

Springer Series in
CLUSTER PHYSICS

Springer-Verlag Berlin Heidelberg GmbH

Physics and Astronomy  **ONLINE LIBRARY**

<http://www.springer.de/phys/>

Springer Series in
CLUSTER PHYSICS

Series Editors:

A. W. Castleman, Jr. R. S. Berry H. Haberland J. Jortner T. Kondow

The intent of the Springer Series in Cluster Physics is to provide systematic information on developments in this rapidly expanding field of physics. In comprehensive books prepared by leading scholars, the current state-of-the-art in theory and experiment in cluster physics is presented.

Mesoscopic Materials and Clusters

Their Physical and Chemical Properties

Editors: T. Arai, K. Mihama, K. Yamamoto and S. Sugano

Cluster Beam Synthesis of Nanostructured Materials

By P. Milani and S. Iannotta

Theory of Atomic and Molecular Clusters

With a Glimpse at Experiments

Editor: J. Jellinek

Dynamics of Clusters and Thin Films on Crystal Surfaces

By G. Rosenfeld

Metal Clusters at Surfaces

Structure, Quantum Properties, Physical Chemistry

Editor: K.-H. Meiwes-Broer

Karl-Heinz Meiwes-Broer

Metal Clusters at Surfaces

Structure, Quantum Properties,
Physical Chemistry

With 275 Figures and 4 Colour Plates



Springer

Professor Dr. Karl-Heinz Meiwes-Broer
Universität Rostock
Fachbereich Physik
Universitätsplatz 3
18051 Rostock
Germany

Series Editors:

Professor A. W. Castleman, Jr.
(*Editor-in-Chief*)
Department of Chemistry
The Pennsylvania State University
152 Davey Laboratory
University Park, PA 16802, USA

Professor Dr. Joshua Jortner
School of Chemistry, Tel Aviv University
Raymond and Beverly Sackler
Faculty of Sciences
Ramat Aviv, Tel Aviv 69978, Israel

Professor R. Stephen Berry
Department of Chemistry
The University of Chicago
5735 South Ellis Avenue
Chicago, IL 60637, USA

Dr. Tamotsu Kondow
Toyota Technological Institute
Cluster Research Laboratory
East Tokyo Laboratory
Genesis Research Institute Inc.
Futamata 717-86
Ichikawa, Chiba 272-0001, Japan

Professor Dr. Hellmut Haberland
Albert-Ludwigs-Universität Freiburg
Fakultät für Physik
Hermann-Herder-Strasse 3
79104 Freiburg, Germany

ISSN 1437-0395

ISBN 978-3-642-63064-4 ISBN 978-3-642-57169-5 (eBook)

DOI 10.1007/978-3-642-57169-5

Library of Congress Cataloging-in-Publication Data

Meiwes-Broer, Karl-Heinz. Metal clusters at surfaces: structure, quantum properties, physical chemistry / Karl-Heinz Meiwes-Broer. p.cm. – (Cluster physics) Includes bibliographical references and index. ISBN 3-540-66562-5 (alk. paper) 1. Metal crystals. 2. Atomic clusters. 3. Surfaces (Physics) I. Title. II. Series. QC173.4.M48 M45 2000 530.4'17-dc21 99-056372

This work is subject to copyright. All rights are reserved, whether the whole or part of the material is concerned, specifically the rights of translation, reprinting, reuse of illustrations, recitation, broadcasting, reproduction on microfilm or in any other way, and storage in data banks. Duplication of this publication or parts thereof is permitted only under the provisions of the German Copyright Law of September 9, 1965, in its current version, and permission for use must always be obtained from Springer-Verlag. Violations are liable for prosecution under the German Copyright Law.

© Springer-Verlag Berlin Heidelberg 2000

Originally published by Springer-Verlag Berlin Heidelberg New York in 2000

Softcover reprint of the hardcover 1st edition 2000

The use of general descriptive names, registered names, trademarks, etc. in this publication does not imply, even in the absence of a specific statement, that such names are exempt from the relevant protective laws and regulations and therefore free for general use.

Typesetting by the author using a Springer T_EX macro package

Production: ProEdit, Heidelberg

Cover concept: eStudio Calamar Steinen

Cover production: *design & production* GmbH, Heidelberg

Printed on acid-free paper

SPIN: 10746488

57/314450 - 5 4 3 2 1 0

Preface

The enormous progress in the miniaturisation of electronic and mechanical devices means that we have now reached a stage in which it is necessary to investigate the underlying physical mechanisms. Similar to semiconductor dots, metal nanostructures also exhibit quantum effects, but now over even smaller physical dimensions. A metallic constriction to about 1 nm induces an energy level splitting in the hundred meV range, values high enough to persist even at room temperature.

Experiments and calculations have shown that isolated metal clusters possess many interesting features, quite different from those known from surface and solid-state physics or from atomic and molecular physics. The technological exploitation of these new properties, e.g., in miniature electronic or mechanical components, requires the cluster to be brought into an environment such as an encapsulating matrix or onto a surface. Due to the interaction with the contact medium, some properties of the clusters may change or even disappear. Thus the physics of the cluster-on-surface systems – the main subject of this book – is of fundamental importance.

The book addresses both beginners in this field as well as the experts. Starting from fundamental concepts of cluster physics and adsorbate–surface interactions, it deals with the modification of electronic properties through quantum size effects, magnetism, physical chemistry and the application of clusters in nanofabrication.

Due to the interdisciplinary nature of the field, the emphasis is initially placed on the electron confinement and magnetic properties of free clusters (Chap. 1). The electron confinement in clusters induces novel properties. The second basic discipline involved is surface physics. When a cluster is brought into contact with a surface, both the cluster and, locally, the surface will be changed. Here, we have to rely on knowledge from surface science studies where the interaction with adsorbates is of special interest. Fundamentals of adsorbate–surface interactions are treated in Chap. 2.

For the production of metal cluster deposits, conventional lithographic techniques fail since many of the interesting properties emerge from very small systems with diameters below 5 nm. Thus new methods had to be developed; these include aggregation by atom diffusion and self-organisation on surfaces (Chap. 3) and the deposition of preformed clusters from beams (Chap. 4). By varying the parameters substrate temperature, deposition energy and flux,

and cluster size, a vast variety of distinct surface modifications have been demonstrated.

The reduced dimensionality of these cluster–surface systems leads to a new electronic structure which can be investigated for small deposited clusters by photoelectron and scanning tunnelling spectroscopy; see Chap. 5. A pronounced peak structure in the conductivity reveals the energy quantisation in small metal clusters, even when in contact with surfaces. In Chap. 6, these results are supplemented by conductance measurements in metallic point contacts, where it is shown that the conductance is due to a well-defined set of quantum modes. Similar to the situation in metal clusters, quantum forces give rise to an electronic and geometrical shell structure.

The electron confinement also determines the spin statistics and thus the magnetic properties. In particular high atomic magnetic moments of ferromagnetic clusters have been demonstrated in beams (Chap. 1). The magnetism of single-domain magnetic particles can be analysed with the SQUID technique, as described in Chap. 7. There, the quantum tunnelling in the magnetisation reversal is demonstrated.

The distinct cluster energy-level structure is governed by the laws of quantum mechanics and, in turn, determines the chemical reactivity. Thus, like the elements in a periodic table, clusters can exhibit pronounced periodicities in their chemical properties as function of size. These properties are also seen with deposited clusters (Chap. 8).

Finally, as an example of the wealth of potential technological application, Chap. 9 reviews a method which uses clusters as tools for the fabrication of silicon nanopillars.

This book is the first in its field and necessarily covers only a selection of the many topics connected with the physics of metallic clusters and dots. It is the interdisciplinary nature which makes this area so interesting, both in terms of fundamental science and from the applications viewpoint. For many of the effects and problems described here, our understanding is still at an early stage; hence, a lively future can be predicted for research into clusters at surfaces.

It is my pleasure to thank all authors who carefully introduced their topics while simultaneously succeeding in giving an overview of the current state of the art. I am indebted to Dr. Josef Tiggesbäumker who was a great help in editing the final manuscript. Furthermore, I like to thank the members of our cluster group who gave technical assistance, in particular Brigitte Schädel, Hans Hermann, Tilo Döppner, Silvio Teuber, Dr. Andreas Bettac. I also thank Springer-Verlag for undertaking thorough language editing.

Contents

1 Confinement and Size Effects in Free Metal Clusters	1
Walt A. de Heer	
1.1 Introduction	1
1.2 Free Simple Metal Clusters	6
1.2.1 The Shell Model	6
1.2.2 Extended Theoretical Models	10
1.2.3 Liquid and Solid Clusters	11
1.2.4 Molecular Beam Methods for Cluster Research	12
1.2.5 Electronic and Geometrical Structure	14
1.2.6 Optical Excitations and Plasma Resonances	20
1.3 Magnetic Particles in Molecular Beams	24
1.3.1 Stern–Gerlach Deflections of Ferromagnetic Metal Clusters . . .	26
1.3.2 Magnetic Moments of 3d Transition Metal Clusters	28
1.3.3 Other Ferromagnetic Cluster Systems	31
1.4 Conclusion	33
2 Fundamentals of Adsorbate-Surface Interactions	37
Heinz Hövel, Lars S. O. Johansson, Bruno Reihl	
2.1 Introduction	37
2.2 Physisorption of Xenon on Graphite: Superstructure and Domain Boundaries	38
2.3 Chemisorption of Alkali Atoms on Semiconductor Surfaces	41
2.3.1 Ionic vs. Covalent Bonding and Charge-Transfer Monitoring . .	41
2.3.2 Li, Na, K and Cs on Cleaved Si(111)	43
2.3.3 Li, Na, K and Rb on Si(100)	46
2.4 Bonding of C ₆₀ Molecules on Ag and Au(110) Surfaces	52
2.4.1 Geometric Properties	53
2.4.2 Electronic Properties	54
2.5 Electronic Response within the Cluster–Surface Interaction	58
2.6 Summary	62
3 Growth of Metal Clusters at Surfaces	67
Harald Brune	
3.1 Introduction	67
3.2 The Elementary Processes of MBE Growth	68

3.3 Nucleation	71
3.4 Aggregation	75
3.5 Coarsening	84
3.6 Anisotropic Surfaces	86
3.7 Growth of Cluster Arrays	90
3.8 Single Crystal Oxide Surfaces	95
3.9 Conclusion	99
4 Collision of Clusters with Surfaces	107
Wolfgang Harbich	
4.1 Introduction	107
4.2 Cluster–Surface Collisions: General Remarks	108
4.3 Experimental Considerations	114
4.4 Molecular Dynamics Calculations	116
4.5 Softlanding	116
4.6 Fragmentation	122
4.6.1 Clusters Scattering off the Surface	123
4.6.2 Fragmentation Studies on Molecules and Clusters	125
4.7 Implantation	128
4.8 Sputtering	131
4.9 Thin Film Formation by Energetic Cluster Impact	132
4.10 Cluster Impact Chemistry	134
4.11 Crater Formation and Cluster Impact Induced Erosion	135
4.12 Electronic Processes	136
4.13 Summary and Outlook	140
5 Electronic Level Structure of Metal Clusters at Surfaces ..	151
Karl–Heinz Meiwes-Broer	
5.1 Introduction	151
5.2 Photoelectron Spectroscopy of Deposited Clusters	153
5.3 Scanning Tunnelling Spectroscopy and Inverse Photoemission	158
5.3.1 Target Preparation and Experimental Methods	160
5.3.2 STS on Platinum, Silver and Sodium Clusters	163
5.3.3 Photon Maps of Silver Islands	168
5.4 Summary	170
6 Conductance Quantisation in Metallic Point Contacts	175
Jan M. van Ruitenbeek	
6.1 Introduction	175
6.2 Landauer Theory for Ballistic Conductance	176
6.3 Experimental Techniques	178
6.4 Conductance of Atomic-Scale Contacts	179
6.5 Histograms of Conductance Values	183
6.6 The Character of the Conductance Modes Through a Single Atom ..	187
6.6.1 Subgap Structure in Superconducting Contacts	187

6.6.2 Valence-Orbital-Based Description of the Conductance Modes .	191
6.6.3 Further Experimental Techniques	194
6.6.4 Implications for Conductance Curves and Histograms	200
6.7 Chains of Atoms	201
6.8 Quantum Forces and Shell Structure in Alkali Nanowires	203
6.9 Discussion and Outlook	205
7 Magnetism of Nanometer-Sized Particles and Clusters	211
Wolfgang Wernsdorfer	
7.1 Introduction	211
7.2 Single Particle Measurement Techniques	213
7.2.1 Micro-SQUID Magnetometry	214
7.3 Mechanisms of Magnetisation Reversal in Single Domain Particles at Zero Kelvin	215
7.3.1 Magnetisation Reversal by Uniform Rotation	215
7.3.2 Generalisation of the Stoner–Wohlfarth Model	218
7.3.3 Experimental Verification	218
7.4 Influence of Temperature on Magnetisation Reversal	221
7.4.1 Superparamagnetism – Néel–Brown Model	221
7.4.2 Experimental Methods	222
7.4.3 Experimental Evidence for the Néel–Brown Model	224
7.5 Magnetisation Reversal by Quantum Tunnelling	225
7.5.1 Molecular Clusters	226
7.5.2 Individual Single-Domain Nanoparticles	228
7.5.3 Single-Domain Nanoparticles and Wires at Low Temperatures	231
8 Physical Chemistry of Supported Clusters	237
Ueli Heiz and Wolf-Dieter Schneider	
8.1 Introduction	237
8.2 Supported Size-Distributed Model Catalysts	243
8.2.1 Preparation and Characterisation	243
8.2.2 CO Dissociation on Supported Rh Clusters	244
8.2.3 Kinetic Effects in the CO Oxidation Reaction on Supported Pd Particles	245
8.2.4 Catalytic Activity of Supported Au Clusters	247
8.3 Supported Monodispersed Model Catalysts	249
8.3.1 Preparation and Characterisation of Monodispersed Supported Clusters	249
8.3.2 Size-Dependent CO Dissociation on Small Ni Clusters	252
8.3.3 The Catalytic Role of Small Silver Clusters for the Latent Image Generation in Photography	254
8.3.4 The Hydrogenation of Toluene on Monodispersed Ir ₄ and Ir ₆ Supported on Oxide Surfaces	255
8.3.5 Size-Dependent Cyclotrimerisation of Acetylene on Monodispersed Palladium Clusters Supported on MgO	258

8.3.6 The Oxidation of CO on Monodispersed Platinum Clusters Supported on MgO	261
8.3.7 The Oxidation of CO on Monodispersed Gold Clusters Supported on MgO	266
8.4 Conclusions and Outlook	268
9 Application of Clusters to the Fabrication of Silicon Nanostructures	275
Katrin Seeger and Richard E. Palmer	
9.1 Prospects for the Application of Clusters	275
9.1.1 Clusters as Building Blocks	275
9.1.2 Clusters as Tools	278
9.2 Silicon Nanostructures	278
9.2.1 Motivation	278
9.2.2 Experimental Approaches	280
9.3 Production of Cluster Films for Fabrication	283
9.3.1 Cluster Growth on Surfaces	283
9.3.2 Deposition of Size-Selected Clusters	285
9.3.3 Organised Arrays of Clusters	287
9.4 Application of Metal Clusters as Plasma Etching Masks	289
9.4.1 Fabrication of Silicon Pillars and Cones using Cluster Films Grown on the Surface	289
9.4.2 Production of Silicon Pillars Using Cluster Beam Deposition ..	292
9.4.3 Ordered Arrays of Silicon Pillars	296
9.5 Summary	298
Index	303

Contributors

Walt A. de Heer

Georgia Institut of Technologie
School of Physics
Atlanta, GA 30332
USA
deheer@electra.physics.gatech.edu

Jan M. Ruitenbeek

Kamerlingh Onnes Laboratorium
Universiteit Leiden
PObox 9504
2300 RA Leiden
The Netherlands
ruitenbe@phys.LeidenUniv.nl

**Heinz Hövel, Lars S.O. Johansson,
Bruno Reihl**

Universität Dortmund
Experimentelle Physik I
Otto-Hahn-Strasse 4
44227 Dortmund
Germany
hoevel@physik.uni-dortmund.de

Wolfgang Wernsdorfer

CNRS
Lab. Louis Néel
BP 166, 25 Avenue des Matyrs
38042 Grenoble Cedex 9
France
wernsdor@labs.polycnrs-gre.fr

Harald Brune

Institut de Physique Expérimentale
Ecole Polytechnique Federale de Lausanne
PHB-ECUBLENS
1015 Lausanne
Switzerland
harald.brune@ipe.dp.epfl.ch

Ueli Heiz, Wolf-Dieter Schneider

Institut de Physique de la Matière Con-
densée
Université de Lausanne
1015 Lausanne
Switzerland
Ulrich.Heiz@ipmc.unil.ch
Wolf-Dieter.Schneider@ipmc.unil.ch

Wolfgang Harbich

Institute de Physique Expérimentale
Ecole Polytechnique Federale de Lausanne
PHB-ECUBLENS
1015 Lausanne
Switzerland
wolfgang.harbich@epfl.ch

Katrin Seeger, Richard E. Palmer

Nanoscale Physics Research Laboratory
School of Physics and Astronomy
The University of Birmingham
Edgbaston
Birmingham B 15 2TT
U.K.
R.E.Palmer@bham.ac.uk

Karl-Heinz Meiwes-Broer

Universität Rostock
FB Physik
Universitätsplatz 3
18051 Rostock
Germany
meiwes@physik.uni-rostock.de

1 Confinement and Size Effects in Free Metal Clusters

Walt A. de Heer

1.1 Introduction

Small metallic particles or metal clusters have been intensively studied during the past two decades (for reviews and broad treatments, see [1–8] and also the proceedings of the biannual ISSPIC conferences), while interest in small particles dates back for centuries. Even the artisans of the middle ages were aware of the colours produced by introducing metals into their stained glasses. For example elaborate recipes were known to introduce gold into glass and then to ripen the systems to obtain the desired colour.

Faraday spent a year of his extremely productive scientific career studying small colloidal gold particles. His ultimate aim was to gain insight into the properties of the hypothetical ether: the medium in which light waves were supposed to undulate. He argued that once particle sizes are small enough (and he was able to estimate sub-microscopic sizes rather accurately), then the effects of the ether would be manifested in optical properties. Although he never succeeded in his ultimate goal, in the course of his investigations he nevertheless found effects that are related to reduced dimensionality: the red colour of colloidal gold and the colours of thin films due to surface plasmons. The electrostatics of the phenomena remained unexplained until after the theoretical analyses of Rayleigh and Mie[9], which continue to be seminal discussions on the subject of small metallic particles.

During the 1970s, work on the optical properties of small metal particles had progressed significantly in particular through the work of Kreibitz [10] and others who systematically studied the optical properties of these particles in various supporting matrices.

In the free electron picture, the Drude dielectric function [11] (Fig. 1.1) can be used to determine the resonance frequency ω_r for a spherical metallic particle with N electrons and radius R that is much smaller than the wavelength:

$$\omega_r = Ne^2/mR^3 \quad (1.1)$$

where m is the electronic mass [3,12]. However the Drude dielectric function only applies for simple metals. For the noble metals there is an important contribution from the d electrons [13,14].

The colours of the very small noble metal particles were an issue of interest early in the game, in particular the question as to whether resonances shifted

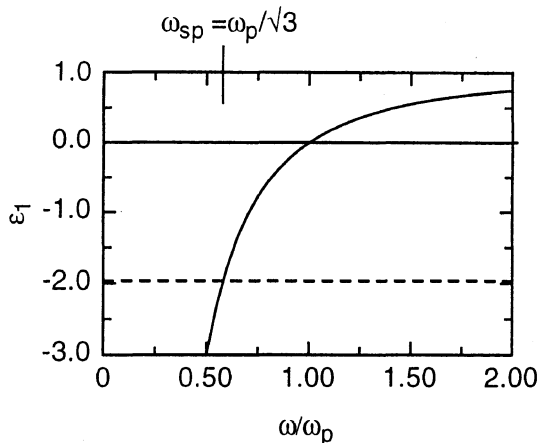


Fig. 1.1. The dielectric function $\epsilon(\omega)$ for a free electron gas. A small spherical particle with this dielectric function will exhibit a sharp resonance for $\epsilon = -2$, which occurs at $\omega_p/\sqrt{3}$. Several simple metal particle systems approximately exhibit these plasma resonances

towards red or blue with decreasing size [13]. Experimentally determined absorption spectra for very small gold particles[14] are shown in Fig. 1.2. According to Mie's theories, if the particle size is much smaller than the wavelength of the excitation, then a maximum in the absorption cross section $\sigma(\omega)$ should occur at the surface plasma resonance which is related to the dielectric function by

$$\sigma(\omega) = C(R)\omega\epsilon_2/[(\epsilon_1 + 2)^2 + \epsilon_2^2], \quad (1.2)$$

where ϵ_1 and ϵ_2 are the real and imaginary parts of the dielectric function of the material and $C(R)$ is a constant which does not depend on ω [13,15]. Hence for $\epsilon_1 = -2$, there is a peak in the absorption.

The Drude model [13] predicts that

$$\begin{aligned} \epsilon_1 &= 1 - \omega_p^2/(\omega^2 + \Gamma^2), \\ \epsilon_2 &= \omega_p^2\Gamma/(\omega^3 + \omega\Gamma^2), \end{aligned} \quad (1.3)$$

where $\omega_p^2 = \pi n e^2/m$; Γ is the damping rate, and n and m are the electronic density and mass. Hence, from equations (1.2) and (1.3) the absorption of small particles can be calculated. For example, for Au, $\omega_p = 8.89$ eV (see e.g. [14]). The Drude analysis suggests that for small particles there should be no size dependence on the shape of the absorption cross sections apart from an overall factor.

For reasonably large simple metal particles the bulk dielectric function can be used, but this approximation will eventually break down for small sizes due to electronic confinement effects [12,15] that cause discreteness of the electronic energy level spectrum (which in turn produces discrete structure in the dielectric function), and due to the increasing importance of the surface (which for example causes damping of the electronic oscillations with

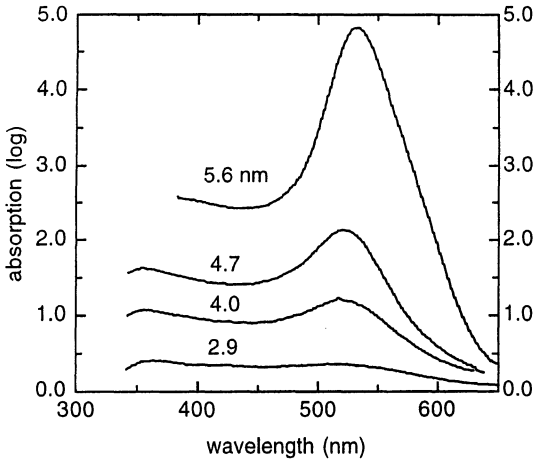


Fig. 1.2. Several examples of measured optical absorption spectra of small gold particles imbedded in a noble gas matrix showing evidence of a single large absorption peak which is identified as the plasma resonance. (Adapted from [13])

a characteristic time of the order of $v_F/(2R)$ where v_F is the Fermi velocity [13,16]). Damping is caused by a coupling of the collective electronic motion to single particle excitations due to the boundaries (wall dissipation)[17,18] and is related to Landau damping in the extended solid [19].

Experimentally, the bulk dielectric function describes the optical properties of gold colloidal particles down to about 10 nm, but for even smaller particles important deviations are observed. This indicates a breakdown of the bulk dielectric description for these sizes as demonstrated in recent experiments for extremely small passivated particles (Fig. 1.3) [14].

Besides optical work, in the earlier investigations there was considerable interest in other electronic properties. In particular, experimental efforts to study the electron spin and nuclear spin resonance produced various results. The purpose of these investigations was to study finite size effects, which were considered to be effects caused by the small number of electrons in the systems [20].

The search for size effects related to electronic confinement (quantum size effects) has been a primary motivating factor in metal cluster research and these effects should be especially significant for particles with diameters that are of the same order of magnitude as the Fermi wavelength so that the shape of the cluster will be reflected in the electronic structure.

One interesting feature of small metallic particles is that the electronic structure is discrete compared with the (quasi) continuous bands of the bulk material. In particular, if one assumes that the electronic levels are non-degenerate (except for spin degeneracies) and equally spaced, then the energy gap between adjacent levels is approximately equal to the Fermi energy divided by the total number of conduction electrons, as discussed in more detail below. The discrete nature of the energy level spectrum will manifest itself in physical properties in particular when the temperature T is low enough, i.e. $kT < \Delta E$. For a simple metal system like sodium, with $E_F = 3.2$ eV and

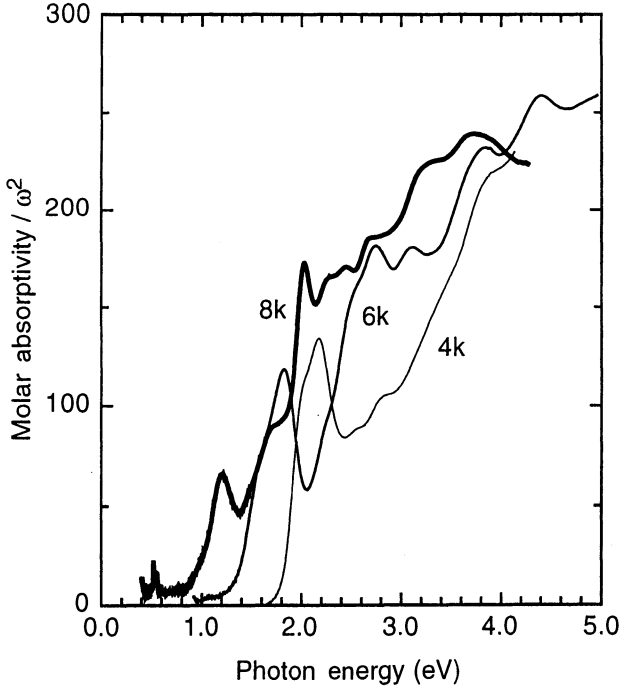


Fig. 1.3. Examples of measured absorption spectra of suspended gold clusters with well defined sizes which have been passivated with a surfactant. The cluster sizes are labelled according to their masses in kilo daltons. The absorption cross sections have been weighted with ω_p^2 . Note the size dependence of shapes of the absorption profiles which reflect the size dependence of the dielectric function. Adapted from the PhD dissertations of T.G. Schaff (Georgia Institute of Technology, Atlanta 1999) and J.T. Koury (University of California at Los Angeles, 1999)

$T = 300$ K, this criterion predicts confinement effects for $N < 250$, assuming a uniform energy level spacing.

One way to probe this effect is through the magnetic susceptibility χ in particular for odd valence systems (alkalis, noble metals). In those cases, there will be one unpaired spin in the highest occupied level, and hence the system is paramagnetic (with a magnetic moment $1 \mu_B$), while if N is even, then the system will be diamagnetic. In the former case the magnetic susceptibility will diverge at low temperatures (i.e. $\chi = K/T$) while in the latter case it will tend towards 0.

In order to test these ideas, various growing and embedding methods were applied to clusters whose size distributions could be controlled to some extent. The earlier results were mildly encouraging. There was evidence for the predicted size effects, but often the interpretation remained ambiguous.

Much of the ambiguity stemmed from two circumstances: one was that the size distributions were quite broad, and the second was that in the most

interesting size range, the metal clusters have more surface than volume [13]. For example, the fraction of surface atoms in a spherical particle with N atoms is approximately $3N^{-1/3}$. Hence not only are small clusters highly sensitive to surface contamination but their properties can be significantly modified by stresses due to the embedding matrices. Towards the end of the 1970s, it became clear that accurate probing of size effects in metal clusters required perfect size selectivity and a matrix free environment. These conditions are met in molecular beams using mass spectrometric methods to detect the clusters.

The most obvious property of small simple metal systems is that the conduction electrons are confined. From elementary quantum mechanical considerations, this confinement implies that the electronic energy level spectrum is discrete in contrast to the continuous spectrum of the infinite bulk. The average spacing between energy levels at the Fermi level for a box shaped simple metal particle with N conduction electrons is [11]

$$\Delta E = (2/3)E_F/N . \quad (1.4)$$

The Fermi energy is the width of the conduction band, which for a simple metal is [11]

$$E_F = \hbar^2(3\pi^2n)^{1/3}/2m , \quad (1.5)$$

where n is the density of states: $n = 1/\Delta E$.

Equation (1.4) is rather powerless if nothing further can be said about the distribution of the energy levels. Several theoretical approaches have been applied before experimental evidence was available. The quantum chemical approach attempts to reconstruct the electronic energy level spectrum by precise calculations of the structure (geometrical and electronic) of these systems. The most sophisticated of these involves full consideration of all the participating atoms with all of their electrons and their mutual interactions[21]. This task is so formidable that only the very smallest clusters can actually be calculated using fully ab initio methods. Hence approximations are always used. (Note that many calculations which are labelled as ab-initio quantum chemical approaches nevertheless still use approximations, and sometimes rather important ones.) Early results along these lines treated metal clusters much like molecules: in fact the resulting electronic spectra of the clusters appeared to have little to do with the parent bulk material.

At the other extreme from these sophisticated approaches were attempts to characterise the electronic structure of clusters where the interactions were treated statistically using methods derived from nuclear physics. These led to predictions of features of the energy level spectrum which could be extended to large particles. An important early application of the statistical approach was to predict magnetic susceptibilities of these systems [20]. Clearly a system with an odd number of electrons will be paramagnetic. If the energy levels are random (which implies that the system has no symmetry) than the ground

states of even electron systems will be diamagnetic. Measurements of the electronic spin susceptibility (ESR, NMR) should register these behaviours at low temperature [22].

1.2 Free Simple Metal Clusters

After molecular beam probes for the electronic structure of small clusters were constructed (see below), it soon became clear that the quantum confinement effects were in fact quite different from those originally assumed. The first evidence came from measurements of the mass spectra of alkali cluster beams, which were performed using a supersonic nozzle beam in conjunction with a quadrupole mass analyser. The mass spectra (Figs. 1.4, 1.5) were found to reflect a remarkable pattern of cluster intensity variations, where clusters with $N = 8, 20, 40, \dots$ were significantly enhanced compared with their neighbours with one more atom [1,3,23]. These are known as the magic numbers, according to the nomenclature used analogous abundance peaks in nuclei. The spectra were correctly interpreted in terms of the stability of the clusters: the larger the cluster binding energy the greater its abundance in the molecular beam [23]. The experimental mass spectra were clearly correlated to the electronic energy level structure of a rather simple confining potential.

1.2.1 The Shell Model

Small simple metal clusters behave in many respects as small metallic droplets. That is to say that to lowest order, the electronic structure resembles that due to a smooth spherical confining potential. Such a potential supports electronic angular momentum and consequently, as in an atom or a nucleus, the electronic structure consists of shells of electrons where all the electrons in a given shell (in the independent electron picture) have the same radial quantum numbers (n) and angular momentum quantum numbers (l) but the shell can contain $2(2l + 1)$ electrons. When the electrons in a cluster exactly fill an energy level (n, l) it is called a closed shell cluster. Reports and reviews can be found in [1,3,21,25] and references therein.

Cluster nomenclature follows that of nuclei, due to the strong similarity between these systems (as far as the fermions are concerned)[25]. Hence for a given angular momentum quantum number l , the lowest energy state is given the radial quantum number $n = 1$, etc. The energy level spectrum for a spherical well then depends on the shape of the well but only in the ordering of the levels as demonstrated in Fig. 1.6. This may be understood by recognising that high l states probe mainly the outer regions of the potential (due to centrifugal effects) while the low angular momentum states are more sensitive to the interior. For example a potential bump in the middle of the cluster will increase the energies of the low l states while leaving the high l states relatively undisturbed.

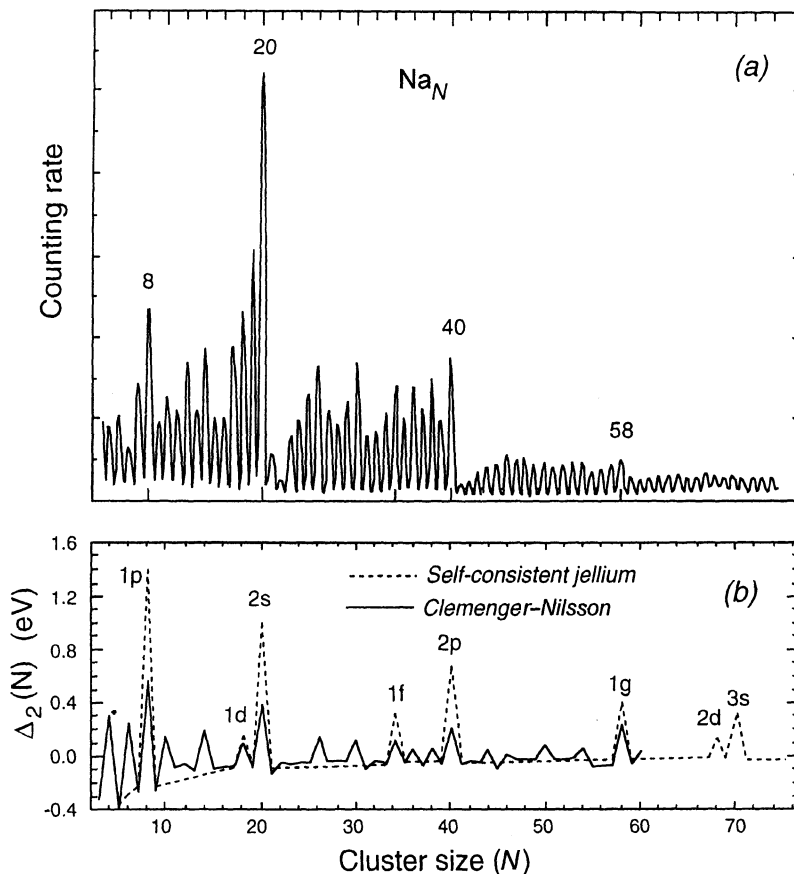


Fig. 1.4. Mass spectrum of sodium clusters and theoretical analysis. The clusters were produced in a helium-seeded high temperature cluster source, ionised with broad band UV light and detected using a quadrupole mass analyser. (a) The intense peaks (compared with neighbours) indicate enhanced stability. Major peaks occur at 8, 18, 20, 40, 58, and several minor peaks are observed as well. (b) The experimental mass spectrum is compared with calculations of the second differences in total electronic energies in the jellium model. The correspondence is clear. Even better correspondence is obtained if spheroidal distortions are taken into account as in the Clemenger–Nilsson calculations which reproduce much of the fine structure. (Adapted from [3])

Note also that sensitivity to the details of the potential is greatest for higher energy electrons. This is due to the fact that the electronic wavelengths are smaller for those energy levels, so that the higher energy electrons can probe smaller details of the potentials.

In any case, the spherical shell model immediately gives a qualitative explanation for the occurrence of abundance maxima. These occur at electronic shell closing numbers which means that it is relatively more costly (by

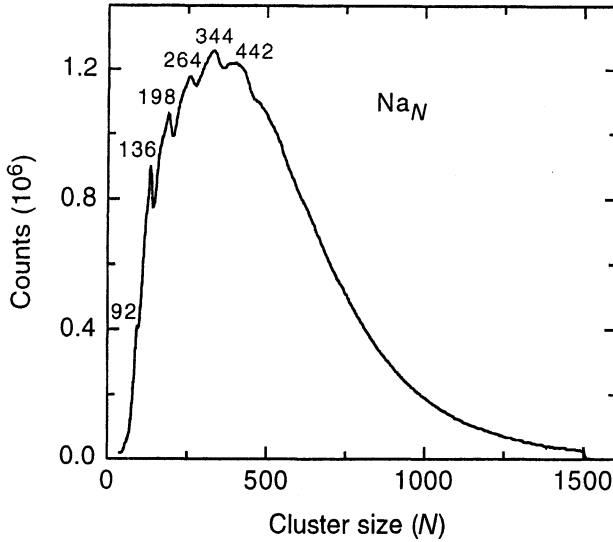


Fig. 1.5. Sodium mass spectrum extending to Na_{1500} . The peaks correspond to spherical shell closing numbers. The abundance maxima become weaker with increasing particle size due to the reduction in the energy gaps with increasing size. Adapted from [24]

an amount given by the energy gap) to add one more atom to a closed shell cluster than to an open shell cluster.

The spherical shell model adequately describes the gross structure in the cluster mass spectra, however it glosses over details; see for example the fine structure in Fig. 1.4. In fact due to crudeness of the approximation (an 8 atom cluster is hardly a sphere), one might assume that the next level would involve the inclusion of the actual ionic core potentials. These introduce undulations in the potential well which may be the source of fine structure in the mass spectra. Perhaps, more profoundly, the independent electron model itself may break down due to correlation effects.

However, it turns out that much of the fine structure in simple metal clusters is well described by allowing the cluster to respond to electronic pressure effects. These give rise to spontaneous distortion from spherical symmetry [26]. This mechanism is essentially the Jahn–Teller effect which was studied in detail for nuclei by Nilsson [27,28]. The physical principle is that for open shell clusters (which are electronically degenerate in their spherical conformation), the total energy can be lowered by distorting the cluster and thereby lifting the degeneracy.

The effect is most simply demonstrated by constraining the volume of the cluster and allowing it to distort along one axis to produce a spheroid.

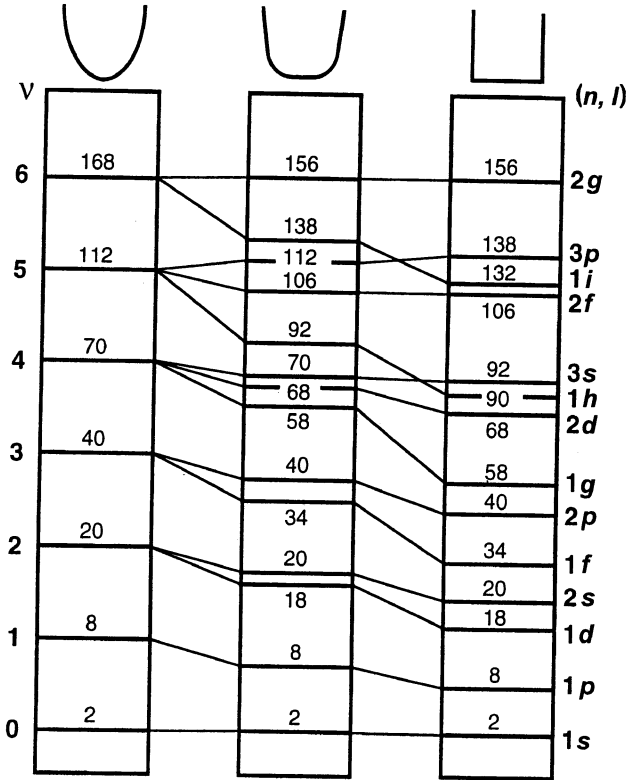


Fig. 1.6. Examples of the electronic energy levels in various spherical potential wells. The simplest case is the isotropic harmonic well where the energy levels are equally spaced and each level has a degeneracy of $\nu(\nu + 1)$. The rounded square well lifts the degeneracies for different angular momentum values l . The splittings get even larger for the square well, although the spherical symmetry preserves the angular momenta of the states. Adapted from [3]

Following Nilsson, the independent electron Hamiltonian can be written with an angular momentum dependent term to accommodate the distortion [26]:

$$H = p^2/2m + m\omega_0^2 q^2/2 - U\hbar\omega_0[l^2 - n(n+3)/6], \quad (1.6)$$

where p and q are the momentum and position operators, l is the angular momentum, and n is the shell number; U is an anharmonic term, without which the effective potential is a harmonic oscillator.

This model goes a long way to describe several of the fine structure features as demonstrated in Fig. 1.4b.

Allowing distortions along all three axes to produce ellipsoidal clusters is only slightly more complex, but feasible and follows methods derived from nuclear physics. In its simplest form the electronic structure of an ellipsoidal simple metal cluster is found from a model where the confining potential is assumed to be an anisotropic harmonic oscillator (i.e., by setting $U=0$ in

(1.6)) [3]. The potential is modelled to conserve the cluster volume and since it is harmonic, the energy level spectrum can be trivially determined analytically for a given choice of axes and number of electrons. The minimum ground state energy configuration can then be determined (as well as excited state energy configurations). Thus predictions for the electronic energy dependent part of the total energy can be made, and from this, features in the abundance spectra can be rationalised. For development of a shell-correction method pertaining to shape deformations of clusters, see Ref. [29–31].

1.2.2 Extended Theoretical Models

The success of the simple shell model and the fact that electronic shell effects exist at all, indicates that the ionic cores do little more than provide a relatively featureless confining well for the electrons. While the simple shell theoretical methods outlined above go some way towards rationalising features in simple metal mass spectra, they tremendously oversimplify the real systems. The electrons are treated independently in an ad-hoc potential. The theoretical situation is much improved by treating the electrons self-consistently in a uniform positively charged sphere. This constitutes the spherical jellium model [1,5,32,33]. The spherical jellium approximation is the starting point for electronic structure calculations which are usually performed using density functional methods (i.e., the local density approximation (LDA) and its extensions).

The spherical jellium model for simple metal clusters was rapidly embraced, primarily due to its simplicity and predictions for very large clusters, even though it is clearly a gross simplification of real systems. Nevertheless, it provides a framework and a reasonable starting point to calculate the electronic properties of small particles. Moreover, the method allows electronic response properties to be calculated using time dependent LDA methods and the random phase approximation (RPA) [34,33].

Methods to calculate the electronic structure of metal clusters have evolved greatly during the past two decades, primarily due to the rapid development of computers and improved computational approaches. Noteworthy are methods which combine high level ab-initio electronic calculations (for example, those where all electrons including those of the atomic cores are treated) with molecular dynamics (MD), like the Car-Parinello method that efficiently combines molecular dynamics with LDA (see [35–39]). Through molecular dynamics, clusters can be annealed from high temperatures to low temperatures, to more or less ensure that ground state structures can be identified. Moreover, the method also allows finite temperature effects to be determined (i.e., melting transitions, vibrational spectra). Molecular dynamics is becoming increasingly more powerful due to the steady improvement of density functional methods (for example, by including non-local corrections). Furthermore, improved methods to treat electronic excitations (i.e., RPA) further enhance the computations.

Density functional methods are still not perfect but at the moment they appear to be the most promising, especially for large metal cluster systems which remain too complex for traditional quantum chemical approaches.

Shell structure is readily understood in terms of the electronic degeneracies in a spherical potential. The origin of the shell structure in this potential is clear since every level with angular momentum l has a degeneracy of $2(2l + 1)$. However, the phenomenon is much more general and bunching of electronic levels (i.e., near and accidental degeneracy) are common. Furthermore, semi-classical methods have proved to be a very powerful tool.

For example, the semi-classical approach explains level bunching in a spherical square well as follows. Energy levels are filled successively with electronic angular momenta from 0 to p_F where p_F is the Fermi momentum with associated Fermi wavelength λ_F . In the spirit of semi-classical orbit theory, only those classical orbits can exist which close on themselves and whose path consists of an integral number of wavelengths. The simplest classical closed paths are lines through the centre, triangles and squares. The circumference of a square which inscribes a circle of radius R is $L_S = 4\sqrt{2}R$, while that of an inscribed triangle is $L_t = 3\sqrt{3}R$. These two orbits (and to a lesser degree the pentagons) are the most important ones to consider. The other orbits rapidly lose coherence around an orbit.

The density of states at the Fermi level will be strongly enhanced for those R where L_S and L_t are both simultaneously integral multiples of λ_F . Hence, the density of states at the Fermi level will oscillate with increasing R with different periods for squares and triangle, so that a beat pattern will occur in the magnitude of the shell effect. This super-shell beating effect has in fact been observed with a period that indeed corresponds to the interference between square and triangular classical orbits [24,40].

The above argument can be extended to other confining potentials. In general it is found that the electronic structure is quasi-periodic in R . For example if the intensities of a mass spectrum are plotted as a function of $N^{1/3}$ (which is proportional to R) then the oscillations are clearly observed, as shown in Fig. 1.7. [24,40].

1.2.3 Liquid and Solid Clusters

The thermodynamic phases of free clusters are difficult to ascertain experimentally, but much information has been obtained from mass spectra. It is known that the melting point of a small particle is reduced from the bulk, essentially due to surface effects [41,42]. Liquid clusters tend to be spherical or spheroidal and the sequence of magic numbers reflects that fact. However, when the clusters become solid, they develop facets and attain specific crystallographic shapes (polyhedra). The facets of solid clusters will affect the magic numbers which may differ from the spherical shell closing numbers [42] and thereby provide evidence for the solid and liquid state.

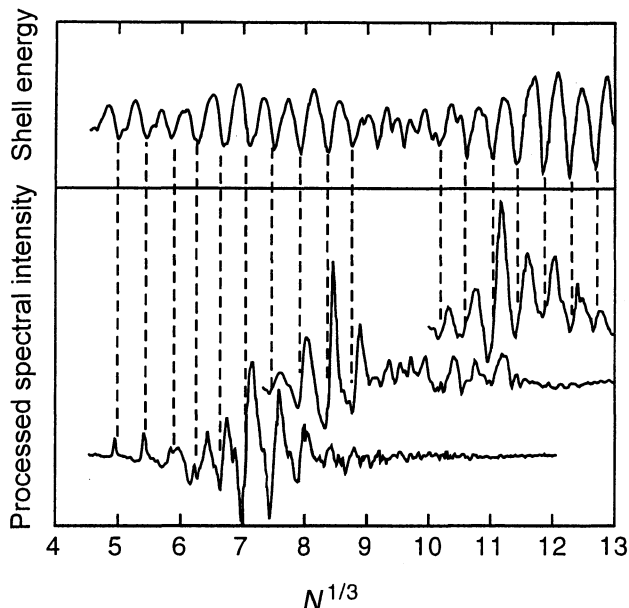


Fig. 1.7. Supershell structure in gallium clusters. Very weak structure in mass spectra like those shown in Fig. 1.5 are revealed by the logarithmic derivative of the intensities of several mass spectra using different source conditions. The data are presented as a function of $N^{1/3}$ and reveal a series of peaks that match those expected for the shell energies in supershell theory. The supershell structure, which can be regarded as a beating effect between triangular and square classical orbits, is clear from the absence of structure at $8.5 < N^{1/3} < 10$. This analysis also shows that electronic shell effects are important at least up to $N = 2200$. After [40].

Direct evidence for melting has been obtained using molecular beam mass spectroscopy [42] and calorimetry [43], where the evaporation rates of a cluster which absorbs a photon are measured and related to the temperature increases. These measurements confirm the lowered melting points of alkali clusters and also demonstrate that certain clusters have anomalous melting points.

1.2.4 Molecular Beam Methods for Cluster Research

Some comprehension of molecular beam methods is useful in order to appreciate the relevance of the results and the limitations of the methods. A typical cluster beam apparatus consists of a cluster source, a drift region and a mass spectrometer. The system is in a vacuum chamber, or more usually consists of several sequential chambers to facilitate differential pumping.

Cluster sources: Various cluster source designs are typically employed, of which the most common ones are described here. Further descriptions can be found in [3,6]. The high temperature nozzle source consists of a reservoir

and a nozzle. The material under investigation is vaporised in the reservoir and the pure vapour is expanded into a high vacuum through a heated pinhole nozzle. Metal vapour pressure from tens of millibars to hundreds of millibars are typically employed. Due to the high pressure differentials at the nozzle, the metal atoms do not effuse out of the nozzle but rather experience an adiabatic expansion which causes the vapour temperature to drop significantly whereby the vapour condenses into clusters. The clustering process is greatly enhanced by utilising an inert carrier gas (with pressures up to several bar), since the adiabatic expansion of the carrier out of the nozzle causes the beam to cool to very low temperatures. These supersonic seeded nozzle beam sources typically produce clusters in the size range from single atoms to several thousands of atoms per cluster. The peak of the distribution can be varied by adjusting the source temperature, the nozzle temperature and the carrier gas pressure. The seeded cluster beams are very intense (typically using about 0.1 mol of material per hour) and continuous.

Alternatively, cluster beams can be produced in the gas aggregation cluster source where the vapour from a heated reservoir of metal is injected into a cold carrier gas, whereby the vapour supersaturates and clusters are formed. The cluster/carrier gas are then ejected out of a nozzle into the drift tube. These cluster sources are less bright and produce larger clusters than the nozzle sources. Typical sizes range from $100 < N < 10^6$. The size distributions can be adjusted by varying the source parameters (vapour pressure, gas pressure, dimensions of the source, etc.). One advantage of the gas aggregation source is that the cluster temperature corresponds more closely to that of the carrier gas compared with laser vaporisation sources.

The third important category of cluster sources is the pulsed laser vaporisation cluster source. In these sources the material under investigation is locally vaporised with an intense pulse of focused light from a laser. The hot metal plasma is quenched in inert gas (which is usually introduced into the source using a pulsed valve), after which the mixture expands out of a nozzle. During the cooling of the gas, clusters are formed. The ultimate temperature of the clusters may be adjusted to equal the nozzle temperature, although this requires a properly designed nozzle which provides sufficient cluster/carrier gas interaction to cause equilibration. At the same time the supersonic expansion must be suppressed to inhibit adiabatic cooling effects. Another advantage of the laser vaporisation cluster source is that clusters can be produced in their ionic forms. Both cationic as well as anionic clusters are produced, indispensable for many experiments.

Related cluster sources depend on vapours produced in electric arc discharges (i.e., the PACIS source [44]) and are somewhat similar to laser vaporisation sources.

Clusters and cluster ions are also produced in sputtering processes of high energy ions with metallic surfaces. These sources produce continuous beams of hot clusters.

Cluster detectors: Mass sensitive detection is an essential feature in cluster science, since it is precisely this information which facilitates the determination of the size dependence of physical properties. The two main categories of detector are the quadrupole mass filter and the time-of-flight mass spectrometer [3,6].

In the Quadrupole Mass Analyser (QMA), cluster ions are created in an ion volume by ionising neutral clusters by various means. Either electron impact ionisation, or more usually photoionisation, is used in this step. The ions are then accurately focused to a point on the axis of four parallel symmetrically positioned rods (typically about 15 cm long, about 5 mm in diameter 1 cm apart). By applying appropriate time dependent potentials on the rods, only those ions with corresponding charge to mass ratios (q/m) will pass through the filter.

Mass selection in the QMA relies on the dynamic stability of ions in a quadrupolar electric field which has both DC and AC components. As was first discovered by Paul, the ion trajectories may be stable or unstable in the direction perpendicular to the quadrupole axis. The equations of motion and stability of the trajectories are described by an analysis of Matthew's equation, which shows that for a given AC amplitude and the DC amplitude ions within a corresponding range $\Delta(q/m)$ will have stable trajectories. By properly tuning the potentials, this range can be made very small, thus ensuring good mass selectivity.

A major advantage of the QMA is that it can detect particles of chosen q/m continuously, which is particularly convenient if a specific cluster is under investigation. The major disadvantage of the QMA is that the potentials required increase linearly with particle mass which limits the mass range to typically below 10.000 amu.

The time of flight mass spectrometer (TOF) is often the best mass spectrometer. Its operation is relatively straightforward. Clusters are introduced in the ionisation volume and then ionised, typically with a pulse of ionising radiation. The ions are accelerated by a series of electric fields and then detected. The arrival time is carefully measured and the mass (or more correctly, the mass to charge ratio) is determined. TOF's are capable of extremely high mass resolutions (> 10.000). Their mass range, which is bounded primarily by the detection efficiency of large particles ($\approx 10^7$ amu). Their main disadvantage is their rather low duty cycle.

1.2.5 Electronic and Geometrical Structure

Mass spectra and the limits of electronic shell structure: Electronic shell effects are observed in all simple metal cluster systems up to very large cluster sizes [45]. In fact, mass spectra with up to about $N = 2200$ still reveal the characteristic pattern of shell closings (see Fig. 1.7). However, for larger sizes, electronic shell structure gives way to order related to the successive completion of atomic layers or geometrical shell structure. Figure 2 in Chap.8

shows evidence for icosahedral shell closings from $N = 1980$ to $N = 21300$ [45]. The observed magic numbers in this range correspond closely to those expected for the Mackay icosahedra with from 10 to 19 layers of atoms: a Mackay icosahedron with K shells has

$$N = (10K^3 - 15K^2 + 11K - 3)/3 \quad (1.7)$$

atoms [46]. Thus the observations indicate that when the system becomes large enough, variations in the binding energies due to electronic effects become small compared to geometrical effects which drive the clusters towards well defined crystalline structures. Incidentally, the Mackay icosahedra do not correspond to crystals with bcc structure which is the bulk crystal structure of sodium, so that for even larger clusters a phase transition to the bulk structure can be expected.

The mass spectra provide evidence for patterns and regularities in metal cluster systems. In fact there are two important reasons for structure in the mass spectra: a large mass peak may indicate a dominant presence of the corresponding neutral particle or, alternatively, it may signify an enhanced ionisation probability. The first property relates to the relative stability of the cluster (since weakly bound systems are less likely to be produced in the source), while the second property relates to the ionisation potential. Both effects are observed and frequently have opposite influence: often a strongly bound cluster has a higher ionisation potential, so that even though it may be abundantly produced, it appears only weakly in the mass spectrum when the photon energy is near threshold [42]. This is why magic numbers appear as peaks in the mass spectra in Figs. 1.4 and 1.5 and as dips in the mass spectra in Fig. 2 of Chap. 8.

While mass spectra are powerful indicators, they are usually not considered as definitive proof for structure. However, in many cases reproducible patterns in mass spectra have stimulated detailed interpretations of electronic and geometric structure of small particles.

Photoionisation spectroscopy: Mass spectra only provide a first glimpse of the electronic and geometric structure of cluster systems. Far more powerful methods exist which directly address the electronic system. Photoionisation spectra measure ion yields as a function of the photoionising light energy, whereby the photoionisation threshold or ionisation potential (IP) can be determined.

A plot of the photoionisation threshold as a function of cluster size (see Fig. 1.8) typically reveals that the photoionisation energy decreases as a function of cluster size, roughly proportional to the inverse of the classical cluster radius $R_N = N^{1/3}R_1$, converging to the bulk work function W (Fig. 1.9). The $1/R$ dependence is a classical term which is related to capacitance of a classical metal particle. Hence, to lowest order,

$$\text{IP}_N = W + e^2/2R_N, \quad (1.8)$$

where e is the electronic charge.

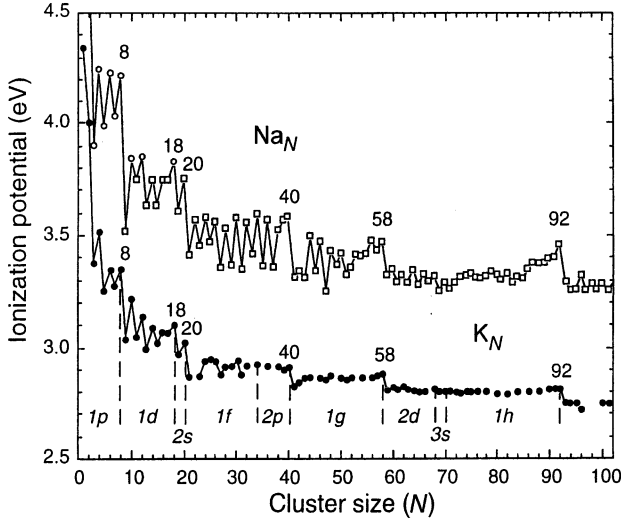


Fig. 1.8. Ionisation potentials of Na and K clusters. The IPs show typical shell structure features: high IPs for closed shell clusters $N = 8, 20, 40, 58, 92$, after which the IP drops dramatically. Note the similarities with the mass abundance spectrum. The structure for K clusters is less pronounced than for Na clusters due to the lower Fermi energy of K compared to Na, since the Fermi energy fixes overall energy scaling. The spherical shell structure indices (n,s) are shown. Furthermore, analysis [5] of the above data showed that finite-temperature electronic entropy effects are largely responsible for the absence of fine-structure between major shell closures in the IPs of K_N with $N > 20$. Adapted from [3]

Two important corrections are required to obtain better correspondence with the measured values. One is the electronic shell correction Δ_N , which may be seen as a correction to the work function (or Fermi level), that causes closed shell systems to have relatively larger IPs. The other is a correction to the classical radius due to the kinetic energy of the confined electrons, that causes the electrons to spill out beyond the classical radius (called the electronic spillout δ). The spillout is also a property of bulk surfaces where the electronic density does not abruptly terminate at the surface but in fact decays approximately exponentially. Hence

$$IP_N = W + \Delta_N + e^2/2(R_N + \delta) . \quad (1.9)$$

This behaviour is observed in many simple metal clusters.

Photoelectron spectroscopy: The development of anion photoelectron spectroscopy has been particularly important in obtaining deep insights into the electronic structure of clusters (for review, see [47]). The method involves a source of negatively charged clusters (a pulsed laser vaporisation cluster source for example). The clusters are mass selected, typically with a TOF, whereafter they are de-ionised using a UV laser. The kinetic energy of the emitted photoelectron is measured using time-of-flight methods. The electron

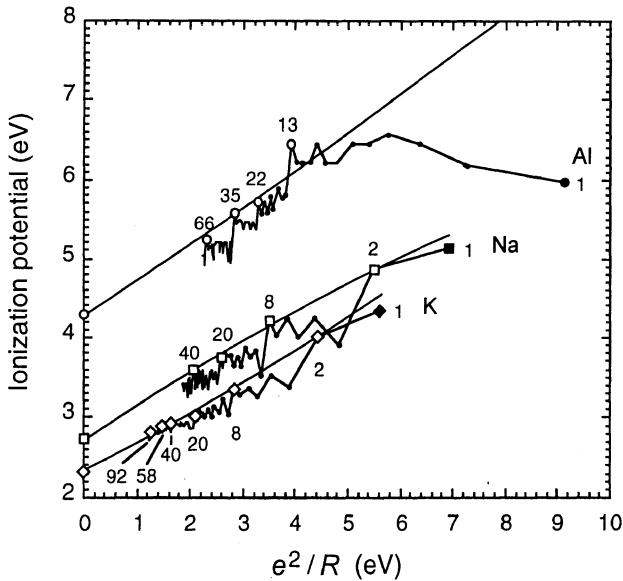


Fig. 1.9. Ionisation potentials of simple metal clusters as a function of e^2/R . The open symbols reflect results for closed-shell or near closed-shell systems. The approximately linear trends can be seen as reflecting the classical part of the IP which relates to the charging of a capacitor with a capacitance of $1/R$ as for a classical sphere. The large deviation in the case of Al clusters can be attributed to incomplete s-p hybridisation for very small clusters. Adapted from [3]

binding energy is defined as the difference between the UV photon energy and the electron kinetic energy. It is clearly closely related to the electronic binding energies obtained from photoionisation spectroscopy and hence the interpretations are similar. However, the method gives information on the binding energies of all the electrons which can be ionised with the light used in the experiment.

Within a level of approximation similar to that above, the binding energy of the n_{th} electron in a simple metal cluster with N atoms is given by

$$BE_{N_n} = W + \Delta_{N_n} - e^2/2(R_N + \delta) \quad (1.10)$$

so that the relative peak positions in the photoelectron spectra reflect the position of the electronic energy levels (in the independent electron picture). These can be compared with shell model predictions (see [3], for example).

The size dependence of the electron affinity is given to the same level of approximation as (1.8) by

$$EA_N = W - e^2/2R_N, \quad (1.11)$$

which implies that the size dependence of the electron affinity and the ionisation potentials are complementary. This feature is indeed (approximately)

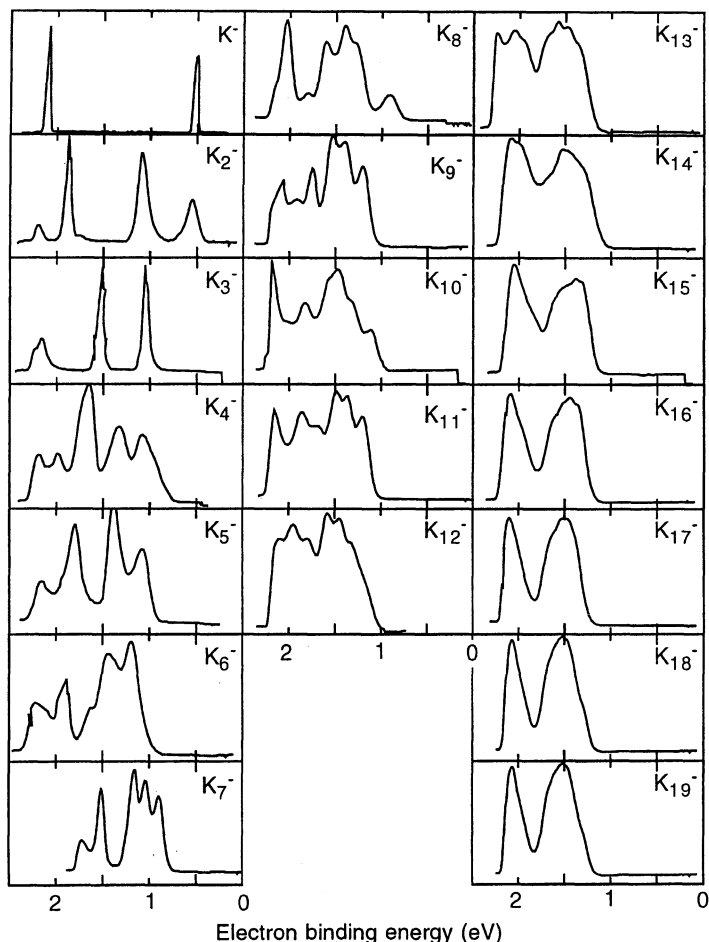


Fig. 1.10. Photoelectron spectra of potassium anions. These spectra have been obtained by illuminating mass-selected anions with laser light and recording the energy of emitted electrons. Note the shell structure. For example K_7^- clearly shows the $1s$ peak (at $E_B=1.5$ eV) and the $1p$ peak (at $E_B \approx 1$ eV). The latter is split into three components due to crystal field effects. K_{19}^- shows two broad peaks, one due to the $1p$ states and the other from the $1d$ states. (The subsequent $2s$ states at $E_B \approx 1.25$ eV are not resolved.) Adapted from [48]

observed [3,49]. However, the anion spectroscopy is more sensitive to quantum mechanical effects like exchange interactions. When including those, a quite far going correspondence between the measured affinity energies and results of local density calculations are found[49].

The photoelectron spectra of rather long series of metal clusters are now available. Those of the alkali metal cluster systems have been particularly important and have provided deeper insight into the electronic structure of

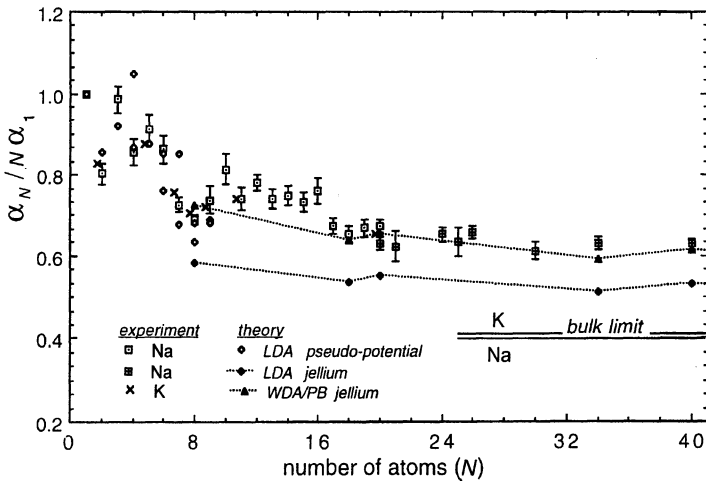


Fig. 1.11. Per atom polarisabilities of Na and K clusters, normalised to their respective atomic polarisabilities. The bulk limits are also shown. The two Na data sets refer to slightly different source conditions, which has a small effect (vs. Na_{20}). The decrease with increasing size is related to the electronic spillout that causes small clusters to have relatively larger polarisabilities. Three theoretical data sets are also shown. Adapted from [3]

these clusters. They have clearly demonstrated the electronic shell structure within specific clusters as shown in Fig. 1.10, where the p levels and d levels can be distinguished. Note also that these anion photoelectron spectra clearly show that the alkali magic numbers are related to the number of valence electrons rather than the number of atoms, so that for example, K_7^- and K_{19}^- represent closed shell clusters [48].

Not only simple metal clusters but also the noble metal clusters show evidence for electronic shell structure. However, the photoelectron spectra of those systems also indicate the important effect of the d bands.

Cluster polarisabilities: The static polarisability of clusters can be determined by measuring their deflections in a molecular beam due to a strong inhomogeneous electric field. The electric field \mathbf{E} causes the cluster to acquire an induced electric dipole moment $\mathbf{P} = \alpha_N \mathbf{E}$ where α_N is the polarisability, and the field gradient supplies a force to the dipole. Examples for Na and K clusters are shown in Fig. 1.11. These measurements reveal that the static polarisabilities are closely related to those of a classical metal sphere:

$$\alpha_N = R_N^3. \quad (1.12)$$

However, as in the case of the IP's, the radius must be adjusted to account for spillout effects, so that

$$\alpha_N = (R_N + \delta)^3. \quad (1.13)$$

Besides this correction, since open shell clusters are not spherical, there is a classical ellipsoidal correction due to this which enhances the polarisabilities. Hence the polarisabilities of simple metal clusters are approximately equivalent to those of classical metal ellipsoids with slightly enhanced radii.

1.2.6 Optical Excitations and Plasma Resonances

The coloration of metal-particle containing glasses was the first cluster property to be identified and investigated. Although the electrodynamics of sub-micron metallic particles was understood in principle for a century [9], extrapolations to very small sizes remained problematic. For example, it was known that the colours are caused by collective electromagnetic resonances (or plasma resonances) of the valence electrons. The resonances shift towards the blue as the size of gold particles in host matrices is decreased, but the origin of the shift was not well understood [13].

Experiments on unsupported clusters in the molecular beam have shed much light on the problem. The method of longitudinal beam depletion spectroscopy was developed in order to detect the optical properties of small alkali clusters [12]. In this method an alkali cluster beam is illuminated with light from a pulsed laser which is directed at the cluster beam. If a cluster absorbs a photon and if this energy is redistributed among the vibrational degrees of freedom, then the cluster temperature will increase significantly: in fact the temperature rise will be of the order of

$$\Delta T = h\nu / (3Nk) , \quad (1.14)$$

where $h\nu$ is the photon energy, and k is Boltzmann's constant. The temperature rise of a cluster may be many hundreds of degrees after absorption of an optical photon for $N < 100$. This temperature increase is often more than enough to cause the cluster to evaporate one or more atoms. In the evaporation process, the cluster fragments are kinetically deflected from the collimated beam. The relative fraction of the clusters that are removed is measured and converted to an absorption cross-section. With further knowledge of the laser fluence, the absolute absorption cross-sections can be determined as a function of cluster size and photon energy.

Alkali cluster photoabsorption cross-section spectra typically have one or more rather broad peaks. The position of the peaks, their relative intensities and the integrated intensities all provide important information on the optical absorption process which is closely related to the plasmons (or Mie resonances) in larger particles.

For example, for a spherical simple metal particle (such as a closed shell cluster), the plasma resonance should consist of a single peak. Its position is given approximately by

$$\omega^2 = e^2 N / m\alpha , \quad (1.15)$$

where α is the static polarisability [3]. If the cluster is non-spherical (this occurs when it has a partially filled electronic shell), then in general there will be either two or three peaks, depending on how many inequivalent axes there are in the cluster [26]. Collective electronic oscillation frequencies depend on the direction of the oscillation in the cluster (like water sloshing in a glass). The resonance shifts toward lower frequencies along the long axes and towards higher frequencies along the short axes. For a classical metal ellipsoid, the intensities of each of the three peaks are equal and according to the dipole sum rule [50], the integral of the intensities is

$$\int \sigma(\omega) d\omega = 2\pi^2 N e^2 / mc, \quad (1.16)$$

where N is the total number of electrons and m the electronic mass.

These properties are reasonably well obeyed for several simple metal cluster systems. In particular, the multi-peaked structures appear to follow the trends dictated by the ellipsoidal shell model (Fig. 1.12). The integrated intensities do indeed approximately exhaust the dipole sum rule, which indicates that the entire optical dipole response is concentrated in these plasma resonances [5]. Furthermore, the closed shell cationic clusters ($N a_N^+$, $N=9,21,41,59,93$) [51] all appear to have a single peak which exhausts the sum rule, thus confirming that they have quasi-spherical shapes (Fig. 1.13). For analysis of the different plasmon profiles for $N a_{20}$ and $N a_{21}^+$, see Ref.[52]

This is an interesting observation, since it is reasonable to expect that these very small cluster systems should behave more like molecules with forests of optical excitations corresponding to a multitude of possible optical excitations. In fact, when the depletion spectra are measured for very cold clusters, the rather smooth broad peaks (or bands) do indeed break up into several resolved peaks, which indicates that these plasma resonances are really envelopes of lines (each of which may have single electron excitation characteristics).

Nevertheless, the collective dipole description of the resonance remains valid, since one may consider that the single particle excitations derive their dipole strength by coupling to the plasmon so that only those excitations which are near the plasma frequency are excited. Those that are far away are dipole forbidden and therefore too weak to be observed.

The simple metal particle plasmon picture is a lowest order approximation to the optical response. Its failure is clear under close examination for simple metal cluster systems and more dramatic in more complex metals like the noble metals. Even though particles of these metals may have very intense plasmon bands (e.g., Au and Ag), the position of the peaks are strongly affected by the d bands [53,14]. Nevertheless, even in those cases, for larger particles the resonances are reasonably well described by classical electrodynamics using the empirical dielectric function as first demonstrated by Mie. In effect, the dielectric function captures the essentials of the response of a

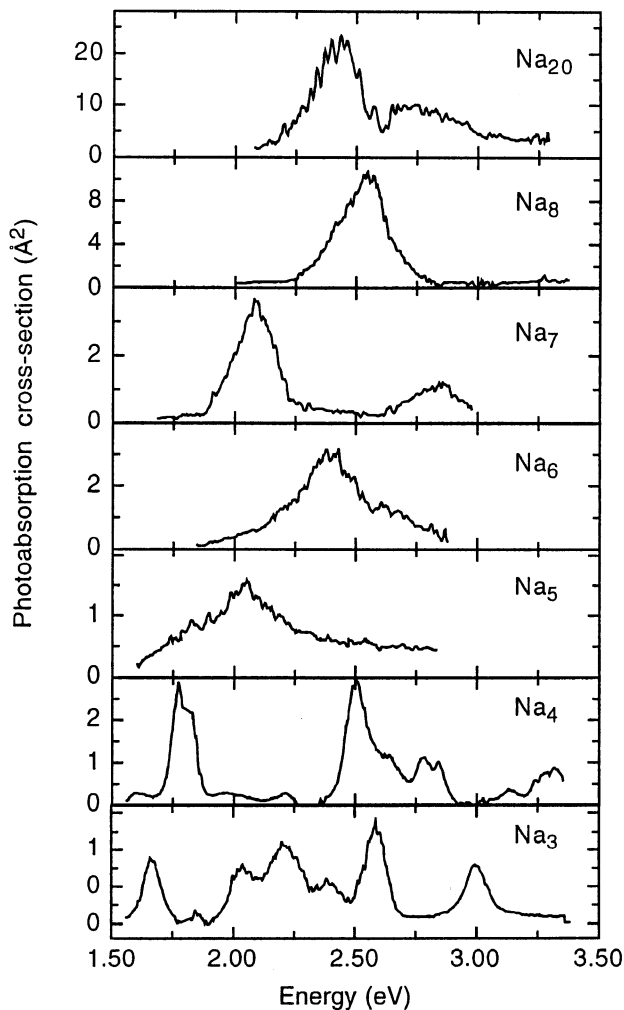


Fig. 1.12. Optical absorption spectra of small Na clusters using the beam depletion method. The position, structure and intensities of the peaks indicates that they are closely related to plasma resonances. Split peaks are usually found for open shell clusters (i.e., Na₇). Adapted from Brechignac and Cahuzac in [5]

material to electromagnetic excitations. The shape of the particle imposes the boundary conditions and hence the response to electromagnetic radiation can then be calculated. This procedure requires the dielectric function to be known and, for larger particles, it is well approximated by its bulk counterpart.

For very small particles, deviations are expected and observed since for them the electronic structure of the particle surface plays an increasingly important role (see [54] for example). One could also say that electronic

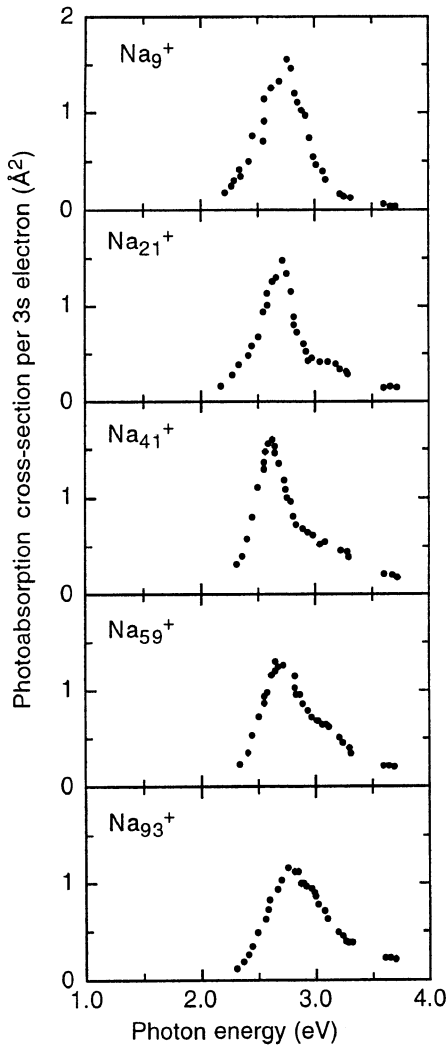


Fig. 1.13. Optical absorption spectra of small closed shell Na_N^+ clusters divided by $(N + 1)$. The peaks closely exhaust the dipole sum rule. Note that the peaks shift to the blue with increasing size, an effect closely related to the decrease in polarisability. (Adapted from [51])

confinement affects electronic structure and thereby modifies the dielectric function. For alkali clusters the most conspicuous modification is the red shift with decreasing N , which is ascribed to the electronic spillout effect, and splittings (fragmentation) of the plasma band partly due to shape effects as described above. Resonances between single particle excitations and plasmons also lead to this spectral fragmentation.

The response of metal clusters to light (i.e., the dynamic polarisability) has been extensively theoretically studied at several levels: from simple jellium-based calculations on spherical systems to the response of particles calculated in high level molecular dynamics algorithms.

1.3 Magnetic Particles in Molecular Beams

If the simple metallic clusters previously discussed are at one extreme of complexity, the transition metal clusters, and in particular those which exhibit ferromagnetic behaviour, are at the opposite extreme. Clusters of these materials do not satisfy any of the criteria which could classify them as simple metal systems, due to the strong exchange and correlation effects which cause their spin systems to order magnetically. (For in-depth general treatments on magnetism, see for example [11,55,56]; a brief introduction to magnetism follows.) The third row transition metals with more than half filled 3d band (i.e., Mn, Cr, Fe, Co and Ni) fall into this category. The latter three of these elements produce ferromagnetic solids. Moreover these are itinerant ferromagnets since the ferromagnetic properties are due to alignment of the valance electron spins in contrast to localised magnetic systems (i.e., the rare earth magnets).

Magnetic order in these metals derives from a competition between kinetic and Coulomb terms in the total energy, in much the same way that atoms with partially filled electronic shells attain magnetic moments (c.f. Hund's rules) [19,55]. In particular when two 3d electrons are near an atomic core at the same time, their Coulomb interaction term is minimised by maximising the inter-electron distance. This is accomplished by mutually aligning the spins and thereby ensuring minimal overlap of the electronic wave functions due to the Pauli exclusion principle.

In contrast, the (independent) electronic states in an otherwise featureless confining potential (i.e., a rectangular box) are spin doublets. Hence if they are occupied with non-interacting electrons, the overall spin of the system is 0 for an even electron system and 1/2 for an odd system. This spin order is predicted and observed for simple metal systems. The reduced electronic density favours successive occupation of the electronic states because this minimises kinetic energy, the dominant contribution to the total energy.

In a simplified picture, confinement due to central Coulomb potentials near the cores favours aligned spins (when possible) whereas itineracy favours paired spins. Since the vast majority of metals are non-magnetic the magnetic ordering exchange interaction is only rarely effective in producing large magnetic moments. Nevertheless, there are several important metals which have magnetic order.

Magnetically ordered bulk elemental metals are classified as ferromagnetic or antiferromagnetic (Fig. 1.14) [11,55]. For ferromagnetic metals (in the localised moment picture), the spins of the electrons at neighbouring atomic sites are mutually aligned, whereas in the antiferromagnetic case, they are oppositely aligned. Antiferromagnetic order (as for example in Mn and Cr) should not be confused with non-magnetic order (i.e., Na). In the former the local spin densities at the atomic site are non-zero while they are zero for non-magnetic systems. Furthermore, antiferromagnetic systems have characteristic magnetic susceptibilities which we will not discuss here.

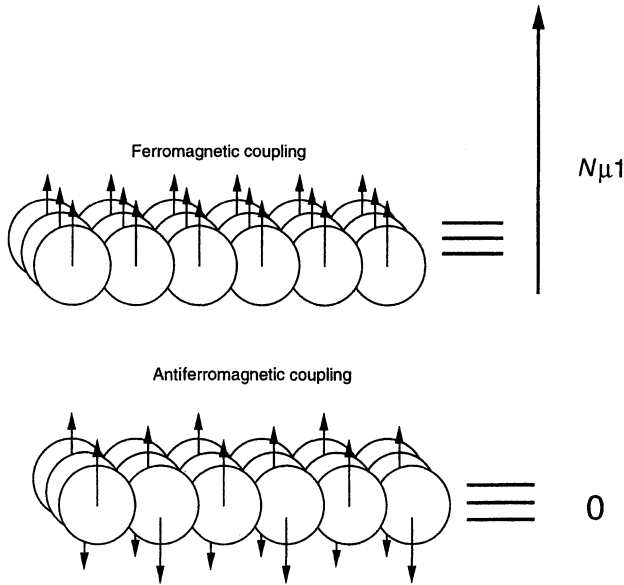


Fig. 1.14. Examples of spin order. In ferromagnetic systems the magnetic moments of neighbouring atoms are mutually aligned at low temperatures. In antiferromagnetic systems they are anti-aligned. In both cases the alignment is due to the exchange interaction. At elevated temperatures thermal vibrations overcome the alignment causing the systems to become paramagnetic. Ferromagnetic systems undergo a second order phase transition to a paramagnetic state at the Curie temperature beyond which the system cannot support a permanent magnetic moment

Less subtle are the ferromagnetic systems due to the obvious effect of macroscopic magnetic moments which give rise to large spontaneous magnetic fields. Regions of mutually aligned magnetic moments are called magnetic domains. The domain size is primarily determined by a competition between the exchange interaction, which aligns the spins, and the magnetic field energy, which prefers minimal spin alignment. The latter is a long-range interaction which ultimately dominates for sufficiently large systems producing a complex structure of domains within each of which all the spins are mutually aligned.

Since the domain sizes are typically of the order of a micron, we may assume that the clusters we are concerned with here are single domain particles so that we can ignore complications due to domain structure. Whereas the following section reviews work on magnetic clusters in a beam, Chap. 7 describes results on larger but still single domain particles investigated with the SQUID technique.

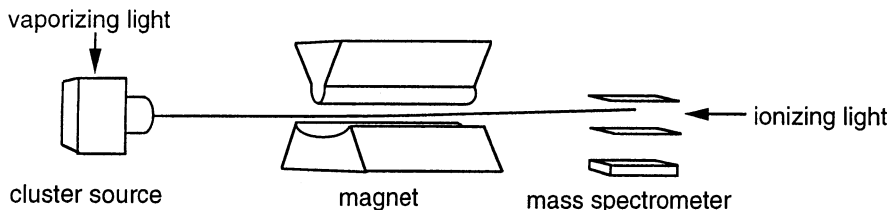


Fig. 1.15. Experimental configuration for magnetic deflection measurements. A collimated cluster beam passes between the pole faces of a Stern–Gerlach magnet that causes the particles to deflect. The deflection is measured as a function of the cluster mass using a time-of-flight mass spectrometer after the clusters are ionised with a pulse of laser light

1.3.1 Stern–Gerlach Deflections of Ferromagnetic Metal Clusters

From the above it is clear that the majority of atoms have non-zero magnetic moments but the majority of bulk metals are non-magnetic. Apparently the process of forming metallic bonds tends to quench the large spin states which are expected from Hund’s rules for atomic systems. This then naturally raises important questions about how the spin systems of clusters evolve as a function of cluster size. For simple metal clusters (for example, the alkalis), it appears that the spin pairing mechanism is immediately effective: even clusters have no spin and odd clusters have spin $1/2$.

Clusters of the $3d$ ferromagnetic transition metals (Fe, Co, Ni) have been measured and they are found to be ferromagnetic [57,58], at least for $N > 8$. Their magnetic properties are probed by deflecting molecular cluster beams in the magnetic field of a Stern–Gerlach magnet (Fig. 1.15). The Stern–Gerlach magnet is essentially an electromagnet with specially contoured pole faces to produce a calibrated magnetic field and magnetic field gradient that is applied to particles in the molecular beam.

The results of these measurements are surprising since it is found that all clusters deflect uniquely in the direction of increasing magnetic field (Fig. 1.16) [57]. This seemingly trivial observation indicates not only that the particles have large magnetic moments (and hence large spins) but also that the spins spontaneously align in the direction of increasing magnetic field, which signifies a spin relaxation mechanism. For example, if spin relaxation did not occur then the clusters would deflect both towards and away from the increasing field direction, as is the case for paramagnetic atoms in the famous Stern–Gerlach experiment. While spin relaxation is well understood for macroscopic systems and causes ferromagnetic objects to be attracted to magnets, we do not expect this for very small systems since the relaxation mechanism requires conservation of energy and angular momentum of the system and this must be provided by the degrees of freedom of the particle. In fact the spins of the silver atoms in atomic beams cannot relax, which explains the result of the original Stern–Gerlach experiment.

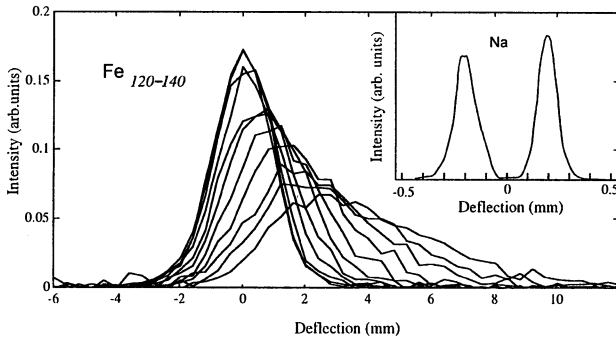


Fig. 1.16. Magnetic deflection profiles of iron clusters with 120–140 atoms per cluster. As the magnetic field strength is increased, the clusters are deflected more. The deflection is uniquely in one direction indicating that spin relaxation occurs. The Stern–Gerlach deflections for Na atoms are also shown in the *inset*. Since these atoms are spin $1/2$ particles with a magnetic moment of $1\mu_B$, the beam splits into two directions due to quantisation of angular momentum. In this case, there is no spin relaxation. Adapted from [57].

The relaxation effect is poorly understood. In particular for clusters in which rotational degrees of freedom have been cooled by a supersonic expansion (which may reduce the rotational temperature to below 10 K), anomalies are observed [58]. However, if care is taken to suppress the supersonic expansion effects and to ensure full equilibration of all the degrees of freedom, then the clusters are emitted from the nozzle under a rather well defined set of initial conditions, for which a unique temperature can be assigned to all degrees of freedom.

In that case, spin relaxation effects appear to operate similarly to the analogous bulk effect: it is as if the spin system were in thermal contact with a heat bath [59]. This heat bath must be provided by the few atoms in the cluster. For a paramagnetic system with angular momentum quantum number J , and a magnetic moment $\mu = Jg_J\mu_B$, the magnetisation M (the projection of the magnetic moment in the direction of the magnetic field B) at temperature T is given by [11]:

$$M = \sum m_J g_J \mu_B \exp(m_J g_J \mu_B B / kT) / \sum \exp(m_J g_J \mu_B B / kT). \quad (1.17)$$

Defining $x = Jg_J\mu_B B / kT = \mu B / kT$, we obtain the Brillouin function [11]

$$M = g_J \mu_B (2J + 1) / 2J \coth\{(2J + 1)x / 2J\} - (1/2J) \coth(x/2J). \quad (1.18)$$

For large J , this reduces to the well known Langevin function [11]

$$M = g_J \mu_B \coth(x) - 1/x. \quad (1.19)$$

The Stern–Gerlach deflection D of a cluster is given by

$$D = K \cdot M \cdot B / mv^2 \quad (1.20)$$

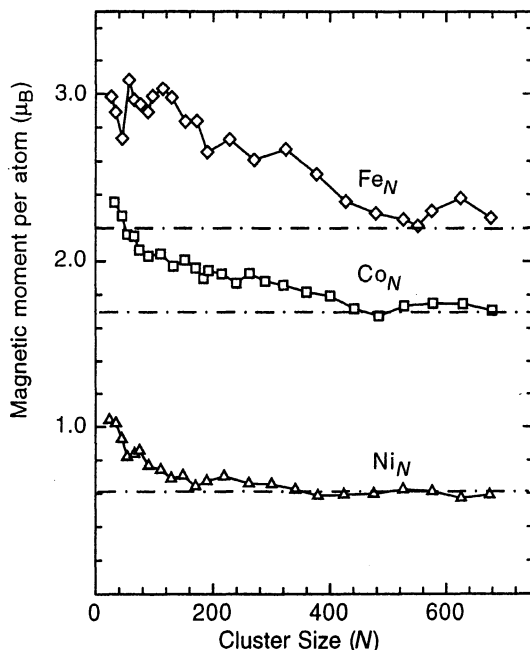


Fig. 1.17. Measured magnetic moments of ferromagnetic 3d clusters. The magnetic moments of the small clusters are close to the maximum values for the spin according to Hund's rules. The magnetic moments decrease quite rapidly towards their respective bulk values. Adapted from [61]

where m is the cluster mass, v its velocity, and K an apparatus dependent constant.

Hence measurements of the mass, velocity, temperature, magnetic field and deflection yield the magnetic moment. Usually the magnetic moment is normalised to the number of atoms in the cluster N .

1.3.2 Magnetic Moments of 3d Transition Metal Clusters

Stern–Gerlach measurements of the 3d transition metal clusters (Fe, Co, Ni) have been made at several temperatures for a large range of cluster sizes [60,61]. An overall decreasing trend of the magnetic moment per atom with increasing cluster size is observed in all three cases, with some oscillating fine structure features (Fig. 1.17).

This decreasing trend can be understood from general arguments, relating to the cluster surface [61]. The magnetic moment of an atom at the surface is generally larger than in the bulk. This is due to the lower coordination of these atoms. Electrons tend to dwell near the atomic cores for relatively longer times before hopping to a neighbouring site, compared with electrons at the higher coordinated interior atoms. Hence the lower coordination causes surface atoms to have more of a free-atom-like character than the interior

atoms. The electrons are more confined near these sites than at interior sites and the arguments which lead to Hund's rules (i.e., large spins) also produce relatively large surface spins.

Note that for small sizes the magnetic moments per atom for Fe, Co and Ni are approximately $3\mu_B$, $2\mu_B$ and $1\mu_B$ respectively. (Co is slightly higher, probably due to orbital effects.) These values correspond to the maximum spin that can be obtained with 7, 8 and 9 electrons in a d orbital. For example a nearly-free iron atom has 8 valence electrons of which 1 is in the 4s orbital and 7 in the 3d orbital. Of those 7, 5 are in spin up states (forming the majority spin band) and 2 in spin down states (the minority spin band). Hence the net magnetic moment per atom due to the 3d orbitals is $3\mu_B$ (the s band is not spin polarised). This is roughly the situation for a surface atom, where the majority spin band is entirely below the Fermi surface. Analogous arguments predict $2\mu_B$ for Co surface atoms and $1\mu_B$ for Ni surface atoms.

Increased coordination of the interior atoms causes broadening of the bands (as a consequence of more frequent hopping) so that the minority band partially rises above the Fermi level (from which some electrons leak into the half empty 4s band), causing a reduction in the spin imbalance. Consequently, the magnetic moments of the interior atoms are reduced compared with surface atoms. In fact for Fe, $\mu_{\text{bulk}} = 2.2\mu_B$; for Co, $\mu_{\text{bulk}} = 1.6\mu_B$; for Ni, $\mu_{\text{bulk}} = 0.7\mu_B$.

This simple picture suggest a model: for a hypothetical spherical particle, the ratio of surface atoms to total atoms is about $3N^{-1/3}$, so that for $N = 1000$, about 30% of the atoms are on the surface. Hence, one can estimate that the size dependence of the magnetic moment is

$$\mu = \mu_{\text{bulk}} + (\mu_{\text{surf}} - \mu_{\text{bulk}})3N^{-1/3}. \quad (1.21)$$

Measurements show that the convergence to the bulk value occurs much more rapidly than predicted and that clusters with as few as 1000 atoms may already have bulk-like magnetic moments. Moreover, the evolution to the bulk is not smooth. This indicates that the picture is far too simplistic, although it has the merit of describing extremes reasonably well.

It is interesting to note that measurement of Cr clusters ($N > 10$) have demonstrated that these clusters do not deflect. This may indicate that they are non-magnetic or antiferromagnetic (as in the bulk).

1.3.2.1 The Temperature Dependence of Magnetic Moments

Loss of ferromagnetic order occurs at the Curie temperature where thermal motion overcomes the order imposed by the interatomic exchange interaction. In itinerant magnetism there are two distinct pictures [55,56]: in the band picture, the magnetic moment reduction is caused by thermally induced electronic excitations (Stoner excitations) which reduce the total moment. In the localised moment picture, the global moment is reduced through local misalignments, although the local moments remain intact. The Curie temperature predicted by the Stoner model (see Chap. 7) is too large, while the

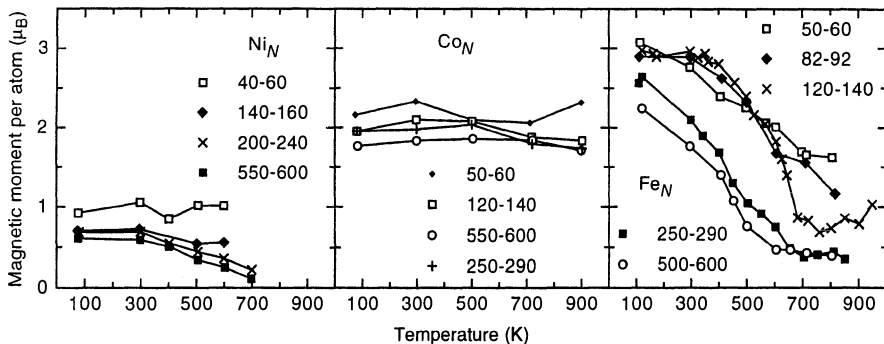


Fig. 1.18. Magnetic moments as a function of cluster temperature for several cluster size ranges. Ni clusters appear to converge to the bulk magnetisation curves with an apparent Curie temperature of about 700 K for larger clusters. Fe clusters are quite anomalous and there is no clear convergence to the bulk magnetisation curve, in fact the apparent Curie temperature of larger clusters is far below the bulk value of 1041 K. Adapted from [61]

local moment picture misrepresents the itinerant nature of the 3d electrons. (It rests on fairly solid ground for rare earth metals where moment-carrying electrons are well localised).

The molecular beam method favours measurements of magnetic moments as a function of temperature over a wide range of temperatures, ranging from 80 K and below to 1000 K and above (Fig. 1.18). In this way the ferromagnetic to paramagnetic phase transition can be probed. Magnetic moments have been measured as a function of temperature for several sizes and it is clear that they decrease with increasing temperature.

Several interesting general observations can be made. Magnetic moments reduce with increasing temperature although they do not vanish at a well defined temperature. This property may be expected since finite systems cannot have sharp phase transitions. It is also observed that for Ni and Co, with increasing size, the magnetisation curves appear to converge to their respective bulk behaviours. However, Fe is anomalous and no obvious trend can be discerned. We suspect that this may be related to the various crystallographic phases of Fe which differ in their magnetic properties. In particular, bulk Fe is bcc. In the bulk this structure is stabilised compared with the fcc structure, due to magnetic interactions. Small clusters usually prefer icosahedral structures (to minimise surface energy). These steric considerations cause further complications in the structure, and consequently in the magnetic properties, as appears to be revealed by the measurements.

At sufficiently low temperatures it is expected that the magnetic moment becomes pinned to a preferred axis in the cluster giving rise to the so-called blocking effect [59,62]. In supported cluster systems this is manifested as an abrupt vanishing of the magnetisation at and below the blocking temperature, since the spin system is no longer able to respond to the applied field.

It is not clear how the effect will manifest in free clusters, since the cluster as a whole can still orient with respect to the applied field. However it is unlikely that the response is still given by the Langevin equation. In fact it has been predicted that below the blocking temperature, the magnetic moment is still given by a Langevin-like equation, although it is uniformly reduced by a factor of $2/3$ [63].

In contrast, low temperature measurements (down to 80 K) do not reveal obvious anomalies although a slight reduction is observed in the Co data. Hence, it seems that the blocking temperatures are lower than 80 K for these cluster systems for all measured sizes, from which upper bounds to the strength of the crystalline anisotropy coupling can be estimated. (Note that shape anisotropies are not expected to be important for these sizes).

1.3.2.2 Magnetism of Ferromagnetic Clusters at Low Rotational Temperatures

Thermal spin relaxation of free ferromagnetic clusters remains problematic because of the apparent violation of angular momentum conservation in the spin reorientation process. For example, if a cluster with spin $S = 100\hbar/2$ (e.g., Fe_{35}) enters the magnet with its spin anti-aligned to the magnetic field and exits it with its spin aligned, then the change in spin angular momentum is $S = 100\hbar$. Consequently, the rotational angular momentum R must have undergone an equal and opposite change. If $R \gg 100\hbar$, the change can be accommodated by a reorientation of R , keeping its magnitude constant; however, if $R < 100\hbar$, then spin relaxation must also involve a change in the rotational state which may be prohibited (since this requires a further change in the total rotational energy). Hence, we may expect that spin relaxation is inhibited for rotationally cold clusters (i.e., $T < 10\text{K}$) (Fig. 1.19).

Clusters are very efficiently rotationally cooled in supersonic expansions since the rotations only involve three degrees of freedom (compared with $3N$ for the vibrations). Evidence for reduced spin relaxation for rotationally cold clusters is found in large deviations from the Langevin function for clusters subjected to source conditions which favoured supersonic expansions [57,58].

Not only is the magnetisation strongly suppressed, we also observe evidence of non-monotonic behaviour in the magnetisation as a function of applied field. An explanation for this effect is given in terms of an intra-cluster resonance which occurs when the cluster rotational frequency is comparable to the Larmor precession frequency of the spin in the magnetic field [58].

Whether this explanation is correct remains to be seen. However, it is clear that several anomalous effects manifest themselves at low temperatures.

1.3.3 Other Ferromagnetic Cluster Systems

The magnetic properties of several rare earth metals have been investigated and in particular those of gadolinium [64,65]. Magnetism in these systems is

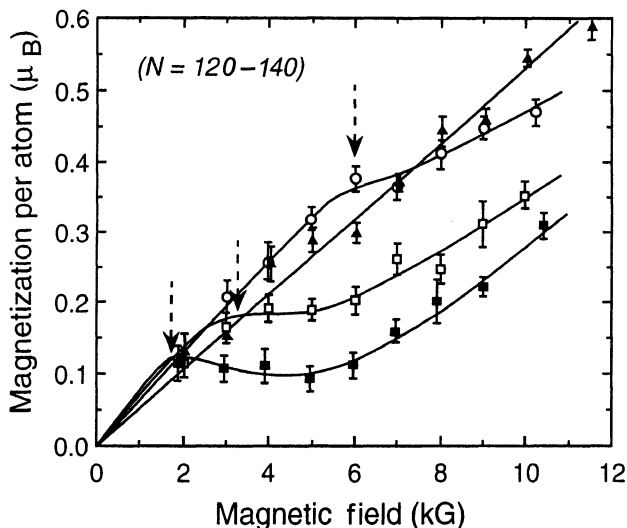


Fig. 1.19. Examples of anomalous magnetisation behaviours. The magnetisation of Fe_N as a function of magnetic field is shown for different expansion conditions. For those conditions which produce rotationally warm clusters (*solid triangles*) a very nearly linear behaviour is observed as may be expected for super paramagnetic particles in the low field limit. For conditions which produce rotationally cold clusters (progressive expansion for \circ , \square and filled \square), important deviations from linear behaviour are observed which cannot be accounted for in a simple relaxation model. The effect is not well understood and may represent a very important property of spin dynamics in free ferromagnetic clusters. Adapted from [58]

caused by partially filled 5f atomic orbitals which are essentially bound to the atomic cores in contrast to the itinerant 3d electrons. Consequently, these systems satisfy the conditions for the localised magnetic moment picture, where ferromagnetic order is induced by an indirect exchange mechanism involving polarisation of conduction electrons (super-exchange). Gadolinium clusters are reported to have magnetic magic numbers, i.e., several Gd clusters with less than 92 atoms are significantly more magnetic than neighbouring clusters [64]. From the localised magnetic moment picture this suggests that the spin alignment of neighbouring spins must be rather sensitive to the cluster structure (assuming that the magnitude of the spin at each atomic site is unaltered). Furthermore, it has also been reported that the clusters deflect not only in the direction of the applied field but also in the opposite direction [64]. The effect was explained in terms of locked moment behaviour and other spin dynamic effects. However, recent measurements failed to reproduce the effect [65].

A new ferromagnetic material has also been found. Magnetic deflections of small rhodium clusters have been observed which indicate that they are ferromagnetic, in contrast to the bulk[66]. Hence ferromagnetism in this sys-

tem is due to small-size effects. The magnetic moment is quite small but this nevertheless indicates that novel nanoscopic magnetic systems may exist.

1.4 Conclusion

The molecular beam provides a unique non-interacting environment to study properties of nanoscopic objects. Quantum confinement effects which give rise to the electronic shell structure are readily identified in molecular cluster beams, but are difficult to detect for small imbedded clusters or clusters deposited on substrates.

This is not because these properties are illusive or subtle; they are not. It is because it is very difficult to produce sufficient quantities of identical supported clusters to produce unambiguous results. Even if all clusters are identical, the substrate may strain the clusters and thereby modify their electronic structure, see Chap. 5.

Now that a rather large body of information has been obtained on the properties of pure clusters, it has become possible to distinguish intrinsic properties from those which are caused by substrate interactions.

The ideal experimental environment provided by the molecular beam will continue to be exploited and pushed in new directions. While most experiments are presently performed on simple systems, much more complex alloy systems can be studied and analysed using the molecular beam production and detection methods described here. For example, molecular beam prospecting methods can be employed to identify novel magnetic alloys, which educe properties from size effects.

References

1. W. A. de Heer, W. D. Knight, M. Y. Chou, and M. L. Cohen, in *Solid State Physics Vol.40*, edited by H. Ehrenreich, F. Seitz, and D. Turnbull (Academic Press, New York, 1987), pp. 94–180.
2. *Physics and Chemistry of Small Clusters*, edited by P. Jena, B. K. Rao, and S. N. Khanna (Plenum, New York, 1987).
3. W. A. de Heer, *Rev.Mod.Phys.* **65**, 611 (1993).
4. *Physics and Chemistry of Finite Systems: From Clusters to Crystals, C*, edited by P. Jena, S. N. Khanna, and B. K. Rao (NATO ASI series, Kluwer, Dordrecht, 1992).
5. *Nuclear Aspects of Simple Metal Clusters*, edited by C. Bréchnignac and P. Cahuzac (OPA, Amsterdam, 1995), Vol. 31.
6. *Clusters of Atoms and Molecules*, edited by H. Haberland (Springer, Berlin, 1995), Vol. I+II.
7. *Large Clusters of Atoms and Molecules*, Vol. 313 of *NATO ASI Series E: Applied Sciences*, edited by T. P. Martin (Kluwer, Dordrecht, 1996).
8. S. Sugano and H. Koizumi, *Microcluster Physics*, Vol. 20 of *Springer Series in Material Sciences* (Springer, Berlin, 1996).

9. G. Mie, *Ann. Phys.* **25**, 377 (1908).
10. U. Kreibig and P. Zacharias, *Z.Phys.* **231**, 128 (1970).
11. C. Kittel, *Introduction to Solid State Physics* (Wiley, New York, 1976).
12. W. A. de Heer *et al.*, *Phys. Rev. Lett.* **59**, 1805 (1987).
13. U. Kreibig and M. Vollmer, *Optical Properties of Metal Clusters* (Springer, Berlin, 1995).
14. M. M. Alvarez, J. T. Khoury, T. G. Schaaff, M. N. Shafiqullin, I. Vesmar, and R. L. Whetten, *J.Phys.Chem.* **101**, 3706 (1997).
15. V. Kresin, *Phys.Rep.* **220**, 1 (1992).
16. A. Kawabata and R. Kubo, *J. Phys. Soc. Jap.* **21**, 1765 (1966).
17. C. Yannouleas, *Nucl.Phys.A* **439**, 336 (1985).
18. C. Yannouleas and R. A. Broglia, *Ann. Phys.* **217**, 105 (1992).
19. N. W. Ashcroft and N. D. Mermin, *Solid State Physics* (Holt, Rinehart and Winston, New York, 1976).
20. R. Kubo, *J. Phys. Soc. Jpn.* **17**, 1975 (1962).
21. V. Bonačić-Koutecký, P. Fantucci, and J. Koutecký, *Chem. Rev.* **91**, 1035 (1991).
22. R. Denton, B. Mühlischlegel, and D. J. Scalapino, *Phys. Rev. B* **7**, 3589 (1973).
23. W. D. Knight, K. Clemenger, W. A. de Heer, W. A. Saunders, M. Y. Chou, and M. L. Cohen, *Phys. Rev. Lett.* **52**, 2141 (1984).
24. J. Pederson, S. Bjørnholm, J. Borggreen, K. Hansen, T. P. Martin, and H. D. Rasmussen, *Nature* **353**, 733 (1991).
25. *Nuclear Physics Concept in the Study of Atomic Cluster Physics*, Vol. 404 of *Lecture Notes in Physics*, edited by R. Schmidt, H. Lutz, and R. Dreizler (Springer, Berlin, 1992).
26. K. Clemenger, *Phys. Rev. B* **32**, 1359 (1985).
27. B. Mottelson and S. G. Nilsson, *Phys. Rev.* **99**, 1615 (1955).
28. A. Bohr and B. R. Mottelson, *Nuclear Structure* (Benjamin, New York, 1975), Vol. II.
29. C. Yannouleas and U. Landman, *Phys.Rev.B* **48**, 8376 (1993).
30. C. Yannouleas and U. Landman, *Phys.Rev.B* **51**, 1902 (1995).
31. C. Yannouleas and U. Landman, *Phys.Rev.Lett.* **78**, 1424 (1997).
32. W. Ekardt, *Phys. Rev. B* **29**, 1558 (1984).
33. M. Brack, *Rev. Mod. Phys.* **65**, 677 (1993).
34. W. Ekardt, *Phys. Rev. B* **31**, 6360 (1985).
35. U. Röthlisberger and W. Andreoni, *J. Chem. Phys.* **94**, 8129 (1991).
36. R. N. Barnett, U. Landman, and G. Rajagopa, *Phys.Rev.Lett.* **67**, 3058 (1991).
37. R. N. Barnett and U. Landman, *Phys.Rev.B* **48**, 2081 (1993).
38. R. N. Barnett and U. Landman, *Nat.* **387**, 788 (1997).
39. W. D. Luedtke and U. Landman, *J. Phys. Chem.* **100**, 13323 (1996).
40. M. Pellerin, B. Bagueard, C. Bordas, M. Broyer, J. Lerme, and J. L. Vialle, *Phys. Rev. B* **48**, 17645 (1993).
41. P. Buffat and J. P. Borrel, *Phys. Rev. A* **13**, 2287 (1976).
42. T. P. Martin, Y. Naher, H. Schaber, and U. Zimmermann, *J.Chem. Phys.* **100**, 2322 (1994).
43. M. Schmidt, R. Kusche, W. Kronmüller, B. von Issendorff, and H. Haberland, *Phys.Rev.* **79**, 99 (1997).
44. H. R. Siekmann, C. Lüder, J. Fähmann, H. O. Lutz, and K. H. Meiwes-Broer, *Z. Phys. D* **20**, 417 (1991).

45. T. P. Martin, T. Bergmann, H. Göhlich, and T. Lange, *J. Phys.Chem.* **95**, 6421 (1991).
46. A. L. Mackay, *Acta Crystallogr.* **15**, 916 (1962).
47. K. H. Meiwes-Broer, in *Advances in Metal and Semiconductor Clusters* (JAI, Greenwich, 1993), Vol. 1, p. 27.
48. J. G. Eaton, L. H. Kidder, H. W. Sarkas, K. M. McHugh, and K. M. Bowen, in *Physics and Chemistry of Finite Systems: From Clusters to Crystals* (Kluwer, Dordrecht, 1992).
49. M. Seidl, K. H. Meiwes-Broer, and M. Brack, *J. Chem. Phys.* **95**, 1295 (1991).
50. J. D. Jackson, *Electromagnetic Fields and Waves* (Wiley, New York, 1975).
51. T. Reiners, C. Ellert, M. Schmidt, and H. Haberland, *Phys.Rev.Lett.* **74**, 1558 (1995).
52. C. Yannouleas, R. B. Brack, and P. F. Bortignon, *Phys. Rev. Lett.* **63**, 255 (1989).
53. J. Tiggesbäumker, L. Köller, K. H. Meiwes-Broer, and A. Liebsch, *Phys. Rev. A* **48**, R1749 (1993).
54. L. Wöste, *Z. Phys. Chem.* **196**, 1 (1996).
55. D. C. Mattis, *Theory of Magnetism* (Springer, Berlin, 1985).
56. J. Crangle, *Solid State Magnetism* (Van Nostrand Reinhold, New York, 1991).
57. W. de Heer, P. Milani, and A. Châtelain, *Phys. Rev. Lett.* **65**, 488 (1990).
58. J. Becker and W. de Heer, *Ber. der Bunsenges. Phys. Chem.* **30**, 1239 (1992).
59. C. Bean and J. Livingston, *J. Appl. Phys.* **30**, 120 (1958).
60. I. M. L. Billas, A. Châtelain, and W. A. de Heer, *J. Mag. Mag.Mat.* **168**, 64 (1997).
61. I. M. L. Billas, A. Châtelain, and W. A. de Heer, *Science* **265**, 1682 (1994).
62. *Magnetic Properties of Fine Particles*, edited by J. Dormann and D. Fiorani (North-Holland, Amsterdam, 1992).
63. G. F. Bertsch and K. Yabana, *Phys. Rev. A* **40**, 1930 (1994).
64. D. C. Douglass, J. P. Bucher, and L. A. Bloomfield, *Phys. Rev.Lett.* **68**, 1774 (1992).
65. D. Gerion, A. Hirt, and A. Châtelain, *Phys. Rev. Lett.* **83**, 532 (1999).
66. A. J. Cox, J. G. Louderback, and L. A. Bloomfield, *Phys.Rev.Lett.* **71**, 923 (1993).

2 Fundamentals of Adsorbate-Surface Interactions

Heinz Hövel, Lars S. O. Johansson, and Bruno Reihl

2.1 Introduction

Certain atomic and molecular species play the role of model systems for the understanding of fundamental chemical and physical concepts in adsorbate-surface interactions. Although the *commercial* value of these species may be rather low, their value must be appreciated by the conclusions which can be drawn from them, and their possible subsequent implementations into technical processes and/or the engineering of novel materials. Amongst these model species are the rare-gas atoms with their closed electronic shells, the alkali metal atoms with just one valence electron, the highly symmetric C₆₀ molecule, and metal clusters, all adsorbed on the best-understood single-crystal surfaces. These are those of graphite, silicon, silver, and gold. Various combinations of these model systems and surfaces will be presented here with the special focus on the adsorbate-surface interaction, and the resulting modifications of both the adsorbed species and the substrate surface.

A key issue in this context is the question of bonding, its nature and strength. Weakly bound species may be desorbed from the substrate surface by a small energy transfer as, e.g., given by a small temperature increase. As an example, we mention xenon on graphite, which bonds by the Van-der-Waals interaction below 65 K. Usually, this is referred to as physisorption. In the other extreme of a very strong bond, the energy equivalent of several hundred Kelvin is required to break the bond and allow the adsorbed species to desorb from the substrate surfaces. This bonding regime is usually termed chemisorption and comprises, e.g., alkalis and C₆₀ on silicon, if we restrict ourselves to the above-mentioned list of model systems. The strong bonding case is usually accompanied by a charge transfer. Depending on the degree of localisation and direction of the involved electronic orbitals, the literature distinguishes *ionic*, *covalent* and *metallic* bonding [1].

For an understanding of the interplay between the electronic and geometric properties of the adsorbate-surface system it is important to know and understand the properties of the clean, possibly reconstructed surfaces, since the adsorbing species may induce or alter any reconstruction, which is then usually accompanied by a modification of the electronic structure, changing, e.g., the composite surface from metallic to semiconducting or vice versa. In most cases, the degree of surface modification is scaling with the bonding

strength: As we will discuss below, adsorbed xenon leaves the graphite surface unchanged, while C_{60} adsorbed on the $Au(110)1 \times 2$ surface causes a complete rearrangement of the top atomic layer, resulting in a new $Au(110)1 \times 5$ reconstruction of the substrate underneath.

Besides the surface reconstruction, the adsorbate can form an ordered overlayer, which may or may not be in registry with the surface periodicity, and is usually dependent on the amount of adsorbed species and its interfacial morphology given by the overlayer–surface strain and annealing temperature applied. Important here is also the relative strength of the adsorbate–surface versus adsorbate–adsorbate interaction. For a strong bonding to the surface the overlayer forms a commensurate structure which fits into the surface periodicity. If the bonding within the adsorbed species is dominating, this leads to an incommensurate overlayer or even to three dimensional growth. As we shall show in the next section a submonolayer of xenon on graphite forms an incommensurate overlayer with a honeycomb-like domain structure.

2.2 Physisorption of Xenon on Graphite: Superstructure and Domain Boundaries

As an example for physisorption we discuss xenon on graphite. Monolayers of rare gases on graphite provide ideal testing grounds for 2D adsorbate phases and phase transitions [2], as they exhibit a large variety of different phases originating from the fact that the lateral interaction of the rare gas atoms is of the same order of magnitude as the corrugation of the graphite surface potential [3]. The phase diagram of Xe on graphite is well-known [4] along with many details in the monolayer-coverage regime [5]. Hong et al. [5] found a commensurate $(\sqrt{3} \times \sqrt{3})R30^\circ$ Xe phase for the monolayer coverage at temperatures below $T = 60$ K, which was confirmed by other studies [4]. As the $(\sqrt{3} \times \sqrt{3})R30^\circ$ lattice constant is about 3% smaller than the Xe bulk lattice constant, Xe forms an incommensurate phase in the submonolayer regime, because compressive strain would be needed for the formation of the commensurate phase.

The scanning tunnelling microscopy (STM) topograph in Fig. 2.1(a) shows an atomically resolved surface area of $16 \times 16 \text{ nm}^2$ of xenon on graphite. It exhibits a nearest-neighbor distance of 0.45 ± 0.05 nm in agreement with the expected $(\sqrt{3} \times \sqrt{3})R30^\circ$ value of 0.425 nm for a Xe adlayer on a graphite surface (for experimental details see [6,7]). The Xe atoms resolved in Fig. 2.1(a) form hexagonal patches about 15 atomic rows wide, separated by domain walls which appear in the STM signal as a smooth contrast several atomic rows in width. Xe atoms forming domain walls are slightly darker in the image than the surrounding Xe atoms in the domains. The origin of this contrast will be discussed below. The Xe domains are arranged in a hexagonal honeycomb-like structure. This is in agreement with an incommensurate phase observed for Xe coverages well below the completion of the first monolayer at tem-

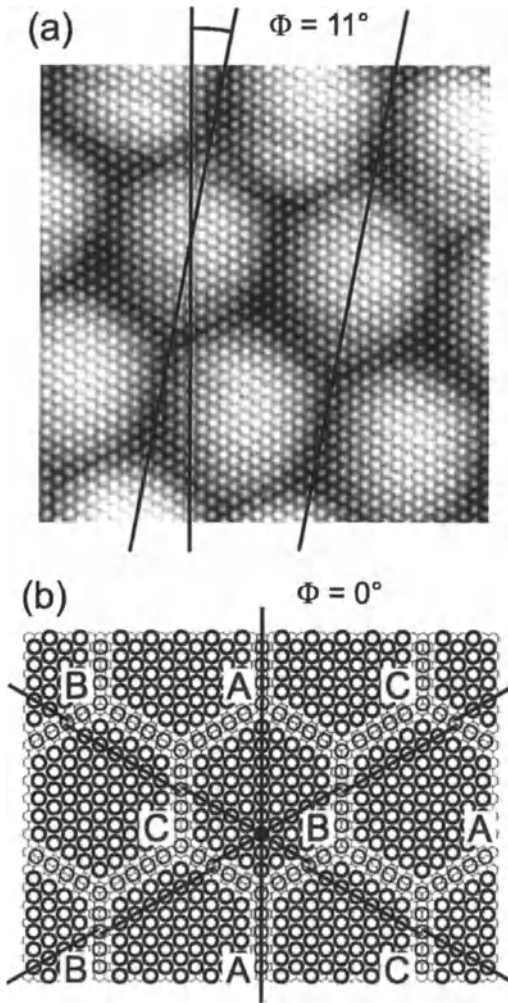


Fig. 2.1. (a): STM image of Xe on graphite showing atomically resolved hexagonal Xe domains arranged in a hexagonal honeycomb-like structure. Image parameters: scan area $16 \times 16 \text{ nm}^2$, tip bias: 3.2 V, current: 0.1 nA, $T = 5 \text{ K}$. (b): Schematic model of the Xe overlayer structure. Φ denotes the angle between the domain walls and the Xe atomic rows. Xe atoms are arranged in three possible domains (bold circles) denoted A, B, C. Xe atoms forming domain walls are shown as thin circles. See text for a further discussion. (From Ref. [6])

peratures $T < 60 \text{ K}$ [5]. It is also supported by theoretical predictions for a hexagonal domain-wall structure [8]. For a better illustration a schematic model of the Xe overlayer is shown in part (b) of Fig. 2.1. The Xe atoms are arranged in three possible domains denoted A, B, and C, each of which having a registered $(\sqrt{3} \times \sqrt{3})R30^\circ$ structure with respect to the graphite surface. In going from one domain to the neighboring one the Xe rows are shifted by $a/2 = 0.12 \text{ nm}$ where a denotes the lattice constant of graphite. In the STM image of Fig. 2.1 this shift can best be seen as a slight distortion of the Xe rows across the domain walls.

We note that the symmetry axes of the honeycomb dislocation pattern in the STM image of Fig. 2.1(a) are not aligned with the symmetry axes of the

Xe atoms as it is drawn in Fig. 2.1(b), but tilted by about $\Phi = 11^\circ$. With a more detailed evaluation of our STM images [6] we have identified this large tilting angle of the domain walls to be the origin of the small rotation angle predicted by theory [9] and observed in diffraction studies [4,5].

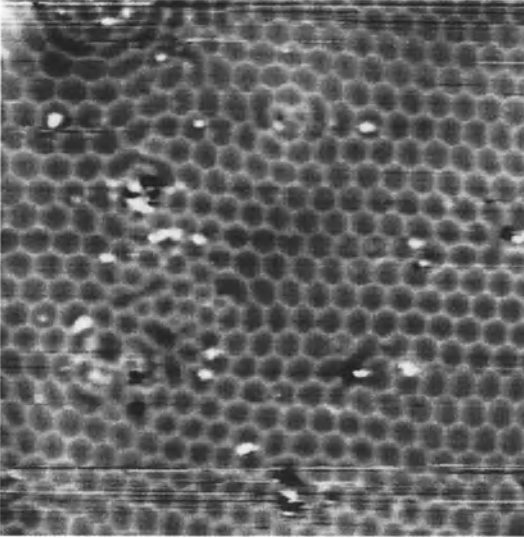


Fig. 2.2. STM image of Xe on graphite showing contamination-induced distortions in the hexagonal honeycomb-like overlayer structure. Image parameters: scan area $200 \times 200 \text{ nm}^2$, tip bias: 4.5 V, current: 0.1 nA, $T = 5 \text{ K}$. (From Ref. [6])

Fig. 2.2 shows a typical large-area STM image of $200 \times 200 \text{ nm}^2$. The domain walls are clearly visible as a bright honeycomb pattern. The surface is locally contaminated by randomly distributed adsorbates appearing as bright spots. These adsorbates create distortions of the regular honeycomb-like domain walls as has been discussed by Villain [10]. The presence of adsorbates creates a local preference for one certain domain leading to distortions of the wall structure. The contrast inversion in comparison with the measurement of Fig. 2.1(a) is due to the higher gap voltage applied (4.5 V), increasing the tip-sample separation, which was an advantage when taking large area overviews of the domain structure without atomic resolution. The contrast between domains and domain walls is an electronic effect which can be attributed to the lateral interaction of the Xe atoms within the adsorbate layer. This lateral interaction is strongly dependent on the interatomic distance as has been shown for the occupied states of the Xe monolayer [11,12]. In Fig. 2.1(a) (gap voltage 3.2 V) the interaction causes a broadening of the unoccupied Xe bands in the compressed areas of the domains. These are then contributing to the tunneling current at lower gap voltages as compared to the domain-wall regions, which consequently appear darker in the STM images. The inversion of the contrast between domains and domain walls around 4.5 V can be related to the unoccupied Xe 6p level located 4.3 V above the Fermi level in the monolayer coverage regime as has been shown for the system Xe on Au(110)

by inverse photoemission [13]. A sharp peak in the energy distribution curve of the inverse-photoemission signal corresponds to a high density of states and causes an extra contribution in the STM signal of the domain walls, while in the case of the domains the broadening of the energy bands smears out and possibly shifts this contribution to higher energies.

2.3 Chemisorption of Alkali Atoms on Semiconductor Surfaces

2.3.1 Ionic vs. Covalent Bonding and Charge-Transfer Monitoring

There is a longstanding controversy [14] about the nature of the bonding of the alkali-metal atoms to semiconductor surfaces, in particular to silicon surfaces. Two extreme pictures may describe the situation: in case of a complete charge transfer of the alkali valence s electron to the semiconductor surface, the bonding is *ionic*, and the metallisation as a function of coverage is caused by a partial filling of the surface state bands [15–19]. The strong dipole field created by the positive alkali ion and the negative image charge are causing the strong workfunction change with coverage. In the other case, the charge transfer is fractional and rather small, and a weak *covalent* bonding explains the strong workfunction reduction by a polarization-dependent interaction [20–22]. The metallisation occurs within the alkali metal overlayer as soon as the valence electron orbitals can overlap as a function of coverage, hence a critical surface atom density is required in contrast to the ionic-bonding picture. Some theories also favor a mixed-type of bonding, i.e. almost ionic at low coverages, while the covalent character increases with coverage [23,24]. As we will show below, direct and inverse photoemission results favor the second or third alternatives in most cases (with one significant exception).

A common belief in the literature of alkali-metal-on-semiconductor research is the equivalency of the different alkali atoms (with the exception of Li), and in particular of potassium and cesium. Often, calculations performed for potassium are compared to experiments with cesium and vice versa. For example, the electronic-structure calculations of Ciraci and Batra [16] for Si(111)(2×1)-K were compared to photoemission results of Cs [25] on the same surface. Later it was found from self-consistent total-energy calculations [17] that the (2×1) surface reconstruction is unstable against K adsorption, favoring a (1×1) structure which may become insulating at higher coverages. We will prove below that alkali atoms do not behave iso-electronically on the same semiconductor surface. Their atomic radii and polarizabilities also play important roles, as they determine the relative strength of the adsorbate-adsorbate versus adsorbate-surface interaction.

The experimental techniques of angle-resolved direct and inverse photoemission (Angle Resolved Ultraviolet Photoelectron Spectroscopy, ARUPS

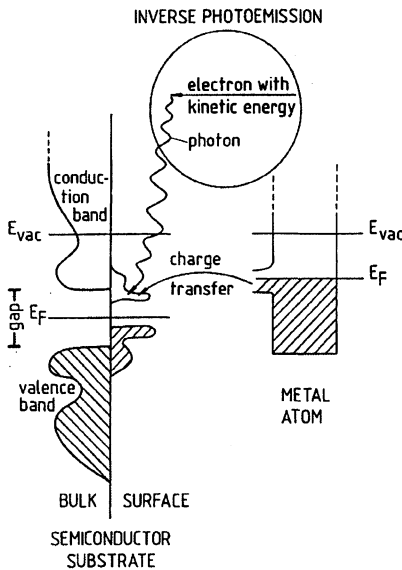


Fig. 2.3. Illustration of inverse photoemission as a monitor of charge-transfer processes which may occur when a metal atom interacts with a semiconductor surface with bulk and surface states

and Inverse Photoelectron Spectroscopy, IPES) are particularly well suited for investigating the amount of charge transfer as relevant parameter for the ionic versus covalent character of the Si-alkali metal bond. The empty electronic states at the surface may get filled by charge transfer from the alkali atom, and hence are no longer available as final states in the IPES process. On the other hand, they should then become visible in the ARUPS spectra. This is illustrated in Fig. 2.3. The changes of the ARUPS and the IPES signals thus provide a monitor of the semiconductor-metal interaction. In addition, ARUPS and IPES provide the needed surface sensitivity owing to the limited penetration depth of the incoming and outgoing electrons, respectively. An important aspect is the availability of both techniques in the same spectrometer, allowing IPES and ARUPS measurements on the same surface, with the same alkali metal coverage.

We are mainly interested in ordered surfaces, because then surface states may form bands with well-defined $E(k)$ dispersion relationships in the plane of the surface. The measurement of their dispersions allows us to identify the surface states, i.e. distinguish them from bulk states. In cases where they cross the Fermi energy, a necessary condition for a metallization of the interface system is fulfilled. By comparison to electronic-structure calculations we can even derive structural information and determine alkali adsorption positions as demonstrated below. The wave vector k of surface states as two-dimensional entities has only a component parallel to the surface k_{\parallel} which can be related to the kinetic energy E_k and polar angle θ of the incident electron beam (or outgoing beam for ARUPS) by $k_{\parallel} = 0.512 \sin \theta (E_k)^{1/2}$,

where $E_k = h\nu - \phi + E_B$ and E_B is the measured binding energy, referred to E_F , of the spectral features in the IPES and the ARUPS spectra. Energies are in electron volts (eV) and wave vectors in inverse Ångströms, ϕ denotes the workfunction. Details about the ARUPS and IPES experiments, the sample preparation, the surface characterization, etc. of the various alkali-metal interfaces may be found in the original publications (see references within the following text).

2.3.2 Li, Na, K and Cs on Cleaved Si(111)

It was found from total-energy calculations [17] that K deposition on the cleaved Si(111) surface destroys the 2×1 reconstruction and forms a 1×1 surface. In contrast, we find that K deposition leaves the p-bonded chains unchanged and observe a 2×1 LEED pattern throughout the coverage regime [26]. However, cesium does destroy the 2×1 registry and forms a new $\sqrt{3} \times \sqrt{3} - R30^\circ$ surface atom arrangement at exactly the 1-monolayer (ML) coverage [27]. Sodium [28] and lithium [29] also destroy the 2×1 pattern and form 1×1 phases as it had been predicted [17] for K.

In Fig. 2.4 we show the relevant angle-resolved inverse photoemission spectra for one ML of potassium on Si(111) 2×1 . As discussed in more detail in Ref. [26], the K-induced surface state U'_1 in Fig. 2.4 shifts towards the Fermi level and loses spectral intensity. Such behavior is proof for an IPES peak moving through the Fermi level as measured with a finite energy resolution [30], hence the surface state crosses the Fermi level about midway along the $\bar{\Gamma}$ – \bar{J} axis, proving a metallization. Plotting the peak position of the spectra in Fig. 2.4 (and other spectra not shown), we find that the overall shape and bandwidth of the surface-state band is consistent with Ciraci and Batra’s calculations [16] for one K atom per 2×1 unit cell. This is essentially the clean-surface band structure with the Fermi level shifted so that it cuts through the unoccupied band, rendering the substrate surface metallic. Finally, we note that we also observe [26] this surface-state band to cross E_F at smaller coverages, i.e. less workfunction reductions, indicating metallicity in a broad coverage range, which makes the K/Si(111) interface consistent with the ionic picture. Its ingredients were substrate metallization through filling of the surface-state bands [16], and no critical coverage needed for metallization.

The monolayer-covered Cs/Si(111) surface is quite different from the K/Si(111) case, as cesium destabilizes the p-bonded chain structure and induces a $(\sqrt{3} \times \sqrt{3})R30^\circ$ reconstruction [27]. The Cs-induced surface-state features exhibit only little dispersion as function of ϕ and never approaches the Fermi level for all Surface Brillouin Zone (SBZ) symmetry directions measured (data not shown). This holds true for the unoccupied surface band dispersion as obtained by IPES as well as the occupied surface band as derived from ARUPS. Their combination yields an indirect surface bandgap of 1.5 eV. All these observations are at variance with previous predictions and experiments of the Cs/Si(111) 2×1 interface system.

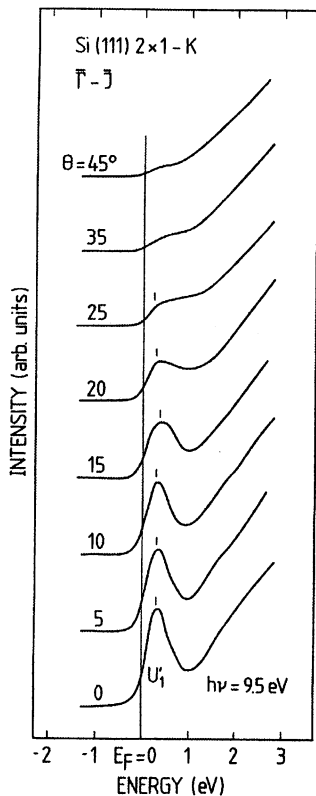


Fig. 2.4. Angle-resolved inverse photoemission spectra at $h\nu = 9.5$ eV for different incidence angles Θ , probing states along the $\bar{\Gamma}$ - \bar{J} line of the Si(111) 2×1 -K surface Brillouin zone (from Ref. [26])

We have also investigated sodium and lithium on the cleaved Si(111) surface [28,29]. The workfunction minima are less pronounced (-2.40 eV for Li and -2.7 eV for Na) as compared to K and Cs on the same surface. At about half of the saturated-monolayer coverage, the LEED pattern changes from 2×1 to 1×1 which implies the existence of yet another alkali phase on the same silicon surface. Angle-resolved UPS and IPES measurements (not shown) reveal that at 1-ML coverage both interfaces are semiconducting. In Fig. 2.5 we compare our measured energy dispersion for the Na-induced unoccupied (U'_1) and occupied (S) surface state features to existing band-structure calculations which we have split for the two different azimuths. Along $\bar{\Gamma}$ - \bar{K} we have reproduced the bands from a first-principles pseudopotential calculation [15], which finds $\Delta\phi = -2.7$ eV in perfect agreement with our value and an ionic bond of the Na 3s with the 3p dangling bonds of the Si substrate. Amongst the various adsorption sites, this calculation favors the three-fold hollow site. The latter is in contrast to the calculations of Ossicini et al. [31], which favor the three-fold filled site with a charge transfer of 0.14 electrons per atom, indicating a covalent bonding. Their electronic structure is based upon the linear muffin-tin orbital method in the atomic-sphere approxima-

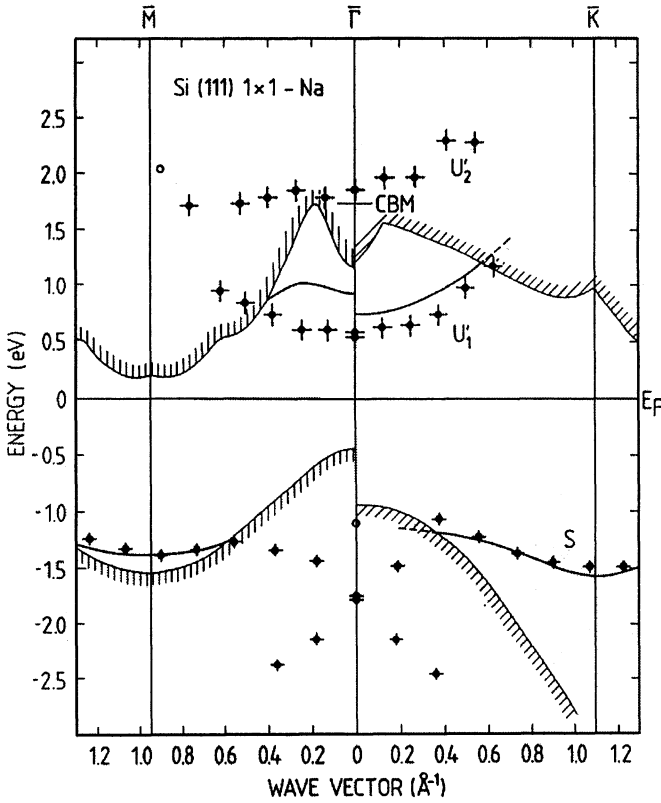


Fig. 2.5. The energy dispersion $E(k_{\parallel})$ of the occupied and empty surface-state features of 1 ML Na on Si(111) as measured by angle-resolved UPS and IPES, respectively. The crosses indicate the estimated uncertainty. Along $\bar{\Gamma}-\bar{K}$ (right side) we compare to the calculated bands of Northrup [15], along $\bar{\Gamma}-\bar{M}$ (left side) to those of Ossicini et al. [31]. (The theoretical surface-state bands have been adjusted in energy to give the best agreement for the occupied part. The hatched area represents the projected bulk bands of each calculation.) (From Ref. [28])

tion and are shown in Fig. 2.5 along the $\bar{\Gamma}-\bar{M}$ azimuth. Clearly, their empty surface-state band does not follow our measured dispersion. Recently, *ab initio* molecular dynamics simulations using a plane-wave expansion have been performed for both Na- [32] and Li- [33] covered Si(111). These calculations simulate temperature annealing with a random displacement of atoms in order to find the equilibrium structure. The authors also find the 1×1 surface structure with the three-fold filled site for Li and the three-fold hollow site for Na as the most stable configurations with the lowest total energy. Their surface-state dispersions calculated for the two different adsorption sites agree almost perfectly with our measured dispersions for Li and Na, respectively.

2.3.3 Li, Na, K and Rb on Si(100)

The important questions about the alkali-metal–semiconductor interface, e.g. the nature of the alkali–Si bond, the amount of charge transfer from the alkali metals to the substrate, the metallization, the adsorption positions, the saturation coverage at room temperature (RT), has been most hotly debated for the Si(100) 2×1 surface. In early studies of alkali-metal adsorption on Si(100) 2×1 , Levine’s model for Cs adsorption [34] was assumed to be valid for all the alkali-saturated surfaces at RT. In that model, the alkali atoms are placed in the so-called pedestal sites, i.e. in the middle between two neighboring dimers in the same row, which gives a coverage of 0.5 ML of alkali-metal atoms. (1 ML is defined as 6.78×10^{14} atoms per cm^2 , i.e. the same density as for one Si-atom surface layer). Originally, both theoretical [19] and experimental [35] studies of the K/Si(100) 2×1 surface supported this model. In particular electron-energy loss spectroscopy of the overlayer plasmon indicated the existence of one-dimensional alkali-metal chains [35], as expected from Levine’s model. The room temperature saturation coverage and the adsorption sites were then for several years under discussion, partly because of the experimental difficulties in determining the alkali-metal coverages. However, in recent years broad agreement (with few exceptions [36]) has developed around the so-called double-layer model for alkali-metal adsorption on Si(100), originally proposed for the K/Si(100) system [37]. In this model, which is illustrated in Fig. 2.6, the room-temperature alkali-metal saturation coverage is about one ML, and the alkali atoms sit in two different adsorption sites: the pedestal site and the valley-bridge site (in the trough between the dimer rows, straight between two pedestal sites). A large body of experimental evidence has been obtained, which wholly or partially supports this model, e.g. with X-ray photoelectron diffraction [37], angle-resolved photoemission [38,39] and inverse photoemission [40–42], core-level spectroscopy [43,44], and ion scattering [45]. Similarly, recent theoretical total-energy calculations also support this model [21,22].

The nature of the alkali–Si bond and the surface metallization are two other widely debated topics, in particular after the early proposal by Ciraci and Batra [19,46] that the alkali–Si bond is strongly ionic at saturation coverages, and consequently that metallization occurs by simple charge transfer from the alkali metal to the substrate surface states. More recent theoretical studies [21,22] have come to a different conclusion, describing the bond as a hybridization of Si dangling bonds and alkali ns – np orbitals, which is then called a polarized covalent bond. Many experimental studies have confirmed the covalent-bond picture, in particular photoemission [36,38,39,43,47] and inverse photoemission studies [40–42,48]. The ARUPS studies have shown a transformation of the dangling-bond band into at least two new bands at alkali-metal saturation coverages, whereas the IPES results have shown the emergence of new dispersing overlayer-derived bands.

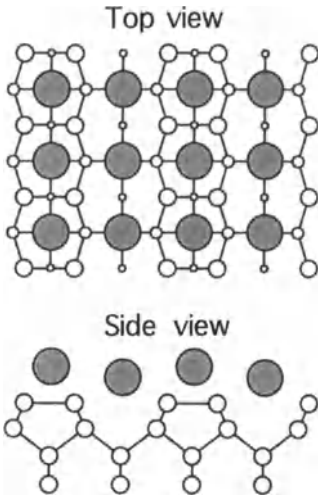


Fig. 2.6. Schematic illustration of the double-layer model originally proposed for the Si(100)2-K surface in Ref.[37]. The alkali atoms (large shaded circles) are located both between and on top of the dimer rows right above the third Si layer. (From Ref. [48])

The onset of metallization of the RT-saturated K/Si(100) 2×1 surface was demonstrated experimentally in our early combined IPES/ARUPS study [40], where it was shown that metallization occurs through occupation of the minimum of a strongly dispersing empty overlayer-derived band at saturation. This is illustrated in Fig. 2.7 which shows ARUPS and IPES spectra recorded in normal emission and incidence, respectively, for increasing K coverages. A single-domain 2×1 -reconstructed surface was obtained by using vicinal samples. In the spectra from the clean surface ($\Delta\phi = 0.0$) contributions can be seen from the filled and empty dangling-bond surface state, denoted S_1 and U_1 . A small contribution from the U_1 state can be seen also in the UPS spectrum owing to the high n-doping of the sample crystal. The structures above 3 eV and below -2 eV are attributed to the Si conduction-band and valence-band emission, respectively. At low K coverages, the emission from the small U'_1 peak at the Fermi level in the ARUPS spectra is increased. This Fermi peak corresponds to the partial occupation of the previously empty U_1 dangling-bond state, by charge transfer from the outer s-level of the alkali adsorbate to the substrate. This effect has been observed much clearer on low-doped on-axis cut Si substrates for low coverages of Li [49], Na [43], K [38,43], Rb [48], and Cs [44] on Si(100). This simple charge transfer effect suggests a mainly ionic bonding at low coverage (up to 0.2 ML), a conclusion that is also supported by low-energy ion scattering studies of K and Cs adsorption on Si(100) [50].

At a coverage corresponding to $\Delta\phi = -2.0$ eV an empty surface state denoted U_2 appears at 2.4 eV energy, which shifts with further increasing coverage downwards in energy until it reaches the Fermi level at the same coverage where the work function reaches its minimum at $\Delta\phi = -3.38$ eV. Then the U_2 state becomes also visible in the ARUPS spectra (denoted U'_2).

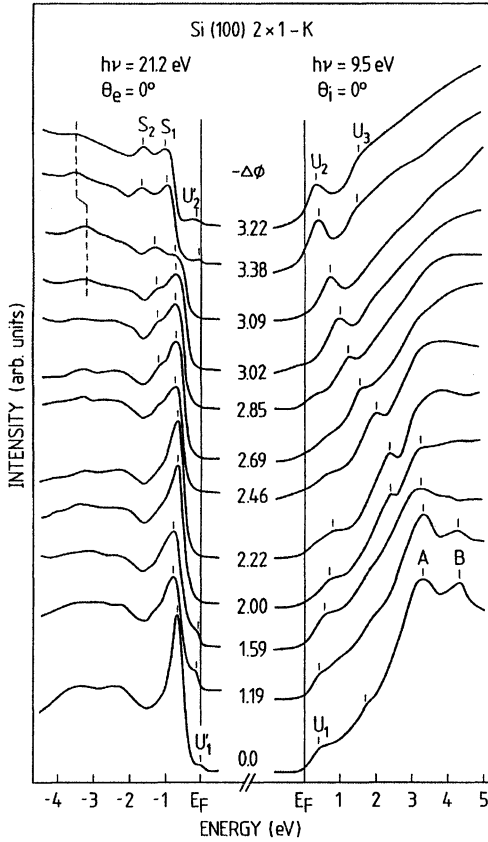


Fig. 2.7. ARUPS normal-emission and IPES normal-incidence spectra recorded on the Si(100)2×1-K surface for increasing K coverage. The coverage was indirectly controlled by the measured work function shift ($\Delta\Phi$). The symbols are explained in the text. (From Ref. [40])

In the ARUPS spectra, a second surface state denoted S_2 appears to split off from the S_1 peak for $\Delta\phi = -2.85$ eV and move to lower energies for increasing coverage. Between $\Delta\phi = -3.09$ eV and -3.38 eV, all ARUPS features shift downwards by 0.3 eV, as indicated in Fig. 2.7. This energy shift thus coincides with the minimum in the $\Delta\phi$ curve and occurs quite abruptly with respect to the K-evaporation time. We interpret this shift to be a band-bending shift caused by the onset of the filling of the previously empty surface state U_2 .

The dispersion of the U_2 state was measured by recording IPES spectra for various incidence angles along the main symmetry directions of the surface Brillouin zone (SBZ). This could be done unambiguously due to the single-domain character of the 2×1 -reconstructed surface. Large parabolic-like dispersions were found in both the $\bar{\Gamma}$ - \bar{J} and the $\bar{\Gamma}$ - \bar{J}' directions of the SBZ, which are plotted in Fig. 2.8.

The data presented above were the first direct and conclusive evidence for overlayer metallization in the case of Si(100), since in the IPES and ARUPS spectra we directly observe the crossing of the Fermi level of the

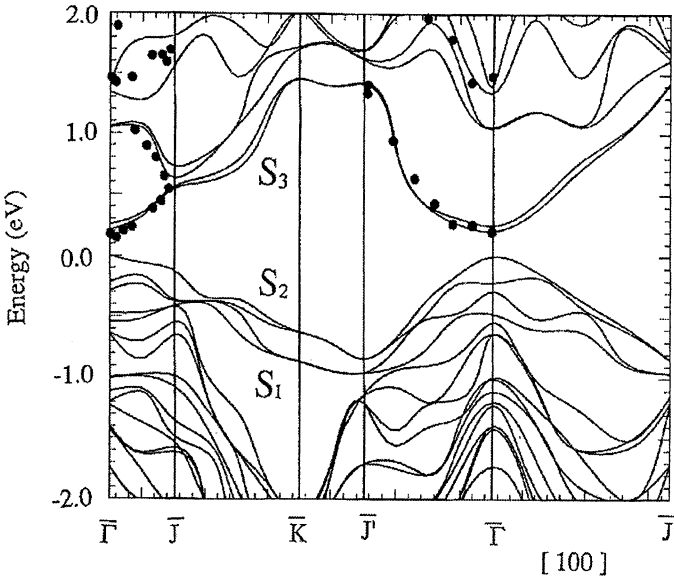


Fig. 2.8. The theoretical and experimental energy dispersion $E(k_{\parallel})$ of the surface-state features of 1 ML K on Si(100) 2×1 . The experimental data as measured by angle-resolved IPES (Ref. [40]) are indicated by dots and are shifted in energy to achieve the best agreement with the theoretical bands, as calculated by Morikawa et al. (From Ref. [21])

overlayer-derived U_2 band. Further evidence for a metallic overlayer is given by the parabolic-like dispersion of the U_2 band, which indicates a metallic bonding within the overlayer with strong K–K interaction both parallel and perpendicular to the dimer rows. Later photoemission [39,51] and STM [52] studies confirmed these results. This metallization occurs at the coverage corresponding to the minimum workfunction value, whereas at a slightly lower K coverage, at $\Delta\phi = -3.09$ eV, the surface is still semiconducting. This indicates that the metallization occurs at a coverage that is nominally slightly above 1 ML. Thus at 1 ML coverage we expect a semiconducting surface, in agreement with the double-layer model.

By comparing to calculated band structures for Si(100) 2×1 -K [19,21,22], it is clear that our results are consistent with atomic models based on 1 ML coverage, e.g. the double-layer model [37], but not with 1/2-ML models, e.g. Levine’s model [34]. The main features of the 1/2-ML models (one filled surface band and one half-filled, with the empty part dispersing downwards from $\bar{\Gamma}$) are widely different from the experimental results presented here and in Ref. [38] (two filled surface bands well below the Fermi level, a semiconducting surface just before saturation and a mainly empty surface band

dispersing upwards from $\bar{\Gamma}$). The steep dispersion of U_2 in the direction perpendicular to the dimer rows is also clearly inconsistent with Levine's model, since it indicates a strong K–K interaction in this direction.

In contrast, our results are in very good agreement with ab-initio theoretical studies of Kobayashi et al. and Morikawa et al. [21]. This is illustrated in Fig. 2.8, which shows our experimental dispersions together with the calculated bandstructure of Morikawa et al. for a 1 ML K coverage on the Si(100) 2×1 surface. For the double-layer model they found a semiconducting surface band structure with two filled bands derived from the Si dangling bonds and K 4s and 4p_{x,y} orbitals, and one empty band with mixed K 4p_z and 4s orbital content. The character of the empty band agrees well with the U_2 band in the present work. Our results thus give strong support to the polarized covalent Si–K bonding picture proposed in Ref. [21].

Our IPES/ARUPS investigations of alkali-metal adsorption on Si(100) were later extended to Na [41] and Li [42] and Rb [48]. The adsorption of these alkali metals on Si(100) 2×1 have shown general similarities to the K/Si(100) 2×1 results, but also significant differences in the electronic structure, in particular the lack of metallization in the Li and Na cases. However, in all cases an overlayer-derived surface state appeared and shifted downwards towards the Fermi level with increasing alkali metal coverage. For K and Rb it reached the Fermi level leading to a metallization of the surface, whereas for Li and Na, the overlayer state remained above E_F , leaving the surface semiconducting.

Our results fit very nicely into the overall picture that has emerged for RT saturation coverage of alkali metals on Si(100) 2×1 , i.e. about a full monolayer coverage, arranged into a double-layer above the still dimerized 2×1 -reconstructed substrate, a relatively weak polarized covalent Si-alkali bond, and a semiconducting surface band structure (in the ideal 1-ML case, see discussion above). These results provide a database that allows us to systematically investigate the effects of the size of the adsorbed alkali atoms. The combination of ARUPS and IPES in one spectrometer made it possible to unambiguously determine important parameters of the surface electronic band structure. In particular, the maximum energy of the topmost occupied band at $\bar{\Gamma}$ and the minimum energy of the unoccupied band could be determined by recording an IPES and an ARUPS spectrum directly after each other on the same surface preparation. Thereby the surface band gap could be (almost) unambiguously determined. This parameter provides information about the strength of the Si–alkali bond. A strong bond leads to a smaller Si–alkali bond length and a larger band gap, whereas a weak bond leads to the opposite [21]. In addition, the bandwidth of the empty overlayer-derived U_2 band gives a qualitative information about the strength of the alkali-alkali interaction within the overlayer. Fig. 2.9 illustrates the differences in energy positions of the surface states at $\bar{\Gamma}$ for saturation coverage of the different alkali-metal adsorbates. One can clearly see how the surface band gap mono-

tonically changes from a quite large gap for Li, down to a quite small gap for Rb. This is mainly caused by the movement of the U_2 band minimum downwards towards the Fermi level for increasing alkali-atom size. However, also the occupied states move slightly towards the Fermi level for increasing alkali atom size.

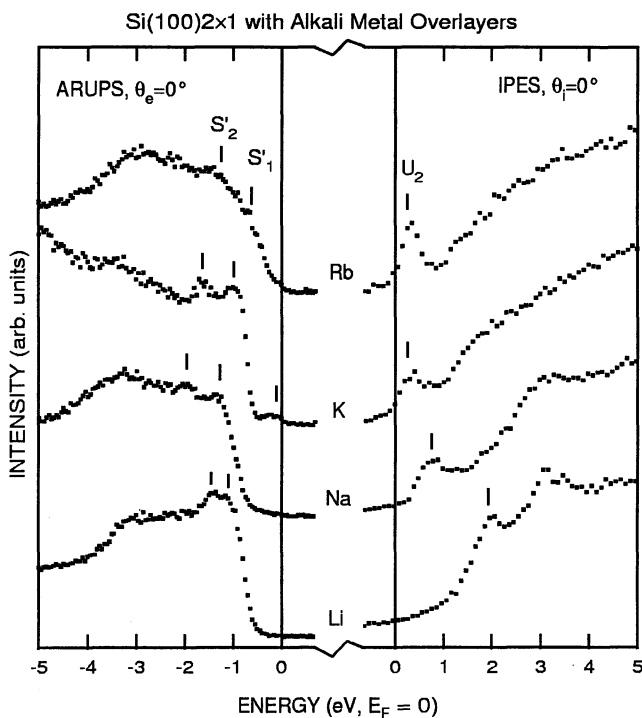


Fig. 2.9. Comparison of ARUPS normal-emission and IPES normal-incidence spectra recorded from alkali-saturated Si(100)2×1 surfaces for Li, Na, K and Rb adsorbates. The data are taken from Refs. [40–42,48], respectively. (From Ref. [48])

The values of the band gaps and U_2 minimum positions, as well as atomic radii and the U_2 bandwidths are shown in Table 1. The U_2 bandwidths display the opposite trend as compared to the band gaps. For Li the U_2 dispersion is flat and for increasing alkali-atom size, the bandwidth increases up to about 1.4 eV for K and Rb. The reason for this change can be found by considering the adsorption positions on the Si(100)2×1 surface. In the double-layer model (see Fig. 2.6) the nearest-neighbor distances for the alkali atoms are 3.84–4.0 Å, giving an atomic radius of about 1.9–2.0 Å. This can be compared to

the atomic radii for the alkali atoms in the metallic phase (see Table 2.1). One observes that the larger alkalis (K, Rb) sit considerably closer to each other on the Si(100) 2×1 surface as compared to the K and Rb bulk metals, respectively, leading to a strong alkali-alkali interaction and thereby a large U_2 dispersion. The atomic radius of Li, however, is considerably smaller than the Li–Li distance on the Si(100) 2×1 surface, leading to small wave function overlap, i.e. small Li–Li interaction and thus no dispersion for U_2 . In general, the wave function overlap and the corresponding interaction should hence be larger for increasing alkali-atom size. This is precisely what the U_2 bandwidth differences indicate.

Table 2.1. Metallic atomic radii for the alkali atoms and measured surface electronic-structure parameters for saturation coverages of Li, Na, K and Rb on Si(100) 2×1 . The data are from Refs. [40–42,48]. The uncertainties in determining the energy positions are given by the energy resolution of the experimental techniques and the resulting cut-off effects by the Fermi level. The resulting errors for the surface band-gap values are estimated to be ± 0.2 eV.

Alkali- atom	Metallic atom radius (Å)	Surface band gap (eV)	U_2 -min. rel. to E_g (eV)	U_2 -min. rel. to VBM (eV)	U_2 bandwidth (eV)
Li	1.52	3.0	2.0	2.3	0
Na	1.86	2.1	0.7	1.25	0.3
K	2.27	1.0	0	0.3	1.4
Rb	2.48	0.6	0	0.2	1.4

2.4 Bonding of C_{60} Molecules on Ag and Au(110) Surfaces

The cage-like arrangement of 60 carbon atoms on equivalent sites to form a soccer-ball (named fullerene), which again condenses on fcc lattice sites to build up a solid called fullerite, is established by now [53]. There exists a great body of experimental and theoretical papers [54–60] dealing with the energy positions of the highest-occupied and lowest-unoccupied molecular orbitals and the resulting HOMO-LUMO gap.

Surprisingly, there exist only few detailed investigations on the interplay of the geometric and electronic properties of fullerite formation. In many cases fullerite is formed by growing films of C_{60} on metal or semiconductor substrate surfaces. Hence, interfacial epitaxy, possible charge transfer, and different adsorption phases play a crucial role and determine the electronic

and geometric properties of the first layers of the fullerene film. We discuss our findings of C_{60} adsorption on the clean $Ag(110)$, $Au(110)1 \times 2$, and $Si(100)2 \times 1$ surfaces employing the techniques of STM, tunneling spectroscopy, and direct and inverse photoemission.

2.4.1 Geometric Properties

Fig. 2.10 shows an STM topograph of $Au(110)1 \times 2$ covered with about $2/3$ monolayers C_{60} , in which large platelets of ordered C_{60} are observed. In the regions of the bare surface a high density of Au steps appears, indicating the retreat of surface steps under the influence of the advancing edge of a growing fullerene island. The same phenomenon was observed for C_{60} on $Ag(110)$ [61]. This step bunching along with the Au material transport involved already provides evidence for the strong interaction of C_{60} with the open-structured noble-metal (110) surface at monolayer coverage.

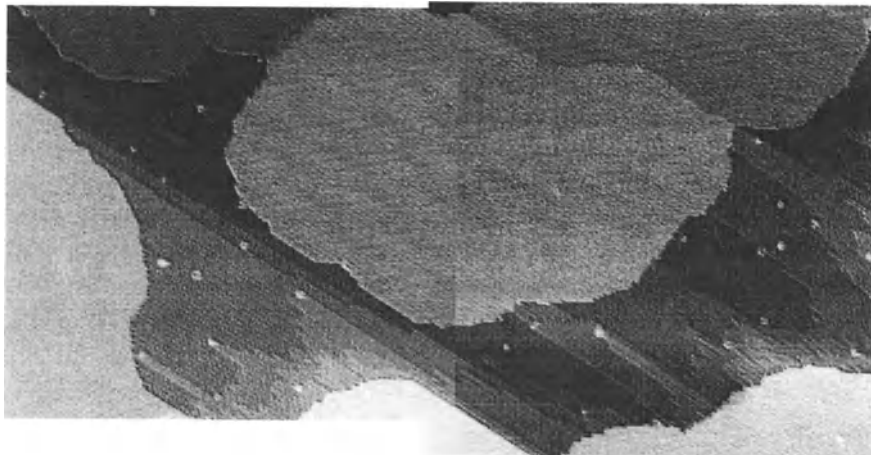


Fig. 2.10. STM topograph ($\sim 200 \times 400 \text{ nm}^2$) of about $2/3$ monolayer C_{60} on $Au(110)$ showing well-ordered platelets of C_{60} and a high-density of surface steps in-between. Tip bias: $+0.55 \text{ V}$, current: 0.23 nA , $T = 5 \text{ K}$

Zooming into one C_{60} island we observe in Fig. 2.11 a quasi-hexagonal overlayer structure with a "zigzag" superstructure with respect to the simple hexagonal C_{60} lattice, as originally found by Gimzewski et al. [62]. The zigzag lines (bright is higher, dark is lower) run parallel to the $[1\bar{1}0]$ gold rows and are vertically displaced by $0.05\text{--}0.08 \text{ nm}$. Close inspection of the STM topographs and rigid-ball modeling of the composed surface reconstruction reveal a $Au(110)6 \times 5\text{--}C_{60}$ structure, whereby the mere gold surface underneath exhibits a 1×5 reconstruction, which continues to persist even in between the C_{60} islands, as can be seen in Fig. 2.12. In the case of $Ag(110)$, the strong

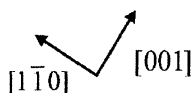
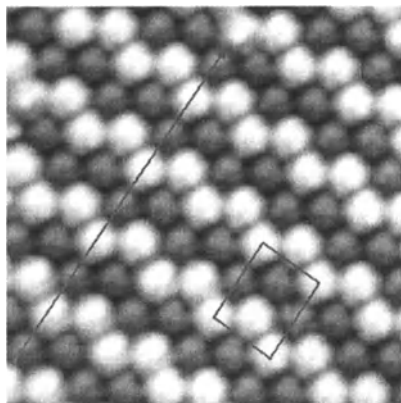


Fig. 2.11. STM topograph ($10 \times 10 \text{ nm}^2$) of an ordered C_{60} monolayer on $\text{Au}(110)$ with the typical zigzag arrangement with the 6×5 unit cell depicted as a rectangle. Tip bias: -0.2 V , current: 0.24 nA , $T = 5 \text{ K}$

C_{60} -noble metal interaction manifests itself in an unexpected growth behavior of the C_{60} overlayer perpendicular to the surface, which follows the $[110]$ direction and not the typical $[111]$ direction of an epitaxial fcc crystal growth mode [61]. In contrast to the gold case, the reconstructed surface leaves the silver surface unaffected and exhibits a $\text{Ag}(110)c(4 \times 4)\text{-C}_{60}$ symmetry.

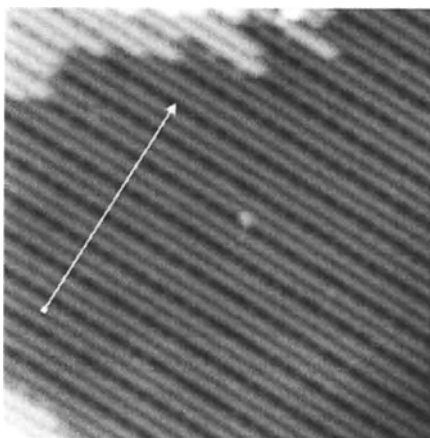


Fig. 2.12. STM topograph ($27 \times 27 \text{ nm}^2$) of the $\text{Au}(110) 1 \times 5$ substrate reconstructed area in between the C_{60} islands. Tip bias: $+0.36 \text{ V}$, current: 0.21 nA , $T = 5 \text{ K}$

2.4.2 Electronic Properties

The strong interaction of C_{60} with both the Ag and $\text{Au}(110)$ surfaces manifesting itself as major atomic rearrangements, is also expected to show up in the electronic structure of the C_{60} film in both cases. One way to look at the electronic structure is by means of the STM performing tunneling spectroscopy, i.e. measuring the normalized conductance $(dI/dV)/(I/V)$ as

a function of tip–sample voltage V (see Chap. 5). This provides a local view of the electronic structure. As presented in section 2.3 for alkali metals on semiconductors, electronic-structure investigations have also been performed employing direct- and inverse- photoemission spectroscopy which are, however, spatially averaging. In the following we discuss the results for Ag(110)c(4×4)-C₆₀.

We have performed tunneling spectroscopy on C₆₀ monolayer and multilayer covered Ag(110) surfaces. The spectrum for the 1-ML coverage exhibits features above and below but close to the Fermi level. They are both found at energies further away from the Fermi energy, when additional layers are adsorbed (not shown, see [61]). These measurements are consistent with our observations in photoemission (see below). The electronic structure of fullerene films has been studied by UPS and IPES [54–56,58], but other techniques have also been applied to measure the energy position of the HOMO and/or determine the band gap of solid C₆₀. Unfortunately, the experimentally obtained values for the energy positions of the HOMO- and LUMO-derived bands and the corresponding band gap E_g differ substantially [63]. We have performed UPS and IPES measurements at $h\nu = 21.2$ eV and 9.5 eV, respectively, as a function of C₆₀ monolayer coverage at room temperature [64]. Fig. 2.13 shows the clean-silver spectra at the bottom, which are dominated by the occupied silver 3d bands between -4 eV and -8 eV. The 1-ML spectra reveal the characteristic [54–56,58] five-peak structure of the occupied regime and the four unoccupied spectral features with the HOMO and LUMO peaks, respectively, closest to the silver Fermi level, E_F . However, in contrast to the literature the LUMO spectral feature crosses E_F rendering the ordered 1-ML C₆₀ metallic. With the deposition of the 2nd monolayer additional features occur in the spectra (cf. Fig. 2.13). Using the multilayer spectra (top curves) the 2-ML spectra can be interpreted as superposition of a 1-ML spectrum and a 2nd-layer spectrum shifted by ~ 0.9 eV for the unoccupied states and ~ 0.2 eV for the occupied states away from the Fermi level, respectively. The multilayer spectra are then dominated by these shifted peaks with a clear semiconducting signature, as they are known in the literature. Also shown in Fig. 2.13 are the workfunction changes with respect to the clean surface: after an initial increase of 0.40 eV, the workfunction practically stays constant within ± 0.05 eV.

The opposite energetic shifts of the occupied and unoccupied molecular levels reveal the metallic image-charge screening in the photoemission final states [13]. In an initial-state picture the energy position of the adsorbed molecule is pinned to the vacuum level. It changes simultaneously as a function of coverage for, e.g., the HOMO and LUMO, as $E_{2\text{nd ML}} = E_{1\text{st ML}} + \Delta\phi$ in contrast to our observation in Fig. 2.13 with no further workfunction changes after the 1st-ML deposition. On the other hand, the final-state picture yields

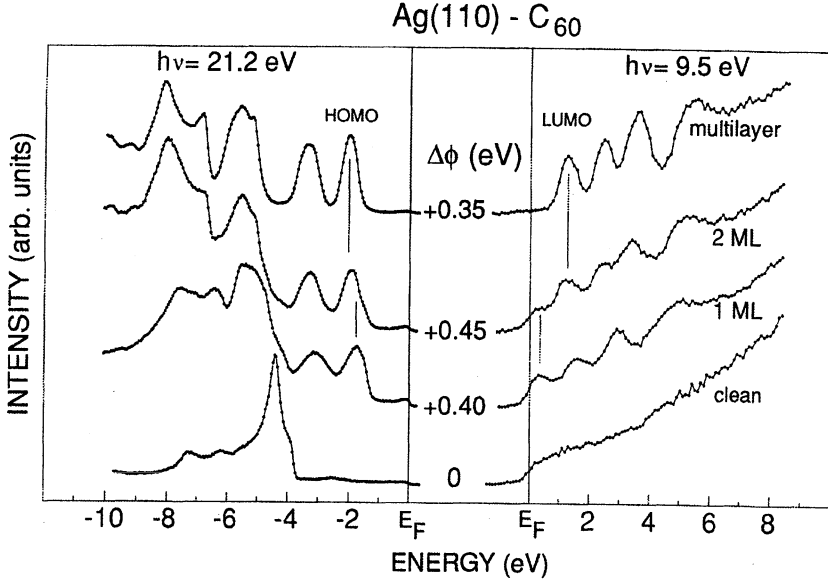


Fig. 2.13. Direct and inverse photoemission spectra C_{60} on Ag(110) as a function of monolayer coverage. Also given are the workfunction changes $\Delta\Phi$ with respect to the clean surface. (From Ref. [64])

$$E_{\text{measured}} = E_{\text{initial}} + E_{\text{relax}}, \quad (2.1)$$

where

$$E_{\text{relax}} = E_{\text{intra, screen}} + E_{\text{inter, screen}} + (-e^2/4z) \quad (2.2)$$

takes into account the intra- and intermolecular screening energies and the image-charge screening term. The image charge is induced in the silver surface by the positive (negative) C_{60} ion, with the screening energy depending on the average distance z of the photo-ionized (electron-added in case of IPES) molecule to the image plane of the surface. This naturally explains the coverage dependence and the opposite shifts observed for the UPS and IPES features in Fig. 2.13. Our findings are in agreement with valence-band photoemission and C 1s core-hole absorption of C_{60} on Au(110) and their interpretation [65] and similar measurements for xenon on Au(110) [13].

As a test we have also deposited C_{60} on Si(100) wafers and measured the analogous UPS and IPES curves as a function of coverage (see Fig. 2.14 and Table 2.2). In accordance with our interpretation above we do not observe any shifts of the HOMO and LUMO, as we do not expect any metallic image-charge screening for the Si(100) surface. Table 2.2 summarizes the measured values of E_g for the C_{60} monolayer and multilayer on Ag(110) and Si(100). Now it is evident why the literature values of the energy positions of the C_{60}

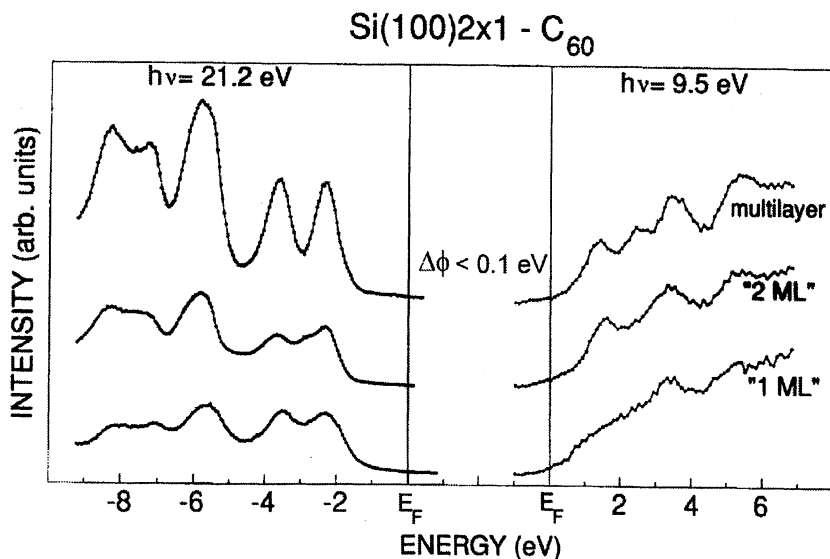


Fig. 2.14. Direct and inverse photoemission spectra of C_{60} on Si(100) as a function of coverage. Also given is the workfunction change $\Delta\phi$ with respect to the clean surface

HOMO and LUMO and the corresponding gaps differ so much: there is a coverage dependence, a substrate dependence (metallic or semiconducting), and a dependence on the experimental technique applied, as each technique implies a different relaxation energy.

As an intermediate conclusion we may state that the highly symmetric and unique cluster C_{60} exhibits different "signatures" depending on the substrate and on the spectroscopic technique employed. The screening and relaxation energies involved in these spectroscopies are well-known and established phenomena for any highly-correlated electronic system, as already manifested in free d-metal atoms, solids and compounds. Asymmetric core-

Table 2.2. Experimentally determined minimum gap E_g and HOMO–LUMO peak differences for C_{60} on Ag(110) and Si(100).

Method	E_g (eV)	HOMO–LUMO gap (eV)	specimen
UPS/IPES	2.2	3.1	> 2 ML on Ag(110)
UPS/IPES	1.1	2.0	1 ML on Ag(110)
UPS/IPES	2.0 ± 0.2	3.8 ± 0.2	≥ 1 ML on Si(100)2 \times 1

level lineshapes and satellite structures in the valence-band emission of, e.g., nickel are just two such examples. New in the present case of C_{60} adsorption is the cluster-substrate interaction which opens an additional dimension to the "old" question of screening and relaxation. As we shall present in the next section, this will hold true for any type of cluster and not just C_{60} , and will affect both the spectral emission from the valence bands as well as for the localized levels. Questions like the metallicity of low-dimensional systems will hence find a natural answer.

2.5 Electronic Response within the Cluster–Surface Interaction

Nanostructures which include low-dimensional systems and clusters of nanometer size exhibit new and unexpected properties. Their experimental verification, however, may in itself exhibit surprises and reveal novel phenomena linked to nanometer dimensions. For example, there is an ongoing controversy about cluster size effects in photoelectron spectroscopy: Are they due to changes in the electronic structure of the clusters, i.e. initial-state effects, or caused by the final-state effect originating from the positive charge remaining on the cluster in the photoemission process? [66]

The electron energy measured in a photoemission experiment is influenced by the interaction with the remaining positive charge. In general, this is a dynamic process on a femtosecond timescale. An adiabatic and a sudden regime have been distinguished. In the adiabatic limit the ejected electron picks up the relaxation energy, while this is missing in the sudden limit, giving rise to satellite structures or asymmetric line shapes. It was suspected [67] that these dynamic effects could be different for finite systems, like, e.g., clusters. Finally, in low dimensional samples the localized positive charge has been discussed as one possible effect responsible for unusual spectral shapes in photoemission [68], in particular near the Fermi level.

Here we present experimental UPS results of the Fermi-level onset of quasi size-selected silver clusters produced by controlled condensation in preformed nanopits on a graphite surface [69]. They show that in these experiments neither the sudden nor the adiabatic approximation is applicable, but that dynamic effects on a femtosecond timescale determine the spectral shape of the Fermi-level onset. The experiments are described in detail in [7,70]. We present results for four different cluster sizes (cf. Fig. 2.15). Details of cluster growth by atom diffusion and aggregation are given in Chap. 3. The mean number of atoms in the clusters measured by a combination of STM and transmission electron microscopy are $N = 4 \times 10^2$, 9×10^2 , 2×10^3 , and 4×10^3 , respectively. The silver clusters produce a distinct additional signal in the photoemission spectra. In Fig. 2.16 we present the spectra (taken at $T = 40$ K with $h\nu = 21.2$ eV) of the silver clusters, for the four different cluster sizes of Fig. 2.15. The corresponding STM and the UPS data were

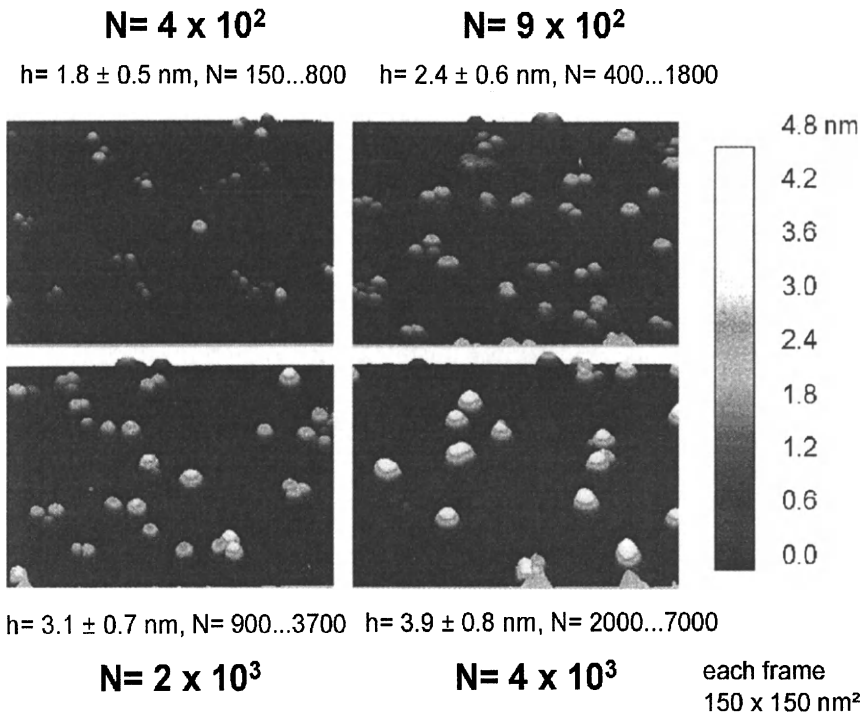


Fig. 2.15. STM topographs ($150 \times 150 \text{ nm}^2$) of silver clusters on graphite (HOPG) produced by controlled condensation in preformed nanopits. The height distribution h and the mean number of atoms in one cluster N are given in the figure

taken in situ on one and the same sample. For comparison we have also measured the analogous spectrum of a thick polycrystalline silver film and show it as the lowest curve in Fig. 2.16. All four spectra show similar features. Especially we note that at the Fermi energy there is a kink as sharp as the Fermi-level onset of bulk silver (see arrows in Fig. 2.16). At first glance these spectra seem to indicate that the clusters are non-metallic, because there is a vanishing density of states at the Fermi energy, which, however, is impossible for such large clusters and inconsistent with the pronounced plasmon resonance at approximately 3.5 eV which we observed (not shown) for all cluster sizes employing electron energy loss spectroscopy. The existence of a cluster plasmon proves the collective motion of the s-electrons typical for a metal.

Instead, we explain the observed spectral shape with a model which takes into account the influence of the photohole remaining on the metal cluster during the photoemission process and the cluster-surface interaction. The photohole finally vanishes, when an electron is regained from the surface. In a simple model, the elimination of the positive charge is described by

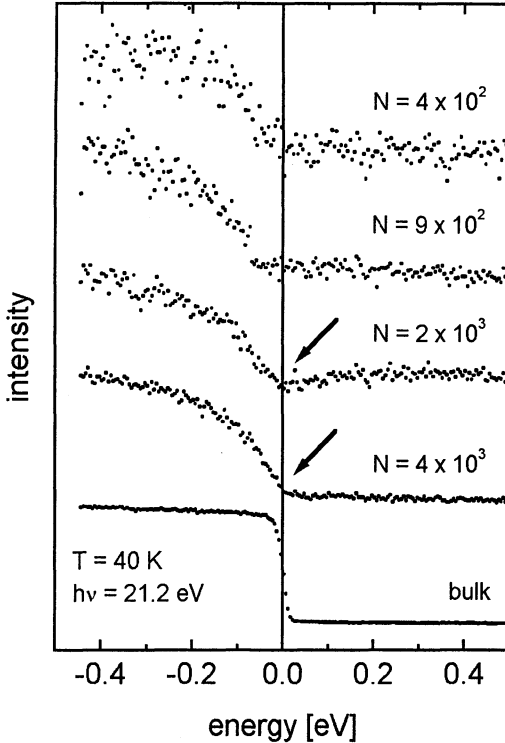


Fig. 2.16. The spectral contribution of the silver clusters in UPS, measured for the four different samples of Fig. 2.15. The bottom curve represent the bulk silver spectrum. $T = 40$ K. (From Ref. [70])

a characteristic time τ , with the probability that the charge is eliminated during the time interval $[t, t + dt]$ given by $P(t) dt = (1/\tau) \exp(-t/\tau) dt$.

In order to calculate the energy of the electron arriving at the electron energy analyzer, we take a Coulomb potential acting on the electron on its way from the cluster to infinity. If the charge on the cluster is neutralized after a time t , when the electron has covered a distance vt , this gives the energy shift W for this electron. The measured spectra average over a large number of photoelectrons with different times t . This leads - even if all clusters are identical in radius R and coupling to the surface - to a distribution of energy shifts $P(W)$. The measured Fermi onset at low temperatures (where the thermal broadening is negligible) is formed by a superposition of sharp Fermi edges shifted with the distribution $P(W)$. With E_B being the binding energy this leads to the calculated spectra $S(E_B)$ near E_F , which are plotted for several values of $C = R/v\tau$ in Fig. 2.17. For $C \ll 1$ the Fermi onsets are shifted by W_{\max} . This corresponds to the case of free clusters with an infinite lifetime of the photohole [71]. For $C \gg 1$ we observe Fermi onsets at $E_B = 0$, because the photohole is immediately neutralized. In the intermediate range, we find curves with different curvatures, depending on the value of C . To check on the influence of the cluster size distribution we assumed a Gaussian distribution with $R = \bar{R} \pm 0.2\bar{R}$, which corresponds to the measured cluster

sizes [69]. Calculated $S(E_B)$ curves for the different values of C were summed up with varying $W_{\max} \propto 1/R$ according to the size distribution. The results are also shown in Fig. 2.17. It is remarkable that the curves for $C > 1$ are almost unchanged by the cluster size distribution. Especially the kink at the Fermi energy remains as sharp as for monodispersed clusters.

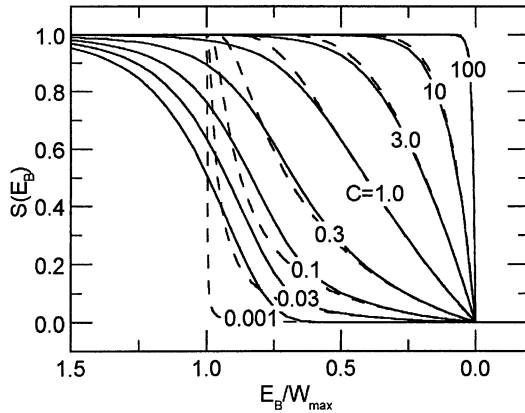


Fig. 2.17. Photoemission spectra calculated for several values of $C = R/vt$ assuming clusters identical in radius (dashed lines) and assuming a Gaussian distribution with $R = \bar{R} \pm 0.2\bar{R}$ (solid lines). (From Ref. [70])

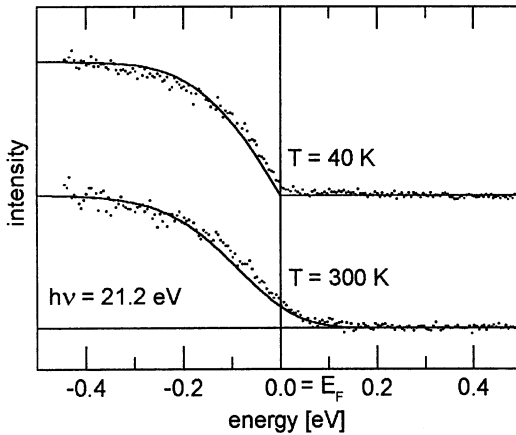


Fig. 2.18. Comparison of the experimental spectra (data points) for clusters with 4×10^3 atoms and calculated spectra (solid lines) for $T = 40$ K and $T = 300$ K. (From Ref. [70])

In Fig. 2.18 we show that the experimental spectrum for the clusters with $N = 4 \times 10^3$ atoms at $T = 40$ K can be described by our model if we choose the parameters $C = 3.0$ and $W_{\max} = 0.49$ eV. In a recent work [72] we proved that the same model with identical parameters applies also to the d-band structure of the silver clusters. Together with the mean cluster radius $\bar{R} = 2.5$ nm this results in $\tau = 0.3 \times 10^{-15}$ s which is of the expected order of magnitude for a coupling with significant cluster–surface interaction as in the case of

graphite. We also show in Fig. 2.18 the cluster signal at the Fermi energy with the measurements made at room temperature. In this case the thermal broadening of the Fermi edge masks the sharp kink at the Fermi energy, which is also evident in the calculated spectrum using identical parameters as for low temperatures, but convoluting a room temperature Fermi function. Therefore, performing UPS with high energy resolution at low temperatures was crucial for the clarification of the cluster–surface interaction.

2.6 Summary

In this chapter we have shown how a combination of experimental techniques can be used to address various aspects of the adsorbate-surface interaction, with the adsorbates being atoms, molecules and clusters. Example systems were presented along an increasing interaction strength in going from physisorption to chemisorption. In particular, we have presented and discussed xenon on graphite, alkali metals on silicon surfaces, C_{60} on noble-metal surfaces, and Ag clusters on graphite. Our ansatz employs the so-called "complete surface-science experimental approach", in which the electronic and geometric structure of each sample system and their interdependencies were investigated by direct and inverse photoemission, scanning tunneling microscopy and spectroscopy, LEED and Auger Electron Spectroscopy. Ideally, this ansatz left the sample system in the same UHV apparatus to apply all techniques mentioned and hence minimize any problems related to their cumbersome preparation and characterization.

As an important result of our investigation we like to point out that screening and relaxation effects, which were well known in electron spectroscopic measurements of single atoms, molecules, and solids, now also manifest themselves in the new dimension of the adsorbate-surface interaction. Although we may say that a very high energy resolution combined with low temperatures is a necessary requirement to observe such subtle effects at all, it is also true as a rule of thumb that the stronger the adsorbate-surface interaction is the more important screening phenomena do become. Two example systems for this stronger adsorbate-surface interaction have been discussed in this chapter: For C_{60} on noble-metal surface image-charge screening is the prevailing phenomenon, which renders the composite surface C_{60} -Ag metallic for the monolayer coverage. On the other hand, for Ag clusters on graphite the dynamic response during a small, but finite time period (femtoseconds) causes a distribution of energy shifts for all spectral features, which may mask ground-state properties of the electronic structure as measured in photoemission, i.e. the composite system Ag clusters on graphite appears to be semiconducting, although the clusters are clearly metallic. As stated above we can deduce that the occurrence of such final-state effects point to strongly bound species, i.e. chemisorption.

Future research will have to enlarge the base of relevant adsorbate-surface systems, in particular it will be interesting and necessary to study systems with different numbers of electrons per bandwidth interval near the Fermi level, and with a different degree of correlation. The latter would certainly comprise superconducting clusters and substrate surfaces in any combination.

Acknowledgment: We thank our collaborators H. Bernhoff, R. Dudde, T. Düttemeyer, B. Grimm, K. J. Magnusson, M. Pollmann, and D. Purdie for their help.

References

1. N. W. Ashcroft, N. D. Mermin, *Solid State Physics*, Holt-Saunders (1976).
2. R. J. Birgeneau and P. M. Horn, *Science* 232, 329 (1986).
3. W. J. Nuttall, K. P. Fahey, M. J. Young, B. Keimer, R. J. Birgeneau, and H. Suematsu, *J. Phys. Condens. Matter* 5, 8159 (1993).
4. M. Hamichi, A. Q. D. Faisal, J. A. Venables, and R. Kariotis, *Phys. Rev. B* 39, 415 (1989).
5. H. Hong, C. J. Peters, A. Mak, R. J. Birgeneau, P. M. Horn, and H. Suematsu, *Phys. Rev. B* 40, 4797 (1989).
6. B. Grimm, H. Hövel, M. Pollmann, and B. Reihl, *Phys. Rev. Lett.* 83, 991 (1999).
7. H. Hövel, T. Becker, D. Funnemann, B. Grimm, C. Quitmann, and B. Reihl, *J. Electron Spectros. Rel. Phenom.* 88-91, 1015 (1998).
8. B. Joos, B. Bergersen, and M. L. Klein, *Phys. Rev. B* 28, 7219 (1983).
9. A. D. Novaco and J. P. McTague, *Phys. Rev. Lett.* 38, 1286 (1977).
10. J. Villain, *Phys. Rev. Lett.* 41, 36 (1978).
11. K. Hermann, J. Noffke, and K. Horn, *Phys. Rev. B* 22, 1022 (1980).
12. T. Mandel, M. Domke, and G. Kaindl, *Surf. Sci.* 197, 81 (1988).
13. K. Horn, K. H. Frank, J. A. Wilder, and B. Reihl, *Phys. Rev. Lett.* 57, 1064 (1986).
14. *Metallization and Metal-Semiconductor Interfaces*, ed. by I. P. Batra, NATO Advanced Study Institute, Series B, Vol. 195 (Plenum, New York 1989).
15. J. E. Northrup, *J. Vac. Sci. Technol. A* 4 1404 (1986).
16. S. Ciraci and I. P. Batra, *Phys. Rev. Lett.* 58, 1982 (1987).
17. I. P. Batra and S. Ciraci, *Phys. Rev. B* 37, 8432 (1988).
18. R. Ramirez, *Phys. Rev. B* 40, 3962 (1989).
19. S. Ciraci and I. P. Batra, *Phys. Rev. Lett.* 56, 877 (1986); 60, 547 (1988); *Phys. Rev. B* 37, 2955 (1988).
20. H. Ishida and K. Terakura, *Phys. Rev. B* 40, 11519 (1989).
21. K. Kobayashi, Y. Morikawa, K. Terakura, and S. Blügel, *Phys. Rev. B* 45, 3469 (1992); Y. Morikawa, K. Kobayashi, and K. Terakura, *Surf. Sci.* 283, 377 (1993).
22. P. Krüger and J. Pollmann, *Appl. Phys. A* 59, 487 (1994), *Phys. Rev. B* 47, 1898 (1993).
23. Y. Ling, A. J. Freeman, and B. Delley, *Phys. Rev. B* 39, 10144 (1989).
24. T. Kato, K. Ohtomi, and M. Nakayama, *Surf. Sci.* 209, 131 (1989).
25. H. Tochiyama, M. Kubota, M. Miyao, and Y. Murata, *Surf. Sci.* 158, 497 (1985).

26. B. Reihl and K. O. Magnusson, *Phys. Rev. B* 42, 11839 (1990).
27. K. O. Magnusson and B. Reihl, *Phys. Rev. B* 39, 10456 (1989).
28. B. Reihl, S. L. Sorensen, R. Dudde, and K. O. Magnusson, *Phys. Rev. B* 46, 1838 (1992).
29. B. Reihl, unpublished.
30. R. Clauberg, K. H. Frank, J. M. Nicholls, and B. Reihl, *Surf. Sci.* 189, 44 (1987).
31. S. Ossicini, C. Arcangelia, and O. Bisi, *Phys. Rev. B* 42, 7671 (1990).
32. I. Moullet, W. Andreoni, and M. Parrinello, *Phys. Rev. B* 46, 1842 (1992).
33. I. Moullet, unpublished.
34. J. D. Levine, *Surf. Sci.* 34, 90 (1973).
35. T. Aruga, H. Tochiyara, and Y. Murata, *Phys. Rev. Lett.* 53, 372 (1984).
36. P. Soukiassian, J. A. Kubby, P. Mangat, Z. Hurych, and K. M. Schirm, *Phys. Rev. B* 46, 13471 (1992).
37. T. Abukawa and S. Kono, *Phys. Rev. B* 37, 9097 (1988).
38. Y. Enta, T. Kinoshita, S. Suzuki, and S. Kono, *Phys. Rev. B* 36, 9801 (1987); 39, 1125 (1989).
39. P. Segovia, G. R. Castro, A. Mascaraque, P. Prieto, H. J. Kim, and E. G. Michel, *Phys. Rev. B* 54, R14277 (1996).
40. L. S. O. Johansson and B. Reihl, *Phys. Rev. Lett.* 67, 2191 (1991); *Appl. Surf. Sci.* 56-58, 486 (1992).
41. L. S. O. Johansson and B. Reihl, *Phys. Rev. B* 47, 1401 (1993).
42. L. S. O. Johansson and B. Reihl, *Surf. Sci.* 287/288, 524 (1993).
43. Y. C. Chao, L. S. O. Johansson, and R. I. G. Uhrberg, *Phys. Rev. B* 52, 2579 (1995); *Phys. Rev. B* 55, 7198 (1997).
44. Y. C. Chao, L. S. O. Johansson, and R. I. G. Uhrberg, *Phys. Rev. B* 54, 5901 (1996).
45. A. J. Smith, W. R. Graham, and E. W. Plummer, *Surf. Sci.* 243, L37 (1991).
46. I. P. Batra, *Phys. Rev. B* 43, 12322 (1991).
47. E. G. Michel, P. Pervan, G. R. Castro, R. Miranda, and K. Wandelt, *Phys. Rev. B* 45, 11811 (1992).
48. L. S. O. Johansson T. Düttemeyer, L. Duda, and B. Reihl, *Phys. Rev. B* 58, 5001 (1998).
49. M. K.-J. Johansson, S. M. Gray and L. S. O. Johansson, *Phys. Rev. B* 53, 1362 (1996).
50. R. Souda, W. Hayami, T. Aizawa, and Y. Ishizawa, *Surf. Sci.* 290, 245 (1993); *Phys. Rev. B* 47, 9917 (1993); *Phys. Rev. B* 48, 17255 (1993).
51. J. A. Martin-Gago, M. C. Asensio, F. Soria, P. Aebi, R. Fasel, D. Naumovic, and J. Osterwalder, *Surf. Sci.* 307-309, 995 (1994).
52. A. Brodde, T. Bertrams, and H. Neddermeyer, *Phys. Rev. B* 47, 4508 (1993).
53. For a review see K. Prassides and H. Kroto, *Physics World* 5, 44 (1992).
54. T. Takahashi, S. Suzuki, T. Morikawa, H. Katayama-Yoshida, S. Hasegawa, H. Inokuchi, K. Seki, K. Kikuchi, S. Suzuki, K. Ikemoto, Y. Achiba, *Phys. Rev. Lett.* 68, 1232 (1992).
55. P. J. Benning, D. M. Poirier, T. R. Ohno, Y. Chen, M. B. Jost, F. Stepniak, G. H. Kroll, J. H. Weaver, J. Fure, R. E. Smalley, *Phys. Rev. B* 45, 6899 (1992).
56. T. R. Ohno, Y. Chen, S. E. Harvey, G. H. Kroll, J. H. Weaver, R. E. Hauffer, R. E. Smalley, *Phys. Rev. B* 44, 13747 (1991).
57. Y. Kuk, D. K. Kim, Y. D. Suh, K. H. Park, H. P. Noh, S. J. Oh, S. K. Kim, *Phys. Rev. Lett.* 70, 1948 (1993).

58. R. W. Lof, M. A. van Veenendaal, B. Koopmans, H. T. Jonkman, G. A. Sawatzky, *Phys. Rev. Lett.* 68, 3924 (1992).
59. N. Troullier and J.L. Martins, *Phys. Rev. B* 46, 1754 (1992).
60. E. L. Shirley and S. G. Louie, *Phys. Rev. Lett.* 71, 133 (1993).
61. T. David, J. K. Gimzewski, D. Purdie, B. Reihl, R. R. Schlittler, *Phys. Rev. B* 50, 5810 (1994).
62. J. K. Gimzewski, S. Modesti, and R. R. Schlittler, *Phys. Rev. Lett.* 72, 1036 (1994).
63. B. Reihl, in: *Science and Technology of Fullerene Materials*, eds. P. Bernier et al., *Mat. Res. Soc. Symp. Proc. Vol. 359*, 375 (1995).
64. D. Purdie, H. Bernhoff, and B. Reihl, *Surf. Sci.* 364, 279 (1996).
65. A. J. Maxwell, P. A. Bruhwiler, A. Nilsson, N. Martensson, P. Rudolf, *Phys. Rev. B* 49, 10717 (1994).
66. G. K. Wertheim, S. B. DiCenzo, and S. P. Youngquist, *Phys. Rev. Lett.* 51, 2310 (1983); M. G. Mason, in: *Cluster Models for Surface and Bulk Phenomena*, NATO-ASI Series B, vol. 283, Plenum Press New York (1992), page 115.
67. J. W. Gadzuk and M. Sunjic, *Phys. Rev. B* 12, 524 (1975).
68. B. Dardel, D. Malterre, M. Grioni, P. Weibel, and Y. Baer, *Phys. Rev. Lett.* 67, 3144 (1991).
69. H. Hövel, Th. Becker, A. Bettac, B. Reihl, M. Tschudy, and E. J. Williams, *J. Appl. Phys.* 81, 154 (1997); H. Hövel, Th. Becker, A. Bettac, B. Reihl, M. Tschudy, E. J. Williams, *Appl. Surf. Sci.* 115, 124-127 (1997).
70. H. Hövel, B. Grimm, M. Pollmann, B. Reihl, *Phys. Rev. Lett.* 81, 4608-4611 (1998).
71. M. Seidl, K.-H. Meiwes-Broer, and M. Brack, *J. Chem. Phys.* 95, 1295 (1991).
72. H. Hövel, B. Grimm, M. Pollmann, B. Reihl, *Eur. Phys. J. D* 9, 595 (1999).

3 Growth of Metal Clusters at Surfaces

Harald Brune

3.1 Introduction

In the present chapter we will discuss the creation of surface supported metal clusters through nucleation and growth in Molecular Beam Epitaxy (MBE). MBE is commonly used to grow thin epitaxial films from the vapour phase onto single crystal substrates under ultra-high vacuum (UHV) conditions [1]. In thin film growth the nucleation of stable clusters is the preliminary step to the immobilisation and further condensation of film atoms or molecules. If one is close to thermodynamic equilibrium it is irrelevant how and where this nucleation takes place and the film topography is given by the balance of the free energies of film surface, substrate surface, and the interface between the two [2]. However, the prerequisite to the growth is to be away from thermodynamic equilibrium, at least to some extent, since detailed balance arguments require that in equilibrium all processes appear with equal rates, including condensation and desorption. Therefore, the entire growth system hardly adopts equilibrium and is thus in a state always influenced to a certain extent by kinetics. The history of when and where the film atoms were added begins to matter and the film morphology is determined by the microscopic pathway taken by the system. This pathway comprises the interplay of only a few elementary processes, such as terrace diffusion of single adatoms, cluster formation and diffusion, as well as aggregation and interlayer diffusion. All diffusion events take place on a time scale set by the coverage divided by the deposition flux. The importance of kinetics in thin film growth was realized early on, leading to the development of mean-field nucleation theory which relates the cluster density to monomer and cluster diffusion rates and to cluster dissociation rates [3–5]. Continued interest in the elementary processes of epitaxial growth has led to the quantification of energy barriers for the most important of these processes. On the experimental side techniques such as Field Ion Microscopy (FIM) [6–9] and by Variable Temperature Scanning Tunnelling Microscopy (VT-STM) [10] have been used. On the theoretical side the barriers for these processes were evaluated using approximative methods such as the Embedded Atom Method (EAM) or Effective Medium Theory (EMT) and ab initio theoretical concepts based on Density Functional Theory (DFT). The study of the elementary processes in-

volved in epitaxial growth and their relation to cluster and film morphology are topics of ongoing interest.

The knowledge gained from such surface science studies can be employed to grow clusters at surfaces with well defined size, shape and even regular spacing. The idea of assembling supported clusters from adatoms might appear unusual to readers belonging to the cluster community, as typically in cluster physics, clusters are condensed, cooled and mass selected in the gas phase before they eventually become (soft-) landed onto the support. The aim of the present chapter is to convince the reader of the high degree of control on cluster size, shape and spacing that can be achieved in the MBE growth of clusters at single crystal surfaces. Of course, the attempt to grow well defined structures at specific sites is a struggle against the statistics inherent in deposition and in the Brownian character of thermally activated adatom diffusion. The statistics of both processes expresses itself in the clusters' spatial and size distributions. These distributions are coupled to each other and their width and shape are given by well known scaling laws of nucleation [11–14]. However, we will show below that there are means to overcome statistical limitations and, to some extent, to create order out of randomness.

The chapter is organised as follows. We will start with an introduction to the elementary processes of epitaxial growth. In the following Sects. 3.3–3.5 we discuss cluster growth on isotropic metal surfaces. First we give a brief outline of the basic results of nucleation theory in its simplest form of stable and immobile dimers. We show experiments that confirm the theory for that case and permit a direct link between nucleation densities and terrace diffusion parameters. In Sect. 3.4 we discuss the transitions from fractal to various compact clusters tracing back the cluster shape to the atomic processes of aggregation. The last section on isotropic substrates is devoted to Ostwald ripening as a means of preparing compact two-dimensional (2D) clusters with a narrow size distribution centred at almost any desired value. Section 3.6 discusses cluster growth on anisotropic metal substrates where diffusion and/or sticking anisotropy give rise to the formation of elongated clusters, and in the extreme case to 1D atomic chains. In the following section we turn to surfaces with dislocation networks or Moiré patterns. Such substrates provide inhomogeneous potential energy surfaces that may guide diffusing monomers to singular sites where they nucleate clusters. The result is a periodic cluster array, the regularity in spacing being accompanied by narrow cluster size distributions. The nucleation of metal clusters on single crystal oxides and sulfides is discussed in Sect. 3.8. We will end this chapter with a brief conclusion and outlook.

3.2 The Elementary Processes of MBE Growth

In molecular beam epitaxy, film atoms are deposited onto the substrate with thermal energy (~ 0.1 eV) and flux F (expressed in atoms per lattice site,

equivalent to monolayers (ML), per second). Typically, the energy gained in the adsorbate–substrate bond formation is effectively dissipated into the lattice, so that adatoms are brought into thermal equilibrium with the substrate already at their site of impact [15]. This can be inferred for instance from experiments at low temperatures revealing cluster sizes in agreement with the predictions of statistical growth, allowing no diffusion at all [10,16–18]. Therefore transient jumps are the exception, if they exist at all for metal on metal adsorption. (In contrast, there is evidence for transient motion for the dissociative chemisorption of molecules on metals [19,20].) Transient non-thermal motion has to be distinguished from thermal motion with small energy barriers towards next nearest neighbours [21] and clusters [22,23]. For certain combinations of elements the adsorption energy might be used to trigger transient exchange processes, even at low T [24]. However, in the absence of exchange and sufficiently far away from clusters or adatoms, the film atoms generally adsorb where they land from the vapour phase. From there on, adatom diffusion sets in.

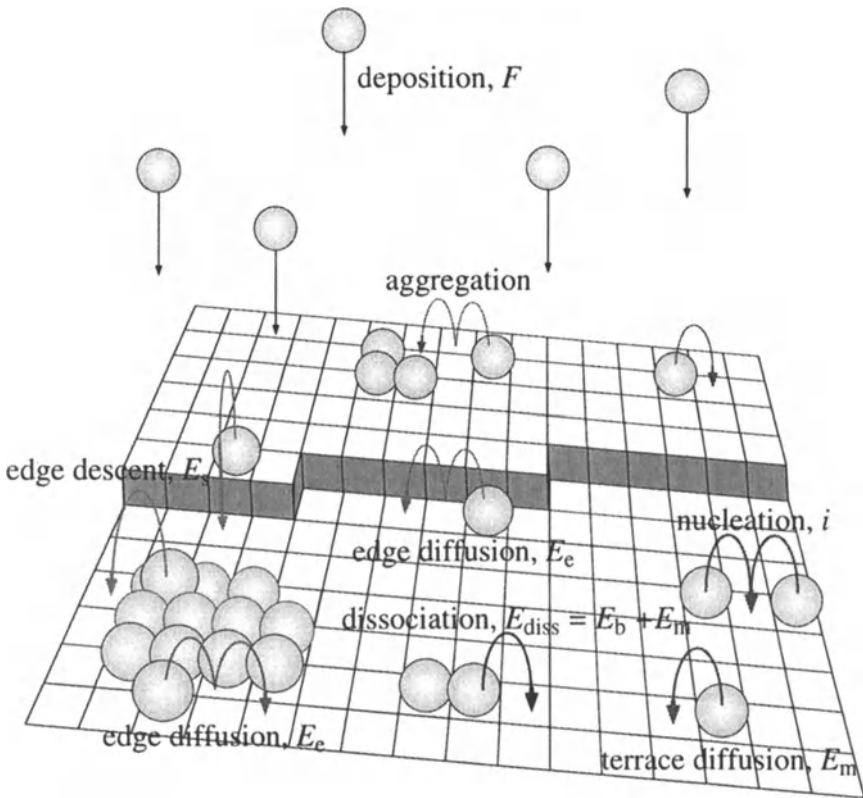


Fig. 3.1. The elementary diffusion processes of MBE growth

The diffusion processes participating in epitaxial growth are thermally activated jumps mostly in the form of straight adatom movements between adjacent lattice sites. However, concerted motion of several atoms may also be involved. Transition State Theory (TST) [25] assumes that the atoms stay between two subsequent jumps long enough in their adsorption wells to thermally equilibrate, in addition, recrossing of the barrier is assumed to be negligible. These assumptions are justified if the energy barrier separating the binding from the transition site satisfies $E \ll k_B T$. The jump rate of a diffusion process of type n is then given by Boltzmann statistics as $\nu_n = \nu_{0,n} \exp(-E_n/k_B T)$, with the attempt frequency $\nu_{0,n}$ typically being in the range $10^{12} - 10^{13}$ Hz of Debye frequencies.

Terrace migration of single adatoms (E_m in Fig. 3.1) is the most fundamental of these diffusion processes. It gives rise to nucleation of islands on substrate terraces or to step flow growth at elevated temperatures. Depending on the density of simultaneously diffusing particles, one distinguishes the *collective* diffusion coefficient (also known as *chemical* or *Fickian* diffusion coefficient) of an ensemble of mutually interacting particles from the *tracer* (or *intrinsic*) diffusion coefficient describing the mean square displacement of one isolated random walker per unit time [26]. For typical growth rates the density of diffusing particles is rather small (the monomer density $n_1 < 10^{-3}$ adatoms per adsorption site). The mean inter particle distance is therefore large compared to typical interaction ranges for metal adatoms on metal substrates [27,28] and cluster densities are determined by the tracer diffusion coefficient D defined as

$$D = D_0 \exp(-E_m/k_B T), \text{ with } D_0 = \frac{1}{4} \nu_0, \quad (3.1)$$

where D is expressed in substrate unit cells per second. The factor of $1/4$ in D_0 is valid for 2D diffusion, whilst in one dimension this factor is $1/2$.

Diffusion across the terrace ends when the adatoms collide with one or more of their own (for sake of simplicity structural and chemical defects are not considered). Depending on the lateral bond energy (E_b in Fig. 3.1) and the number of neighbors, the formed cluster remains stable or decays again. A stable nucleus is a cluster that is large enough to grow more rapidly than it decays on the time-scale of deposition. One defines the critical cluster size i by the number of atoms in the smallest stable nucleus minus one, i.e., attachment of one atom turns a critical cluster into a stable one.

The two-dimensional cluster shape is determined by the mobility of aggregating adatoms along the cluster edge (barrier E_e in Fig. 3.1), more specifically along straight steps and around kinks and corners, in the case of trigonal substrates also from 1-fold coordinated corner to 2-fold coordinated step sites. Low mobility leads to ramified clusters with fractal dimension, similar to Diffusion Limited Aggregation (DLA) scenarios [29–31]. Anisotropic terrace diffusion imposed by the substrate symmetry, in conjunction with anisotropic sticking to the edges, can lead to the formation of 1D monoatomic wires.

Compact 2D clusters are created if edge diffusion is fast compared to the cluster growth rate. The thermodynamic 2D equilibrium shape forms when corner and kink crossing become activated.

The rate of adatom descent at cluster steps determines whether or not adatoms deposited onto the cluster top are able to descend to the substrate level before other adatoms become deposited onto the cluster top. In the latter case a stable nucleus forms on top of the cluster giving rise to the kinetic growth of 3D clusters, whereas in the first case clusters remain 2D until they coalesce. An adatom approaching a descending step encounters a barrier E_s for descent which is typically larger than E_m . The extra diffusion barrier to overcome atomic steps was experimentally discovered [32] and theoretically conjectured [33] long ago. It is caused by the strongly reduced coordination of the adatom to the substrate in the transition state, or in the case of exchange interlayer diffusion, by the reduced coordination of the complex transition state configuration. Ab initio calculations give insight into why exchange diffusion is preferred for specific step orientations and combinations of metallic elements whereas for other step orientations and systems interlayer diffusion is a simple roll down process. The values for E_s derived from such calculations [34–36] can be compared to results from FIM experiments [15,37]. Experiment and theory agree that the mechanism of interlayer diffusion is strongly system specific. Complementary to direct FIM inspection there are also various indirect ways to infer experimental estimates on E_s from layer occupation numbers [38,39], from the nucleation probability on cluster tops [40], from island decay in suitable geometries [41], or from step densities [42,43] and slopes of mounds evolving through kinetic roughening [44,45]. The values of E_s derived from such observations of the film morphology are all effective barriers for interlayer diffusion. Despite their relevance for predicting the epitaxial growth morphology and cluster dimension, association to a particular microscopic interlayer diffusion process is often not unambiguously possible. For sake of simplicity the following discussion of metal on metal systems will be restricted to 2D islands only, i.e., the STM images below show monolayer high islands. For kinetically caused 3D island growth the reader is referred to the references given in this paragraph.

3.3 Nucleation

We will now address the relationship between cluster density and terrace diffusion coefficient, cluster binding energy and deposition flux. For simplicity we discuss the case of 2D islands in the irreversible growth regime where the critical cluster is a monomer, i.e., $i = 1$, and a dimer is stable and immobile. For an extension of this discussion to more complicated cases of larger critical cluster sizes, 3D clusters, incomplete condensation, or cluster diffusion, we refer to [4,46–48].

The simplest MBE growth scenario has monomers as the only mobile species and dimers represent stable nuclei. In the initial phase of deposition the adatoms arriving from the gas phase with rate F diffuse with rate D on the substrate terraces until they meet a second diffusing adatom and create a dimer. As deposition proceeds, the number of dimers will increase linearly until their density n_2 becomes comparable to the monomer density n_1 . From there on, the probabilities that a diffusing monomer encounters one of its own or a dimer become comparable and the growth of stable clusters starts to compete with the nucleation of new ones. As a consequence, the increase in density of stable nuclei n_x (x standing for any size that is stable, $x \geq 2$) levels off until n_x saturates at a coverage of typically $\theta_{\text{sat}} \sim 0.15$ ML. When the saturation island density is reached, the mean free path of diffusing adatoms is equal to the mean island separation and any further deposition will exclusively lead to island growth since all adatoms reach and attach themselves to existing islands. At coverages beyond 0.2 ML the 2D clusters start to coalesce until the monolayer film percolates at typically $\theta = 0.5$ ML. For metal on metal growth this scenario was experimentally verified for Ag/Pt(111) by means of VT-STM [49]. The STM observations ranged from the pure nucleation phase with its linear increase of n_x and an average cluster size of 2–3 atoms up to saturation and finally coalescence. Figure 3.2 shows the 2D Ag clusters formed at three deposition temperatures in the irreversible growth regime. To avoid coarsening of the metastable clusters they have been imaged at the deposition temperature.

Mean-field nucleation theory relates the saturation cluster density n_x to the ratio of diffusion D to deposition rate F and to the cluster binding energy E_i by the following expression for complete condensation and 2D clusters [4,50]

$$n_x = \eta(\theta, i) \left(\frac{D}{F} \right)^{-\chi} \exp \left(\frac{E_i}{(i+2)k_B T} \right), \quad \text{with } \chi = \frac{i}{i+2}. \quad (3.2)$$

From (3.2) it becomes clear that the most direct link between n_x and D is obtained at low temperatures where $i = 1$. Then the cluster binding energy is by definition $E_i = 0$, and (3.2) reduces to

$$n_x = \eta(\theta, 1)(D/F)^{-1/3}, \quad (3.3)$$

with $\eta(\theta, 1) = 0.25$ in the coverage range of saturation [4,18]. At higher temperature the cluster binding energy E_i can for instance be expressed in a pair binding model involving multiples of the energy per bond E_b [46] (for dimers $E_i = E_b$, see Fig. 3.1).

The Arrhenius plot of n_x in Fig. 3.2d shows a roughly linear regime in the range of $10^5 \leq D/F \leq 10^9$, in accordance with (3.3). The application of this equation to $n_x(T)$ data inferred from STM has proven to yield valid numbers for the barrier and attempt frequency of terrace diffusion [51,52,49]. It was pointed out that the accuracy of these numbers can be considerably

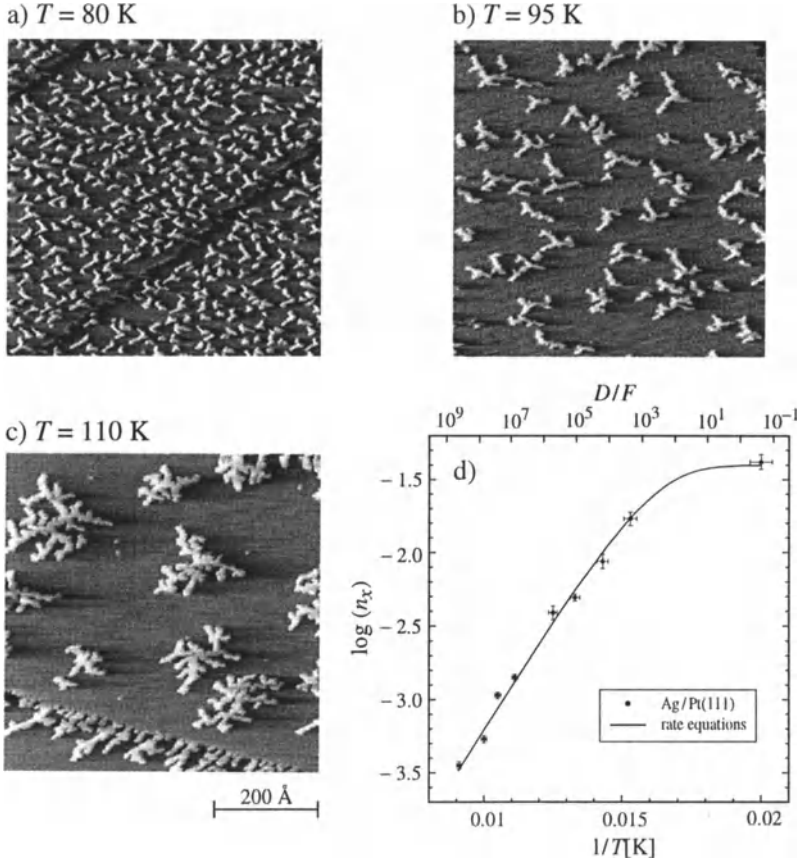


Fig. 3.2. Variation of saturation island density with temperature for deposition of $\theta = 0.12$ ML Ag onto a Pt(111) surface. (a)–(c). Common length scale STM images taken at the respective deposition temperatures. (d) Arrhenius plot of the saturation island densities in the temperature regime where dimers are stable nuclei (for the applied deposition flux of $F = 1.1 \times 10^{-3}$ ML/s). Experimental island densities for Ag/Pt(111) are compared with results from integrating rate equations from mean-field nucleation theory using self-consistent calculations for capture numbers (solid line) [18]

increased in analyzing cluster densities down to lower temperatures [18,53]. There ($D/F < 10^5$), however, (3.3) no longer holds since monomers are diffusing too slowly to reach each other and create all nuclei during deposition. Therefore monomers are stable nuclei ($i = 0$) in the sense that many of them remain monomers *during* deposition. However, they continue to diffuse after deposition. This post-deposition mobility gives rise to cluster growth and cluster nucleation in the time between deposition and imaging with STM. It is clearly visible in Fig. 3.2d that this leads to a reduced slope ending with

a plateau where all islands are created after deposition and thus n_x becomes independent from the deposition temperature [49,54]. Post-deposition mobility can be accounted for in rate equations using mean-field nucleation theory. These equations have been integrated using self-consistent solutions to the capture numbers derived by Bales et al. [55]. As a result, the experimental data for Ag/Pt(111) could be fitted over a range of almost 10 orders of magnitude in D/F yielding $E_m = 168 \pm 5$ meV and $\nu_0 = 7 \times 10^{13 \pm 0.3} \text{ s}^{-1}$ [18]. Similar precision was obtained by Bott et al. for Pt(111) self-diffusion [53].

The experiments studying $n_x(T)$ in the irreversible growth regime ($i = 1$) yield a precision for E_m close to that of state-of-the-art FIM studies, which up to now presented our most precise source of information on atomic diffusion barriers. In contrast to FIM, however, the nucleation method is not limited to highly refractive elements and therefore enables the study of monomer diffusion for a wide range of metal and semiconductor systems. In the past, the influence of isotropic strain on diffusion on fcc(111) surfaces was studied [56]. This inspired ab initio calculations revealing that the binding energy of the bridge site becomes less affected by strain than that of the three-fold hollow site, leading to the observed strong effect of strain on E_m , which is the difference of both energies [57,41]. Also systems with extremely small diffusion barriers which were formerly inaccessible by experiment, such as Al/Al(111) and Al/Au(111)-($\sqrt{3} \times 22$) could be addressed [10,58,59]. However, the nucleation studies revealing extremely small diffusion barriers ($E_m < 100$ meV) systematically yielded prefactors smaller by several orders of magnitude than the universal one discussed above. This may be due to a breakdown of transition state theory, since E_m becomes of the order of $k_B T$ and the adatoms no longer thermally equilibrate between jumps. The low apparent prefactors might equally well indicate the limit of applicability of the nucleation method, i.e., of (3.3). Since the E_m values are small, the cross-sections of cluster formation get sensitive to small variations in the binding energy of an adatom approaching one of its own. Such variations can be substrate-mediated interactions [60] which in the case of surface sites can be of extremely long range. If these interactions were repulsive over several lattice constants, cluster formation would be delayed with the result of larger cluster densities than expected from (3.3). Application of this equation would then lead to smaller apparent prefactors.

Apart from this extreme case of exceptionally small E_m values, Eqs. (3.2) and (3.3) have been subjected to extensive experimental tests and to tests with Kinetic Monte Carlo (KMC) simulations, all showing that for the general case these equations unambiguously relate D/F to n_x . Therefore the cluster density at terraces can be tuned for each system to the desired value by choosing an adequate substrate temperature and/or deposition flux. The average cluster size is then adjusted by the coverage.

The cluster size distributions obtained by nucleation on homogeneous substrates all fall onto common curves that depend only on the critical cluster

size i [61–64,12]. The scaling law is obtained when the size distributions are plotted as $n_N \times \langle N \rangle^2 / \theta$ vs. $N / \langle N \rangle$, where N and $\langle N \rangle$ are the size and its mean value, and n_N is the density of N -sized clusters. The shape of the size distributions is Gaussian with a Half Width at Half Maximum (HWHM) of $\sigma \sim 0.55$ in the case of $i = 1$ [12]. We will discuss below several methods for significantly narrowing down the size distributions. For the prospect of growing small clusters the low temperature plateau of constant cluster densities shown in Fig. 3.2d is of interest, since through post-nucleation, exponentially decreasing island size distributions with mostly dimers and trimers are formed.

3.4 Aggregation

The similarity of patterns formed in non-equilibrium growth processes in physics, chemistry and biology is conspicuous, and many attempts have been made to discover common mechanisms underlying their formation [65,66]. The most prominent examples are snowflakes. The correlation of their shape with meteorological crystal growth conditions leads to valuable conclusions concerning the meteorology in the upper atmosphere [67]. The manifold growth patterns in nature commonly evolve from non-equilibrium growth at an interface with material transport via diffusion being the rate limiting process. Exactly these conditions govern aggregation of clusters at single crystal surfaces held at low temperatures. Aggregation of submonolayer coverages of metal atoms is often two-dimensional and therefore easier to understand than many more complex growth patterns. Nevertheless, it bears enough complexity that knowledge gained in 2D may be transferred to the understanding of more complicated 3D patterns appearing in nature. This makes low temperature metal aggregation an ideal model system for tracing back mechanisms by which single diffusion events of atoms along a growing interface translate can determine an overall pattern. STM opened access to the structure of monolayer high 2D aggregates formed by atoms at surfaces [68]; and its extension to variable low temperatures enabled the investigation of the kinetics underlying the formation of such patterns down to temperatures where irreversible growth occurs [69–72]. The knowledge gained from microscopic studies in turn provides control over the shape of MBE grown surface-supported clusters. In this section we discuss ramified clusters with fractal dimension, and various compact island shapes formed on isotropic single crystal metal surfaces. For the sake of controlled cluster growth we focus on the link between cluster shape and system parameters and growth conditions.

Let us assume we perform an MBE experiment on an isotropic substrate at low temperature. If adatoms would irreversibly stick to the site where they hit the growing aggregate ($i = 1$), and if edge diffusion were entirely frozen, then so-called Diffusion Limited Aggregation (DLA) clusters [29,30] would form with monoatomic branches spreading out into random directions. The

formation of branches is caused by low mobility along the edge leading to the so-called *tip- or Saffman-Taylor instability* [73]. This instability is due to the fact that protrusions at the edge resulting from statistical fluctuations capture more adatoms from the terrace diffusion field than straight or concave step sections. If these atoms cannot be transported away sufficiently fast, the protrusions grow out as a branch with a width related to the step edge diffusion barrier [74–77]. With increasing length the branch tip becomes exposed to an increased solid angle of aggregating adatoms causing ramification into more branches. The continued ramification leads to the self-similarity of the DLA patterns and a fractal Hausdorff [66] dimension of 1.7, i.e., the cluster area increases as $A = r^{1.7}$, with r being the radius.

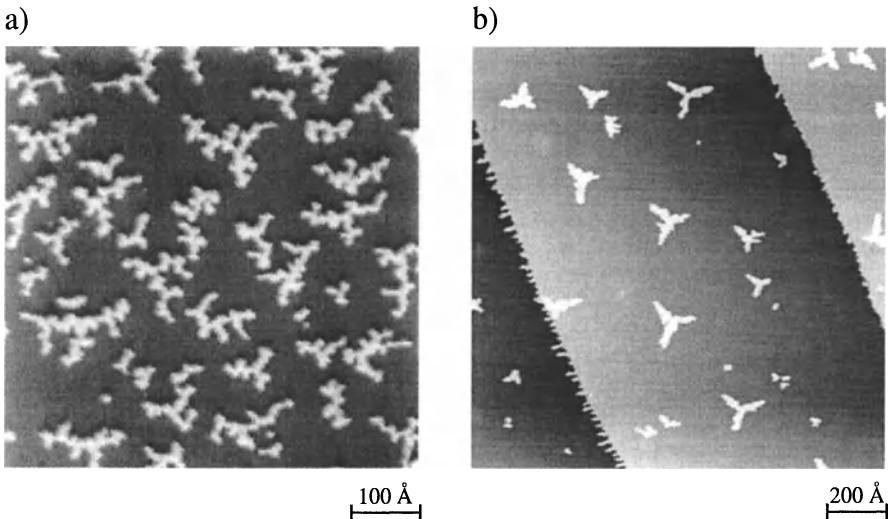


Fig. 3.3. Dendritic patterns formed for low temperature metal deposition onto hexagonal close-packed substrates. (a) Pt(111) homoepitaxy at 180 K ($\theta = 0.094$ ML) [78]. (b) Pt heteroepitaxy on Ru(0001) at 300 K ($\theta = 0.1$ ML) [79]

However, the classical DLA clusters have so far never been observed in MBE growth on single crystal surfaces and there are strong indications that, if ever observed, DLA growth will be the exception for these systems. Depending on the surface symmetry there are different reasons for the observed lack of DLA clusters. On square lattices there are only one-fold coordinated step sites and therefore edge diffusion has a barrier comparable to that of terrace diffusion [80–82]. As soon as terrace diffusion (the process needed for cluster formation) gets thermally activated, diffusion along the cluster edge is also activated. This generally leads to compact square clusters at any deposition temperature [83,84,54,85–88]. An exception is the formation of non-compact islands observed for Cu/Ni(100), thought to be due to the strain induced increase of step length [89]. On hexagonally close-packed surfaces,

there are corner sites with 1-fold lateral coordination and sites at straight $\langle 1\bar{1}0 \rangle$ -oriented edges with 2-fold coordination. Atoms bound to the two-fold edge sites have high E_e values and thus low mobility and this can indeed generate branched clusters (see Figs. 3.2a–c and 3.3). However, in contrast to DLA clusters these clusters have trigonal symmetry and their branches are at least 2–3 atoms wide. Nevertheless their fractal dimension is close to the DLA value of 1.7. These islands have been called dendrites by analogy with other patterns in nature revealing preferred growth directions [70]. The three preferred growth directions lead to Y-shapes for small cluster sizes (see Figs. 3.2a, b and 3.3b - due to the absence of further branching these Y's have a Hausdorff dimension of 1) and to a triangular envelope for larger dendrites (see Figs. 3.2c and 3.4c). Note that in the case of Pt/Ru(0001) shown in Fig. 3.3b the substrate has hcp stacking leading to a rotation of the dendrites by 60° from terrace to terrace.

The reason for the slightly larger than monoatomic branch width in dendrites is connected with the relaxation of 1-fold corner atoms to 2-fold step sites. This relaxation is asymmetric being one of the reasons for the preferred growth directions [72,78]. The diffusion asymmetry from corner to edge sites can be inferred from the ball model in Fig. 3.4a. It shows that there are two different micro-facets **A** ($\{100\}$ -facet) and **B** ($\{111\}$ -facet) formed by the $\langle 1\bar{1}0 \rangle$ -oriented edges of any pseudomorphic cluster placed on a hexagonal substrate. Diffusion from a 1-fold corner-site (**C**) to an **A**-step involves an hcp-site at just the right distance from the corner, whereas diffusion to the **B**-step has either an on top site or the hcp-site very close to the island as transition state. From these geometric considerations one would generally expect that corner to **A**-step diffusion has a lower barrier than diffusion from a corner to a **B**-step. This picture is confirmed by EMT [90,80] calculations for a number of metal/metal combinations for which dendritic growth perpendicular to **A**-steps is observed [10]. Fig. 3.4b shows the case of Ag/Pt(111). Diffusion from a corner site to an **A**-step has a barrier as low as E_m , whereas diffusion to a **B**-step costs 5 times as much activation energy. KMC simulations (see Fig. 3.4d) have demonstrated that the asymmetric corner relaxation leads to a preferred population of **A**-steps over **B**-steps and thus to the three preferred growth directions. The experimentally observed cluster shapes for Ag/Pt(111) (see Fig. 3.4c) are very well reproduced by these simulations [72].

For some systems such as Cu and Pt/Pt(111), however, EMT calculations show the corner-to-edge diffusion asymmetry to be the other way around [10]. For Pt/Pt(111) this result is confirmed by a recent ab initio calculation [91]. Pt reveals a large tensile stress leading to a strong inward relaxation of the island edge. This can facilitate diffusion towards **B**-steps as it renders the hcp-site located between corner and **B**-step more attractive as a transition state; in the absence of strain this site is located too close to the island (see 3.4a). Despite this inversion of the corner to **A**- and **B**-step diffusion asymmetry,

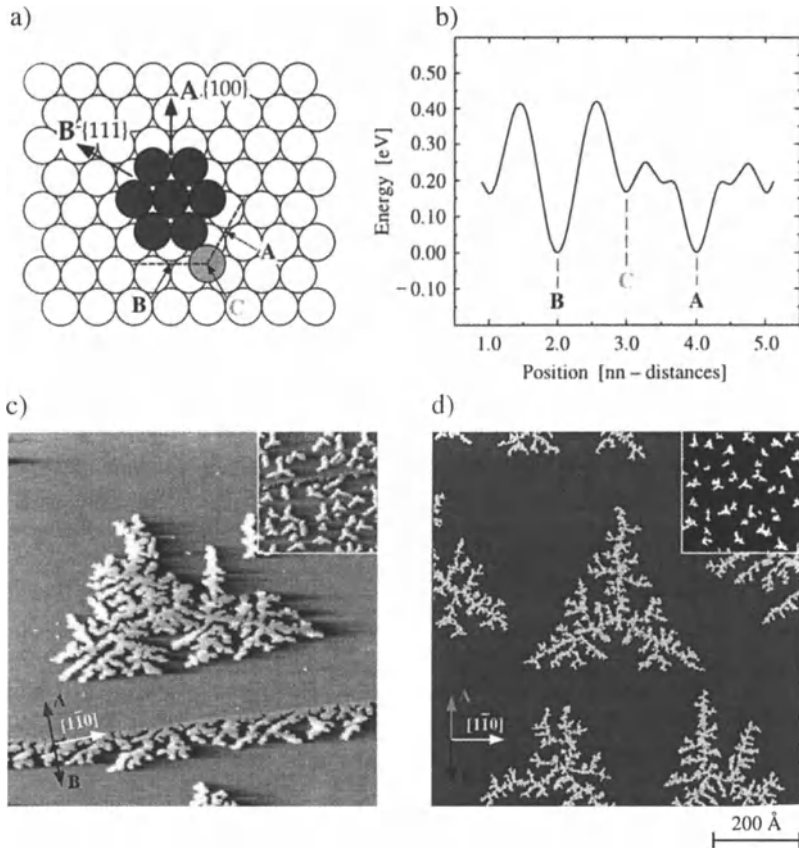


Fig. 3.4. (a) Ball model of a heptamer on a hexagonal lattice revealing the existence of A- and B-steps. (b) The EMT calculation for Ag/Pt(111) shows that this geometric difference implies different corner diffusion barriers. (c) Experiment for Ag/Pt(111) at 130 K (*main figure*) and 80 K (*inset*). (d) The KMC simulations identify the difference in corner diffusion as the origin of dendritic growth; they reproduce the dendrites found in experiment (scale bar common to (c) and (d)) [72]

Pt/Pt(111) shows dendritic growth with the same preferred growth direction as Ag/Pt(111) and Ag/Ag(111), i.e., perpendicular to A-steps (see Fig. 3.3a).

Apart from the aspect of diffusion along the island edge treated so far it was pointed out that the different diffusion paths of atoms from the terrace towards the two kinds of steps give rise to a second asymmetry favoring population of A-steps [72]. Considering the different diffusion paths from second-neighbor fcc sites via hcp sites towards a heptamer one readily finds that there is a strong statistical preference of 3/6 vs. 1/6 for attachment to A- vs. B-steps, whereas corners are visited with a probability of only 2/6 [10]. The attachment asymmetry is more general than corner diffusion

asymmetry. Both effects have to be considered in conjunction to understand and predict cluster morphology. If corner diffusion is faster towards **B**-steps, it could counterbalance attachment and random growth may result. For systems with faster diffusion towards **A**-steps, both effects push towards exclusive population of **A**-steps resulting in dendritic growth perpendicular to these steps. For Pt/Pt(111) there is a slightly smaller barrier for diffusion from corners to **B**-steps. This anisotropy is too weak to fully counterbalance the preferred attachment to **A**-steps, leading to dendrites with preferred growth perpendicular to these steps. In agreement with this weak preference, the trigonal symmetry is less pronounced for that system (see Fig. 3.3a).

The growth of dendrites with trigonal symmetry can be considered as understood. This growth morphology is generally expected for low temperature ($i = 1$) 2D cluster aggregation on hexagonal metal surfaces. Dendritic clusters undergo several mutations upon increasing the temperature and/or reducing the flux, i.e., when going to $i > 1$ conditions. For some systems the branches begin to grow into random directions, lifting the trigonal symmetry of the low temperature dendrites [70]; in addition the branches become wider. Despite a considerable effort, the shape transition from dendritic to random isotropic growth patterns [68,77,92] is not yet fully understood. Also a quantitative understanding of the relationship between the degree of edge diffusion and the branch width is presently lacking. We briefly review the present understanding of isotropic fractal clusters. Similar to the dendrites, these patterns reveal the fractal dimension 1.7 of classical DLA aggregates [68].

Examples of this species are shown in Fig. 3.5. The Au clusters formed at room temperature on Ru(0001) have branches 60 atoms wide and the Ag aggregate grown at 220 K on Pt(111) has an average branch width of 20 ± 2 atoms [77]. The cluster branches spread out and meander into random directions. Formation of partial surface dislocations between fcc- and hcp-stacking has been suggested to understand the loss of directional growth [10]. This was motivated by the fact that both systems shown in Fig. 3.5 reveal considerable misfit possibly leading to partial dislocations where strain is relieved. Each stacking variation from hcp to fcc alters the orientation of **A**- and **B**-steps and thus the branches' preferred growth directions. Regular stacking faults could thus explain the observed random isotropic growth. Partial surface dislocations have been observed for Ag/Pt(111) upon a critical island size [93], which is however beyond the branch width for which the onset of random growth is observed. It was thus proposed that partials were generated by kinetics, and a KMC model showed that the transition from dendritic to random fractal clusters can be generated that way [10]. A second possible origin for the loss of directional growth is the detachment from 1-fold coordinated corner sites since $i > 1$. The arguments of corner diffusion and diffusion paths for attachment to the different step types given above have to be re-examined under reversible growth. This might well lead to the finding

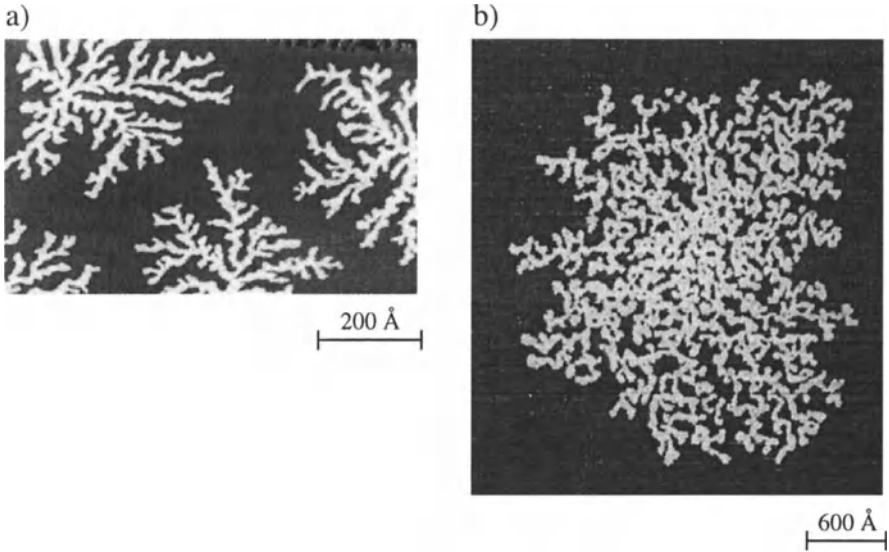


Fig. 3.5. Examples for random fractals typically following dendrites at elevated temperatures. (a) STM image of Au islands grown on Ru(0001) at room temperature ($F = 3.3 \times 10^{-3}$ ML/s, $\theta = 0.30$ ML) [68]. The aggregate's branches spread out into random directions. Although the branches are significantly wider than those of the DLA clusters, the aggregate's fractal dimension is the DLA value of 1.72. (b) STM image of a Ag fractal grown on Pt(111) at 220 K similarly showing wide branches that frequently alter their growth direction ($F = 1.1 \times 10^{-3}$ ML/s, $\theta = 0.12$ M) [94]

that frequent detachment of one-fold atoms leads to the observed random growth directions.

The branch width was related to edge diffusion, both by analytic models [88,76,74] and through KMC simulations [95]. The basic idea underlying these studies is that the lateral impingement rate I competes with the rate for an adatom to scan the edge of a compact seed particle. The seed particle stays compact until the edges reach a critical width w where both rates become comparable. At that point nucleation of protrusions at the edge can no longer be flattened out and the aggregate becomes unstable upon ramification through the Mullins–Sekerka instability introduced above. This instability argument defines the critical cluster size for ramification and equally the mean branch width taken on by the cluster after ramification. However, the models presented in the literature disagree on the exact dependence of w on D_e/I , where $I = F/n_x$, and D_e is the 1D diffusion rate at the edge. Therefore these models give contradicting results for the attempt frequencies and barriers for edge diffusion when experimental data of $w(T)$ (available for Ag/Ag(111) and Ag/Pt(111) [77]) are analyzed. Realistic models have to incorporate a set of parameters where diffusion barriers are attributed to step atoms de-

pending on their coordination and the step orientation. Evidently this leads to the well known problem of models invoking too many parameters to allow a sensible comparison with experiment. This problem is encountered also in recent papers dealing with cluster diffusion, a similarly complex issue [96]. Ways out are either to simplify the model, or to use additional input from calculations to ascribe reasonable values to the barriers. The first attempt has been made by disregarding the difference between **A**- and **B**-steps with a view to extracting an effective E_e value and its attempt frequency for diffusion between 2-fold coordinated sites along straight steps [10]. The result ($E_e = 370$ meV and $\nu_0 = 1 \times 10^{13}$ Hz) is more realistic than the values obtained from the former analysis [77]. The second attempt will certainly follow in the near future. Ab initio calculations become feasible for larger systems allowing the calculation of various energy barriers for adatom displacement along cluster edges [97,81,98,91], thus generating valuable input parameters for KMC simulations. Random fractal islands with wide branches will certainly be of ongoing interest until we can answer the open question of how they evolve from dendrites and how their branch width is linked to the edge diffusion barrier.

With increasing deposition temperature various compact clusters form on hexagonal substrates. These polygonal clusters are first triangles, whose orientation is set by the trigonal symmetry of the dendrites preceding them at low temperatures. Examples for triangular clusters with preferred orientation are Co/Ru(0001) [92,99,100], Co/Pt(111) [101], and Fe/Au(111) [102,103]. The triangles are followed at larger deposition temperature by hexagons, which can mutate back into triangles before reaching the thermodynamic equilibrium shape, by further increasing the deposition temperature or by annealing. The equilibrium shape of a 2D cluster on a trigonal substrate is a hexagon where, according to the Wulff construction, the different surface free energies of **A**- and **B**-steps are reflected in the lengths of these facets [104]. Since interlayer diffusion generally has different barriers for both step types their respective length, or in the case of triangles their orientation, can be decisive for 2D versus 3D growth.

The sequence of the various polygonal compact clusters has been reported for Pt/Pt(111) [105], and is reproduced in Fig. 3.6. At 400 K triangles bound by **A**-steps were observed, at 455 K hexagons, and deposition at 640 K yielded again triangles, this time bound by **B**-steps. Finally the clusters attained the quasi-hexagonal equilibrium shape, which was proven to be independent of cluster history (compare Figs. 3.6d1 and d2).

Inversion of triangle orientation with increasing deposition temperature was a puzzle for theorists [107–109,81] until it recently became solved by a repetition of the experiments under extremely clean evaporation conditions [106]. Taking up the Pt/Pt(111) experiments once more was motivated by a discrepancy between results on island orientation and interlayer diffusion, and ab initio calculations [36]. The experiments led to the important

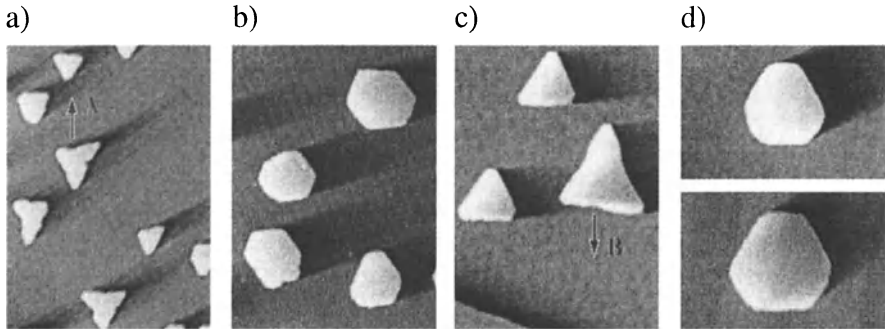


Fig. 3.6. The formation of various polygonal islands during Pt(111) homoepitaxy [105,106]. The deposition temperatures are as follows. (a) $T = 400$ K ($\theta = 0.08$ ML, $1300 \times 1900 \text{ \AA}^2$), (b) $T = 455$ K ($\theta = 0.14$ ML, $770 \times 1100 \text{ \AA}^2$), (c) $T = 640$ K ($\theta = 0.15$ ML, $2300 \times 3300 \text{ \AA}^2$), (d1) $T = 710$ K ($\theta = 0.08$ ML, $1540 \times 1100 \text{ \AA}^2$), (d2) deposition at $T = 455$ K as in (b) and subsequent annealing to 710 K for 1 min ($\theta = 0.08$ ML, $630 \times 900 \text{ \AA}^2$). Common deposition flux $F = 1 \times 10^{-2}$ ML/s

conclusion that minute amounts of impurities (CO) were responsible for inversion of triangle orientation. Depositing at extremely low CO partial pressure ($p_{\text{CO}} \leq 5 \times 10^{-12}$ mbar, see Fig. 3.7) the island shape evolves from dendrites via fractals with large branches to triangles only bound by B-steps; the triangles increase in size with increasing temperature but they keep their orientation [106].

Before we go into the details specific to the system Pt/Pt(111), let us discuss the mechanism generally responsible for triangular cluster shapes on trigonal substrates. In the kinetic regime, the cluster shape is determined by the growth rate perpendicular to A and B steps, i.e., by the rate with which adatoms accumulate at both steps. The slowly growing facets prevail in the final crystal shape whereas the faster ones disappear during growth, as is generally the case in crystal growth. There are two temperature regimes, in each of which the step progression rate is determined by different atomic processes. At temperatures where diffusion around corners is frozen, and thus material exchange between both step types inhibited, the diffusion rates along the two edges will determine the cluster shape. The step type with fast edge diffusion grows smoothly with few kinks, whereas at the other step edge diffusion is slow and growth involves many kinks. Hence, the first step propagates only slowly whereas the latter progresses rapidly [105,109]. We note, however, that this first case can be artificial since barriers for corner crossing are often quite close to those for edge diffusion [98,91]. Therefore the temperature regime where corner crossing is frozen but edge diffusion active is small, if it exists at all. Much more important is the case where corner crossing becomes activated. The diffusion bias around the corners between A and B-steps, and the progression of the respective steps, is given by the difference in their

adatom binding energies, $\Delta E_{\mathbf{A}-\mathbf{B}} = E_{\mathbf{A}\rightarrow\mathbf{c}} - E_{\mathbf{c}\rightarrow\mathbf{A}} - E_{\mathbf{c}\rightarrow\mathbf{B}} + E_{\mathbf{B}\rightarrow\mathbf{c}}$ (\mathbf{c} denotes the one-fold corner site) [110]. Thus the shape of compact islands, in the kinetic regime, depends on a small difference of large activation energies. If both edges bind adatoms equally well compact irregular spherical islands form, if there is a small energy difference triangles form, their orientation being given by the sign of the binding energy difference.

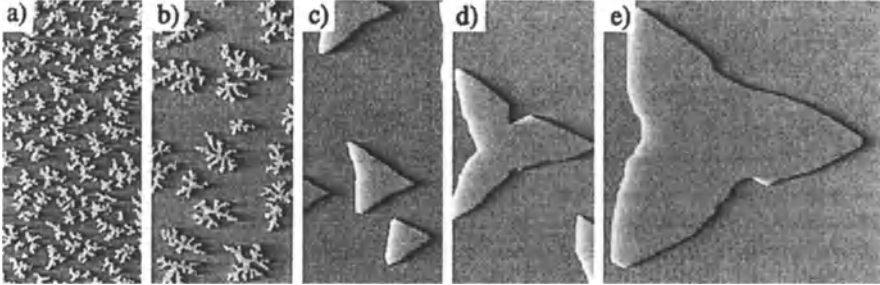


Fig. 3.7. Island morphology for 0.17 ML Pt/Pt(111) under extremely clean evaporation conditions (during evaporation $p_{tot} < 2.0 \times 10^{-11}$ mbar) [111]. The deposition temperatures are as follows. (a) $T = 200$ K, (b) $T = 300$ K, (c) $T = 400$ K, (d) $T = 500$ K, (e) $T = 600$ K ($630 \times 900 \text{ \AA}^2$), image sizes (a–d) $670 \times 1340 \text{ \AA}^2$, (e) $1340 \times 1340 \text{ \AA}^2$

Accordingly, the triangles with **B**-steps shown in Figs. 3.7c–e are due to better binding to **A**-steps. Note that this is in contradiction with recent results from theory [91]. The binding energy difference obtained in these calculations is weak, but it favors population of **B**-steps, and this is not in agreement with their prevalence. Triangles with the inverse orientation, however, are due to minor amounts of CO present during deposition. The effect of CO adsorption on the energetics and kinetics of edge diffusion has not yet been explored theoretically.

The example of Pt(111) homoepitaxy shows that the island shape is a sensitive indicator for small energy differences which can therefore be rather useful to test ab initio calculations. It is clear that the binding energy difference between the two step types is a thermodynamic argument, however, it also determines the diffusion bias around corners in the kinetic regime. In thermodynamic equilibrium the step formation energy comes into play. The total step length is then reduced by the formation of quasi hexagons. The example of Pt(111) homoepitaxy also shows that the effect of defects does not belong to the past even in careful UHV experiments. Chemically influenced diffusion is now being systematically addressed for a number of metal/metal systems [112,113].

3.5 Coarsening

Coarsening by Ostwald ripening is a means of preparing compact surface supported 2D clusters with narrow size distributions and average sizes $\langle N \rangle$ adjustable from 3 to 10^3 atoms [69]. This is of particular importance, since currently much experimental and theoretical effort focuses on exploring the evolution of chemical and physical properties of small agglomerations of matter as a function of the number of atoms they contain [114].

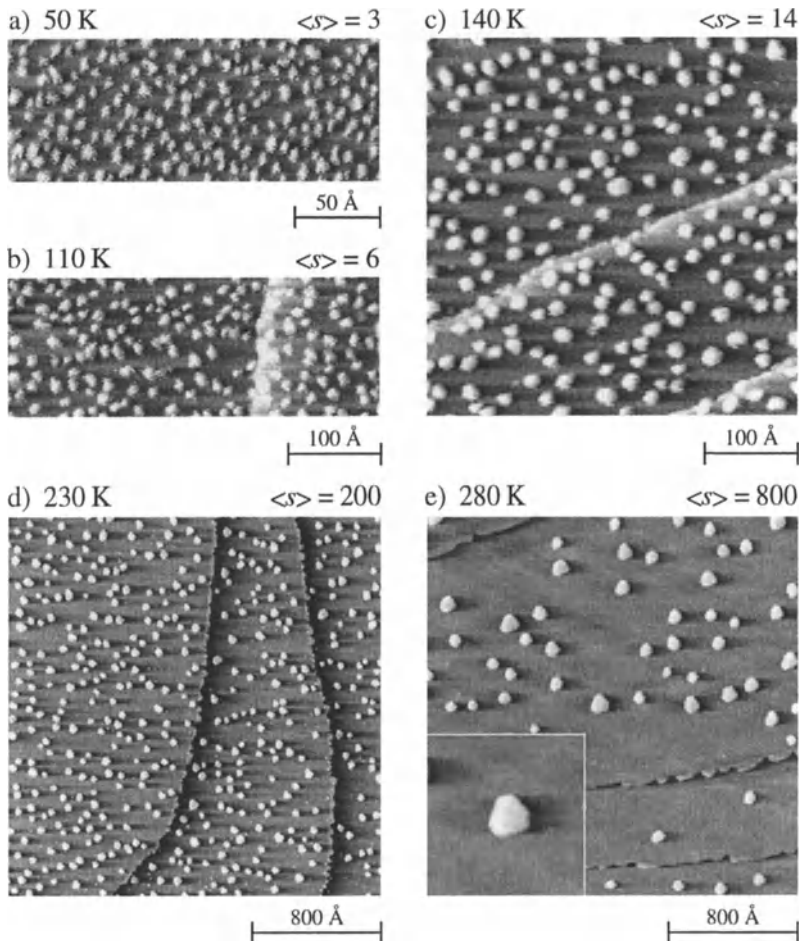


Fig. 3.8. STM images showing Ostwald ripening in two dimensions as a way to create compact 2D islands with their size $\langle N \rangle$ being well defined by the annealing temperature [69]. The starting population of mostly dimers and trimers was produced via deposition of 0.1 ML Ag onto Pt(111) at 50 K

Ostwald ripening [115–117] is caused by a more rapid dissociation of smaller islands in favor of larger ones. Through the availability of surface microscopy at the atomic level this phenomenon has received considerable attention in two dimensions [69,118,119].

The starting point for the preparation method is a large density of small clusters, mostly dimers, prepared by deposition of ~ 0.1 ML at a temperature chosen such that there is little mobility in the time of deposition ($D/F < 10^3$). In this post-nucleation regime (see Sect. 3.3) monomers diffuse towards each other mostly *after* deposition leading to a mean cluster size of $\langle N \rangle \sim 3$ atoms. The same result is obtained when depositing at temperatures where diffusion is frozen and subsequently gently annealing the surface to activate diffusion [54,18]. After preparation of the small clusters, their densities and thus their average sizes (since θ is a known constant) are monitored by STM as a function of annealing temperature. The Ag clusters on Pt(111) shown in Fig. 3.8 are compact spherical until they adopt a quasi-hexagonal shape with different lengths of the A- and B-facets. This shape can be considered as the equilibrium shape of a 2D cluster for that system since further annealing leads to island decay. This is believed to be promoted by the compressive strain inherent in the clusters [120,121].

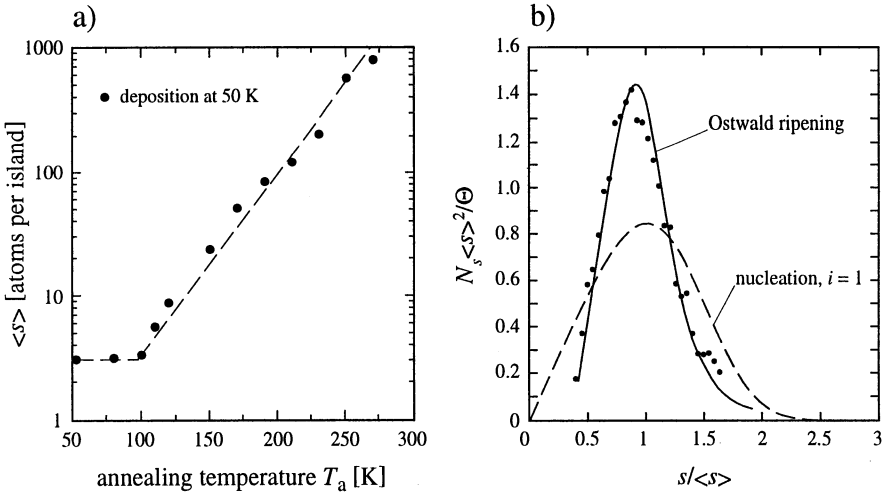


Fig. 3.9. Investigation of 2D Ostwald ripening for Ag/Pt(111) by means of STM [10]. (a) The mean island size $\langle N \rangle$ stays constant until it exhibits an exponential increase due to Ostwald ripening for annealing temperatures $T_a > 100$ K. (b) Scaled island size distributions for Ostwald ripening (data from Fig. 3.8, *solid line* serves as guide to the eye) are significantly more narrow as compared to nucleation (*dashed line* theoretical $i = 1$ scaling curve [12])

The evolution of the mean island size while annealing shows a plateau followed by an exponential increase characteristic of Ostwald ripening (see Fig. 3.9a). The constant regime implies that the most fragile objects in the population, namely the dimers (and on square lattices also the trimers), neither dissociate nor diffuse, since both would lead to coarsening. The temperature threshold for the onset of 2D Ostwald ripening thus defines the $i = 1$ regime and yields the dimer dissociation barrier, which contains the dimer bond energy E_b via $E_{\text{diss}} \sim E_m + E_b$ ($E_b = 150 \pm 20$ meV has been inferred in this way for Ag/Pt(111) [18]).

As an advantage to island nucleation, the size distributions obtained from Ostwald ripening, starting from the exponentially decreasing size distributions of post-nucleation [54], are significantly sharper. This becomes evident from inspection of the STM images in Fig. 3.8 and from the size distributions shown in Fig. 3.9b. The half width at half maximum decreases from $\sigma = 0.55$ for regular $i = 1$ nucleation to $\sigma = 0.3$ for coarsening. Similar to nucleation, the island size distributions obtained from Ostwald ripening at various temperatures become congruent when scaled the same way as for nucleation.

3.6 Anisotropic Surfaces

Anisotropic substrates show directional dependence of adatom diffusion rates and/or of lateral sticking coefficients of adatoms to clusters. Both effects lead to the creation of elongated clusters, in the extreme case of one-dimensional chains of atoms (see Figs. 3.10a and 3.11a). The 1D structures can be considered as quantum wires, the physical properties of which are of considerable scientific interest. Their fabrication with high abundance by MBE growth is thus highly appreciated.

There are various ways to grow quasi-1D clusters at surfaces. One is step decoration [122–124] that has advanced as far as the controlled row-by-row growth at steps of vicinal surfaces [125–127]. We focus our present discussion, however, on clusters formed amid substrate terraces. The desired 1D or elongated structures imply the use of anisotropic substrates. Candidates for metal substrates with diffusion anisotropy are the hex-reconstructed fcc(100) surfaces of Au, Pt and Ir [128,129]. The clusters formed on these surfaces are rectangles elongated along the direction of fast diffusion [130–133]. However, pure 1D structures do not form since sticking to clusters is isotropic on these surfaces. In addition, cluster formation on the hex-reconstructed surfaces is associated with lifting the underlying reconstruction and this makes an understanding on the atomic level difficult. Substrates that permit the growth of 1D strings of atoms, and where cluster formation is easier to understand, are the (1×2) reconstructed and unreconstructed fcc(110) surfaces. We will concentrate on these surfaces where anisotropic diffusion and anisotropic lateral bonding of adatoms in conjunction lead to real 1D clusters.

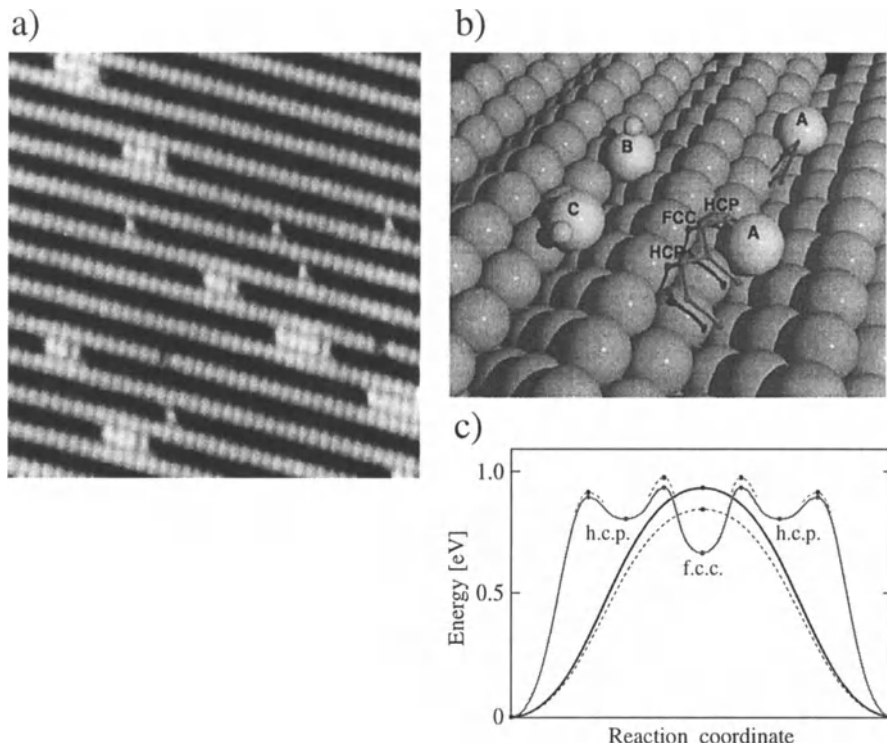


Fig. 3.10. (a) STM image showing the (1×2) -reconstructed Pt(110) surface after a submonolayer amount of Pt has been deposited at 313 K (image size $97 \times 102 \text{ \AA}$) [134]. (b) Model of the (1×2) reconstruction showing two possible diffusion paths for a Pt adatom (A) along the troughs. The first is direct and the second indirect over fcc and hcp sites on the $\{111\}$ -oriented ridge. (c) Ab initio-calculation of the total energy along the reaction coordinate for both diffusion processes (*full lines*). Both diffusion paths are degenerate in activation energy. In the presence of atomic H this degeneracy is lifted and the direct diffusion path has a considerably lowered barrier (*dashed lines*) [112]

The clean Pt(110) surface exhibits a (1×2) reconstruction where every other close-packed atomic row is missing, leading to troughs bound by the energetically favored $\{111\}$ -facets (see Fig. 3.10b). Diffusion of Pt adatoms on this surface is one-dimensional and occurs by a certain number ($\sim 10\%$) of double jump events, i.e., jumps to second neighbor sites, as revealed from an analysis of time-lapsed STM images [134] such as the one shown in Fig. 3.10a. An adatom (labelled A in Fig. 3.10b) has two diffusion paths to move along the trough, a direct one along the bottom of the trough, and an indirect one where the atom walks ‘up’ on the $\{111\}$ -facet. There it passes an hcp, an fcc and another hcp site before it goes down again to the bottom of the trough. Calculations with DFT (Fig. 3.10c) showed that both reaction paths have

equal activation energies [112]. The existence of the two diffusion paths has also been found by molecular dynamics (MD) simulations for self-diffusion on the (1×2) -reconstructed Au(110) surface. These simulations show that the indirect path is the cause for the long jumps [135]. DFT calculations show that the degeneracy of paths is lifted by adsorption of atomic hydrogen (see dashed lines in Fig. 3.10c). Furthermore it is found that the activation energy is lowered as compared to the clean case for diffusion of the Pt–H complex (B and C in Fig. 3.10b) along the bottom of the troughs. In accordance with the smaller activation energy STM revealed significantly enhanced diffusion rates for the Pt–H complexes showing up as brighter Pt adatoms in constant current topographs [112].

Apart from the lessons regarding the complex pathways of 1D surface diffusion and its sensitivity to adsorbates, the example of Pt/Pt(110)- (1×2) also illustrates the effect of anisotropic sticking on the cluster shape. The clusters in Fig. 3.10a are 1D strings a few atoms in length. The 1D shape is caused by the fact that diffusion along troughs of neighboring chains is unperturbed; the distance between two troughs is large and interaction across the ridge is weak. In contrast to the negligible lateral sticking coefficient the binding energy of an atom at the end of an atomic string is large. Small 1D clusters have also been observed for Au, Ni, and Cu deposition on the (1×2) -reconstructed Au(110) surface [17,16,136]. We note that above certain temperatures these systems involve exchange diffusion leading in heteroepitaxial cases to alloyed islands and ridges.

The anisotropies of diffusion and sticking are much weaker on the unreconstructed fcc(110) surfaces since there the troughs are closer and the ridges between them are less protruding. Nevertheless, it was on the unreconstructed surface that 1D metal clusters were observed for the first time [69,137]. The STM image reproduced in Fig. 3.11a shows chains of Cu atoms aligned along the troughs of the Pd(110) surface. The formation of monoatomic Cu wires up to 1000 Å long was reported for that system, corresponding to aspect ratios as large as $A \sim 300$ [69]. With increasing deposition temperature, to values above room temperature, clusters become compact while remaining elongated along the $\langle 1\bar{1}0 \rangle$ -direction. Atomic chains were also observed for Pd [138] and Fe [139] deposition onto Pd(110).

The mechanism underlying cluster growth for Cu/Pd(110) and in general on unreconstructed fcc(110) surfaces has been the subject of various models. A KMC model (see Fig. 3.11c) accounting for the fcc(110) symmetry involves the following assumptions. Diffusion within a trough adjacent to a chain is unperturbed ($E_{h,y} = E_{e,y} = 0.3$ eV) whereas adatoms are less mobile along the short cluster edge ($E_{e,x} = 0.65$ eV); cross channel diffusion was allowed ($E_{h,x} = 0.45$ eV) and a net mass transport along the island perimeter towards the short island end was incorporated (corner rounding $E_{c,y} = 0.3$ eV, whereas $E_{c,x} = 0.65$ eV). The model reproduced well the temperature dependence of average experimental quantities such as cluster aspect ratio (see

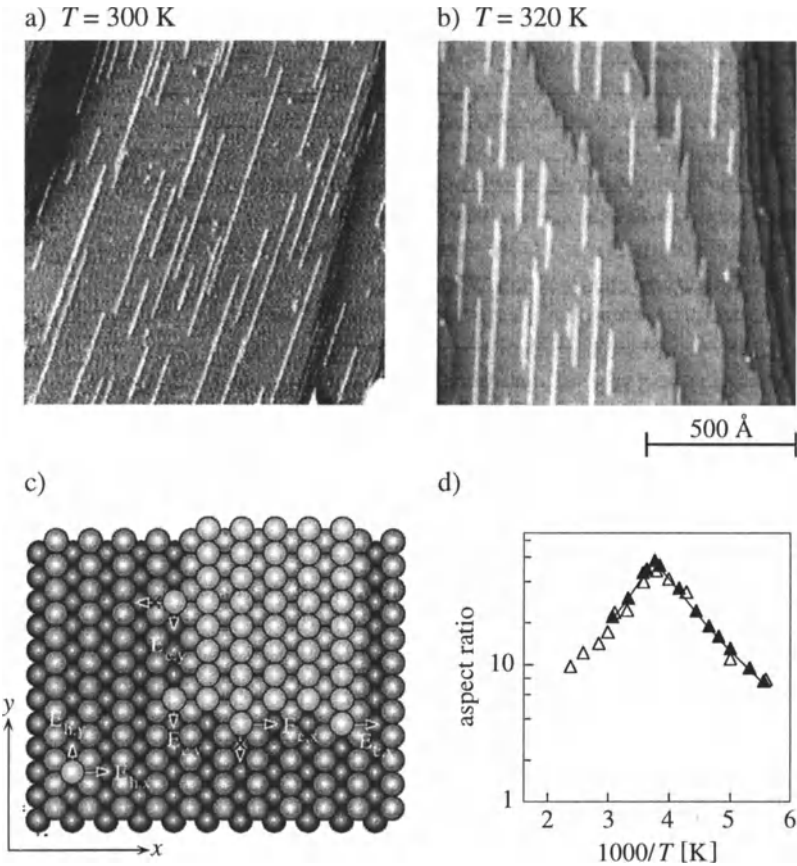


Fig. 3.11. (a) STM image of monoatomic Cu chains on Pd(110) grown at room temperature ($\theta = 0.07$ ML). (b) Rectangular clusters form upon deposition at 320 K ($\theta = 0.1$ ML, common scale bar for (a) and (b)) [137]. (c) Anisotropic edge diffusion and sticking are the dominant mechanisms giving rise to elongated islands on fcc(110) surfaces. The ball model shows the processes considered in the KMC simulation (for simulation parameters see text). (d) Simulated (*filled symbols*) vs. experimental (*open symbols*) cluster aspect ratios [140]

Fig. 3.11d) and density [140]. According to the simulations, the 1D cluster regime is extended to temperatures far beyond the 1D diffusion regime, leading to the large chain lengths. This is due to the corner rounding process, i.e., to adatoms diffusing along the chains and then attaching via cross channel diffusion to chain ends. The 2D cluster shape at higher temperatures is caused by transport from short to long island edges competing with the opposite one. With a second model it was argued that the mechanism leading to the morphology transition from 1D chains to 2D clusters is not direct diffusion

around the corner but rather detachment, terrace diffusion and reattachment to the cluster [141,142].

The essential point to be learned from the KMC simulations is that anisotropic sticking (or similarly anisotropic adatom diffusion around the cluster perimeter) is much more important for the cluster shape than diffusion anisotropy. This fact is illustrated by Si/Si(100) where anisotropic sticking and diffusion anisotropy are turned by 90° to each other. Since the role of sticking overwhelms that of diffusion, clusters are elongated along the slow diffusion direction [143]. Nevertheless diffusion anisotropy is essential for the understanding of island density scaling with flux and temperature. On the (1×2) -reconstructed fcc(110) surfaces diffusion is strictly 1D. Thus there is no possibility of net adatom flux around the cluster perimeter explaining the fact that 1D clusters on these surfaces are generally much shorter than on unreconstructed ones.

3.7 Growth of Cluster Arrays

The strain energy present in heteroepitaxial systems and the surface stress characterizing clean surfaces can give rise to the formation of weakly incommensurate layers, respectively surface reconstructions. On fcc(111) surfaces these layers have surface partial dislocations marking transitions between fcc and hcp-stacking domains. These dislocations (or domain walls) have long-range mutual repulsive interactions, and this has two general implications. Firstly, there is a well defined density of dislocations due to the compromise between optimum strain relief achieved through introduction of dislocations and their mutual repulsion. Secondly, the dislocations order into regular patterns. Examples are the herringbone reconstruction of Au(111) (see Fig. 3.12a), or dislocation networks (for a general account of strain relief on fcc(111) surfaces see [144–146]).

There is clear experimental evidence that for many epitaxial systems the surface partial dislocations represent strongly repulsive line defects for diffusing adatoms [56,147,58]. Their influence on nucleation can go as far as to drive the most perfect layer-by-layer growth yet observed [148]. The two ingredients, ordering of dislocations into periodic patterns and strong influence of dislocations on adatom diffusion, can be employed to grow periodic arrays of almost monodispersed islands [149]. In this section we will discuss results obtained for nucleation on such patterned substrates.

Our first example is Ni nucleation at the ‘elbows’ of the Au(111) $(\sqrt{3} \times 22)$ -reconstruction. Fig. 3.12a shows the clean Au(111) surface with the $\langle 11\bar{2} \rangle$ -oriented partials appearing bright since they involve bridge sites. Strain relief is unidirectional in the $(\sqrt{3} \times 22)$ unit cell. To achieve overall isotropic strain relief a well ordered mesoscopic pattern of two domains with alternating orientation of $\pm 120^\circ$ evolves on large terraces. The Ni clusters formed at room temperature deposition are all lined up along the elbows of this so-called

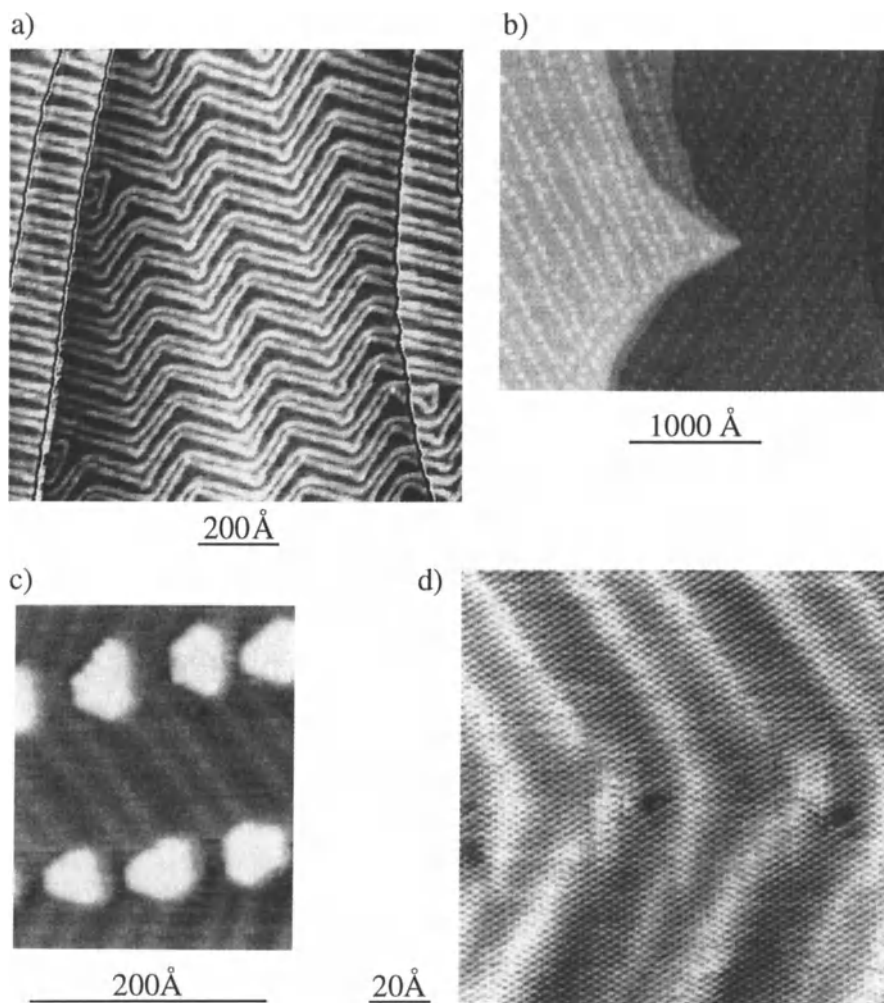


Fig. 3.12. (a) STM image of the herringbone pattern characterizing the mesoscopic order of the Au(111)-($\sqrt{3} \times 22$)-reconstruction [150]. Partial surface dislocations are imaged 0.20 Å higher than fcc areas and thus appear bright. Ni nucleation on that surface at room temperature takes place exclusively at the elbows of the reconstruction (b) ($\theta = 0.11$ ML) leading to monolayer high Ni islands aligned in rows along the $\langle 11\bar{2} \rangle$ -directions (c) ($\theta = 0.14$ ML) [151]. This preferential nucleation at elbows is due to exchange of Ni into Au at these sites [152]. (d) The formation of adislands can be suppressed by performing adsorption at 350 K giving access to the embedded Ni islands; they are comprised of 4 to 5 atoms each ($\theta = 0.002$ ML)

herringbone reconstruction pattern (Figs. 3.12b and c). Note that the regular spacing is accompanied by narrow cluster size distributions. The ordered nucleation was long believed to be caused by the influence of dislocations on diffusion. They were thought to generate attractive potential dips at the elbows [151]. However, the origin of ordered nucleation was revealed by Meyer et al. to be site selective exchange of Ni atoms with Au surface atoms [152]. The exchange is localized at the elbows since there a close-packed atomic row terminates, giving rise to Au atoms with reduced lateral coordination which are especially susceptible to exchange processes. The embedded Ni clusters each comprising only 4–5 atoms are clearly detected as depressions in Fig. 3.12d. The site selective exchange is followed by preferential nucleation of Ni adislands on top of substitutional Ni islands; the adislands appear bright in Figs. 3.12b and c.

The ordering mechanism present in the Ni/Au(111) system is presumably also active for Fe [102,103], Co [153,154] and Rh [155] showing clusters lined up at elbows, too. The argument given by Meyer et al. was that these elements have a larger surface free energy and heat of sublimation than Au [152]. Accordingly, for elements with lower values of these quantities such as Ag [156] and Al [58] the ordering is absent. However, predicting instability towards exchange solely on the basis of bulk quantities does not always work; Al/Au(111) shows exchange at $T > 245$ K [157,158]. Nevertheless, the picture is consistent that site selective exchange is generally responsible for ordered nucleation on the elbows of the reconstructed Au(111) surface. With that in mind it is clear that ordering is specific to that surface and to the elements of the periodic table exhibiting exchange on it.

A more general approach relying on pure adatom diffusion on networks of dislocations has been suggested [149]. Dislocations confine adatoms by their repelling them into the unit cell in which they were deposited leading to the nucleation of exactly one cluster per unit cell. The partial dislocations are a smooth stacking transition extended over many atoms, as is the repulsion of adatoms away from the dislocations. In addition, fcc- and hcp-domains often have different adatom binding energies. Both effects cause clusters to form on a well defined site within the unit cell, thereby congruently transferring the order of the template surface to the cluster array.

Figure 3.13 illustrates an example where an array of 2D Ag clusters formed on the dislocation network of 2 ML Ag on the Pt(111) surface. The misfit between Ag and Pt leads to a (25×25) -network with surface partials representing 'soft' walls, with lower surface atom density, where the compressive strain is relieved [144] (Fig. 3.13a). Ag nucleation on top of this network reveals a transition between two rate limiting diffusion processes with an intermediate temperature regime where exactly one island forms per unit cell (see Figs. 3.13b and d). Note that all of the clusters nucleate on the distorted hexagon of the unit cell implying preferential binding to these fcc-stacking areas, in agreement with theory [159]. The Arrhenius slopes (Fig. 3.13d) below

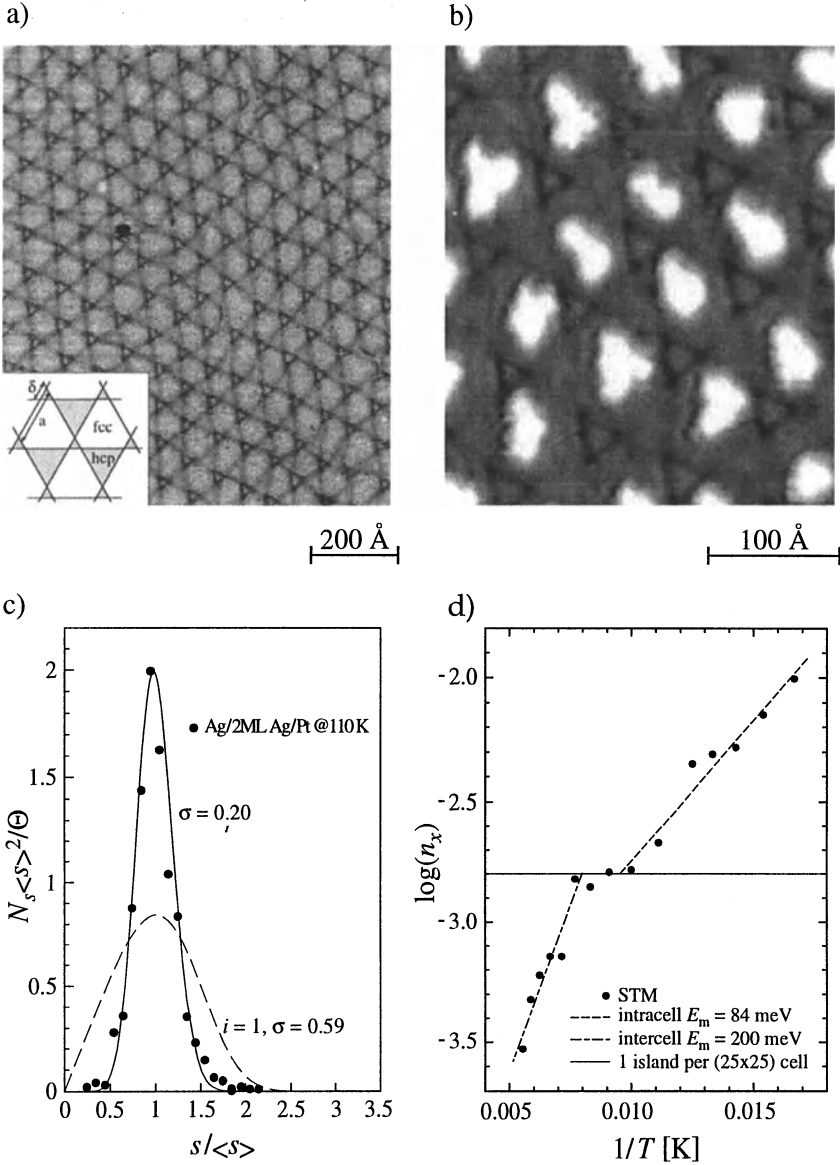


Fig. 3.13. Nucleation of a cluster superlattice on a dislocation network with a period of 7 nm. (a) STM image of the network of $\langle 1\bar{1}0 \rangle$ -oriented partial dislocations formed by the second Ag monolayer on Pt(111) upon annealing to 800 K. The inset shows a model of the trigonal strain relief pattern with its fcc- and hcp-stacking domains. (b) Ag nucleation on this network at $T = 110$ K yields an island superlattice ($\theta = 0.10$ ML). (c) Narrow size distributions are associated with the periodic island spacing (data as *full symbols* and binomial distribution as *full line*) as compared to nucleation on isotropic substrates (*dashed line*). (d) Arrhenius plot of experimental island densities showing the crossover in the rate limiting diffusion process from intracell diffusion to crossing of dislocations [149]

and above the plateau give the activation energies for intracell and intercell diffusion, respectively. From the steeper slope of the latter the repulsive character of the dislocations becomes apparent. At the plateau intracell diffusion is fast enough for adatoms to visit the entire unit cell, although their thermal energy does not yet suffice to cross dislocations and exactly one island forms per unit cell.

In general there is a correlation between cluster spacings and cluster sizes [14]. Material deposited onto the area closest to an island is likely to attach to that island. This capture area of an island is its Voronoi polygon. For equidistant islands these areas are identical thus leading to very narrow island size distributions. In our example the Voronoi areas are the (25×25) network unit cells. The scaled island size distribution (see Fig. 3.13c) is accordingly significantly sharper than that obtained for homogeneous nucleation. We note that the measured standard deviation of $\sigma = 0.20$ (σ equals approximately half the width at half maximum of the size distribution) represents an upper bound due to the residual width caused by STM-tip convolution. The theoretical lower bound for σ is given by the case of ideal confinement of adatoms by infinite barriers. Then the cluster size distribution reduces to the statistics of deposition into the unit cells: for deposition of an average coverage p into unit cells with size n substrate atoms, the probability of finding k atoms within a unit cell obeys a binomial distribution. This distribution, when normalized according to Fig. 3.13c, has a standard deviation of $(\sigma = \sqrt{q/np})$. For our example ($p = 0.1$, $q = 1 - p = 0.9$ and $n = 625$) this yields $\sigma = 0.12$. This result from confined nucleation compares favorably to the best size distributions currently obtained in self-organized growth of quantum dots, which have $\sigma = 0.16$ [160]. Due to reduced fluctuations σ decreases for larger unit cells and larger coverages. For example deposition of 0.5 ML into (25×25) unit cells leads to extremely sharp island size distributions with $\sigma = 0.04$. These values refer to island areas, the distribution of island diameters having only half this width.

The prerequisites for confined nucleation are that dislocations must arrange themselves into periodic patterns, they must be repulsive for adatom diffusion, and there must be no exchange. The first condition is met by numerous heteroepitaxial systems. Well-ordered trigonal dislocation networks are found in a number of epitaxial metal [38,145,146] and semiconductor systems [161]. The requirement for surface dislocations to be repulsive is found to be met by many metal systems. Exchange can be avoided by proper choice of the template. A Cu template formed on Pt(111) [162] was used instead of Ag to avoid exchange processes for the growth of Co and Fe arrays (see Fig. 3.14). In addition a low deposition temperature had to be used to avoid exchange (note that Cu(111) is unstable upon exchange with Co down to 170 K [163]) leading to the formation of many small clusters which were subsequently transferred into an ordered array by Ostwald ripening. Moiré structures [164–166] are also possible templates for self-organized growth of

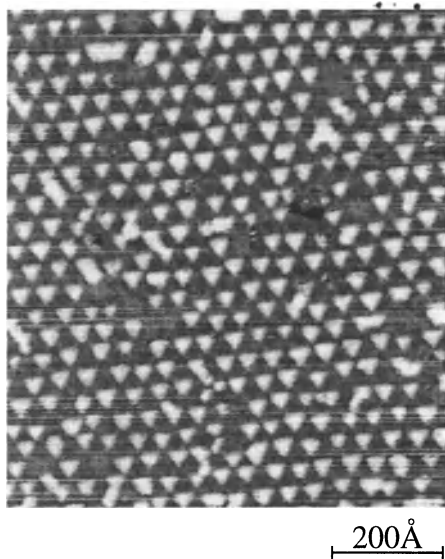


Fig. 3.14. STM image of a periodic array of 2D Fe islands (lattice constant 3.6 nm) nucleated on the dislocation network of the Cu (13×13) bilayer on Pt(111) (deposition at 60 K, ripening at 250 K) [149]

cluster arrays. Similar to dislocation patterns they reveal periodic variations in adatom binding energy. In any of these cases the lattice constant of the array will be a fixed number given by the misfit of overlayer and substrate. However, the lattice constant of 2D alloy layers is a function of the composition and generally given by Vegard's law. Therefore the misfit and the supercell size are adjustable as has been shown for $\text{Au}_x\text{Ni}_{1-x}$ -layers on Ni(111) [165]. This renders alloy layers interesting as templates for ordered nucleation.

We discussed two methods of self-organized growth of almost monodispersed, equally spaced nanostructures on substrates with periodic strain-relief patterns. Whereas the first relies on site specific exchange and risks being highly system specific, the second involving pure adatom diffusion seems to be more generally applicable. Since both methods require surface partial dislocations or Moiré structures that are known to form on hexagonal surfaces only, it is still a challenge to find a method for creating arrays with square symmetry.

3.8 Single Crystal Oxide Surfaces

The motivation for studying metal clusters on single crystal oxide supports is two-fold. The oxide support reduces electronic coupling with respect to metal or semiconductor surfaces, and metal clusters on oxide surfaces provide a model system for industrial supported catalysts [167], see also chapter 8 of this book. Such model catalysts can also be created by MOCVD [168] and by wet impregnation [169]. As in the case of metal/metal systems there is the need to achieve a detailed understanding of nucleation and growth in order to create the uniformity in cluster sizes and shapes required to draw

conclusions from integral measurements of, e.g., reactivity and selectivity in a heterogeneous catalytic reaction. In the near future it is likely that the magnetism, electronic structure and superconductivity of clusters on weakly interacting supports will also be studied. Nucleation and growth of metals on oxides has been intensively studied in the past [167,170–172]. We focus in this section on two model cases with which we illustrate the role of substrate preparation, shed light on nucleation kinetics in the presence of attractive point defects characteristic of single-crystal oxide surfaces, and finally compare the information gained from local probes with that from Transmission Electron Microscopy (TEM).

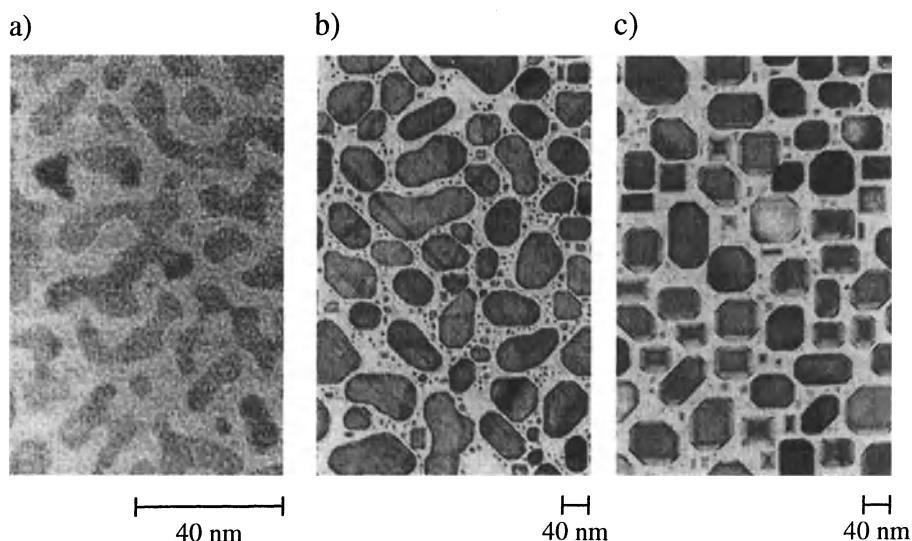


Fig. 3.15. TEM micrographs of Pd particles epitaxially grown on MgO(100) at (a) 300 K, (b) 433 K, and (c) 673 K, respectively ($\theta = 5\text{--}10$ ML) [173]

The evolution of cluster shape with growth temperature is shown for the case of Pd/MgO(100) in Fig. 3.15. The cluster shape at 300 K is 2D and the edges are rough, both of which are signatures for kinetically controlled clusters. Upon deposition at 673 K clusters are truncated half-octahedrons. This cluster shape is considered to be the thermodynamic equilibrium shape since the height/base ratio was found to be independent of cluster size [173]. The cluster shape as a Wulff polyhedron gives access to the surface free energies of the respective facets. For the equilibrium shape to be reached the adatoms deposited onto the substrate ($\theta = 5\text{--}10$ ML) have to be able to climb up to the cluster tops where they are more strongly bound than on MgO(100). However, equilibrium is only reached for isolated clusters, while for the coalesced clusters, deviations from the equilibrium shape show that the system is still to some extent affected by kinetic limitations.

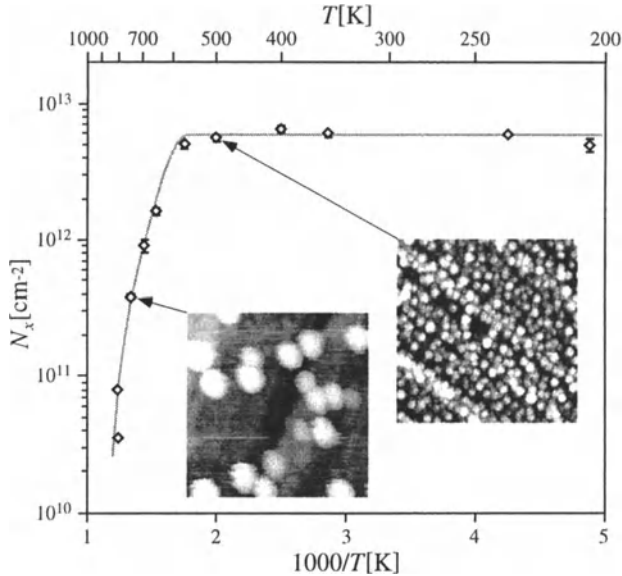


Fig. 3.16. Arrhenius plot of island densities for Pd deposits on Ar-cleaved MgO(100) obtained with non-contact AFM (size of images $1000 \times 1000 \text{ \AA}$) [174]. The *solid line* is a mean-field rate equation model accounting for defect trapping ($\theta = 0.1 \text{ ML}$, $F = 2.7 \times 10^{-4} \text{ ML/s}$). See text for model parameters

The cluster density is critically dependent on the preparation of the single crystal MgO(100) surface. Cleavage in air and subsequent evaporation under UHV conditions yields a 10-times larger island density than UHV cleavage and in situ deposition [167]. This is indicative of heterogeneous nucleation at defects created upon exposure to the ambient atmosphere. On the other hand, cleavage in Ar atmosphere with subsequent annealing in oxygen (750 K, $p_{\text{O}_2} = 1 \times 10^{-4} \text{ mbar}$) gives the same densities as UHV cleavage [174]. Information concerning nucleation kinetics for Pd on MgO(100) was obtained from average cluster densities deduced from AFM images taken as a function of deposition temperature [174]. The AFM images reproduced in Fig. 3.16 show that cluster nucleation takes place at terraces and only occasionally at steps. On the other hand, the Arrhenius plot of the island density is clear evidence for heterogeneous nucleation at defects with large trapping energies. The trapping defects must thus be located at substrate terraces. There are *ab initio* calculations investigating the Pd trapping energies of several possible defects on MgO(100) terraces; one which seems likely to be involved is an oxygen vacancy, the so-called neutral F_s -center [175].

Comparing experimental data with calculations using mean-field nucleation theory including trapping defects (solid line in Fig. 3.16), the relevant system parameters could be derived. The diffusion energy on the defect-free MgO(100) terraces must be rather low ($E_m \leq 0.2 \text{ eV}$) for all the Pd atoms to

reach the defect sites down to $T = 200$ K. The length of the plateau towards higher T defines the minimum trapping energy, $E_t \geq 1.2$ eV. This bound compares reasonably well with the theoretical value of $E_t = 1.55$ eV [175]. The knee at 600 K is best fitted by a transition from $i = 1$ to $i = 3$, i.e., traps remain populated by one Pd atom, but the second and third bound to it break up while only 4 atoms represent a stable cluster at a trap. The deduced lateral bond energy of $E_b = 1.2$ eV lies slightly below the theoretical gas phase value which is reasonable on a weakly bonding substrate. Incomplete condensation starts at 750 K, as evidenced by the decrease in sticking deduced from AES measurements, and by the final increase in the slope of $\log(n_x)$ vs. $1/T$, obtained in the model for an adsorption energy of

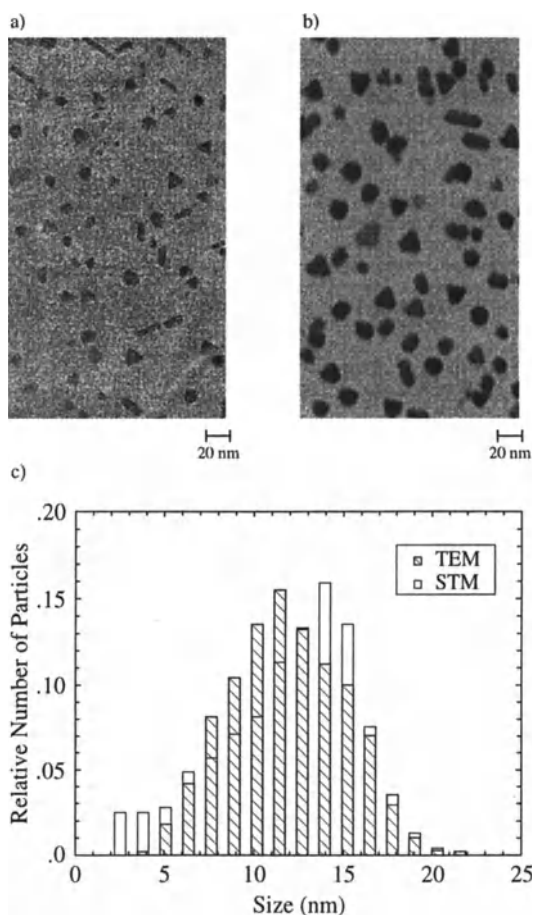


Fig. 3.17. Pd clusters grown on MoS₂ at 623 K. (a) Ex situ image by TEM as compared to (b) in situ STM image. The effect of tip convolution on the size distributions (c) in the case of STM imaging is evident [176]

$E_a = 1.2$ eV. The parameter set derived for the model system Pd/MgO(100) constitutes a valid basis for comparison with theory and is a step towards a quantitative understanding of nucleation and growth in metal/insulator systems.

The imaging of clusters with local probes enables in situ studies and gives access to the cluster height. However, the convolution with the tip falsifies absolute values of the projected surface area, which are reliably obtained by ex situ TEM. In our example of Pd/MoS₂ the convolution is clearly visible since clusters appear distinctly larger in the STM topograph than they are in reality (see Fig. 3.17). Accordingly the size distribution derived from STM is centered at larger average sizes. The effect of tip convolution is expected to be even more dramatic for AFM images of metal clusters, e.g., on MgO. Such images have to be taken in non-contact mode to prevent displacement of the weakly bound clusters by the tip-sample interaction forces appearing in contact mode. Awareness of the convolution effect when deriving absolute cluster sizes and size distributions from local probe techniques is therefore important.

We end our section about metals on insulators by discussing a method that reduces the width of the cluster size distribution for these systems. It is based on the fact that the optical absorption coefficient of metal particles is strongly size dependent. Laser irradiation of clusters (Ag on a quartz support) with a frequency chosen in resonance with the plasmon modes for a certain cluster size selectively heats these clusters which then evaporate atoms and shrink in size. Specific cluster sizes can thereby be reduced or even totally removed. Successive irradiation with two laser wavelengths removes the smallest clusters and causes a size reduction of the largest ones. Thus both tails of the size distribution are removed which reduces its width (to $\sigma \sim 0.26$), as verified by means of AFM and optical extinction spectra [177]. In the sense of leading to better defined cluster sizes the method is similar to Ostwald ripening of small clusters discussed in Sec. 3.5, although it is not coarsening because the mean cluster size remains unchanged.

3.9 Conclusion

The presented methods of cluster growth on metal surfaces are transferable to semiconductor surfaces and possibly also to thin oxide layers. Kinetically or thermodynamically controlled cluster growth represents an alternative to the creation of ordered nanostructures at surfaces by lithography, atom optics, colloids, or soft landing of size selected clusters. Self-organized cluster growth at surfaces will become particularly important for an extension of basic science and applications towards objects with smaller length scales. Questions that may be addressed in the near future are chemical reactivity, transport, and magnetic properties of surface supported clusters evolving from the quantum confinement of electrons in the clusters. The advantage of

cluster growth with respect to atomic manipulation with local probes is the high cluster density enabling access to the clusters' chemical and physical properties with integrating experimental techniques. In order to get the relevant information from integrating measurements, however, size and shape uniformity are essential, requiring detailed understanding and control of the atomic processes underlying cluster growth at surfaces.

References

1. *Growth and Properties of Ultrathin Epitaxial Layers*, Vol. 8 of *The Chemical Physics of Solid Surfaces and Heterogeneous Catalysis*, edited by D. A. King and D. P. Woodruff (Elsevier Science, Amsterdam, 1997).
2. E. Bauer, *Z. Kristallographie* **110**, 372 (1958).
3. M. J. Stowell, *Phil. Mag.* **26**, 349 (1972).
4. J. A. Venables, *Philos. Mag.* **17**, 697 (1973).
5. B. Lewis and J. C. Anderson, *Nucleation and Growth of Thin Films* (Academic Press, New York, San Francisco, London, 1978).
6. G. Ehrlich, *Surf. Sci.* **246**, 1 (1991).
7. G. Ehrlich, *Appl. Phys. A* **55**, 403 (1992).
8. G. L. Kellogg, *Surf. Sci. Rep.* **21**, 1 (1994).
9. T. T. Tsong, *Atom-probe field ion microscopy* (Cambridge University Press, New York, 1990).
10. H. Brune, *Surf. Sci. Rep.* **31**, 121 (1998).
11. M. C. Bartelt, M. C. Tringides, and J. W. Evans, *Phys. Rev. B* **47**, 13891 (1993).
12. J. G. Amar and F. Family, *Phys. Rev. Lett.* **74**, 2066 (1995).
13. M. C. Bartelt and J. W. Evans, *Phys. Rev. B* **54**, R17359 (1996).
14. P. A. Mulheran and J. A. Blackman, *Phys. Rev. B* **53**, 10261 (1996).
15. S. C. Wang and G. Ehrlich, *J. Chem. Phys.* **94**, 4071 (1991).
16. A. Hitzke, M. B. Hugenschmidt, and R. J. Behm, *Surf. Sci.* **389**, 8 (1997).
17. S. Günther, A. Hitzke, and R. J. Behm, *Surf. Rev. and Lett.* **4**, 1103 (1997).
18. H. Brune, G. S. Bales, C. Boragno, J. Jacobsen, and K. Kern, *Phys. Rev. B* **60**, 5991 (1999).
19. H. Brune, J. Wintterlin, R. J. Behm, and G. Ertl, *Phys. Rev. Lett.* **68**, 624 (1992).
20. J. Wintterlin, R. Schuster, and G. Ertl, *Phys. Rev. Lett.* **77**, 123 (1996).
21. G. Vandoni, C. Félix, R. Monot, J. Buttet, and W. Harbich, *Surf. Sci.* **320**, L63 (1994).
22. S. C. Wang and G. Ehrlich, *Phys. Rev. Lett.* **70**, 41 (1993).
23. S. C. Wang and G. Ehrlich, *Phys. Rev. Lett.* **71**, 4174 (1993).
24. G. L. Kellogg, *Phys. Rev. Lett.* **76**, 98 (1996).
25. A. F. Voter and J. D. Doll, *J. Chem. Phys.* **80**, 5832 (1984).
26. R. Gomer, *Rep. Prog. Phys.* **53**, 917 (1990).
27. G. Ehrlich and F. Watanabe, *Langmuir* **7**, 2555 (1991).
28. F. Watanabe and G. Ehrlich, *J. Chem. Phys.* **96**, 3191 (1992).
29. T. A. Witten and L. M. Sander, *Phys. Rev. Lett.* **47**, 1400 (1981).
30. P. Meakin, in *Phase Transitions and Critical Phenomena*, edited by C. Domb and J. L. Lebowitz (Academic Press, New York, 1988), Vol. 12, p. 335.

31. A. L. Barabási and H. E. Stanley, *Fractal concepts in surface growth* (Cambridge University Press, New York, 1995).
32. G. Ehrlich and F. G. Hudda, *J. Chem. Phys.* **44**, 1039 (1966).
33. R. L. Schwoebel and E. J. Shipsey, *J. Appl. Phys.* **37**, 3682 (1966).
34. R. Stumpf and M. Scheffler, *Phys. Rev. Lett.* **72**, 254 (1994).
35. B. D. Yu and M. Scheffler, *Phys. Rev. Lett.* **77**, 1095 (1996).
36. P. J. Feibelman, *Phys. Rev. Lett.* **81**, 168 (1998).
37. G. Ehrlich, *Surf. Sci.* **331–333**, 865 (1995).
38. J. A. Meyer, J. Vrijmoeth, H. A. van der Vegt, E. Vlieg, and R. J. Behm, *Phys. Rev. B* **51**, 14790 (1995).
39. P. Smilauer and S. Harris, *Phys. Rev. B* **51**, 14798 (1995).
40. K. Bromann, H. Brune, H. Röder, and K. Kern, *Phys. Rev. Lett.* **75**, 677 (1995).
41. K. Morgenstern, G. Rosenfeld, E. Lægsgaard, F. Besenbacher, and G. Comsa, *Phys. Rev. Lett.* **80**, 556 (1998).
42. I. Markov, *Phys. Rev. B* **56**, 12544 (1997).
43. K. R. Roos, R. Bhutani, and M. C. Tringides, *Surf. Sci.* **384**, 62 (1997).
44. C. M. Zhang, M. C. Bartelt, J. M. Wen, C. J. Jenks, J. W. Evans, and P. A. Thiel, *J. Cryst. Growth* **174**, 851 (1997).
45. J. Alvarez, E. Lundgren, X. Torrelles, and S. Ferrer, *Phys. Rev. B* **57**, 6325 (1998).
46. J. A. Venables, *Phys. Rev. B* **36**, 4153 (1987).
47. S. Liu, L. Bönig, and H. Metiu, *Phys. Rev. B* **52**, 2907 (1995).
48. M. C. Bartelt, S. Günther, E. Kopatzki, R. J. Behm, and J. W. Evans, *Phys. Rev. B* **53**, 4099 (1996).
49. H. Brune, H. Röder, C. Boragno, and K. Kern, *Phys. Rev. Lett.* **73**, 1955 (1994).
50. J. A. Venables, G. D. T. Spiller, and M. Hanbücken, *Rep. Prog. Phys.* **47**, 399 (1984).
51. Y. W. Mo, J. Kleiner, M. B. Webb, and M. G. Lagally, *Phys. Rev. Lett.* **66**, 1998 (1991).
52. J. A. Stroschio, D. T. Pierce, and R. A. Dragoset, *Phys. Rev. Lett.* **70**, 3615 (1993).
53. M. Bott, M. Hohage, M. Morgenstern, T. Michely, and G. Comsa, *Phys. Rev. Lett.* **76**, 1304 (1996).
54. B. Müller, B. Fischer, L. Nedelmann, H. Brune, and K. Kern, *Phys. Rev. B* **54**, 17858 (1996).
55. G. S. Bales and D. C. Chrzan, *Phys. Rev. B* **50**, 6057 (1994).
56. H. Brune *et al.*, *Phys. Rev. B* **52**, R14380 (1995).
57. C. Ratsch and M. Scheffler, *Phys. Rev. B* **58**, 13163 (1998).
58. B. Fischer, H. Brune, A. Fricke, J. V. Barth, and K. Kern, *Phys. Rev. Lett.* **82**, 1732 (1999).
59. J. V. Barth, H. Brune, B. Fischer, J. Weckesser, and K. Kern, *Phys. Rev. Lett.* in press (1999).
60. T. B. Grimley, *Proc. Phys. Soc.* **90**, 751 (1967).
61. M. C. Bartelt and J. W. Evans, *Phys. Rev. B* **46**, 12675 (1992).
62. L. H. Tang, *J. Phys. (Paris)* **13**, 935 (1993).
63. C. Ratsch, A. Zangwill, P. Smilauer, and D. D. Vvedensky, *Phys. Rev. Lett.* **72**, 3194 (1994).

64. J. A. Stroschio and D. T. Pierce, *Phys. Rev. B* **49**, 8522 (1994).
65. T. Vicsek, *Fractal Growth Phenomena* (World Scientific, Singapore, 1989).
66. H. Takayasu, *Fractals in the physical sciences* (Manchester University Press, Manchester, New York, 1990).
67. Y. Furukawa, *Chemie in unserer Zeit* **2**, 58 (1997).
68. R. Q. Hwang, J. Schröder, C. Günther, and R. J. Behm, *Phys. Rev. Lett.* **67**, 3279 (1991).
69. H. Röder, E. Hahn, H. Brune, J. P. Bucher, and K. Kern, *Nature* **366**, 141 (1993).
70. H. Brune, C. Romainczyk, H. Röder, and K. Kern, *Nature* **369**, 469 (1994).
71. T. Michely, M. Hohage, M. Bott, and G. Comsa, *Phys. Rev. Lett.* **70**, 3943 (1993).
72. H. Brune *et al.*, *Surf. Sci.* **349**, L115 (1996).
73. Y. Couder, N. Gérard, and M. Rabaud, *Phys. Rev. A* **34**, 5175 (1986).
74. A. Pimpinelli, J. Villain, and D. E. Wolf, *J. Phys. (Paris)* **3**, 447 (1993).
75. M. C. Bartelt and J. W. Evans, *Surf. Sci.* **314**, L829 (1994).
76. G. S. Bales and D. C. Chrzan, *Phys. Rev. Lett.* **74**, 4879 (1995).
77. H. Röder, K. Bromann, H. Brune, and K. Kern, *Phys. Rev. Lett.* **74**, 3217 (1995).
78. M. Hohage, M. Bott, M. Morgenstern, Z. Zhang, T. Michely, and G. Comsa, *Phys. Rev. Lett.* **76**, 2366 (1996).
79. F. B. de Mongeot, M. Scherer, B. Gleich, E. Kopatzki, and R. J. Behm, *Surf. Sci.* **411**, 249 (1998).
80. P. Stoltze, *J. Phys. Condens. Matter* **6**, 9495 (1994).
81. P. Ruggerone, C. Ratsch, and M. Scheffler, in *Growth and Properties of Ultrathin Epitaxial Layers*, edited by D. A. King and D. P. Woodruff (Elsevier Science, Amsterdam, 1997), Vol. 8, p. 490.
82. C. L. Liu, *Surf. Sci.* **316**, 294 (1994).
83. D. D. Chambliss and K. E. Johnson, *Phys. Rev. B* **50**, 5012 (1994).
84. J. A. Stroschio, D. T. Pierce, and R. A. Dragoset, *Phys. Rev. Lett.* **70**, 3615 (1993).
85. E. Kopatzki, S. Günther, W. Nichtl-Pecher, and R. J. Behm, *Surf. Sci.* **284**, 154 (1993).
86. E. Hahn, E. Kampshoff, N. Wälchli, and K. Kern, *Phys. Rev. Lett.* **74**, 1803 (1995).
87. J. M. Wen, J. W. Evans, M. C. Bartelt, J. W. Burnett, and P. A. Thiel, *Phys. Rev. Lett.* **76**, 652 (1996).
88. Z. Zhang, X. Chen, and M. G. Lagally, *Phys. Rev. Lett.* **73**, 1829 (1994).
89. B. Müller, L. Nedelmann, B. Fischer, H. Brune, J. V. Barth, and K. Kern, *Phys. Rev. Lett.* **80**, 2642 (1998).
90. J. K. Nørskov, K. W. Jacobsen, P. Stoltze, and L. B. Hansen, *Surf. Sci.* **283**, 277 (1993).
91. P. Feibelman, *Phys. Rev. B* **60**, 4972 (1999).
92. C. Günther *et al.*, *Ber. Bunsenges. Phys. Chem.* **97**, 522 (1993).
93. K. Bromann, H. Brune, M. Giovannini, and K. Kern, *Surf. Sci.* **388**, L1107 (1997).
94. K. Bromann, H. Brune, and K. Kern, unpublished results (1997).
95. M. C. Bartelt and J. W. Evans, *Surf. Sci.* **314**, L829 (1994).
96. A. Bogicevic, S. Liu, J. Jacobsen, B. I. Lundquist, and H. I. Metiu, *Phys. Rev. B* **57**, R9459 (1998).

97. R. Stumpf and M. Scheffler, *Phys. Rev. B* **53**, 4958 (1996).
98. A. Bogicevic, J. Strömquist, and B. I. Lundquist, *Phys. Rev. Lett.* **81**, 637 (1998).
99. R. Q. Hwang, C. Günther, J. Schröder, S. Günther, E. Kopatzki, and R. J. Behm, *J. Vac. Sci. Technol. A* **10**, 1970 (1992).
100. J. Vrijmoeth, C. Günther, J. Schröder, R. Q. Hwang, and R. J. Behm, in *Magnetism and Structure in Systems of Reduced Dimension*, edited by R. F. C. Farrow (Plenum Press, New York, 1993), p. 55.
101. C. Boragno, H. Röder, H. Brune, and K. Kern, to be published (1999).
102. B. Voigtländer, G. Meyer, and N. M. Amer, *Surf. Sci.* **255**, L529 (1991).
103. J. A. Stroscio, D. T. Pierce, R. A. Dragoset, and P. N. First, *J. Vac. Sci. Technol. A* **10**, 1981 (1992).
104. T. Michely and G. Comsa, *Surf. Sci.* **256**, 217 (1991).
105. T. Michely, M. Hohage, M. Bott, and G. Comsa, *Phys. Rev. Lett.* **70**, 3943 (1993).
106. M. Kalff, G. Comsa, and T. Michely, *Phys. Rev. Lett.* **81**, 1255 (1998).
107. S. Liu, Z. Zhang, G. Comsa, and H. Metiu, *Phys. Rev. Lett.* **71**, 2967 (1993).
108. J. Jacobsen, K. W. Jacobsen, and J. K. Nørskov, *Surf. Sci.* **359**, 37 (1996).
109. C. Ratsch, P. Ruggerone, and M. Scheffler, in *Surface Diffusion: Atomistic and Collective Processes*, edited by M. C. Tringides (Plenum Press, New York, 1997), Vol. 360, p. 83.
110. S. Ovesson, A. Bogicevic, and B. L. Lundqvist, *Phys. Rev. Lett.* **83**, 2608 (1999).
111. M. Kalff, Ph.D. thesis, Forschungszentrum Jülich, 1999.
112. S. Horch *et al.*, *Nature* **398**, 134 (1999).
113. F. Besenbacher, personal communication (1999).
114. *Physics and Chemistry of Finite Systems: From Clusters to Crystals*, edited by P. Jena, S. N. Khanna, and B. K. Rao (Kluwer, Dordrecht, 1992).
115. W. Ostwald, *Z. Phys. Chem. (Leipzig)* **34**, 495 (1900).
116. C. Wagner, *Z. Elektrochem.* **65**, 581 (1961).
117. L. M. Lifshitz and V. V. Slyozov, *J. Phys. Chem. Solids* **19**, 35 (1961).
118. K. Morgenstern, G. Rosenfeld, and G. Comsa, *Phys. Rev. Lett.* **76**, 2113 (1996).
119. W. Theis, N. C. Bartelt, and R. M. Tromp, *Phys. Rev. Lett.* **75**, 3328 (1995).
120. P. Blandin, C. Massobrio, and P. Ballone, *Phys. Rev. Lett.* **72**, 3072 (1994).
121. H. Röder, H. Brune, and K. Kern, *Phys. Rev. Lett.* **73**, 2143 (1994).
122. P. M. Petroff, A. C. Gossard, and W. Wiegmann, *Appl. Phys. Lett.* **45**, 620 (1984).
123. Y. W. Mo and F. J. Himpsel, *Phys. Rev. B* **50**, 7868 (1994).
124. J. Shen, R. Skomski, M. Klaua, H. Jenniches, S. S. Manoharan, and J. Kirschner, *Phys. Rev. B* **56**, 2340 (1997).
125. V. Marsico, M. Blanc, K. Kuhnke, and K. Kern, *Phys. Rev. Lett.* **78**, 94 (1997).
126. M. Blanc, K. Kuhnke, V. Marsico, and K. Kern, *Surf. Sci.* **414**, L964 (1998).
127. P. Gambardella, M. Blanc, H. Brune, K. Kuhnke, and K. Kern, *Phys. Rev. B* in press (1999).
128. M. A. v. Hove *et al.*, *Surf. Sci.* **103**, 189 (1981).
129. V. Fiorentini, M. Methfessel, and M. Scheffler, *Phys. Rev. Lett.* **71**, 1051 (1993).

130. S. Günther, E. Kopatzki, M. C. Bartelt, J. W. Evans, and R. J. Behm, *Phys. Rev. Lett.* **73**, 553 (1994).
131. L. Bönig, S. Liu, and H. Metiu, *Surf. Sci.* **365**, 87 (1996).
132. T. R. Linderoth, J. J. Mortensen, K. W. Jacobsen, E. Lægsgaard, I. Stensgaard, and F. Besenbacher, *Phys. Rev. Lett.* **77**, 87 (1996).
133. J. J. Mortensen, T. R. Linderoth, K. W. Jacobsen, E. Lægsgaard, I. Stensgaard, and F. Besenbacher, *Surf. Sci.* **400**, 290 (1997).
134. T. R. Linderoth, S. Horch, E. Lægsgaard, I. Stensgaard, and F. Besenbacher, *Phys. Rev. Lett.* **78**, 4978 (1997).
135. F. Montalenti and R. Ferrando, *Phys. Rev. B* **58**, 3617 (1998).
136. M. B. Hugenschmidt, M. Ruff, A. Hitzke, and R. J. Behm, *Surf. Sci.* **388**, L1100 (1997).
137. J. P. Bucher, E. Hahn, P. Fernandez, C. Massobrio, and K. Kern, *Europhys. Lett.* **27**, 473 (1994).
138. N. Waelchli, Ph.D. thesis, Ecole Polytechnique Fédérale de Lausanne, 1997.
139. J. V. Barth, personal communication (1999).
140. Y. Li *et al.*, *Phys. Rev. B* **56**, 12539 (1997).
141. R. Ferrando, F. Hontinfinde, and A. C. Levi, *Phys. Rev. B* **56**, R4406 (1997).
142. C. Mottet, R. Ferrando, F. Hontinfinde, and A. C. Levi, *Surf. Sci.* **417**, 220 (1998).
143. C. Pearson, M. Krueger, and E. Ganz, *Phys. Rev. Lett.* **76**, 2306 (1996).
144. H. Brune, H. Röder, C. Boragno, and K. Kern, *Phys. Rev. B* **49**, 2997 (1994).
145. C. Günther, J. Vrijmoeth, R. Q. Hwang, and R. J. Behm, *Phys. Rev. Lett.* **74**, 754 (1995).
146. H. Brune and K. Kern, in *Growth and Properties of Ultrathin Epitaxial Layers*, edited by D. A. King and D. P. Woodruff (Elsevier Science, Amsterdam, 1997), Vol. 8, p. 149.
147. J. A. Meyer, P. Schmid, and R. J. Behm, *Phys. Rev. Lett.* **74**, 3864 (1995).
148. T. Michely, M. Hohage, S. Esch, and G. Comsa, *Surf. Sci.* **349**, L89 (1996).
149. H. Brune, M. Giovannini, K. Bromann, and K. Kern, *Nature* **394**, 451 (1998).
150. J. V. Barth, H. Brune, G. Ertl, and R. J. Behm, *Phys. Rev. B* **42**, 9307 (1990).
151. D. D. Chambliss, R. J. Wilson, and S. Chiang, *Phys. Rev. Lett.* **66**, 1721 (1991).
152. J. A. Meyer, J. D. Baikia, E. Kopatzki, and R. J. Behm, *Surf. Sci.* **365**, L647 (1996).
153. B. Voigtländer, G. Meyer, and N. M. Amer, *Phys. Rev. B* **44**, 10354 (1991).
154. S. Padovani, P. Molinás-Mata, F. Scheurer, and J. P. Bucher, *Appl. Phys. A* **66**, S1199 (1998).
155. E. I. Altman and R. J. Colton, *Surf. Sci.* **304**, L400 (1994).
156. D. D. Chambliss and R. J. Wilson, *J. Vac. Sci. Technol. B* **9**, 928 (1991).
157. M. A. Krzyzowski, Ph.D. thesis, Universität Bonn, 1995.
158. B. Fischer, J. V. Barth, A. Fricke, L. Nedelmann, and K. Kern, *Surf. Sci.* **389**, 366 (1997).
159. C. Ratsch, A. P. Seitsonen, and M. Scheffler, *Phys. Rev. B* **55**, 6750 (1997).
160. S. Fafard, R. Leon, D. Leonard, J. L. Merz, and P. M. Petroff, *Phys. Rev. B* **52**, 5752 (1995).
161. M. H. von Hoegen, A. A. Falou, H. Pietsch, B. H. Müller, and M. Henzler, *Surf. Sci.* **298**, 29 (1993).
162. B. Holst, M. Hohlen, K. Wandelt, and W. Allison, *Surf. Sci.* **377-379**, 891 (1997).

163. M. Ø. Pedersen *et al.*, Surf. Sci. **387**, 86 (1997).
164. T. Wiederholt, H. Brune, J. Wintterlin, R. J. Behm, and G. Ertl, Surf. Sci. **324**, 91 (1994).
165. F. Besenbacher, L. P. Nielsen, and P. T. Sprunger, in *Growth and Properties of Ultrathin Epitaxial Layers*, edited by D. A. King and D. P. Woodruff (Elsevier, Amsterdam, 1997), Vol. 8, p. 207.
166. M. Böhringer, Q. Jiang, R. Berndt, W. D. Schneider, and J. Zegenhagen, Surf. Sci. **367**, 245 (1996).
167. C. R. Henry, Surf. Sci. Rep. **31**, 231 (1998).
168. S. K. Purnell, X. Xu, D. W. Goodman, and B. C. Gates, J. Phys. Chem. **98**, 4076 (1994).
169. M. Valden, J. Aaltonene, E. Kuuisto, M. Pessaand, and C. J. Barnes, Surf. Sci. **307-309**, 193 (1994).
170. H. Poppa, Catal. Rev. Sci. Eng. **35**, 359 (1993).
171. R. J. Lad, Surf. Rev. Lett. **2**, 109 (1995).
172. C. T. Champbell, Surf. Sci. Rep. **27**, 1 (1997).
173. C. Henry, C. Chapon, S. Giorgio, and C. Goyhenex, in *Chemisorption, Reactivity of Clusters, Thin Films*, edited by R. M. Lambert and G. Pacchioni (Kluwer, Dordrecht, 1997), p. 117.
174. G. Haas, A. Menck, H. Brune, J. V. Barth, J. A. Venables, and K. Kern, Phys. Rev. B submitted for publication (1999).
175. A. M. Ferrari and G. Pacchioni, J. Phys. Chem. **100**, 9032 (1996).
176. E. Perrot, Ph.D. thesis, Université de Marseille, 1996.
177. J. Bosbach, D. Martin, F. Stietz, T. Wenzel, and F. Träger, Appl. Phys. Lett. **74**, 2605 (1999).

4 Collision of Clusters with Surfaces: Deposition, Surface Modification and Scattering

Wolfgang Harbich

4.1 Introduction

In the preceding chapter we saw how clusters are formed on surfaces starting from atom deposition. Nucleation and aggregation processes determine the surface morphology and these are governed by diffusion barriers on terraces, kinks and steps. Cluster formation in this context is strongly determined not by the minimisation of the total energy of the cluster alone but rather by the total energy and the energy barriers of the cluster–surface system. These two are fundamentally different. An example for strongly interacting surfaces is given below: the binding energy of a silver dimer Ag_2 in the gas phase is 1.6 eV [1], which is a medium strength bond. If this dimer is formed on a Pt(111) surface, the energy corresponding to the bond reduces roughly by a factor of 10 [2]. The gas phase structure of Ag_7 is a bipyramidal pentagon [3], while Ag_7 on Pt(111) has been calculated to be a compact two-dimensional island [4].

The deposition process itself is different if atoms or clusters land on the surface. Cluster speed and size can be varied over a wide range giving rise to new phenomena not accessible within conventional deposition methods. Low energy cluster beam deposition leads to thin films which clearly keep the memory of the deposition [5,6]. Energetic deposition of cluster ions has been shown to give strongly adhering films of high quality [7–11]. Higher energy cluster deposition leads to shallow implantation and better defined interfaces [12]. Giant sputtering yields are found at elevated impact energies [13–15]. Even nuclear fusion processes have been reported at the very highest energies [16]. Clusters are precursors for particular etching and growth procedures on surfaces [17], see Chap. 9. Energetic rare gas clusters are used to polish insulator surfaces very much like an atomic scale sand blasting machine [18,19]. Charging problems by bombarding insulating surfaces are strongly reduced since the charge to mass ratio decreases with increasing N .

Energetic cluster impact gives rise to enormous pressures and temperatures [20–26] which are hardly accessible otherwise. The choice of substrate and cluster material define the reaction partners in cluster collision induced chemical reactions. The surface can either serve as a hard wall [22] simply transforming translational kinetic energy into internal energy or participate

in the reaction. A nice example is the oxidation of silicon surfaces by energetic oxygen cluster impact [27,28]. This allows oxidation to take place at low surface temperatures thus preserving the structures formed before.

4.2 Cluster–Surface Collisions: General Remarks

The description of cluster–surface collisions has to take into account a variety of different phenomena. We can define two timescales in cluster–surface deposition or scattering experiments: The collision itself which lasts for several picoseconds and the evolution of the cluster–surface system with time (evaporation, diffusion, aggregation) which can extend to hours or even days. This is illustrated in Fig. 4.1 which shows a molecular dynamics simulation of a Cu_{1000} cluster colliding at an energy of 10 keV ($v_0 = 5600$ m/s) with a Cu(100) surface. Most of the collision dynamics is over after 50 ps and we can consider Fig. 4.1 as the final configuration (configuration 1) of the collision event. However, from an energetic point of view we expect the minimum energy as a configuration of an island of monatomic height with $(N - M)$ atoms, where M is the number of atoms which are ejected from the surface (configuration 2).

The local temperature of the collision zone after 50 ps is already very close to the initial surface temperature T_0 . The transition from configuration 1 to configuration 2 takes place via thermally activated processes and the time t necessary to reach configuration 2 depends on the surface temperature. This time t lies anywhere between nanoseconds and hours, days or even longer. An example is given in Fig. 4.2 for the system $\text{Ag}_{19}/\text{Pd}(100)$. Fig. 4.2a shows snapshots of a Ag_{19} cluster colliding with a Pd(100) surface at 1 eV/atom kinetic impact energy. These results have been obtained from molecular dynamics calculations by Massobrio et al. [4,30]. The collision outcome is shown in Fig. 4.2a left. The energetic ‘ground state’ of this system is given in Fig. 4.2a right. Thermal energy helium scattering experiments (TEAS)[31] for this system performed as a function of surface temperature T_s show this transition, which happens around room temperature. The idea of the method is as follows. Helium atoms at thermal energy are reflected under specular conditions from a surface. The specular reflected intensity I/I_0 decreases due to adsorbates (in this case the clusters) on the surface with a cross section σ which depends on the morphology of the adsorbate. The deposition curve recorded at $T_s = 200$ K can be fitted with the cross section σ_A shown in Fig. 4.2b left. Since the experimental data can be fitted with the so-called lattice gas model, which describes a statistical distribution of clusters on the surface, one can further conclude that the cluster–surface morphology at this temperature is frozen, i.e., no post-collision dynamics takes place in the time scale of the experiment. At $T_s = 300$ K we see a clear deviation from the lattice gas behaviour which can be well described by a morphology change from σ_A to σ_B .

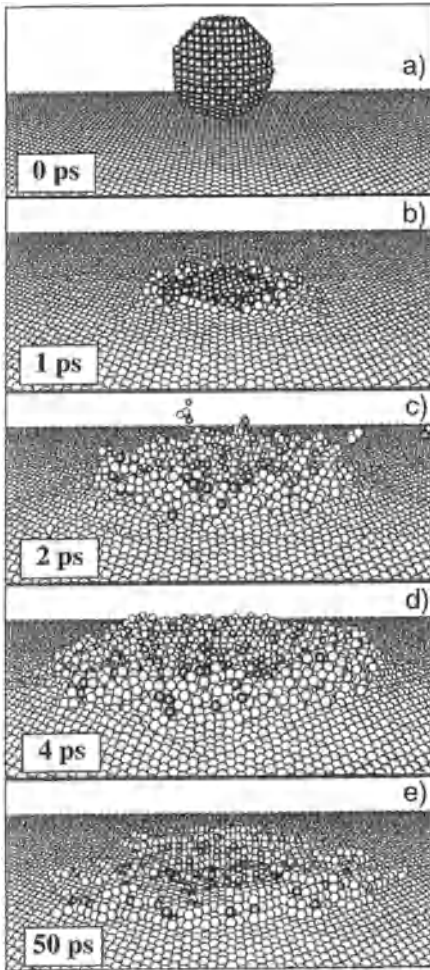


Fig. 4.1. Molecular dynamics calculation for a Cu_{1000} cluster colliding with a $\text{Cu}(100)$ surface. Impact energy $E_0=10$ keV. After Moseler [29]

This means that cryogenic surface temperatures are often required to freeze in all post-collision processes which alter the system under study.¹ The present chapter deals as far as it is possible with the description of the collision dynamics. Experimental results have been obtained in a time window of seconds to hours after the collision event and tracing the fundamental processes back is sometimes difficult.

¹ Generally liquid nitrogen temperature is considered to be sufficient. This is not always the case, in particular for the compact metal surfaces like $\text{Pt}(111)$. The energy barrier for adatom diffusion amounts to 168 meV [32], which corresponds to a hopping frequency of 300 Hz at this temperature. Another example is HOPG. High Ag atom and cluster mobilities have been found at surface temperatures as low as 50 K [33].

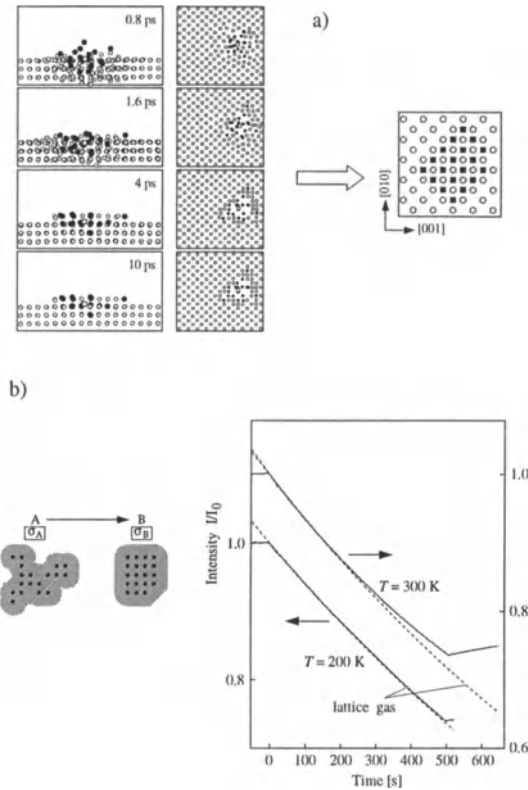


Fig. 4.2. Molecular dynamics calculations and experiment for a Ag_{19} collision with $\text{Pd}(100)$ at $E_0 = 1$ eV/atom; (a) time evolution of the collision (*side and top view*) and the energetic ‘ground state’ configuration. After Massobrio et al. [4,30]. (b) Thermal energy helium scattering experiment for the same system at surface temperatures $T_s = 200$ K corresponding to configuration A (*left*) and $T_s = 300$ K showing the transformation from configuration A to configuration B [31]. The deposition starts at $t = 0$ and stops at $t = 500$ s. The specular intensity recovers for the higher surface temperature when the deposition is stopped since the transformation from σ_A to σ_B is not complete.

For the following discussion it is instructive to draw an intuitive picture of an energetic cluster–surface collision process. When the cluster arrives at the surface, first the front atoms collide with the substrate atoms and are abruptly stopped. The cluster atoms further away from the surface still have their initial velocity and pile up, colliding with the front atoms. This compression leads to an increase in potential energy and internal kinetic energy (heating) of both cluster and surface. A microscopic shock wave is formed which propagates through the cluster. Temperatures, densities and pressures can reach enormous values. Numerical values for an Ar_{561} cluster hitting a $\text{NaCl}(100)$ surface at 1050 eV (1.86 eV/atom) are 3000 K, $1.4 \rho_0$ and 10^4 atm

respectively [23]. For Al_N on Cu, the maximum local temperature increase is found to be proportional to the impact energy per atom and independent of cluster size [34]. At these temperatures the cluster and the surface around the impact are molten. The release of pressure leads to bulging up of material on the rim of the impact area (crater formation), backscattering of atoms and spreading (deformation and dissociation).

It should be asked whether temperature is still a defined quantity in this transient process. Betz et al. [34] have made an analysis of the velocity distribution of the atoms in the heated volume around the impact and found a Maxwell–Boltzman (MB) distribution for the lower impact energies. Deviations from the MB distribution were found for impact energies of 10 eV/atom and this only in the very initial phase of the collision ($\tau < 300$ fs). As will become clear later, the concept of a superheated cluster reasonably explains experimental data.

Another problem consists in classifying cluster–surface collisions. The parameter space is large. I will try to account for the most important parameters in order to attribute them to the different collision processes.

- Cluster size N ($2 \leq N \leq 10^5$).
- Cohesive energies of the cluster $E_{\text{coh}}^{\text{cl}}$ and surface $E_{\text{coh}}^{\text{s}}$, and the bonds formed between cluster atoms and substrate atoms $E_{\text{coh}}^{\text{cl-s}}$. (It is not the same to shoot a stainless steel bullet in wax or hit a stainless steel surface with a sphere of wax). The ratio

$$R = \frac{E_{\text{coh}}^{\text{cl}}}{E_{\text{coh}}^{\text{s}}} \quad (10^{-2} \leq R \leq 10^2) \quad (4.1)$$

spans almost 4 orders of magnitude. The extreme cases are not at all pathological ones. Rare gas clusters are used to smooth metal and semiconductor surfaces [35,36] and rare gas surfaces are used as shock absorbers in softlanding experiments [37,38]. $E_{\text{coh}}^{\text{cl-s}}$ is an important parameter when softlanding conditions apply (see below). In this case, the impact energy is so small that no considerable bond breaking occurs. If $E_{\text{coh}}^{\text{cl-s}} \ll E_{\text{coh}}^{\text{cl}}$, plastic deformation of the cluster is not favourable similar to a non wetting behaviour in atom deposition on surfaces.

- Impact energy E_0 . The cluster impact energy can be considered as one of the key parameters in cluster–surface collisions and covers 10 orders of magnitude from 10^{-2} to 10^8 eV. E_0 defines to a large extent the transient temperatures, pressures and densities.
- Impact angle Φ_{in} determines the amount of lateral momentum with respect to the surface plane. In collisions of C_{60} with HOPG for example, this lateral component is transformed in rotation of the molecule while the normal component is responsible for vibrational excitation [39]. Φ_{in} is closely connected to the mass transport of cluster material parallel to the surface plane and can be considered as one of the key processes in surface smoothing effects for metal deposits [40].

- The charge state of the particle. The neutralisation process in cation or anion deposition is a source of energy which cannot be neglected in low energy cluster deposition.
- Cluster and surface temperature have to be considered. They become increasingly important as the cluster size grows and the deposition energy is reduced. Molecular dynamics simulations [30,41] have shown that the cluster temperature does not greatly influence the collision outcome for Ag_7 and $\text{Ag}_{19}/\text{Pd}(100)$. However, if we approach larger cluster systems, both temperatures play an important role [29]. It is clear that a liquid drop hitting a solid surface behaves quite differently to a solid particle hitting a liquid surface.

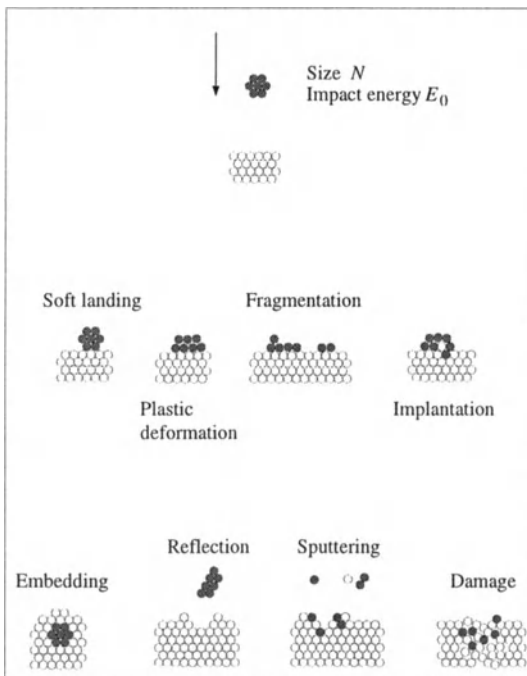


Fig. 4.3. Fundamental processes in cluster-surface collisions

The parameters described above will strongly influence the outcome of a complex collision process. Fig. 4.3 is an attempt to decompose the collision into fundamental processes. The depicted sequence will be treated step by step and will serve as a guideline throughout this chapter. The following processes will be considered:

- Soft landing. The particle sticks at the impact point and keeps its identity. Collision induced deformation is elastic.
- Ballistic deposition: the transformation of translational kinetic energy into potential energy leads to plastic deformation of the particle.

- **Fragmentation:** the incoming cluster decomposes upon impact. This means not only that coordination within the cluster is reduced but that bonds are broken. Fragmentation together with the reformation of new different bonds will be called cluster impact chemistry.
- **Implantation:** part of the cluster is implanted in the surface resulting in an intermixing of cluster and substrate. The depth of implantation depends strongly on the ratio R defined above and impact energy E_0 . If the incident energy is sufficiently high and R sufficiently large the cluster can be completely buried in the solid.
- **Reflection:** the cluster or a cluster fragment is backscattered from the surface. Information about charge- and energy transfer is obtained.
- **Sputtering:** substrate and cluster atoms are ejected from the surface. The overlapping trajectories of the individual cluster atoms lead to highly nonlinear collision cascades.
- **Crater formation:** when the cluster increases in size (≥ 100 atoms) an enormous pressure is built up during the collision accompanied by local melting. The substrate reacts by lateral material transport which induces crater formation.
- **Radiation damage:** collision induced displacements are not completely annealed, producing vacancies, interstitials or completely amorphous zones.

These fundamental processes normally do not occur separately but coexist (except for the first two items). They become important in a certain range of impact energy and cluster size. Fig. 4.4 shows a mechanism diagram which is in close analogy to the one proposed by Averback and coworkers [42]. They have generated this diagram on the basis of molecular dynamics calculations. I have added more processes which will be discussed below to complete the picture. The main parameters in this diagram are the reduced impact energy

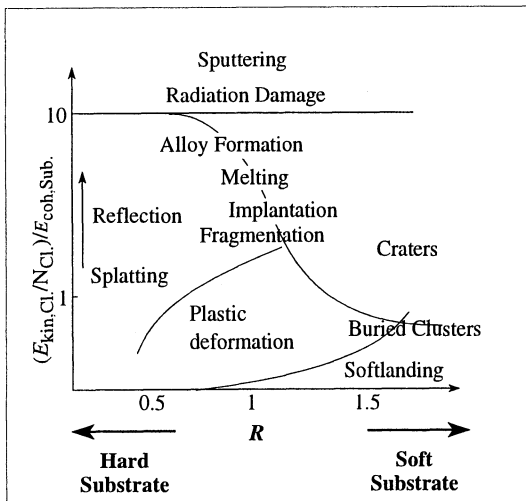


Fig. 4.4. Mechanism diagram in cluster-surface collisions. The x -coordinate represents the relative binding energies of the surface and the cluster $R = E_{coh}^{cl}/E_{coh}^s$; the y coordinate is the reduced energy (after [42])

(per atom of the cluster and cohesive energy of the substrate) and the ratio R defined above. Small R means that a soft cluster collides on a hard surface and large R that a hard cluster impinges on a soft surface. Deposition on a hard surface at elevated energies leads preferentially to splatting and reflection while deposition on a soft surface results in penetration of the particle as one would intuitively expect. Melting, sputtering and radiation damage become important at higher impact energies while softlanding is restricted to the lowest impact energies. This diagram, however, should only be used as a guideline. Cluster size does not appear as a separate parameter. When the particle size decreases to only a few atoms, implantation for example becomes easily possible even for very hard substrates. Before going into a more detailed description of the different processes some remarks on experimental and (to a lesser extent) ‘theoretical’ techniques will be added.

4.3 Experimental Considerations

To study energetic cluster–surface depositions two, in the past separate fields, had and still have to merge: the well established field of surface physics on one side and the much younger field of cluster physics on the other side. Experimental control of surface cleanliness, substrate morphologies and surface temperature which is everyday practice in surface physics is not always an element of common language in the cluster deposition community. If large cluster fluxes are employed, as for example in the experiments of Haberland on energetic cluster deposition [8–10] or Yamada in surface smoothing by cluster impact [43] vacuum requirements are not so strict. On the other hand, when mass selected clusters are employed, cluster currents which can be obtained today are still so small that ultra high vacuum conditions are absolutely necessary. This is particularly true when the surface is held at cryogenic temperatures $T_s \leq 77$ K in order to freeze in diffusion and aggregation processes, since the sticking coefficient for residual gases in the vacuum system approaches unity.

Fig. 4.5 shows the ratio of cluster vs. residual gas flux on the surface as a function of background pressure for the equivalent cluster currents of 0.1, 1 and 10 nA cm⁻². The 10 nA range is about the limit obtainable today [44–46] and most of the state-of-the-art mass selected cluster sources operate well below these values. The two horizontal lines in Fig. 4.5 delimit operation conditions where we have at least as many clusters deposited as ‘dirt’ and where we deposit 10 times as many clusters as residual gas, assuming a sticking coefficient of one. To obtain larger cluster fluxes than impurities on the surface, pressures in the low 10⁻¹⁰ mbar range are mandatory.

Cluster sources which are used for deposition experiments are mostly continuous sources like the gas aggregation source [47], sputter sources [48] and a mixture of gas aggregation and sputter sources [49], see also Chap. 1 and 9. Only very recently, have pulsed sources, which have a high cluster

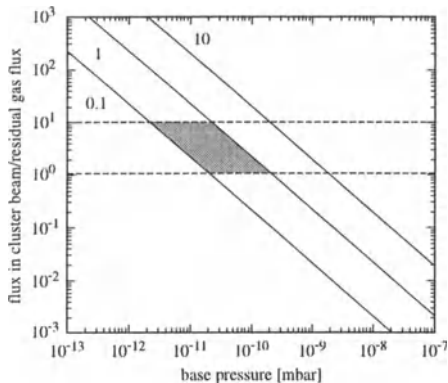


Fig. 4.5. Ratio of cluster flux to residual gas flux for 0.1, 1 and 10 nA cm^{-2} cluster current densities as a function of base pressure in the vacuum chamber. The *shaded area* corresponds to operating conditions in which, as a lower bound, as many clusters hit the surface as impurities and in which, as an upper bound, ten times more clusters than impurities hit the surface for typical mass selected cluster sources employed today

density in the pulse but a small duty cycle, been employed [50,46]. These sources are based on material evaporation following the impact of a high power laser pulse (laser vaporisation sources, LVPS) [51] or an electrical arc (pulsed arc ion source, PACIS [52]). Gas aggregation sources have a high mass flux but only neutral clusters are produced and post-ionisation of the cluster is rather inefficient. Sputter sources, LVPS and PACIS have the advantage that charged clusters are produced directly and can be formed into a beam. Sputter sources which are still the most intense ones for a selected number of elements and small clusters ($N < 20$) have the drawback that the ejected clusters have a rather large energy distribution (≈ 10 eV) [53–55] and this prevents them from forming an energetically well defined beam. This is of particular importance in softlanding experiments where total deposition energies below 10 eV are desired. An elegant way out of this problem has been devised in Wöste’s group [56] and in Anderson’s group [57]. The energetic clusters produced in the sputtering process are thermalized in a helium buffer gas inside a quadrupole field. This procedure, which has been introduced and used for many years by Gerlich and co-workers [58,59], leads to a momentum and spatial compression of the ion beam.

High repetition rates in pulsed sources (LVPS and PACIS) increase the intensity of this type of source to an amount which makes them suitable for deposition experiments. These are in my opinion the sources which will be most often employed in the near future. Unlike sputter or gas aggregation sources, almost any material can be evaporated, even refractory metals and the mean cluster size distribution can be adjusted over a wide range by adjusting the carrier gas pressure, source temperature and nozzle geometry. Heiz et al. [46] have developed a source which is close to the ‘ideal’ experiment supplying mass selected clusters at well defined energies under clean ultra high vacuum conditions. The energy spread is very small ($\delta E < 1$ eV) thus allowing defined collision conditions down to very low energies. For more detailed information see Chap.8.

4.4 Molecular Dynamics Calculations

Powerful computers today allow us to simulate cluster–surface collisions containing some ten thousand atoms up to impact energies in the high keV regime. Since this method solves Newtons equations for all particles integrating the trajectories, we can consider this technique as a dynamical microscope where we get insight into the collision process with femtosecond time resolution (see Fig. 4.1). Experimentally that much detail could never be expected. Commercial software is available but the true bottleneck in this type of numerical experiment is the appropriate choice of the interaction potentials. Detailed experimental information on cluster–surface collision outcomes is consequently highly desired for testing the potentials employed. Once being confident in the appropriate choice, MD is a very powerful predictor for experiments. Here it is much faster and cheaper to set up a computer experiment than a real one. Still there are a couple of problems connected to this method: to properly describe the dynamics of all atoms in the system, time steps of $\tau \leq 10$ fs are necessary, and even smaller ones during the collision phase itself where high energies are still present. This restricts the method to integration times in the order of ns, which is much shorter than laboratory time-scales. However, the collision process which lasts a few ps can be very well described. A further complication arises from the fact, that an experiment averages over millions of collision events (excepting of local probes) while in a MD calculation each run is unique and a large number of calculations have to be performed to obtain reasonable statistics.

4.5 Softlanding

A simple criterion for defining softlanding would be that the cluster sits on the surface without atom exchange with the surface (no implantation) and without any collision-induced plastic deformation. This directly implies that no fragmentation occurs (see Fig. 4.2). Applying this criterion, softlanding conditions can only be obtained for rather exotic systems, at least for small clusters. Consider a neutral cluster of 7 Ag atoms approaching a Pd(100) surface with essentially zero kinetic energy, just enough for the cluster to arrive eventually at the surface. Two energy terms apply in this situation: the cohesive energy between cluster and surface atoms $E_{\text{coh}}^{\text{cl-s}}$ and the difference in the potential energy corresponding to the atomic arrangement of the free gas phase clusters and the final cluster shape on the surface, in this case a compact island of monatomic height. Fig. 4.6 shows results of a MD calculation by Nacer et al. [4] for $\text{Ag}_7/\text{Pd}(100)$. The kinetic energy of the cluster T_{cm} and the temperature T_{int} both expressed in units of temperature (Fig. 4.6a) can be compared to the collision dynamics represented as snapshots in Fig. 4.6b. Ag_7 approaches the surface with its gas phase structure. When the cluster ‘feels’ the surface it accelerates in a short time interval. The maximum temperature

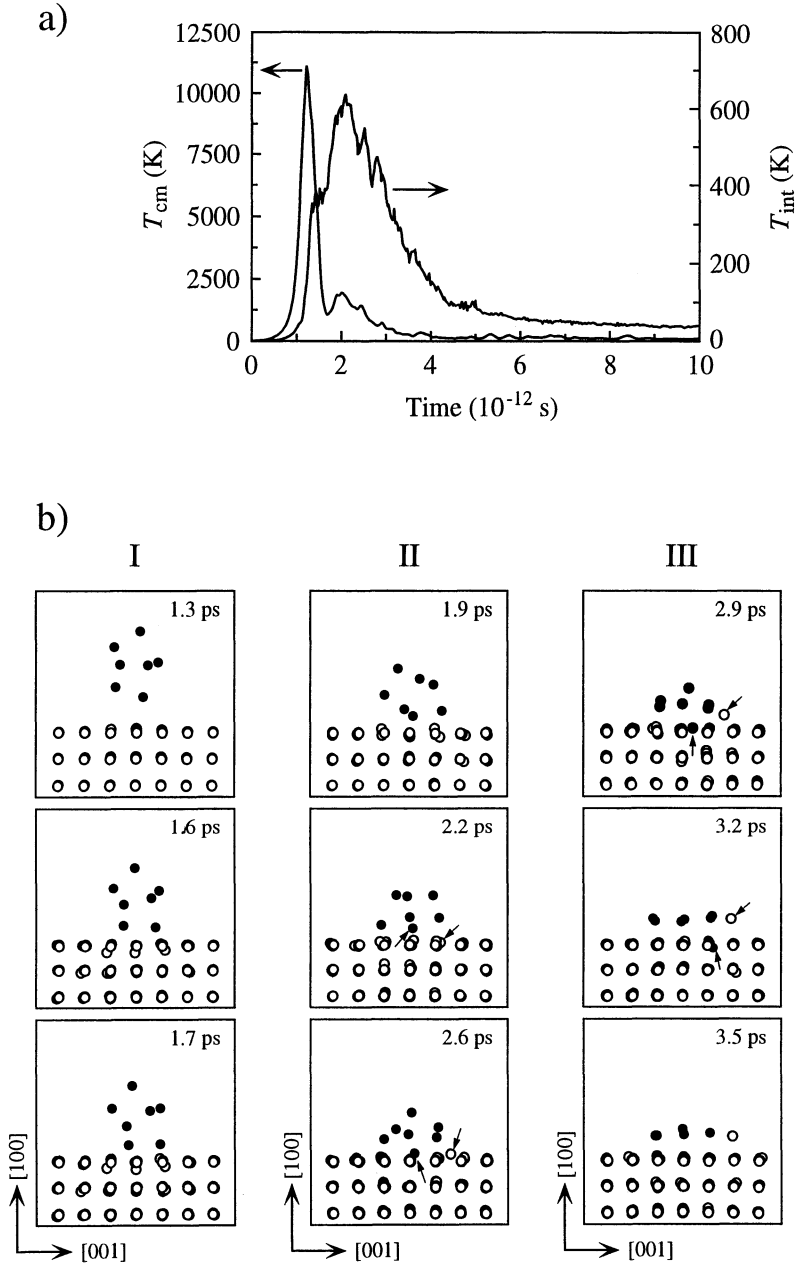


Fig. 4.6. Molecular dynamics calculation of a zero kinetic energy deposition of $\text{Ag}_7/\text{Pd}(100)$. (a) Kinetic energy of the centre of mass T_{cm} and internal temperature T_{int} of the cluster as a function of time; (b) snapshots of cluster and surface atom positions at different times. The trajectories of an implanted cluster atom and a removed surface atom are indicated by little arrows. After Nacer et al. [4]

T_{cm} of 10^4 K corresponds to roughly 1 eV of kinetic energy. When the cluster hits the surface, translational energy is transformed into internal energy and both surface and cluster are heated. As shown in Fig. 4.6bI, the cluster has undergone almost no structural change at this point. The relevant energy for this temperature rise is the adsorption energy of the 3-dimensional cluster to the surface. The cluster's centre of mass motion is stopped at around 1.7 ps but heating continues to take place. This is attributed to the structural change of the cluster, visualised in snapshots II and III. The energy which can be associated to the formation of bonds and to the structural transformation is high enough for implantation of cluster atoms into the surface to take place in 79 % of the simulated collisions for Ag_7 and 10 % for Ag_{19} . It is worth mentioning here that implantation at zero kinetic energy is unique to clusters, since the deposition of thermal atoms does not lead to implantation (at least for the case of Ag on Pd(100)).

Structural deformation and implantation become also less important when the cluster size is increased. This can be understood in the following way [4]: implantation requires a cluster to overcome the exchange barrier which is 0.75 eV for the Ag/Pd(100) system. The energy available per atom for larger clusters decreases making the exchange mechanism less and less probable. Cheng and Landman [21] for example, did not find evidence for implantation for the system $\text{Cu}_{147}/\text{Cu}(111)$ at a total impact energy of $2.6 \cdot 10^{-2}$ eV which corresponds to thermal energy. Further on, the acceleration of the cluster due to the attractive range of the interaction potential leads to a cluster temperature of about 410 K (starting from room temperature), well below the melting temperature, resulting in a 3D crystalline structure. No surface damage was observed in these calculations. Going to even larger clusters leads to softlanding closer and closer to the conditions which have been defined above. The tendency extracted from these selected examples is clear. For $R \approx 1$ softlanding with negligible deformation of the cluster can only be obtained for larger clusters where $N \geq 100$ can be considered as a yardstick. This behaviour is not at all surprising if we extrapolate to macroscopic particles landing at negligible thermal energy on a surface. Intuitively one does not expect a silver sphere of 1 mm diameter to flatten on a clean Ag(111) surface and form an ordered arrangement of epitaxial layers. When the cluster substrate interaction decreases the critical sizes on which softlanding conditions can be obtained will shift to smaller N . The extreme case are covalent or metallic clusters deposited in van der Waals solids like the condensed rare gases or N_2 .

Experimental proof can be obtained for softlanding in van der Waals solids since due to the small cluster substrate interaction, cluster specific (size and structure) information is accessible [60,61,50]. A nice example from Honea et al. [50] is shown in Fig. 4.7. Mass selected small silicon clusters were deposited in solid N_2 and subsequently studied by Raman spectroscopy. Raman spectroscopy gives access to geometrical information via the vibrational modes of

the particle. Fig. 4.7 shows the Raman spectra with the corresponding Raman active modes for the geometrical structures shown with each spectrum. The geometrical structures found are the same as in the gas phase, which means that softlanding in its most strict form has been achieved. Optical absorption spectra have been obtained by our group for Ag_N in Ar for $N=2-40$ [60,61]. Each cluster size shows a distinct optical absorption spectrum. Further analysis of these spectra prove the three dimensional structure of the clusters similar to the gas phase ones [62]. Impact energies in these deposition experiments reach from 0.5 eV/atom (Ag_{40}) to 10 eV/atom (Ag_2). Extrapolating these experiments to 0 eV kinetic energy leads again to true softlanding conditions in the form defined at the beginning of this chapter. A further advantage of this technique, which is known more commonly as Matrix Isolation Spectroscopy (MIS) is that the condensation of these substrates need cryogenic temperatures, freezing in almost all post-collisional dynamics.

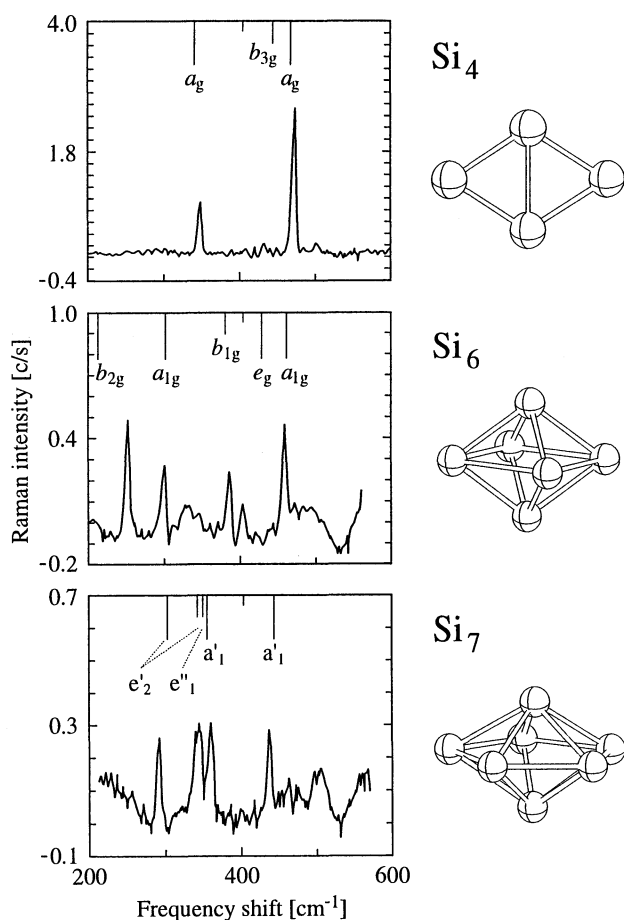


Fig. 4.7. Raman spectra of Si_N in solid N_2 . The spectra are obtained after codepositing mass selected Si_N with N_2 on a cryogenic surface. The bars on the top of each graph represent the Raman active modes of the structures shown on the right of each spectrum. After Honea et al. [50]

Limited information, however, is obtained in these experiments on implantation or even substrate damage induced by the collision process. Photoemission studies [63] on small mass selected Ag clusters on rare gases report considerable sputtering of the substrate for collision energies of 30 eV. Apart from the matrix isolation experiments very limited experimental information is available for deposition on real surfaces and conclusive evidence as to whether softlanding conditions have been obtained does not exist. These experiments are very difficult to perform. Photoemission experiments have been performed on mass selected cluster deposits at low impact energies [64–66] (see also Chap. 5). XPS and UPS spectra are not detailed enough to inform about fragmentation or deformation processes. Local probes (STM, AFM, TEM) at cryogenic temperatures coupled to mass selected cluster deposition can in principle provide this information. Considerable effort in this direction is underway and more data can be expected in the near future.

Indirect confirmation on softlanding has been obtained in some experiments which show very size selective results: the work of Wöste and coworkers on the photographic process initiated by Ag₄ deposition [48] (see also Chap. 8), the catalytic activity of small supported size selected clusters [67,46] and the photoemission results in two photon electron spectroscopy with femtosecond pump and probe lasers of Busolt et al. [68]. In all these experiments a strong dependence on cluster size in an atom by atom manner is found which gives confidence that deposition without fragmentation has been achieved. Plastic deformation or implantation, however, cannot be excluded.

The Lyon group [5,69] deposited larger metal clusters on carbon substrates as these are suitable for subsequent electron microscopy studies. In most cases, cluster sizes obtained on the surface are considerably larger than the cluster size of the beam, induced by surface diffusion and coalescence of the clusters (see also Chap.3). Under some conditions, however (in particular when clusters are sufficiently large to suppress merging of small clusters into large ones), the supported clusters show the same size histogram as the gas phase ones measured during the same experimental run. Similar results have been obtained by Hövel et al. [70] and Palpant et al. [71] for larger clusters deposited at thermal energy. However, it should always be kept in mind that these experiments have been performed on large clusters which are not size selected. This means that qualitative but no quantitative information can be extracted.

If softlanding is defined as a collision outcome allowing for plastic deformation of the cluster but no fragmentation and implantation into the substrate, higher impact energies can be used (see discussion about implantation below). The upper bound of the deposition energy is then defined by the onset of fragmentation and implantation. All molecular dynamics studies analysed for this article showed implantation at about 1 eV/atom, regardless of the cluster–substrate system, while implantation which is not driven by the cohesive energy of the cluster to the substrate and shape deformation (as

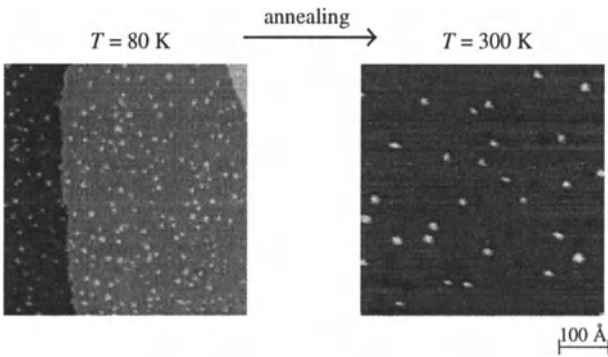
discussed above) is absent for impact energies below 0.1 eV/atom, i.e., well above thermal energies (rare gas substrates are not considered). Analysing fragmentation and implantation processes in more detail as we shall do in the following, allows us to define an upper bound for softlanding conditions to be achieved, which is:

$$E_0 < 1 \text{ eV/atom} \quad (4.2)$$

Another way to reach controlled softlanding conditions on 'hard' surfaces even at hyperthermal energies is deposition into rare gas buffer layers which have been condensed onto the surface prior to deposition [37,38].

"Hard" landing of Ag_7 on Pt(111)

impact energy 20 eV (2.9 eV per Ag atom)



"Soft" landing of Ag_7 on 10 ML Ar/Pt(111)

Dissipation of impact energy into Ar - film

Impact energy 20 eV (2.9 eV per atom), $T_{\text{dep}} = 26 \text{ K}$

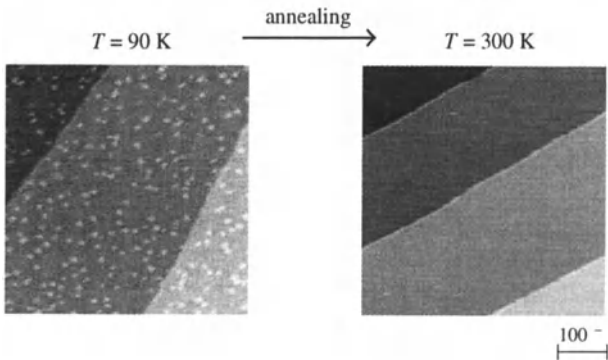


Fig. 4.8. STM images for hardlanded Ag_7 (top) and softlanded Ag_7 (bottom) on Pt(111). (After Bromann et al. [38])

Three-dimensional clusters with a small fragmentation rate (see below) can be obtained when metal clusters are deposited into rare gases at impact energies $E_{\text{dep}} \approx 20 \text{ eV}$ [72,73]. The trick is now to adapt the thickness of the rare gas layer in such a way that the subsequent evaporation does not lead to diffusion induced aggregation of the clusters before they reach the metal surface. Experimental proof for this idea, which was theoretically worked out by the Landman group in molecular dynamics simulations [20], has been obtained by combining variable temperature STM measurements with mass selected cluster deposition in rare gas layers [37,38]. Fig. 4.8 shows a comparison of ‘hard landed’ silver heptamers at 20 eV (2.9 eV/atom) on Pt(111) with ‘soft-landed’ Ag_7 on a 10 monolayer thick Argon buffer layer on top of Pt(111) at the same impact energy. It is instructive to compare the cluster experiment with the deposition of atoms at thermal energies. If the Pt(111) surface is held at cryogenic temperatures beautiful ramified islands are obtained (see Chap.3) but on annealing to 300 K, all atoms are finally condensed at the steps of the Pt(111) surface. This is not the case in energetic deposition of Ag_7 . Ag_7 deposited at 20 eV on the uncovered surface at a surface temperature $T_s = 26 \text{ K}$ (picture taken at 80 K) results in a random distribution of clusters with approximately the same size. Annealing the surface to 300 K gives a result very different to thermal deposition. The silver is still concentrated within (larger) islands on the terraces which indicates stabilisation of the particles by implantation. This is very different when the clusters are slowed down in an argon buffer layer. Heating the surface to 90 K results in complete evaporation of the rare gas and the metal clusters stick to the surface. The islands are very homogeneous in size showing that no cluster aggregation has taken place and the size distribution should be equal to the ones obtained in matrix isolation spectroscopy. Annealing to 300 K leads to complete condensation of the clusters on the Pt steps, identical to thermal deposition.

4.6 Fragmentation

We define fragmentation by decomposition of the cluster into two or more constituents. The amount of fragmentation can vary significantly from the loss of just one atom to complete shattering of the particle upon impact. Experimental access to fragmentation rates in cluster-surface scattering experiments are obtained by mass spectrometry of the backscattered fragments [22,74–79]. Two main problems are inherent in these measurements: first, only a fraction F of the incoming particles is backscattered. F depends strongly on the system and the scattering geometry and can become very small. In this case only very few selected trajectories of the total contribute to the measured signal and these do not have to be representative at all in a statistical sense. Second, usually charged backscattered particles are detected unless post-ionisation is performed [80]. The amount of neutralisation can become

very important ($\geq 90\%$) and the mechanisms of charge transfer are not well understood, making quantitative analysis difficult. In cluster deposition experiments the surface has to be analysed during or after deposition giving clear fingerprints of the size distribution. By measuring the size distribution of the deposit and comparing it to the parent cluster size, the different fragmentation channels can be quantified. To my knowledge such experiments only exist for rare gas supports, where the fingerprint for any particular size can be obtained by optical spectroscopy, see below.

4.6.1 Clusters Scattering off the Surface

Experiments investigating the scattering of clusters off surfaces at thermal and hyperthermal energies have been carried out for a variety of chemical elements from van der Waals to covalent systems. Chatelet and coworkers have made extensive studies for large ($N \approx 1000$) Ar_N , Kr_N and mixed clusters scattering off HOPG surfaces at thermal velocities ($v = 500 \text{ m/s}$) [81–88]. It is clear that any scattering process at moderate energy with a surface having a temperature higher than the rare gas condensation temperature will inevitably lead to complete evaporation of the rare gas. However, the angular and velocity distribution of the scattered particles give insight into the energy transfer processes. A cluster which hits the surface at a small angle glides on the surface in analogy to the well known Leidenfrost phenomenon. The authors distinguish three different exit channels:

- monomers evaporate from the gliding cluster;
- large cluster fragments leave the surface at angles close to the surface plane (that means they split from the gliding cluster);
- atoms are temporarily trapped to the surface, thermalize and are subsequently evaporated with a thermal energy distribution.

Molecular dynamics calculations by Pettersson et al. [89] support this interpretation.

Diatomic molecules embedded in van der Waals clusters ($\text{I}_2^-(\text{CO}_2)_N$) fragment upon collision with a surface [77]. The fragmentation rate depends on N for collision energies extending to 30 eV per I_2 molecule. Part of the fragmentation events is explained by a molecular wedge effect very much like a wedge splitting a piece of wood, the CO_2 molecules serving as the wedge.

Simple metal clusters scatter off surfaces at low to moderate energies by monomer loss [90]. Metal clusters interacting with surfaces generally show more inelasticity, which can be translated into a longer interaction time and better repartition of the initial translation energy into inner degrees of freedom. As a consequence, neutral atoms are evaporated from the scattered parent cluster ion for simple metals in contrast to small clusters as, for example in Sb_N [91]. The fragmentation patterns found for Sb_N and Bi_N in the

low energy collision range very much reflect the stability of the clusters [91–93] pointing again to a thermal evaporation process for the collision heated cluster.

Prominent candidates for covalent clusters colliding with surfaces are the particularly stable fullerenes, more specifically C_{60} . Depending on the impact energy, two different fragmentation mechanisms can be distinguished. At lower collision energies $E_0 \leq 300$ eV even numbered fullerene fractions like C_{58} , C_{56} and so on are found [94], indicating a sequential fragmentation by dimer evaporation. A typical fragmentation pattern is given in Fig. 4.9. Fragmentation kinetics has been modelled using a simple unimolecular reaction diagram. An activation energy of 6.6 eV was found for the decomposition process: $C_{60}^+ \rightarrow C_{58}^+ + C_2$. In contrast to the ‘low energy’ process, where C_2 fragments boil off the superheated cluster, prompt fragmentation occurs on impact (shattering) for higher impact energies. As E_0 increases, the fragmentation pattern changes in nature and small carbon clusters C_N^- ($2 \leq N \leq 28$) are formed. Beck et al. [94] were able to reproduce their data qualitatively

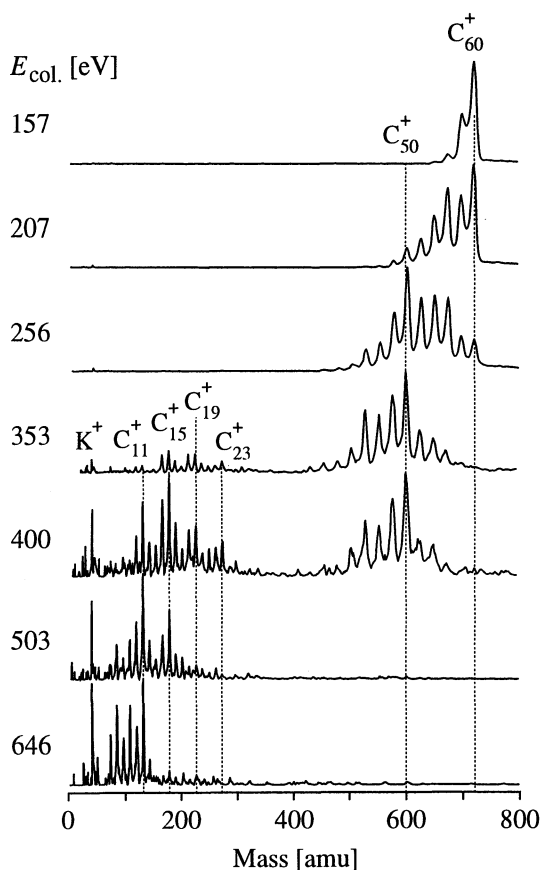


Fig. 4.9. Fragmentation pattern of C_{60} as a function of impact energy. After Beck et al. [94]

using a bond percolation model, taking into account the electron attachment efficiency. It is worth noting here that we are dealing with a very particular molecule which is capable of storing an enormous amount of internal energy.

Fragmentation of silicon clusters colliding with silicon and graphite surfaces have been investigated by St. John et al. [95] and the Kondow group [96] using collision energies of 5 eV/atom. Fragment ions of Si_N parent ions were typically $\text{Si}_{N/2}$, indicating that fragmentation proceeds unimolecularly after the parent ion is scattered from the surface without dissociation. This is further supported by the fact that about 40 % of the initial energy is found as translational kinetic energy of the scattered products.

The picture which emerges from these results is the following: at small collision energies, rapid heating of the cluster leads to evaporation of atoms or small fragments reflecting the stability of the clusters. This is similar to the sputtering process where cluster abundance is modulated by the stability of the clusters. At higher collision energies shattering of the incoming particle takes place and backscattered fragments are typically small clusters or cluster–substrate compounds. The scattering scenario is similar for metals and covalent clusters. Although rather detailed information about the reaction pathways can be obtained from these scattering experiments it should be kept in mind that scattering off the surface might not be the major channel but rather deposition on the surface. Information extracted from scattering always refers to specific collision trajectories, complicated by the charge transfer mechanism which is not well understood.

4.6.2 Fragmentation Studies on Molecules and Clusters

When the fragments or the fragmented parent ions stay on the surface, which is the case in most thermal and hyperthermal experiments at normal incidence, experimental information is sparse because of the above mentioned technical difficulties.

Metal clusters on rare gas substrates are the only systems to my knowledge which have so far supplied quantitative information on fragmentation F in cluster deposition [62]. The distinct size dependent optical absorption spectra for Ag_N allow us to measure the fragmentation rate F as a function of E_0 , N and the substrate material and to deduce on the fragment channels. Qualitatively, fragmentation decreases as the cohesive energy of the substrate decreases in agreement with MD calculations by Cheng et al. [20]. This is shown in Fig. 4.10, where Ag_2 and Ag_7 have been deposited in different rare gases. Clearly discernible in the optical spectra are the well known atomic $s - p$ transitions centred at 4 eV [97], which are a clear indication of fragmentation. The presence of a signal from atoms in Fig. 4.10 further indicates that an important fragmentation channel for metal cluster deposition on these substrates is the evaporation of atoms from the clusters. We could indeed show that Ag_3 can be deposited up to 100 eV primary energy in Ar always giving the same ratio Ag_2/Ag_1 , which means that up to this energy

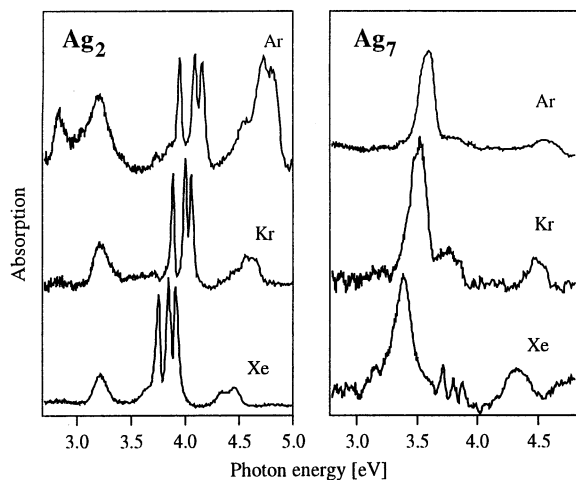


Fig. 4.10. Optical absorption spectra of Ag_2 and Ag_7 in different rare gases. The total deposition energy is $E_{\text{dep}} \approx 20$ eV. Apart from the spectroscopic signatures of the parent clusters, fragments are also present, in particular atoms

the trimer always decomposes in a dimer and a monomer. Quantitative information on the fragmentation rate F can be obtained for dimers, as shown in Fig. 4.11. F has been determined as a function of impact energy for Ag_2 in Xe, Kr and Ar. Clearly there is a hierarchy in the fragmentation curves to lower fragmentation rates with smaller cohesive energy of the substrate (small R) and the minimum values found around 20 eV impact energy are of the order of $F = 20\%$.² The surprising result in Fig. 4.11 is that up to 50% of the incoming dimers survive a collision of 50 eV with the substrate. The reason for this, as we will see later also for the ‘real’ solid, is a cage effect when the dimer (or cluster) is implanted in the solid. Lateral spreading of

² The levelling off at $F = 20\%$ rather than at $F = 0$ for the lowest deposition energies is caused by the large energy distribution of the cluster beam used in these experiments.

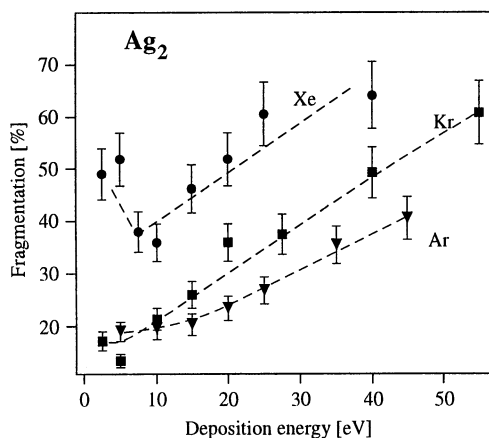


Fig. 4.11. Fragmentation F of Ag_2 as a function of impact energy in Ar, Kr and Xe

cluster atoms is hindered. The case of a van der Waals solid and in particular the rare gas is special. The energy deposited by the cluster impact is sufficient to break hundreds of support atom bonds around the impact point. In a simplified picture, the metal cluster is caged in a small gas ball, as in an atomic scale gas aggregation source. So even when fragmentation occurs in this bubble, reaggregation can happen with reasonable probability [98] and the so called softlanding process is in reality a fragmentation re-aggregation process. Molecular dynamics calculations have been performed to test this model [99]. Typical trajectories for a fragmentation–reaggregation process as well as for a dissociative collision are given in Fig. 4.12 for Cu_2 in Ar. Besides the effect discussed above, the "soft" energy transfer from translational into internal energy has been confirmed by these calculations.

The fragmentation F is expected to depend directly on the bond strength of the colliding cluster. Fig. 4.13 shows F as a function of the bond energy of the neutral dimers in different condensed gases. The experimental conditions are not identical since the data points have been collected from the literature. Deposition energies vary slightly (10 to 30 eV). Nevertheless, the expected trend is clearly visible, showing a very strong dependence on the binding energy.

Quantitative fragmentation data on metallic or covalent surfaces do not exist to my knowledge. Qualitatively, strong fragmentation is found for Ag_7 hitting $\text{Pd}(100)$ at $E_0 = 3$ eV/atom, while much less fragmentation is found for Ag_{19} at $E_0 = 1$ eV/atom [31].

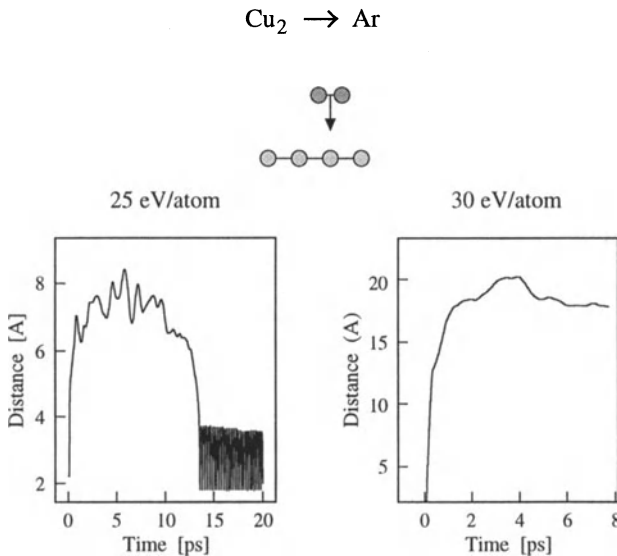


Fig. 4.12. MD calculation for Cu_2 colliding with an Ar surface. The interatomic distance of the two Cu atoms is plotted as a function of time showing dissociation and reaggregation (*left*) and dissociation (*right*). After Ratner et al. [99]

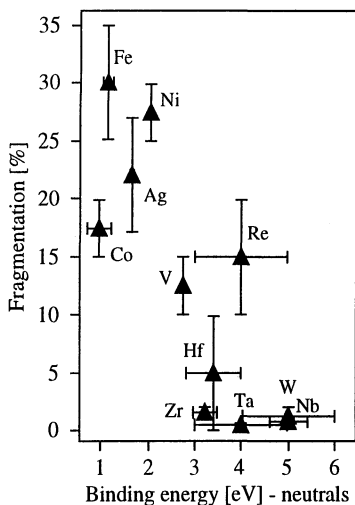


Fig. 4.13. Dimer fragmentation as a function of bond energy. After Fedrigo et al. [98]

4.7 Implantation

Implantation processes have always been important in ion-surface interactions specially in semiconductor technology. Implantation of clusters instead of atomic ions opens new ways with better defined interfaces [11] and less radiation damage in hetero nuclear systems. The stability of cluster structures on surfaces is strongly dependent on the stabilisation of the cluster by implanting some of the cluster atoms into the surface (pinning). The energy range in which implantation processes are involved is comprised between thermal energy and MeV/atom. It was quickly realised that the correlated motion of the individual cluster atoms give rise to an overlap of the collision cascade. These effects will be discussed for implantation and more particularly for sputtering phenomena induced by cluster impact in the next chapter.

One question to be addressed is whether there is a threshold for this process, which means that at least one of the cluster atoms is embedded in the surface layer (see Fig. 4.2). This threshold will depend on the material combination. Referring to Fig. 4.4 we would expect implantation into rare gases well below $E_0 = 1$ eV while implantation starts at around 3 eV/atom in the case of a metal cluster on a metal surface ($R \approx 1$). The cluster size will play a role since macroscopic effects, like shock-wave generation are not active in dimer or trimer depositions. A reasonably good idea for the onset of implantation (for metallic and covalent systems) is given in Fig. 4.14 which shows a compilation of MD results from the literature and two experimental points. Significant implantation sets in at around 1 eV/atom and is complete at around 100 eV/atom. The scattering in the data points can be correlated with the ratio R as discussed above. Quantitative data for implantation in this energy range have been obtained in our group for Ag_7^+ -Pd(100) using Thermal Energy Atom Scattering (TEAS) [100,41]. Implantation yields of 1

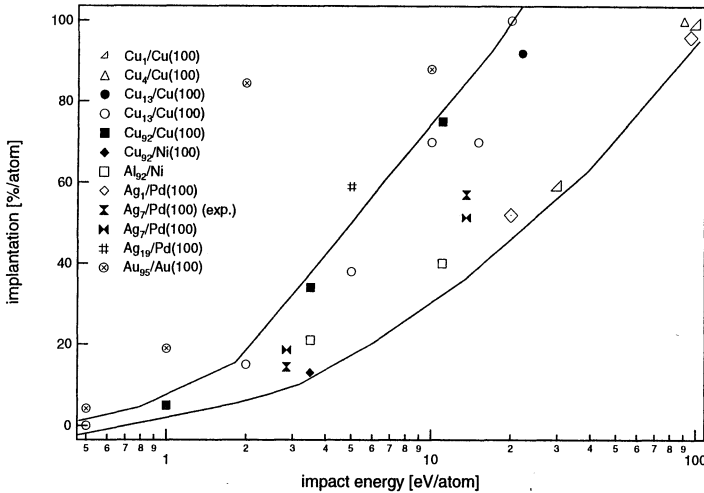


Fig. 4.14. Relative implantation yield (100% corresponds to a completely buried cluster) as a function of impact energy. All data except for $\text{Ag}_7/\text{Pd}(100)$ [100,41] are extracted from MD calculations. Cu_1 [104], $\text{Cu}_{4,13,92}$ [42], Cu_{13} [105], Al_{92} [42], Au_{95} [106], Ag_1 [107], Ag_7 [41], Ag_7 [30]

atom per heptamer at 3 eV/atom and 3–4 atoms per heptamer at 14 eV/atom have been found. These values are in nice agreement with MD calculations for the same system [101] and follow well the trend in Fig. 4.14. Kaiser et al. [102] find a size dependent threshold for Sb_N cluster deposition on HOPG, which is higher than the values reported in Fig. 4.14. However, their values have to be considered as upper bounds. Their conclusions are drawn on the basis of the feasibility of finding particles in the STM images for HOPG at room temperature and the authors do suspect the presence of intercalated particles at lower deposition energies, corresponding to almost complete implantation. The collision trajectory for small clusters hitting the surface depends strongly on the orientation of the cluster and the impact point, as was shown by Carroll et al. [103]. The penetration depth and also the damage zone created by the atoms or small clusters show a large spread corresponding to the large amount of possible orientations.

Time Evolution Monte Carlo (DYACAT) and molecular dynamics simulations have shown that the penetration of small to medium sized clusters in metal and covalent cluster-surface systems are always significantly larger than for the corresponding ions at the same incident velocity [108–112]. This phenomenon has been explained by a clearing-the-way effect (CLW) where the ‘front’ atoms of the incident cluster push target atoms out of the way. The CLW is directly related to the collective motion of the cluster atoms. It depends on the respective masses of cluster (m_c) and surface (m_s) atoms. The CLW effect is much more pronounced when $m_c \gg m_s$ and could not be observed when $m_c \ll m_s$ [113]. The implantation depth of the clusters

decreases with increasing cluster size for the same cluster velocity. This is attributed to a ‘multiple collision effect’ [109]. The transfer of the initial cluster momentum to the lateral direction is more effective than in the atom case due to the enhanced number of collisions between cluster and surface atoms. Aoki et al. [114,109] find a cube root dependence of the penetration depth on impact energy for C_{60} on carbon and Ar_N ($13 \leq N \leq 3000$) on Si(100). This dependence reflects isotropic energy transport through the solid. Note that even the rare gas clusters keep a correlated motion when penetrating into the solid at these elevated energies. The multiple collision effect gets less important when the cluster energy is further increased since scattering cross sections decrease. The collision trajectories of the clusters atoms finally become similar to those of the monomer.

Experimental access to the penetration depth for clusters into substrates is difficult to come by. An elegant solution has been found in the group of Kappes [115]. They use a ‘chemical developing technique’ to measure the penetration depth of C_{60} in HOPG. Oxidation only takes place at defect sites of the HOPG surface in atmospheric oxygen pressure at temperatures below 950 K. Each defect results in a one monolayer deep etch pit of roughly round geometry. Etching stops when no defect is present in the following layer. The penetration depth of the fullerenes is then obtained by measuring the depth of the etch pits with an STM. Fig. 4.15 shows the average penetration depth as a function of impact energy. Comparing their measurements with TRIM calculations for monomer penetration they find an increase in cluster penetration depth by a factor of 1.7 in qualitative agreement with the MD findings discussed above. Baudin et al. [116] have measured the energy loss

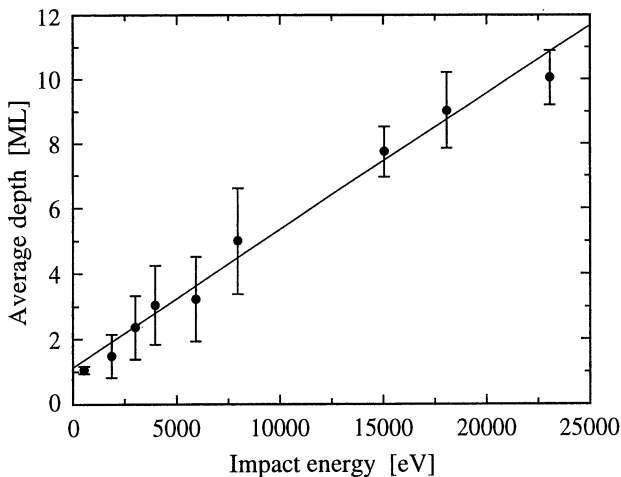


Fig. 4.15. Penetration depth of C_{60} in HOPG as a function of impact energy. After Bräuchle et al. [115]

of MeV C_{60}^+ through thin carbon foils. They find an energy loss which is the same as for a carbon atom having the same impact energy per atom.

The effects discussed above suggest that implantation can be improved by cluster impact. Yamadas group [12,117] has successfully generated ultra-shallow (7 nm) implantation profiles by bombarding a Si(100) substrate with Decaborane ($B_{10}H_{14}$).

4.8 Sputtering

Sputtering phenomena for monatomic ions colliding with a surface in the keV energy regime are well understood on the atomic scale [53–55]. Sputtering yields for most of the ion target combinations can be described by the linear cascade theory by Sigmund [118]. Nonlinear effects should be expected when polyatomic ions are used as projectiles. Nonlinear effects in the sputtering yield Y means $Y(X_M) > MY(X_1)$. In fact already more than 20 years ago experimental evidence for these nonlinear effects by dimer bombardment have been found [119,120]. Since then an increasing data set has been established ranging from keV to MeV impact energy [15,19,121,35,122–129]. An example of such a nonlinear sputtering yield with cluster size is given in Fig. 4.16 which shows the normalised sputtering yield Y/N as a function of impact energy for Au_N with up to 5 atoms per cluster hitting a gold surface [122]. In this energy range only nuclear stopping has to be considered (in contrast to electronic stopping which becomes important above 1 MeV/atom). An enhancement of Y by a factor of 55 is measured in the maximum between Au_5 and the monomer ion. No saturation effect is found in the experimental data and one can speculate that even higher enhancement factors apply for larger clusters.

One of the key words used to explain these effects is ‘energy density’ due to the overlap of the individual trajectories of the impinging cluster atoms,

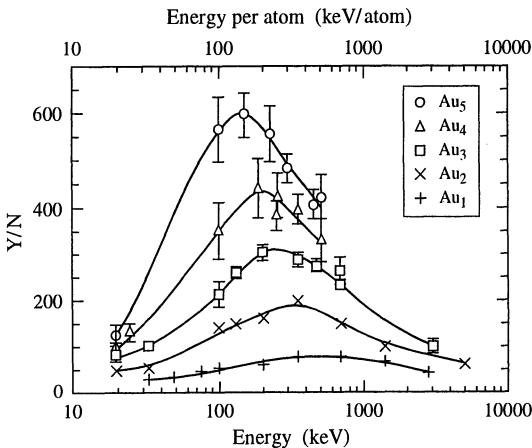


Fig. 4.16. Normalised sputtering yield as a function of impact energy and cluster size. After Andersen et al. [122]

which stay close together, at least in the vicinity of the surface. Although the energy loss of the cluster atoms is reduced with respect to the monomer at identical velocities, this reduction factor is smaller than the number of atoms in the cluster and becomes one for very high energies (see above). A gradual transition from a linear collision cascade to a thermal spike has been proposed by Thompson et al. [130] and Sigmund et al. [131]. However, so far no satisfactory agreement has been obtained between model and experiment.

In the case of electronic stopping, quantitative reproduction of the enhancement has been obtained by a simple energy density argument. Tomaschko et al. [15] have measured the secondary ion yield of CsI bombarded by C_N^+ ($N=1-12$). The authors used the sputtering yield dependence on the energy density ϵ of the monomer and replaced ϵ by the corresponding cluster value.

It is worth noting that in all cases where emission of larger molecules or cluster emission has been measured, the enhancement factors increased with the size of the secondary particle. In other words, cluster impact increases the probability of emitting clusters instead of monomers as secondary ions. However, these data have to be considered with some caution since no corrections have been made to the ionisation efficiency of the emitted particles which can become very important [132].

Apart from the sputtering yield, the angular distribution of sputtered particles merit some attention. Large lateral components in the sputtered particles have been reported experimentally [128,35,129,129] and by molecular dynamics simulations [121,18,127]. Using this 'lateral sputtering effect' the authors explain the surface smoothing obtained in gas cluster bombardment of surfaces at normal incidence.

4.9 Thin Film Formation by Energetic Cluster Impact

About 25 years ago Takagi et al. [133] proposed to use energetic clusters instead of monomer ions in thin film production. The Ionised Cluster Beam Deposition method (ICBD) has attracted considerable attention since and some hundred papers have been published. Remarkable results have been obtained in thin film formation which can be summarised as follows:

- the morphology of thin films can be changed from amorphous to crystalline by increasing the acceleration voltage;
- strongly adhering films with low surface roughness can be produced.

An example is the epitaxial growth of aluminium on Si(100) at room temperature, a system with a very large (25%) lattice mismatch [134]. The results have been explained by phenomenological arguments (adatom migration, high mass density, low energy/atom deposition) but no clear picture has emerged and no theoretical or numerical effort was instigated until 1989 [135]. It was realised that the cluster content in the early ICB sources was very low if existed at all [136-138]. The situation became even more puzzling when Zuhr

et al. [139] showed that energetic monomer ions gave equivalent results in the epitaxial growth of Al on Si(100). Systematic work, specifying the cluster size, has been published more recently by the Haberland group [8–10,49,140–144] and corroborated by molecular dynamics calculations [7,145,146]. The technique has been renamed to Energetic Cluster Impact (ECI).

Adherence of the films can be attributed to surface cleaning effects induced by cluster impact and by partial implantation (pinning) of the clusters in the substrate. The elevated transient temperatures generated locally during the impact allow for recrystallisation even on room temperature substrates.

The reduction in surface roughness has been attributed to an effect, not discussed so far. Surface roughness on a microscopic scale can be visualised as small surface areas which are tilted by ϕ_{in} with respect to the surface plane. It is therefore instructive to discuss the collision mechanism at oblique impact angles. Moseler et al. [40] have proposed a downhill mechanism which has been verified experimentally by STM measurements on asymmetrical crater shapes for oblique cluster impact [128]. The idea is simple. The velocity component parallel to the surface which depends on ϕ_{in} leads to shear stress on the cluster and results in a net mass flow of cluster atoms. Fig. 4.17 shows a molecular dynamics calculation of the collision of a Cu_{2000} cluster with a Cu(100) surface at an incidence angle $\phi_{in} = 7^\circ$. The memory effect on the incident angle is clearly visible. The net mass transport leads to a filling of the protrusions in the case of a rough surface, hence a surface smoothing. The model shows good agreement with experimental data obtained by AFM measurements. Closer inspection of Fig. 4.17 shows that not only cluster

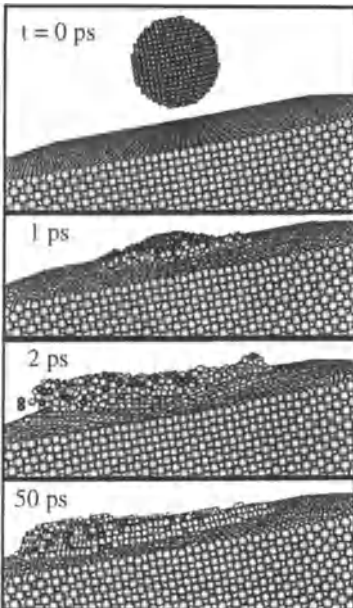


Fig. 4.17. Downhill mass transport in a collision of Cu_{2000} with Cu(100) at an impact angle of 7° with respect to the surface normal. After Moseler [29]

atoms but also substrate atoms are transported downhill. This effect may also be responsible for the surface smoothing induced by rare gas cluster impact reported by the Yamada group [129,36].

4.10 Cluster Impact Chemistry

As already mentioned at the beginning of this chapter, cluster collisions with a surface can lead to extreme temperatures,

densities and pressures in the cluster and on the surface. Together with the transformation from translational kinetic energy into potential energy this may induce bond breaking and formation of new bonds putting forward the idea to search for chemical reactions induced by cluster impact. Two different approaches can be distinguished in the search for cluster-impact-induced chemical reactions. In the first, followed by the groups of Levine and Even, the surface is used in a hard cube model as an ‘energy transformer’ to efficiently heat the cluster. Molecular dynamics studies as well as experiments have been performed giving detailed insight into the energy acquisition mechanisms of the cluster during collision [22,24–26,79,147–149]. Very recently [22] experimental proof of such homogenous reactions has been given. Iodomethane clusters were transformed to molecular iodine and trifluoromethane clusters to molecular fluorine by colliding the parent molecular ions with a *p*-type

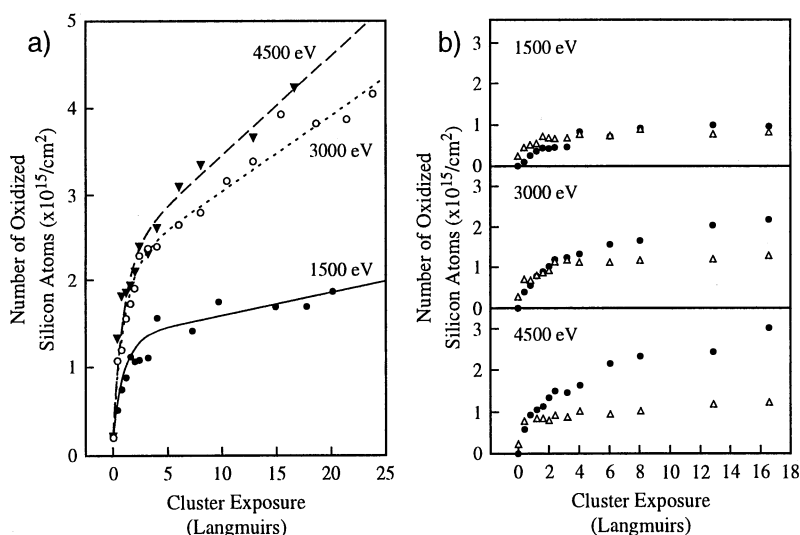


Fig. 4.18. Oxidation of Si by energetic $(\text{O}_2)_N$ ($N \approx 1600$) impact. (a) production of oxidised Si atoms as a function of exposure and impact energy; (b) production of suboxides SiO_x (open triangles) and SiO_2 (filled circles) as a function of exposures for impact energies of 1.5, 3.0 and 4.5 keV. After Klopčič et al. [28]

diamond coated silicon surface. The chemical reaction rates have been found surprisingly high.

In the second approach heterogeneous reactions between the cluster molecules and the substrate are addressed. Yamada's group [27] and Jarrold's group [28] have studied the oxidation of Si by energetic cluster impact at room temperature. Surface oxidation of silicon at room temperature by exposing the surface to O₂ at thermal energies is very inefficient and produces primarily suboxides SiO_x [150]. Surface temperatures T_s > 700° C are required to produce stoichiometric SiO₂ surface layers [151]. This problem can be overcome by energetic cluster deposition. Fig. 4.18a shows the number of oxidised silicon atoms N₀ as a function of O₂ exposure for different impact energies (measured by XPS). The mean cluster size in these experiments was 1600 oxygen molecules per cluster ion. The efficiency of the oxidation process is clearly shown. A steep increase of N₀ at low coverage followed by a much smaller slope at high exposures is observed. Even more interesting are the amounts of SiO_x and SiO₂ as a function of exposure and impact energy, shown in Fig. 4.18b. While the suboxide levels off quite rapidly, SiO₂ continues to grow in particular at high impact energies. This is a nice example of how impact induced heating can drive a chemical reaction.

4.11 Crater Formation and Cluster Impact Induced Erosion

A cluster which hits the surface at elevated energy ($E_0 \gg 1 \text{ eV/atom}$) penetrates the surface and exerts a large pressure between the front atoms of the cluster and the substrate. This pressure is released via the perimeter of the impact zone which is liquid-like and a crater rim is formed. Moseler [29] has studied crater formation in MD calculations of a Cu_N (1000 < N < 3000) cluster hitting a copper single crystalline surface. The following observations can be extracted from this study:

- the crater depth increases with the impact energy;
- the form of the crater depends on the crystallographic orientation;
- the form of the crater depends on the impact angle due to mass transport parallel to the surface;
- the diameter of the crater is not very sensitive to cluster size.

Crater or crater-like formation can be obtained already for very small cluster sizes. Fig. 4.19 shows an STM image obtained by our group of a Pt(111) surface after impact of 1 keV Ag₇. The impacts are characterised by a central impact region of 10–15 Å diameter. Small, approximately round islands of ejected substrate atoms decorate the rim of the crater. The overall diameter of the impact zone is approximately 40 Å.

For larger clusters and higher energies, cluster induced erosion takes place. This effect has been applied by Gspann and coworkers to use cluster impact

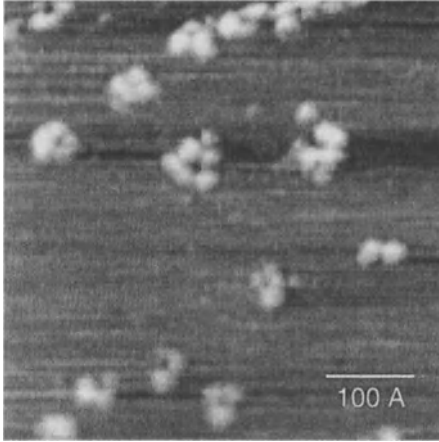


Fig. 4.19. STM image of Pt(111) after the impact of Ag₇ at $E_0 = 1$ keV. Surface temperature $T_s = 93$ K. After Joedicke [152]

erosion for the production of nanostructures [153–156]. $(\text{CO}_2)_N$ clusters with $N \approx 1000$ are accelerated up to 120 keV. Physical erosion as well as chemical etching processes (Reactive Accelerated Cluster erosion RACE) are active during the collision, leading to much smoother eroded surfaces than obtained by sputtering with monatomic ions. Submicron structures with various wall inclinations have been generated on glass, quartz and diamond films.

4.12 Electronic Processes

So far we have neglected electronic processes during cluster–surface collisions. They can provide valuable information about the collision dynamics. The impact energy (or better velocity) and the charge state of the colliding cluster play a decisive role in which kind of electronic processes have to be considered. Using the Bohr velocity as a reference we can distinguish between the low energy regime ($E_0 \approx \text{keV/atom}$) and the high energy regime ($E_0 \approx \text{MeV/atom}$). In the first case the energy loss proceeds via atomic collisions. Charge exchange processes are important as well as thermionic processes of the collisionally heated scattered clusters or cluster fragments. In the high energy range electronic stopping starts to dominate the energy loss mechanism. Several recent reviews treat this subject [157–159].

Electronic processes during and after a cluster–surface collision can manifest themselves in different ways:

- photon emission;
- secondary ion emission;
- electron emission.

Most of the literature concentrates on electron emission which will be briefly reviewed. Electron emission by ion impact is an established field which is fairly well documented [160]. Focusing first on low energies, two important

Electron Emission (EE) mechanisms can be distinguished, Potential Emission (PE) and Kinetic Emission (KE). In a PE process the potential energy of the projectile is dissipated through a two-electron Auger process and in principle there is no threshold behaviour for the impact particle velocity. However, the energy release in the Auger process has to be larger than the binding energy for the electron which is to be emitted. PE is contrasted with KE, where the energy to release the electron is provided by the kinetic energy of the projectile. This channel is inactive below a threshold impact velocity.

Baragiola [158] has reviewed the differences between PE and KE in the case where clusters or molecules collide with the surface instead of monatomic ions. The PE mechanism shows a reduced emission yield γ/N for molecules or clusters with respect to monatomic ions. In addition, a strong velocity dependence for γ is observed for clusters in contrast to the case for atoms. Two possible explanations are given. The first concerns resonant electron capture which becomes more likely, since the number of (empty) excited states increases as the cluster size increases. De-excitation of the hole left in the valence band is filled by Auger interband transitions which favour small energy transfers. This competing process, which explains the reduction in γ for polyatomic molecules also explains the velocity dependence, since higher impact velocities favour electron capture into the ground state of the ion, leading to higher γ values, as observed experimentally.

Another mechanism which becomes possible in cluster-surface collisions is electron capture into repulsive states of the molecule. In very slow collisions this means that electronic energy is transformed into atomic motion, leaving less energy for the electron emission.

Kinetic electron emission is important in atomic and cluster ion detection. Secondary electron multipliers are based on this mechanism. Since the electron yield depends on velocity rather than on energy of the incoming ion, problems arise in the detection of large clusters. The threshold for kinetic electron emission (KE) depends on the projectile target combination with minimum values of $v_{\text{thr}} \approx 2 \cdot 10^4 \text{ m/s}$ [160,158]. One of the most striking findings when clusters are considered is that the apparent threshold for KE decreases. Beuhler et al. [161] have measured KE induced by the impact of H_2O on copper and aluminium oxide and find thresholds of $v_{\text{thr}} = 1.8 \cdot 10^4 \text{ m/s}$ and $v_{\text{thr}} = 0.9 \cdot 10^4 \text{ m/s}$ respectively. Even more surprising is the work reported by Even et al. [162]. The authors report on electron emission induced by CCl_4 clusters produced in a supersonic ($1.6 \cdot 10^3 \text{ m/s}$) expansion. Since the incoming clusters are neutral, PE can be excluded and one can speculate whether this result is a case of Thermionic Emission (TE).

Thermionic emission can be considered as a two-step process and is, at least for low impact energies (no formation of secondary ion clusters) unique to clusters. The question arises as to whether cooling of the collisionally heated cluster via electron emission, as from a hot tungsten wire, will be an active channel. As stated by Thum et al. [163] and references therein, it is

unlikely that any thermionic emission arises from the hot spot created during the impact of the energetic ion. The main argument is that the lifetime of the collision cascade or the thermal spike ($\tau \approx 10^{-12}$ s) is too short for this process to be effective. This is not the case for scattered clusters, cluster fragments or substrate fragments. Dissipation of internal energy gained by the collision cannot proceed via the support and is basically restricted to three cooling mechanisms: a) atom evaporation, b) electron emission (thermionic emission), c) photon emission (black body radiation). Which of these three will be the dominant channel depends strongly on the ratio of the binding energy to the ionisation potential. While coinage metal clusters like Ag or Au will cool by atom evaporation, refractory metal clusters like W, Va and in particular C_{60} can emit electrons. This has been shown in the gas phase by laser heating of the cluster [164–168] and also identified as a mechanism in cluster–surface collisions [169–171]. Cooling by photon emission (black body radiation) has been shown in the gas phase [172,173] but to my knowledge not in cluster surface collisions.

The question arises as to whether EE in cluster–surface collisions is determined by electronic processes of the atomic constituents independently or whether molecular effects play an important role. The relevant quantity here is the ratio

$$Q_N = \frac{\gamma(M_N^+)}{N\gamma(M^+)} \quad (4.3)$$

for the cluster ion M_N^+ . For hydrogen cluster ions a sublinear effect ($Q_N < 1$) is found at impact energies ($E_0 < 300$ keV) while $Q_N > 1$ for $E_0 > 300$ keV [174]. The mechanisms involved in these positive and negative molecular effects are not really understood. Gold clusters ($1 < N < 5$) colliding with a CsI surface at impact energies comprised between 30 keV/atom and 6 MeV/atom always show a sublinear effect increasing with impact energy [175]. The authors explain this behaviour by a reduced cross-section for multiple ionisation.

A nice experiment has been performed by the group of Meiwes-Broer [176,177] which gives insight into the neutralisation or better charge exchange dynamics during a cluster–surface collision on a femtosecond time scale. Electron emission yields $\gamma(N, E_0)$ have been measured as a function of size N and impact energy E_0 for the impact of negatively and positively charged clusters on metal and HOPG surfaces (see Fig. 4.20). The authors find in their experiment a monotonic decrease in $\gamma(N, E_0)$ for impact on metal surfaces while pronounced oscillations are found in collisions with HOPG substrates, which depend on the impact energy. Although the origin of the electron emission process is not revealed, detailed information on neutralisation dynamics is obtained. The underlying idea is the following: EE can only happen when the cluster reaches the surface in its initial charge state. Charge transfer however can already take place between target and projectile via electron tunnelling. Even further, the electron is allowed to jump back and forth. Essential for

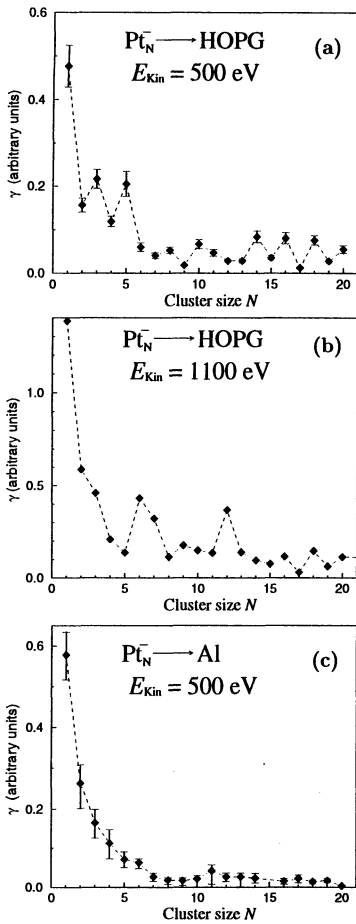


Fig. 4.20. Measured relative electron yield $\gamma(N)$ as a function of cluster size for collisions between Pt_N^- clusters and HOPG and Al surfaces. After Speer et al. [177]

this ansatz is that the projectile velocities are sufficiently low in order to provide the time for this tunnelling to happen. In the case of discrete levels for the two collision partners (which corresponds to zero bandwidth of the substrate or a low density of states as in HOPG), resonant or quasi-resonant tunnelling between the two approaching states takes place, resulting in an oscillatory behaviour of γ as a function of collision time. The cluster size in Fig. 4.20 translates into a time scale via the velocity of the incoming cluster. The time dependence of the effect emerges from the broader oscillation for $E_0 = 1100 \text{ eV}$ impact energy (Fig. 4.20b) compared to $E_0 = 500 \text{ eV}$ (Fig. 4.20a). For metal substrates which have a broad bandwidth the approach results in a monotonic decrease in $\gamma(N)$ again in agreement with experiment. In the case of finite bandwidth damped oscillations result.

4.13 Summary and Outlook

Collisions between clusters and surfaces show a rich and complex spectrum of phenomena. The fundamental difference between atomic and cluster projectiles can be found in the correlated motion of the atoms which form the cluster. This correlated motion is valid up to very high impact energies and only in the range of MeV/atom can we treat the system as if independent atoms collide with the surface.

One of the key problems in low energy cluster deposition experiments is whether the cluster is softlanded or breaks apart upon impact. Deposition of clusters at thermal energies clearly demonstrate a memory effect resulting in surface morphologies which cannot be obtained with conventional deposition techniques. Slightly higher impact energies ($E_0 > 1$ eV/atom) lead to implantation of cluster atoms into the substrate, stabilising the nanostructures formed. Energetic cluster-surface collisions provide a unique possibility for increasing the impact energy while keeping the impact velocity constant. In this way very high energy densities can be obtained close to the surface which manifest themselves through in giant sputtering yields and cluster-induced impact chemistry.

A solid understanding of the fundamental processes involved in cluster-surface collisions can only be obtained by dedicated experiments which are technically very demanding. The last few years have seen a growing effort in performing experiments with size selected clusters and well defined supports, and progress in this field is only a matter of time.

References

1. M. D. Morse, Chem. Rev. **86**, 1049 (1986).
2. P. Blandin and C. Massobrio, Surf. Sci. **279**, L219 (1992).
3. V. B. Koutecky, L. Cespiva, P. Fantucci, and J. Koutecky, J. Chem. Phys. **98**, 7981 (1993).
4. B. Nacer, C. Massobrio, and C. Felix, Phys. Rev. B **56**, 10590 (1997).
5. P. Melinon *et al.*, Int. J. Mod. Phys. B **9**, 4 (1995).
6. P. Melinon *et al.*, Mat. Sci. Eng. A **30**, 69 (1996).
7. H. Haberland, Z. Insepov, and M. Moseler, Phys. Rev. B **51**, 11061 (1995).
8. G. Kleer, E. Schaffer, M. Bodmann, J. Kraft, Y. Qiang, and H. Haberland, Materialwissenschaft und Werkstofftechnik **29**, 545 (1998).
9. J. Nordiek, M. Moseler, and H. Haberland, Rad. Eff. **142**, 27 (1997).
10. Y. Qiang, Y. Thurner, T. Reiners, O. Rattunde, and H. Haberland, Surface and Coatings Technology **100**, 27 (1998).
11. I. Yamada, NIM B **99**, 240 (1995).
12. D. Takeuchi, T. Aoki, J. Matsuo, and I. Yamada, AIP **392**, 491 (1997).
13. S. F. Belykh, I. S. Bitensky, D. Mullaev, and U. Rasulev, NIM B **129**, 451 (1997).
14. J. Chaumont, H. Bernas, A. Kusnetsov, C. Clerc, and L. Dumoulin, NIM B **129**, 436 (1997).

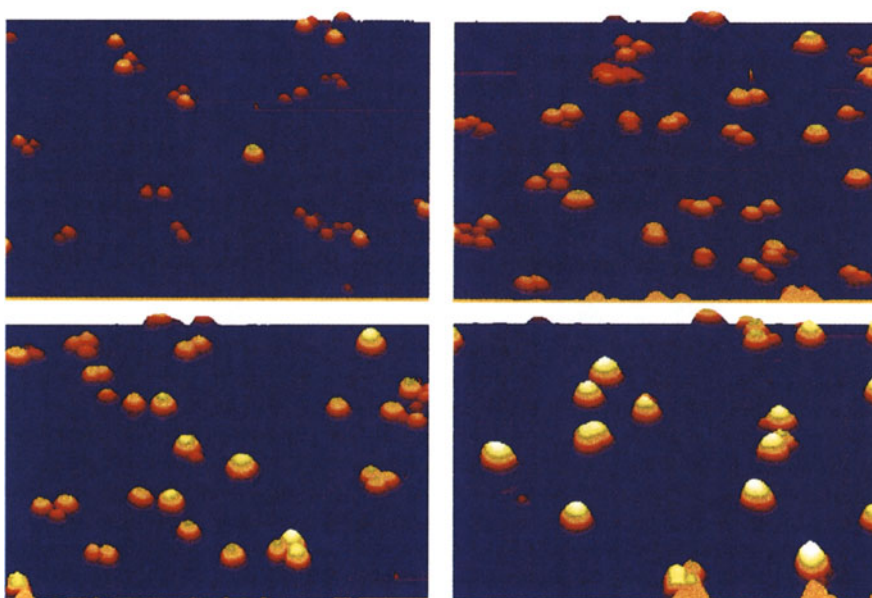
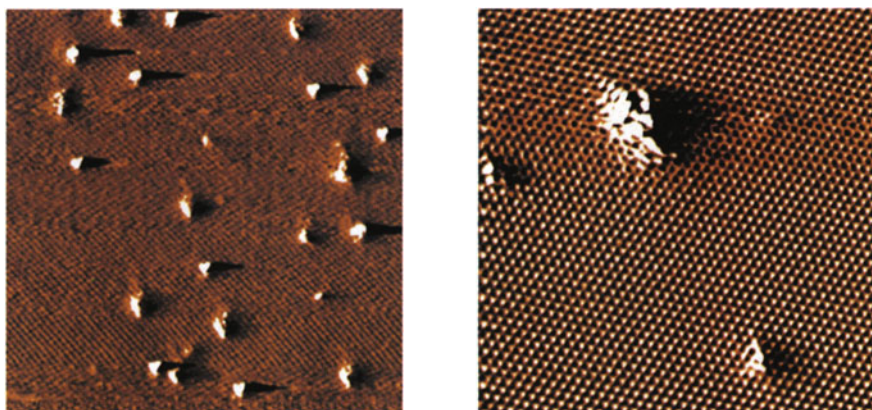
15. C. Tomaschko, K. H. Herrmann, J. Kaeshammer, R. Kuegler, C. Schoppmann, and H. Voit, *NIM B* **132**, 371 (1997).
16. R. J. Beuhler, G. Friedlander, and L. Friedman, *Phys. Rev. Lett.* **63**, 1292 (1989).
17. T. Tada, T. Kanayama, P. Weibel, S. J. Carroll, K. Seeger, and R. E. Palmer, *Microelectr. Eng.* **35**, 293 (1997).
18. Z. Insepov, I. Yamada, and M. Sosnowski, *J. Vac. Sci. Techn.* **15**, 981 (1997).
19. N. Toyoda, H. Kitani, J. Matsuo, and I. Yamada, *NIM B* **121**, 489 (1997).
20. H. P. Cheng and U. Landman, *Science* **260**, 1304 (1993).
21. H. P. Cheng and U. Landman, *J. Phys. Chem.* **98**, 3527 (1994).
22. W. Christen and U. Even, *J. Phys. Chem.* **102**, 9420 (1998).
23. C. L. Cleveland and U. Landman, *Science* **257**, 355 (1992).
24. T. Raz, I. Schek, M. B. Nun, U. Even, J. Jortner, and R. D. Levine, *J. Chem. Phys.* **101**, 8606 (1994).
25. I. Schek, J. Jortner, T. Raz, and R. D. Levine, *Chem. Phys. Lett.* **257**, 3 (1996).
26. I. Schek, T. Raz, R. D. Levine, and J. Jortner, *J. Chem. Phys.* **101**, 8596 (1994).
27. M. Akizuki, J. Matsuo, I. Yamada, M. Harada, S. Ogasawara, and A. Doi, *NIM B* **112**, 83 (1996).
28. S. A. Klopčič and M. F. Jarrold, *J. Chem. Phys.* **106**, 8855 (1997).
29. M. Moseler, Thesis, University of Freiburg (1998).
30. C. Massobrio and B. Nacer, *Z. Phys. D* **40**, 526 (1997).
31. C. Felix, G. Vandoni, C. Massobrio, R. Monot, J. Buttet, and W. Harbich, *Phys. Rev. B* **57**, 4048 (1998).
32. H. Brune, H. Roder, K. Bromann, and K. Kern, *Thin Solid Films* **264**, 230 (1995).
33. R. Schaub, H. Joedicke, J. Buttet, R. Monot, and W. Harbich, unpublished (1999).
34. G. Betz and W. Husinsky, *NIM B* **122**, 311 (1997).
35. I. Yamada and J. Matsuo, *Symp. Mater. Res. Soc.* 265 (1996).
36. A. Yoshida *et al.*, *NIM B* **112**, 248 (1996).
37. K. Bromann *et al.*, *Surf. Sci.* **377**, 1051 (1997).
38. K. Bromann *et al.*, *Science* **274**, 956 (1996).
39. E. E. B. Campbell and I. V. Hertel, *NIM B* **112**, 48 (1996).
40. M. Moseler, O. Rattunde, J. Nordiek, and H. Haberland, *Comp. Mat. Sci.* **10**, 452 (1998).
41. G. Vandoni, C. Felix, and C. Massobrio, *Phys. Rev. B* **54**, 1553 (1996).
42. H. Hsieh, R. S. Averback, H. Sellers, and C. P. Flynn, *Phys. Rev. B* **45**, 4417 (1992).
43. I. Yamada, J. Matsuo, N. Toyoda, T. Aoki, E. Jones, and Z. Insepov, *Mat. Sci. Eng.* **253**, 249 (1998).
44. S. Fedrigo, T. L. Haslett, and M. Moskovits, *Z. Phys. D* **40**, 99 (1997).
45. Z. Hu *et al.*, *J. Chem. Phys.* **95**, 2206 (1991).
46. U. Heiz, F. Vanolli, L. Trento, and W. D. Schneider, *Rev. Sci. Instr.* **68**, 1986 (1997).
47. W. Schulze, B. Winter, and I. Goldenfeld, *Phys. Rev. B* **38**, 2937 (1988).
48. P. Fayet, F. Granzer, G. Hegenbart, E. Moisar, B. Pischel, and L. Woste, *Phys. Rev. Lett.* **55**, 3002 (1985).

49. H. Haberland, M. Karrais, and M. Mall, *Z. Phys. D* **20**, 413 (1991).
50. E. C. Honea *et al.*, *Nature* **366**, 42 (1993).
51. T. G. Dietz, M. A. Duncan, D. E. Powers, and R. Smalley, *J. Chem. Phys.* **74**, 6511 (1981).
52. G. Ganteför, H. R. Siekmann, H. O. Lutz, and K. H. Meiwes-Broer, *Chem. Phys. Lett.* **165**, 293 (1990).
53. R. Behrisch, *Sputtering by Particle Bombardment I*, Vol. 47 of *Topics in Appl. Physics* (Springer, New York, 1981).
54. R. Behrisch, *Sputtering by Particle Bombardment II*, Vol. 52 of *Topics in Appl. Physics* (Springer, New York, 1983).
55. R. Behrisch, *Sputtering by Particle Bombardment III*, Vol. 64 of *Topics in Appl. Physics* (Springer, New York, 1991).
56. T. Leisner, C. Rosche, S. Wolf, F. Granzer, and L. Wöste, *Surf. Rev. Lett.* **3**, 1105 (1996).
57. K. J. Boyd, A. Lapicki, M. Aizawa, and S. L. Anderson, *Rev. of Sci. Instr.* **69**, 4106 (1998).
58. E. Teloy and D. Gerlich, *Chem. Phys.* **4**, 417 (1974).
59. D. Gerlich, *Adv. Chem. Phys.* **82**, 1 (1992).
60. W. Harbich, S. Fedrigo, and J. Buttet, *Chem. Phys. Lett.* **195**, 613 (1992).
61. W. Harbich, S. Fedrigo, and J. Buttet, *Z. Phys. D* **26**, 138 (1993).
62. S. Fedrigo, W. Harbich, J. Beljaev, and J. Buttet, *Chem. Phys. Lett.* **211**, 166 (1993).
63. K. Fauth, J. Buttet, and W. Harbich, submitted to *PRB* (1999).
64. W. Eberhardt *et al.*, *Phys. Rev. Lett.* **64**, 780 (1990).
65. H. V. Roy, J. Boschung, P. Fayet, F. Patthey, and W. D. Schneider, *Int. J. Mod. Phys. B* **7**, 556 (1993).
66. H. V. Roy, P. Fayet, F. Patthey, W. D. Schneider, B. Delley, and C. Massobrio, *Phys. Rev. B* **49**, 5611 (1994).
67. U. Heiz, *Appl. Phys. A* **67**, 621 (1998).
68. U. Busolt, E. Cottancin, H. Rohr, L. Socaciu, T. Leisner, and L. Wöste, *App. Phys. B* **68**, 453 (1999).
69. A. Perez *et al.*, *Nanostructured Materials* **6**, 1 (1995).
70. H. Hövel, A. Hilger, I. Nusch, and U. Kreibig, *Z. Phys. D* **42**, 203 (1997).
71. B. Palpant *et al.*, *Phys. Rev. B* **57**, 1963 (1998).
72. S. Fedrigo, W. Harbich, and J. Buttet, *J. Chem. Phys.* **99**, 5712 (1993).
73. S. Fedrigo, W. Harbich, and J. Buttet, *Phys. Rev. B* **47**, 10706 (1993).
74. R. D. Beck, P. S. John, M. L. Homer, and R. L. Whetten, *Chem. Phys. Lett.* **187**, 122 (1991).
75. R. D. Beck, P. S. John, M. L. Homer, and R. L. Whetten, *Science* **253**, 879 (1991).
76. P. M. S. John, R. D. Beck, and R. L. Whetten, *Phys. Rev. Lett.* **69**, 1467 (1992).
77. H. Yasumatsu, U. Kalmbach, S. Koizumi, A. Terasaki, and T. Kondow, *Z. Phys. D* **40**, 51 (1997).
78. W. Christen, U. Even, T. Raz, and R. D. Levine, *J. Chem. Phys.* **108**, 10262 (1998).
79. E. Hendell, U. Even, T. Raz, and R. D. Levine, *Phys. Rev. Lett.* **75**, 2670 (1995).
80. C. Yeretizian, K. Hansen, R. D. Beck, and R. L. Whetten, *J. Chem. Phys.* **98**, 7480 (1993).

81. M. Benslimane, M. Chatelet, A. D. Martino, F. Pradere, and H. Vach, *Chem. Phys. Lett.* **237**, 323 (1995).
82. M. Chatelet, M. Benslimane, A. D. Martino, F. Pradere, and H. Vach, *Surf. Sci.* **352**, 50 (1996).
83. M. Chatelet, A. de Martino, J. Pettersson, F. Pradere, and H. Vach, *Chem. Phys. Lett.* **196**, 563 (1992).
84. A. D. Martino, M. Benslimane, M. Chatelet, F. Pradere, and H. Vach, *J. Chem. Phys.* **105**, 7828 (1996).
85. E. Fort, F. Pradere, A. D. Martino, H. Vach, and M. Chatelet, *European. Phys. Jour. D* **1**, 79 (1998).
86. F. Pradere, M. Benslimane, M. Chatelet, A. D. Martino, and H. Vach, *Surf. Sci.* **375**, 2 (1997).
87. H. Vach, M. Benslimane, M. Chatelet, A. D. Martino, and F. Pradere, *J. Chem. Phys.* **103**, 1972 (1995).
88. H. Vach, A. D. Martino, M. Benslimane, M. Chatelet, and F. Pradere, *J. Chem. Phys.* **100**, 8526 (1994).
89. J. B. C. Pettersson and N. Markovic, *Chem. Phys. Lett.* **201**, 421 (1993).
90. A. Terasaki, T. Tsukuda, H. Yasumatsu, T. Sugai, and T. Kondow, *J. Chem. Phys.* **104**, 1387 (1996).
91. T. M. Bernhardt, B. Kaiser, and K. Rademann, *Z. Phys. D* **40**, 327 (1997).
92. B. Kaiser, T. M. Bernhardt, M. Kinne, K. Rademann, and A. Heidenreich, *J. Chem. Phys.* **110**, 1437 (1999).
93. M. Kinne, M. Bernhardt, B. Kaiser, and K. Rademann, *Int. J. Mass Spectr.* **167**, 161 (1997).
94. R. D. Beck, J. Rockenberger, P. Weis, and M. M. Kappes, *J. Chem. Phys.* **104**, 3638 (1996).
95. P. M. S. John and R. L. Whetten, *Chem. Phys. Lett.* **196**, 330 (1992).
96. A. Terasaki, H. Yamaguchi, H. Yasumatsu, and T. Kondow, *Chem. Phys. Lett.* **262**, 3 (1996).
97. D. M. Lindsay, F. Meyer, and W. Harbich, *Z. Physik D* **12**, 15 (1989).
98. S. Fedrigo, W. Harbich, and J. Buttet, *Phys. Rev. B* **58**, 7428 (1998).
99. M. Ratner, W. Harbich, and S. Fedrigo, *Phys. Rev. B* accepted for publication (1999).
100. G. Vandoni, C. Felix, C. Goyhenex, R. Monot, J. Buttet, and W. Harbich, *Surf. Sci.* **333**, 838 (1995).
101. G. Vandoni, C. Felix, R. Monot, J. Buttet, C. Massobrio, and W. Harbich, *Surf. Rev. Lett.* **3**, 949 (1996).
102. B. Kaiser, T. M. Bernhardt, and K. Rademann, *Appl. Phys. A* **66**, 5711 (1998).
103. S. J. Carroll, S. G. Hall, R. E. Palmer, and R. Smith, *Phys. Rev. Lett.* **81**, 3715 (1998).
104. F. Karetta and H. M. Urbassek, *J. Appl. Phys.* **11**, 5410 (1992).
105. R. Lee, Z. Pan, and Y. Ho, *Phys. Rev. B* **53**, 4156 (1996).
106. H. J. Kang, M. W. Lee, J. H. Kim, and C. N. Whang, *NIM B* **121**, 53 (1997).
107. C. Felix, Thesis, EPFL Lausanne (1995).
108. V. I. Shulga and P. Sigmund, *NIM B* **62**, 23 (1991).
109. T. Aoki, T. Seki, J. Matsuo, Z. Insepov, and I. Yamada, *Mat. Chem. Phys.* **54**, 1 (1998).
110. Z. Pan and P. Sigmund, *NIM* **51**, 344 (1990).
111. Y. Yamamura and T. Muramoto, *Rad. Eff.* **130**, 225 (1994).

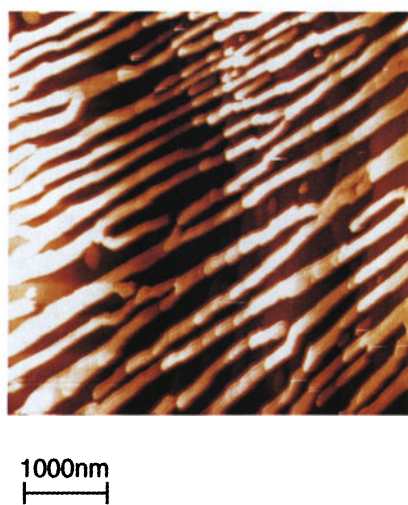
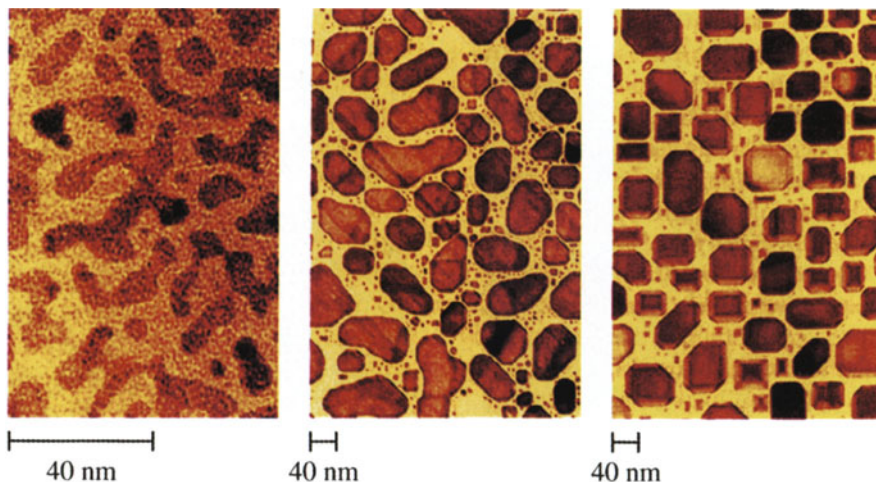
112. S. Ihara, S. Itoh, and J. Kitakami, *Phys. Rev. B* **58**, 10736 (1998).
113. Y. Yamamura and T. Muramoto, *NIM* **72**, 331 (1992).
114. T. Aoki, J. Matsuo, Z. Insepov, and I. Yamada, *NIM* **121**, 498 (1997).
115. G. Braeuchle, S. R. Schneider, D. Illig, R. D. Beck, H. Schreiber, and M. M. Kappes, *NIM B* **112**, 105 (1996).
116. K. Baudin *et al.*, *NIM B* **94**, 341 (1994).
117. N. Shimada, T. Aoki, J. Matsuo, I. Yamada, K. Goto, and T. Sugui, *Mat. Chem. Phys.* **54**, 80 (1998).
118. P. Sigmund, *Phys. Rev.* **184**, 383 (1969).
119. H. H. Andersen and H. L. Bay, *J. App. Phys.* **45**, 953 (1974).
120. H. H. Anderson and H. L. Bay, *J. App. Phys.* **46**, 2416 (1975).
121. Z. Insepov and I. Yamada, *NIM B* **99**, 248 (1995).
122. H. H. Andersen *et al.*, *Phys. Rev. Lett.* **80**, 5433 (1998).
123. K. Baudin *et al.*, *NIM B* **112**, 59 (1996).
124. M. Benguerba *et al.*, *NIM B* **62**, 8 (1991).
125. K. Boussofiane-Baudin *et al.*, *NIM B* **88**, 61 (1994).
126. A. Brunelle *et al.*, *NIM B* **125**, 207 (1997).
127. Z. Insepov, I. Yamada, and M. Sosnowski, *Mat. Chem. Phys.* **54**, 234 (1998).
128. N. Toyoda, H. Kitani, N. Hagiwara, T. Aoki, J. Matsuo, and I. Yamada, *Mat. Chem. Phys.* **54**, 263 (1998).
129. T. Yamaguchi, J. Matsuo, M. Akizuki, C. E. Ascheron, G. H. Takaoka, and I. Yamada, *NIM B* **99**, 237 (1995).
130. D. A. Thompson and S. S. Johar, *Appl. Phys. Lett.* **34**, 342 (1979).
131. P. Sigmund and C. Claussen, *J. App. Phys.* **52**, 990 (1981).
132. K. Franzreb, A. Wucher, and H. Oechsner, *Surf. Sci.* **279**, L225 (1992).
133. T. Takagi, I. Yamada, and A. Sasaki, *Thin Solid Films* **39**, 207 (1976).
134. I. Yamada, H. Usui, H. Inokawa, and T. Takagi, *Surf. Sci.* **168**, 365 (1986).
135. Y. Yamamura, I. Yamada, and T. Takagi, *NIM B* **38**, 902 (1989).
136. I. F. K. Urban, *J. App. Phys.* **67**, 7082 (1990).
137. I. F. K. Urban and A. Bernstein, *Thin Solid Films* **193**, 92 (1990).
138. W. L. Brown *et al.*, *NIM B* **59**, 182 (1991).
139. R. A. Zuhr, T. E. Haynes, M. D. Galloway, S. Tanaka, A. Yamada, and I. Yamada, *NIM* **59**, 308 (1991).
140. H. Haberland *et al.*, *Symp. Mater. Res. Soc* 207 (1995).
141. H. Haberland, Z. Insepov, M. Karrais, M. Mall, M. Moseler, and Y. Thurner, *Mat. Sci. Eng. B* **19**, 31 (1993).
142. H. Haberland, Z. Insepov, M. Karrais, M. Mall, M. Moseler, and Y. Thurner, *NIM B* **81**, 1320 (1993).
143. H. Haberland, M. Karrais, M. Mall, and Y. Thurner, *J. Vac. Sci. Techn.* **10**, 3266 (1992).
144. H. Haberland, M. Mall, M. Moseler, Q. You, T. Reiners, and Y. Thurner, *J. Vac. Sci. Techn.* **12**, 2925 (1994).
145. H. Haberland, Z. Insepov, and M. Moseler, *Z. Phys. D* **26**, 229 (1993).
146. M. Moseler, J. Nordiek, O. Rattunde, and H. Haberland, *Rad. Eff.* **142**, 39 (1997).
147. U. Even, I. Schek, and J. Jortner, *Chem. Phys. Lett.* **202**, 3 (1993).
148. T. Raz, U. Even, and R. D. Levine, *J. Chem. Phys.* **103**, 5394 (1995).
149. T. Raz and R. D. Levine, *J. Chem. Phys.* **105**, 8097 (1996).
150. T. Engel, *Surf. Sci. Rep.* **18**, 91 (1993).

151. J. R. Engstrom, D. J. Bonser, and T. Engel, *Surf. Sci.* **268**, 238 (1992).
152. H. Joedicke, Thesis, EPFL Lausanne (1999).
153. A. Gruber, J. Gspann, and H. Hoffmann, *Appl. Phys. A* **68**, 197 (1999).
154. A. Gruber, J. Gspann, and P. von Blanckenhagen, *J. Vac. Sci. Techn.* **15**, 1382 (1997).
155. J. Gspann, *J. Vac. Sci. Techn.* **13**, 2618 (1995).
156. P. V. Blanckenhagen, A. Gruber, and J. Gspann, *NIM B* **122**, 322 (1997).
157. Y. L. Beyec, *Int. J. Mass Spec.* **174**, 101 (1998).
158. R. A. Baragiola, *NIM B* **88**, 35 (1994).
159. M. Fallavier, *NIM B* **112**, 72 (1996).
160. D. Hasselkamp, *Particle Induced Electron Emission*, Vol. 123 of *Springer tracts in Modern Physics* (Springer, New York, 1992).
161. R. J. Beuhler, *J. Appl. Phys.* **54**, 4118 (1983).
162. U. Even, P. J. de Lange, H. T. Jonkman, and J. Kommandeur, *Phys. Rev. Lett.* **56**, 965 (1986).
163. F. Thum and W. O. Hofer, *Surf. Sci.* **90**, 331 (1979).
164. E. E. B. Campbell, G. Ulmer, and I. V. Hertel, *Phys. Rev. Lett.* **67**, 1986 (1991).
165. K. Athanassenas, T. Leisner, U. Frenzel, and D. Kreisle, *Ber. Bunsenges. Phys. Chem.* **96**, 1192 (1992).
166. A. Amrein, R. Simpson, and P. Hackett, *J. Chem. Phys.* **94**, 4663 (1991).
167. G. Ganteför, W. Eberhardt, H. Weidele, D. Kreisle, and E. Recknagel, *Phys. Rev. Lett.* **77**, 4524 (1996).
168. T. Leisner, K. Athanassenas, D. Kreisle, E. Recknagel, and O. Echt, *J. Chem. Phys.* **99**, 9670 (1993).
169. P. Weis, J. Rockenberger, R. D. Beck, and M. M. Kappes, *J. Chem. Phys.* **104**, 3629 (1996).
170. P. M. S. John, C. Yerezian, and R. L. Whetten, *J. Phys. Chem.* **96**, 9100 (1992).
171. C. Yerezian, K. Hansen, and R. L. Whetten, *Science* **260**, 652 (1993).
172. U. Frenzel, U. Hammer, H. Westje, and D. Kreisle, *Z. Phys. D* **40**, 108 (1997).
173. W. A. Chupka and C. E. Klotz, *Int. J. Mass Spec.* **167**, 595 (1997).
174. H. Rothard *et al.*, *Rad. Eff.* **126**, 373 (1993).
175. K. Baudin, A. Brunelle, S. D. Negra, J. Depauw, Y. L. Beyec, and E. S. Parilis, *NIM B* **117**, 47 (1996).
176. B. Wrenger, K. H. M. Broer, O. Speer, and M. E. Garcia, *Phys. Rev. Lett.* **79**, 2562 (1997).
177. O. Speer, M. E. Garcia, B. Wrenger, and K. H. Meiwes-Broer, *Surf. Sci.* **443**, 195 (1999).



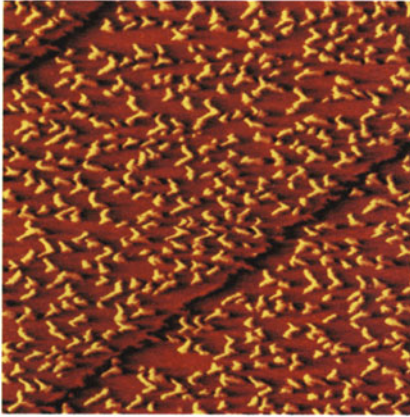
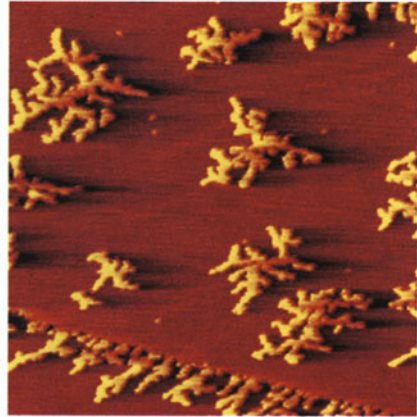
Top: Platinum clusters produced in a Pulsed Arc Cluster Ion Source (PACIS) and deposited from a beam onto HOPG. Image size $67\text{ nm}\times 67\text{ nm}$ (*left*) and $11\text{ nm}\times 11\text{ nm}$ (*right*). See Chap. 5, Fig. 5.6

Bottom: Silver clusters with sizes between $N = 4 \times 10^2$ and $N = 4 \times 10^3$, grown by condensation in preformed nanopits in HOPG. See Chap. 2, Fig. 2.15

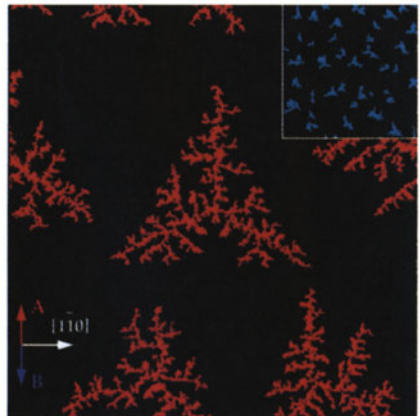
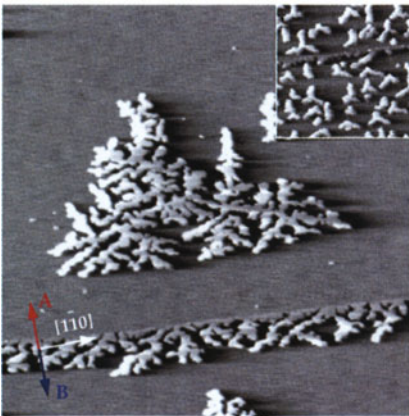


Top: Pd particles epitaxially grown on MgO(100) at 300 K, 433 K, and 673 K, respectively. By Henry et al. See Chap. 3, Fig. 3.15

Bottom: Oriented Fe islands on W(110), grown by self-organisation of Fe atoms and subsequent annealing. After J. Bansmann, V. Senz, L. Lu, A. Bet-tac, and K.H. Meiwes-Broer, *J.Electr.Spectr.Relat.Phenom.* 106,221 (2000). Such nanostructures are interesting systems for magnetic studies, see also Chap. 7

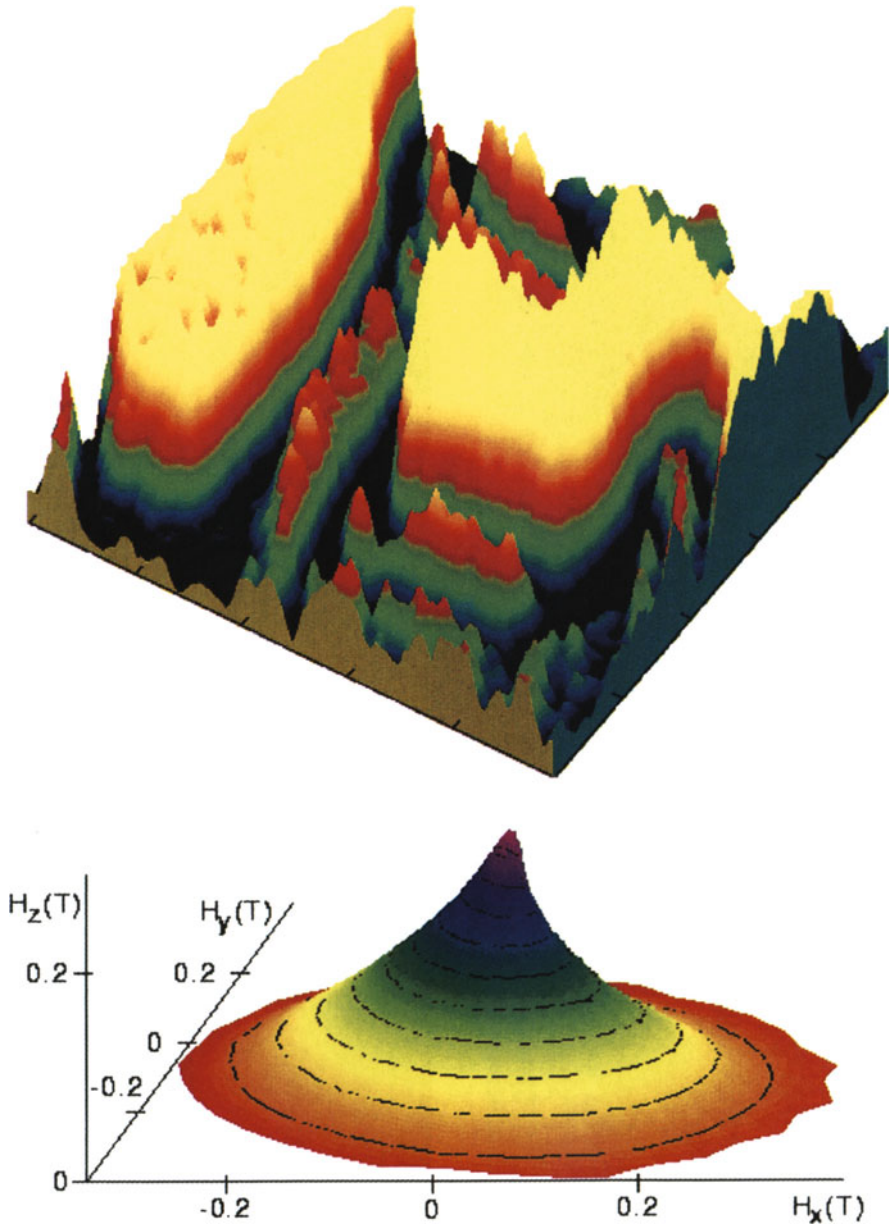
$T = 80 \text{ K}$  $T = 110 \text{ K}$ 

200 Å



200 Å

Self organisation of silver on Pt(111), see Chap. 3. *Top*: Island formation at different temperatures, Fig. 3.2. *Bottom*: A dendritic structure grown at 130 K (and 80 K, *inset*), compared to the results of kinetic Monte Carlo calculations, see Fig. 3.4



Top: Photon map of silver islands on W(110)/C-R(15×3). 50 nm×50 nm. Note that also the very small structures (down to 1 nm) emit light during scanning. 3-dimensional representation of Fig. 5.13 in Chap. 5.

Bottom: Directional dependence of the magnetic switching field of a BaFeCo-TiO particle with about 20 nm. See Chap. 7, Fig. 7.6

5 Electronic Level Structure of Metal Clusters at Surfaces

Karl-Heinz Meiwes-Broer

5.1 Introduction

The electronic properties of free metal clusters depend sensitively on the exact number of atoms N , as has been pointed out by de Heer in Chap.1. For any technical application it is unavoidable to study the influence of a supporting or embedding medium on the electronic level structure. For example, by conserving the distinct energy spacings of a deposited cluster, it would be possible to generate a “new surface” with adjustable electronic, and hence, also optical and chemical properties. Indeed, cluster size dependent surface reactivities have recently been observed, see the work of Schneider and Heiz in Chap. 8 and [1,2]. Furthermore, many investigations dealt with N dependent optical absorption of clusters on surfaces or in matrices [3–6] which were throughout explained by collective electron excitations.

The presence of a surface will significantly influence the electronic level structure in the cluster (see Fig. 5.1). At a large distance the only common energy is the vacuum energy, E_{vac} .

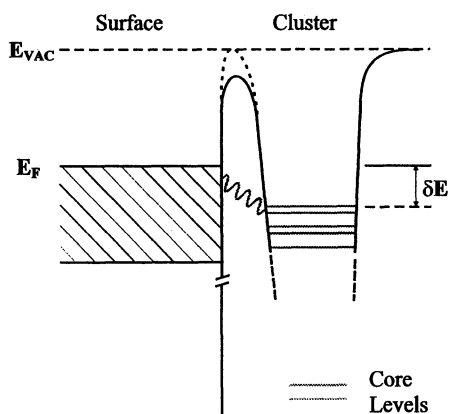


Fig. 5.1. A metal cluster approaches a conducting surface. How will the presence of the surface change the electronic level structure? Will the highest molecular orbital pin to the Fermi level E_F ?

With decreasing separation the energy barrier between cluster and surface will also decrease. Thus the cluster level structure might change when compared to the corresponding free system. The details of the binding determine whether the highest occupied level in the cluster adjusts to the substrate Fermi energy E_F . In this case the contact potential would induce a local charge accumulation. Also, the core levels might shift. Most theoretical investigations deal with structural properties which are dominated by the material combination (see preceding chapters). On a metallic surface the cluster forms a metallic bond and often likes to wet the substrate. If the cluster is of the same material as the surface it will form an epitaxial layer. On a non-metallic and weakly interacting surface clusters might keep their identity and have structures close to those of the free clusters in vacuum. The details of the cluster-surface interaction will determine the changes in geometrical and electronic properties with respect to the unsupported case.

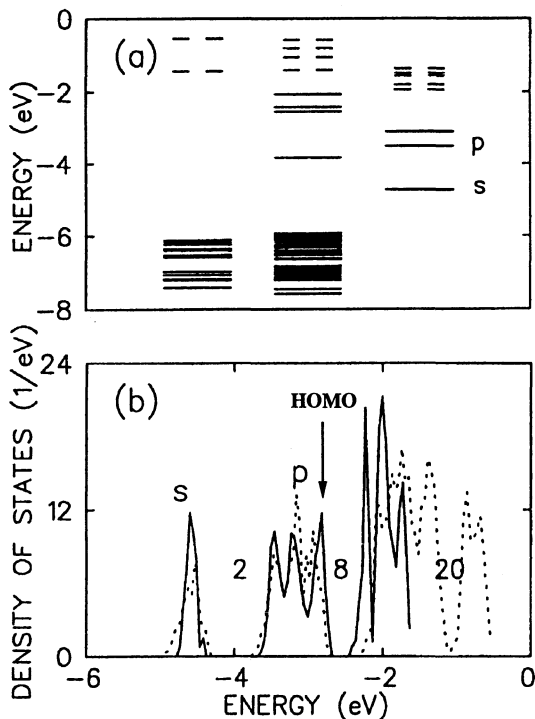


Fig. 5.2. (a) Kohn-Sham eigenvalues for the NaCl(001) substrate (*left*), for the relaxed Na₈/NaCl(001) system (*middle*), and the free Na₈ cluster (*right*). The *broken lines* correspond to empty levels. The HOMO of the free Na₈ has twofold degeneracy which is lifted upon surface contact. (b) Time averaged DOS for the adsorbed cluster at 350 K (*solid curve*), and the corresponding distribution for a free Na₈ at 550 K. After Häkkinen et al. [7]

Whereas a wealth of theoretical information is available on the electronic properties of adsorbed atoms and molecules, the level structure of deposited clusters, on the other hand, has scarcely been considered. In the case of weakly interacting surfaces, e.g., metal clusters on salt, it is found that the density of states (DOS) within the cluster is only weakly affected by the presence of the surface [7]. This is demonstrated in Fig. 5.2 by the Kohn–Sham eigenvalues of free Na_8 when compared to those of deposited ones. The corresponding DOS shows only a slight change in the electronic level structure (see for example the shifts in cluster levels and the lifting of the degeneracy of the HOMO, middle of Fig. 5.2a). Even at elevated temperatures the DOS remains clearly structured (see Fig. 5.2b). As a matter of fact, it can be shown that jellium clusters on inert surfaces possess either a planar or a 3-dimensional ground state, but in many cases both geometries are stable and there is a marked energy barrier between them [8].

For 3-dimensional clusters on surfaces with stronger interactions there are no theoretical results concerning their electronic level structures. As mentioned above, such systems are inherently complex due to the sensitivity of the DOS on structural change and possible charge transfer processes.

So far most information on the electronic situation in deposited metal clusters has been gained by experimental methods. The main results are briefly reviewed, which were obtained either by photoelectron spectroscopy, or with spatially resolving methods, e.g., scanning tunnelling spectroscopy. For the sake of completeness it should be noted that there is also field emission work on single metal particles. The Reifenberger group [9] measured the electron energy distribution from Au_N on tungsten tips. The structure was attributed to energy levels which could be described within the jellium picture.

5.2 Photoelectron Spectroscopy of Deposited Clusters

A very straightforward way to investigate electronic properties is to deposit the clusters and inspect them by conventional Photo Electron Spectroscopy (PES). Vacuum ultraviolet light sources like He lamps or synchrotron radiation have to be chosen for the excitation (see also Chap. 2). This method involves two major problems: (i) with the exception of some transition metals, the cross section for photoemission close to the Fermi level is often low; (ii) as a nonlocal method PES probes the underlying substrate as well, so that usually most of the signal originates from the supporting surface. Consequently much information has been obtained on the core levels of the deposited clusters, and this can be recorded with high efficiency.

In order to illustrate the problem, in Fig. 5.3 photoelectron spectra are depicted which were recorded from an uncovered SiO_2 substrate (dotted curve), and after deposition of lead clusters from a beam ($N \approx 500$). After deposition a strong peak appears at a binding energy of about 18 eV. This can be assigned to the $Pb5d_{5/2}$ core level. Depending on the cluster size, this

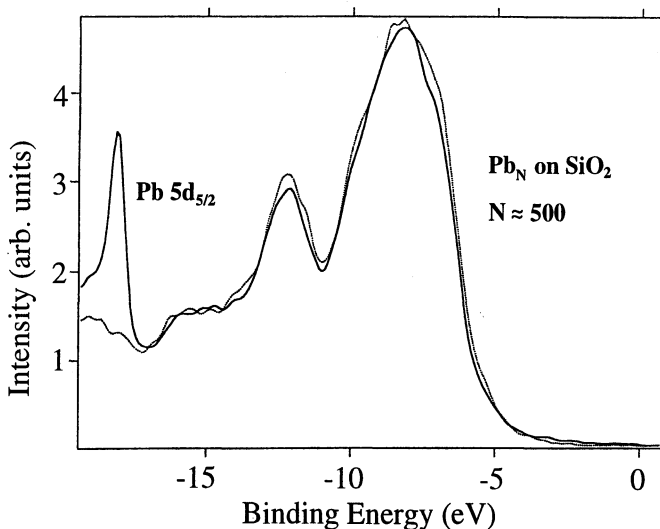


Fig. 5.3. Photoelectron spectra of an uncovered (natural) SiO_2 probe, dotted curve, and after deposition of Pb_N , $N \approx 500$. Excitation energy $h\nu = 50$ eV. Note the extremely low emission from the lead clusters close to the Fermi level at 0 eV even for $N \approx 500$. After Siekmann et al. [10]

peak exhibits a shift to higher or lower values [10]. Close to the Fermi level, however, only an extremely low electron intensity originates from the lead clusters although large clusters and a substrate with a wide band gap are chosen, i.e., a low DOS between -5 eV and the Fermi energy.

As this situation is symptomatic for conventional PES on deposited metal clusters, many investigations concentrated on the N dependence of the cluster atom core levels. For clusters on carbon or even insulating materials, as in Fig. 5.3, core level photoemission is in this case dominated by the effect of *final state charging*, i.e., the photohole cannot be shielded within the short time of the emission event [11–16]. This effect is illustrated in Chap. 2 on the PES thresholds of silver particles [17] where the authors show that the neutralisation dynamics of the photohole is responsible for the missing sharp Fermi edge. The lack of shielding leads to N dependent core level shifts which can be discussed in terms of adsorption and cohesive energies [18]. The low electron intensity close to E_F contrasts PES of *gas phase* lead clusters, which shows several intense peaks at low binding energies. This is illustrated in Figure 5.4 where small Pb_N^- clusters in a beam, were investigated [19]. Similarly, every lead cluster with a given size has a distinct photoelectron spectrum which serves as ‘fingerprint’ for the detailed electronic structure [20,21]. Cluster anions of many different materials have been investigated by this method. They all show distinct material and size specific confinement effects (see also Chap. 1 where alkali anion PES is shown).

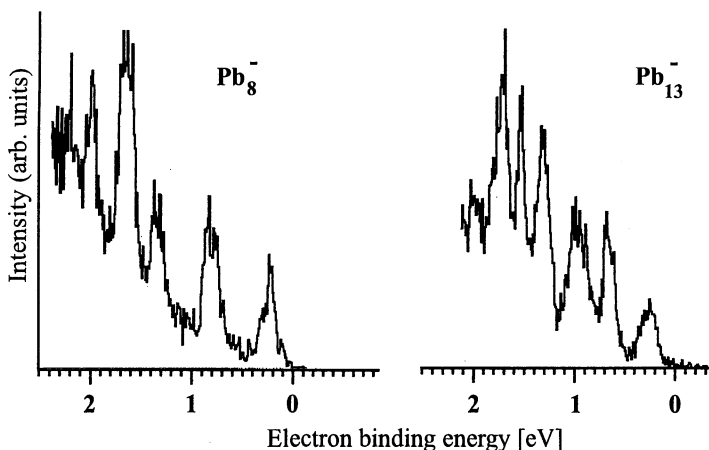


Fig. 5.4. Photoelectron spectra of mass selected negatively charged lead clusters in a beam. Excitation energy $h\nu = 5.0$ eV. Note that the zero point of the energy scale has arbitrarily been shifted to the emission onset. For the method see [20]. After Hector et al. [19]

Clearly the gas phase PES at low excitation energies (usually UV lasers are used with energy from about 4 – 8 eV) reveals the undisturbed electronic level structure.

On the surface, also other clusters show no or only weak s- or p-derived emission: for mass selected Au_N on carbon, extremely weak and barely interpretable electron intensity was reported by DiCenzo et al. [22]. In the case of Siekmann et al., who also investigated Au_N (on silver) [10], no s-derived electron intensity could be recorded, instead a very narrow d-peak hints to a low coordination within the gold cluster.

Clusters of open d-shell metals, on the other hand, do show some interesting features. Roy et al. investigated Pt_N and Pd_N on silver where the spin-orbit split components of the d-level change their separations and centres of gravity with N [23]. The separation between the spin-orbit components in Pt_N and in Pd_N increase and both components gradually move towards the Fermi energy. These clusters are strongly bound to the Ag surface, where the localised adsorbate states are coupled to the delocalised conduction electrons of silver. The increased spin-orbit splitting reflects the increase in cohesive energy due to molecular interaction, whereas the shift in the centre of gravity of the d-emission indicates the trend to metal formation [23]. As a matter of fact, the strong cluster-surface interaction induces a flattening of the clusters until 2-dimensional systems with monoatomic height are obtained. So these results do not reflect the electronic level structure of a 3 dimensional supported cluster.

Takasu et al. [24] investigated Pd particles on silica without mass selection. A structureless electron intensity developed within the band gap of the substrate, gradually approaching the bulk spectrum at high coverages. Weak d derived emission was observed by Eberhardt et al. [25] for small mass selected Pt_N on silica; again no clear signature is found close to the Fermi energy.

Summarising the photoemission work on deposited metal clusters with conventional techniques it can be stated that up to now there is only little information available on their electronic level structure. So far nothing similar to what was observed with PES on mass selected clusters in beams could be found with deposited metal clusters. One reason for the not so encouraging situation is the fragility of the cluster on surface system. Possibly the irradiation by the vacuum UV radiation leads to a change or even a destruction/fragmentation of the clusters. From gas phase experiments it is known that metal clusters can exhibit, at least in certain energy ranges, an enormous photofragmentation cross section with UV light [26]. At the same time, conventional photoelectron spectroscopy with scanning electron energy analysers merely records a vanishing fraction of all electrons emitted. Thus the sample has to suffer a significant radiation dose before a spectrum is recorded with sufficient statistics (typical sampling time at a synchrotron lies around in 500 s at a photon flux of about $10^{12} \text{ s}^{-1} \text{ cm}^{-2}$).

In order to significantly reduce the necessary radiation dose deposited metal clusters were also investigated with time-of-flight (TOF) PES [27]. For this a pulsed UV light source is necessary. The method of resonant four wave mixing of dye laser light in mercury vapour and, alternatively, in a mercury supersonic beam was used. Up to 10^{12} photons per pulse were generated within a pulse duration of about 10 ns at a photon energy of 9.9 eV [28]. The nascent electron pulses enter a 50 cm drift tube and their arrival times are registered. After conversion of the time dependent signal into an energy scale, electron energy spectra are obtained. Due to the simultaneous registration of electrons with different energies, the necessary radiation dose is reduced by four orders of magnitude or more, depending on the chosen resolution. One result obtained by this method is reproduced in Fig. 5.5. Here, roughly mass selected lead clusters with broad size distributions were deposited from a beam on naturally grown SiO_2 on Si(111) [29,27]. The spectra show clear signatures of the cluster deposits which change with the cluster size. In a first approach these features were assigned to transitions of atomic spin-orbit split $6p_{1/2}$ -derived levels. The width ΔE of the peak is connected with the hopping integral V_H by the relation $\Delta E = 2 \cdot \sqrt{N_Z} \cdot V_H$, with N_Z the mean coordination number [30]. The mean cluster size N is estimated from the photoemission thresholds to $N \approx 50$ (5b) up to $N \approx 500$ (5e), thus allowing the determination of N_Z and, finally, the hopping integral V_H . Depending on whether δ - or π -molecular orbitals contribute to the emission, the extracted

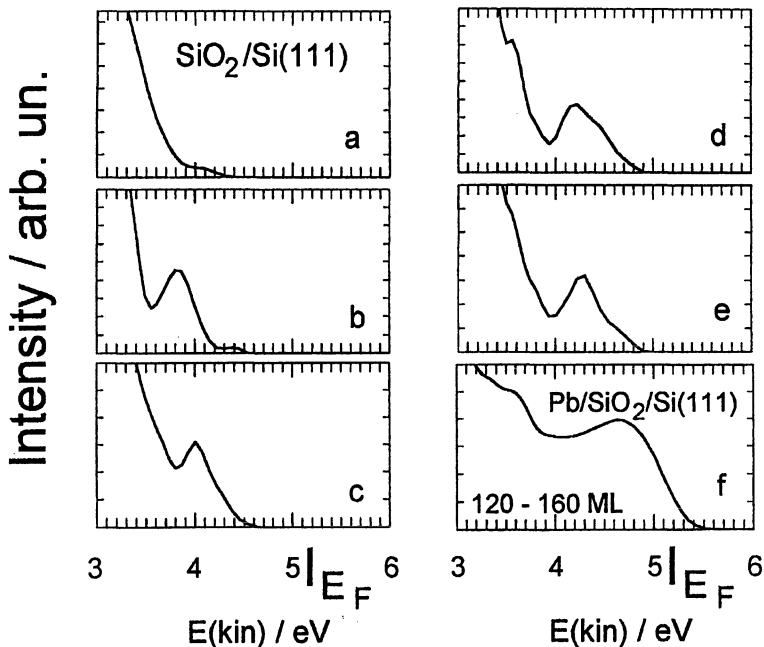


Fig. 5.5. PES of deposited Pb_N on $\text{SiO}_2/\text{Si}(111)$ at 78 K. The spectra are obtained by electron TOF spectroscopy with frequency mixed laser radiation at 9.9 eV (pulse length about 10 ns). **a**) Uncovered $\text{SiO}_2/\text{Si}(111)$ substrate. **b–e**) Increasing coverage with preformed lead clusters. The clusters aggregate on the surface and thus the analysed lead deposits increase in size. **f**) Spectrum of a thick polycrystalline Pb film. From Hector et al. [27]

V_H ranges from around 0.2 eV to 0.5 eV, which is close to theoretical values for alkali-metal clusters [31].

At longer times of exposure the structures in the photoelectron spectra wash out, a clear sign of radiation damage. It is also interesting to note that the overall photoelectron intensity increases by one to two orders of magnitude upon covering the substrate with metal clusters. This raises the question about the process of photoemission from cluster deposits, a point which is currently under contention.

In spite of the still limited resolution (mainly due to the electronics used and the laser pulse length) distinct and intense peaks can be recorded which originate from the deposited clusters. With the third generation of synchrotrons (e.g., BESSY II), and with UV free electron lasers, powerful pulsed UV light sources become available to start a promising new approach in studying the electronic level structure of deposited clusters by time-of-flight PES.

Other current investigations use electron TOF as well, but now with ultra-short (50 – 100 fs) laser light pulses on silver clusters [32] and silver particles on HOPG [33]. In both investigations collective electron excitations appear to play a major role where the pump-probe time resolved results give insight into the charge carrier relaxation processes. As to date, however, no single electron excitations have yet been observed which would give more insight into the electronic level structure of those systems.

In the following, we focus more on spatially resolving techniques, and paying special attention to scanning tunnelling spectroscopy .

5.3 Scanning Tunnelling Spectroscopy and Inverse Photoemission

Scanning tunnelling microscopy is a suitable method for looking at nanometer-sized islands and supported clusters with a resolution on the atomic scale. It is important to note that no direct information can be obtained on the local chemical nature. One promising approach involves analysis of the electronic structure by carrying out Scanning Tunnelling *Spectroscopy* (STS). Here, the current between tip and sample is measured as a function of the applied voltage. The current strongly depends on the density of states of the tip and sample and hence, in principle, extracts information about the local electronic structure and thus the chemical nature.

STS has been widely used for the spectroscopy of surfaces [34,35], for a review see [36,37]. Indeed, recent analyses by STS [38] reveal even the vibrational levels of a molecule in surface contact. Most theoretical approaches use perturbation theory which treats both the tunnelling tip, and the sample independently. In this representation the total current is proportional to the local charge density at the Fermi level evaluated at the tip end [39,40]. A simple picture evolves, whereby the tunnelling current, or more precisely, its derivative dI/dU , maps the DOS of the sample whenever the DOS of the tip displays a smooth energy dependence.

As one goes to decreasing distances and higher lateral resolutions the tip-sample interaction plays an increasing role, and as a consequence, the theoretical perturbation breaks down. Now the tunnelling must be treated as a scattering process where the convolution between the wave functions of the tip and the sample has to be considered. Up to now, this many particle problem has been tackled by first-principles local density functional calculations and the application of Green's functions. A theoretical review and applications to atomic adsorbates can be found in [41]. As there is yet no theoretical treatment of the conductivity of a cluster on a surface, we have to look into related fields, e.g., the physics of metallic atomic size contacts. Recent theoretical approaches deal with quantum electronic transport through microconstrictions with variable shapes (see Chap. 6 of this book). There it is shown that the conductance can be quantised due to the geometry of the constrict-

tion, i.e., even without consideration of the chemical nature of the contact. Along this line, Scherbakov et al. [42] showed that for three-dimensional free electron - like constrictions the charge transport is quantised. This is evident from peaks in the calculated dI/dU .

When considering additionally the orbital electronic structure and the local atomic environment around the region of constriction, the transmission eigenvalues are richly structured as a function of energy. This means that the conductance is strongly connected to the orbitals of the atoms involved, which gives hope that a measurement of the charge transport through a cluster might yield information about its electronic structure. Finally, another feature has to be considered which might be important for the description of a tunnelling experiment on clusters: in the presence of an electrically insulating layer between cluster and surface, the single electron charging energy $e^2/2C$, with C the capacitance of the cluster, might lead to a voltage threshold (the Coulomb barrier) below which electron transport is hindered. With increasing voltage, steps arise (Coulomb staircase) which are caused by changing the charge on the cluster by successively adding single electrons. Since the charging energy is inversely proportional to C , the barrier and the step distances can be increased by choosing smaller clusters. These systems are therefore serious candidates as a basis for future electronic devices on the low - nm scale, even at room temperature [43]. On the other hand, however, single electron experiments on clusters yield only limited information about their electronic structure, since the process is dominated by the capacitance C . It is possible that under certain circumstances some substructure on the plateau of the Coulomb staircase can originate from the electronic structure of the clusters [44].

In order to summarise the current theoretical situation, it can be stated that there has been no study which would describe the charge transport through a deposited cluster on a molecular level. A complete picture has to include the electronic cluster levels in the given geometry in the presence of the surface, the influence of the electrical field under the tip (up to 10^8 V m^{-1}) and possible charging effects.

Notwithstanding the lack of any concrete theory, several experimental investigations have nevertheless dealt with STS on clusters in order to explore electronic structure. The first result on mass selected clusters, i.e., Si_{10} on $\text{Au}(001)$, shows a pronounced broad minimum in the dI/dU record, due to a band gap width of about 1 eV [45]. Iron clusters ($N \approx 13$) on $\text{GaAs}(110)$ were found to exhibit a gap at the Fermi level which was attributed to the non-metallic character [46], whereas for $N > 35$ the gap closes. Flat gold clusters on $\text{GaAs}(110)$ give rise to pronounced band gap states [47]. The dI/dU records of 5 nm palladium clusters on $\text{TiO}_2(110)$ show an astonishingly broad low intensity range which is discussed in terms of a large band gap [48]. Such a large gap, however, is unexpected and cannot be explained

with current theories. Several further experiments have been reported, none of which show interpretable details of the electronic structure of the clusters.

In our group we have investigated the electronic structure of metal clusters, mainly Pt_N , Na_N and Ag_N by STS in ultrahigh vacuum at cryogenic temperatures [49–51]. Platinum deposits on Highly Oriented Pyrolytic Graphite (HOPG) are interesting systems for such studies. Clark et al. [52] already observed weak features in the I–V characteristics of two-dimensional Pt islands at room temperature. At lower temperatures, however, the resolution in STS should increase. Therefore we also apply STS to liquid helium cooled samples. Na_N and Ag_N are prototypes of jellium like clusters, see Chap. 1. The results presented below give evidence that these systems exhibit a pronounced energy level structure even when in contact with a surface.

Complementary to the STS technique, which gives information about *elastic channels* in the charge transport, we will also apply STM-induced inverse photoemission (STIPE) in order to learn about *inelastic channels*. Using the high resolution of an STM, this method was first applied by Coombs et al. [53] and later by Berndt et al. [54–56]. For a recent review see [57]. So far the physical origin of the light emission during tunnelling is discussed in terms of plasmon modes which are localised close to the tip and decay via the emission of light within a broad spectral range. In particular, the noble metals are known to show intensive light emission. In the context of this book we will investigate whether the STIPE method is suitable to investigate small particles and clusters on surfaces. More specifically, we will explore a possible lower N-limit in the light emission of silver.

5.3.1 Target Preparation and Experimental Methods

The experiments are carried out in an UHV system (about 3×10^{-11} mbar base pressure) equipped with a low temperature STM (6 K, 55–78 K, RT), a LEED system, an electron beam evaporator and an UHV transfer system for the beam deposited clusters. Both the tip and the sample can be changed while the system is kept at liquid helium temperature, which considerably reduces the waiting time after a change. The cluster-on-surface system is prepared either by atom diffusion or by depositing particles from a beam under UHV conditions. We employ a Pulsed Arc Cluster Ion Source (PACIS) [58,59,21] which generates clusters with broad size distributions. Starting at a helium seeding gas pressure of 10^{-4} mbar in the source chamber, the beam passes several pumping stages until it reaches the prepared surface with a kinetic energy of about 1 eV/atom.

Usually, a low coverage is chosen as it ensures the absence of interactions between the clusters. Note that with several cluster–surface combinations it is necessary to cool the substrate in order to inhibit diffusion. In the case of Pt_N on HOPG, however, the clusters can be stable at room temperature when pinned to defects or steps. The investigation starts with an imaging of the sample by STM. Figure 5.6a displays an STM image of platinum clusters

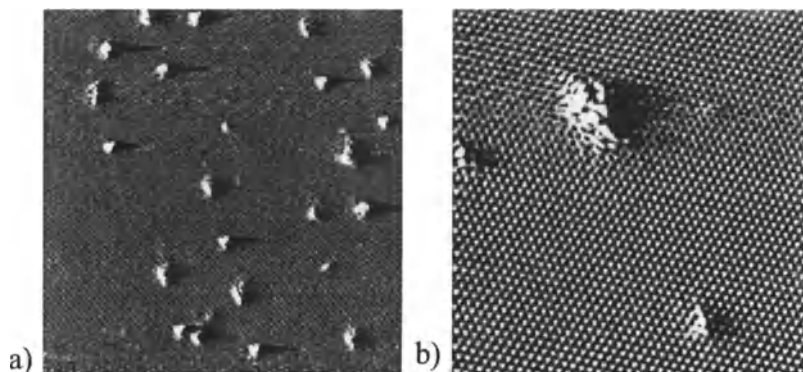


Fig. 5.6. (a) STM constant height image ($67 \text{ nm} \times 67 \text{ nm}$) of Pt clusters on a HOPG surface. The clusters are generated by the PACIS and deposited under ultrahigh vacuum conditions. (b) A close-up showing single clusters ($11 \text{ nm} \times 11 \text{ nm}$). After [51]

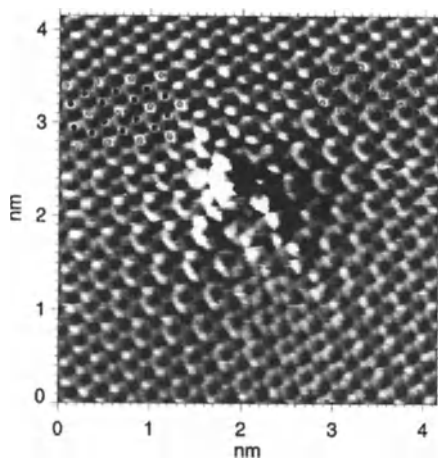


Fig. 5.7. A deposited Pt cluster on HOPG might induce a pronounced superstructure in its vicinity, a sign for a strong cluster substrate interaction. From Bettac[51]

on HOPG for a coverage of about 2%. The apparent particle size varies between 0.5 nm and 4 nm in diameter, which, due to the convolution with the tip shape, exceeds that of the clusters analysed in the mass spectrometer. Figure 5.6b shows a single Pt cluster with about 15 atoms and two smaller ones on atomically resolved graphite. Like the measurement of the particle width, also the height determinations have to be performed with special care since the cluster DOS usually differs from that of the bare surface.

These small clusters often appear flat and in their vicinity a $(\sqrt{3} \times \sqrt{3})R30^\circ$ superstructure is occasionally observed (see Figure 5.7). Similar su-

perstructures have been found near adsorbed particles and point defects on graphite [60–63].

For the STS measurements, either a single cluster is selected and investigated, or STS spectra are taken at regularly separated positions within a selected area. At each position, the tunnelling current is recorded while scanning the sample bias under open feedback conditions. During the investigations, samples are cooled either to liquid helium temperature, yielding 5 K measured at the sample holder, or to liquid nitrogen temperature.

In the STIPE investigations, the emitted photons are collected by a condenser lens inside the vacuum chamber and focused by a second lens outside the vacuum onto a Peltier cooled photomultiplier tube working in photon counting mode. During the imaging process the integral photon intensity is recorded for each scanning point. The energy range of the detected photons is limited by the sensitivity of the photomultiplier (about 200–700 nm).

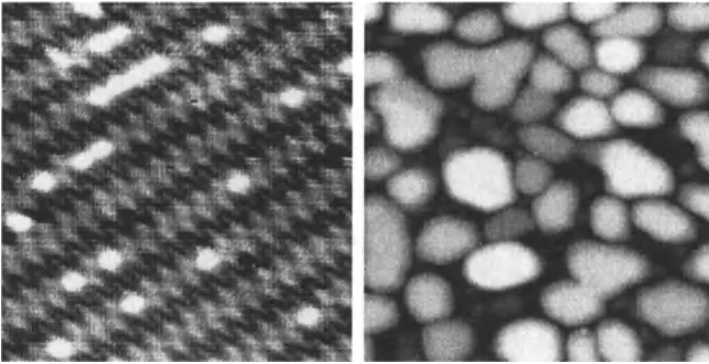


Fig. 5.8. *Left:* Atomically resolved zig zag structure of the carbon-induced (15×3) reconstruction of W(110). The bright spots are atomic and molecular adsorbates from the residual gas (area $8 \text{ nm} \times 8 \text{ nm}$). *Right:* Ag islands on W(110)/C-R (15×3) grown by tempering a thin Ag film ($12 \text{ nm} \times 12 \text{ nm}$). The island size is adjustable by varying the deposition flux and the thermal treatment. From Mayer et al. [66]

A W(110) surface with a carbon-induced (15×3) reconstruction [64,65] is a good substrate to study light emission from silver islands. We prepare the W(110) crystal by heating it to about 1000 K in UHV at an oxygen pressure of about 10^{-5} mbar. Afterwards, the oxygen is removed by flashing the sample. A further brief flash converts the clean W(110) surface into the W(110)/C – R(15×3) (see left side of Fig. 5.8). After this surface treatment, silver is deposited from an electron beam evaporator. Heating the resulting thin Ag film at about 700 K yields an island structure (see the right side of Fig. 5.8). The island size can be adjusted by choosing the initial film thickness, the temperature and the heating time. These islands later serve for STIPE investigations.

5.3.2 STS on Platinum, Silver and Sodium Clusters

In this section we present results on STS measurements of different clusters on HOPG. After deposition, the current-voltage characteristics are obtained at selected positions on a part of the bare surface and on top of a cluster. In order to demonstrate the feasibility of the method we start with platinum where it is known from PES and calculations that a very pronounced peak in the DOS resides at about 100 meV below E_F [67]. In Pt as a metal where the d-electrons dominate the DOS close to E_F , we expect that already quite small clusters with $N \approx 20$ -50 should exhibit an energetic level structure close to that of bulk Pt. Analysing Pt_N , with $N \approx 70$, at different locations on one and the same cluster yields spectra like those in Fig. 5.9. For several local thicknesses of the cluster the spectra are governed by a single pronounced peak in dI/dU . There is an approximately linear relationship between peak intensity and cluster height. Such spectra have to be interpreted in the way that the intensity for voltages below zero, i.e., for negative bias of the sample, maps the situation of the occupied sample states (folded with unoccupied tip states). At positive voltages, unoccupied sample states are recorded. For an interpretation of this spectral feature it is instructive to compare with PES results and calculations of bulk Pt [67]. Obviously the Pt cluster investigated by STS is large enough to exhibit bulk - like properties. Even the spectral feature at and below -0.2 eV finds correspondence to the photoemission results [67]. The slight spectral shift of the peak in the STS data compared to PES on a Pt surface could be due to a weakening of the Pt bond which originates from the decreased coordination or the presence of the surface. Thus, there are situations like those in Fig. 5.9 where STS on clusters closely resembles the corresponding PES data.

The main spectral feature of Fig. 5.9 shows a Fano-like profile. Such a peak shape would result from an electron scattering process where, due to the interference of different channels, certain phase shifts occur [68]. In the case considered here, the direct transmission establishes one channel and scattering at the localised state in the Pt cluster a second one. Similarly, Fano-like peak shapes in STS have been described before on magnetic impurities [69,70]. The quality of a Fano profile fit to a cluster spectrum is demonstrated in Fig. 5.9 (bottom). According to this fit the two channels (scattering and direct transmission) have about equal probability. With a linewidth of 50 meV the high spectral sensitivity of the STS method is demonstrated.

Another group of spectra, now recorded on very small beam-deposited Pt clusters like those in Figure 5.6, shows extremely sharp features, see Fig. 5.10. Several properties for negatively biased samples can be summarised that are common for the results of this group: e.g., the separations of the prominent peaks slightly decrease with increasing height of the clusters; their positions are not strongly affected by the tunnelling conditions, although, in some cases, a part of the spectrum changes when going from one cluster to the other (c.f. the shift Δ); many small spectral features are sensitive to the

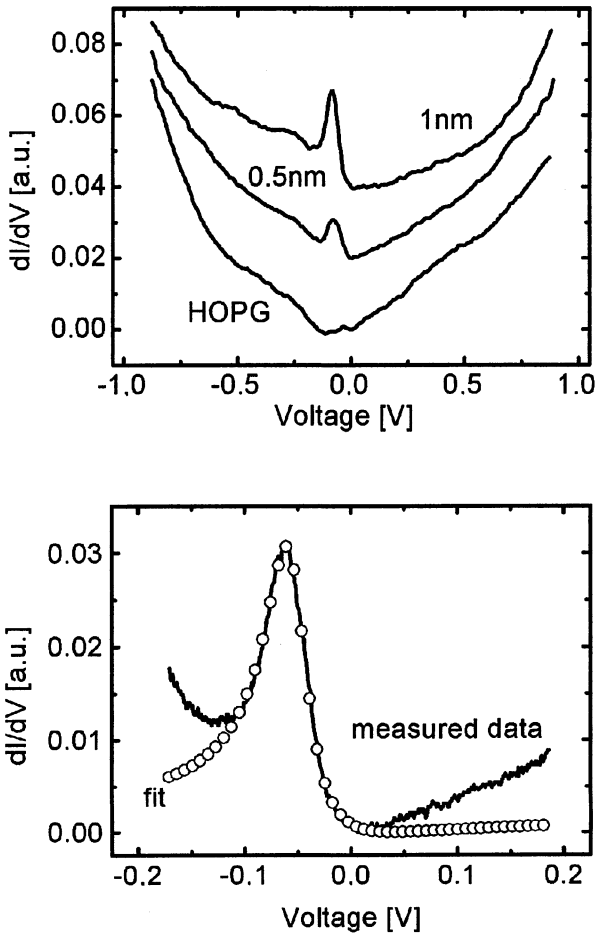


Fig. 5.9. Scanning tunnelling spectra of one Pt cluster at 36 K cluster with $N \approx 70$, measured on different positions on the cluster at the given height, and on the pure HOPG (top). Bottom: A Fano profile fit to an enlarged section of an STS spectrum of a cluster with $N \approx 130$ at 5 K. Fitting parameters: width 0.05 eV, position of the local state at -54.5 meV. From Rank et al. [71]

cluster sizes and the tunnelling parameters. The high energetic resolution as seen in these spectra requires a low substrate temperature. At elevated temperatures (70 K), the peaks in the conductivity curves broaden, and at room temperature they are no longer discernible.

In order to understand these richly structured STS spectra, we checked whether the small size of the cluster might lead to interferences which would induce a quantisation of the electrical conductance. The situation is thus reduced to a simple particle-in-a-box problem where the confining potential is

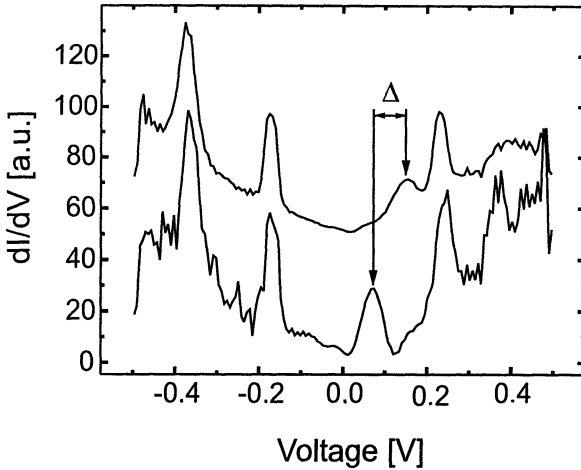


Fig. 5.10. STS spectra recorded over small Pt_N deposited from a PACIS cluster beam onto HOPG. Surface temperature 6 K. After [49]

made up by the cluster boundaries. For a flat cluster, a quantisation perpendicular to the surface, should give rise to peaks with the largest separations. In a simple first model, we assumed that the energy levels are quantised due to a narrow square well potential, where the boundaries originate from the cluster-surface and the cluster-vacuum interfaces, respectively [49]. Indeed, the measured energy separations between the first two prominent peaks (close to -200 mV and -400 mV) loosely correspond to an inverse height dependence thus being in accordance with an electron interference picture. Interestingly, the de Broglie wavelength of a 200 meV electron roughly matches the estimated width of the constriction. Altfeder et al. [72] observed a conductance quantisation in thin Pb films on Si(111). Their measurements also showed peaks due to electron interference phenomena.

It should be noted that the spectra of Fig. 5.10 are recorded with a tungsten tip which yielded not a completely unstructured U-shaped HOPG spectrum, i.e., due to a special tip configuration, some small peaks and shoulders are present. It appears that the presence of a Pt cluster greatly enhances some of the spectral features.

The next example concerns silver clusters on HOPG, now produced by atom diffusion and self organisation. Like in alkali clusters (Chap. 1) it is known that free silver clusters exhibit a strongly N -dependent electronic structure originating from the s -electron confinement. One typical example of an STS spectrum on Ag_N with a cluster height of 0.6 nm is depicted in Fig. 5.11. Whereas the spectrum on the uncovered HOPG shows a clear parabola shape, on top of the cluster a rich structure appears, consisting of two basically different features. First, strong peaked intensity at high negative and positive bias voltages shows up which is separated by a region of low intensity. This apparent gap changes in width from nearly 2 eV at $N \approx$

10 to about 0.7 eV for a big cluster with a height of 3 nm, i.e., some thousand atoms. Second, with higher sensitivity, a pronounced peaked structure emerges inside the apparent gap.

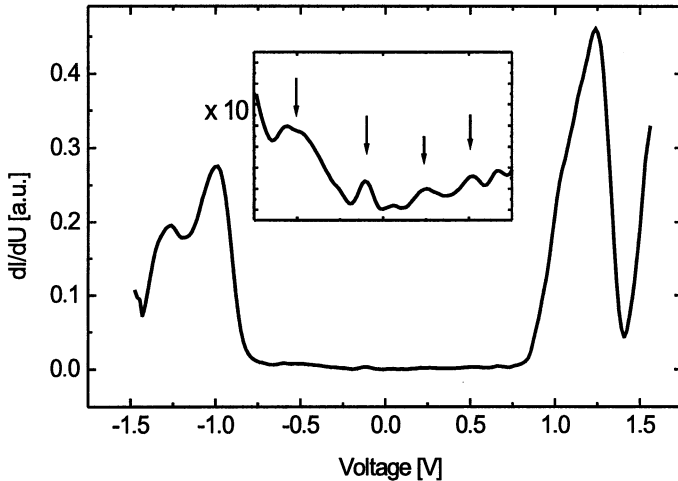


Fig. 5.11. STS spectrum of a silver cluster with $N \approx 50$. Note the richly structured intensity in the apparent gap. From Jonas et al. [73]

At first glance the gap could be interpreted as being due to the electron confinement and thus the electronic structure of the silver cluster. On the other hand, however, effective medium calculations and photoelectron spectra show that the gaps between the occupied and unoccupied levels, i.e., the HOMO-LUMO gaps, range around 1.2 eV for $N=8$ and 0.3 eV for $N=25$ [74,75]. There is no reason why a silver cluster with some hundreds of atoms should possess an energy gap in the eV range. Thus, only the weak intensity in the apparent gap can be connected to the cluster's electronic level structure which might lead to distinct conduction channels. The corresponding transmission eigenvalues depend on the orbital character of cluster, which, so far, have not been investigated. With the method demonstrated by Cuevas et al. [76] it should be possible to calculate the microscopic origin of these STS spectra. Even the largest clusters with $N \approx 500$ show no similarities to bulk silver, clearly indicating that in this size range cluster-specific properties still prevail.

Another and spectrally more open system are alkali clusters: In Chap. 1 it was already shown that the K_N anion photoelectron spectra exhibit very distinct and N -dependent peaks and gaps which can be attributed to electronic

levels. E.g., K_{19}^- has 20 electrons and thus it should be a closed shell system. The corresponding PES shows a distinct gap between the 1p and 1d peaks, see Fig. 1.10 in Chap. 1 of this book. In order to explore whether deposited alkali clusters have also such a level structure, we prepare Na_N on HOPG by atomic vapour deposition. Indeed, the resulting STS spectra are in part richly structured, see Figure 5.12. Again, like in the case of Ag_N , interesting spectral features arise from the deposited cluster.

When comparing an STS spectrum to anion PES the fact that the energy scales are fixed to different zero points has to be considered, i.e., the Fermi level coincides with zero voltage in STS whereas the gas phase PES is pinned to the vacuum energy. Shifting the spectra accordingly leads to a rough agreement between the STS spectrum in Figure 5.12 and the anion PES on K_{15}^- to K_{19}^- in Fig. 1.10. Note that in addition to information on occupied cluster

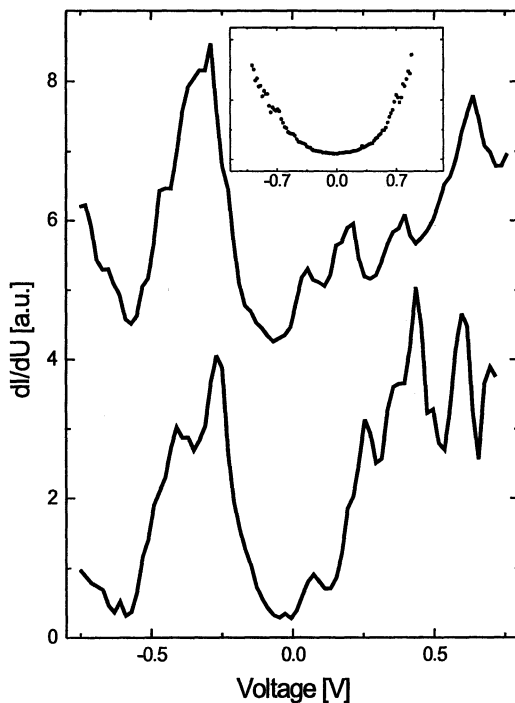


Fig. 5.12. STS on two different Na clusters on HOPG, $N \approx 15 \dots 30$. Possibly the minimum at -0.6 eV separates peaks which originate from two closed shells. The intensity at positive voltage originates from unoccupied levels. The corresponding spectrum of an uncovered HOPG spot close to the cluster is given in the inset. $T = 78$ K. From Jonas et al. [73]

levels, STS also maps unoccupied ones, see the intensity at positive voltage. At first sight the rough agreement in the PES of free and deposited clusters appears to be astonishing since the gas phase clusters are more or less spherically shaped whereas the deposited ones should be flattened and thus show a different spectrum. Indeed, calculations on 2-dimensional alkali clusters prove that also those systems possess electronic shells [77]. As a result of the now changed symmetry the closings are found at $N=6, 12, 20, 30, \dots$. This situation is similar to shell filling in a vertical semiconductor quantum dot which has the shape of a disk with a diameter approximately ten times the thickness. The energy needed to add electrons shows particular high values when 6 and 12 electrons are in the dot, a clear indication for a shell structure in the two dimensional system [78]. With density functional calculations it is shown that such dots exhibit a static spin density-like state [79].

In summary, whilst the situation for STS on metal clusters is promising, with a wealth of spectroscopic details obtainable, there are still, as yet, many features that need further explanation. In particular, the crucial role of the tip has to be questioned. Even with uncontaminated tips, completely different results might be obtained due to the different local orbital character.

5.3.3 Photon Maps of Silver Islands

In the following, light emission is studied using STM in order to check whether this method might give additional information on electronic properties of nanometer-sized metal structures. The system studied is shown on the left side of Figure 5.13 by the topographic image of a silver island structure. The image on the right side displays the corresponding photon map to the same length scale. Clearly the topography and the light emission show a close correspondence. Nevertheless, not all parts of islands contribute equally to the photon map. For example, the dark area in the topographic image on the left side corresponds to a well between two islands. The photon map, on the other hand, shows a significant intensity inside this well which is due to a silver layer at the bottom. With higher resolution, see the 3-dimensional representation of this image on the colour plates, also very small light emitting patches down to 1 nm diameter are resolved. A decreasing particle size leads to a blue shift of the spectra. Similar to photodepletion and -absorption experiments on gas-phase mass-selected Ag_N [26,80,5] we can expect a shift of the spectral peak into the UV, down to about 3.8 eV in the case of $N \approx 10$.

Insight into the light emitting process might be obtained by a study of the voltage dependence. Figure 5.14 displays the influence of the gap voltage on the light intensity observed on a sample with large islands (some hundred nanometer in lateral size). For a fixed tunnelling current of 1 nA, we scan in both the forward and the backward direction in order to eliminate a possible influence of tip and island asymmetries. The emitted light has a maximum in intensity at 3.5 V, and additionally a shoulder at about 2.6 V is observed. Our results on Ag islands are in good agreement with measurements on Ag

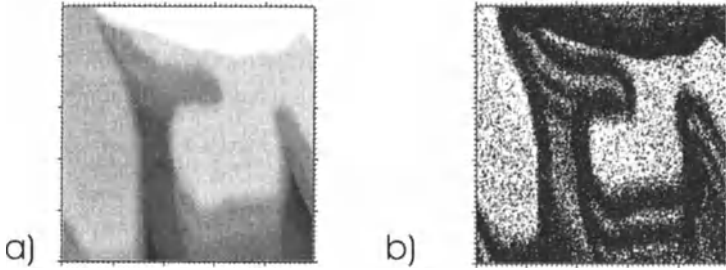


Fig. 5.13. Silver islands on $W(110)/C - R(15 \times 3)$, area $50 \text{ nm} \times 50 \text{ nm}$. The islands are obtained by tempering a thin silver film. *Left:* Topographic image, maximum height 5 \AA , measured at 78 K . *Right:* Simultaneously measured photon map with a maximum photon level of about 1000 cps . The 3-dimensional image, see the color plates, shows that even small spots down to 1 nm can be resolved. Silver tip, bias 3.6 V , 1 nA . From Mayer et al. [66]

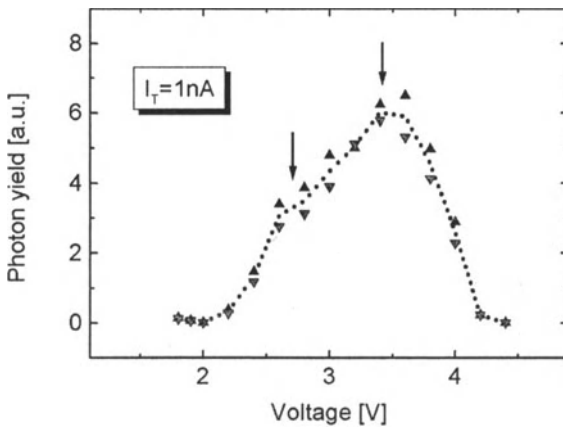


Fig. 5.14. Dependence of the STM-induced light emission from silver islands on the gap voltage. From Mayer et al. [66]

surfaces by Berndt [57]. The maximum at 3.5 V has also been seen for other metal surfaces, and appears to be fairly independent of the tip and the sample materials. Possibly the peak and the strong decrease in intensity which follows are due to the increased tip-surface distance. In the range between $3 - 4 \text{ V}$, the linear dependence of the gap distance (tip-sample) on the applied voltage undergoes a transition to a quadratic behaviour resulting in a lower field enhancement and thus a reduced photon yield. In reference [81] it is

discussed that the increased intensity at around 2,6eV could be caused by the dielectric properties of silver. In this energy range the electronic properties are dominated by the s-electrons, which in this regime have strong free electron character. Under these conditions, localised surface plasmon modes can easily be excited which could lead to an increased photon yield.

So far light emission from silver and silver islands is explained by plasmon formation which should sensitively depend on the tip radius. Furthermore, there are many pointers that indicate that other features, apart from plasmon formation, may play an important role in the observed light emission. In particular, the nature, geometry and orbital character of the tip govern the process of light generation. Nevertheless, STIPE is a valuable method for recording the local chemical nature of very small particles down to the atomic scale.

5.4 Summary

This chapter aimed at giving a brief glimpse into studies of electronic properties of clusters at surfaces. Conventional photoelectron spectroscopy so far yielded only little information on the level structure, which is in contrast to PES on negatively charged mass selected metal clusters in beams. There, highly structured spectra with many sharp features reveals that each cluster with a given size has its own electronic life.

With the scanning tunneling microscope, single clusters at a surface can be addressed. Two different ways of investigating electronic properties of nanoscaled metal particles using STM have been presented. Platinum, silver and sodium clusters on HOPG surfaces clearly show discrete peaks in the tunnelling spectra which can, in part, be related to the electronic level structure. Yet, the STS method itself bears unsolved problems. In a second approach, STM-induced inverse photoemission serves as a local probe for inelastically scattered electrons. High levels of light emission and a fairly good agreement with the topography are observed on Ag islands on $W(110)/C - R(15 \times 3)$. The intensity of the light emission depends on the applied gap voltage. Even very small clusters with diameters of only 1 nm emit light. Although electronic properties due to the confined nature of the islands have not yet been resolved, a further investigation of the STM-induced light emission from clusters would be fruitful.

Acknowledgement

It is my pleasure to thank all members of our STM group for their help, in particular Dr. Viola Rank, Andreas Bettac, Ralf Meyer, and Karl-Ludwig Jonas.

References

1. U. Heiz, F. Vanolli, A. Sanchez, and W.-D. Schneider, *J. Am. Chem. Soc.* **120**, 120 (1998).
2. M. Frank *et al.*, *Chem. Phys. Lett.* **279**, 92 (1997).
3. U. Kreibig and M. Vollmer, *Optical Properties of Metal Clusters*, Vol. 25 of *Springer Series in Materials Science* (Springer, Berlin, Heidelberg, 1995).
4. Stietz and F. Träger, *Appl. Phys. Lett.* (1999).
5. W. Harbich, S. Fedrigo, and J. Buttet, *Chem. Phys. Lett.* **195**, 613 (1992).
6. T. Klar, M. Perner, S. Grosse, G. van Plessen, W. Spirkl, and J. Feldmann, *Phys. Rev. Lett.* **80**, 4249 (1998).
7. H. Häkkinen and M. Manninen, *Phys. Rev. Lett.* **76**, 1599 (1996).
8. J. Kolehmainen, H. Häkkinen, and M. Manninen, *Z. Phys. D* **40**, 306 (1996).
9. M. Lin, R. Andres, and R. Reifenberger, *Phys. Rev. Letters* **67**, 477 (1991).
10. H. Siekmann, B. Wrenger, E. Holub-Krappe, C. Pettenkofer, and K. H. Meiwes-Broer, *Z. Phys. D* **26**, 54 (1993).
11. M. Mason, *Phys. Rev. B* **27**, 748 (1983).
12. T. T. P. Cheung, *Chem. Phys. Lett.* **111**, 219 (1984).
13. S.L. Qiu, X. Pan, M. Strongin, and P. Citrin, *Phys. Rev. B* **36**, 36 (1987).
14. G. Wertheim, S. B. DiCenzo, and D. Buchanan, *Phys. Rev. B* **33**, 5384 (1986).
15. G. Wertheim, *Z. Phys. B* **66**, 53 (1987).
16. G. Wertheim, *Z. Phys. D* **12**, 319 (1989).
17. H. Hövel, B. Grimm, M. Pollmann, and B. Reihl, *Phys. Rev. Lett.* **81**, 4608 (1998).
18. H. Siekmann, E. Holub-Krappe, B. Wrenger, C. Pettenkofer, and K. H. Meiwes-Broer, *Z. Phys. B* **90**, 201 (1993).
19. R. Hector and K. H. Meiwes-Broer, unpublished.
20. G. Ganteför, M. Gausa, and K. H. Meiwes-Broer, *Z. Phys. D* **12**, 405 (1989).
21. M. Gausa, R. Kaschner, G. Seifert, J. Faehrmann, H. O. Lutz, and K. H. Meiwes-Broer, *J. Chem. Phys.* **104**, 9719 (1996).
22. S. B. DiCenzo, S. D. Berry, and J. E. H. Hartford, *Phys. Rev. B* **38**, 8465 (1988).
23. H.-V. Roy, P. Fayet, F. Patthey, W. -D. Schneider, B. Delley, and C. Massobrio, *Phys. Rev. B* **49**, 5611 (1994).
24. Y. Takasu, R. Unwin, B. Tesche, and A. Bradshaw, *Surf. Sci.* **77**, 219 (1978).
25. W. Eberhardt *et al.*, *Phys. Rev. Lett.* **64**, 780 (1990).
26. J. Tiggesbäumker, L. Köller, K. H. Meiwes-Broer, and A. Liebsch, *Phys. Rev. A* **48**, R1749 (1993).
27. R. Hector and K. H. Meiwes-Broer, unpublished; R. Hector, Thesis, University of Bielefeld 1993 (unpublished).
28. R. Hector and K. H. Meiwes-Broer, *Opt. Comm.* **123**, 155 (1996).
29. P. Jonk, R. Hector, and K. H. Meiwes-Broer, *Nucl. Instr. Meth. Phys. Res. B* **80/81**, 818 (1993).
30. G. Pastor and K. B. P. Stampfli, *Z. Phys. D* **12**, 365 (1989).
31. D. Lindsay, Y. Wang, and T. George, *J. Chem. Phys.* **86**, 3500 (1987).
32. U. Busolt, E. Cottancin, H. Röhr, L. Socaciu, T. Leisner, and L. Wöste, *Appl. Phys. B* **68**, 453 (1999).
33. K. Ertel *et al.*, *Appl. Phys. B* **68**, 439 (1999).
34. G. Binnig and H. Rohrer, *Helv. Phys. Acta* **55**, 726 (1982).

35. R. M. Feenstra and P. Mårtensson, *Phys. Rev. Lett.* **61**, 447 (1988).
36. in *Scanning Tunneling Microscopy and Related Methods*, edited by R. B. et al. (Kluwer Academic Publishers, Amsterdam, 1990), Chap. R. M. Feenstra, p. 211.
37. in *Scanning Probe Microscopy: Analytical Methods*, edited by R. Wiesendanger (Springer Verlag, Berlin and Heidelberg, 1998), Chap. T.A. Jung and F.J. Himpfel and R.R. Schlittler and J.K. Gimzewski: Chemical Information from Scanning Probe Microscopy and Spectroscopy, pp. 11–48.
38. B. Stipe, M. Rezaei, and W. Ho, *Science* **280**, 1732 (1998).
39. J. Tersoff and D. Hamann, *Phys. Rev. B* **31**, 805 (1985).
40. J. Bardeen, *Phys. Rev. Lett.* **6**, 57 (1961).
41. *Scanning Tunneling Microscopy III*, Vol. 29 of *Springer Series in Surface Sciences*, 2nd ed., edited by R. Wiesendanger and H.-J. Güntherodt (Springer, Berlin, Heidelberg, 1996).
42. A. Scherbakov, E. Bogachek, and U. Landman, *Phys. Rev. B* **53**, 4054 (1996).
43. C. Schönenberger, H. van Houten, and H. Donkersloot, *Europhys. Lett.* **20**, 249 (1992).
44. T. P. Bigioni, L. E. Harrell, W. G. Cullen, D. K. Guthrie, R. L. Whetten, and P. N. First, *Eur. Phys. J. D* **6**, 355 (1999).
45. Y. Kuk, M. Jarrold, P. Silverman, J. Bower, and W. Brown, *Phys. Rev. B* **39**, 11168 (1989).
46. P. N. First, J. A. Stroscio, R. A. Dragoset, D. T. Pierce, and R. J. Celotta, *Phys. Rev. Lett.* **63**, 1416 (1989).
47. R. M. Feenstra, *Phys. Rev. Lett.* **63**, 1412 (1989).
48. C. Xu, X. Lai, G. W. Zajac, and D. W. Goodman, *Phys. Rev. B* **56**, 13464 (97).
49. A. Bettac, L. Köller, V. Rank, and K. H. Meiwes-Broer, *Surf.Sci.* **402-404**, 475 (1998).
50. A. Bettac, V. Rank, and K. H. Meiwes-Broer, to be published.
51. A. Bettac, thesis, Universität of Rostock, 1999 (unpublished).
52. G. Clark and L. Kesmodel, *J. Vac. Sci. Technol. B* **11**, 131 (1993).
53. J. H. Coombs, J. K. Gimzewski, B. Reihl, J. K. Sass, and R. R. Schlittler, *J. Micr.* **152**, 325 (1988).
54. R. Berndt, R. R. Schlittler, and J. K. Gimzewski, *J. Vac. Technol. B* **2**, 573 (1991).
55. R. Berndt and J. K. Gimzewski, *Phys. Rev. B* **48**, 4746 (1993).
56. R. Berndt *et al.*, *Phys. Rev. Lett.* **74**, 102 (1995).
57. in *Scanning Probe Microscopy: Analytical Methods*, edited by R. Wiesendanger (Springer Verlag, Berlin and Heidelberg, 1998), Chap. R. Berndt: Photon Emission from the Scanning Tunneling Microscope, pp. 97–131.
58. H. Siekmann, C. Lüder, J. Faehrmann, H. O. Lutz, and K. H. Meiwes-Broer, *Z. Phys. D* **20**, 417 (1991).
59. C.-Y. Cha, G. Ganteför, and W. Eberhard, *Rev. Sci. Inst.* **63**, 5661 (1992).
60. J. Xhie, K. Sattler, U. Müller, N. Venkateswaran, and G. Raina, *J. Vac. Sci. Technol. B* **9**, 833 (1991).
61. G. Shedd and P. Russel, *Surf. Sci.* **266**, 259 (1992).
62. J. Valenzuela-Benavides and L. de la Garza, *Surf.Sci.* **330**, 227 (1995).
63. H. Mizes and J. Foster, *Science* **244**, 559 (1989).
64. M. Bode, R. Pascal, and R. Wiesendanger, *Surf.Sci.* **344**, 185 (1996).

65. M. Bode, *Z. Phys. B* **101**, 103 (1996).
66. R.-P. Mayer, A. Bettac, V. Rank, and K. H. Meiwes-Broer, to be published.
67. S. Lin, D. Pierce, and W. Spicer, *Phys. Rev. B* **4**, 326 (1971).
68. U. Fano, *Phys. Rev.* **124**, 1866 (1961).
69. V. Madhavan, W. Chen, T. Jamneala, M. Crommie, and N. Wingreen, *Science* **280**, 567 (1998).
70. J. Li, W. -D. Schneider, R. Berndt, and B. Delley, *Phys. Rev. Lett.* **80**, 2893 (1998).
71. V. Rank, A. Bettac, K.-L. Jonas, and K. H. Meiwes-Broer, to be published.
72. I. B. Altfeder, K. A. Matveev, and D. M. Chen, *Phys.Rev.Lett.* **78**, 2815 (1997).
73. K.-L. Jonas, , V. Rank, and K. H. Meiwes-Broer, to be published.
74. O. B. Christensen, K. W. Jacobsen, and K. Norskov, *Phys. Rev. Lett.* **66**, 2219 (1991).
75. K. H. Meiwes-Broer, *Appl. Phys.* **A55**, 430 (1992).
76. J. C. Cuevas, A. L. Yeyati, and A. Martin-Rodero, *Phys. Rev. Lett.* **80**, 1066 (1998).
77. S. Reimann, M. Koskinen, H. Häkkinen, P. Lindelof, and M. Manninen, *Phys. Rev. B* 12147 (1997).
78. S. Tarucha, D. Austing, T. Honda, R. van der Hage, and L. Kouwenhoven, *Phys. Rev. Lett.* **77**, 3613 (1996).
79. M. Koskinen, M. Manninen, and S. Reimann, *Phys. Rev. Lett.* **79**, 1389 (1997).
80. B. Collings, K. Athanassenas, D. Rayner, and P. Hackett, *Chem. Phys. Lett.* **227**, 490 (1994).
81. P. Johansson and R. Monreal, *Z. Phys. B* **84**, 269 (1991).

6 Conductance Quantisation in Metallic Point Contacts

Jan M. van Ruitenbeek

6.1 Introduction

In metallic clusters the electron wave function is confined in all three spacial dimensions, resulting in a discrete set of energy levels. In quantum wires the confinement of the electron wave function is limited to two spacial dimensions, which gives rise to the formation of a set of one-dimensional energy bands, which we refer to as modes, or channels.

The influence of these quantum modes on the properties of metallic quantum wires has been studied experimentally by forming point contacts between metal electrodes, using scanning tunnelling microscopes, mechanically controllable break junctions, or related techniques. Where the primary observation of quantum size effects in clusters was based on cluster abundance spectra, for metal point contacts there is a somewhat analogous statistical method, which consists in recording a histogram of conductance values observed for large numbers of contacts. For simple, monovalent metals these histograms show a number of pronounced peaks close to multiples of the quantum of conductance, $2e^2/h$.

The interpretation of the histograms is less straightforward compared to that of the cluster abundance spectra, since the former are the result of a combination of atomic structural features, and of the quantisation of the electron states in 1D subbands. Various experimental methods have recently been used to investigate the role of quantised modes in atomic-size contacts. These include measurements of the mechanical force on the contacts, the use of characteristic features in the current–voltage relation of superconducting contacts, measurements of the thermopower, of the voltage-dependence of the conductance and measurements of the shot noise intensity. With the help of these methods it can be shown that the conductance of atomic size contact for simple metals (Au, Na, etc.) is indeed carried by a well defined set of quantum modes. However, in general the conductance is determined by the number and character of the valence orbitals of the metal atoms forming the contact.

A very direct analogy between the physics of metal clusters and the physics of metallic point contacts becomes visible when recording conductance histograms for the alkali metals and for contacts larger than just a few atoms. A large number of peaks is observed, which have the same origin as

the “magic numbers” in cluster abundance spectra. The observations suggest that the electronic quantum mode structure influences the mechanical stability of the nanowire, giving preference to those diameters which correspond to a filled “shell” of conductance modes.

The outline of this chapter is as follows. First a brief introduction is given of the natural formalism for discussing electron transport in ballistic conductors: the Landauer theory. After introducing the experimental techniques, which are used for studying ballistic point contacts in metals, the experimental observations for the conductance of atomic-scale contacts are presented. In order to obtain a full description in terms of the quantum modes for conductance, several recently developed techniques are reviewed, which go beyond straightforward measurement of the conductance. A brief discussion is given of an unusual atomic geometry for gold contacts, which evolve into a chain of freely suspended atoms. Then shell filling effects in sodium nanowires are discussed in the context of the influence of the conductance modes on the total energy of the system. The chapter ends with an outlook on promising new developments.

6.2 Landauer Theory for Ballistic Conductance

The metallic point contacts and nanowires, which we will consider, are all of atomic size, much smaller than all characteristic scattering lengths of the system. In particular, the electron mean free path for elastic scattering on defects and impurities near the contact is assumed to be much longer than the contact size. The only elastic scattering considered is the scattering by the walls forming the boundary of the system. Also, it is assumed that the probability for scattering events, which change the spin and phase of the electron wave function, is negligible. Following the standard approach (for reviews, see [1–3]) we will assume that the system can be schematically represented as in Fig. 6.1. The connection between the ballistic system and the outside world is represented by electron reservoirs on each side of the contact, which are held



Fig. 6.1. Schematic representation of a ballistic point contact. The reservoirs on the left and right fully absorb the incoming electron waves. The lead on the left has a width, which admits N conductance channels, and the one on the right has M channels

at a potential difference eV by an external voltage source. When the leads connecting the reservoirs to the contact are straight wires of constant width, there is a well defined number of conducting modes in each of these wires, say N and M for the left and right lead, respectively. In a free electron gas model the modes are simply plane waves, which can propagate in the current direction (to the left and right) and are standing waves in the perpendicular directions. The modes can be labelled by an index corresponding to the number of nodes in the perpendicular direction. The numbers N and M are limited by the requirement that the energy of the modes is lower than the Fermi energy. The conductance of the system can now be simply expressed as [1–3],

$$G = \frac{2e^2}{h} \text{Tr}(\mathbf{t}^\dagger \mathbf{t}) , \quad (6.1)$$

where e is the electron charge, h is Planck's constant, and \mathbf{t} is an $N \times M$ matrix with matrix element t_{mn} giving the probability amplitude for an electron wave in mode n on the left to be transmitted into mode m on the right of the contact. It can be shown that the product matrix $\mathbf{t}^\dagger \mathbf{t}$ can always be diagonalised by going over to a new basis, consisting of linear combinations of the original modes in the leads. Further, the number, N_c , of non-zero diagonal elements is only determined by the number of modes at the narrowest cross section of the conductor [4,5]. Equation (6.1) thus simplifies to

$$G = \frac{2e^2}{h} \sum_{n=1}^{N_c} T_n , \quad (6.2)$$

where $T_n = |t_{nn}|^2$ and the index refers to the new basis.

Under favourable circumstances, all transmission probabilities, T_n , can be close to unity. As an example, for a smooth (“adiabatic”) and long wire the modes at the narrowest cross section couple exclusively to a single mode at either side of the contact, and the expression for the conductance further simplifies to

$$G = N_c G_0 , \quad (6.3)$$

where $G_0 = 2e^2/h$ is the conductance quantum. For increasing diameter of the contact the number N_c increases each time a new mode fits into the narrowest cross section. This number is limited by the requirement that the kinetic energy for motion in the perpendicular direction is smaller than the Fermi energy. For a 2-dimensional (2D) system this can be expressed as $(\hbar^2/2m)(\pi N_c/W)^2 < E_F$, with W the width of the contact, which leads to $N_c = \text{Int}(2W/\lambda_F)$, with λ_F the Fermi wavelength. For a 3D metallic contact $N_c \approx (\pi R/\lambda_F)^2$, with R the contact radius. This quantisation of the conductance was first observed in experiments on 2D electron gas devices by van Wees et al. [6] and by Wharam et al. [7], where $\lambda_F \simeq 400 \text{ \AA}$ is much larger than the atomic scale.

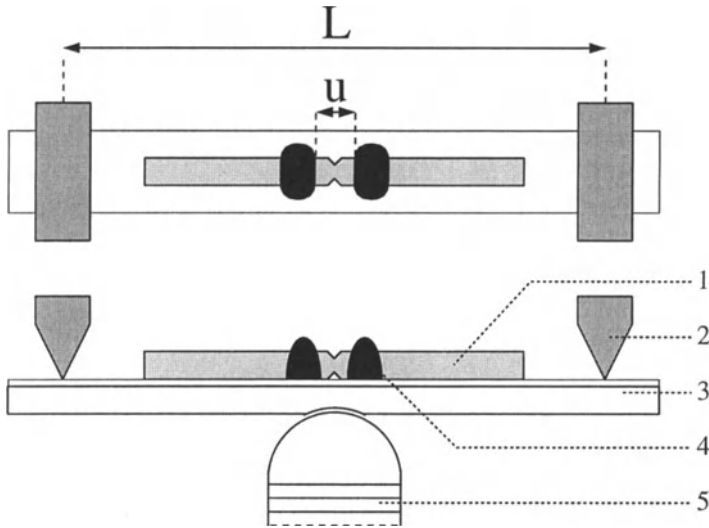


Fig. 6.2. Schematic top and side view of the mounting of a MCB, where the metal to be studied has the form of a notched wire (1), which is fixed onto an insulated elastic substrate (3) with two drops of epoxy adhesive (4) very close to either side of the notch. The substrate is mounted in a three-point bending configuration between the top of a stacked piezo element (5) and two fixed counter supports (2). This setup is mounted inside a vacuum can and cooled down to liquid helium temperatures. Then the substrate is bent by moving the piezo element forward. The bending causes the top surface of the substrate to expand and the wire to break at the notch. Typical sizes are $L \simeq 20$ mm and $u \simeq 0.1$ mm

6.3 Experimental Techniques

The experimental tools for fabricating atomic-scale contacts are mostly based on a piezoelectric actuator for the adjustment of the contact size between two metal electrodes. Standard Scanning Tunnelling Microscopes (STM) are often used for this purpose [8–10]. The tip of the STM is driven into the surface and the conductance is recorded while gradually breaking the contact by retracting the tip. The first experiment of this type was reported by Gimzewski and Möller [11].

A practical tool for the purpose of studying metallic quantum point contacts is the Mechanically Controllable Break-junction (MCB) technique [12]. The principle is illustrated in Fig. 6.2. By breaking the metal, two clean fracture surfaces are exposed, which remain clean due to the cryo-pumping action of the low-temperature vacuum can. This method circumvents the problem of surface contamination of tip and sample in STM experiments, where a UHV chamber with surface preparation and analysis facilities are required to obtain similar conditions. The fracture surfaces can be brought back into contact by relaxing the force on the elastic substrate, while a piezoelectric

element is used for fine control. The roughness of the fracture surfaces results in a first contact at one point, and experiments usually give no evidence of multiple contacts. In addition to a clean surface, a second advantage of the method is the stability of the two electrodes with respect to each other. From the noise in the current in the tunnelling regime one obtains an estimate of the vibration amplitude of the vacuum distance, which is typically less than 10^{-3} Å. The stability results from the reduction of the mechanical loop which connects one contact side to the other, from centimetres, in the case of an STM scanner, to ~ 0.1 mm in the MCB.

Conductance properties of atomic-size contacts can even be studied by still simpler methods. When breaking the contact between two regular wires under ambient conditions [13] or switching a commercial relay [14] and when recording the evolution of the conductance with a time resolution of the order of microseconds, the conductance can be observed to decrease by atomic steps during the last stages of the contact breaking. Such methods allow rapid accumulation of histograms of conductance values for a large number of such scans.

6.4 Conductance of Atomic-Scale Contacts

Figure 6.3 shows some examples of the conductance measured during breaking of a gold contact at low temperatures, using an MCB device. The con-

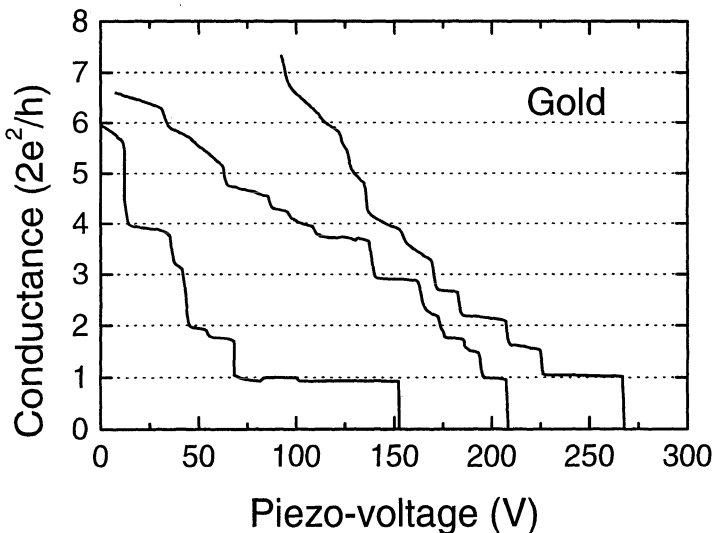


Fig. 6.3. Three typical recordings of the conductance G measured in atomic size contacts for gold at helium temperatures, using the MCB technique. The electrodes are pulled apart by increasing the piezo-voltage. The corresponding displacement is about 0.1 nm per 25 V. After each recording the electrodes are pushed firmly together, and each trace has new structure. (After J.M. Krans [15])

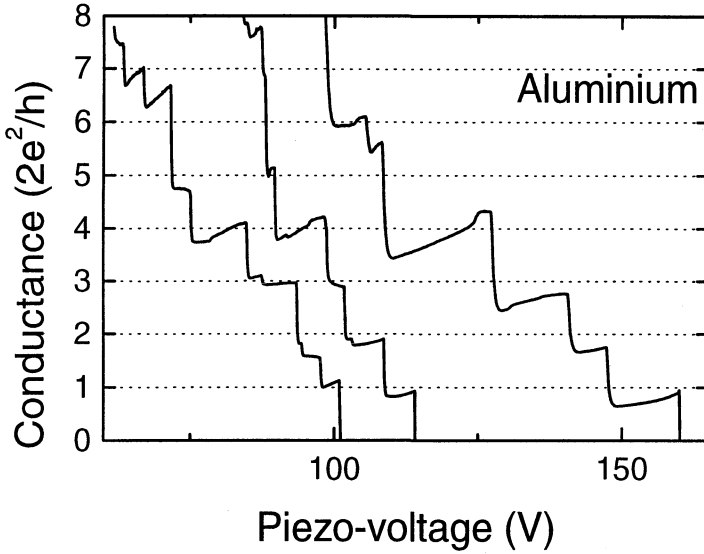


Fig. 6.4. Three examples of the conductance measured in atomic size contacts for an aluminium MCB junction at 4.2 K, as a function of the piezo-voltage. (After [16])

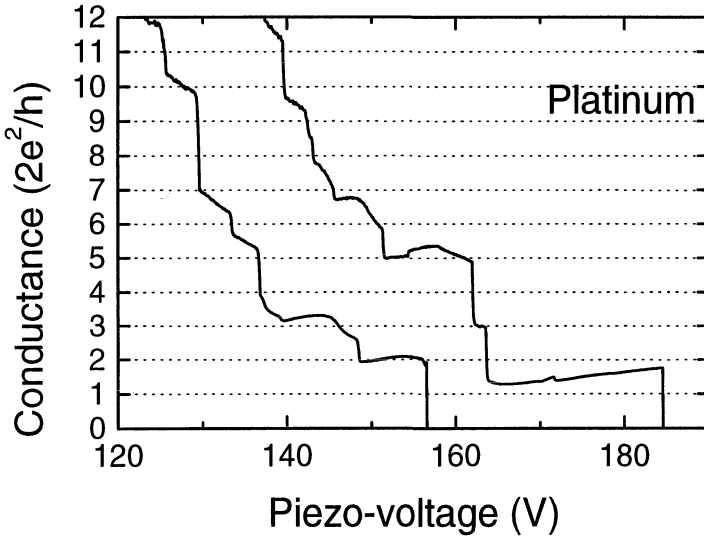


Fig. 6.5. The conductance for a platinum junction at 1.3 K as a function of piezo-voltage for two successive scans. (After [16])

ductance decreases by sudden jumps, separated by plateaux, which have a negative slope, the higher conductance the steeper. Some of the plateaux are remarkably close to multiples of the conductance quantum, G_0 ; in particular the last plateau before loosing contact is nearly flat and very close to $1 G_0$.

Closer inspection, however, shows that many plateaux cannot be identified with integer multiples of the quantum unit, and the structure of the steps is different for each new recording. Also, the height of the steps is of the order of the quantum unit, but can vary by more than a factor of 2, where both smaller and larger steps are found. Drawing a figure such as Fig. 6.3, with grid lines at multiples of G_0 , guides the eye to the coincidences and may convey that the origin of the steps is in quantisation of the conductance. However, in evaluating the graphs, one should be aware that a plateau cannot be farther away than one half from an integer value, and that a more objective analysis is required. Still, it is clear that we can use these fairly simple techniques to produce and study atomic-scale conductors, for which the conductance is dominated by quantum effects. The interpretation of graphs as in Fig. 6.3 will be the subject of this and the following sections.

The fact that the atomic structure and orbital character of the electron modes is important for an interpretation of the conductance can already be deduced by comparing the conductance curves for various metals. Figure 6.4 shows three examples of conductance curves for aluminium atomic-size contacts, and Fig. 6.5 shows results for platinum. In both cases, in particular for aluminium, we find that many plateaux have an anomalous slope: the conductance *increases* when pulling the contact, in contrast to the results for gold. For aluminium, the last plateau before breaking is still close to one unit of conductance, but one frequently observes the conductance diving below this value, and then recovering to nearly $1 G_0$, before contact is lost. Platinum, on the other hand, has a last conductance value, which is usually of order two times larger and also the size of the jumps is somewhat larger.

For all metals the transition between the plateaux is very sudden and sharp. Such sudden transitions would not be expected in a model which describes the conductance in terms of a set of conduction modes, which are gradually pinched-off by reducing the contact diameter. Indeed, the jumps find their origin in sudden rearrangements of the atomic structure of the contact [17,18]. Upon stretching of the contact, the stress accumulates elastic energy in the atomic bonds over the length of a plateau. This energy is suddenly released in a transition to a new atomic configuration, which will typically have a smaller contact size. Such atomic-scale mechanical processes were first described by Sutton and Pethica [19] and by Landman et al. [20].

The first direct proof for atomic rearrangements at conductance steps was provided in an experiment by Rubio, Agraït and Vieira [21], where the conductance for atomic-size gold contacts was measured simultaneously with the force on the contacts (Fig. 6.6). The stress accumulation on the plateaux and the coincidence of the stress relief events with the jumps in the conductance can be clearly distinguished. Presently, the experiment has only been reported for gold at room temperature. At low temperatures, the evidence for the atomic structure related nature of the jumps comes from analysis of the dynamic behaviour of the jumps. Generally, hysteresis is observed in the posi-

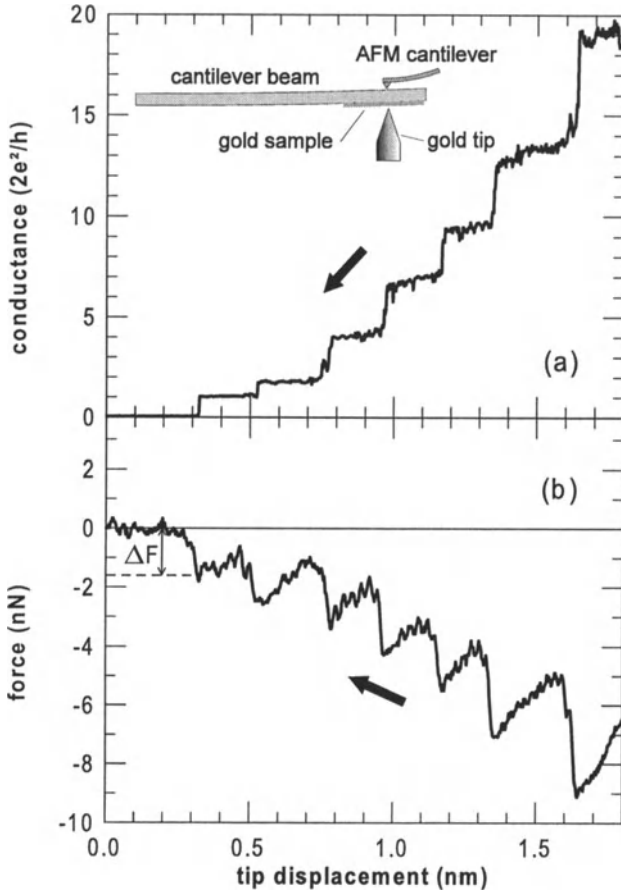


Fig. 6.6. Simultaneous measurement of force and conductance on atom scale point contacts for Au. The sample is mounted on a cantilever beam and the force between tip and sample is measured by the deflection of the beam using an Atomic Force Microscope (AFM). The measurements are done in air at room temperature. (From [21])

tion of the jumps when retracing the curve immediately after a jump is found (Fig. 6.7). When increasing the bath temperature or the current through the contact (which indirectly heats the contact) the width of the hysteresis is seen to gradually decrease until it is reduced to zero, and spontaneous jumps between the two conductance values are observed, which have a thermally activated behaviour [18,22,23]. These observations find a natural interpretation in terms of jumps between two distinct atomic configurations for the contact, separated by an energy barrier. Various recent molecular dynamics simulations confirm this scenario [4,24–27].

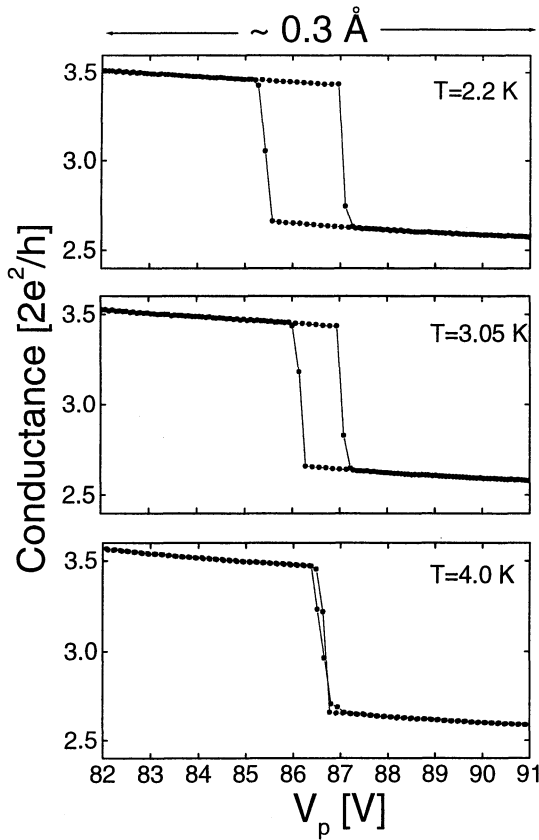


Fig. 6.7. Measurements of the conductance for an atomic-size gold contact while sweeping the piezo-voltage forward and back over a single step. The curves have been recorded at three different temperatures while maintaining the sweep centred around the same jump. Clear hysteresis of the order of 0.1 \AA is observed at 2.2 K . At 3.1 K the hysteresis is half as large, and at 4.2 K it has disappeared. (After J.M. Kras [22])

6.5 Histograms of Conductance Values

The atomic configuration of a contact adjusts itself in response to the externally applied stress, and evolves depending on the starting configuration of the contact at larger size. The fact that each conductance curve differs in many details from previous curves reflects the fact that the atomic configuration of the contact for given conductance is different in each run. However, as observed in the previous section, there appears to be a certain preference for conductance values near integer multiples of the quantum unit. For gold near $1 G_0$ this is immediately obvious from the examples in Fig. 6.3. A general and objective method of analysis was introduced [28,29], which consists in recording histograms of conductance values encountered in a large number of runs. Figure 6.8 shows a histogram for gold measured using a room temperature STM under UHV conditions [30]. Up to four peaks are found centred near the first four multiples of G_0 . For sodium in a low temperature experiment using the MCB technique, a histogram with peaks near 1, 3, 5 and 6 times G_0 was observed [29]. Figure 6.9 shows a similar result for potassium.

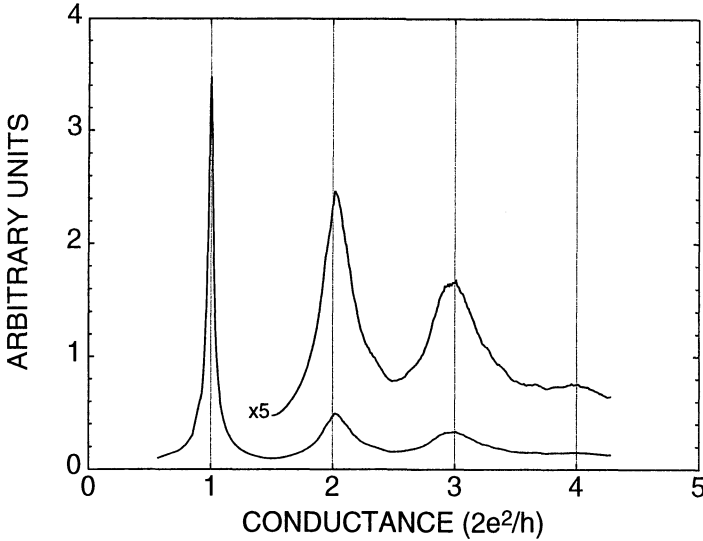


Fig. 6.8. Histogram representing the relative weight which each conductance value has in the experiments. The histogram is constructed from 227 conductance curves recorded while breaking Au contacts, using an STM under UHV at room temperature. (From [30])

The fact that peaks near 2 and $4 G_0$ are absent points at an interpretation in terms of a smooth, near-perfect cylindrical symmetry of the sodium contacts. Sodium indeed forms a very good approximation to a free electron system, and the weakly bound *s*-electrons strongly reduce surface corrugation. This is also why the best abundance spectra for clusters, with pronounced features at magic numbers have been obtained for the alkali metals [31]. For a model smooth, cylindrically symmetric contact with continuously adjustable contact diameter [32,33], the conductance increases from zero to $1 G_0$ as soon as the diameter is large enough, so that the first conductance mode is occupied. When increasing the diameter further, the conductance increases by two units because the second and third modes are degenerate. The modes are described by Bessel functions (assuming a hard wall boundary potential) and the first mode is given by the $m = 0$ Bessel function, which is not degenerate. The second and third modes are the degenerate $m = \pm 1$ modes, followed by $m = \pm 2$ for further increasing contact diameter. The next mode which will be occupied corresponds to the second zero of the $m = 0$ Bessel function, and is again *not* degenerate. Thus the conductance for such a contact should increase by 1, 2, 2 and 1 units, producing just the series of conductance values observed in the sodium experiment. The slight shift of the peaks in Fig. 6.9 below the integer values can be attributed to an effective series resistance due to back-scattering on defects near the contact. Model simulations [34] of the histogram are in close agreement with the experiment, including the shift

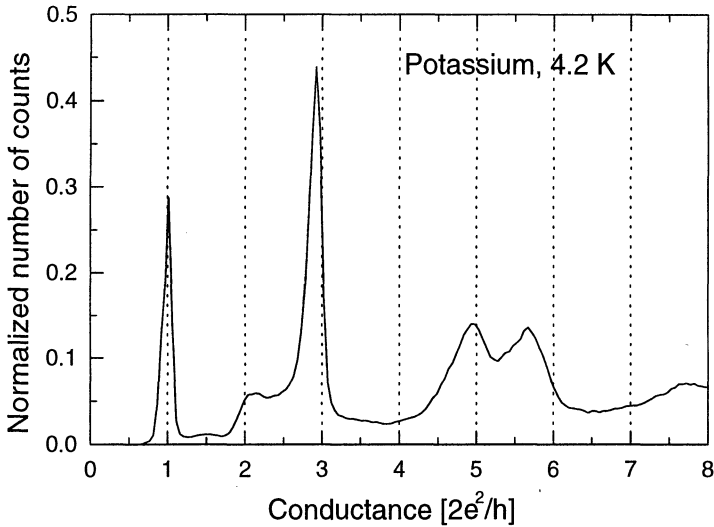


Fig. 6.9. Histogram of conductance values, constructed from $G(V_p)$ -curves measured for potassium at 4.2 K with an MCB device, involving several thousand individual measurements. The characteristic sequence of peaks ($G = 1, 3, 5, 6$) is regarded as a signature for conductance quantisation. (From [38])

of the peaks. The fact that gold histograms show peaks at all the first four quantum values may be explained by a stronger deviation from cylindrical symmetry in gold, which then lifts the degeneracy of the modes. Model simulations are indeed able to reproduce the shape of the gold histograms [30].

Not all metals show such pronounced histogram peaks near integer conductance values. The most clear-cut results are obtained only for monovalent metals. The alkali metals Li, Na and K show a histogram structure as represented by Fig. 6.9, although for Li the shift of the peaks is somewhat stronger [38]. The noble metals Cu, Ag and Au show histograms as in Fig. 6.8 [14]. The details such as the shift in position, the width and relative height of the peaks can be different depending on the experimental conditions [14,30,29,35–37]. Most other metals only show a rather broad first peak, which reflects the conductance of a single atom contact (see below). This peak can generally not be identified with an integer value of the conductance; for example niobium shows a wide peak centred near $2.5 G_0$ (Fig. 6.10) and similar results have been obtained for Pb [39]. On the other hand there are a few examples of multivalent metals, which show pronounced peaks in the histograms, among which aluminium [40]. As we shall discuss below, the histogram for Al throws doubt upon a straightforward interpretation of the histogram peaks in terms of conductance quantisation. For some systems other than simple metals evidence has been obtained for preferred conductance values near multiples of the quantum of conductance (carbon nanotubes, semimetals, metal oxides,

etc.). These will not be discussed here, since the nature of the contact and the mechanism of contact formation is expected to be very different from that in ordinary metals.

When we assume that the contact breaking process produces any effective contact diameter with equal probability, then the histograms represent a derivative of conductance with respect to the effective diameter of the contact. It is instructive to calculate the integral of the histogram, as was first done by Gai et al. [35]. Fig. 6.11 shows such a curve, obtained from a gold histogram similar to the one shown in Fig. 6.3. This curve is to be compared to conductance traces obtained for 2D semiconductor devices [6,7], for which the width of the contact can directly and continuously be adjusted by the gate electrostatic potential. Compared to the latter, the conductance steps in Fig. 6.11 are poorly defined, with the exception of the first conductance quantum. Moreover, we will show that the first quantum feature results from the fact that our assumption mentioned above is not valid. The effective diameters produced during contact breaking are strongly influenced by the possible atomic configurations. As we will argue below, the step at $1 G_0$, corresponding to the strong peak in the histogram for gold, results from the formation of a chain of gold atoms during the last stages of contact breaking. Disregarding the first step in Fig. 6.11, we find that the conductance is not strictly quantised, as the probability of finding a contact with a conductance of, e.g., $2 G_0$ is only twice that of finding $1.5 G_0$. However, the conductance

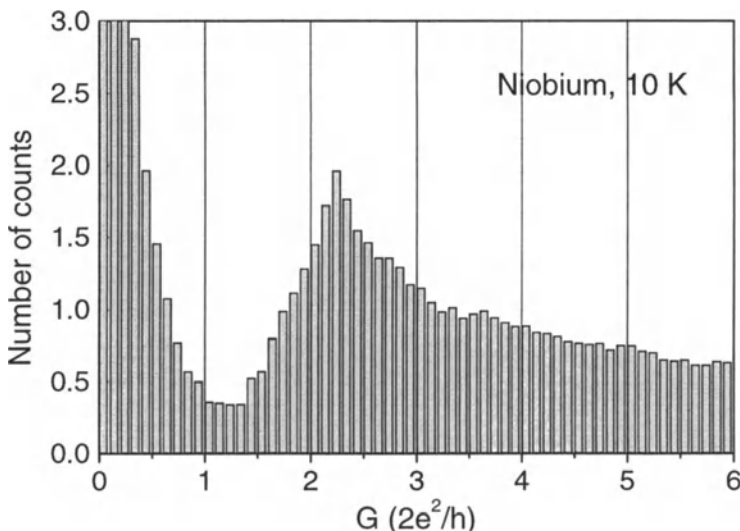


Fig. 6.10. Histogram constructed from 2400 individual conductance curves for a niobium sample. Each curve was recorded while stretching the contact to break, using the MCB technique at a temperature of 10 K, which is just above the superconducting transition temperature. The conductance was measured using a DC voltage bias of 20 mV. (From B. Ludoph [39])

is still determined by the quantum states, as described in Sect. 6.2 and is carried by a limited number of modes. We will show below how the quantum nature for monovalent metals is revealed by a tendency for the modes to open one-by-one as the contact becomes larger.

6.6 The Character of the Conductance Modes Through a Single Atom

Instead of discussing the average properties of many contacts, we now concentrate on the simplest configuration, a single atom bridging the electrodes at either side, and consider the question of what the conductance for this atomic configuration will be. Ideally, we would like to know the number of modes contributing to the conductance and the transmission probability, T_n for each of these. From a measurement of the conductance alone we cannot obtain this information, since the conductance gives only the sum of T_n . Scheer et al. [41] have introduced a method which allows us to obtain this information from experiment. The method exploits the non-linearities in the current–voltage characteristic for contacts in the superconducting state. Other techniques, which give more limited information on the contribution of the various modes, will be discussed at the end of this section.

6.6.1 Subgap Structure in Superconducting Contacts

The principle of the method introduced by Scheer et al. can be illustrated by considering first a contact having a single mode with low transmission

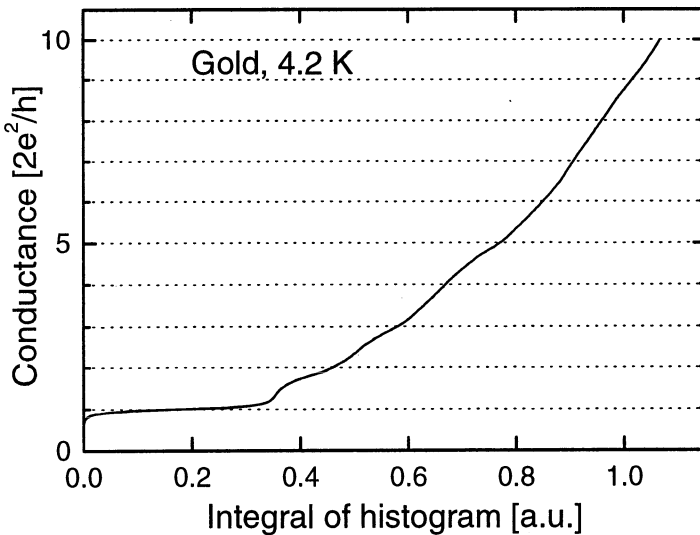


Fig. 6.11. Curve obtained by integrating a gold histogram similar to Fig. 6.3 (from A.I. Yanson [38])

probability, $T \ll 1$. For $T \ll 1$ we have essentially a tunnel junction, and the current–voltage characteristic for a superconducting tunnel junction is known to directly reflect the gap, Δ , in the density of states for the superconductor [42]. As illustrated in Fig. 6.12a no current flows until the applied voltage exceeds $2\Delta/e$ (where the factor 2 results from the fact that we have identical superconductors on both sides of the junction), after which the current jumps to approximately the normal-state resistance line. For $eV > 2\Delta$ single quasiparticles can be transferred from the occupied states at $E_F - \Delta$ on the low voltage side of the junction to empty states at $E_F + \Delta$ at the other side. For $eV < 2\Delta$ this process is blocked, since there are no states available in the gap.

However, when we consider higher order tunnel processes a small current can still be obtained. Figure 6.12(b) illustrates a process, which is allowed for $eV > \Delta$ and consists of the simultaneous tunnelling of *two* quasiparticles from the low bias side to form a Cooper pair on the other side of the junction. The onset of this process causes a step in the current at half the gap value, $V = 2\Delta/2e$. The height of the current step is smaller than the step at $2\Delta/e$ by a factor T , since the probability for two particles to tunnel is T^2 . In general, one can construct similar processes of order n , involving the simultaneous transfer of n particles, which give rise to a current onset at $eV = 2\Delta/n$ with a step height proportional to T^n . An example for $n = 3$ is illustrated in Fig. 6.12c. This mechanism is known as multiple particle tunnelling and was first described by Schrieffer and Wilkins [43]. It is now understood that this is the weak coupling limit of a mechanism which is referred to as multiple Andreev reflection [44–49]. The theory could only be tested recently, since it requires the fabrication of a tunnel junction having a single tunnelling mode with a well-defined tunnelling probability T . For atomic size niobium tunnel junctions the theory was shown to give a very good agreement [50,51], describing up to three current steps, including the curvature and the slopes, while the only adjustable parameter is the tunnel probability, which follows directly from the normal state resistance.

Since the theory has now been developed to all orders in T [45–49], Scheer et al. [41] realised that this mechanism offers the possibility of extracting the transmission probabilities for contacts with a finite number of channels contributing to the current, and is ideally suited to analysing atomic size contacts. Roughly speaking, the current steps at $eV = 2\Delta/n$ are proportional to $\sum T_m^n$, with m the channel index, and when we can resolve sufficient details in the current–voltage characteristics, we can fit many independent sums of powers of T_m 's. When the T_m 's are not small compared to 1, all processes to all orders need to be included for a description of the experimental curves. In practice, the full expression for the current–voltage characteristic for a single channel from theory [46–49] is numerically evaluated for a given transmission probability T_m (Fig. 6.13, inset), and a number of such curves are added independently, where the T_m 's are used as fitting parameters. Scheer et al.

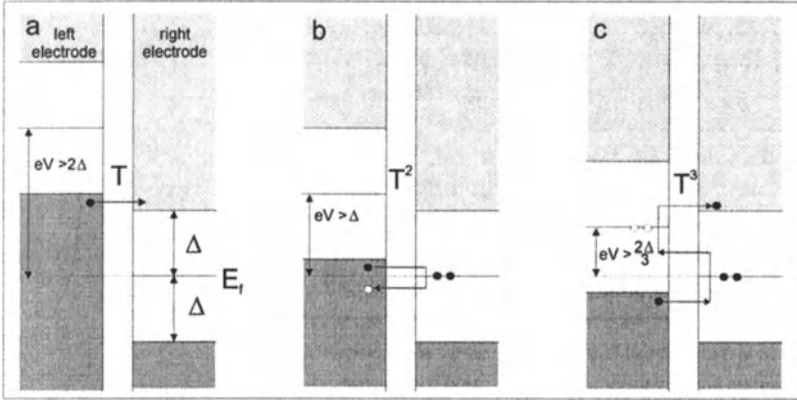


Fig. 6.12. Illustration of the Multiple Particle Tunnelling (MPT), or Multiple Andreev Reflection (MAR) processes. In each of the three diagrams the available quasi-particle states as a function of energy (*vertical axis*) at both sides of the tunnel barrier are given in the semiconductor representation. *Dark grey* are the occupied states, *light grey* the unoccupied states and the *line* in the middle of the gap represents the Cooper pair energy, which is separated by an energy Δ from the occupied and the unoccupied states. Applying an external electrical potential V across the junction shifts the states on the left side of the junction up by an energy eV with respect to those in the right electrode. The ordinary superconducting tunnelling process is given in (a), which shows that a voltage $V > 2\Delta/e$ is required for single quasi-particles to cross the junction. The probability for tunnelling of a particle, determined by the transparency of the barrier, is T . This gives rise to the familiar jump in the current at $eV = 2\Delta$ in the current–voltage characteristic of a superconducting tunnel junction. When we consider higher order processes, the next order is represented in (b). This can be described as two quasi-particles crossing simultaneously to form a Cooper pair in the right electrode (MPT). Alternatively, the process can be regarded as an electron-like quasiparticle falling onto the barrier, which is reflected as a hole-like quasiparticle, forming a Cooper pair on the right (MAR). The two descriptions are equivalent, and give rise to a current step in the current–voltage characteristic of the junction at $eV = 2\Delta/2$. The probability for the process is T^2 , since it requires the crossing of two particles. (c) shows the third order process, which involves breaking up a Cooper pair on the left, combining it with a quasiparticle, to form a Cooper pair and a quasiparticle on the right. It is allowed for $eV > 2\Delta/3$ and has a probability T^3

tested their approach first for aluminium contacts [41]. As shown in Fig. 6.13, all current–voltage curves for small contacts can be very well described by the theory. However, the most important finding was that at the last “plateau” in the conductance, just before the breaking of the contact, typically three channels with different T ’s are required for a good description, while the total conductance for such contacts is of order $1 G_0$, and would in principle require only a single conductance channel. Contacts at the verge of breaking are expected to consist of a single atom, and this atom would then admit

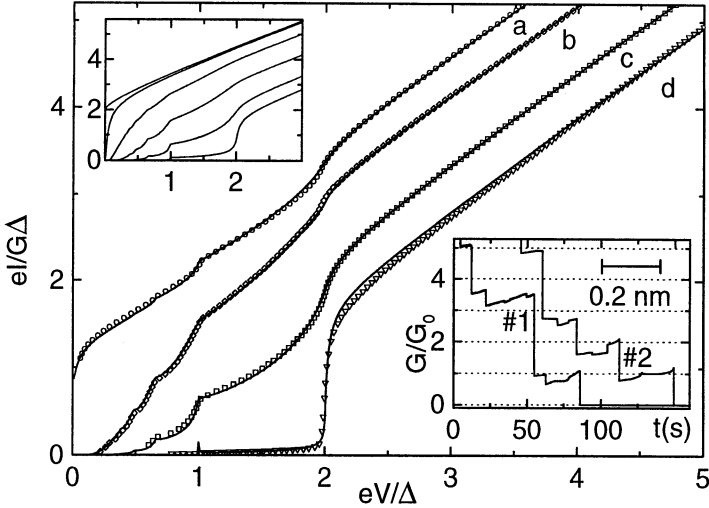


Fig. 6.13. Current–voltage characteristics for four atom-size contacts of aluminium using a lithographically fabricated mechanically controllable break junction at 30 mK (*symbols*). The *right inset* shows the typical variation of the conductance, or total transmission $T = G/G_0$, as a function of the displacement of the electrodes, while pulling, and is similar to the curves for aluminium shown in Fig. 6.4. The bar indicates the approximate length scale. The data in the main panel have been recorded by stopping the elongation at the last stages of the contact (**a–c**) or just after the jump to the tunnelling regime (**d**) and then measuring the current while slowly sweeping the bias voltage. The current and voltage are plotted in reduced units, $eI/G\Delta$ and eV/Δ , where G is the normal state conductance for each contact and Δ is the measured superconducting gap, $\Delta/e = (182.5 \pm 2.0)\mu\text{V}$. The *left inset* shows the current–voltage characteristics obtained from first-principles theory for a single channel junction [46–49] with different values for the transmission probability T (from bottom to top: $T=0.1, 0.4, 0.7, 0.9, 0.99, 1$). The *full curves* in the main panel have been obtained by adding several theoretical curves and optimising the set of T values. The curves are obtained with: (**a**) three channels, $T_1=0.997, T_2=0.46, T_3=0.29$ with a total transmission $\sum T_n = 1.747$, (**b**) two channels, $T_1=0.74, T_2=0.11$, with a total transmission $\sum T_n = 0.85$, (**c**) three channels, $T_1=0.46, T_2=0.35, T_3=0.07$ with a total transmission $\sum T_n = 0.88$. (**d**) In the tunnelling range a single channel is sufficient, here $\sum T_n = T_1 = 0.025$. (From Scheer et al. [41])

three conductance channels, but each of the three would only be partially open, adding up to a conductance close to $1 G_0$. This very much contradicts a simple picture of quantised conductance in atomic size contacts, and poses the question as to what determines the number of channels through a single atom.

6.6.2 Valence-Orbital-Based Description of the Conductance Modes

Cuevas, Levy Yeyati and Martín-Rodero [5] constructed a model to explain these results, using a tight binding calculation, for a geometry of two atomic pyramids touching at the apex through a single atom. They argue that it is very important to make the tight binding calculation self-consistent, by which they mean that local charge neutrality is maintained at each atomic site, by iteration and adjustment of the site energy for each individual atom in the model configuration. Figure 6.14 shows the results of their calculations of the density of states and the transmission probability for the various channels as a function of energy. They find that the conductance channels can be described in terms of the atomic valence orbitals. Aluminium has a configuration $[\text{Ne}]3s^23p^1$, and a total of four orbitals would be available for current transport: one s orbital and three p orbitals, p_x, p_y and p_z . They identify in their calculation three contributions, one which originates from a combination of s and p_z orbitals (where the z coordinate is taken in the current direction), and two smaller identical contributions labelled p_x and p_y . The degeneracy of these two channels is due to the symmetry of the problem, and can be lifted by changing the local environment for the central atom. The fourth possible channel, an antisymmetric combination of s and p_z , is found to have a negligible transmission probability. Thus, their calculation confirms the experimental observation by Scheer et al. that three channels contribute to the conductance for a single aluminium atom. It was also found that the total conductance for the three channels is of order $1 G_0$. The results are very robust against changes in the atomic configuration; only the total conductance varies somewhat between different choices for the atomic geometry. The qualitative features of the model agree with *ab initio* calculations for single atom contacts and a simplified structure for the environment [52–55].

The analysis, both theoretical and experimental, was extended to other metals [5,56], by which it was shown that the number of conductance channels for an atom of a given metallic element depends on the number of valence orbitals. Figure 6.15 shows conductance curves, similar to those in Fig. 6.3, for Pb, Al, Nb and Au, where at each point in the figure current–voltage curves as in Fig. 6.13 were recorded and fitted in order to determine the number of channels involved. This number of channels is indicated along the curves in Fig. 6.15. The number is constant over a plateau in the conductance, where the transmission probability for every mode changes gradually. At the steps in the conductance the number of channels involved is usually found to jump to a smaller number. In tunnelling range, when the contact is broken and the distance is larger than 0.2 nm, the current–voltage characteristics can in all cases be described by a single channel, with a transmission probability which is given by the tunnelling resistance. The number of channels found for the smallest contacts, just before the jump to tunnelling is 1 for Au, 3 for Al and Pb, and 5 for Nb. Note that gold is not a superconductor, and a special device

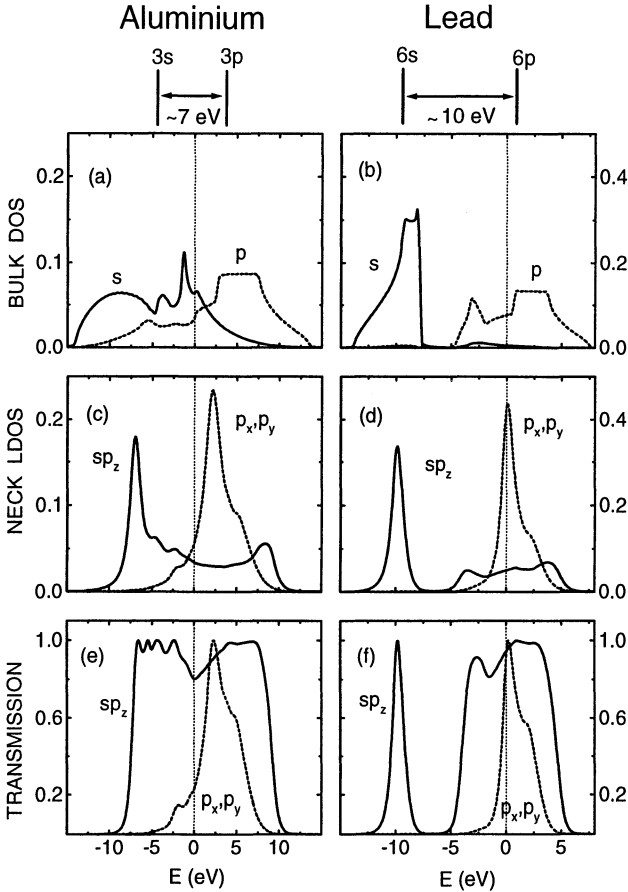


Fig. 6.14. Localised orbital model for electrical conduction through one-atom contacts. The atomic valence levels (*vertical bars* above the figures) develop into bulk conduction bands (a) and (b) for Al and Pb, respectively. The panels (c) and (d) depict schematically the local density of states (LDOS) in eV^{-1} at the central atom of the model geometry for a single atom contact. The global energy dependence of the transmission coefficients T_n is shown in (e) and (f). The *dotted lines* indicate the position of the Fermi level. The sp_z mode is the best transmitted for both materials. The p_x and p_y modes are degenerate due to the symmetry of the model geometry. (From [5,56])

was fabricated which allowed the use of proximity induced superconductivity [56]. The device is a nanofabricated version of a break junction, having a thick superconducting aluminium layer forming a bridge with a gap of about 100 nm. This small gap was closed by a thin gold film in intimate contact with the aluminium. Superconducting properties were thereby induced in the gold film, and by breaking the gold film and adjusting an atomic size contact, the same subgap analysis could be performed. Both the Al and Au junctions

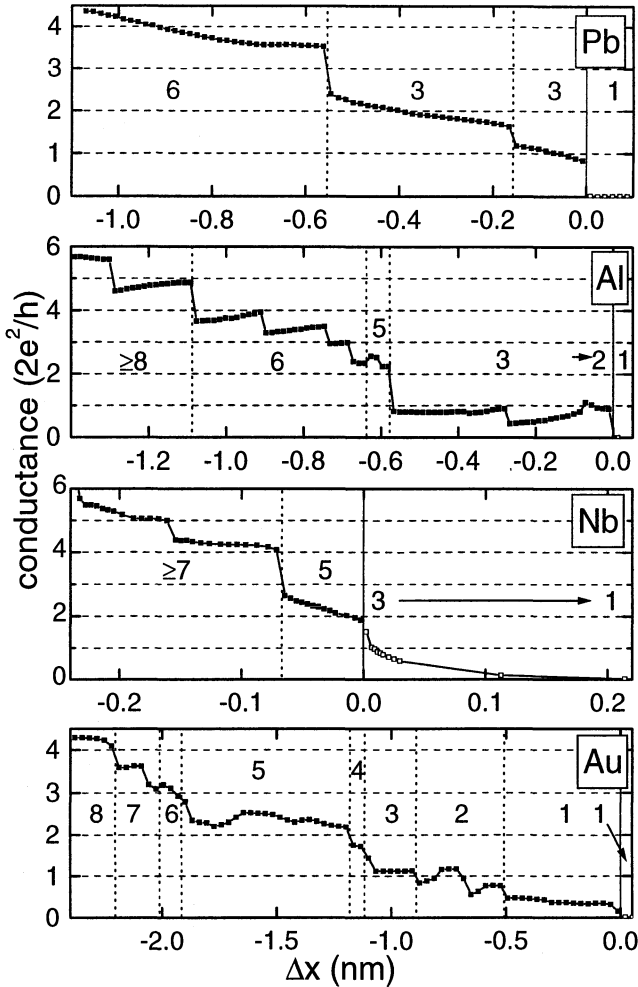


Fig. 6.15. Conductance curves measured as a function of contact elongation for Al, Pb, Nb and Au. The number of channels contributing to the conductance was determined at each point in the curves by recording the current–voltage relation and fitting the curves with the theory for superconducting subgap structure. The *numbers along the curves* in the figure indicate the number of channels obtained in this way. The number is constant over a plateau, and usually jumps to a smaller value at the steps in the conductance. (From [56])

were measured at temperatures of 100 mK, far below the superconducting transition temperatures. Pb and Nb were measured at 1.5 K.

The number of channels and the total conductance at the last plateau before breaking found in the experiment agree very well with the theory, for which the results can be summarised in the following way. Single atom contacts for monovalent metals, including the noble metals Cu, Ag and Au, and

the alkali metals, have a single valence orbital available for current transport, giving rise to a single channel with a transmission probability close to unity. The total conductance for such contacts is thus expected to be close to $1 G_0$. The experiment for gold shows indeed a single channel, but the total conductance is a factor 2–3 smaller than predicted. This was tentatively attributed to the strong scattering in the nano-fabricated device, and other techniques, which will be discussed below, have found more close agreement with the predicted total conductance of $1 G_0$. For *s-p* metals, including Al and Pb, three channels give a noticeable contribution to the current. The fourth channel, i.e., the antisymmetric combination of *s* and p_z is always nearly closed. The total transmission depends on the number of valence *electrons*. Pb has 4 valence electrons while aluminium has only three, and this has roughly the effect that the Fermi energy in Fig. 6.14 is shifted up to the peak in the p_x, p_y channel for Pb. The total conductance for Pb is found to be nearly $3 G_0$ in the calculations, while the conductance at the last plateau for lead does indeed start close to three quantum units, dropping to lower values upon further stretching of the contact. Niobium is a *d*-metal with a configuration $[\text{Kr}]4d^45s^1$ having 6 valence orbitals: 1 *s* and 5 *d*. The theory again predicts one combination with a negligible contribution and that the remaining five channels should add up to a total conductance of about $2.8 G_0$, again in good agreement with the experiment. The overall agreement is good, but some variation is observed between contacts and the information is obtained on a limited number of contacts. Below techniques are discussed which give less detailed information, but directly show the average properties of the contacts, and confirm the picture presented here.

6.6.3 Further Experimental Techniques

Three other methods have recently been introduced in order to investigate the number of channels contributing to the conductance of atomic size contacts: the measurement of shot noise, conductance fluctuations and thermopower.

Shot noise is the result of the discrete character of the current due to the passage of individual electrons. It was originally found in vacuum diodes, and first discussed by Schottky in 1918 [57]. The passage of individual electrons can be regarded as a delta function of the current with time. The total current is the sum of a random distribution of such delta functions, giving a time averaged current I , and a frequency spectrum of fluctuations which is white (up to very high frequencies), with a noise power equal to $2eI$. This shot noise can be observed, e.g., in tunnel junctions.

For a perfect ballistic point contact, in the absence of back-scattering, i.e., all channel transmission probabilities are either 1 or 0, the shot noise is expected to vanish [58–63]. This can be understood from the wave nature of the electrons, for which the wave function extends from the left bank

to the right bank of the contact without interruption. When the state on the left is occupied for an incoming electron, it is occupied on the right as well and there are no fluctuations in this occupation number. In other words, the incoming electron is not given the choice of being transmitted or not, it is always transmitted when it enters an open mode. In order to have noise, the electron must be given the choice of being reflected at the contact. This will be the case when the transmission probability is smaller than 1 and larger than 0. In single-channel quantum point contacts, shot noise is predicted to be suppressed by a factor proportional to $T(1 - T)$, where T is the transmission probability of the conductance channel [58–62]. This quantum suppression has recently been observed in point contact devices in a 2-dimensional electron gas [64,65]. For a general multichannel contact the shot noise power is predicted to be

$$P_I = 2eVG_0 \sum_n T_n(1 - T_n). \quad (6.4)$$

Since this depends on the sum over the second power of the transmission coefficients, this quantity is independent of the conductance, $G = G_0 \sum T_n$, and simultaneous measurement of these two quantities should give information about the channel distribution.

When measuring shot noise on atomic size point contacts [66], it is necessary to work at low temperatures in order to reduce thermal noise, and to shield the contact carefully from external mechanical and acoustic vibrations. Using two sets of preamplifiers in parallel and measuring the cross-correlation of the noise for the two signals eliminates the noise of the preamplifier. Experimental results for shot noise in gold point contacts for a number of conductance values are shown in Fig. 6.16. From the two measured parameters, G and P_I , one can determine at most two independent transmission probabilities. Instead, the results in Fig. 6.16 are compared to models which assume a certain evolution of the values for T_n as a function of the total conductance, G . The full curve shows the simplest model, where all T_n are either 0 or 1, except for a single partially open channel, so that the total conductance is given by $G/G_0 = N - 1 + T_N$. The figure shows that the experimental data closely follow this behaviour, in particular at low conductance. In order to estimate the contribution of additional partially open channels the broken curves show the expected behaviour for an evolution of the channel transmissions as illustrated in the inset. It shows that the deviation from a model with the channels opening one-by-one is only 10% between 1 and 2 G_0 , and about 20% between 2 and 3 G_0 . The scatter in the data points is larger than the experimental error because each point was measured on a different contact, which can have a very different set of transmission values, and a purely systematic behaviour is not expected. Although we cannot determine each individual transmission value, we obtain information from the property that the noise increases the more channels are partially transmitted. The minimum possible noise for a given conductance value is represented by the

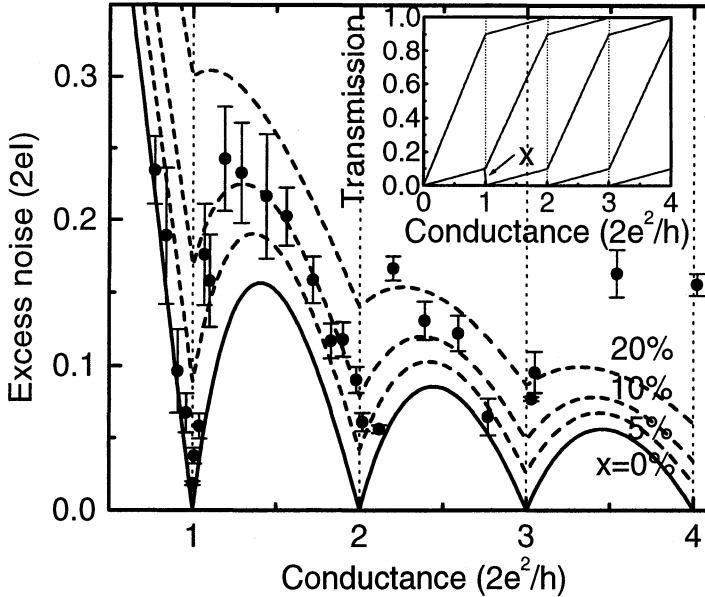


Fig. 6.16. Measured shot noise values for 27 gold contacts at 4.2 K with a bias current of 0.9 μA . Comparison is made with calculations in the case of one single partially transmitted mode (*full curve*) and for various amounts of contributions of other modes according to the model described in the inset (*dashed curves*). In the limit of zero conductance, these curves all converge to full shot noise, i.e., $2.9 \times 10^{-25} \text{ A}^2/\text{Hz}$. (From [66])

full curve in Fig. 6.16, corresponding to a single partially open channel. The broken curves give an impression of the other partially open channels.

There is a very strong suppression, down to 2% of the full shot noise value, for $G = 1 G_0$. It needs to be stressed that this holds for gold contacts. There is a fundamental distinction between this monovalent metal and the multivalent metal aluminium, which shows no systematic suppression of the shot noise at multiples of the conductance quantum, and the intensities lie between 0.3 and 0.6 times $2eI$ for G close to G_0 [66].

Conductance Fluctuations. Interference between electron trajectories scattering on defects near atomic size metallic contacts, gives rise to dominant contributions to the second derivative of the current with respect to bias voltage V , i.e., in dG/dV . This effect has the same origin as the well-known Universal Conductance Fluctuations (UCF) in diffusive mesoscopic conductors [67]. It was studied for point contacts an order of magnitude larger than the atomic size by Holweg et al. [68,69] and by Ralph et al. [70], and the theory was developed by Kozub et al. [71]. In experiments on gold contacts [72] it was found that this voltage dependence is suppressed near multiples of the quantum value of conductance, $n(2e^2/h)$. By applying a constant modulation

voltage at frequency ω and measuring the current with lock-in amplifiers simultaneously at ω and the second harmonic 2ω the conductance and its derivative can be obtained during conductance scans as in Fig. 6.3. From the combined data sets of many such curves one can construct a conductance histogram together with the average properties of dG/dV . It was found that dG/dV for a given conductance value has a bell-shaped distribution centred around zero and that the width of this distribution has a systematic variation with conductance. Figure 6.17 shows the standard deviation of the derivative of the conductance with bias voltage $\sigma_{GV} = \langle (dG/dV)^2 \rangle$, obtained from 3500 curves for gold, where the conductance and the derivative of the conductance were measured simultaneously as a function of contact elongation. The conductance histogram for the same set of data is shown in the lower panel.

The data for σ_{GV} display pronounced minima for G near multiples of G_0 . A similar effect can be recognised in the numerical calculations of Maslov et al. [73]. The explanation for this quantum suppression of the conductance fluctuations as presented in [72] is illustrated in the inset of Fig. 6.17. The contact is modelled by a ballistic central part, which can be described by a set of transmission values for the conductance modes, sandwiched between diffusive banks, where electrons are scattered by defects characterised by an elastic scattering length l_e . An electron wave of a given mode falling onto the contact is transmitted with probability amplitude t and part of this wave is reflected back to the contact by the diffusive medium, into the same mode, with probability amplitude $a_n \ll 1$. This back-scattered wave is then *reflected* again at the contact with probability amplitude r_n , where $T_n = |t_n|^2 = 1 - |r_n|^2$. The latter wave interferes with the original transmitted wave. This interference depends on the phase difference between the two waves, and this phase difference depends on the phase accumulated by the wave during the passage through the diffusive medium. The probability amplitude a_n is a sum over all trajectories of scattering, and the phase for such a trajectory of total length L is simply kL , where k is the wave vector of the electron. The wave vector can be influenced by increasing the voltage over the contact, thus launching the electrons into the other electrode with a higher speed. The interference of the waves changes as we change the bias voltage, and therefore the total transmission probability, or the conductance, changes as a function of V . This describes the dominant contributions to the conductance fluctuations, and from this description it is clear that the fluctuations are expected to vanish either when $t_n = 0$, or when $r_n = 0$.

Elaborating this model Ludoph et al. obtained the following analytical expression for σ_{GV} ,

$$\sigma_{GV} = \frac{2.71 e G_0}{\hbar k_F v_F \sqrt{1 - \cos \gamma}} \left(\frac{\hbar/\tau_e}{eV_m} \right)^{3/4} \sqrt{\sum_n T_n^2 (1 - T_n)}, \quad (6.5)$$

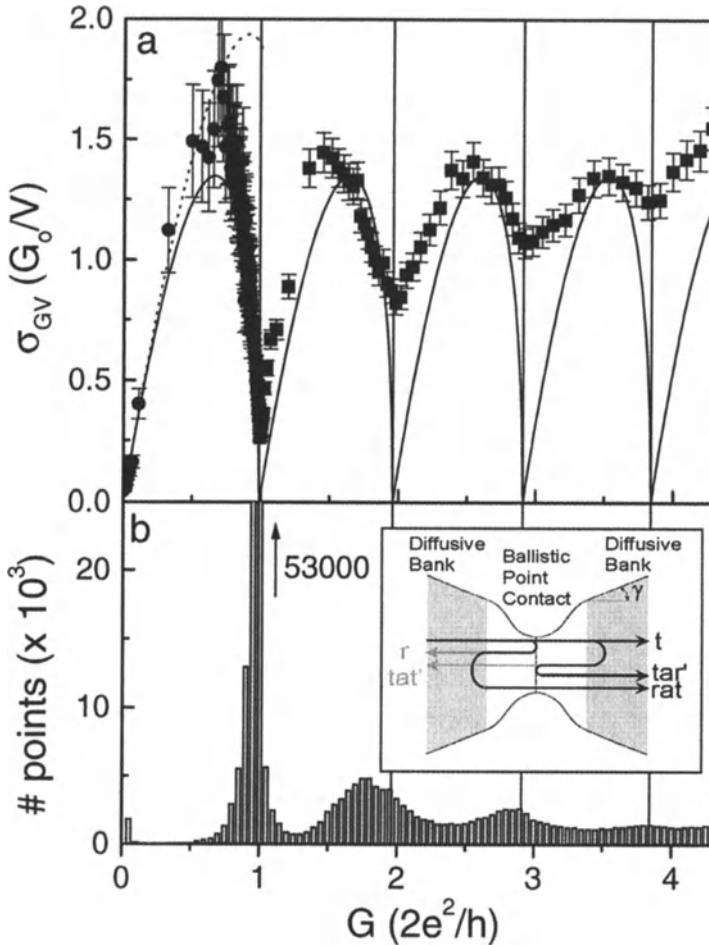


Fig. 6.17. (a) Standard deviation of the voltage dependence of the conductance versus conductance for 3500 curves for gold. All data points in the set were sorted as a function of the conductance after which the rms value of dG/dV was calculated from a fixed number of successive points. The *circles* are the averages for 300 points, and the *squares* for 2500 points. The *solid* and *dashed curves* depict the calculated behaviour for a single partially-open channel and a random distribution over two channels respectively. The *vertical lines* are the corrected integer conductance values (see text). (b) Conductance histogram obtained from the same data set. The peak in the conductance histogram at G_0 extends to 53000 on the y -scale. (*Inset*) Schematic diagram of the configuration used in the analysis. The *dark lines* with arrows show the paths, which contribute to the conductance fluctuations in lowest order. (From [72])

where k_F and v_F are the Fermi wave vector and Fermi velocity, respectively, $\tau_e = l_e/v_F$ is the scattering time. The shape of the contact is taken into account in the form of the opening angle γ (see the inset in Fig. 6.17), and V_m

is the applied voltage modulation amplitude. The full curves in Fig. 6.17a are obtained from (6.5), assuming a single partially-open channel at any point, i.e., assuming that channels open one-by-one as the conductance increases. In agreement with the results discussed above, the conductance for the smallest gold contacts is very well described by this simple approximation. The amplitude of the curves is adjusted to fit the data, from which a value for the mean free path is obtained, $l_e = 5 \pm 1$ nm. Similar experiments [72,74] for copper and silver and for sodium also show the quantum suppression of conductance fluctuations observed here for gold, while for aluminium or niobium it is not observed.

The back-scattering, which produces the conductance fluctuations, has a second observable effect, namely on the average conductance, as opposed to the fluctuating part. This effect is seen as a shift to lower conductance of the minima in σ_{GV} , and can be described to lowest order by an effective resistance in series with the contact. This shift has been taken into account in the calculation of the curves in Fig. 6.17a. Also in the interpretation of conductance histograms, a phenomenological series resistance is often taken into account in order to describe the shift of the peaks to lower values [29,14,36,37]. The estimate of the mean free path obtained from this series resistance is indeed consistent with the value obtained by fitting expression (6.5) to the data.

Thermopower. Further information on the quantum transport properties of atomic size contacts, again for gold, has been obtained from thermopower experiments using a modified MCB technique [75]. By applying a constant temperature difference over the contacts, the thermally induced potential could be measured simultaneously with the conductance. Large thermopower values were obtained, which jump to new values simultaneously with the jumps in the conductance. The values are randomly distributed around zero with a roughly bell-shaped distribution, in contrast to what was expected from elementary free electron gas models [76]. The thermopower was shown to result from the same mechanism as the conductance fluctuations, and the theory was adapted to describe the results. The experimental results were found to follow the law obtained from this defect-scattering model, and quantum suppression of the thermopower was indeed observed. By fitting the curves, a value for the mean free path was obtained which was in close agreement with the value from the conductance fluctuations. Since the two experimental techniques are very different, and the typical energy scales for the effects are at least an order of magnitude apart (this scale is set by the modulation voltage amplitude, 20 mV, in one case and the temperature, ~ 10 K, equivalent to $\simeq 1$ mV, in the other), these results give strong support for the description and interpretation presented above.

6.6.4 Implications for Conductance Curves and Histograms

Let us first focus on results for the monovalent metal, gold, which has been most studied. The results obtained from superconducting subgap structure, shot noise measurements, conductance fluctuations and thermopower are in agreement and show that the conductance for the smallest contacts of monovalent metals (gold) is carried by a single mode. For increasing contact size it is found that the transmission for the first mode goes to unity, before the second mode opens, then the second mode goes fully open, before the third opens, and so on. This property of atomic size contacts has been described as “saturation of the channel transmission” [72]. This property holds to very good approximation (a few percent) up to $G = 1G_0$, but deviations increase to 20% admixture of the next channels at $G = 4G_0$.

It is interesting to compare the positions of the maxima in the conductance histogram and those for the minima in σ_{GV} in Fig. 6.17. It appears that these positions do not all coincide, which is most evident for the peak in the histogram at about $G = 1.8G_0$. The histograms give preferential conductance values, which may reflect a quantisation effect in the conductance as a function of contact diameter, but also a preference for forming contacts of certain effective diameters. Such preferential contact diameters may be expected based on the fact that the contact is only a few atoms in cross section, which limits the freedom for choosing the diameter. It appears that at least the peak at $1.8 G_0$ in the histogram for gold arises from this atomic geometry effect. Although the shot noise and conductance fluctuation experiments both show that the conductance for gold contacts with $G \simeq 2G_0$ is carried by two nearly perfectly transmitted modes, this conductance is not preferred, as evidenced by the conductance histogram.

This observation amplifies the arguments given in the discussion of Fig. 6.11 where it was argued that it is not appropriate to describe the conductance for gold as being quantised. There is no pronounced preference for conductances near multiples of G_0 , with the exception of $1 G_0$, which is due to a special property of gold contact in that it forms chains of atoms at the last stages of contact elongation (see below). Of course, the conductance is a true quantum property in the sense that it is carried by only a few well-defined modes, but the transmission for these modes can add up to any value of the total conductance. Moreover, we identify a property for these contacts, called the saturation of channel transmission, which describes the tendency for the conductance modes to open one-by-one.

For s , s - p and s - d metals the results for the subgap structure on the smallest contacts agree with the predictions of the tight binding model of Cuevas et al. under the assumption that the last plateau, before the jump to tunnelling, consists of a single atom contact. The agreement between the predicted number of channels and the number obtained from the fits of the current-voltage curves, thus confirm the assumption that the contacts consist of a single atom at the last stage of the contact elongation. The results on shot

noise and conductance fluctuations for Al, where no quantum suppression was found, confirm the results by Scheer et al. that the conductance near $G = 1 G_0$ cannot be described by a single mode. We conclude that a saturation of channel transmission is not observed for Al, and is expected to be absent in all metals other than simple *s*-metals. Despite this apparent lack of a simple quantum mode structure, the conductance histogram for aluminium shows pronounced peaks near the first three or four multiples of G_0 [40], albeit considerably shifted from perfect integers. A natural interpretation for the first peak in the histogram, which is consistent with the findings above, would be that it arises from a reproducible last contact configuration of a single atom, with a conductance close to $1 G_0$ and three channels involved in the conductance. In this sense, the histogram peak would arise purely as a result of atomic structure. In analogy, the other peaks are also expected to relate to atomic structure, although it is less evident what this structure should be. In the simplest approach one could imagine that the peaks correspond to 1, 2, 3 and 4 atoms in the contact cross section.

Further support for the model of valence orbitals as a basis for the conductance channels comes from the anomalous slope of the plateaux of the conductance for aluminium, where conductance increases as the contact is stretched (Fig. 6.4). Calculations of the conductance through a single atom, within the tight binding model discussed above, as a function of the bond distance of the atom with its neighbours, reproduce the anomalous dependence of conductance on distance [77]. For gold a nearly flat dependence is found, while for Pb the conductance decreases with increasing elongation, again in agreement with the observations. The anomalous slopes for Al are also found for larger contacts, and have been explained in terms of the stress-dependence of the electronic band structure [78]. It appears that this property of the band structure is conserved in contacts down to the atomic scale.

6.7 Chains of Atoms

All evidence shows that for a single atom contact for monovalent metals the current is carried by a single mode, with a transmission probability close to one. Guided by this knowledge, in experiments on gold Yanson et al. [79] discovered that during the contact breaking process the atoms in the contact form stable chains of single atoms, up to 7 atoms long. Independently, Ohnishi et al. [80] discovered the formation of chains of gold atoms at room temperature in a combined STM and transmission electron microscope, where an atomic strand could be directly seen in the images. Currently, the only material for which this chain formation is observed is gold. It is interesting that for silver the effect is much less pronounced and copper does not seem to show it at all.

Some understanding of the underlying mechanism can be obtained from molecular dynamics simulations. Already before the experimental observa-

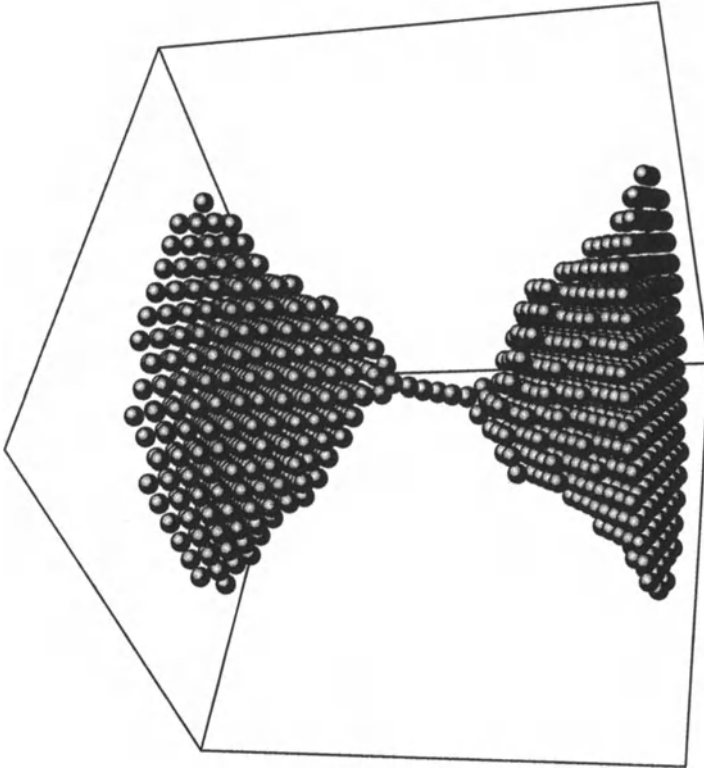


Fig. 6.18. Atomic configuration obtained during the last stages of breaking of a nanowire in a molecular dynamics simulation for gold, using a bath temperature of 12 K. (From [81])

tions, several groups had observed the spontaneous formation of chains of atoms in computer simulations of contact breaking [81–83]. Figure 6.18 shows the results obtained by Sørensen et al. for gold. The authors caution that the interatomic potentials used in the simulation may not be reliable for this unusual configuration. However, from these studies we may learn more about the atomic configuration sequences producing the chains, and they form a good starting point for more advanced model calculations.

Such chains constitute the ultimate one-dimensional metallic nanowires. The current is carried by a single mode, with a transmission probability, which is somewhat below 1 due to back-scattering, but can be tuned to unity by adjusting the stress on the junction. The chains sustain enormous currents, up to 80 μA , due to the ballistic nature of the electron transport [79]. More work is needed to elucidate the mechanism of chain formation, what limits the length of the chains, and why it works best for gold. Further unusual atomic configurations may be found, according to model calculations by Gülseren et al. [84], who show a series of “weird wire” structures depending on the

number of atoms in the cross section of the wires and on the metallic element involved.

6.8 Quantum Forces and Shell Structure in Alkali Nanowires

Apart from their role in determining the electronic transport properties of the contacts, the quantisation of the wave functions may also affect the energy of formation of the contact. In direct analogy with the effect of electronic shell closing on the formation energy of clusters [31], one expects that specific contact diameters will be stabilised by the formation of quantum modes. Several groups have recently presented model calculations on this problem, mostly considering free electrons confined by a hard wall potential [86–91]. Local density calculations taking the atomic structure into account have also appeared [92–94]. There appears to be a consensus on the magnitude of the force fluctuations which may result from this mechanism, which is of the order of 1 nN, and is comparable to the force jumps for the smallest contacts observed in Fig. 6.6. Some authors argue that the jumps observed in the conductance as a function of contact stretching should therefore be considered as being the result of the underlying electronic quantum modes. However, in the experiment many conductance steps are found which are much smaller, or much larger, than a conductance quantum, and all steps show similar mechanical and dynamic behaviour. In addition, the conductance steps in monovalent metals look similar to those in *sp* or *sd* metals, where such simple description definitely breaks down. Experimental methods will have to be developed to test a possible quantum-mode-based atomic force mechanism. One possibility is to measure the charge, or the work function of the nanowire, which is expected to fluctuate in unison with the force within this simple free electron gas picture [87,90].

While the contribution of quantum modes to the force in the smallest contacts is still under debate, a newly observed phenomenon for larger contacts provides strong evidence for quantum force fluctuations. In a recent study of conductance histograms for sodium, potassium and lithium up to conductances much larger than shown in Fig. 6.9, Yanson et al. [85] observed a large number of additional peaks (Fig. 6.19). The peaks are not as sharp as the ones associated with conductance quantisation at low conductance (Fig. 6.9) and cannot be identified with multiples of the conductance quantum. The peaks become more pronounced as the temperature is raised to about 80 K, and the position of the peaks is seen to be periodic in the square root of the conductance, as illustrated in Fig. 6.20.

The interpretation of the phenomenon is based on fluctuations in the density of states as a function of energy (or equivalently as a function of diameter) for a free electron gas inside a cylindrically symmetric wire. At the points where a new mode (the bottom of a 1-dimensional subband) crosses

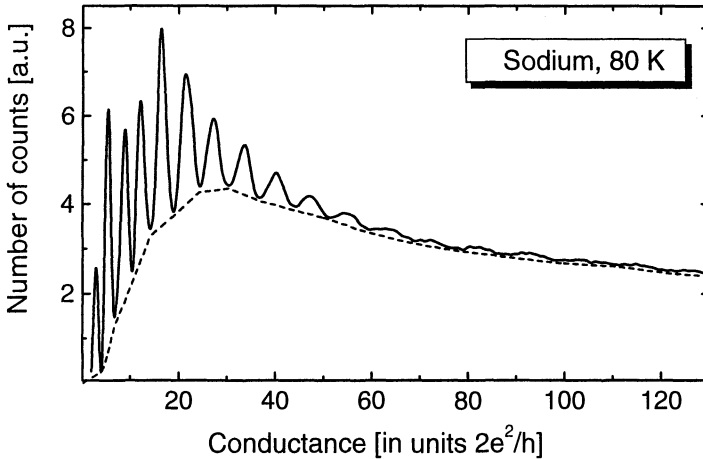


Fig. 6.19. Histogram of the number of times each conductance is observed versus the conductance in units of the conductance quantum, G_0 , for sodium at $T=80$ K and bias voltage $V=100$ mV, constructed from over 10,000 individual scans. The smooth background (*dashed curve*) helps to bring out the smaller amplitude oscillations. (From [85])

the Fermi energy, the density of states shows a $1/\sqrt{E - E_n}$ singularity. These singularities are smeared out by the finite length of the wire and would not have a very pronounced effect were they homogeneously distributed. However, the symmetry of the wire gives rise to a bunching of the singularities, which can be associated with the electronic shells in metal clusters. The resulting density of states fluctuations have been analysed by Stafford and coworkers [86,90], by Yannouleas et al. [88] and by Höppler and Zwerger [91]. The fluctuations in the density of states result in local minima in the total energy for the nanowire, and the stable wire diameters predicted from this model are in fairly good agreement with the observed periodic peak structure in the histograms [85].

It was found that a direct comparison with cluster magic numbers is possible. One can calculate the effective cluster radius from the magic numbers for sodium clusters [31] (see Chap. 1) $N_m = 8, 20, \dots, 1500$ using $R_m = r_S N_m^{1/3}$, where r_S is the Wigner–Seitz radius of the atom. Then the conductance of a nanowire with these magic radii can be found using the semi-classical expression [33], $G_m = G_0(\pi R_m/\lambda_F)^2(1 - \lambda_F/\pi R_m)$. The square root of the conductance values obtained in this way are plotted against the shell number m and compared to the histogram peak positions in Fig. 6.20. A striking agreement is observed, which is believed to result from the fact that the dominant fluctuation terms in the density of states can be described in terms of the lowest order semi-classical trajectories inside the system [95,96,91]. These trajectories (diametrical, triangular and square orbits inscribed inside the sphere and cylinder, respectively, c.f. Chap. 1) are the same for clusters

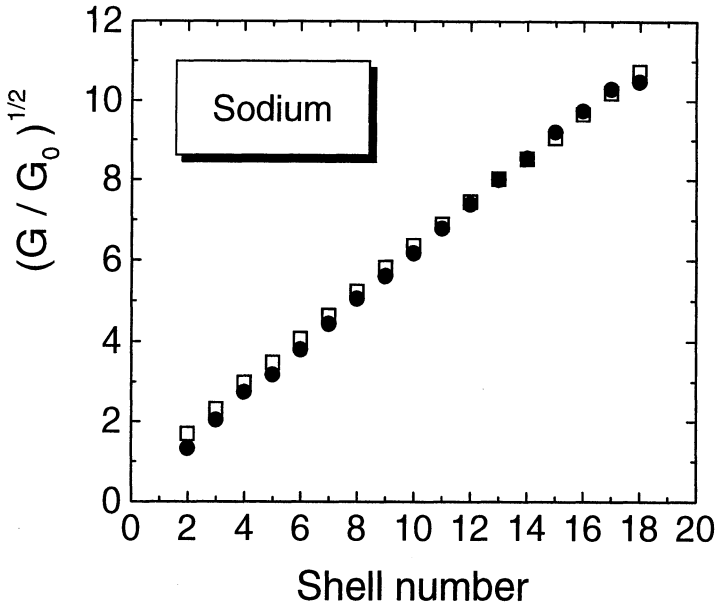


Fig. 6.20. Square root of the positions of the maxima in Fig. 6.19, $\sqrt{G_i/G_0}$, versus the shell number (*open squares*). The experimental peak positions are compared to the expected positions derived from the magic numbers of metallic clusters (*closed circles*). (From [85])

and nanowires. However, the agreement in Fig. 6.20 is better than expected since the relative contribution of each of the trajectories for the two systems should be different. Further work is needed to clarify the details of the shell structure in nanowires.

6.9 Discussion and Outlook

With the developments of the last few years a microscopic understanding of atomic-scale electrical transport properties is beginning to grow. A coherent picture of conductance modes in a single atom derived from atomic valence orbitals is obtained, which finds strong support in the experimental observations for various metallic elements. For contacts of several atoms, monovalent metals demonstrate saturation of channel transmission, which is a very interesting experimental observation, but is not yet fully understood on the microscopic level. Also, the nature of peaks in the histograms is still not fully resolved: quantisation plays a role but not exclusively. This is evident from the histograms for aluminium, in combination with the channel numbers obtained from subgap structure, shot noise and conductance fluctuations. The peak at $5 G_0$ in sodium is stronger than expected from a simple free electron nanowire model, and the peak below $2 G_0$ in gold does not correspond to

the position of the conductance quantum, even after correction for a series resistance, as was seen in conductance fluctuation experiments.

It seems clear that a full understanding of the structure in conductance histograms requires a description of the mechanical evolution of the atomic structure of the contacts. It is possible that conditions such as temperature or bias voltage must be taken into account [97]. Much has been learned already from molecular dynamics calculations, but new experimental tools are probably essential. Promising developments come from two groups, which have recently shown transmission electron microscopy images with atomic resolution of contacts that can be controlled in situ [80,98,99]. By simultaneous measurement of the conductance while observing a single atom contact in the electron micrograph, Ohnishi et al. clearly confirmed that a single atom gold contact has a conductance close to $1 G_0$.

The question of the effect of the conductance modes on the force in metallic contacts will, without doubt, receive a lot of attention in the near future. A related question at present being considered is whether the increased density of states at specific wire diameters may be lifted by deformation of the shape of the wire cross section (in analogy to the Jahn–Teller effect) [87] or by a spontaneous magnetisation [100]. Many other open questions promise new and interesting developments in this area of physics. The dynamics of atomic structures, seen as two-level fluctuations, have not received sufficient attention. A related problem concerns the interaction with the electric current and the heating of the contact [101]. The observed chain formation for gold may lead to a deeper understanding of bonding forces on the atomic scale. We may be able to produce much longer atomic wires, which will open a new field for study of purely one-dimensional solid state physics.

References

1. C.W.J. Beenakker and H. van Houten Quantum transport in semiconductor nanostructures. *Solid State Physics* **44**, H. Ehrenreich and D. Turnbull, eds. (Academic Press, New York, 1–228, 1991)
2. T.J. Thornton, *Rep. Prog. Phys.* **57**, 311–364 (1994)
3. Y. Imry, Introduction to mesoscopic physics (Oxford University Press, Oxford, 1997)
4. M. Brandbyge, M.R. Sørensen, and K.W. Jacobsen, *Phys. Rev. B* **56**, 14956–14959 (1997)
5. J. C. Cuevas, A. Levy Yeyati, and A. Martín-Rodero, *Phys. Rev. Lett.* **80**, 1066–1069 (1998)
6. B.J. van Wees, H. van Houten, C.W.J. Beenakker, J.G. Williamson, L.P. Kouwenhoven, D. van der Marel, and C.T. Foxon, *Phys. Rev. Lett.* **60**, 848–850 (1988)
7. D.A. Wharam, T.J. Thornton, R. Newbury, M. Pepper, H. Ahmed, J.E.F. Frost, D.G. Hasko, D.C. Peacock, D.A. Ritchie, and G.A.C. Jones, *J. Phys. C* **21**, L209–L214 (1988)
8. N. Agraït, J.G. Rodrigo, and S. Vieira, *Phys. Rev. B* **47**, 12345–12348 (1993)

9. J.I. Pascual, J. Méndez, J. Gómez-Herrero, A.M. Baró, and N. García, *Phys. Rev. Lett.* **71**, 1852–1855 (1993)
10. L. Olesen, E. Lægsgaard, I. Stensgaard, F. Besenbacher, J. Schiøtz, P. Stoltze, K.W. Jacobsen, J.K. and Nørskov, *Phys. Rev. Lett.* **72**, 2251–2254 (1994)
11. J.K. Gimzewski, R. and Möller *Phys. Rev. B* **36**, 1284–1287 (1987)
12. C.J. Muller, J.M. van Ruitenbeek, and L.J. de Jongh, *Physica C* **191**, 485–504 (1992)
13. J.L. Costa-Krämer, N. García, P. García-Mochales, and P.A. Serena, *Surf. Sci.* **342**, L1144–L1149 (1995)
14. K. Hansen, E. Lægsgaard, I. Stensgaard, and F. Besenbacher, *Phys. Rev. B* **56**, 2208–2220 (1997)
15. J.M. Krans, Size effects in atomic-scale point contacts. PhD thesis, Leiden, The Netherlands (1996)
16. J.M. Krans, C.J. Muller, I.K. Yanson, Th.C.M. Govaert, R. Hesper, and J.M. van Ruitenbeek, *Phys. Rev. B* **48**, 14721–14724 (1993)
17. T.N. Todorov, and A.P. Sutton, *Phys. Rev. Lett.* **70**, 2138–2141 (1993)
18. C.J. Muller, J.M. van Ruitenbeek, and L.J. de Jongh, *Phys. Rev. Lett.* **69**, 140–143 (1992)
19. A.P. Sutton, J.B. and Pethica, *J. Phys.: Condens. Matter* **2** 5317–5326 (1990)
20. U. Landman, W.D. Luedtke, N.A. Burnham, and R.J. Colton, (1990) *Science* **248**, 454–461 (1990)
21. G. Rubio, N. Agrait, and S. Vieira, *Phys. Rev. Lett.* **76**, 2302–2305 (1996)
22. J.M. Krans, J.M. van Ruitenbeek, and L.J. de Jongh, *Physica B* **218**, 228–233 (1996)
23. H.E. van den Brom, A.I. Yanson, and J.M. van Ruitenbeek, *Physica B* **252**, 69–75 (1998)
24. T.N. Todorov, and A.P. Sutton, *Phys. Rev. B* **54** R14234–R14237 (1996)
25. U. Landman, W.D. Luedtke, B.E. Salisbury, and R.L. Whetten, *Phys. Rev. Lett.* **77**, 1362–1365 (1996)
26. H. Mehrez, S. Ciraci, C.Y. Fong, and S. Erko, *J. Phys.: Condens. Matter* **9**, 10843–10854 (1997)
27. H. Mehrez, and S. Ciraci *Phys. Rev. B* **56**, 12632–12642 (1997)
28. L. Olesen, E. Lægsgaard, I. Stensgaard, F. Besenbacher, J. Schiøtz, P. Stoltze, K.W. Jacobsen, and J.K. Nørskov, *Phys. Rev. Lett.* **74**, 2147–2150 (1995)
29. J.M. Krans, J.M. van Ruitenbeek, Fisun, I.K. Yanson, and L.J. de Jongh, *Nature* **375**, 767–769 (1995)
30. M. Brandbyge, J. Schiøtz, M.R. Sørensen, P. Stoltze, K.W. Jacobsen, J.K. Nørskov, L. Olesen, E. Lægsgaard, I. Stensgaard, and F. Besenbacher, *Phys. Rev. B* **52**, 8499–8514 (1995)
31. W.A. de Heer, *Rev. Mod. Phys.* **65**, 611–676 (1993)
32. E.N. Bogachek, A.N. Zagoskin, and I.O. Kulik, *Sov. J. Low Temp. Phys.* **16**, 796–800 (*Fiz. Nizk. Temp.* **16**, 1404–1411) (1990)
33. J.A. Torres, J.I. Pascual, and J.J. Sáenz, *Phys. Rev. B* **49**, 16581–16584 (1994)
34. J.A. Torres, and J.J. Sáenz, *Phys. Rev. Lett.* **77**, 2245–2248 (1996)
35. Z. Gai, Y. He, H. Yu, and W.S. Yang, *Phys. Rev. B* **53**, 1042–1045 (1996)
36. J.L. Costa-Krämer, *Phys. Rev. B* **55**, R4875–4878 (1997)
37. J.L. Costa-Krämer, N. García, and H. Olin, *Phys. Rev. B* **55**, 12910–12913 (1997)
38. A.I. Yanson, and J.M. van Ruitenbeek, to be published

39. B. Ludoph, and J.M. van Ruitenbeek, to be published
40. A.I. Yanson, and J.M. van Ruitenbeek, *Phys. Rev. Lett.* **79**, 2157 (1997)
41. E. Scheer, P. Joyez, D. Esteve, C. Urbina, and M.H. Devoret, *Phys. Rev. Lett.* **78**, 3535–3538 (1997)
42. E.L. Wolf, *Principles of electron tunneling spectroscopy*. (Oxford University Press, Oxford, 1989)
43. J.R. Schrieffer, and J.W. Wilkins, *Phys. Rev. Lett.* **10**, 17–20 (1963)
44. T.M. Klapwijk, G.E. Blonder, and M. Tinkham, *Physica B* **109–110**, 1657–1664 (1982)
45. G.B. Arnold, *J. Low Temp. Phys.* **68** 1–27 (1987)
46. D. Averin, and D. Bardas, *Phys. Rev. Lett.* **75**, 1831–1834 (1995)
47. J.C. Cuevas, A. Martín-Rodero, and A. Levy Yeyati *Phys. Rev. B* **54**, 7366–7379 (1996)
48. E.N. Bratus, V.S. Shumeiko, and G. Wendin, *Phys. Rev. Lett.* **74**, 2110–2113 (1995)
49. E.N. Bratus, V.S. Shumeiko, E.V. Bezuglyi, and G. Wendin, *Phys. Rev. B* **55**, 12666–12677 (1997)
50. N. van der Post, E.T. Peters, I.K. Yanson, and J.M. van Ruitenbeek, *Phys. Rev. Lett.* **73**, 2611–2613 (1994)
51. N. van der Post, *Superconductivity and magnetism in nano-scale junctions*. PhD thesis, Leiden, The Netherlands (1997)
52. N.D. Lang, *Phys. Rev. B* **36**, 8173–8176 (1987)
53. N.D. Lang, *Phys. Rev. B* **52**, 5335–5342 (1995)
54. N.D. Lang, *Phys. Rev. Lett.* **79**, 1357–1360 (1997)
55. C.C. Wan, J. Mozes, G. Taraschi, J. Wang, and H. Guo, *Appl. Phys. Lett.* **71**, 419–421 (1997)
56. E. Scheer, N. Agraït, J.C. Cuevas, A. Levy Yeyati, B. Ludoph, A. Martín-Rodero, G. Rubio Bollinger, J.M. van Ruitenbeek, and C. Urbina, *Nature* **394**, 154–157 (1998)
57. W. Schottky, *Ann. Phys. (Leipzig)* **57**, 541–567 (1918)
58. G.B. Lesovik, *Sov. Phys. JETP Lett.* **49**, 592–594 (*Pis'ma Zh. Eksp. Teor. Fiz.* **49**, 513–515) (1989)
59. M. Büttiker, *Phys. Rev. Lett.* **65**, 2901–2904 (1990)
60. C.W.J. Beenakker, and H. Van Houten, *Phys. Rev. B* **43**, 12066–12069 (1991)
61. Th. Martin, and R. Landauer, *Phys. Rev. B* **45**, 1742–1751 (1992)
62. M. Büttiker, *Phys. Rev. B* **46**, 12485–12507 (1992)
63. A.G. Scherbakov, E.N. Bogachek, and U. Landman, *Phys. Rev. B* **57**, 6654–6661 (1998)
64. M. Reznikov, M. Heiblum, H. Shtrikman, and D. Mahalu, *Phys. Rev. Lett.* **75**, 3340–3343 (1995)
65. A. Kumar, L. Saminadayar, D.C. Glattli, Y. Jin, and B. Etienne, *Phys. Rev. Lett.* **76**, 2778–2781 (1996)
66. H.E. van den Brom, J.M. and van Ruitenbeek, *Phys. Rev. Lett.* **82**, 1526–29 (1999)
67. B.Z. Spivak, and A.Yu. Zyuzin, In: *Mesoscopic Phenomena in Solids*, Altshuler, B.L., Lee, P.A. and Webb, R.A., eds., (North-Holland, Amsterdam, 1991)
68. P.A.M. Holweg, J.A. Kokkedee, J. Caro, A.H. Verbruggen, S. Radelaar, A.G.M. Jansen, and P. Wyder, *Phys. Rev. Lett.* **67**, 2549–2552 (1991)

69. P.A.M. Holweg, J. Caro, A.H. Verbruggen, and S. Radelaar, *Phys. Rev. B* **48**, 2479–2485 (1993)
70. D.C. Ralph, K.S. Ralls, and R.A. Buhrman, *Phys. Rev. Lett.* **70**, 986–989 (1993)
71. V.I. Kozub, J. Caro, and P.A.M. Holweg, *Phys. Rev. B* **50**, 15126–15137 (1994)
72. B. Ludoph, M.H. Devoret, D. Esteve, C. Urbina, and J.M. van Ruitenbeek, *Phys. Rev. Lett.* **82**, 1530–1533 (1999)
73. D.L. Maslov, C. Barnes, and G. Kirczenow, *Phys. Rev. Lett.* **70**, 1984–1987 (1993)
74. B. Ludoph, and J.M. van Ruitenbeek, *Phys. Rev. B*, in print. Preprint cond-mat/9908139 (1999)
75. B. Ludoph, and J.M. van Ruitenbeek, *Phys. Rev. B* **59**, 12290–12293 (1999)
76. E.N. Bogachek, A.G. Scherbakov, U. Landman, *Phys. Rev. B* **54**, R11091–R11097 (1996)
77. J.C. Cuevas, A. Levy Yeyati, A. Martín-Rodero, G. Rubio Bollinger, C. Untiedt, and N. Agraït, *Phys. Rev. Lett.* **81**, 2990–2993 (1998)
78. D. Sánchez-Portal, C. Untiedt, J.C. Soler, J.J. Sáenz, and N. Agraït, *Phys. Rev. Lett.* **79**, 4198–4201 (1997)
79. A.I. Yanson, G. Rubio Bollinger, H.E. van den Brom, N. Agraït, and J.M. van Ruitenbeek, *Nature* **395**, 783–785 (1998)
80. H. Ohnishi, Y. Kondo, and K. Takayanagi, *Nature* **395**, 780–783 (1998)
81. M.R. Sørensen, M. Brandbyge, and K.W. Jacobsen, *Phys. Rev. B* **57**, 3283–3295 (1998)
82. G.M. Finbow, R.M. Lynden-Bell, and I.R. McDonald, *Mol. Phys.* **92** N4, 705–714 (1997)
83. A.P. Sutton, and T.N. Todorov, unpublished
84. O. Gülseren, F. Ercolessi, and E. Tosatti, *Phys. Rev. Lett.* **80**, 3775–3778 (1998)
85. A.I. Yanson, I.K. Yanson, and J.M. van Ruitenbeek, *Nature* **400**, 144–146 (1999)
86. C.A. Stafford, D. Baeriswyl, and J. Bürki, *Phys. Rev. Lett.* **79**, 2863–2866 (1997)
87. J.M. van Ruitenbeek, M.H. Devoret, D. Esteve, and C. Urbina, *Phys. Rev. B* **56**, 12566–12572 (1997)
88. C. Yannouleas, E.N. Bogachek, and U. Landman, *Phys. Rev. B* **57**, 4872–4882 (1998), and references therein
89. S. Blom, H. Olin, J.L. Costa-Krämer, N. García, M. Jonson, P.A. Serena, and R.I. Shekhter, *Phys. Rev. B* **57**, 8830–8833 (1998)
90. F. Kassubek, C.A. Stafford, and H. Grabert, *Phys. Rev. B* **59**, 7560–7574 (1999)
91. C. Höppler, and W. Zwerger, *Phys. Rev. B* **59**, R7849–R7851 (1999)
92. R.N. Barnett, and U. Landman, *Nature* **387**, 788–791 (1997)
93. H. Häkkinen, and M. Manninen, *Europhys. Lett.* **44**, 80–84 (1998)
94. A. Nakamura, M. Brandbyge, L.B. Hansen, and K.W. Jacobsen, *Phys. Rev. Lett.* **82**, 1538–1541 (1999)
95. R. Balian, and C. Bloch, *Ann. Phys. (N.Y.)* **69**, 76–160 (1972)
96. M. Brack, *Rev. Mod. Phys.* **65**, 677–732 (1993)
97. A.M. Bratkovsky, A.P. Sutton, and T.N. Todorov, *Phys. Rev. B* **52**, 5036–5051 (1995)

98. Y. Kondo, and K. Takayanagi, *Phys. Rev. Lett.* **79**, 3455–3458 (1997)
99. T. Kizuka, *Phys. Rev. Lett.* **81**, 4448–4451 (1998)
100. N. Zabala, M.J. Puska, and R.M. Nieminen, *Phys. Rev. Lett.* **80**, 3336–3339 (1998)
101. T.N. Todorov, *Phil. Mag. B* **77**, 965–973 (1998)

7 Magnetism of Nanometer-Sized Particles and Clusters

Wolfgang Wernsdorfer

7.1 Introduction

Since the late 1940s, nanometer-sized magnetic particles have generated continuous interest as the study of their properties has proved to be scientifically and technologically very challenging. In particular it was recognised that the ferromagnetic state, with a given orientation of the particle moment, has a remanent magnetisation if the particle is small enough. This was the starting point of huge permanent magnets and magnetic recording industries. However, despite intense activity during the last few decades, the difficulties in making nanoparticles of good enough quality has slowed the advancement of this field. As a consequence, for 50 years, these applications concentrated above and then near the micrometer scale. In the last few years, this has no longer been the case because of the emergence of new fabrication techniques which have led to the possibility of making small objects with the required structural and chemical qualities. In order to study these objects new techniques were developed such as magnetic force microscopy, magnetometry based on micro-Hall probes or micro-SQUIDs. This led to a new understanding of the magnetic behaviour of nanoparticles, which is now very important for the development of new fundamental theories of magnetism and in modelling new magnetic materials for permanent magnets or high density recording.

In order to put this chapter into perspective, let us consider Fig. 7.1 which presents a scale of size ranging from macroscopic down to nanoscopic sizes. The unit of this scale is the number of magnetic moments in a magnetic system. At the macroscopic level, magnetism is governed by domains (Weiss 1907) and domain walls. Magnetisation reversal occurs via nucleation, propagation and annihilation of domain walls (see the hysteresis loop on the left in Fig. 7.1 which was measured on an elliptic CoZr particle of $1\ \mu\text{m} \times 0.8\ \mu\text{m}$, and a thickness of 50 nm). Size and width of domain walls depend on the material of the magnetic system, on its size, shape and surface, and on its temperature [1]. The material dependence of the domain walls has motivated the definition of two length scales: (i) the domain wall width δ defined by $\delta = \sqrt{A/K}$ and (ii) the exchange length λ defined by $\lambda = \sqrt{A/M_S}$ where A is the exchange energy, K is the crystalline anisotropy constant and M_S is the spontaneous magnetisation. Qualitatively, the first definition shows that

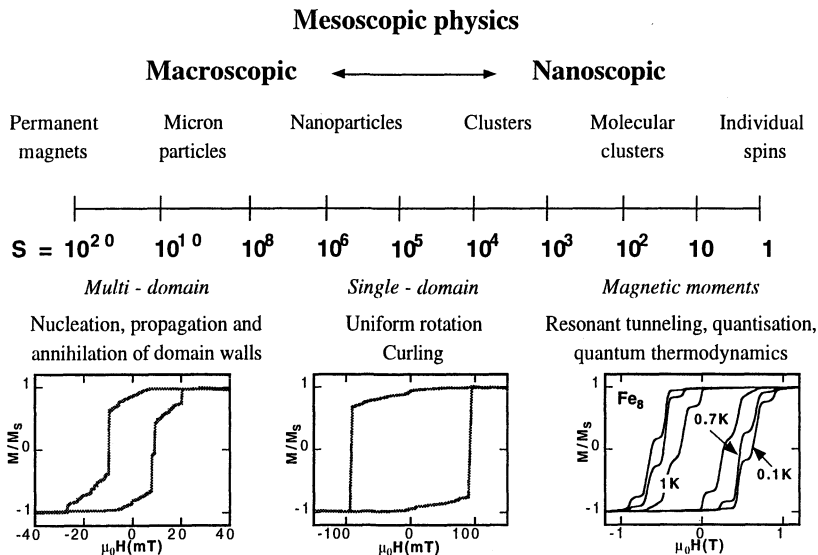


Fig. 7.1. Scale of size which goes from macroscopic down to nanoscopic sizes. The unit of this scale is the number of magnetic moments in a magnetic system (roughly corresponding to the number of atoms). The hysteresis loops are typical examples for a magnetisation reversal via nucleation, propagation and annihilation of domain walls (*left*), via uniform rotation (*middle*), and quantum tunnelling (*right*)

anisotropy energy favours a thin wall, while the exchange energy favours a thick wall. For very small crystalline anisotropy, the first definition suggests an infinite domain wall width which has a large total energy. This is due to the magnetostatic energy term which can be reduced by subdividing the ferromagnetic crystal into domains. Therefore, for very small crystalline anisotropy, the domain wall width is of the order of magnitude of the λ . Both length scales can range from sub-micrometer scales in alloys to atomic scales in rare earth systems.

When the system size is of the order of magnitude of δ and λ , the formation of domain walls requires too much energy, i.e., the magnetisation remains in the so-called single domain state. Hence, the magnetisation has to reverse mainly by uniform rotation (see hysteresis loop in the middle of Fig. 7.1). In this chapter, we discuss mainly this size range where the physics is rather simple.

For system sizes well below δ and λ , one must take into account the band structure of spins which are complicated by band structure modifications at the particle's boundaries [2].

At the smallest size (below which one must consider individual atoms and spins) there are either free clusters made of several atoms [3,4] (see Chap. I) or molecular clusters which are molecules with a central complex containing

magnetic atoms. In the last case, measurements on the Mn_{12} acetate and Fe_8 molecular clusters showed that the physics can be described by a collective moment of spin $S = 10$. By means of simple hysteresis loop measurements, the quantum character of these molecules showed up in well defined steps which are due to resonance quantum tunnelling between energy levels (see hysteresis loop on the right in Fig. 7.1).

In the following sections, we review the most important theories and experimental results concerning the magnetisation reversal of single-domain particles and clusters. Special emphasis is laid on single particle measurements avoiding complications due to distributions of particle size, shape etc. Measurements on particle assemblies has been reviewed in [5]. We mainly discuss the low temperature regime in order to avoid spin excitations.

In Sect. 7.2, we briefly review the commonly used measuring techniques. Among them, electrical transport measurements, Hall probes and micro-SQUID techniques seem to be the most convenient techniques for low temperature measurements. Section 3 discusses the mechanisms of magnetisation reversal in single domain particles at zero Kelvin. The influence of temperature on the magnetisation reversal is reported in Sect. 7.4. Finally, Sect. 7.5 shows that for very small systems or very low temperature, magnetisation can reverse via tunnelling.

7.2 Single Particle Measurement Techniques

The dream of measuring the magnetisation reversal of an individual magnetic particle goes back to the pioneering work of Néel [6]. The first realisation was published by Morrish and Yu in 1956 [7]. These authors employed a quartz-fibre torsion balance to make magnetic measurements on individual micrometer sized $\gamma\text{-Fe}_2\text{O}_3$ particles. With their technique, they wanted to avoid the complication of particle assemblies which are due to different orientations of the particle's easy axis of magnetisation and particle-particle dipolar interaction. They aimed to show the existence of a single-domain state in a magnetic particle. Later on, other groups tried to study single particles but the experimental precision did not allow a detailed study. A first breakthrough came via the work of Knowles [8] who developed a simple optical method for measuring the switching field, defined as the minimum applied field required to reverse the magnetisation of a particle. However, the work of Knowles failed to provide quantitative information on well defined particles. More recently, insights into the magnetic properties of individual and isolated particles were obtained with the help of electron holography [9], vibrating reed magnetometry [10], Lorentz microscopy [11,12], and magnetic force microscopy [13,14]. Most of the studies have been carried out using magnetic force microscopy at room temperature. This technique has an excellent spatial resolution but dynamical measurements are difficult due to the sample-tip interaction.

Recently, magnetic nanostructures have been studied by the technique of magnetic linear dichroism in the angular distribution of photoelectrons or by photoemission electron microscopy [15]. In addition to magnetic domain observations, element-specific information is available via the characteristic absorption levels or threshold photoemission.

Only a few groups were able to study the magnetisation reversal of individual nanoparticles or nanowires at low temperatures. The first magnetisation measurements of individual single-domain nanoparticles and nanowires at very low temperatures were presented by Wernsdorfer et al. [16]. The detector (a Nb micro-bridge-DC-SQUID) and the studied particles were fabricated using electron-beam lithography. Coppinger et al. [17] indirectly investigated the magnetic properties of nanoparticles by resistance measurements. They observed the two-level fluctuations in the conductance of a sample containing self-organising ErAs quantum wires and dots in a semi-insulating GaAs matrix. By measuring the electrical resistance of isolated Ni wires with diameters between 20 and 40 nm, Giordano and Hong studied the motion of magnetic domain walls [18,19]. Other low temperature techniques which may be adapted to single particle measurements are Hall probe magnetometry [20,21], magnetometry based on the giant magnetoresistance [22,23] or spin-dependent tunnelling with Coulomb blockade [24]. At the time of writing, the micro-SQUID technique allows the most detailed study of the magnetisation reversal of nanometer-sized particles [25,26]. The following section reviews the basic ideas of the micro-SQUID technique.

7.2.1 Micro-SQUID Magnetometry

The Superconducting Quantum Interference Device (SQUID) has been used very successfully for magnetometry and voltage or current measurements in the fields of medicine, metrology and science [28,29]. SQUIDs are mostly fabricated from a Nb–AlO_x–Nb trilayer, several hundreds of nanometers thick. The two Josephson junctions are planar tunnel junctions with an area of at least 0.5 μm². In order to avoid flux pinning in the superconducting film the SQUID is placed in a magnetically shielded environment. The sample's flux is transferred via a superconducting pick up coil to the input coil of the SQUID. Such a device is widely used as the signal can be measured by simple lock-in techniques. However, this kind of SQUID is not well suited to measuring the magnetisation of single submicron-sized samples as the separation of SQUID and pickup coil leads to a relatively small coupling factor. A much better coupling factor can be achieved by coupling the sample directly with the SQUID loop. In this arrangement, the main difficulty arises from the fact that the magnetic field applied to the sample is also applied to the SQUID. The lack of sensitivity to a high field applied in the SQUID plane, and the desired low temperature range led to the development of the micro-bridge-DC-SQUID technique [26] which allows us to apply several teslas in the plane of the SQUID without dramatically reducing the SQUID's sensitivity.

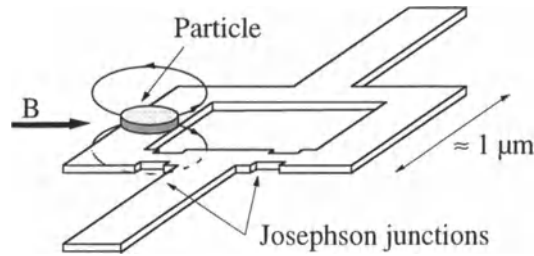


Fig. 7.2. Drawing of a planar Nb micro-bridge-DC-SQUID on which a ferromagnetic particle is placed. The SQUID detects the flux through its loop produced by the sample magnetisation. Due to the close proximity between sample and SQUID a very efficient and direct flux coupling is achieved

The planar Nb micro-bridge-DC-SQUID can be constructed by using standard electron beam lithography, and the magnetic particle is directly placed on the SQUID loop (Fig. 7.2) [16]. The SQUID detects the flux through its loop produced by the sample magnetisation. For hysteresis loop measurements, the external field is applied in the plane of the SQUID, so that the SQUID is only sensitive to the flux induced by the stray field of the sample magnetisation. Due to the close proximity between sample and SQUID, magnetisation reversals corresponding to $10^3 \mu_B$ can be detected, i.e., the magnetic moment of a Co nanoparticle with a diameter of 2–3 nm.

7.3 Mechanisms of Magnetisation Reversal in Single Domain Particles at Zero Kelvin

As already briefly discussed in the introduction, for a sufficiently small magnetic sample it is energetically unfavourable for a domain wall to be formed at remanence. The specimen then behaves as a single domain. For extremely small particles, the magnetisation should reverse by uniform rotation of magnetisation. For somewhat larger particles, the curling reversal mode should be dominant [1]. For even larger particles, magnetisation reversal occurs via a domain wall nucleation process starting in a rather small volume of the particle. In the following, we discuss in detail the uniform rotation mode which is used in many theories, in particular in Néel, Brown and Coffey's theory of magnetisation reversal by thermal activation (Sect. 7.4) and in the theory of macroscopic quantum tunnelling of magnetisation (Sect. 7.5). In this section, we neglect temperature and quantum effects.

7.3.1 Magnetisation Reversal by Uniform Rotation

The model of uniform rotation of magnetisation, developed by Stoner and Wohlfarth [30], and Néel [31], is the simplest classical model describing mag-

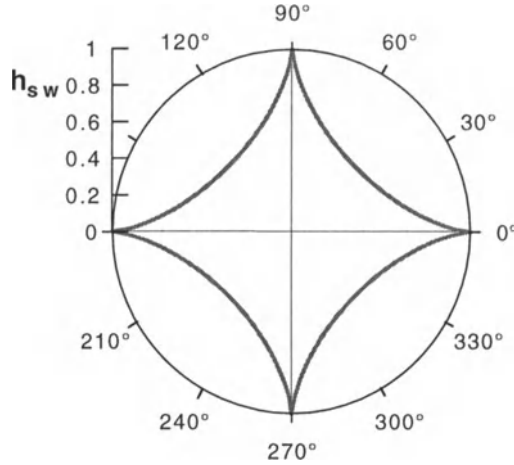


Fig. 7.3. Angular dependence of the Stoner–Wohlfarth switching field $h_{sw} = H_{sw}^0/H_a$ (7.2). This curve is often called the ‘Stoner–Wohlfarth astroid’

netisation reversal. One supposes a particle of an ideal material where exchange energy holds all spins tightly parallel to each other, and the magnetisation does not depend on space. In this case, the exchange energy is constant, and does not enter energy minimisation. Consequently, there is competition only between the anisotropy energy of the particle and the effect of the applied field. The original study by Stoner and Wohlfarth assumed only uniaxial shape anisotropy which is the anisotropy of the magnetostatic energy of the sample induced by its non-spherical shape. Later on, we will see that Thivaille has generalised this model for an arbitrary effective anisotropy which includes any magnetocrystalline anisotropy and even surface anisotropy [32]. The energy of a Stoner–Wohlfarth particle is given by

$$E = KV \sin^2 \phi - \mu_0 M_S V H \cos(\phi - \theta), \quad (7.1)$$

where KV is the uniaxial anisotropy energy constant which depends on the shape of the particle, V is the volume of the particle, M_S is the spontaneous magnetisation, H the magnitude of the applied field, and ϕ and θ are the angles of magnetisation and applied field respectively, with respect to the easy axis of magnetisation. The potential energy of (7.1) has two minima separated by an energy barrier. For given values of θ and H , the magnetisation selects the angle ϕ which minimises the energy. This position can be found by equating to zero the first derivative with respect to ϕ of (7.1): $dE/d\phi = 0$. The second derivative provides the condition for maxima and minima. The magnetisation reversal is defined by the minimal field value at which there is no energy barrier between the metastable minimum and the stable one, i.e.,

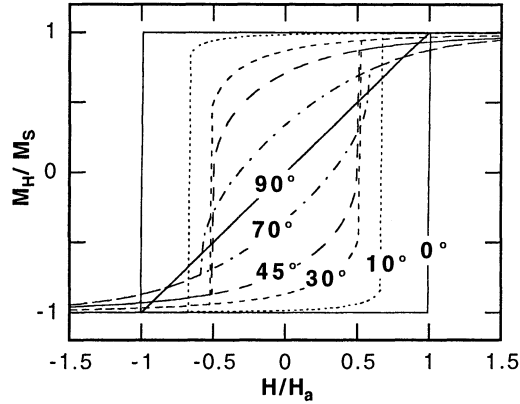


Fig. 7.4. Hysteresis loops of a Stoner–Wohlfarth particle for different field angles θ . The component of magnetisation in direction of the applied field is plotted, i.e., $M_H = M_S \cos \phi$

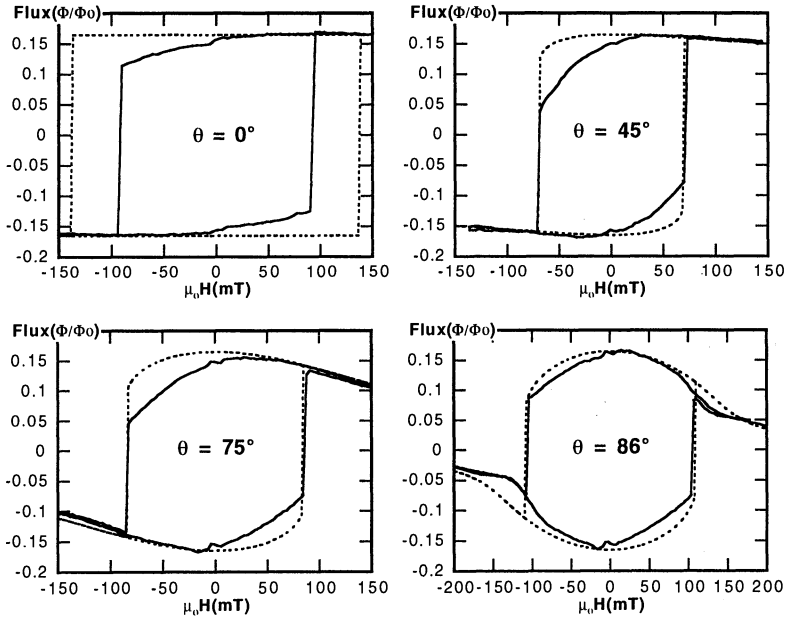


Fig. 7.5. Hysteresis loops of a nanocrystalline elliptic Co particle of $70 \times 50 \times 25 \text{ nm}^3$. The *dashed line* is the prediction of the Stoner–Wohlfarth model of uniform rotation of magnetisation

at $dE/d\phi = d^2E/d\phi^2 = 0$. A short analysis gives the angular dependence of this field, called the switching field H_{sw}^0 (Fig. 7.3):

$$H_{sw}^0 = H_a / \left(\sin^{2/3} \theta + \cos^{2/3} \theta \right)^{3/2}, \quad (7.2)$$

where $H_a = 2K/(\mu_0 M_S)$ is the anisotropy field.

The hysteresis loops have to be calculated numerically. The result is seen in Fig. 7.4 showing the component of magnetisation in the direction of the applied field, i.e., $M_H = M_S \cos \phi$. Such loops are often called Stoner–Wohlfarth hysteresis loops. It is important to note that single particle measurement techniques do not measure this component M_H . For example for the micro-SQUID technique, with the easy axis of magnetisation in the plane of the SQUID and perpendicular to the current direction in the SQUID wire (Fig. 7.2), one measures a magnetic flux which is proportional to $M_S \sin \phi$ (Fig. 7.5).

The main advantage of this classical theory is that it is sufficiently simple to add some extra features to it, as presented in the following.

7.3.2 Generalisation of the Stoner–Wohlfarth Model

The original model of Stoner and Wohlfarth assumed only uniaxial anisotropy with one anisotropy constant (one second order term). This is sufficient to describe high symmetry cases like a prolate spheroid of revolution or an infinite cylinder. However, real systems are often quite complex and the anisotropy is a sum of mainly shape (magnetostatic), magnetocrystalline and surface anisotropy. Shape anisotropy can be written as a biaxial anisotropy with two second order terms. Magnetocrystalline anisotropy is in most cases either uniaxial (hexagonal systems) or cubic, yielding mainly second and fourth order terms. Finally, in the simplest case, surface anisotropy is of second order. One additional complication arises because the various contributions of the anisotropies are aligned in an arbitrary way with regard to each other. All these facts motivated a generalisation of the Stoner–Wohlfarth model for an arbitrary effective anisotropy, this was done by Thiaville [32]. It is a geometrical method to determine the switching field for all angles of the applied magnetic field yielding the critical surface of switching fields, and to calculate the particle energy.

The main interest in Thiaville’s calculation is that measuring the critical surface of the switching field allows one to find the effective anisotropy of the nanoparticle. Knowledge of the latter is important for temperature dependent studies (Sect. 7.4) and quantum tunnelling investigations (Sect. 7.5). Knowing precisely the particle shape and crystallographic axis allows one to determine the various contributions to the effective anisotropy.

7.3.3 Experimental Verification

In order to demonstrate experimentally the uniform rotation mode, the angular dependence of the magnetisation reversal has often been studied (see references in [1]). However, a comparison of theory with experiment is difficult because magnetic particles often have a nonuniform magnetisation state which is due to rather complicated shapes and surfaces, crystalline defects,

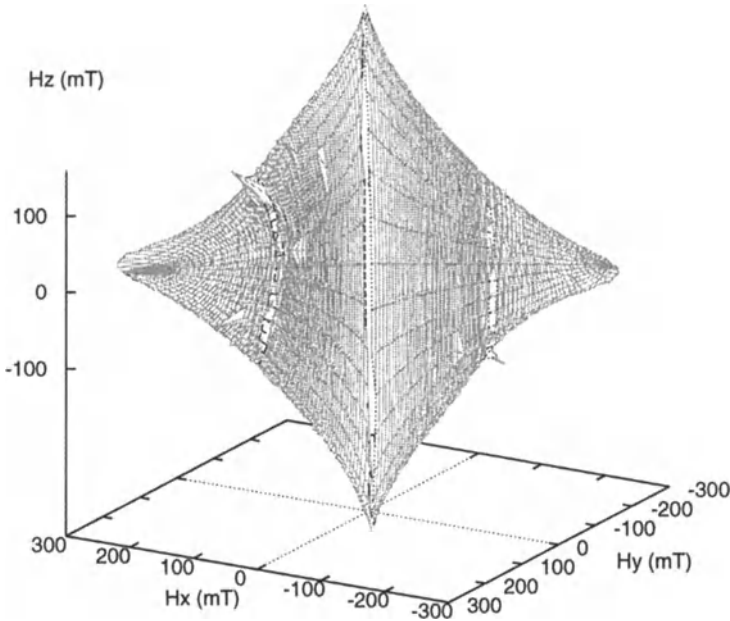


Fig. 7.6. Three-dimensional angular dependence of the switching field of a BaFeCo-TiO particle [33] with a diameter of about 20 nm. The anisotropy field is $H_a \sim 0.4$ T

and surface anisotropy. In general, for many particle shapes the demagnetisation fields inside the particles are nonuniform leading to nonuniform magnetisation states [1]. An example is presented in Fig. 7.5 which compares typical hysteresis loop measurements of an elliptical Co particle, fabricated by electron beam lithography, with the prediction of the Stoner–Wohlfarth model. Before magnetisation reversal, the magnetisation decreases more strongly than predicted because the magnetic configuration is not collinear as in the Stoner–Wohlfarth model, but presents deviations mainly near the particle surface. The angular dependence of the switching field agrees with the Stoner–Wohlfarth model only for angles $\theta \gg 0^\circ$ where non-linearities and defects play a less important role. It is therefore important to choose a proper system which minimises nonuniform magnetisation states. This can be done by choosing a system in which one particular anisotropy contribution is dominant.

For example, the magnetisation reversal in a single-crystalline nanowire, of a material with low magnetocrystalline anisotropy, is dominated by uniaxial

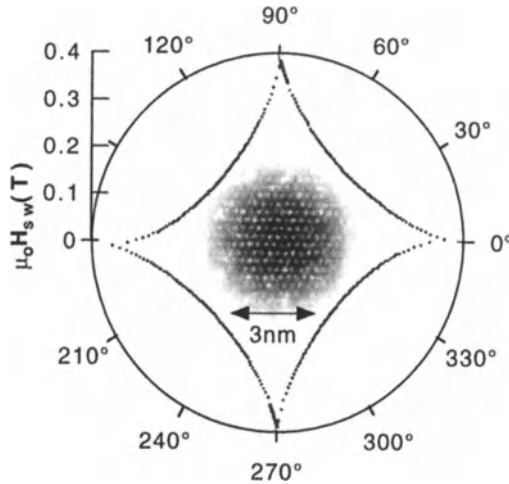


Fig. 7.7. Angular dependence of the switching field of a cobalt cluster of 3 nm in diameter. The astroid shape obtained is predicted by the model of uniform rotation of magnetisation proposed by Stoner and Wohlfarth (see Fig. 7.3). The *inset* displays a high resolution transmission electron microscopy micrograph of a 3 nm Co cluster with a f.c.c. structure

shape anisotropy as shown by measurements on a Fe wire of 20 nm diameter and 200 nm length [34].

Another example are BaFeO nanoparticles which have a dominant uniaxial magnetocrystalline anisotropy. Figure 7.6 shows the three dimensional angular dependence of the switching field measured on a BaFeO particle of about 20 nm. Although this particle has a simple critical surface being close to the original Stoner–Wohlfarth astroid (7.2), it cannot be generated by the rotation of a 2D astroid. However, taking into account the shape anisotropy and hexagonal crystalline anisotropy of BaFeO, good agreement with the Stoner–Wohlfarth model is found [35].

Finally, nearly spherical nanometer sized clusters are also nice model systems as ellipsoids favour uniform magnetisation inside the particle. Figure 7.7 shows the angular dependence of the switching field of a Co cluster of 3 nm in diameter. The cluster was elaborated by a laser vaporisation source which allows us to work in the Low Energy Cluster Beam Deposition regime (clusters do not fragment when they arrive on the substrate, see also Chap. 4) [36]. For these clusters, surface anisotropy also makes a significant contribution, in addition to magnetocrystalline and shape anisotropies. This renders clusters very attractive for future studies.

7.4 Influence of Temperature on Magnetisation Reversal

7.4.1 Superparamagnetism – Néel–Brown Model

The thermal fluctuations of the magnetic moment of a single-domain ferromagnetic particle and its decay towards thermal equilibrium were introduced by Néel [6] and further developed by Bean and Livingston [38], and Brown [39]. For an assembly of independent particles, the influence of temperature on the magnetisation state is called superparamagnetism. In the absence of magnetic anisotropy and without an applied magnetic field, the magnetic moments of the particles are randomly oriented. The situation is the same as for paramagnetic atoms, leading to a Curie behaviour in the magnetic susceptibility and to the Brillouin function for the field dependence of magnetisation. The only difference is that the magnetic moments of the particles are much larger than those of the paramagnetic atoms. Therefore, the quantum mechanical Brillouin function can be replaced by the classical limit for larger magnetic moments, namely the Langevin function.

These properties do change however as soon as magnetic anisotropy is present which establishes one or more preferred orientations of the particle's magnetisation. In Néel and Brown's model of thermally activated magnetisation reversal, a single domain magnetic particle has two equivalent ground states of opposite magnetisation separated by an energy barrier which is due to shape and crystalline anisotropy. The system can escape from one state to the other by thermal activation over the barrier. Just as in the Stoner–Wohlfarth model, they assumed uniform magnetisation and uniaxial anisotropy in order to derive a single relaxation time. Néel supposed further that the energy barrier between the two equilibrium states is large in comparison to the thermal energy $k_B T$ which justified a discrete orientation approximation. Brown criticised Néel's model because the system is not explicitly treated as a gyromagnetic one [39]. Brown considered the magnetisation vector in a particle to wiggle around an energy minimum, then jump to the vicinity of the other minimum, then wiggle around there before jumping again. He supposed that the orientation of the magnetic moment may be described by a Gilbert equation with a random field term which is assumed to be white noise. On the basis of these assumptions, Brown was able to derive a Fokker–Planck equation for the distribution of magnetisation orientations. Brown did not solve his differential equation. Instead he tried some analytic approximations and an asymptotic expansion for the case of the field parallel or perpendicular to the easy axis of magnetisation. More recently, Coffey et al. [40] found by numerical methods an exact solution of Brown's differential equation for uniaxial anisotropy and an arbitrary applied field direction. They also derived an asymptotic general solution for the case of large energy barriers in comparison to the thermal energy $k_B T$. In

the following, we consider a simplified version of the Néel–Brown Model and propose three techniques to check the validity of this model.

7.4.2 Experimental Methods

7.4.2.1 Waiting time measurements. The waiting time method corresponds to magnetisation relaxation measurements on assemblies of particles. In this case, the decay of magnetisation is often logarithmic in time, due to the broad distribution of switching fields. For individual particle studies, waiting time measurements give direct access to the switching probability (Fig. 7.8). At a given temperature, the magnetic field H is increased to a waiting field H_w near the switching field H_{sw}^0 . Next, the elapsed time until the magnetisation switches is measured. This process is repeated several hundred times, yielding a waiting time histogram. The integral of this histogram yields the switching probability. Finally, the switching probability is measured at different waiting fields H_w in order to explore several barrier heights, and at different temperatures.

According to the Néel–Brown model, the probability that the magnetisation has not switched after a time t is given by:

$$P(t) = e^{-t/\tau}, \quad (7.3)$$

and τ (inverse of the switching rate) can be expressed by an Arrhenius law of the form:

$$\tau(T, H) = \tau_0 e^{E(H)/k_B T}, \quad (7.4)$$

where τ_0 is the inverse of the attempt frequency. A simple analytical approximation for the field dependence of the energy barrier $E(H)$ is:

$$E(H) = E_0 \left(1 - H/H_{sw}^0\right)^\alpha = E_0 \varepsilon^\alpha, \quad (7.5)$$

where E_0 is the energy barrier at zero field, and ε is defined as a reduced field difference value. It can be shown that the exponent α is in general equal to 1.5 [41]. Using the Stoner–Wohlfarth analytical expressions of $E(H)$ [30], we can show numerically that α is near 1.5 [26] and increases up to a value of 2 (more frequently cited in the literature) if the applied field forms an angle smaller than a few degrees with the easy axis of magnetisation.

7.4.2.2 Switching field measurements. For single particle studies, it is often more convenient to study magnetisation reversal by ramping the applied field at a given rate and measuring the field value as soon as the particle magnetisation switches. In this case, the switching process is characterised by a distribution of switching fields (Fig. 7.8) evaluated by Kurkijärvi [42] and Garg [43]. The most probable switching field H_{sw} is given by:

$$H_{sw} = H_{sw}^0 \left(1 - \left[\frac{k_B T}{E_0} \ln \left(\frac{cT}{v\varepsilon^{\alpha-1}}\right)\right]^{1/\alpha}\right), \quad (7.6)$$

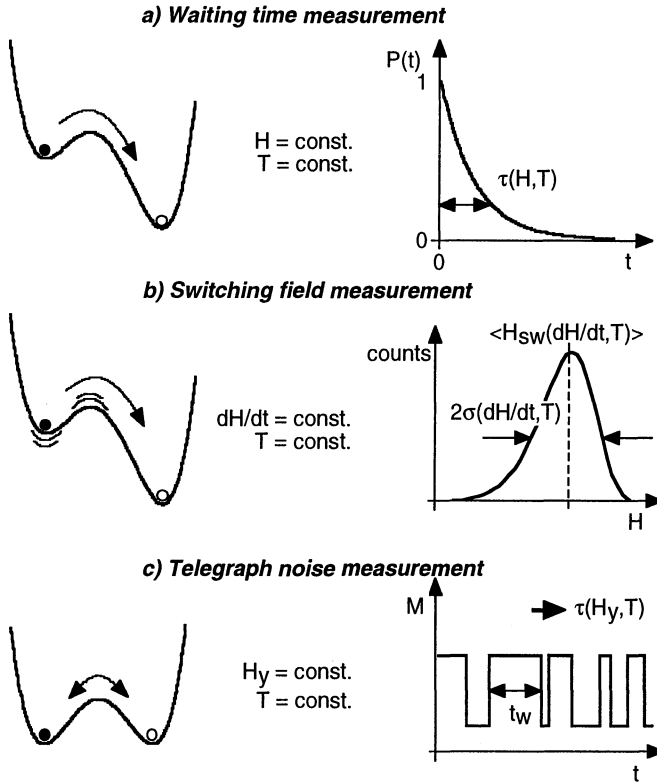


Fig. 7.8. Scheme of three methods for studying escape from a metastable potential well: waiting time and telegraph noise measurements give direct access to the switching time probability $P(t)$, whereas switching field measurements yield histograms of switching fields.

where $c = k_B H_{sw}^0 / (\tau_0 \alpha E_0)$ and v is the field sweeping rate. The width of the switching field distribution is given by:

$$\sigma \approx H_{sw}^0 \frac{1}{\alpha} \left(\frac{k_B T}{E_0} \right)^{1/\alpha} \left[\frac{k_B T}{E_0} \ln \left(\frac{cT}{v \varepsilon^{\alpha-1}} \right) \right]^{(1-\alpha)/\alpha} \quad (7.7)$$

7.4.2.3 Telegraph noise measurements. At zero applied field, a single domain magnetic particle has two equivalent ground states of opposite magnetisation separated by an energy barrier. When the thermal energy $k_B T$ is sufficiently high, the total magnetic moment of the particle can fluctuate thermally, like a single spin in a paramagnetic material.

In order to study the superparamagnetic state of a single particle, it is simply necessary to measure the particle's magnetisation as a function of time.

This is called telegraph noise measurement as stochastic fluctuations between two states are expected. According to the Néel–Brown model, the mean time τ spent in one state of magnetisation is given by an Arrhenius law of the form of (7.4). As τ increases exponentially with decreasing temperature, it is very unlikely that an escape process will be observed at low temperature. However, applying a constant field in direction of a hard axis (hard plane) of magnetisation reduces the height of the energy barrier (Fig. 7.8). When the energy barrier is sufficiently small, the particle’s magnetisation can fluctuate between two orientations which are close to a hard axis (hard plane) of magnetisation.

The time spent in each state follows an exponential switching probability law as given by (7.3)–(7.5) with $\alpha = 2$. Note that for a slightly asymmetric energy potential, one switching probability can be so long that two-level fluctuation becomes practically unobservable.

7.4.3 Experimental Evidence for the Néel–Brown Model

The Néel–Brown model is widely used in magnetism, particularly in order to describe the time dependence of the magnetisation of collections of particles, thin films and bulk materials. However until recently, all the reported measurements, performed on individual particles, were not consistent with the Néel–Brown theory. This disagreement was attributed to the fact that real samples contain defects, ends and surfaces which could play an important, if not dominant, role in the physics of magnetisation reversal. It was suggested that the dynamics of reversal occurs via a complex path in configuration space, and that a new theoretical approach is required to provide a correct description of thermally activated magnetisation reversal even in single-domain ferromagnetic particles [14,44]. Similar conclusions were drawn from numerical simulations of the magnetisation reversal [45,46].

A few years later, micro-SQUID measurements on Co nanoparticles showed for the first time a very good agreement with the Néel–Brown model by using waiting time, switching field and telegraph noise measurements [47,37,48]. It was also found that sample defects, especially sample oxidation, play a crucial role in the physics of magnetisation reversal.

One of the important predictions of the Néel–Brown model concerns the exponential not-switching probability $P(t)$ (see (7.3)) which can be measured via waiting time measurements. At a given temperature, the magnetic field is increased to a waiting field H_w which is close to the switching field. Then, the elapsed time is measured until the magnetisation switches. This process is repeated several hundred times, in order to obtain a waiting time histogram. The integral of this histogram gives the not-switching probability $P(t)$ which is measured at several temperatures and waiting fields H_w . The inset of Fig. 7.9 displays typical measurements of $P(t)$ performed on a Co nanoparticle. All measurements show that $P(t)$ is given by an exponential function described by a single relaxation time τ .

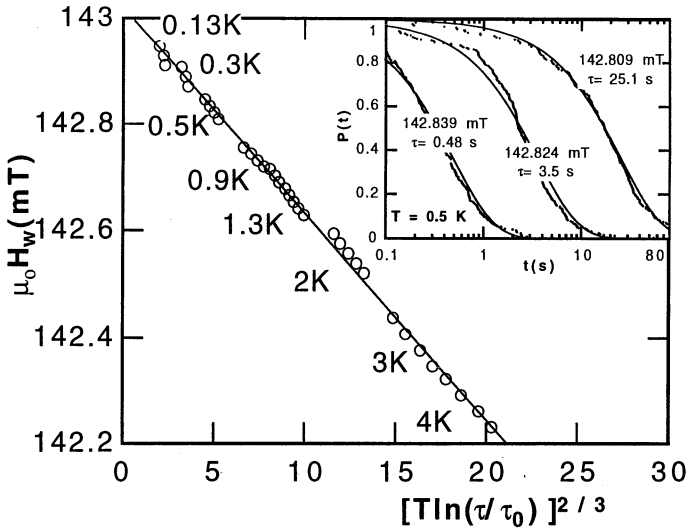


Fig. 7.9. Scaling plot of the mean switching time $\tau(H_w, T)$ for several waiting fields H_w and temperatures ($0.1 \text{ s} < \tau(H_w, T) < 60 \text{ s}$) for a Co nanoparticle. The scaling yields $\tau_0 \approx 3 \times 10^{-9} \text{ s}$. *Inset:* examples of the probability of not-switching of magnetisation as a function of time for different applied fields and at 0.5 K. *Full lines* are data fits with an exponential function: $P(t) = e^{-t/\tau}$

The validity of (7.4) is tested by plotting the waiting field H_w as a function of $[T \ln(\tau/\tau_0)]^{2/3}$. If the Néel–Brown model applies, all points should collapse onto one straight line (master curve) by choosing the proper values for τ_0 . Figure 7.9 shows that the data set $\tau(H_w, T)$ falls on a master curve provided $\tau_0 \approx 3 \times 10^{-9} \text{ s}$. The slope and intercept give the values $E_0 = 214000 \text{ K}$ and $H_{\text{sw}}^0 = 143.05 \text{ mT}$. The energy barrier E_0 can be approximately converted to a thermally “activated volume” by using $V = E_0 / (\mu_0 M_S H_{\text{sw}}^0) \approx (25 \text{ nm})^3$ which is very close to the particle volume estimated by SEM. This agreement is another confirmation of a magnetisation reversal by uniform rotation. The result of the waiting time measurements are confirmed by switching field and telegraph noise measurements [47,37,48]. The field and temperature dependence of the exponential prefactor τ_0 is taken into account in [49].

7.5 Magnetisation Reversal by Quantum Tunnelling

Studying the boundary between classical and quantum physics has become a very attractive field of research which is known as ‘mesoscopic’ physics (Fig. 7.1). New and fascinating mesoscopic effects can occur when characteristic system dimensions are smaller than the length over which the quantum wave function of a physical quantity remains sensitive to phase changes. Quantum interference effects in mesoscopic systems have, until now, involved

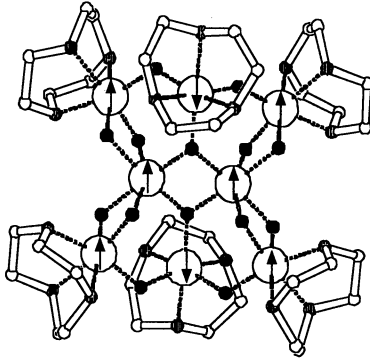


Fig. 7.10. Schematic view of the Fe₈ molecule. The large *open circles* represent iron atoms; *full, hatched, and empty small circles* stand for oxygen, nitrogen and carbon atoms, respectively. The spin structure of the $S = 10$ ground state is schematised by the *arrows* [53]

phase interference between paths of particles moving in real space as in SQUIDS or mesoscopic rings. For magnetic systems, similar effects have been proposed for spins moving in spin space, such as magnetisation tunnelling out of a metastable potential well, or coherent tunnelling between classically degenerate directions of magnetisation [50,51].

We have seen in the previous sections that the intrinsic quantum character of the magnetic moment can be neglected for nanoparticles with dimensions of the order of the domain wall width δ and the exchange length λ , i.e., particles with a collective spin of $S = 10^5$ or larger. However, recent measurements on molecular clusters with a collective spin of $S = 10$ suggest that quantum phenomena might be observed at larger system sizes with $S \gg 1$. Indeed, it has been predicted that macroscopic quantum tunnelling of magnetisation can be observed in magnetic systems with low dissipation. In this case, it is the tunnelling of the magnetisation vector of a single-domain particle through its anisotropy energy barrier or the tunnelling of a domain wall through its pinning energy. These phenomena have been studied theoretically and experimentally [51].

7.5.1 Molecular Clusters

Magnetic molecular clusters are the final point in the series of smaller and smaller units from bulk matter to atoms. Up to now, they have been the most promising candidates for observing quantum phenomena since they have a well defined structure with well characterised spin ground state and magnetic anisotropy. These molecules are regularly assembled in large crystals where

all molecules often have the same orientation. Hence, macroscopic measurements can give direct access to single molecule properties. The most prominent examples are a dodecanuclear mixed-valence manganese-oxo cluster with acetate ligands, Mn_{12} acetate [52], and an octanuclear iron(III) oxo-hydroxo cluster of formula $[\text{Fe}_8\text{O}_2(\text{OH})_{12}(\text{tacn})_6]^{8+}$, Fe_8 [53], where tacn is a macrocyclic ligand (Fig. 7.10). Both systems have a spin ground state of $S = 10$, and an Ising-type magneto-crystalline anisotropy, which stabilises the spin states with $M = \pm 10$ and generates an energy barrier for the reversal of the magnetisation of about 67 K for Mn_{12} acetate and 25 K for Fe_8 .

Fe_8 is particularly interesting because its magnetic relaxation time becomes temperature independent below 360 mK showing for the first time that a pure tunnelling mechanism between the only populated $M = \pm 10$ states is responsible for the relaxation of the magnetisation [54].

The simplest model describing the spin system of Fe_8 molecular clusters (called the giant spin model) has the following Hamiltonian:

$$H = -DS_z^2 + E(S_x^2 - S_y^2) + g\mu_B\mu_0\mathbf{S} \cdot \mathbf{H}. \quad (7.8)$$

S_x , S_y , and S_z are the three components of the spin operator, D and E are the anisotropy constants, and the last term of the Hamiltonian describes the Zeeman energy associated with an applied field H . This Hamiltonian defines a hard, medium, and easy axes of magnetisation in x , y and z directions, respectively. It has an energy level spectrum with $(2S+1) = 21$ values which, to a first approximation, can be labelled by the quantum numbers $M = -10, -9, \dots, 10$. The energy spectrum, shown in Fig. 7.11, can be obtained by using standard diagonalisation techniques of the $[21 \times 21]$ matrix describing the spin Hamiltonian $S = 10$. At $H = 0$, the levels $M = \pm 10$ have the lowest energy. When a field H is applied, the energy levels with $M \ll 0$ increase, while those with $M \gg 0$ decrease. Therefore, different energy values can cross at certain fields. It turns out that for Fe_8 the levels cross at fields given by $\mu_0 H_n \approx n \cdot 0.22$ T, with $n = 1, 2, 3, \dots$. The inset of Figure 7.11 displays the details at a level crossing where transverse terms containing S_x or S_y spin operators turn the crossing into an ‘avoided level crossing’. The spin S is ‘in resonance’ between two states when the local longitudinal field is close to an avoided level crossing.

The effect of these avoided level crossings can be seen in hysteresis loop measurements (Fig. 7.12). When the applied field is near an avoided level crossing, the magnetisation relaxes faster, yielding steps separated by plateaus. As the temperature is lowered, there is a decrease in the transition rate due to reduced thermal-assisted tunnelling. The hysteresis loops become temperature independent below 0.35 K demonstrating quantum tunnelling at the lowest energy levels.

The energy gap at an avoided level crossing, the so-called ‘tunnel splitting’ Δ , can be tuned by an applied transverse field via the $S_x H_x$ and $S_y H_y$ Zeeman terms. It turns out that a field in the H_x direction (hard anisotropy

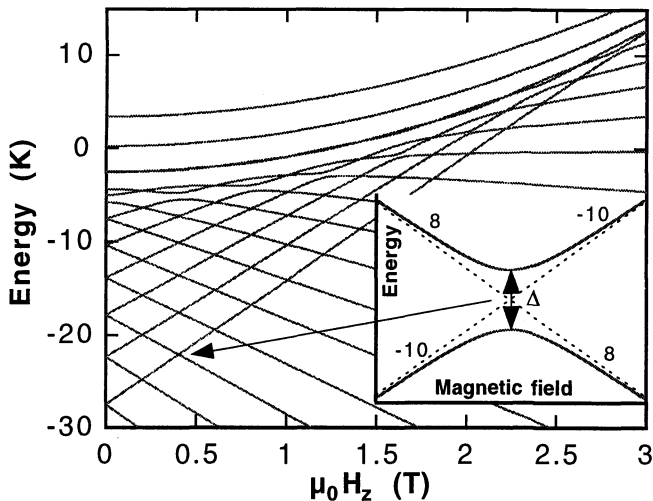


Fig. 7.11. Zeeman diagram of the 21 levels of the $S = 10$ manifold of Fe_8 as a function of the field applied along the easy axis (7.8). From bottom to top, the levels are labelled with quantum numbers $M = \pm 10, \pm 9, \dots, 0$. The levels cross at fields given by $\mu_0 H_n \sim n \cdot 0.22\text{T}$, with $n = 1, 2, 3, \dots$. The *inset* displays the detail at a level crossing where the transverse terms (terms containing S_x or/and S_y spin operators) turn the crossing into an avoided level crossing. The greater the gap Δ , the higher is the tunnel rate

direction) can periodically change the tunnel splitting Δ . In a semi-classical description [55,56], these oscillations are due to constructive or destructive interference of quantum spin phases of two tunnel paths [57]. Such interference effects have been observed for the first time in Fe_8 clusters [58]. Furthermore, parity effects were observed when comparing the transitions between different energy levels of the system [58] which are analogous to the parity effect between systems with half integer or integer spins [59,60]. Hence, molecular chemistry has had a large impact on research into quantum tunnelling of magnetisation on molecular scales.

7.5.2 Individual Single-Domain Nanoparticles

This section focuses on Magnetic Quantum Tunnelling (MQT) studied in individual nanoparticles or nanowires where the complications due to distributions of particle size, shape, and so on are avoided. The experimental evidence for MQT in a single-domain particle or in assemblies of particles is still a controversial subject. We shall therefore concentrate on the necessary experimental conditions for MQT and review some experimental results. We start by reviewing some important predictions concerning MQT in a single-domain particle.

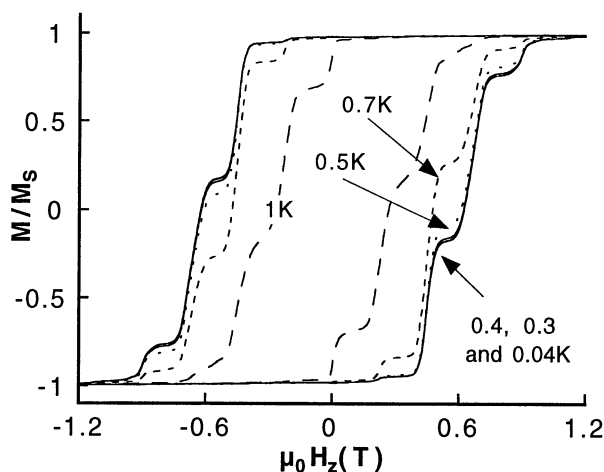


Fig. 7.12. Hysteresis loops of a single crystal of Fe_8 molecular clusters at different temperatures. The longitudinal field (z -direction) was swept at a constant sweeping rate of 0.014 T/s. The loops display a series of steps, separated by plateaus. As the temperature is lowered, there is a decrease in the transition rate due to reduced thermal assisted tunnelling. The hysteresis loops become temperature independent below 0.35 K, demonstrating quantum tunnelling at the lowest energy levels

On the theoretical side, it has been shown that in small magnetic particles, a large number of spins coupled by strong exchange interaction, can tunnel through the energy barrier created by magnetic anisotropy. It has been proposed that there is a characteristic crossover temperature T_c below which the escape of the magnetisation from a metastable state is dominated by quantum barrier transitions, rather than by thermal over barrier activation. Above T_c the escape rate is given by thermal over barrier activation (Sect. 7.4).

In order to compare experiment with theory, predictions of the crossover temperature T_c and the escape rate Γ_{QT} in the quantum regime are relevant. Both variables should be expressed as a function of parameters which can be changed experimentally. Typical parameters are the number of spins S , effective anisotropy constants, applied field strength and direction, etc. Many theoretical papers have been published during the last few years [51]. We discuss here a result specially adapted for single particle measurements, which concerns the field dependence of the crossover temperature T_c .

The crossover temperature T_c can be defined as the temperature where the quantum switching rate equals the thermal one. The case of a magnetic particle, as a function of the applied field direction, has been considered by several authors [61–63]. We have chosen the result for a particle with biaxial anisotropy as the effective anisotropy of most particles can be approximately

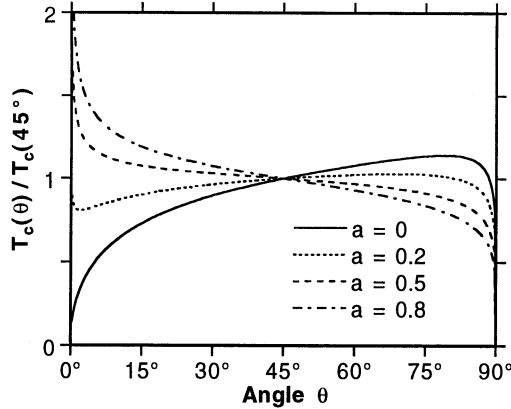


Fig. 7.13. Normalised crossover temperature T_c as given by (7.9), and for several values of the ratio $a = H_{\perp}/H_{\parallel}$

described by strong uniaxial and weak transverse anisotropy. The result due to Kim can be written in the following form [63]:

$$T_c(\theta) \sim \mu_0 H_{\parallel} \varepsilon^{1/4} \sqrt{1 + a(1 + |\cos \theta|^{2/3})} \frac{|\cos \theta|^{1/6}}{1 + |\cos \theta|^{2/3}}, \quad (7.9)$$

where $\mu_0 H_{\parallel} = K_{\parallel}/M_S$ and $\mu_0 H_{\perp} = K_{\perp}/M_S$ are the parallel and transverse anisotropy fields given in tesla, K_{\parallel} and K_{\perp} are the parallel and transverse anisotropy constants of the biaxial anisotropy, θ is the angle between the easy axis of magnetisation and the direction of the applied field, and $\varepsilon = (1 - H/H_{sw}^0)$. Equation (7.9) is valid for any ratio $a = H_{\perp}/H_{\parallel}$. The proportionality coefficient of (7.9) is of the order of unity (T_c is in units of Kelvin) and depends on the approach used for calculation [63]. Equation (7.9) is plotted in Fig. 7.13 for several values of the ratio a . It is valid in the range $\sqrt{\varepsilon} < \theta < \pi/2 - \sqrt{\varepsilon}$.

The most interesting feature which may be drawn from (7.9) is that the crossover temperature is tunable using the external field strength and direction (Fig. 7.13) because the tunnelling probability is increased by the transverse component of the applied field. Although at high transverse fields, T_c decreases again due to a broadening of the anisotropy barrier. Therefore, quantum tunnelling experiments should always include studies of angular dependencies. When the effective magnetic anisotropy of the particle is known, MQT theories give clear predictions with no fitting parameters. MQT could also be studied as a function of the effective magnetic anisotropy. In practice, it is well known for single particle measurements that each particle is somewhat different. Therefore, the effective magnetic anisotropy has to be determined for each particle (Sect. 7.3.2).

Finally, it is important to note that most of the MQT theories neglect damping mechanisms. We discussed the case of ohmic damping in [49] which is the simplest form of damping. More complicated damping mechanisms might play an important role. We expect more theoretical work on this in future.

7.5.3 Single-Domain Nanoparticles and Wires at Low Temperatures

In order to avoid the complications due to distributions of particle size, shape, and so on, some groups have tried to study the temperature and field dependence of magnetisation reversal of individual magnetic particles or wires. Most of the recent studies were done using Magnetic Force Microscopy at room temperature. Low temperature investigations were mainly performed via resistance measurements (Sect. 7.2).

The first magnetisation measurements of individual single-domain nanoparticles at low temperature ($0.1 \text{ K} < T < 6 \text{ K}$) were presented by Wernsdorfer et al. [16]. The detector (a Nb micro-bridge-DC-SQUID, see Sect. 7.2.1) and the particles studied (ellipses with axes between 50 and 1000 nm and thickness between 5 and 50 nm) were fabricated using electron beam lithography. Electrodeposited wires (with diameters ranging from 40 to 100 nm and lengths up to 5000 nm) were also studied [26]. Waiting time and switching field measurements (Sect. 7.4.2) showed that the magnetisation reversal of these particles and wires results from a single thermally activated domain wall nucleation, followed by a fast wall propagation reversing the particle's magnetisation. For nanocrystalline Co particles of about 50 nm and below 1 K, a flattening of the temperature dependence of the mean switching field was observed which could not be explained by thermal activation. These results were discussed in the context of MQT. However, the width of the switching field distribution and the probability of switching are in disagreement with such a model because nucleation is very sensitive to factors like surface defects, surface oxidation and perhaps nuclear spins. The fine structure of pre-reversal magnetisation states is then governed by a multivalley energy landscape (in a few cases distinct magnetisation reversal paths were effectively observed [25]) and the dynamics of reversal occurs via a complex path in configuration space.

Coppinger et al. [17] used telegraph noise spectroscopy to investigate two-level fluctuations (TLF) observed in the conductance of a sample containing self-organising ErAs quantum wires and dots in a semi-insulating GaAs matrix. They showed that the TLF could be related to two possible magnetic states of a ErAs cluster and that the energy difference between the two states was a linear function of the magnetic field. They deduced that the ErAs cluster should contain a few tens of Er atoms. At temperatures between 0.35 K and 1 K, the associated switching rates of the TLF were thermally activated, whilst below 350 mK the switching rate became temperature independent.

Tunnelling of the magnetisation was proposed in order to explain the observed behaviour.

Some open questions remain: what is the object which is really probed by TLF? If this is a single ErAs particle, as assumed by the authors, the switching probability should be an exponential function of time. The pre-exponential factor τ_0^{-1} (sometimes called attempt frequency) was found to lie between 10^3 and 10^6 s⁻¹ whereas expected values are between 10^9 and 10^{12} s⁻¹. Why must one apply fields of about 2 T in order to measure two-level fluctuations which should be expected near zero field? What is the influence of the measurement technique on the sample?

By measuring the electrical resistance of isolated Ni wires with diameters between 20 and 40 nm, Hong and Giordano studied the motion of magnetic domain walls [18]. Because of surface roughness and oxidation, the domain walls of a single wire are trapped at pinning centres. The pinning barrier decreases with an increase in the magnetic field. When the barrier is sufficiently small, thermally activated escape of the wall occurs. This is a stochastic process which can be characterised by a switching (depinning) field distribution. A flattening of the temperature dependence of the mean switching field and a saturation of the width of the switching field distribution (rms deviation σ) were observed below about 5 K. The authors proposed that a domain wall escapes from its pinning site by thermal activation at high temperatures and by quantum tunnelling below $T_c \sim 5$ K.

These measurements pose several questions: what is the origin of the pinning centre which may be related to surface roughness, impurities, oxidation and so on? The sweeping rate dependence of the depinning field, as well as the depinning probability, could not be measured even in the thermally activated regime. Therefore, it was not possible to check the validity of the Néel–Brown model [6,39] or to compare measured and predicted rms deviations σ . Finally, a crossover temperature T_c of about 5 K is three orders of magnitude higher than T_c predicted by current theories.

Later, Wernsdorfer et al. published results obtained on nanoparticles synthesised by arc discharge, with dimensions between 10 and 30 nm [37]. These particles were single crystalline, and the surface roughness was about two atomic layers. Their measurements showed for the first time that the magnetisation reversal of a ferromagnetic nanoparticle of good quality can be described by thermal activation over a single-energy barrier as proposed by Néel and Brown [6,39] (see Sect. 7.4.3). The activation volume, which is the volume of magnetisation overcoming the barrier, was very close to the particle volume, predicted for magnetisation reversal by uniform rotation. No quantum effects were found down to 0.2 K. This was not surprising because the predicted cross-over temperature is $T_c \sim 20$ mK. The results of Wernsdorfer et al. constitute the preconditions for the experimental observation of MQT of magnetisation on a single particle.

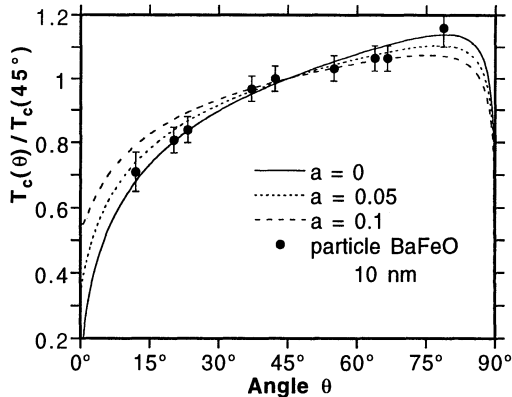


Fig. 7.14. Angular dependence of the crossover temperature T_c for a 10 nm $\text{BaFe}_{10.4}\text{Co}_{0.8}\text{Ti}_{0.8}\text{O}_{19}$ particle with $S \approx 10^5$. The lines are given by (7.9) for different values of the ratio $a = H_{\perp}/H_{\parallel}$. The experimental data are normalised by $T_c(45^\circ) = 0.31$ K

Just as the results obtained with Co nanoparticles [37], a quantitative agreement with the Néel–Brown model of magnetisation reversal was found on $\text{BaFe}_{12-2x}\text{Co}_x\text{Ti}_x\text{O}_{19}$ nanoparticles ($0 < x < 1$) [48], which we will call BaFeO, in the size range of 10 – 20 nm. However, strong deviations from this model were evidenced for the smallest particles containing about $10^5 \mu_B$ and for temperatures below 0.4 K. These deviations are in good agreement with the theory of macroscopic quantum tunnelling of magnetisation.

The measured angular dependence of $T_c(\theta)$ is in excellent agreement with the prediction given by (7.9) (Fig. 7.14). The normalisation value $T_c(45^\circ) = 0.31$ K compares well with the theoretical value of about 0.2 K.

Although the above measurements are in good agreement with MQT theory, we should not forget that MQT is based on several strong assumptions. Among them, there is the assumption of a giant spin, i.e., all magnetic moments in the particle are rigidly coupled together by strong exchange interaction. This approximation might be good in the temperature range where thermal activation is dominant but is it not yet clear if this can be made for very low energy barriers. Future measurements will tell us the answer.

The proof for MQT in a magnetic nanoparticle could be the observation of level quantisation of its collective spin state. This was recently evidenced in molecular Mn_{12} and Fe_8 clusters having a collective spin state $S = 10$ (Sect. 7.5.1). Also the quantum spin phase or Berry phase associated with the magnetic spin $S = 10$ of the Fe_8 molecular cluster was evidenced [58]. In the case of BaFeCoTiO particles with $S = 10^5$, the field separation associated with level quantisation is rather small: $\Delta H = H_a/2S \sim 0.002$ mT. Future measurements should focus on the level quantisation of collective spin states of $S = 10^2$ to 10^4 and their quantum spin phases.

References

1. A. Aharoni (1996) *An Introduction to the Theory of Ferromagnetism*, Oxford University, London
2. A.J. Freemann and R. Wu, *J. Magn. Magn. Mat.*, **100**, 497 (1991).
3. I. M. L. Billas, A. Châtelain, and W. A. de Heer, *Science*, **265**, 1682 (1994); I.M.L. Billas, A. Châtelain, W.A. de Heer, *J. Magn. Magn. Mat.*, **168**, 64 (1997).
4. S. E. Apsel, J. W. Emmert, J. Deng, and L. A. Bloomfield, *Phys. Rev. Lett.*, **76** 1441 (1996).
5. J.L. Dormann, D. Fiorani, E. Tronc, *Adv. Chem. Phys.*, **98**, 283 (1997).
6. Néel L., *Ann. Geophys.*, **5**, 99 (1949) and *C. R. Acad. Science, Paris*, **228**, 664 (1949).
7. A. H. Morrish and S. P. Yu, *Phys. Rev.*, **102**, 670 (1956).
8. J. E. Knowles, *IEEE Trans. Magn.*, **MAG-14**, 858 (1978) and *IEEE Trans. Magn.*, **MAG-20**, 84 (1984).
9. A. Tonomura T. Matsuda, J. Endo, T. Aarii, K. Mihama, *Phys. Rev. B*, **34**, 3397 (1986).
10. H. J. Richter, *J. Appl. Phys.*, **65**, 9 (1989).
11. S.J. Hefferman, J. N. Chapman and S. McVitie, *J. Magn. Magn. Mat.*, **95**, 76 (1991).
12. C. Salling, S. Schultz, I. McFadyen, M. Ozaki, *IEEE Trans. Magn.*, **27**, 5185 (1991).
13. T. Chang and J. G. Chu, *J. Appl. Phys.*, **75**, 5553 (1994).
14. M. Ledermann, S. Schultz and M. Ozaki, *Phys. Rev. Lett.*, **73** 1986 (1994).
15. J. Bansmann, V. Senz, L. Lu, A. Bettac, and K.H. Meiwes-Broer, *J. Electron Spectrosc. Relat. Phenom.*, **106**, (2000)221; K. H. Meiwes-Broer, *Phys. Bl.*, **55** (1), 21 (1999).
16. W. Wernsdorfer, K. Hasselbach, D. Mailly, B. Barbara, A. Benoit, L. Thomas and G. Suran, *J. Magn. Magn. Mat.*, **145**, 33 (1995).
17. F. Coppinger, J. Genoe, D.K. Maude, U. Genner, J.C. Portal, K.E. Singer, P. Rutter, T. Taskin, A.R. Peaker, A.C. Wright, *Phys. Rev. Lett.*, **75**, 3513 (1995).
18. K. Hong and N. Giordano, *J. Magn. Magn. Mat.*, **151**, 396 (1995) and *Europhys. Lett.*, **36**, 147 (1996).
19. J.E. Wegrowe, S.E. Gilbert, D. Kelly, B. Doudin, J.-Ph. Ansermet, *IEEE Trans. Magn.*, **34**, 903 (1998).
20. A.D. Kent, S. von Molnar, S. Gider, D.D. Awschalom, *J. Appl. Phys.*, **76**, 6656 (1994).
21. J.G.S. Lok, A.K. Geim, J.C. Maan, S.V. Dubonos, L. Theil Kuhn, and P.E. Lindelof, *Phys. Rev. B*, **58**, 12201 (1998).
22. V. Gros, Shan-Fab Lee, G. Faini, A. Cornette, A. Hamzic, and A. Fert, *J. Magn. Magn. Mat.*, **165**, 512 (1997).
23. W. J. Gallagher, S. S. P. Parkin, Yu Lu, X. P. Bian, A. Marley, K. P. Roche, R. A. Altman, S. A. Rishton, C. Jahnes, T. M. Shaw and Gang Xiao, *J. Appl. Phys.*, **81**, 3741 (1997).
24. L.F. Schelp, A. Fert, F. Fetta, P. Holody, S. F. Lee, J. L. Maurice, F. Petroff, and A. Vaures, *Phys. Rev. B*, **56**, R5747 (1997).
25. W. Wernsdorfer, K. Hasselbach, A. Benoit, B. Barbara, D. Mailly, J. Tuailleon, J.P. Perez, V. Dupuis, J.P. Dupin, G. Guiraud, A. Perez, *J. Appl. Phys.*, **78**, 7192 (1995).

26. W. Wernsdorfer, Ph.D. thesis, Joseph Fourier University, Grenoble, (1996).
27. W. Wernsdorfer, K. Hasselbach, A. Sulpice, A. Benoit, J.-E. Wegrowe, L. Thomas B. Barbara, D. Maily, Phys. Rev. B, **53**, 3341 (1996).
28. J. Clarke, A. N. Cleland, M. H. Devoret, D. Esteve, J. M. Martinis, Science, **239**, 992 (1988).
29. M. Ketchen, D.J. Pearson, K. Stawiaasz, C-H. Hu, A. W. Kleinsasser, T. Brunner, C. Cabral, V. Chandrashekhar, M. Jaso, M. Manny, K. Stein and M. Bhushan, IEEE Applied Superconductivity **3**, 1795 (1993).
30. E. C. Stoner and E. P. Wohlfarth, Philos. Trans. London Ser. A, **240**, 599 (1948) ; reprinted in IEEE Trans. Magn., **MAG-27**, 3475 (1991).
31. L. Néel, C. R. Acad. Science, Paris, **224**, 1550 (1947).
32. A. Thiaville, J. Magn. Magn. Mat., **182**, 5 (1998).
33. O. Kubo, T. Ido and H. Yokoyama, IEEE Trans. Magn., **MAG-23**, 3140 (1987).
34. W. Wernsdorfer, E. Bonet Orozco, B. Barbara, K. Hasselbach, A. Benoit, D. Maily, B. Doudin, J. Meier, J.E. Wegrowe, J.-Ph. Ansermet, N. Demoncey, H. Pascard, A. Loiseau, L. Francois, N. Duxin, M.P. Pileni, J. Appl. Phys., **81**, 5543 (1997).
35. E. Bonet Orozco, Ph.D. thesis, Joseph Fourier University, Grenoble (1999).
36. A. Perez, P. Melinon, V. Depuis, P. Jensen, B. Prevel, J. Tuaillon, L. Bardotti, C. Martet, M. Treilleux, M. Pellarin, J.L. Vaille, B. Palpant, and J. Lerme, J. Phys. D, **30**, 709 (1997).
37. W. Wernsdorfer, E. Bonet Orozco, K. Hasselbach, A. Benoit B. Barbara, N. Demoncey, A. Loiseau, D. Boivin, H. Pascard and D. Maily, Phys. Rev. Lett., **78**, 1791 (1997).
38. C.P. Bean, J. Appl. Phys., **26**, 1381 (1955); C.P. Bean, J.D. Livingston, J. Appl. Phys. **30**, 120S (1959).
39. W. F. Brown, J. Appl. Phys., **30**, 130S (1959); J. Appl. Phys., **34**, 1319 (1963); Phys. Rev., **130**, 1677 (1963); IEEE Trans. Magn., **15**, 1196 (1979).
40. W.T. Coffey, D.S.F. Crothers, J.L. Dormann, Yu. P. Kalmykov, and J.T. Waldron, Phys. Rev. B **52**, 15951 (1995); L.J. Geoghegan, W.T. Coffey and B. Mulligan, Adv. Chem. Phys. **100**, 475 (1997); W.T. Coffey, Adv. Chem. Phys. **103**, 259 (1998).
41. R. H. Victora, Phys. Rev. Lett., **63**, 457 (1989).
42. J. Kurkijärvi, Phys. Rev. B, **6**, 832 (1972).
43. A. Garg, Phys. Rev. B, **51**, 15592 (1995).
44. W. Wernsdorfer, K. Hasselbach, A. Benoit, G. Cernicchiaro, D. Maily, B. Barbara, L. Thomas, J. Magn. Magn. Mat., **151**, 38 (1995).
45. H. L. Richards, S. W. Sides, M. A. Novotny and P. A. Rikvold, J. Appl. Phys., **79**, 5749 (1996); E. D. Boerner and H. Neal Bertram, IEEE Trans. Magn., **33**, 3052 (1997).
46. D. Hinze and U. Nowak, Phys. Rev. B, **58**, 265 (1998).
47. W. Wernsdorfer, B. Doudin, D. Maily, K. Hasselbach, A. Benoit, J. Meier, J.-Ph. Ansermet, B. Barbara, Phys. Rev. Lett., **77**, 1873 (1996).
48. W. Wernsdorfer, E. Bonet Orozco, K. Hasselbach, A. Benoit, D. Maily, O. Kubo, H. Nakano and B. Barbara, Phys. Rev. Lett., **79**, 4014 (1997).
49. W.T. Coffey, D.S.F. Crothers, J.L. Dormann, Yu. P. Kalmykov, E.C. Kennedy and W. Wernsdorfer, Phys. Rev. Lett., **80**, 5655 (1998).
50. A. J. Leggett, S. Chakravarty, A. T. Dorsey, M. P. A. Fisher, A. Garg, W. Zwerger, Rev. Mod. Phys., **59**, 1 (1987).

51. Quantum Tunneling of Magnetization - QTM'94, NATO ASI, Serie E: Applied Sciences, Vol. 301, ed. L. Gunther and B. Barbara, (1995).
52. R. Sessoli, D. Gatteschi, A. Caneschi, and M.A. Novak, *Nature (London)*, **365**, 141 (1993).
53. A.-L. Barra, P. Debrunner, D. Gatteschi, Ch. E. Schulz and R. Sessoli, *Europhys. Lett.*, **35**, 133 (1996).
54. C. Sangregorio, T. Ohm, C. Paulsen, R. Sessoli., D. Gatteschi, *Phys. Rev. Lett.*, **78**, 4645 (1997).
55. M. V. Berry, *Proc. R. Soc. London A*, **392**, 45 (1984).
56. F.D.M.Haldane, *Phys. Rev. Lett.*, **50**, 1153 (1983); *Phys. Rev. Lett.*, **61**, 1029 (1988).
57. A. Garg, *Europhys. Lett.*, **22**, 205 (1993).
58. W.Wernsdorfer and R. Sessoli, *Science*, **284**, 133 (1999).
59. D. Loss, D.P. DiVincenzo, and G. Grinstein, *Phys. Rev. Lett.*, **69**, 3232 (1992)
60. J. von Delft and C. L. Henley, *Phys. Rev. Lett.*, **69**, 3236 (1992)
61. O.B. Zaslavskii, *Phys. Rev. B*, **42**, 992 (1990).
62. M.C. Miguel and E.M. Chudnovsky, *Phys. Rev. B*, **54**, 388 (1996).
63. Gwang-Hee Kim and Dae Sung Hwang, *Phys. Rev. B*, **55**, 8918 (1997).

8 Physical Chemistry of Supported Clusters













Ueli Heiz and Wolf-Dieter Schneider

8.1 Introduction

Scientists have always tried to classify and systematise their observations in order to extract trends or even propose simple models for the understanding of their results with the aim of predicting properties of new materials. As early as in the 19th century this strategy led to the discovery of the periodicity of oxide formation for different elements by D.I. Mendelejev [1] and shortly afterwards he presented the first Periodic Table in his presentation "On the relation of the properties to the atomic weights of the elements" at the Russian Chemical Society in 1869 [2]. Today we know that the laws of quantum mechanics are responsible for the beautiful order of the elements of our universe and this Periodic Table is used to predict chemical and physical properties of the elements. In a chemical compound the atoms try to acquire a closed shell electronic structure and this is the reason for the high reactivity of the alkalines or halides or for the inertness of rare gases. Today it is possible to construct a Periodic Table of a single element, e.g., sodium, because atoms of an element can form clusters or particles with pronounced periodicities in their chemical and physical properties as a function of their size, shape and form. Sodium clusters were first produced by the groups of Schumacher [3] and Knight [4] in the early eighties, see Chap. 1. They discovered striking discontinuities in the mass spectra at magic numbers (of Na atoms per cluster) 8, 20, 34, and 40 and achieved a fundamental understanding of these abundance spectra within the jellium model [4–7], well known to nuclear physicists. In this way the electronic shell structure of small alkaline clusters was established. By analogy with the classic Periodic Table an "Electronic Periodic Table" for clusters can be constructed simply by filling the electronic shells in the different periods (Fig. 8.1). We find monovalent clusters, like Na_3 , Na_9 , and Na_{19} or halide-like clusters, like Na_7 and Na_{17} which might reveal enhanced reactivities. This simple analogy suggests that for small clusters, where the electronic structure is dominant in changing the cluster's properties, a new and exciting chemistry is waiting to be discovered.

More recently, the group of Martin [8] succeeded in forming and detecting sodium particles with sizes up to several thousand of atoms. Again distinct periodicities in the cluster stabilities were discovered. For clusters larger than about Na_{1500} geometrical packing of atoms into closed shells dominates the

Electronic Periodic Table : Free Na_N Clusters

Shell	Monovalent				Closed shells
1s	 Na				 Na ₂
1p	 Na ₃	 Na ₄	⋯ →	 Na ₇	 Na ₈
1d	 Na ₉	 Na ₁₀	⋯ →	 Na ₁₇	 Na ₁₈
2s	 Na ₁₉				 Na ₂₀

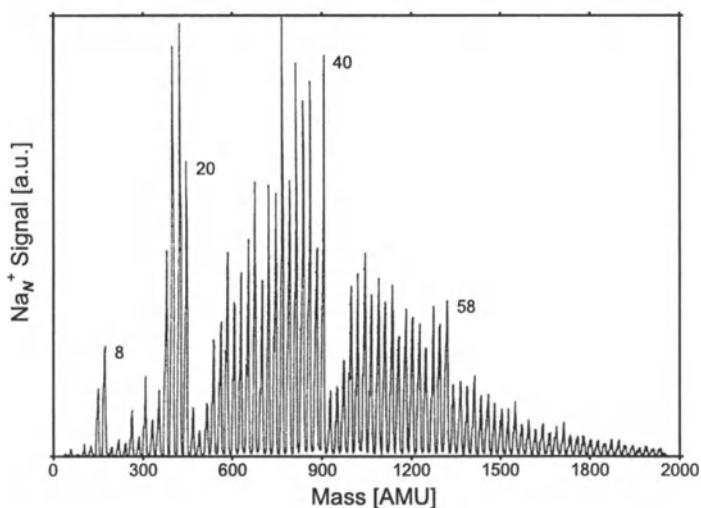


Fig. 8.1. Electronic Periodic Table (*above*) for small sodium clusters. The periods (1s, 2p, 2s,...) are defined by the electronic shells obtained within the jellium model. The first group in this table is formed by the monovalent clusters with an expected high chemical reactivity. The closed shell clusters Na_2 , Na_8 , Na_{20} , Na_{40} are also found in the mass spectrum (*below*) [3] as magic numbers indicating high chemical stability

observed shell structure [9]. In fact, for sodium, shell closings can be correlated with the construction of Mackay icosahedra [10]. In the proposed "Geometric Periodic Table" of the particles (Fig. 8.2) the closed shell particles behave like rare gas particles [11]. In this size range the bulk electronic structure is already fully developed and it is the geometry, i.e., the decreasing step and kink density within a period proceeding towards geometrical shell closing which characterises the particles and which is mainly responsible for the changing chemical properties as a function of size.

These 'Periodic Tables' provide the framework for a classification of size effects in supported clusters and particles. Here we define aggregates consisting of less than hundred atoms as clusters and larger ones as particles. We will show that for supported clusters and particles the intrinsic differences in their electronic and geometric properties are indeed important for an understanding of the observed size effects. The examples presented reveal that for the relatively large sizes, step and kink densities directly influence the kinetics of a catalytic reaction. For very small and size-selected clusters on surfaces the characteristic electronic structure of each cluster size directly changes the potential energy surfaces, e.g., binding energies and activation energies, along a catalytic reaction path.

Clusters composed of a few or a few tens of atoms or molecules are also promising building blocks for future intelligent nanomaterials as they reveal peculiar properties different both from individual atoms and molecules and from bulk materials. The rapid progress in nanoscience and nanotechnology reveals innovative possibilities for potential applications of clusters in material science, e. g., the miniaturisation of electronic devices, the development of highly selective sensors, or the fabrication of selective and efficient catalysts. Clusters are also known to play important roles in crystallisation, liquefaction, and phase separation. Their physical and chemical properties, however, in spite of ongoing and very active research, have not yet been thoroughly understood. Of special interest is the variation of the catalytic activity of a cluster as function of its size. Small gas phase clusters exhibit pronounced variations in their physical and chemical properties as the number of metal atoms in the cluster is varied [12]. These results suggest that supported clusters, i.e., clusters stabilised on solid surfaces, in functionalised matrices or on micromechanical devices may also display novel and distinct cluster size dependencies. A basic understanding of the characteristics of the clusters, such as structure, reactivity, physical and chemical properties, as well as their interaction with the support will open fascinating routes to design catalysts or chemical sensors with tailored properties and complex functions for technical applications.

For example, the active components in the control of automotive pollution are small platinum, palladium and rhodium particles supported on oxide surfaces. Here the catalytic oxidation of carbon monoxide is one of the most important steps. The conversion of CO and O₂ into CO₂ in the gas phase has

Geometric Periodic Table : Free Na_N Particles

Shell (K):	Open Shells			Closed Shells
11	Na_{2870}	Na_{2871}	...	Na_{3871}
12	Na_{3872}	Na_{3873}	Na_{3873} ...	Na_{5083}
13	Na_{5084}	Na_{5085}	...	Na_{6525}
...			...	
17	Na_{12431}	Na_{12432}	...	Na_{14993}
18	Na_{14994}	Na_{14995}	...	Na_{17885}
19	Na_{17886}	Na_{17887}	...	Na_{21127}

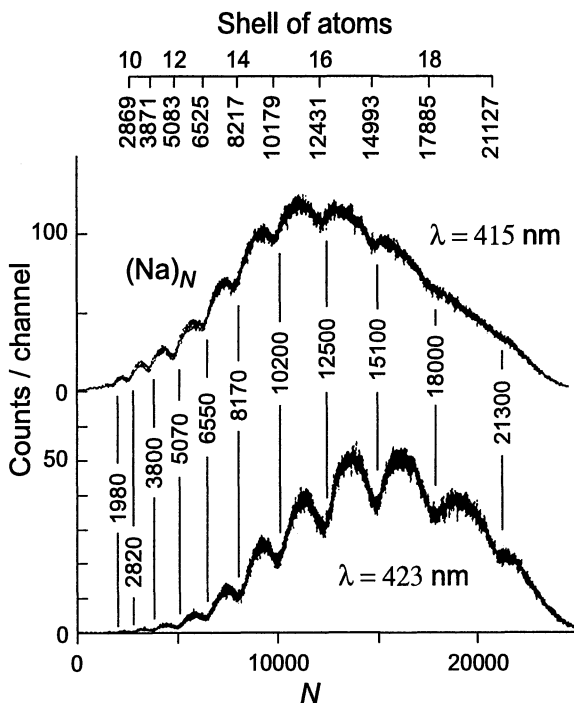


Fig. 8.2. Geometric Periodic Table (*above*) and mass spectra (*below*) for large sodium particles ionised at two different wavelengths λ . The periods are defined by K , the shell number of the Mackay icosahedra, see Eq. 7 in Chap. 1. Along a period K the corresponding shell is filled. Note that the closed shell numbers are found as intensity minima in the sodium mass spectrum [8]. For the closed shell clusters the density of steps is changed within the group directly influencing the catalytic properties (see text)

a free enthalpy of ~ 280 kJ/mol and is therefore thermodynamically allowed. However, in order to initiate this reaction, the activation energy for the dissociation of O_2 has to be overcome, and it is the task of the catalyst to reduce this energy. Studies on single crystals, on supported particles as well as on real catalysts revealed many details about this catalytic process. On highly coordinated Pt atoms, like a Pt(111) single crystal, carbon monoxide can be oxidised at low temperature (160 K) [13–15]. In this case, oxygen atoms produced during the dissociation process of O_2 on the surface oxidise carbon monoxide. In such a mechanism oxygen atoms react with CO before they reach the energy minimum of the oxygen–surface interaction potential and therefore no additional activation for the actual oxidation step is needed [13]. A second reaction channel on Pt(111) involves chemisorbed oxygen atoms, which oxidise adsorbed CO at temperatures higher than 200 K. This mechanism can also be observed on low coordinated platinum sites, e.g., the ones on a Pt(355) surface [16,17] and the oxidation temperature of this mechanism is sensitively dependent on the character of the reactive site [16]. In addition to this rather detailed picture of the energetics of the process, a complex spatial and temporal pattern was discovered for this seemingly simple reaction [18]. Studies on Pt(100) and Pt(110) surfaces revealed a complicated modification of the overall CO-oxidation caused by an adsorption induced change in the surface structure, which leads to oscillations during the reaction [19].

Real catalysts for the oxidation of CO consist of highly dispersed metal particles on refractory metal oxides [20–22]. Besides changes in reactivity due to the existence of different crystalline facets on particles [23,24] a few nanometres in size, very small clusters consisting only of a few atoms should show pronounced size effects in their catalytic behaviour. This is caused by the changing coordination number in different geometric structures and/or the changing electronic structure as a function of cluster size. Such a size-dependent variation in the chemical properties was observed in several gas phase studies, where reactivities of small metal clusters were investigated. Bérces et al. [26] measured absolute rate coefficients for the reaction of Nb_N clusters ($N = 2$ –20) with H_2 and N_2 at different temperatures, confirming the low reactivities of Nb_8 , Nb_{10} , and Nb_{16} measured in earlier experiments [25,27]. They recognised an anticorrelation of the reactivity with an effective ionisation potential of the cluster that includes the polarisation of the charge on the cluster cation. Consequently reactivities of such small clusters are directly related to their intrinsic electronic properties. This correlation between the electronic structure and the reactivities of niobium clusters was also observed experimentally by Kietzmann et al. [28]. These authors estimated the gap between the Highest Occupied Molecular Orbital (HOMO) and the Lowest Unoccupied Molecular Orbital (LUMO) from photoelectron spectra and observed closed shells and a large HOMO–LUMO gap for the unreactive cluster sizes. In addition, Bérces et al. [26] observed clearly biexponential kinetic plots, indicating the presence of different isomers with distinct reactivities.

They suggested that in addition to electronic effects, steric effects also play a decisive role in determining cluster reactivities.

Supported clusters on well characterised oxide surfaces are of primordial interest in modelling the high complexity of real catalysts. This concept has been introduced by Poppa [29]. The important questions to be answered are the role of intrinsic size effects which are closely related to structure sensitive or insensitive catalytic reactions and the influence of the cluster support on the physical chemistry of such small clusters. One key to finding the optimum cluster size and material for a specific catalytic reaction is the atom-by-atom understanding of the electrophilic character of the deposited cluster, i.e., the energy and symmetry of the HOMO and/or LUMO in a one electron picture as a function of size and structure. Another key is to find the specific particle morphology which stabilises the optimum density of steps and kinks for a particular catalytic reaction. In this way one may be able to build designer catalysts by judicious choice of material, size, structure, and support.

There exist excellent recent reviews on various aspects of supported model catalysts. For the interested reader we recommend specifically Henry [31] concerning surface science studies of supported model catalysts. Decomposition of organometallic precursors [32] and wet impregnation [33] close to those used for industrial catalysts have also been reviewed recently [34]. Nucleation and growth of metals on oxides have been treated by Poppa [29], Lad [35], and Campbell [36]. Deposition methods and characterisation techniques with emphasis to non-UHV preparation techniques can be found in [34,37]. The preparation, characterisation and properties of oxide surfaces are well documented in recent books [38,39] and review papers [40,41].

The present review is organised as follows. Section 8.2 presents a few selected examples of *size-distributed* supported particles containing a few hundred atoms, in order to highlight the trends found for their catalytic activity and for the influence of the cluster support on their physical chemistry. Section 8.3 focuses on the relatively small number of existing experiments on *size-selected*, supported clusters consisting only of a few to a couple of tens of atoms. Some of these experiments are chosen to illustrate specifically the possibilities and challenges in this rather young but highly exciting field in cluster science. As far as possible, recent developments in the theoretical understanding of well defined catalysts and the resulting implications for the development of real industrial catalysts will also be addressed.

During the remainder of this review the reader should be well aware of the inherent difficulty of our subject, highlighted by R. P. Feynman. "A chemical reaction is indeed the physical process of rearranging electrons and atoms, resulting in the transformation of molecules. Chemistry is the most complicated physics, the highest physics, unattainable for physicists to understand. The reason is that too many electron-electron and electron-nuclear time-dependent interactions are involved in a chemical event".

8.2 Supported Size-Distributed Model Catalysts

There is growing activity in modelling disperse metal catalysts by studying systems consisting of size-distributed metal particles on well characterised oxide surfaces. In the following we review briefly the key methods used in the preparation and characterisation of small supported particles. We then discuss a few selected examples which emphasise different aspects of the chemical activity of small particles: (i) a size-effect in the CO dissociation on small Rh-particles, (ii) a size- and site-effect in the catalytic oxidation of CO on Pd-particles, and (iii) a size-effect in the catalytic oxidation of CO on small Au-particles.

8.2.1 Preparation and Characterisation

Model catalysts can be prepared by evaporating metal atoms on an oxide surface. Different particle sizes can be grown by changing the growth kinetics. The work of Frank *et al.* [42] represents a typical example for this approach. Their model catalysts consist of a NiAl(110) single crystal covered by a thin oxide layer onto which Rh metal is evaporated under control of the substrate temperature and the metal vapour flux [22,20]. This allows the preparation of relatively narrow particle size distributions of metal deposits. Scanning probe techniques as well as electron diffraction have been applied to determine the size, shape and height of the metal particles and, from their density, the number of atoms per particle is obtained [44,45]. Since these model systems have been prepared under ultrahigh vacuum conditions, the chemical composition of the substrate and of the supported particles is well controlled, a situation not easily achievable for real catalysts.

Modern micro- and nano-fabrication methods provide a new avenue to prepare controlled model catalysts, which realistically mimic real supported catalysts [46,47]. Such catalysts consist of two dimensional (2D) arrays of active catalysts deposited on active or inactive support materials which have been structured by electron beam lithography and lift-off techniques. Particle size, shape, separation and support can be systematically varied. With this approach Pt particles in a size range 10–500 nm have been deposited on alumina, ceria and silica.

Recently, a novel and very interesting method for the preparation of almost monodisperse supported metal nanoparticles has been found [48]. It relies on substantial narrowing of broad size distributions through irradiation with short laser pulses (7 ns) by exploiting the size dependent optical absorption coefficient of the metal particles. Successive irradiation by applying two laser wavelengths completely removes the smallest particles of the distribution and causes a size reduction of the largest particles. Finally, only particles with diameters in a very narrow size interval remain on the surface. In this way Ag particles with mean diameters of 10 nm and size distributions with standard deviations of 0.13 have been obtained.

8.2.2 CO Dissociation on Supported Rh Clusters

In a heterogeneous catalytic process the chemisorption of molecules represents the starting point for an understanding of catalytic properties of small particles. Due to the technical importance, but also because of experimental considerations, carbon monoxide is the most commonly used adsorbate, compared to O_2 , H_2 , and NO , in the investigation of chemisorption on supported model catalysts [31].

Recently, Frank *et al.* [42] and Andersson *et al.* [43] reported on the observation of a particle size dependent CO dissociation on alumina-supported Rh particles. In their study they specifically addressed the question of whether particular sizes or morphologies of deposited particles are relevant in optimising the rate of a given chemical reaction. After adsorption of CO on the Rh particles the probabilities for thermally induced dissociation of CO at temperatures between 350 K and 500 K were determined from C 1s photoelectron spectra. The authors found that for small aggregates the dissociation activity increases with average particle size. After reaching a maximum for particles containing an average of 500 to 1000 Rh atoms, the fraction of dis-

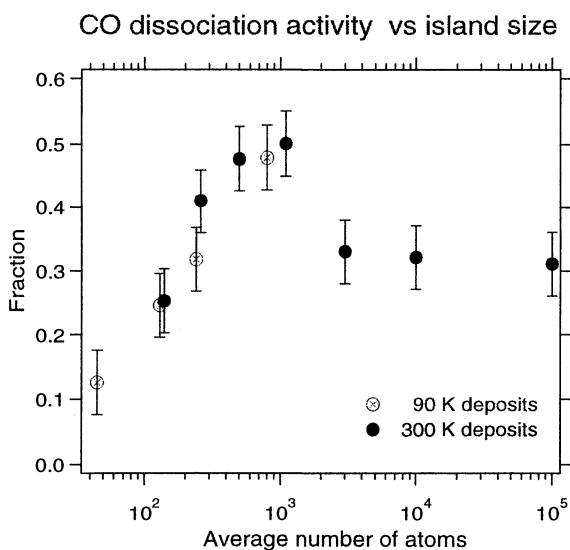


Fig. 8.3. Effect of size of catalytically active Rh particles on alumina: the fraction of initially adsorbed CO (saturation coverage) which dissociates for different Rh particle sizes (measured by the average number of Rh atoms per particle). This dissociation activity was determined by comparing the original intensities of the CO photoemission peak and the final (after heating the sample to 500 K) atomic C 1s peak (corrected for initial 90 K C 1s intensity) for the different preparations. After [43]

sociated CO decreases to values closer to those on well-prepared Rh single crystal surfaces (see Fig. 8.3).

This finding indicates, as proposed by the authors, that the particle morphology, i.e., a particular range of particle sizes, which stabilises an especially high density of steps, is responsible for this peculiar behaviour of the dissociation rate, rather than the unique electronic structure of the corresponding aggregates. In addition, this study might provide an explanation for two contradictory observations which report both an increase and a decrease in CO dissociation probability with size [49–51], as they might probe the dissociation activity on both sides of the maximum. Following the dissociation rate curve from the left the peak can be rationalised [52]: "The smallest particles grow as two-dimensional layers. Before the aggregates contain 100 atoms, the second layer starts to grow. Eventually, three-dimensional particles grow, but their height never exceeds their width. When the particles contain fewer than about 1000 atoms, they coalesce and the island density decreases considerably. That is when the dissociation rate decreases and the maximum has been surpassed. It turns out that the size of particles near 5 nm where the highest dissociation rates are found coincides with those sizes where high catalytic activities have been observed in various chemical reactions. For a given metal/substrate combination, certain particle sizes stabilise a maximum of active sites and thus maximise the reaction rate. Particle morphology, however, is only one ingredient in optimising a catalytic reaction." As is shown in Sect. 8.3 this behaviour is fundamentally different from the very small clusters where the distinct electronic structure of the clusters is responsible for the observed size effects.

8.2.3 Kinetic Effects in the CO Oxidation Reaction on Supported Pd Particles

Compared to chemisorption and dissociation not much has yet been done to study true catalytic reactions with an atomic-level understanding, e.g., the CO oxidation on supported model catalysts [31]. However, the recent increasing number of publications on this subject indicates that the situation is changing rapidly.

Here we present a striking example where the particle morphology clearly influences the kinetics of a catalytic reaction [53]. In general, CO oxidation on Pd is considered to be structure insensitive and is not expected to depend on the size of the Pd particles. However, several size effects have already been evidenced for this reaction [31]. Near the temperature where the steady-state reaction rate is maximum, the reactivity per Pd surface atom (turnover frequency) increases for small particles. At low temperature, in transient molecular beam experiments, a second peak of CO₂ appears after the CO beam is closed but while oxygen is still supplied to the model catalyst. This peak shifts and its shape changes with temperature and oxygen pressure (see Fig. 8.4). The authors [53] interpret this peak by the presence of CO strongly

bound on the particle edges (and possibly other defects on the particle surface) which reacts well after the CO adsorbed on the facets has desorbed. A kinetic model is presented which accounts well for the evolution of this peak with temperature and oxygen pressure. These results show again that the CO oxidation reaction on small particles is more complicated than on extended surfaces. At steady state, near the maximum of reactivity (around 500 K) the reaction rate on the small particles is larger than on extended surfaces [31] because the CO coverage on the edges is much higher than on

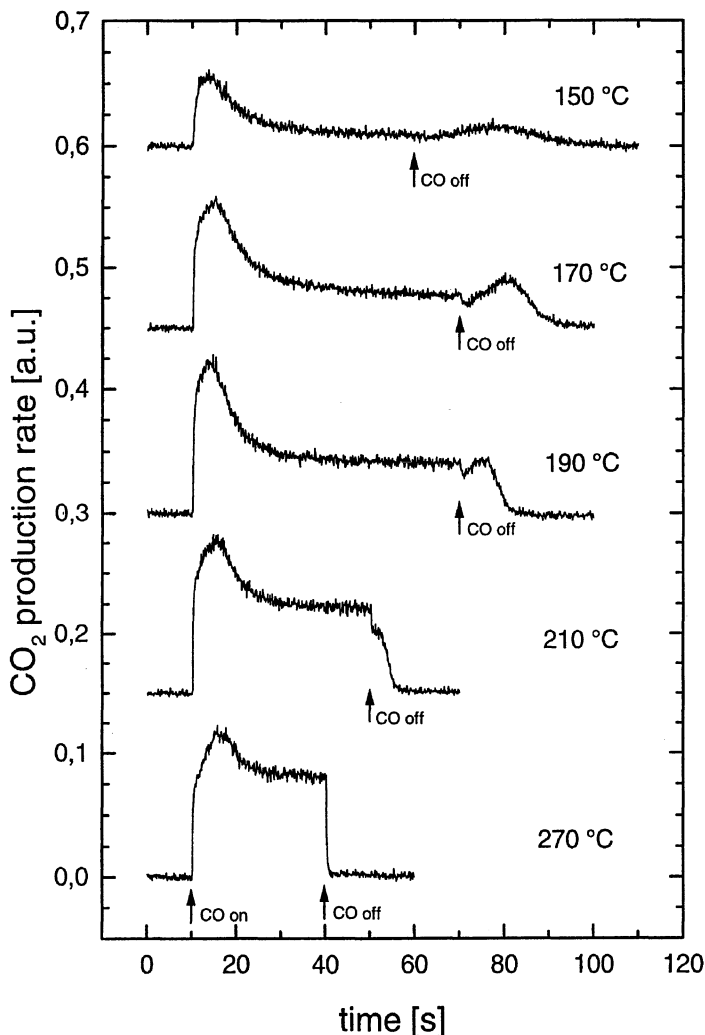


Fig. 8.4. CO₂ transients on 4 nm Pd particles supported on MgO(100) as a function of the sample temperature. The isotropic oxygen pressure is 5×10^{-8} torr and the equivalent pressure in the CO beam is 3.4×10^{-7} Torr. After [53]

the facets although still below saturation. At lower temperature CO saturates the edges, then mainly the facets are active for the CO oxidation and the reaction rate is equal or even smaller than on extended surfaces [54]. The size effects observed for this reaction and also for the CO adsorption are due to the presence of strong adsorption of CO on the edges of the Pd particles.

8.2.4 Catalytic Activity of Supported Au Clusters

As a specific and inspiring example of a size effect observed when reducing one dimension of supported particles we discuss the observed onset of the catalytic activity of gold clusters supported on titania [55].

Gold has long been known to be catalytically far less active than other transition metals. Recently, however, it was found that when dispersed as ultrafine particles and supported on metal oxides such as TiO_2 , Au shows a very high activity for low-temperature catalytic combustion, partial oxidation of hydrocarbons, hydrogenation of unsaturated hydrocarbons, and reduction of nitrogen oxides [56]. For example, Au clusters can promote the reaction between CO and CO_2 at temperatures as low as 40 K [57]. The catalytic properties of Au depend on the support, the preparation method, and particularly on the size of the Au clusters. The structure sensitivity of the low-temperature oxidation of CO on supported Au clusters is reflected in a marked increase in the reaction rate per surface Au site per second, or turnover frequency, when the diameter of the Au clusters is decreased below ~ 3.5 nm [58,59] (see Fig. 8.5). A further decrease in cluster diameter below \sim

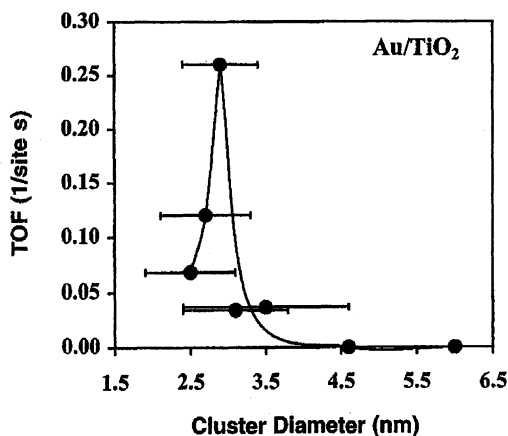


Fig. 8.5. CO oxidation TurnOver Frequencies (TOF) at 300 K as a function of the average size of the Au clusters supported on a high surface area TiO_2 support. The Au/TiO_2 catalysts were prepared by deposition-precipitation method, and the average cluster diameter was measured by Transmission Electron Microscopy (TEM). The *solid line* serves to guide the eye. After [59]

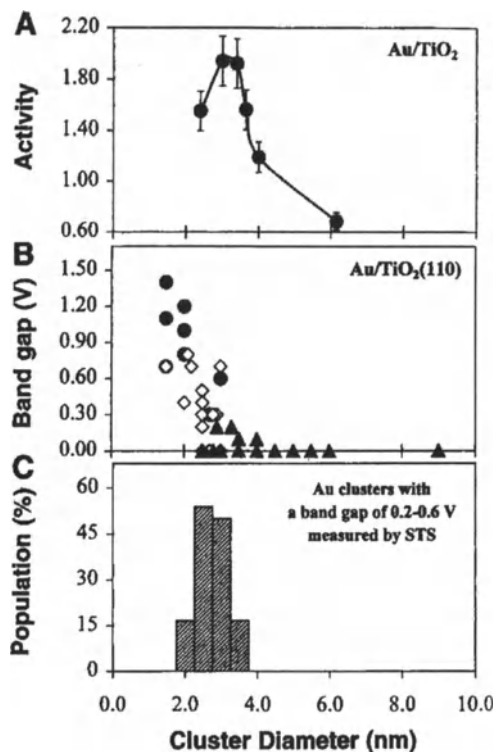


Fig. 8.6. (A) The activity for CO oxidation at 350 K as a function of the Au cluster size supported on TiO₂(110)-(1×1) assuming total dispersion of Au. The CO:O₂ mixture was 1:5 at 40 torr. Activity is expressed as (product molecules)×(total number of Au atoms)⁻¹s⁻¹. (B) Cluster band gap measured by STS as a function of the Au cluster size supported on TiO₂(110)-(1×1). The band gaps were obtained while the topographic scan was acquired on various Au coverages ranging from 0.2 to 4.0 monolayers. *Filled circles*: two-dimensional (2D) clusters; *open squares*: 3D clusters, two atom layers in height; *filled triangles*: 3D clusters with three atom layers or greater in height. (C) Relative population of the Au clusters (two atom layers in height) that exhibited a band gap of 0.2 to 0.6 eV as measured by STS from Au on titania. After [55]

3 nm leads to a decrease in the catalytic activity of Au. The new experiments of [55], reporting on the onset of the catalytic activity of gold clusters on titania with the concomitant appearance of the nonmetallic properties of the gold clusters, provide now a glimpse towards an atomic-level understanding of this extraordinary catalytic behaviour.

These authors prepared Au particles by evaporation on single crystalline surfaces of titania in ultrahigh vacuum. The obtained particle sizes range in diameter from 1 to 6 nm. Scanning Tunnelling Microscopy (STM) and

Scanning Tunnelling Spectroscopy (STS) as well as elevated pressure reaction kinetics show (see Fig. 8.6) that the structure sensitivity of this reaction on gold clusters supported on titania is related to a quantum size effect, i.e., the opening of a band gap, with respect to the thickness of the gold islands. Islands with two layers of gold and a band gap of 0.3 eV are found to be most effective for catalysing the reaction of CO. These results suggest that supported clusters, in general, may have unusual catalytic properties as one dimension of the clusters becomes smaller than three atomic spacings. The authors conclude that the observed tailoring of the properties of small metal clusters by altering the cluster size and its support could prove to be universal for a variety of metals and will likely be quite useful in the design of nanostructured materials for catalytic applications.

8.3 Supported Monodispersed Model Catalysts

In small gas phase clusters consisting only of a few atoms, quantum size effects are pronounced and cluster properties change drastically when their size is varied just by a single atom (see Chap. 1). Therefore, when studying size-dependent properties of such small entities on surfaces, it is necessary to be able to prepare samples of monodispersed clusters supported on well-characterised supports. In the following we first review the key experimental methods to achieve this goal. Then we present selected examples where chemical reactions on metallic particles are studied as a function of the precise number of atoms in the clusters. In a first example which is related to Sect. 8.2.3 we discuss the size-dependent CO dissociation on small supported Ni clusters. Then the catalytic role of small silver clusters for latent image generation in photography is elucidated. Subsequently, the hydrogenation of toluene on supported Ir₄ and Ir₆ is studied, showing that such small particles are already catalytically active and are robust for practical applications. We then present selected cases where the size-dependent catalytic properties of supported clusters are studied in a larger size range under UHV conditions. This allows for the development of simple concepts, which determine the catalytic properties of nanometer size metal particles and which may lead to a molecular understanding of the elementary steps important in catalytic processes. These case studies illustrate how catalytic properties can be tuned by changing the electronic or geometric structure of the metal clusters as a function of size. They also reveal how the support can influence the intrinsic properties of supported metal clusters and how it couples with the catalytic action of supported clusters.

8.3.1 Preparation and Characterisation of Monodispersed Supported Clusters

Today there exist essentially two completely different approaches for assembling monodispersed clusters: chemical methods in solutions and physical

methods using molecular beams. Subsequently the clusters are deposited on the chosen support. In the following we introduce these preparation and deposition methods.

Organometallics are compounds consisting of a well-defined metal core, which is stabilised by organic ligands. The large variety of such compounds is an obvious choice to be used as precursors for the preparation of monodispersed metal clusters supported on surfaces. They can either be deposited on appropriate substrates by evaporation in ultrahigh vacuum (UHV) [60] or by slurring a solution of the organometallics with an oxide powder [61]. These techniques are feasible for the types of metals and sizes where stable organometallic precursors exist. An alternative way is the synthesis of the organometallic compound directly on the substrate [62]. Finally, stripping off the ligands may then result in monodispersed cluster samples. For example, monodispersed tetra- and hexairidium clusters supported on oxide surfaces are produced by applying these chemical methods. The presence of the metallic core is then detected by using Extended X-ray Absorption Fine Structure (EXAFS) spectroscopy [61,63–65]. Once such samples are successfully assembled, their chemical and physical properties as well as their interaction with a support can be studied.

A related approach has been undertaken recently by the group of Whetten [66]. They focused their attention on the preparation of alkanethiolate monolayer-protected metal clusters (MPCs). They found that gold MPCs in particular are quite stable and can be prepared with average core diameters of 1.1 to 5 nm. Electrochemical studies have demonstrated that Au MPCs are equivalent to diffusing, nanometer-sized electrodes and can provide electrocatalytic advantages. In order to use these size-selected Au-clusters as supported model catalysts the ligands have to be removed without changing the stability of the clusters, an interesting task for future applications.

A more general approach to producing monodispersed clusters supported on surfaces is the use of size-selected molecular beams. With this method monodispersed cluster samples of in principle all materials and cluster sizes can be assembled. In a few case studies presented in the following sections the clusters are produced by a sputter source or by a laser evaporation source. Silver clusters (see Sect. 8.3.4) are produced by a sputter source in combination with a phase-space compressor [67] allowing for the production of clusters, e.g., Ag_{21} with kinetic energy distributions of 3.7 eV at Full Width Half Maximum (FWHM) and for smaller clusters like Ag_4 of only 1 eV FWHM. In this arrangement a primary ion beam with an energy between 10^2 to 10^5 eV and a typical current of 5–20 mA is focused onto a target producing neutrals and ions. The secondary ions are then drawn into ion optics for mass-selection and beam transport [68,69]. With such a source, for materials like Ag, Au, or Pd, beam currents for small clusters are typically in the range of a few to a few tens of nanoamperes in state-of-the-art experimental setups. The clusters

produced are boiling hot with temperatures estimated for sputter-produced alkali dimers to be between 1000 K and 1500 K [69].

In the case studies presented in Sects. 8.3.3 and 8.3.6–8.3.8, the size-dependent dissociation of CO on Ni, the cyclotrimerisation of acetylene on Pd_N and the oxidation of CO on Pt_N and Au_N, the model catalysts are prepared using cluster beams generated by a recently developed laser vapourisation source. In detail, the clusters are prepared in the gas phase by a high-frequency laser evaporation source, producing high currents (nA) of singly charged clusters. Subsequently, one single cluster size is selected with a quadrupole mass filter and deposited with low energy onto an oxide surface [70]. The total energy of the deposition process is composed of the kinetic energy of the cluster ($E_{kin} \leq 0.2$ eV/atom) [70], the chemical binding energy between the Pd, Pt, and Au clusters and the MgO surface (0.4–1.4 eV per interacting atom [71]), as well as a negligible Coulomb interaction between the incoming cluster ion and its induced polarisation charge on the oxide film surface. Consequently, as the kinetic energies of the impinging clusters correspond to soft-landing conditions ($E_{kin} \leq 1$ eV/atom, see Chap. 4) [72,73], and as the total energy gained upon deposition is at least a factor of two smaller than the binding energy of the investigated clusters, ranging from 2.0 to 5 eV [74,75], fragmentation of the clusters is excluded. In the experiments presented below less than 0.4 % of a monolayer of size-selected clusters (1 ML = 2×10^{15} clusters/cm²) are deposited at 90 K, in order to land them in isolation on the surface and to prevent agglomeration of the clusters on the support [76]. In the three examples below thin MgO films are used as support material. They are prepared *in situ* for each experiment by epitaxially growing the oxide films on a Mo(100) surface by evaporating magnesium in a ¹⁶O₂ background [77]. The inertness of the thin MgO films is tested for the cyclomerisation of acetylene and the oxidation of CO. In these experiments the clusters are exposed to a well known amount of acetylene or CO and isotopically labelled O₂ [13,16,17,78] and in a Temperature Programmed Reaction (TPR) the products of an eventual chemical reaction are monitored by mass spectrometry. The catalytic action is determined by integrating the TPR signal of the benzene or CO₂ molecule and normalising to the number of deposited clusters. For this procedure the mass spectrometer has been calibrated using the known amount of desorbing CO from a Mo(100) single crystal [79] and taking into account its different sensitivity for benzene, CO and CO₂. The number of deposited clusters is obtained by integrating the measured ion current on the substrate over the deposition time. The prepared model catalysts are then studied to gain insights and give trends in the size-dependent chemical properties of nanometer size supported metal particles.

8.3.2 Size-Dependent CO Dissociation on Small Ni Clusters

The interaction of CO with size-selected nickel clusters (Ni_{11} , Ni_{20} , Ni_{30}) deposited on MgO is studied with Thermal Desorption Spectroscopy (TDS) and Fourier Transform InfraRed (FTIR) spectroscopy. TDS reveals two binding sites of CO on all three clusters. One type of adsorption site chemisorbs CO molecularly and results in CO-desorption between 200 and 300 K as shown for Ni_{30} in Fig. 8.7 for $^{13}\text{C}^{16}\text{O}$ and $^{12}\text{C}^{18}\text{O}$, respectively. On a sec-

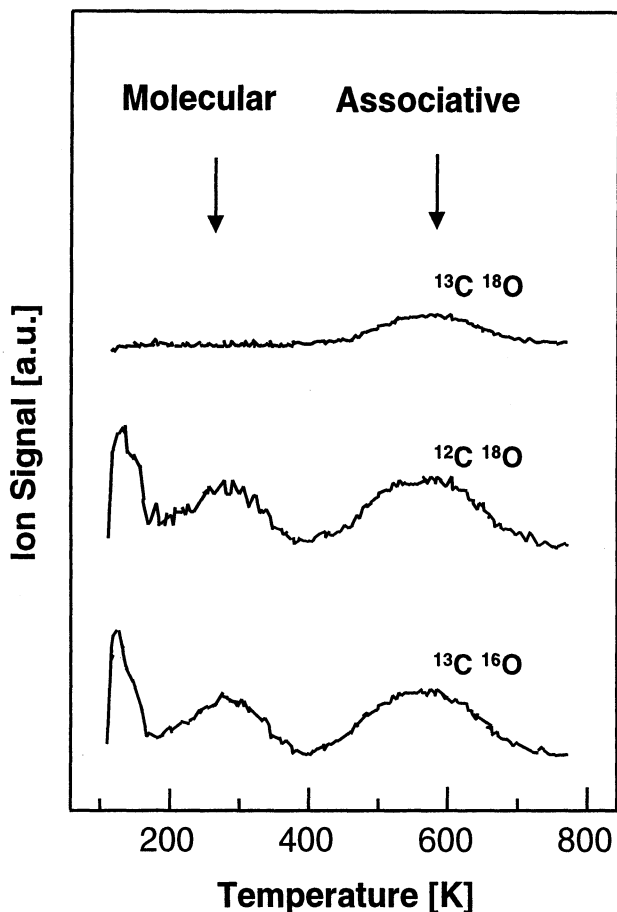


Fig. 8.7. Thermal desorption spectra of an isotopic mixture of $^{12}\text{C}^{18}\text{O}$ and $^{13}\text{C}^{16}\text{O}$ adsorbed on $\text{Ni}_{30}/\text{MgO}/\text{Mo}$. Shown is the desorption of the three indicated isotopes. $^{13}\text{C}^{18}\text{O}$ can only be formed if carbon monoxide is dissociated by the cluster and is subsequently desorbed associatively. This experiment characterises different binding sites on the cluster, showing that the low-temperature peaks around 100 and 260 K originate from molecularly adsorbed CO and the high-temperature peak from dissociated CO. $^{12}\text{C}^{16}\text{O}$ is also formed but due to the weak signal-to-noise ratio not visible in the spectra. After [80]

ond adsorption site the CO molecule is dissociated and desorbs associatively between 500 and 600 K. Isotopic exchange experiments confirm the dissociation on the high-temperature desorption site. In these experiments the monodispersed clusters are exposed to a mixture of $^{12}\text{C}^{18}\text{O}$ and $^{13}\text{C}^{16}\text{O}$. Isotopic exchange occurred only at the high temperature site, producing $^{12}\text{C}^{16}\text{O}$ and $^{13}\text{C}^{18}\text{O}$ (Fig. 8.7 for $^{13}\text{C}^{18}\text{O}$). The two different binding sites are also confirmed by infrared studies, where absorption bands at around 2100 cm^{-1} and $1385/1329\text{ cm}^{-1}$ are observed for Ni_{30} . The former frequency is typical for molecularly adsorbed CO whereas the latter is attributed to CO in a predissociated state. The reactivity of the size-selected clusters is expressed by the number of molecularly adsorbed and dissociated CO molecules per nickel cluster. By contrast to predictions, which suggest that the smaller the cluster the higher the reactivity, in the investigated size range the opposite behaviour is observed. Ni_{30} adsorbs 16 CO molecules, where 10 of them are dissociated. On the other hand, Ni_{11} adsorbs 5 CO molecules where only one CO is dissociated. These results show that by varying the cluster size from Ni_{11} to Ni_{30} the average number of dissociated CO can be changed deliberately. The different reactivities indicate that these small particles have very distinct chemical properties, as they have different electronic and structural properties [80,81]. One possible interpretation is that there exists a transition from a 2-dimensional to a 3-dimensional structure when going from Ni_{11} to Ni_{30} . This argument was tested by investigating the vibrational coupling of the molecularly bound CO's on Ni_{11} [82]. With a simple model using dipole-dipole coupling the measured vibrational coupling shift can be fitted with average CO-CO distances of maximal 2.5 to 3.1 Å. In addition, the observed vibrational frequencies are typical for CO adsorbed on nickel in an on-top configuration. Consequently, for a cluster as large as Ni_{11} , the 4 CO molecules can bind in configurations with CO-CO distances of once or twice the Ni-Ni interatomic distance. The model suggests that the CO's are bound to neighbouring Ni atoms as typical Ni-Ni distances in clusters are between 2 and 2.5 Å. For 2-dimensional cluster morphologies this is unlikely as the CO's tend rather to adsorb on the low-coordinated Ni atoms on the edge of the clusters instead of adsorbing on neighbouring atoms. Therefore it is believed that a 3-dimensional cluster morphology with the 4 CO's adsorbed on a facet with at least 4 nickel atoms is more likely. A 3-D structure is also supported by considering the energetics of supported Ni_4 clusters on MgO, as the Ni-Ni binding energy is about a factor of three larger than the Ni-oxide interaction. It is informative to compare these results with gas phase studies, where the reactivity of bare nickel ions with carbon monoxide was studied in molecular beam experiments. Vajda et al. [83] measured saturation limits of thermalized positively charged nickel clusters with carbon monoxide and observed among others the following saturated nickelcarbonyl species: $\text{Ni}_{11}(\text{CO})_{19}$, $\text{Ni}_{20}(\text{CO})_{25}$, $\text{Ni}_{28}(\text{CO})_{31}$, and $\text{Ni}_{31}(\text{CO})_{32}$. These results clearly show the different CO adsorption behaviour of gas phase and supported nickel

clusters, where the saturation limits are a factor of two (Ni_{30}) to four (Ni_{11}) smaller. For Ni_{30} this is not surprising since each dissociated CO molecule occupies two adsorption sites on the cluster. In addition, the size-dependent interaction with the substrate plays a significant role in changing the chemical properties of such small supported metal clusters, as will be shown in Sect. 8.3.8.

8.3.3 The Catalytic Role of Small Silver Clusters for the Latent Image Generation in Photography

In 1985 the group of Wöste [68] used for the first time size-selected molecular beams to deposit clusters on a support and to investigate the size-dependent reactivity of the supported clusters. They studied the catalytic activity of monodispersed silver clusters for the latent image generation in photography. In the photographic process light-sensitive silver bromide microcrystals absorb a critical number of photons leading to the formation of the latent image, which consists of small silver clusters. They are created by the coagulation of mobile silver ions and photoelectrons produced during illumination. These clusters then catalyse the development of the real image by accelerating the kinetics of the reduction process of the silver bromide microcrystals to metallic silver. Therefore sufficiently exposed silver bromide microcrystals carry the information for the final photographic image. One of the basic questions in this process is whether a critical size for the silver clusters is needed in order to form the latent-image speck [84–87].

Wöste proposed an experiment where the photographic latent image is modelled by size-selected silver clusters deposited onto a silver halide system. In a first experiment size-selected silver clusters (Ag , Ag_3 , Ag_4 , Ag_5 , Ag_7 , and Ag_9) were deposited at relatively high kinetic energy (8 eV/cluster) onto specimens containing binder-free silver bromide microcrystals prepared from a photographic emulsion [68]. The specimen consisted of a glass support covered with a conductive indium–tin oxide layer on which a gelatin layer stabilised the cubic shaped silver bromide microcrystals. The prepared samples were then developed in a conventional photographic developer. The fraction of the developed grains was determined for the different cluster sizes. Figure 8.8 clearly shows that for the development a minimum cluster size of Ag_4 is necessary. Recently these results were reproduced by performing the experiment under better controlled experimental conditions, where cold Ag clusters were deposited with a kinetic energy of only 1 eV/cluster [67].

In addition, in these recent experiments the influence of the redox potential of the developer for the critical sizes Ag_2 , Ag_3 , and Ag_4 was studied. Again Ag_4 shows distinct differences in its catalytic behaviour. These experiments unambiguously prove that a critical minimum cluster size is necessary for the generation of the latent image, an important contribution to the understanding of the photographic process.

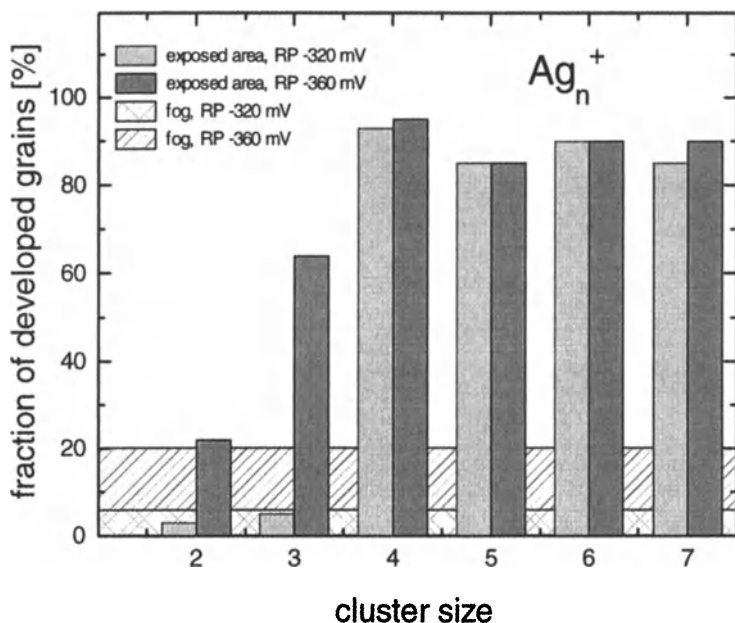


Fig. 8.8. Fraction of developed grains after deposition of size-selected silver clusters for two different redox potentials of the developer. After [67]

8.3.4 The Hydrogenation of Toluene on Monodispersed Ir_4 and Ir_6 Supported on Oxide Surfaces

Supported tetrairidium clusters are obtained by slurring dissolved $\text{Ir}_4(\text{CO})_{12}$ in a solution of either hexane or pentane with calcined MgO powders. The deposited $\text{Ir}_4(\text{CO})_{12}$ clusters are then characterised by FTIR, Raman and Extended X-ray Absorption Spectroscopy (EXAFS). Infrared and Raman data suggest tetrairidium clusters to be mainly present in the form of adsorbed $[\text{H}\text{Ir}_4(\text{CO})_{12}]^-$ or $[\text{Ir}_4(\text{CO})_{12}]^{2-}$ [63,64]. The metalcarbonyls are then decarbonylated by heating the sample in He to 300 C for 2h. EXAFS and FTIR data suggest complete decarbonylation. In addition, the Ir–Ir coordination number is three, suggesting a tetrahedral iridium frame (Table 8.1). EXAFS results further show two Ir–O contributions attributed to the interaction of cluster atoms with the oxygen of the support. The calculated Ir–O distances are 2.1 and 2.7 Å (Table 8.1). The short distance indicates a strong bonding interaction between the iridium frame and the oxide surface, while the long distance is associated with non-bonding Ir–O interactions resulting from nonepitaxial fits of the iridium clusters with the MgO surface. From these data the authors suggest a simplified structural model of the adsorbed Ir_4 cluster on the oxide surface, see Fig. 8.9.

$[\text{Ir}_6(\text{CO})_{15}]^{2-}$ can be formed by surface-mediated synthesis on $\gamma\text{-Al}_2\text{O}_3$ powders. In *n*-hexane dissolved $[\text{Ir}(\text{CO})_2(\text{acac})]$ is slurred with an uncalcined

Table 8.1. EXAFS results characterising the coordination number and the average shell radial distance r . Also indicated are the precursors used for the formation of the metal core, the support and the treatment of the model catalyst. After [88]

Precursor	Support	Treatment	Shell	Coord. No	r [Å]
a) Ir ₄ (CO) ₁₂	MgO	Decarbonylation	Ir–Ir	3.1	2.73
			Ir–O	3.4	2.73
			Ir–O	0.8	2.07
c) Ir ₄ (CO) ₁₂	MgO	Catalysis of toluene hydrogenation	Ir–Ir	2.8	2.69
b) (Ir ₆ (CO) ₁₅) ²⁻	γ -Al ₂ O ₃	Decarbonylation	Ir–Ir	4.05	2.704
			Ir–O	0.83	2.227
			Ir–O	0.61	2.707
c) (Ir ₆ (CO) ₁₅) ²⁻	MgO	Catalysis of toluene hydrogenation	Ir–Ir	4.1	2.69

From a) [61], b) [62], c) [88].

γ -Al₂O₃ support and treated in flowing CO at 100 C for 10h. As inferred from IR data this procedure leads to the formation of [Ir₆(CO)₁₅]²⁻ [62]. In addition to hexairidium clusters, small amounts of unconverted mononuclear iridium as well as tetrairidium species are detected by IR. The EXAFS data are consistent with the 4-coordinated iridium atoms of hexairidium clusters. The metalcarbonyls are then decarbonylated by ramping the sample to 300° C in He. The complete decarbonylation is inferred from the total disappearance of the CO infrared band. In addition, after this treatment EXAFS data (see Table 8.1) confirm the presence of 4-coordinated iridium, and reveal two metal-support contributions indicative of a bonding and a non-bonding Ir–O interaction similar to supported Ir₄ clusters. The catalytic hydrogenation of toluene on Ir₄ and Ir₆ supported on different oxide supports is then investigated. The catalytic activity is expressed as reaction rate per iridium atom (turnover frequency) (see Table 8.2). The authors report Ir₆ to be several times less reactive than Ir₄. However, both clusters are significantly less reactive than supported aggregates of metallic iridium. Increasing the average size of the aggregates from about 5.4 Å to more than about 30 Å increases reactivity by one and two orders of magnitude, respectively [63]. Interestingly, the Ir–Ir distances observed for the clusters and metallic aggregates are the same within the experimental accuracy of the EXAFS measurements. It is therefore suggested that not the geometry but rather the different electronic structure is responsible for the changed reactivity. In addition, it is reported that the low catalytic activity of Ir₄ relative to that of aggregated metallic iridium correlates well with the capacities of these structures to chemisorb hydrogen. This indicates also that the catalytic activity is related to the individual elec-

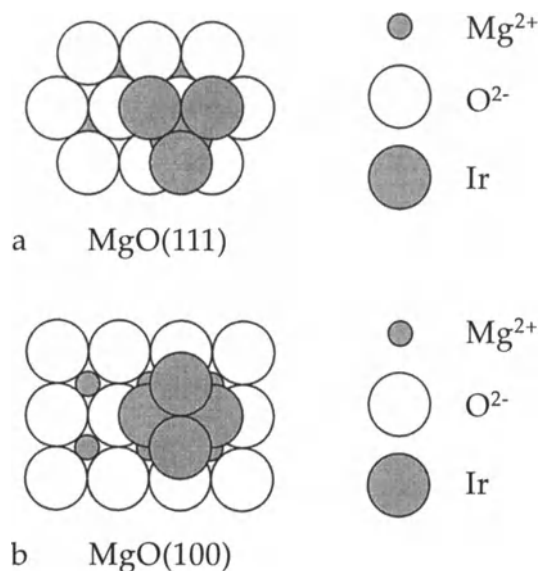


Fig. 8.9. Proposed models representing siting of an Ir_4 tetrahedron on a MgO surface. (a) Tetrahedron with corner in interstice of Mg(111) surface; (b) tetrahedron edge-bonded to oxygen atoms of the MgO(100) surface. After [61]

tronic structure of the metal core. These studies show that molecular iridium clusters manifest a different chemical behaviour than their metallic counterparts. Hence it is proposed that the concept of structure insensitivity breaks down or has to be strictly limited to the catalytic properties of solid surfaces. The supported clusters are regarded as quasi-molecular, with the support providing part of a ligand shell, which affects the activity in the same way as ligands affect the activities of molecular metal-cluster catalysts. This cluster-support interaction is certainly size-dependent and it is suggested that the decrease in catalytic activity as the aggregates become smaller and approach the size of Ir_6 clusters might largely be a consequence of the increasing effect of the support. Here the support is regarded as a ligand, which bonds to the iridium cluster and makes it less bulk-like, metallic iridium [64]. Remarkably, these MgO-supported Ir_4 and Ir_6 clusters are stable catalysts, as is shown both by the lack of significant changes in their activities in steady-state operation in a flow reactor for days and by EXAFS results indicating retention of the metal framework structures during catalysis (see Table 8.1). In addition, the reactivity seems to be independent of the support because the two sizes supported either on MgO or $\gamma\text{-Al}_2\text{O}_3$ show similar reactivities. These results suggest that molecular clusters show different catalytic properties compared to supported metals. However, in order to develop general models and trends in the size-dependent reactivities of nanometer size metal clusters a larger size range has to be investigated, as will be shown in the following subsections.

Table 8.2. Catalytic activities in the toluene hydrogenation of supported metal clusters and supported metallic particles. The catalytic reactivity is expressed in the TurnOver Frequency (TOF) measured at 333K. After [61]

Catalyst	Support	TOF [10^{-3}s^{-1}]
Ir ₄	MgO	0.63
Ir ₄	γ -Al ₂ O ₃	0.94
Ir ₆	MgO	0.23
clusters of ~ 20 atoms each, formed from Ir ₄	γ -Al ₂ O ₃	9.9
Ir-particles	MgO	2.0

8.3.5 Size-Dependent Cyclotrimerisation of Acetylene on Monodispersed Palladium Clusters Supported on MgO

The cyclisation of three molecules of acetylene to benzene over palladium single crystals and supported palladium particles is an example of a structure sensitive reaction. The Pd(111) facet is shown to be the most active surface [89–91]. Acetylene is adsorbed in the three-fold hollow site, leading to a strongly distorted acetylene molecule on palladium. The existence of isolated three-fold sites alone, however, is not a sufficient condition for the cyclotrimerisation of acetylene, and it has been suggested that the catalytically effective surface ensemble corresponds to three C₂H₂ molecules adsorbed on 3-fold sites around a given Pd atom [91]. This geometrical requirement defines the critical ensemble consisting of seven Pd atoms for the cyclotrimerisation of acetylene. The elementary steps in this reaction are summarised as follows [91].

In a first step, at low temperature (≤ 200 K), a stable surface intermediate C₄H₄ is formed by combining two adsorbed acetylene molecules. The addition of a third acetylene molecule leads then to the formation of benzene (~ 200 K). At high coverage or pronounced surface roughness the formed benzene is forced into a weaker binding configuration with the molecular axis tilted with respect to the surface. From this tilted configuration benzene desorbs at a temperature of $T = 230$ K. At low coverage and on flat surfaces the formed C₆H₆ binds strongly to the surface in a flat-lying configuration and desorbs at $T \sim 500$ K. The reaction takes place without C–C bond scission, but a rehybridisation to sp^2 is necessary to form the pentadiene metallocycle (PdC₄H₄) proposed as intermediate species [90]. The formation of benzene on nanometer sized palladium particles is very similar to the analogous low-index single-crystal results, with desorption of benzene at 230 K and 530 K [89]. The larger palladium particles, regular polyhedra comprised exclusively of $\langle 111 \rangle$ and $\langle 100 \rangle$ facets, favour the low-temperature reaction pathway, whereas the smaller particles desorb benzene at 530 K. In

addition, all investigated particles produce benzene at 370 K at defect sites. Remarkably, a drop-off in activity at a particle diameter smaller than 1.5 nm is observed and suggests a manifestation of the anticipated ensemble effect.

In what follows, results for the cyclotrimerisation on small molecular Pd_N clusters down to the atom are presented [92] in order to complete the picture of this structure sensitive reaction (Fig. 8.10). The production of benzene on these small Pd_N clusters ($1 \leq N \leq 30$) is characterised by two main features, the desorption of benzene at 430 K and at 300 K. The high temperature desorption is only present for the larger clusters down to Pd_7 . The low temperature desorption is observed already for a single Pd atom, indicating that one atom is enough to produce benzene [92]. These results are distinctly different from the ones obtained for larger metallic particles and for solid surfaces. Desorption of benzene, typical for the reactive Pd(111) facet at temperatures of about 230 and 500 K, is not present as these molecular clusters are too small to be comprised of crystalline facets. Experimentally it was possible to show that at 430 K benzene desorbs, this being completely produced on the cluster surface. On the other hand the 300 K feature characterises benzene produced at single or low coordinated Pd atoms. This atom-by-atom size-dependent catalytic reactivity for the cyclotrimerisation of acetylene has been investigated in more detail. From the TPR studies shown in Fig. 8.10, the number of catalytically formed benzene molecules per cluster is estimated and displayed in Fig. 8.11. Up to Pd_6 the cyclotrimerisation of acetylene on the cluster surface and desorption of benzene at 430 K is zero (indicated by the absence of the 430 K feature in Fig. 8.10). An abrupt increase in the overall production of benzene is observed when going from Pd_7 to Pd_8 due to the benzene production at 430 K (Fig. 8.10). For the octamer an average of one benzene molecule is produced at 430 K. This catalytic benzene formation increases when going to larger cluster sizes and an average of 4–5 benzene molecules is produced for Pd_{30} . These results suggest that for the cyclotrimerisation of acetylene on molecular clusters at 430 K a critical ensemble of seven palladium atoms is necessary.

The investigated model catalysts consisting of size-selected Pd_N ($N \leq 30$) clusters supported on MgO(100) thin films revealed a new reaction mechanism for the cyclotrimerisation of acetylene at 300 K for single low coordinated palladium atoms. Density functional calculations showed that single Pd atoms can be catalytically activated only when adsorbed on basic defect sites of MgO and when charge is transferred to the metal atom [92]. In addition, it could be shown that a critical ensemble of seven atoms is necessary for the cyclotrimerisation to occur at 430 K. This suggests that geometrical arguments, e.g., the existence of three 3-fold sites, which are responsible for a rehybridisation to sp^2 of acetylene, may explain the minimum size of the critical ensemble. Finally the different desorption temperatures of benzene compared to single crystals suggest that on such small clusters $\langle 111 \rangle$ and $\langle 100 \rangle$ facets are not present.

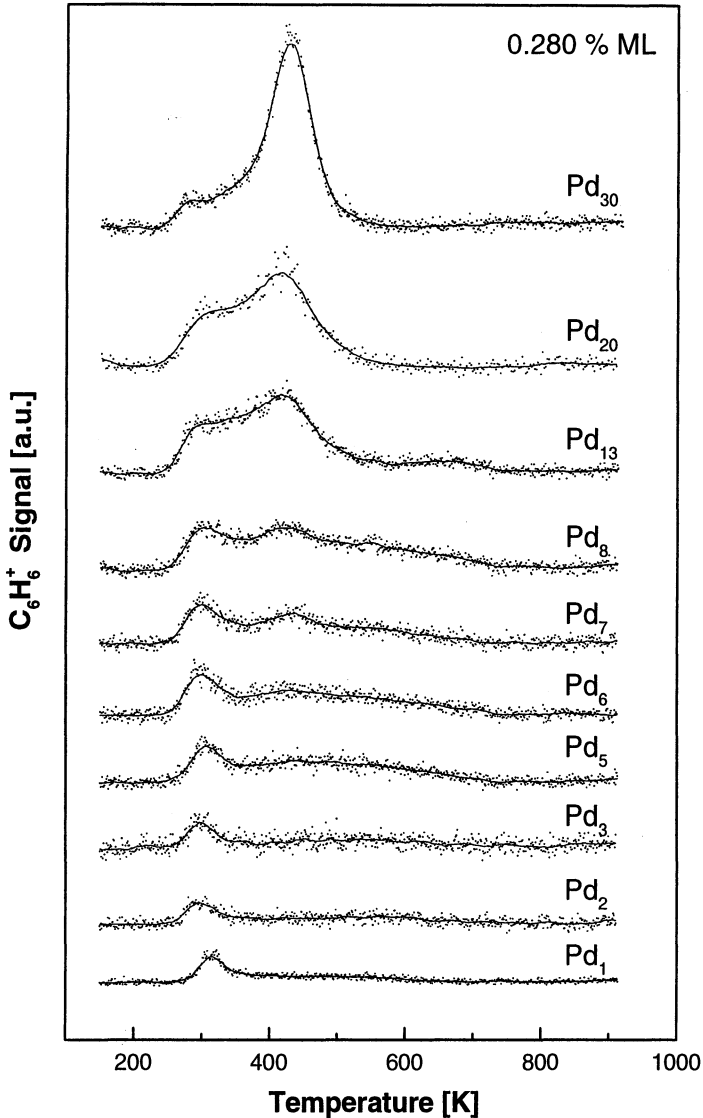


Fig. 8.10. Catalytic formation of benzene for different cluster sizes from a Temperature Programmed Reaction (TPR) experiment. Cluster coverages are 0.28% of a monolayer for all sizes, where one monolayer corresponds to 2.2×10^{15} molecules/cm². For clusters up to Pd₃ benzene is formed at around 300 K. Note the appearance of an additional peak for Pd₇ at around 430 K. This benzene formation increases for larger sizes. For intermediate sizes (Pd₅ to Pd₈) a broad feature is observed between 400 K and 700 K. The origin of the three features is discussed in the text. After [92]

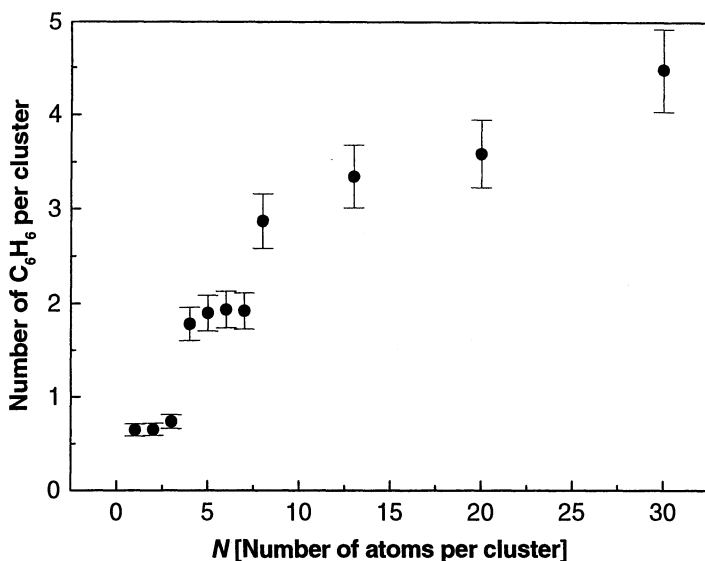


Fig. 8.11. Reactivity of size-selected palladium clusters (Pd_N ; $N \leq 30$) supported on a MgO film obtained from a temperature programmed reaction experiment. The overall reactivity is expressed in the number of formed benzene molecules per cluster. After [92]

8.3.6 The Oxidation of CO on Monodispersed Platinum Clusters Supported on MgO

In this example the catalytic oxidation of CO on platinum is investigated and a distinct atom-by-atom size-dependency is observed for monodispersed platinum clusters consisting of up to 20 atoms on thin MgO(100) films [93].

Fig. 8.12 shows the TPR spectra for the CO-oxidation on supported Pt_N ($8 \leq N \leq 20$) clusters. Because only CO_2 molecules containing one isotopically labelled ^{18}O atom are detected, oxygen is dissociated prior to or during the catalytic oxidation of CO. Thus these small Pt particles are already catalytically active. Remarkably, each cluster size reveals different oxidation temperatures, labelled α , β_1 , and β_2 , and a different catalytic activity as reflected in the different ion signal intensities.

The main CO_2 production, labelled β_1 , occurs at temperatures between 200 K and 400 K. For Pt_{15} to Pt_{20} the CO_2 production is also detected at temperatures around 150 K, labelled α , while Pt_{20} clusters display an additional reaction at 460 K, labelled β_2 . The different oxidation temperatures (peaks α , β_1 , β_2 in Fig. 8.12) indicate different catalytic processes occurring on different active sites on the Pt clusters. Results of FTIR experiments on clean Pt clusters, displayed in the inset of Fig. 8.12, support this assumption, showing only one CO absorption frequency (2065 cm^{-1}) for Pt_8 but two absorption frequencies (2045 cm^{-1} , 1805 cm^{-1}) for Pt_{20} .

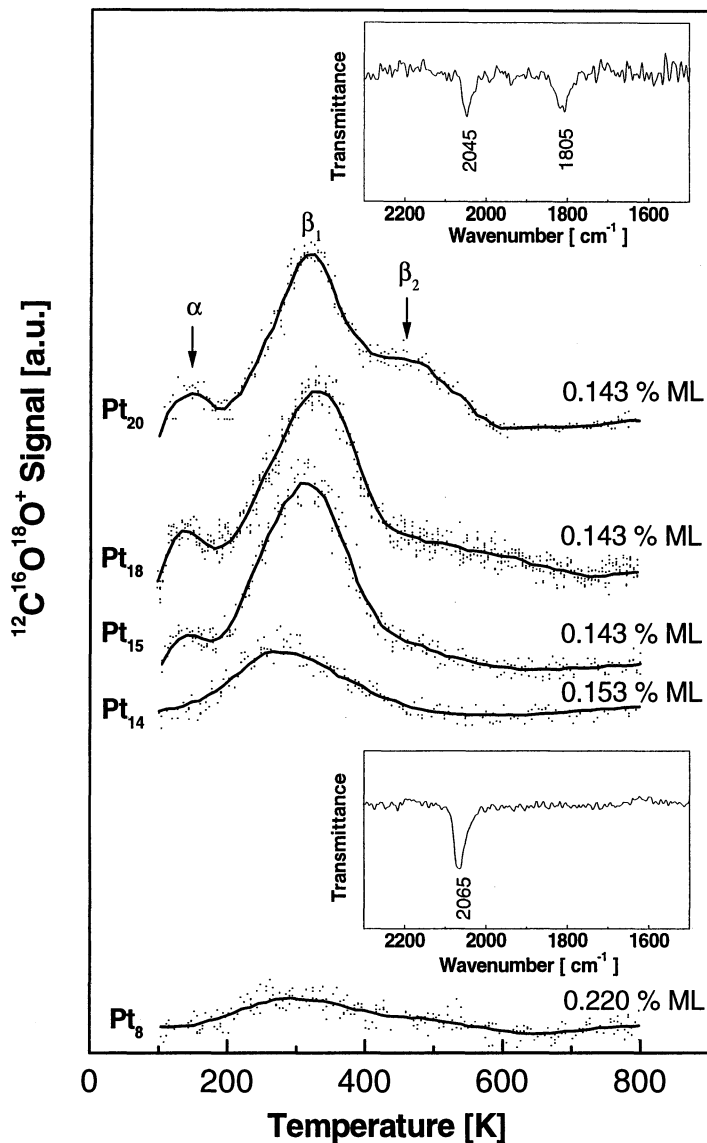
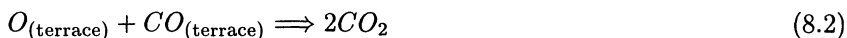


Fig. 8.12. Catalytic CO_2 formation for different platinum cluster sizes obtained from temperature programmed reaction experiments. Cluster coverages are expressed in % of a monolayer, where one monolayer corresponds to 1×10^{15} clusters/ cm^2 . For these experiments the cluster coverages are scaled with an estimated area covered by each cluster size to obtain similar experimental conditions. Different CO_2 -formation mechanisms (α , β_1 , β_2) are labelled according to single crystal studies. The insets show measured vibrational frequencies of CO adsorbed on clean deposited Pt_{20} (above) and Pt_8 (below) clusters. After [93]

A comparison of these results with the catalytic oxidation of CO on Pt single crystal surfaces is elucidating. Two main mechanisms have been observed. (i) On Pt(111) terrace sites the reaction α



has been found at 160 K involving hot oxygen atoms [13,94]. (ii) On a stepped Pt(355) surface the reactions β , i.e., β_1 ,



β_2 ,



and β_3 ,



at 290 K, 350 K, and 200 K, respectively, have been identified [16]. Because the oxidation temperatures on size-selected Pt clusters are in similar ranges, the reaction mechanisms are identified accordingly. The omnipresence of the β -mechanism indicates dissociation of O_2 on all cluster sizes. The α -mechanism is only observed for larger clusters, Pt₁₅ to Pt₂₀, implying that oxygen is adsorbed molecularly only on these species. Thus the presence of higher coordinated and therefore less reactive atoms on the cluster (as on single crystal terraces) is suggested. This is not unexpected as the average coordination number of atoms in clusters increases with size. Expressing the catalytic activity of the monodispersed Pt clusters as the number of catalyzed CO₂ molecules per cluster (Fig. 8.13a) and per atom (Fig. 8.13b) it is noted that CO₂ production increases nonlinearly with cluster size. Up to Pt₈, less than one CO₂ molecule per cluster is formed (Fig. 8.13a).

The reactivity increases abruptly between Pt₈ and Pt₁₅, on which about 6 CO molecules are oxidised. Representing the catalytic oxidation of CO per Pt atom (Fig. 8.13b), a maximum of 0.4 and a minimum of 0.1 is observed for Pt₁₅ and Pt₈, respectively. In addition the reactivity shows a local decrease for Pt₁₃ clusters.

In order to understand this size-dependent reactivity the geometric and electronic structure of each Pt cluster have to be considered. Local Density Functional (LDF) calculations showed that free clusters up to Pt₆ are planar [74] and it is likely that they remain planar on MgO as additional energy is gained by the cluster-substrate interaction for 2-dimensional as compared with 3-dimensional structures. LDF and Embedded Atom Method (EAM) calculations predict three-dimensional structures for Pt_N clusters, $N \geq 13$ [75]. The change in the measured reactivity, expressed in the number of CO₂ produced per cluster (Fig. 8.13a), roughly correlates with the predicted morphological transition from 2- to 3-dimensional structures for Pt cluster sizes

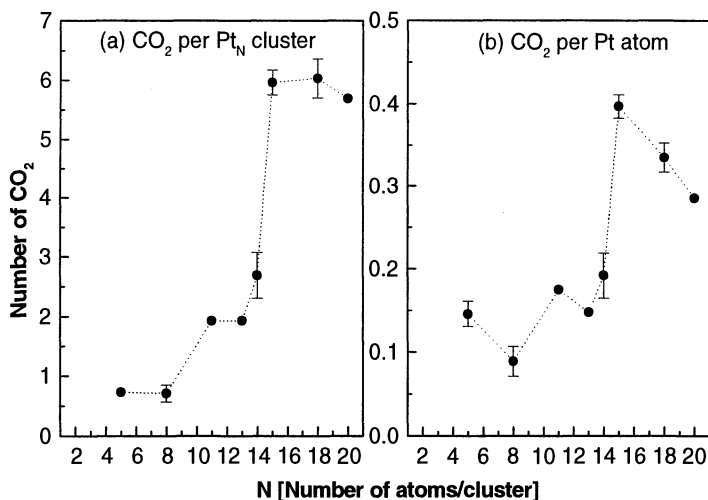


Fig. 8.13. (a) Total number of catalytically produced CO₂ as a function of cluster size. (b) Total number of produced CO₂ per atom as a function of cluster size. After [93]

between Pt₆ and Pt₁₃. It is interesting to note that Pt₁₃ shows a local decrease in the reactivity per atom (Fig. 8.13b), with Pt₁₃ being the first atomic-shell closing of both icosahedral and cubo-octahedral structures. In addition to morphological changes as a function of cluster size, the different electronic structure of the Pt_N clusters is important for an understanding of their catalytic behaviour. As shown above the dissociation of O₂ is the first step in this catalytic reaction. In the absence of model calculations for the CO oxidation on small Pt clusters, the chemical interaction is analysed qualitatively in terms of the frontier orbitals of the oxygen molecule and the Pt cluster (see Fig. 8.14) [95]. Here the molecule–surface interaction is simply replaced by the molecule–cluster interaction. For the oxygen molecule the electronic states of interest are the bonding, fully occupied π_u and σ_g and the antibonding, half-occupied π_g^* orbitals. Providing there exists a resonance (energetically and symmetrically) between one of these orbitals and the cluster's density of state (DOS), adsorption and dissociation of O₂ is possible [95]. As shown by Density Functional Theory (DFT) calculations the position of the centre of the *d*-band is the decisive parameter, when describing molecule–surface bonding [96]. Fragmentation occurs when there is enough backdonation from the clusters into the antibonding π_g^* state or a sufficient donation from the π_u or σ_g into the cluster [97]. Both processes reduce the bond order of oxygen. The energies of the fragment orbitals are -9.23 eV, -8.32 eV, and -6.1 eV for π_u , σ_g , and π_g^* , respectively [95]. On the other hand the energy of the HOMO of the clusters can be tuned by changing the cluster size from -9.0 eV, and the Ionisation Potential (IP) of the atom to -5.32 eV, the Fermi en-

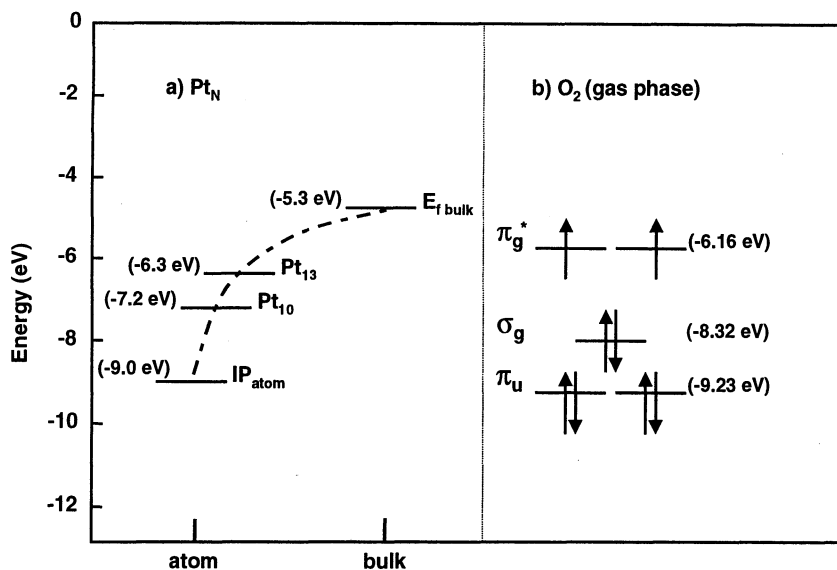


Fig. 8.14. Energy diagram of the relevant electronic states for oxygen dissociation in gas phase clusters and free oxygen. The cluster HOMO lies between the atomic limit (-9.00 eV) and the bulk limit (-5.32 eV). Dissociation is favoured if the energy of the cluster's HOMO is close to the antibonding π_g^* state of oxygen. *Dot-dashed curve*: classical conductive droplet model [100] (the expected fine structure of the ionisation potentials observed for small metal clusters [101,102], see also Chap. 1, is not taken into account). After [93]

ergy of bulk platinum (Fig. 8.14) [93], and can be associated with the centre energy of the d -band [98].

Now the increase in the catalytic activity from Pt₈ to Pt₁₅ can be correlated with the decrease in IP and the change in position of the centre of the d -band with increasing cluster size and the concomitant enhanced resonance with the antibonding π_g^* state of O₂. The maximum reactivity for Pt₁₅ suggests that the resulting backdonation is largest for this cluster. Increasing the cluster size further, lowers the cluster's HOMO even more and may result in a weaker resonance with the antibonding π_g^* state of O₂, as the HOMO's energy passes the energy of this antibonding state. For very small particles this backdonation grows smaller as the energy mismatch of the cluster's HOMO and the π_g^* grows larger (Fig. 8.14).

This example shows that for a single pass heating cycle every single Pt atom composing the supported cluster counts for the catalytic activity of the oxidation of carbon monoxide. Surprisingly, simple geometric and especially molecular orbital arguments seem to be sufficient to describe the general trend of the observed catalytic activity with cluster size. The prospect of tuning catalytic processes as a function of cluster size, a long-sought goal in heterogeneous catalysis, becomes a little less remote.

8.3.7 The Oxidation of CO on Monodispersed Gold Clusters Supported on MgO

High activation barriers for the adsorption or dissociation of small molecules on gold surfaces are responsible for the inertness of this coinage metal. Using DFT, Hammer and Nørskov [99] showed for the dissociation of hydrogen on various metal surfaces, that the nobleness of gold is directly related to its electronic properties. They suggest that the coupling of the fully occupied *d*-band of gold with the adsorbate states is not strong enough to push the resulting antibonding state above the Fermi level of the metal. This leaves this state partially populated and causes a repulsive interaction and a reduced probability of forming new stable compounds (such as hydrides, oxides and carbides). However, studies on free gold clusters revealed a change in the chemical behaviour for very small clusters [103]. Gold cluster cations are reactive towards D₂ and CH₄ with no reaction observed on clusters larger than ~15 atoms. For oxygen, gold cluster anions exhibit a dramatic reactivity variation with only the even-atom cluster anions interacting with oxygen. Recent studies by Haruta et al. [56,104,105] on small supported gold particles showed that nanometer size gold particles (≤ 1 nm prepared by precipitation methods) supported on Mg(OH)₂ are active for CO oxidation. Furthermore, their results suggest that the oxidation of CO is structure dependent as they observe different reactivities for icosahedral and fcc cuboctahedral geometries of their small gold particles. In a recent work, Valden et al. [55] observed a size-dependent oxidation of CO on planar gold islands supported on thin TiO₂ films which depends on the average diameter and height of the particles as shown in Sect. 8.2.5. Islands with diameters in the range of 2.5 to 3.5 nm and a thickness of two atomic layers revealed maximum reactivity. These islands are characterised by a band gap of 0.2–0.6 eV as measured by Scanning Tunnelling Spectroscopy (STS). The authors relate the observed structure sensitivity in the catalytic conversion of CO on gold to a quantum size effect with respect to the thickness of the gold islands.

In the following we discuss briefly the catalytic oxidation of carbon monoxide on small supported gold clusters in the size range of 1 to 20 atoms. In contrast to previous studies, an atom-by-atom size dependency is observed, which is related to the electronic structure of the supported gold clusters on magnesia and their distinct interaction with support defects [106,107]. Figure 8.15 shows the TPR spectra for CO oxidation on supported Au₈ and Au₂₀ clusters. The detected ¹³CO₂ molecules contain one isotopically labelled ¹⁸O atom. No other CO₂ molecules are produced which would be indicative of an oxidation on the cluster–support interface or a disproportion reaction of CO. Therefore the adsorbed ¹⁸O₂ molecule is dissociated prior to or during the reaction.

Thus small Au particles become catalytically active for the oxidation of CO when strongly interacting with defect sites [107]. At low temperature all clusters larger than Au₇ oxidise a small amount of CO at around 160 K.

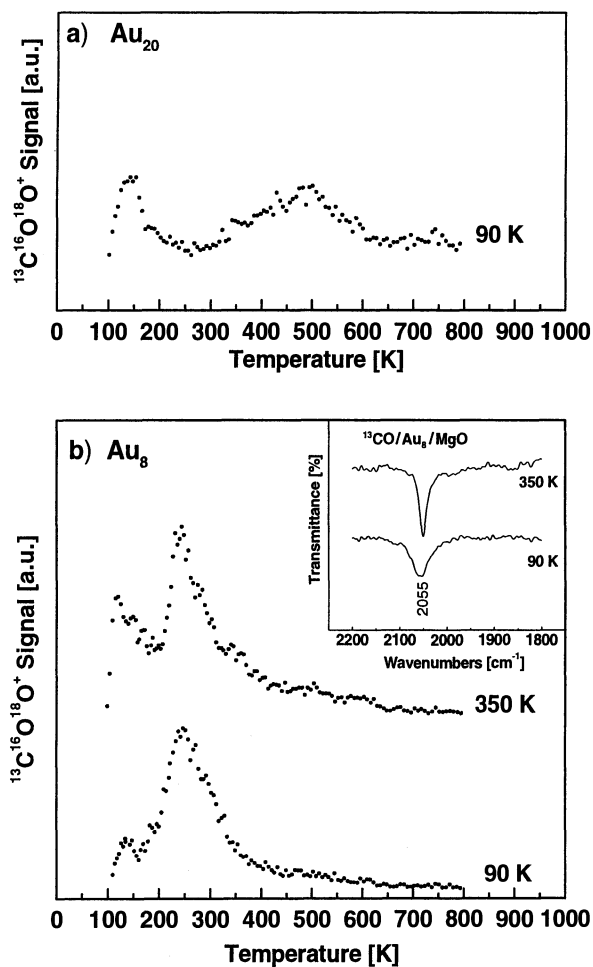


Fig. 8.15. Temperature Programmed Reaction (TPR): CO_2 production on Au_{20} (a) and on Au_8 (b) as a function of temperature. Isotopically labelled $^{13}\text{C}^{16}\text{O}$ and $^{18}\text{O}_2$ are used to unambiguously attribute the catalytic reactivity to the gold clusters. The number of produced $^{13}\text{C}^{16}\text{O}^{18}\text{O}$ is determined by integrating the TPR spectra (see text). Cluster coverages are between 0.2 and 0.4 % of a monolayer (ML). 100% of a ML corresponds to 2.25×10^{15} clusters/ cm^2 . (b, upper): CO_2 production of a Au_8/MgO sample after annealing to 350 K. *Inset*: vibrational frequency of CO adsorbed on Au_8 deposited at 90 K (lower) and annealed to 350 K (upper). After [106,107]

Remarkably, at higher temperature each cluster size reveals a distinctly different oxidation temperature with a transition observed from 240 K for the first closed shell-cluster Au_8 , to 500 K for Au_{20} (Fig. 8.15). In the case of Au_8 several reaction cycles were performed up to a temperature of 350 K with only minor changes in the oxidation of CO at 240 K (Fig. 8.15b, upper), indicating that the Au_8/MgO model catalyst is stable at least up to 350 K. Infrared studies support this observation (Fig. 8.15b). When measuring the vibrational frequency of adsorbed ^{13}CO on Au_8 before and after annealing the sample to 350 K no change in the integrated absorption intensity or frequency is observed. Note that in contrast to gold single crystal surfaces or macroscopic gold particles, CO is adsorbed on the small gold octamer and reveals an untypically high CO frequency. Heating the catalyst to 840 K changes the reactivity probably due to migration and coalescence of Au_8 . Expressing the catalytic reactivity by the number of produced CO_2 per cluster, leads to a

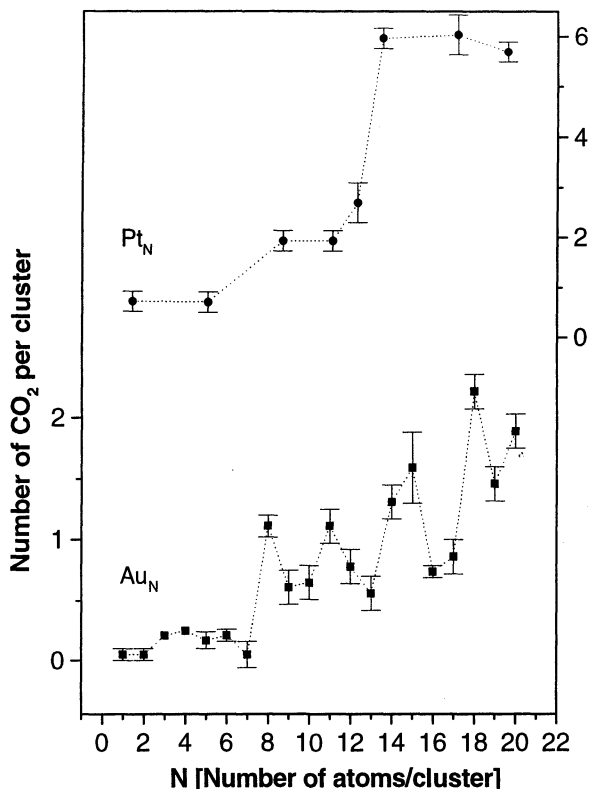


Fig. 8.16. Reactivity of size-selected supported Au_N and Pt_N clusters ($1 \leq N \leq 20$): The reactivity is expressed in the number of produced CO_2 molecules per cluster estimated by the integral of the TPR spectra and the number of deposited cluster ions. After [106,107]

low reactivity for all cluster sizes (Au_N , with $8 \leq N \leq 20$) (Fig. 8.16). This behaviour is in contrast to the strongly size-dependent reactivities found for Pt_N and Pd_N .

This work reveals that small gold particles consisting of only a couple of atoms become reactive for the oxidation of CO. The comparison between reactivities of free and supported-closed shell gold clusters establishes the importance of cluster-surface interactions.

8.4 Conclusions and Outlook

In this review we have seen the appearance of two size ranges in the reactivity of supported clusters. Particles consisting of more than a few hundred atoms display geometrical shell filling effects which manifest themselves as steps and kinks and which determine the kinetics of a chemical reaction at the particle surface. On the other hand, small, size-selected supported clusters (1–30 atoms) on oxide surfaces reveal atom-by-atom, size-dependent catalytic properties, where the individual electronic structure of each cluster size plays a decisive role.

Much more needs to be done. For example, an important aspect of understanding the details of a catalytic reaction is the restructuring of the catalyst under working conditions on local and long-range scales [108,109,47,110]. Tuning the chemical and physical properties of supported metallic, bimetallic or semiconducting nanostructures in a controlled manner by changing the cluster size as well as by choosing different functionalised support materials seems a little less remote. The control of heterogeneous catalytic reactions and photocatalytic properties to eventually build highly selective designer catalysts comes gradually into focus. The adjustment of a chemical interaction of supported clusters with small molecules may lead to the design of novel chemical sensors. The possible tuning of optical properties of nanostructured materials by changing cluster size may be a promising and alternative route to bandgap engineering. Deposition of clusters on intelligent support materials, such as micromechanical sensors consisting of bilayer cantilevers, may be used for calorimetry (reaction and adsorption heats) and photothermal spectroscopy on a local scale. The control of the dynamics of photo-induced catalytic reactions on clusters in the molecular beam or supported on surfaces by real-time pump-probe experiments may open the way to a selected final state which is thermally inaccessible. The link to catalysis in industry will consist in the investigation of the catalytic activity of the designed model catalysts in conventional reactors under real conditions. Thus their catalytic selectivity and efficiency as well as their stability may be optimised under working conditions.

The investigation of the evolution of matter from the atom to the bulk will create many opportunities for finding atomic-scale particles with novel and unique properties. Together with advanced theoretical modelling a deeper understanding of the underlying physical and chemical concepts will be gained which might stimulate the development of novel, functionalised and intelligent nanostructured materials.

Acknowledgements

This work has been supported by the Swiss National Science Foundation. We are delighted to thank S. Abbet, A. M. Ferrari, H. Häkkinen, U. Landman, G. Pacchioni, F. Patthey, N. Rösch, A. Sanchez, L. Trento, and F. Vanolli for an excellent collaboration and for stimulating discussions. It is a pleasure to acknowledge fruitful discussions with D.M. Cox, P. Fayet, H.-J. Freund, C. Henry, A. Kaldor, N. Mårtensson, A. Nilsson, K. Sattler, E. Schumacher, L. Wöste, and J.T. Yates, Jr.

References

1. D. Mendeleeff, *The Principle of Chemistry*, 3rd Ed. (Longmans, Green and Co., London, 1905)
2. T.E. Thorpe, Scientific worthies XXVI. Dimitri Wanowitch Mendeleeff. *Nature* **XL**, 193–197 (1889)
3. M. Kappes, R.W. Kunz, E. Schumacher *Chem. Phys. Lett.* **91**, 413–418 (1982)
4. W.D. Knight, K. Clemenger, W.A. de Heer, W.A. Saunders, M.Y. Chou, M.L. Cohen, *Phys. Rev. Lett.* **52**, 2141–2143 (1984)
5. W. Ekardt, *Phys. Rev. B* **29**, 1558–1564 (1984)
6. K. Clemenger, *Phys. Rev. B* **32**, 1359–3162 (1985)
7. W.A. de Heer, *Rev. Mod. Phys.* **65**, 611–676 (1993)
8. T.P. Martin, T. Bergmann, H. Gölich, T. Lange, *Chem. Phys. Lett.* **172**, 209–213 (1990)
9. P. Stampfli, K.H. Bennemann, *Phys. Rev. Lett.* **69**, 3471–3474 (1992) ; *Z. Phys. D* **25**, 87–94 (1992)
10. A.L. Mackay, *Acta Crystall.* **15**, 916–921 (1962)
11. O. Echt, K. Sattler, E. Recknagel, *Phys. Rev. Lett.* **47**, 1121–1124 (1981)
12. See articles in "Clusters of Atoms and Molecules", Vol. I and II, ed. H. Haberland (Springer, Berlin, 1994)
13. K.-H. Allers, H. Pfnuer, P. Feulner, D. Menzel, *J. Chem. Phys.* **100**, 3985–3998 (1994)
14. T. Matsushima, *Surf. Sci.* **127**, 403–423 (1983)
15. Y. Ohno, T. Matsushima, *Surf. Sci.* **241**, 47–53 (1991)
16. J. Xu, J.T. Yates, *Chem. Phys.* **99**, 725–732 (1993)
17. A. Szabo, M.A. Henderson, J.T. Yates, *J. Chem. Phys.* **96**, 6191–6201 (1992)
18. G. Ertl, P.R. Norton, J. Ruestig, *Phys. Rev. Lett.* **49**, 177–180 (1982)
19. H.H. Rotermund, *Surf. Sci. Rep.* **29**, 265–364 (1997)
20. H.J. Freund, *Angew. Chem. Int. Ed. Eng.* **36**, 452–475 (1997)
21. D.W. Goodman, *Surf. Rev. Lett.* **2**, 9–24 (1995)
22. D.W. Goodman, *Chem. Rev.* **95**, 523–536 (1995)
23. C. Duriez, C.R. Henry, C. Chapon, *Surf. Sci.* **253**, 190–204 (1991)
24. C.R. Henry, C. Chapon, C. Duriez, *Surf. Sci.* **253**, 177–289 (1991)
25. M.R. Zakin, R.O. Brickman, D.M. Cox, et al. *J. Chem. Phys.* **88**, 3555–3560 (1988)
26. A. Berces, P.A. Hackett, L. Lian, et al. *J. Chem. Phys.* **108**, 5476–5490 (1998)
27. M.D. Morse, M.E. Geusic, J.R. Heath, et al. *J. Chem. Phys.* **83**, 2293–2304 (1985)
28. H. Kietzmann, J. Morenzin, P.S. Bechthold, G. Ganteför, W. Eberhardt, *J. Chem. Phys.* **109**, 2275–2278 (1998)
29. H. Poppa, *Catal. Rev. Sci. Eng.* **35**, 359–398 (1993)
30. M. Thomas, J.T. Dickinson, H. Poppa, G.M. Pound, *J. Vac. Sci. Technol.* **15**, 568–571 (1978)
31. C.R. Henry, *Surf. Sci. Rep.* **31**, 231–326 (1998)
32. S.K. Purnell, X. Xu, D.W. Goodman, B.C. Gates, *J. Phys. Chem.* **98**, 4076–4082 (1994)
33. M. Valden, J. Aaltonene, E. Kuuisto, M. Pessaand, C.J. Barnes, *Surf. Sci.* **307–309**, 193–198 (1994)

34. P.L.J. Gunter, J.W.H. Niemantsverdriet, F.H. Ribeiro, G.A. Somorjai, *Catal. Rev. Sci. Eng.* **39**, 77–168 (1997)
35. R.J. Lad, *Surf. Rev. Lett.* **2**, 109–126 (1995)
36. C. T. Campbell, *Surf. Sci. Rep.* **27**, 1–111 (1997)
37. G.B. Raupp, T.J. Udovic, J.A. Dumesic, In: Davenas, J., Rabette, P. S. (Eds.) *Contribution of Cluster Physics to Material Science and Technology*, NATO ASI Series E, pp. 255–261 (1997)
38. V.E. Henrich, P.A. Cox, *The Surface Science of Metal Oxides* (Cambridge Univ. Press, Cambridge, UK, 1992)
39. C. Noguera, *Physics and Chemistry of Oxide Surfaces* (Cambridge Univ. Press, Cambridge, UK, 1996)
40. M. Bäumer, J. Libuda, H.J. Freund, In: Lambert, R. M, Pacchioni, G. (Eds.) *Chemisorption and Reactivity on Supported Clusters and Thin Films*. (Kluwer Academic Publishers, The Netherlands, 61–104, 1997)
41. S.C. Street and D.W. Goodman, In: King, D. A., Woodruff, D. P. (Eds.) *Growth and Properties of Ultrathin Epitaxial Layers*. (Elsevier Science B. V., North-Holland, 375–406, 1997)
42. M. Frank, S. Andersson, J. Libuda, S. Stempel, A. Sandell, B. Brena, A. Giertz, P.A. Brühwiler, M. Bäumer, N. Mårtensson, H.-J. Freund, *Chem. Phys. Lett.* **279**, 92–99 (1997)
43. S. Andersson, M. Frank, A. Sandell, A. Giertz, B. Brena, P.A. Brühwiler, N. Mårtensson, J. Libuda, M. Bäumer, H.-J. Freund, *J. Chem. Phys.* **108**, 2967–2974 (1998)
44. M. Bäumer, J. Libuda, A. Sandell, H.-J. Freund, G. Graw, Th. Bertrams, H. Neddermeyer, *Ber. Bunsenges. Phys. Chem.* **99**, 1381–1386 (1995)
45. C. Xu, D.W. Goodman, *Chem. Phys. Lett.* **263**, 13–18 (1996)
46. K. Wong, S. Johansson, B. Kasemo, *Faraday Discuss.* **105**, 237–246 (1996)
47. S. Johansson, K. Wong, V.P. Zhdanov, B. Kasemo, *J. Vac. Sci. Technol.* **A 17**, 297–302 (1999)
48. J. Bosbach, D. Martin, F. Stietz, T. Wenzel, F. Träger, *Appl. Phys. Lett.*, 3 May (1999)
49. V. Matolín, M.H. Elyakhloufi, K. Masek, E. Gillet, *Cat. Lett.* **21**, 175–182 (1993)
50. V. Matolín, K. Mašek, M.H. Elyakhloufi, E. Gillet, *J. Catal.* **143**, 492–498 (1993)
51. V. Nehasil, I. Stará, V. Matolín, *Surf. Sci.* **331/333**, 105–109 (1995)
52. G. Ertl, H.-J. Freund, *Physics Today*, January, p.32–38 (1999)
53. L. Piccolo, C. Becker, C. Henry, *Eur. J. Phys.* in press (1999)
54. C. Becker, C. Henry, *Surf. Sci.* **352–354**, 457–462 (1996)
55. M. Valden, X. Lai, D.W. Goodman, *Science* **281**, 1647–1650 (1998)
56. M. Haruta, *Catal. Today* **36**, 153–166 (1997)
57. H. Huber, D. McIntosh, G.A. Ozin, *Inorg. Chem.* **16**, 975–979 (1977)
58. M. Haruta et al. *J. Catal.* **144**, 175–192 (1993)
59. G.R. Bamwenda, S. Tsubota, T. Nakamura, M. Haruta, *Catal. Lett.* **44**, 83–87 (1997)
60. F. Vanolli, U. Heiz, W.-D. Schneider, *Surf. Sci.* **414**, 261–270 (1998)
61. S.E. Deutsch, G. Mestl, H. Knoetinger, B.C. Gates, *J. Phys. Chem.* **B 97**, 1374–1384 (1997)
62. A. Zhao, B.C. Gates, *J. Am. Chem. Soc.* **118**, 2458–2469 (1996)

63. O. Alexeev, B.C. Gates, *J. Catal.* **176**, 310–320 (1998)
64. Z. Xu, F.S. Xiao, S.K. Purnell, O. Alexeev, S. Kawi, S.E. Deutsch, B. C. Gates, *Nature* **372**, 346–348 (1994)
65. S.A. Deutsch, F.S. Xiao, B.C. Gates, *J. Catal.* **170**, 161–167 (1997)
66. S. Chen, R.S. Ingram, M.J. Hostetler, J.J. Pietron, R.W. Murray, G. Schaaff, J.T. Khoury, M.M. Alvarez, R.L. Whetten, *Science* **280**, 2098–2101 and refs. therein (1998)
67. T. Leisner, C. Rosche, S. Wolf, F. Granzer, L. Wöste, *Surf. Rev. Lett.* **3**, 1105–1108 (1996)
68. P. Fayet, F. Granzer, G. Hegenbart, E. Moisar, B. Pischel, L. Wöste, *Phys. Rev. Lett.* **55**, 3002–3004 (1985)
69. P. Fayet, J.P. Wolf, L. Wöste, *Phys. Rev. B* **33**, 6792–6797 (1986)
70. U. Heiz, F. Vanolli, L. Trento, W.-D. Schneider, *Rev. Sci. Instrum.* **68**, 1986–1994 (1997)
71. I. Yudanov, G. Pacchioni, K. Neyman, N. Rösch, *J. Phys. Chem.* **101**, 2786–2792 (1997)
72. H.-P. Cheng, U. Landman, *J. Phys. Chem.* **98**, 3527–3537 (1994)
73. K. Bromann, C. Felix, H. Brune, W. Harbich, R. Monot, J. Buttet, K. Kern, *Science* **274**, 956–958 (1996)
74. S.H. Yang, D.H. Drabold, J.B. Adams, P. Ordejon, K. Glassford, *J. Phys. Condens. Matter* **9**, L39–L45 (1997)
75. A. Sachdev, R.I. Masri, J.B. Adams, *Z. Phys.* **D26**, 310–312 (1993)
76. M.-H. Schaffner, F. Patthey, W.-D. Schneider, L.G.M. Pettersson, *Surf. Sci.* **450**, 402–404 (1998)
77. M.C. Wu, J.S. Corneille, C.A. Estrada, J.-W. He, D.W. Goodman, *Chem. Phys. Lett.* **182**, 472–478 (1991)
78. A. Rar, T. Matsushima, *Surf. Sci.* **318**, 89–96 (1994)
79. F. Zaera, E. Kollin, J.L. Gland, *Chem. Phys. Lett.* **121**, 464–468 (1985)
80. U. Heiz, F. Vanolli, A. Sanchez, W.-D. Schneider, *J. Am. Chem. Soc.* **120**, 9668–9671 (1998)
81. U. Heiz, *Appl. Phys.* **A67**, 621–626 (1998)
82. F. Vanolli, U. Heiz, W.-D. Schneider, *Chem. Phys. Lett.* **277**, 527–531 (1997)
83. S. Vajda, S. Wolf, T. Leisner, U. Busolt, L. Wöste, *J. Chem. Phys.* **107**, 3492–3497 (1997)
84. J. F. Hamilton, P.C. Logel, *Photogr. Sci. Eng.* **18**, 507–512 (1974)
85. W.J. Reinders, *J. Phys. Chem.* **38**, 783–795 (1934)
86. I. Konstantinov, J. Malinowski, *J. Photogr. Sci.* **23**, 145–151 (1973)
87. E. Moisar, F. Granzer, D. Dautrich, E. Palm, *J. Photogr. Sci.* **28**, 71–81 (1980)
88. B.C. Gates, *Chem. Rev.* **95**, 511–522 (1995)
89. P.M. Holmblad, D.R. Rainer, D.W. Goodman, *J. Phys. Chem. B* **101**, 8883–8886 (1997)
90. G. Pacchioni, R.M. Lambert, *Surf. Sci.* **304**, 208–222 (1994)
91. R.M. Ormerod, R.M. Lambert, *J. Phys. Chem.* **96**, 8111–8116 (1992)
92. S. Abbet, A. Sanchez, U. Heiz, W.-D. Schneider, A.M. Ferrari, G. Pacchioni, N. Rösch, *J. Am. Chem. Soc.*, in press (1999)
93. U. Heiz, A. Sanchez, S. Abbet, W.-D. Schneider, *J. Am. Chem. Soc.* **121**, 3214–3217 (1999)
94. T. Zambelli, J.V. Barth, J. Winterlin, G. Ertl, *Nature* **390**, 495–497 (1997)
95. A.W.E. Chen, R. Hoffmann, W. Ho, *Langmuir* **8**, 1111–1119 (1992)

96. B. Hammer, O.H. Nielsen, J.K. Nørskov, *Catal. Lett.* **46**, 31–35 (1997)
97. R. Hoffman, *Solids and Surfaces: A Chemist's View of Bonding in Extended Structures* (VCH Verlagsgesellschaft, GmbH, Weinheim 1988)
98. N. Watari, S. Ohnishi, *J. Chem. Phys.* **106**, 7531–7540 (1997)
99. B. Hammer, J.K. Nørskov, *Nature* **376**, 238–240 (1995)
100. R.M. Watwe, B.E. Spiewak, R.D. Cortright, J.A. Dumesic, *Catal. Lett.* **51**, 139–147 (1998)
101. E. Schumacher, F. Blatter, M. Frey, U. Heiz, U. Röthlisberger, M. Schär, A. Vayloyan, C. Yeretizian, *CHIMIA*, **42**, 357–376 (1988)
102. U. Heiz, A. Vayloyan, E. Schumacher, *J. Phys. Chem.* **100**, 15033–15040 (1996)
103. D.M. Cox, R. Brickman, K. Creegan, A. Kaldor, *Z. Phys.* **D19**, 353–355 (1991)
104. M. Haruta, T. Kobayashi, H. Sano, N. Yamada, *Chem. Lett.* **100**, 405–408 (1987)
105. M. Haruta, T. Kobayashi, S. Iijima, *J. Catal.* **115**, 301–309 (1989)
106. U. Heiz, A. Sanchez, S. Abbet, W.-D. Schneider, *Eur. J. Phys. D* **9**, in press (1999)
107. A. Sanchez, S. Abbet, U. Heiz, W.-D. Schneider, H. Häkkinen, U. Landman,
108. G.A. Somorjai, *J. Mol. Catal. A* **107**, 39–53 (1996)
109. A. Berko, G. Menesi, J. Solymosi, *J. Phys. Chem.* **100**, 17732–17734 (1996)
110. V.P. Zhdanov, B. Kasemo, *Phys. Rev. Lett.* **81**, 2482–2485 (1998)

9 Application of Clusters to the Fabrication of Silicon Nanostructures

Katrin Seeger and Richard E. Palmer

9.1 Prospects for the Application of Clusters in Nanotechnology

The field of cluster physics is a relatively young area of science which developed because of the wide range of interesting properties which clusters exhibit. After a period in which these fundamental properties were studied intensively, the possible technological application areas of clusters are now the subject of increased attention. It is difficult to present a complete picture of all these areas, so this chapter aims first to give a brief overview of some applications of clusters in nanotechnology and then, by way of illustration, to discuss in more detail some processes in which metal clusters are utilised to fabricate silicon nanostructures.

Generally, the role of atomic clusters in nanotechnology can be seen as twofold. On the one hand, clusters can be used as *building blocks*; for example, to assemble structures such as wires or porous films. On the other hand, one can also see clusters as possible *tools* in fabrication processes, e.g. as nanometre-scale masks in a plasma etching process (as discussed in detail below), as the etchant itself or as dopants in semiconductors.

9.1.1 Clusters as Building Blocks

Looking first at clusters as building blocks, we have to remember that clusters have properties which can change dramatically with their size, such as their electronic (see Chaps. 1 and 5) and magnetic properties (see Chap. 7) or chemical reactivity (see Chap. 8). Besides that, it is possible to produce clusters from almost any sort of material in a wide variety of sizes, presenting the prospect of "tuning" these properties for different applications.

A typical example is the fabrication of thin films from size-selected clusters, which have completely different properties from films grown by atomic deposition. Depending on the deposition energy the initial cluster morphology will or will not be preserved. Haberland et al. [1] developed a high energy cluster deposition process which allows the production of smooth films which contain very few pinholes and have properties which are not attainable with conventional deposition methods (see Chap. 4). This method makes it

possible to coat, for example, untreated teflon with a metal film, which is impossible with conventional sputtering or evaporation methods. The cluster deposition method could also find application in the fabrication of integrated circuits where the formation of micrometre sized contact holes appears to be a problem. These holes can be filled by cluster deposition at relatively low temperatures, which are necessary to preserve the delicate silicon structures.

Perez et al. [2], who are researching the low energy deposition of clusters, create films with variable physical properties, such as electrical conductivity, optical absorption and hardness. They are able to modify these properties for carbon cluster films from graphitic to diamond-like by changing the size of deposited carbon clusters from 900 atoms to 20 atoms. A film of silicon clusters containing around 50 atoms shows strong luminescence in the red, which is not seen from amorphous or crystalline silicon. This opens opportunities for the application of silicon in opto-electronics.

The influence of the cluster size on the chemical reactivity of clusters is of great interest for the fabrication of sensors and catalysts [3], as the desired properties of the device can be specifically tailored using the appropriately sized clusters (see Chap. 8). A very thorough review of the clusters as model catalysts is given by Henry [4], where he discusses the influence of different parameters, such as substrate, morphology and cluster size. Typical gases studied on supported model catalysts are CO, O₂, H₂ and NO.

A very interesting optical application of clusters was presented by Dirix et al. [5], where silver clusters are used to produce polarisation dependent colour filters. The clusters are embedded in a polymer and have been drawn to form pear-necklace-type arrays of the nanoparticles. The film exhibits a strong colour dependency on the polarisation direction of the incident light. Different colours can also be produced by varying the size of the cluster arrays or the cluster material. The authors point out that these films are potentially useful for the fabrication of LCDs with an enhanced brightness and energy efficiency.

Another field where clusters have started to attract attention is the further miniaturisation of electronic devices [6]. The integration of single electron devices would allow an extreme lowering in power consumption and device sizes [7,8]. As the circuit feature sizes reach the limits for conventional fabrication techniques new methods have to be developed. One possible route is the use of clusters as building blocks for these single electron devices, based on Coulomb blockade [9]. Looking at the conditions to observe Coulomb blockade, we see that the charging energy E_c , necessary to add an electron to the cluster, has to be larger than the thermal energy of the electrons $E_c \gg k_B T$ to avoid thermal fluctuations. The charging energy depends on the capacity of the cluster, $E_c = e^2/2C$ and therefore on the radius $E_c \sim 1/r$. Thus to observe single electron phenomena either very low temperatures or very small clusters have to be used. A typical method of probing these single electron effects is shown in Fig. 9.1 a. The tunnelling current through a passivated cluster is observed

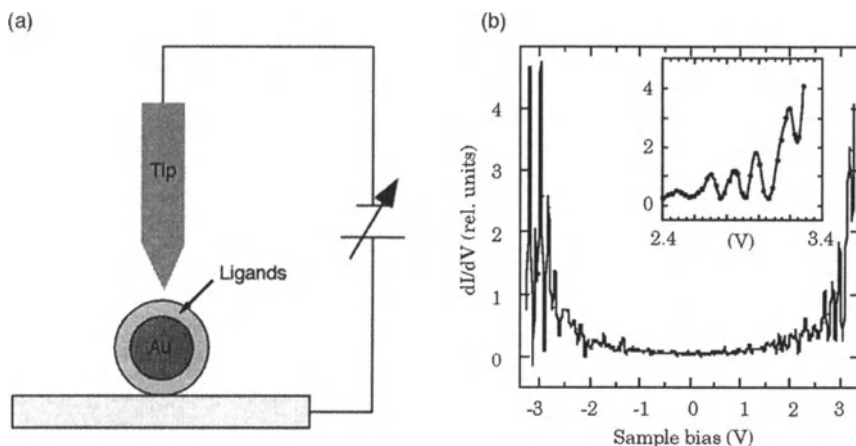


Fig. 9.1. (a) Schematic of the use of a passivated gold cluster as a capacitor. The passivating ligands act as an insulator. (b) Typical dI/dV curve measured between a STM tip and sample across a passivated cluster gold cluster (core size 4.5 nm). The equidistant peaks are proof for a coulomb blockade effect

by addressing the cluster with a Scanning Tunnelling Microscope (STM) tip. The passivation layer acts as an electron tunnelling barrier, allowing electrons to tunnel only at critical voltages, which leads to the formation of Coulomb staircases in the $I - V$ curve. Figure 9.1 b illustrates the staircase effect, as the dI/dV curve shows equidistant peaks. Measurements like the one described above have been performed by many different groups. For example, Andres et al. [10] measured the Coulomb staircase of bare gold clusters (1–2 nm) on a passivated gold surface at room temperature. Chen et al. [11] investigated the influence of the cluster size on the Coulomb staircase experiments and found that the charging undergoes a transition from metal-like double-layer capacity charging to redox-like charging when the core size is reduced.

Other groups are working on the development of real devices, where passivated clusters are deposited between two electrodes and $I - V$ -measurements are performed. One of the main problems here is to create a chain of clusters positioned exactly between these electrodes. Sato et al. [12] developed a chemical method to create short chains of passivated gold clusters. They first create submonolayers by using aminosilane as an adhesion agent and then, after treating the sample with dithiol, deposit additional gold colloidal particles which assemble in short chains. In this way they manage to bridge 30 nm gaps between metal electrodes and observe a Coulomb staircase in the electron transport across the device.

9.1.2 Clusters as Tools

The main body of this chapter will be devoted to a discussion of the role of clusters as tools in nanotechnology, with emphasis, by way of example, on the fabrication of silicon nanostructures. In this work the (metal) clusters act as nanoscale masks for plasma etching of silicon substrates. However, this is not the only way that clusters can be used as tool. For example, Matsuo et al. [13] applied reactive gas phase cluster ions as an etchant to produce nanometre-scale silicon structures. The advantage of cluster ion beams over etching with monomer ions lies in the different characteristics of bombardment. The kinetic energy of the clusters is carried by hundreds of atoms, so the actual impact energy per atom is very low. This allows a low damage processing and also gives a much higher sputter yield, due to multiple collisions between the incoming cluster atoms and the surface atoms. A similar approach was chosen by Gspann [14] who is using ionised cluster beams for mask projective cluster impact lithography. Using clusters of CO_2 and SF_6 allows the microstructuring of various materials, such as natural diamond, silicon and Pyrex glass with very smooth surfaces and steep sidewalls.

As indicated previously, the remainder of this chapter will focus on one particular example of the application of clusters in nanotechnology: the use of clusters as etch mask to fabricate silicon nanostructures. In order to set these novel fabrication processes in context, it is first helpful to understand why the production of nanostructures is desirable, this is discussed in Sect. 9.2.1. Then we give a brief survey of some of the key techniques currently employed in silicon fabrication, describing both, lithographic and plasma etching techniques (Sect. 9.2.2). The new fabrication processes we want to describe are based on cluster films, produced either by growth on the surface or by deposition of clusters grown in the gas or liquid phase (with subsequent size selection as appropriate). Section 9.3.3 reviews methods used to produce ordered arrays of clusters which are grown on the surface at predefined positions. A detailed description of the processes for fabrication of silicon nanostructures, such as pillars and cones, using the cluster films is given in Sect. 9.4.

9.2 Background to the Fabrication of Si Nanostructures

9.2.1 Motivation

Why are silicon nanostructures interesting? Of course, silicon is the most commonly used material in the semiconductor industry, and therefore it enjoys the big advantage that it is relatively inexpensive to produce. However, there is one area in which the use of silicon is severely limited – optoelectronics. Besides some weak IR emission, crystalline silicon is optically inactive because of its indirect band structure. This indirect band gap only allows an electron-hole recombination across the gap when a momentum conserving

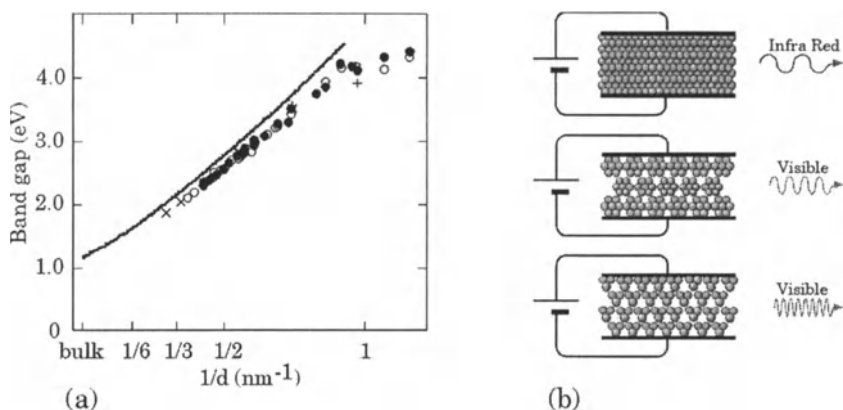


Fig. 9.2. (a) Energy band gap of hydrogen terminated clusters calculated with different techniques: Empirical Tight Binding (*continuous line*) [25,26], Empirical Pseudopotential (\times) [27], Local Density Approximation (\bullet , \circ) [28] and ($+$) [29]. (Taken from [30]). (b) Schematic for the integration of silicon clusters into electronic devices. The generated wavelength depends on the size of the clusters

phonon participates. The result is that the radiative lifetime of crystalline silicon is in the millisecond region, and so non-radiative transitions are more likely to occur.

In 1990 Canham [15] discovered that the optical properties of highly porous silicon, i.e. electrochemical etched crystalline silicon composed of nanometre-scale silicon wires and clusters, are very distinct from those of bulk crystalline silicon. Structures in the nanometre-size range show strong photoluminescence in the visible region at room temperature; later evidence for electrically excited luminescence was also found [16,17]. The reason for the appearance of this effect remains the subject of debate. While many groups support the thesis of a quantum confinement effect [15,18,19], others believe surface effects [20–23] are responsible for producing the visible light emission. A good review of the properties of porous silicon and the possible mechanisms is given by Hamilton [24]. The fact that nanoscale silicon is able to emit light suggests the possibility of replacing the expensive compound semiconductor materials such as GaAs in optoelectronic devices with porous silicon or, more likely, other nanometre-scale silicon structures.

One interesting feature observed from light emitting nanoscale silicon is that the wavelength shifts as the structures get smaller, which is accredited to a band gap widening. Figure 9.2 a shows a diagram of the calculated band gap of Si clusters depending on the confinement parameter $1/d$ (d : cluster diameter) for different theoretical models. As the silicon particles reach the sub-5 nm region a strong widening of the gap appears [31], which leads to a blue shift of the emitted light. Similar behaviour was reported from silicon rods, where the important factor is the nanoscale diameter [31].

Now integration of this effect into optoelectronic devices would be the next aim. Figure 9.2 b illustrates how the light emission effect expected from films of Si clusters might be exploited in such a device. The wavelength of electroluminescence can be varied by using different sized clusters. Instead of clusters it would be possible to use other nanostructures, as is shown by Nassiopoulos et al. [32], who built an electroluminescent device based on silicon nanopillars. In order to produce devices based on nanostructures, methods have to be found to fabricate these structures in a controlled manner.

9.2.2 Experimental Approaches

In microelectronics, the most commonly used technique to produce controlled patterns in silicon structures (and other semiconductors) is photolithography. A subsequent etching step transfers the pattern into the silicon. Photolithography is quite an inexpensive technique which allows a high throughput, ideal for industrial applications. However, patterning in the nanoscale regime is rather difficult, as size limitations are introduced by the wavelength of light. There are numerous techniques such as the use of shorter wavelength light, or phase shift lithography, to improve the resolution in photolithography. IC manufactures are currently working with processes which allow the production of 0.25 μm devices, while the "state of the art" lies at 80 nm [33]. Good reviews of lithographic techniques are given in references [34] and [33].

In order to overcome the resolution limits inherent in photolithography, research is progressing into new methods of lithography. One option is the use of scanning techniques, such as electron beam lithography, which has attracted the attention of the microfabrication community. The small spot of the e-beam, which can be as small as 1 nm [33], allows very fine patterning. But even the resolution of this scanning technique is limited, this time by the resist. Other effects limiting the resolution are proximity effects (scattering of incoming electrons) and backscattering effects in the resist, which leads to linewidth variations. The practical resolution for e-beam lithography lies currently at 10–20 nm. One disadvantage of the scanning techniques is that it is slow compared with photolithography since every part of the pattern has to be exposed serially. Efforts are being made, e.g., in the development of parallel scanning techniques employing more than one beam, to increase the throughput [35].

Other methods of lithography include the use of Scanning Probe Microscopes (SPM) such as the Atomic Force Microscope (AFM) and the Scanning Tunnelling Microscope (STM). These techniques allow the modification or manipulation of material deposited on the surface at the atomic scale, but of course the patterning of a large area with only a single tip will take a considerable time.

An alternative to lithographic techniques is, as mentioned earlier, the possibility to use clusters as etch masks. Compared to the lithographic techniques clusters have the advantage that the size of clusters is not limited.

Thus it is possible to create very small patterns on the surface which allow the fabrication of structures such as nanometre size pillars or cones. We will not go into detail at this point since a discussion of these methods will be given in Sect. 9.4.

Now, after discussing some techniques to produce patterns on a surface, we want to explore the possibility of transferring this 2D pattern into a 3D pattern. Usually this is done by chemical etching. Considering the size of the features in nanofabrication, it is necessary to apply etching techniques which achieve a high directionality in the etching. This can be accomplished in the case of wet chemical etching by exploiting preferential substrate reactivity in certain crystal directions [36]. Unfortunately, it is only possible to apply this technique in very few systems. Thus the development of plasma etching has been a great step forward in device production, because it offers directional etching, as well as cleanliness and compatibility with vacuum processing technology [37]. There are many different plasma etching processes, and here we want to describe only two of the most commonly used types: Reactive Ion Etching (RIE) and Electron Cyclotron Resonance (ECR) etching.

The principle of RIE is to create a plasma from a gas which is able to form ionic species which react chemically with the material to be etched. The typical gases for silicon etching are halogen (i.e. fluorine, chlorine or bromine) based. By combining etch gases, or adding other gases to the etching gas mixture, different effects can be obtained. Good reviews of etch chemistry are given in references [37] and [38]. Figure 9.3 shows a schematic of a typical RIE reactor. It contains one electrode on which the sample is mounted while the reactor walls act as the second, ground electrode. RF power is applied to the electrode, igniting the plasma and inducing a negative DC-bias on the sample electrode (originating from the higher mobility of the electrons compared to the ions). The electrode bias leads to the formation of a plasma sheath at the electrode, which causes the acceleration of ions onto the sample. If the kinetic energy is high enough these impinging ions are able to sputter the surface, assisting the chemical etching process. Reaction products which have a lower vapour pressure, and so do not evaporate immediately, can be removed by this sputtering process, exposing the silicon to the reactive species. At the same time material which is condensed on the side walls of a nanostructure developing in the substrate can not be sputtered because of the directionality of the incoming ions, preventing chemical reactions in the sideways direction. In the case of fluorine based gases, where the etch products are too volatile to condense at room temperature, directed etching requires either that polymer forming gases such as CF_4 or CHF_3 are used [39], or that etching is performed at low temperature in order to condense the reaction products on the side wall surface [40].

One problem with the RIE technique is that the physical sputtering influences the etch selectivity, i.e. the etch rate ratio between the mask material and the underlying (to be etched) material. Therefore the mask material

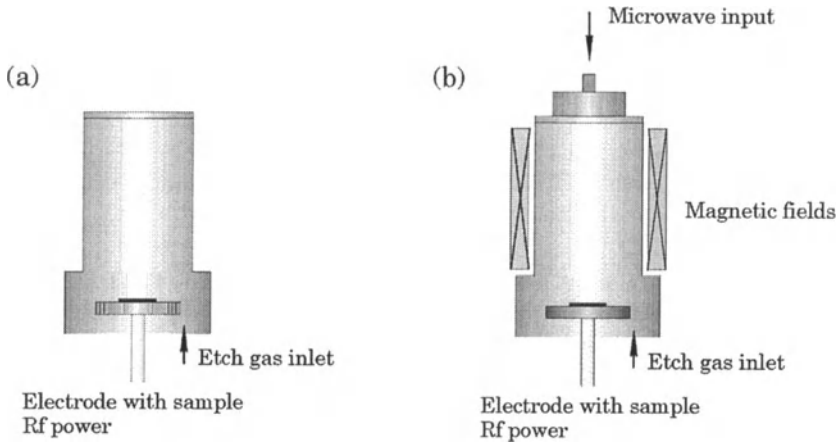


Fig. 9.3. (a) Reactive ion etching (RIE) system. (b) Electron cyclotron resonance (ECR) etching system

should be either strongly resistant to sputtering or thick enough that it endures the etching process. Another disadvantage of the RIE technique is that high pressures (typically 1–30 Pa) are necessary to maintain the plasma, which can lead, for example, to surface roughness. Additionally, the high energy ion bombardment can lead to degradation of the device characteristics, for example, by ion implantation [41].

The ECR etching technique, which has emerged in the last decade, overcomes these problems of RIE etching by allowing independent control over the plasma density and RF power, making it possible to create a higher plasma density at low induced DC bias. This leads to higher etch rates and better control over directionality. Figure 9.3 b shows a schematic of an ECR etching reactor. The features are very similar to those of an RIE reactor, except that microwave power is introduced in addition to the RF power and a magnetic field is applied to the chamber. The static magnetic field induces a cycloidal movement of the electrons. At the same time, microwave power is coupled into the plasma, which is in resonance with the cyclotron movement of the electrons. This resonance effect gives very high energy to the electrons, efficiently increasing the ionisation of the etching gas. Therefore it is possible to work at a much lower pressure with a *higher* plasma density. The application of RF power to the electrode leads, as in RIE etching, to a self bias of the electrode and the formation of a plasma sheath. This independent control of the ion energy and the ion density allows higher etch selectivity and low surface damage during the etching process.

Both techniques, RIE and ECR, have been used to transfer patterns of clusters on a silicon surface into the substrate as described later (Sect. 9.4).

9.3 Production of Cluster Films for Fabrication

In order to exploit atomic clusters in nanofabrication it is necessary to deposit them onto the surface in a controlled way, i.e. important factors, such as shape, size and the position of the clusters should be correctly tailored by the deposition process. There are two different methods of producing cluster films on the surface. One can either grow the clusters (from atoms) directly on the substrate, influencing the position, size and shape by the growth conditions or subsequent treatment (see also Chap. 3). The other possibility is to grow clusters in the gas phase, or in a liquid environment and then deposit them intact onto the substrate. In principle, this process allows the best control over the cluster size distribution, while deposition factors influence the resulting shape (see also Chap. 4). Special techniques also allow the production of organised arrays of clusters, which are very interesting for the production of nanostructures. Although some of the mentioned techniques are partly reviewed more thoroughly in other parts of this book, we want to study it in this section again, from the point of application. Cluster films used for applications in nanofabrication (as they will be described later in Sect. 9.4) should have a 3-dimensional morphology, so they are able to resist the etch plasma. Furthermore we want to influence the density and position of the clusters, to control the position of resulting nanostructures. Thus, some of these different techniques are explained by reviewing the work of different groups. Firstly, we will explore the growth of 3D cluster films on surfaces, then the deposition of size-selected clusters and finally, how to achieve ordered arrays of clusters.

9.3.1 Cluster Growth on Surfaces

The growth of clusters from atoms on surfaces has been studied by many surface science groups, investigating, for example, growth models or chemical reactivity. The techniques used to deposit the atoms, from which the clusters grow, vary; typical methods include thermal evaporation, magnetron sputtering and chemical vapour deposition. The conditions during deposition (e.g. temperature, flux, pressure), the material deposited and the substrate, together influence the growth mode of the film.

The influence of the substrate temperature during atom deposition on the resulting cluster film was, for example, demonstrated by Francis et al. [42]. They investigated the growth of noble metal (Ag, Au) clusters on graphite, deposited by atomic vapour deposition. The deposition of silver, keeping the temperature at 20°C, (deposition of 0.029 ML in 2 s) led to the formation of groups of clusters (typical diameter 10 nm) on the surface as well as lines of clusters along naturally occurring surface steps. By changing the deposition temperature to 165°C (deposition of 0.046 ML in 3 s), it was possible to collect all the material at surface steps, leaving the terraces between them

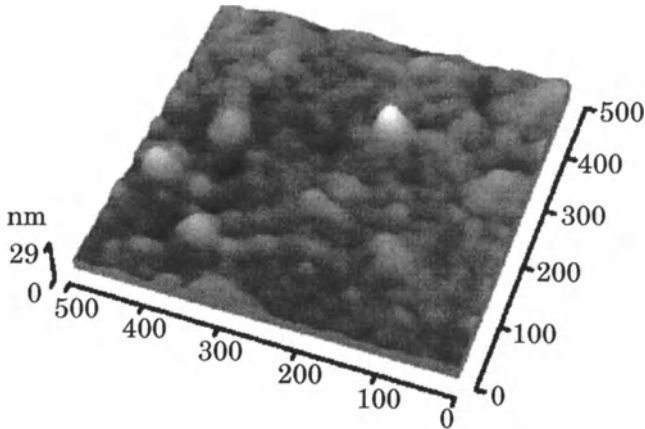


Fig. 9.4. AFM image of a rough silver layer deposited onto a silicon wafer by magnetron sputtering [43]

undecorated. This method allows the production of chains of clusters of order 10 nm diameter on these steps.

The influence of the deposition rate and time as well as the substrate on the cluster film morphology can be seen from the following example, where the deposition of silver onto Si(001) by RF magnetron sputtering was investigated by Je et al. [44]. They found that Ag grains are epitaxial in the initial stages at low sputtering rates (0.22 W/cm^2). As deposition proceeds and the coverage increases the growth mode changes into nonepitaxial 3-dimensional island growth. At higher sputter rates (0.44 W/cm^2), 3D islands form from the outset. They also state that the surface passivation plays an important role in the growth process. Native oxide layers influence the growth mode, leading to 3D islands even at low sputtering rates. Figure 9.4 shows a typical AFM picture of a silver film grown on silicon with a native oxide layer by magnetron sputtering (0.25 W/cm^2). The film thickness is approximately 20 nm. Here the growth is 3D, i.e., the morphology of the film is rough exhibiting silver clusters with a typical diameter of 20 to 40 nm [43]. We will see later that this sort of cluster film has been used as etching mask to fabricate nanostructures in the underlying silicon (see Sect. 9.4.1).

Now we want to look how the atom deposition techniques influence the shape of the clusters grown on the surface. Nguyen et al. [45] compared the growth of aluminium particles on oxidised silicon, when Al atoms were deposited by evaporation and by magnetron sputtering at similar deposition rates. It was found that the particle morphology at low deposition rates (43 \AA/min and 36 \AA/min , respectively) is more spherical in shape for evaporation while flatter nuclei are formed from sputter deposition. This difference can be accounted for by the difference in energy of the incoming Al atoms.

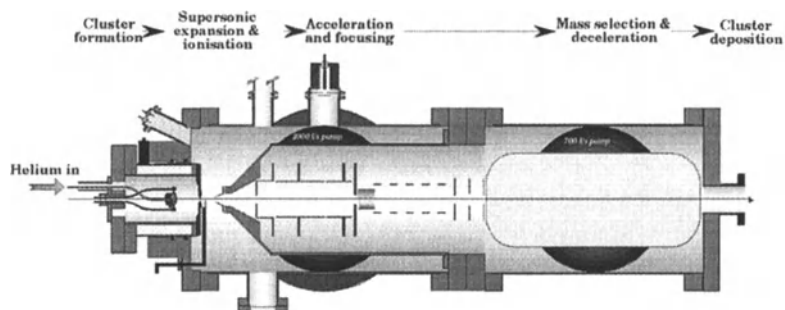
For evaporation thermal deposition energies of ~ 0.1 eV are typical, while for sputter deposition the atoms have energies of 1–2 eV [46].

In summary we can see that it is possible to influence the cluster films by varying the deposition parameters. The temperature influences the mobility of atoms on the surface, thus at higher temperatures atoms diffuse more and are able to form bigger clusters with a lower number density. Clusters are preferentially trapped at nucleation sites, like steps. The mobility is also dependent on the material and underlying substrate. The flux and energy of incoming atoms plays an important role for the film morphology; at a higher flux or lower energy a 3-dimensional cluster film it is more likely to grow.

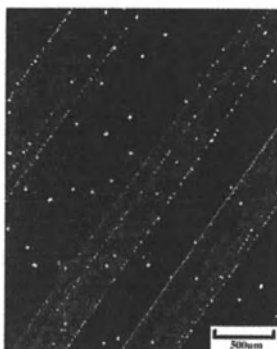
9.3.2 Deposition of Size-Selected Clusters

As demonstrated in the previous section, the detailed deposition parameters as well as the material deposited and the substrate all influence the growth of clusters on surfaces. In order to achieve the best control over the cluster size on the surface, an attractive possibility is to grow the clusters in the gas phase or even in solution prior to depositing them onto the sample, which allows the clusters to be mass (i.e. size) selected before deposition. For the production of clusters in the gas phase, many different cluster sources have been designed [47], see Chap. 1. Here we just want to give a brief description of the gas condensation cluster source [48] which has been used for the experiments described in Sect. 9.4.2. Figure 9.5 a shows a diagram of the source. A metal is thermally evaporated into the flow of a cold inert gas. The vapour becomes supersaturated and condensation of vapour into clusters occurs. The resulting cluster size distribution is broad, and can be influenced by the source parameters, such as evaporation rate, gas pressure or length of the cluster growth region. The clusters are extracted from the condensation chamber through a nozzle into vacuum. They are then ionised by a hot-cathode plasma, so that they can be accelerated and focused into a beam before entering the mass filter. The typical size-selection method employs a quadrupole mass spectrometer [47], which allows the selection of clusters with a small size distribution before deposition of the cluster ion beam onto the sample. For the experiments of Sect. 9.4.2, either a Wien velocity filter or a novel time-of-flight mass filter was employed with the source of Fig. 9.5 a. The deposition energy, which influences the shape and mobility of the clusters after deposition [49], can be modified by applying a voltage to the sample in order to accelerate or decelerate the incoming clusters. In Figure 9.5 b, a scanning electron micrograph of a graphite sample is shown onto which Ag_{400} clusters were deposited at 500 eV. This illustrates an example of the result of cluster deposition with the source in question. At this energy these larger clusters are "soft landed" and are mobile on the surface. This mobility leads to the formation of bigger islands and enhanced attachment of the deposited clusters at step edges. In contrast, Fig. 9.5 c shows a scanning tunnelling micrograph of a Ag_{100} cluster deposited at 2 kV onto graphite.

(a)



(b)



(c)

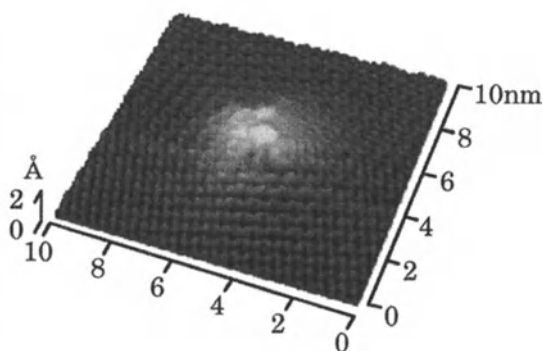


Fig. 9.5. (a) Gas aggregation cluster source [48]. (b) SEM picture of graphite sample with Ag_{400} clusters deposited at 500 eV. The clusters are mobile and can aggregate into bigger islands, and collect atoms along the steps. (c) STM picture of Ag_{100} cluster deposited on graphite with an energy of 2 kV. The cluster is implanted and not able to diffuse across the surface

The cluster, having originally a diameter of ~ 1.1 nm, has now on the surface a diameter of 2 nm. Even though the cluster flattening can be contributed to by STM tip effects, molecular simulations show that after landing on the surface clusters deposited with such high energy become flattened and pinned to the surface [50].

An alternative to the method described above, where bare clusters are deposited on the surface, is the use of passivated clusters. Colloids of metals, such as gold covered with organic passivating ligands are commercially available in sizes up to 100 nm in a narrow size distribution. There are two ways of producing them, either with an aerosol technique or with the soft chemistry technique where they are grown from metal ions reduced at the

oil-water interface in the presence of an alkylthiolate surfactant and a reducing agent [51]. The clusters are covered with a passivation layer which prevents them from direct contact with other particles and from interparticle bonding. The clusters are kept in solution, e.g. in toluene. In order to adsorb the clusters onto the sample, drops of the solution are deposited onto the substrate which should be wetted by the solvent in order to spread the clusters over the surface. The cluster density can be changed by variation of the concentration before deposition and it has been shown that under certain drying conditions the passivated clusters (usually smaller than 10 nm) form an ordered close-packed monolayer on the surface [52].

9.3.3 Organised Arrays of Clusters

For the application of clusters in nanotechnology, ordered patterns of clusters are desirable. In general, neither the growth of clusters on the surface, nor the deposition of complete clusters from the gas phase, permit precise control over the positions of the clusters on the surface. Thus it is desirable to develop new methods of controlling the arrangement of the clusters.

As mentioned above, many research groups are currently working on the deposition of passivated clusters from solution, which under certain conditions assemble themselves into ordered structures, as shown, for example, by Whetten et al. [51]. They report the assembly of gold nanocrystals into a superlattice, characterised by long range translational and orientational order (in both two and three dimensions). Wang [52] presents a general analysis of the structure of such "nanocrystal superlattices", describing 2D and 3D assemblies of the nanoparticles and analysing stacking faults and interparticle bonds. Ohara et al. [53] observed the formation of a sub-micrometre, ring-like superlattice of passivated silver particles, when depositing an organic solution containing the clusters onto solid carbon. These effects are accounted for by the evaporation of the solvent, during which holes open as the evaporation progresses, pushing particles along the receding rim into a ring-shape feature. This shows that passivated clusters are able to produce regular arrays which may be utilised for fabrication processes.

The drop deposition of passivated clusters allows the production of ordered patterns on the surface, but does not allow a predefinition of the area where the patterns are. Vossmeier et al. [54] reported the preferential adsorption of passivated nanoparticles within optically predefined areas. After treating an amino-functionalised silicon or glass surface with a carboxyl acid group, the sample was exposed to light through a mask, creating a pattern of free and protected amino groups. The deposition of amine-stabilised Au particles leads to an exchange of particle ligands with exposed free amino groups, and thus Au particles assemble only in areas previously exposed by light.

Besides predefining the area in which the passivated clusters adsorb it is possible to manipulate the position of clusters after deposition with SPM

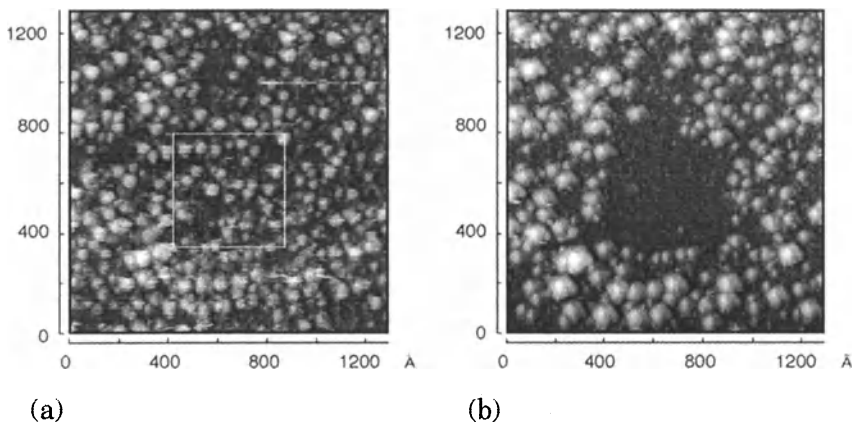


Fig. 9.6. (a) Passivated gold clusters on graphite imaged in the STM at 30 pA and -1.5 V. The marked area was then scanned twice at 30 nA, -15 V leaving (b) a cleared square on the sample [55]

techniques, as described in Sect. 9.2.2. Durston et al. [55] demonstrated the manipulation of passivated gold clusters on graphite. Two scanning tunnelling micrographs of the cluster layer before and after manipulation are shown in Fig. 9.6. After imaging the clusters with an STM at a voltage of -1.5 V and a tunnelling current of 30 pA, the marked region was afterwards scanned twice at -15 V and 30 nA. The STM tip removed the clusters from this area leaving a cleared square in this region. This, of course, only demonstrates the possibility of manipulating the position of the clusters; more complicated patterns could be achieved with a considerable time effort.

Bretzger et al. [56] showed that it is possible to deposit atoms in a periodic structure by using forces induced by the interaction with photons. Chromium atoms are thermally evaporated, laser cooled and then sent through a standing laser field before deposition onto a sample. The neutral atoms interfere with the optical field, leading to a two dimensional chromium structure on the sample surface. Dependent on the laser frequency, chromium dots are formed at points of maximum or minimum light intensity. Chromium features with approximately 100 nm width could be produced with this method.

Another method of masking the sample, which has been termed "Natural Lithography" by Deckman and Dunsmuir [57], employs spherical colloidal polymer particles as lithographic masks. These particles, which are commercially available in sizes from 50 nm to 30 μm [58] dissolved in water, are known to assemble themselves in a well ordered, densely packed array on appropriate substrates. The balls can then be used as deposition masks [57] (or indeed directly as etching masks [59]). After evaporation of material onto the masked surface, and subsequent dissolution (or cleaving) of the balls from the surface, hexagonal patterns of triangular dots remain on the surface. Single crystalline monolayers of polymer balls can be produced by drop deposition

onto the sample followed by very careful evaporation of the water. Different drying methods are reviewed in [60]. Hulteen et al. [61] add a surfactant to the solution, and spin coat the balls onto the surface, in order to achieve large areas of monolayers (ML) or double layers (DL), depending on the particle concentration. Since the wettability of the solution and smoothness of the sample surface plays an important role in successfully achieving a stacking fault free ML, a more flexible way of producing the masks has been developed by Burmeister et al. [62]. They show that it is possible to produce a ML of the colloids on glass slides and, after annealing, to float off the film in order to transfer it onto any other substrate for use as a lithographic mask.

9.4 Application of Metal Clusters as Plasma Etching Masks

In the following section we describe examples of the application of clusters in the production of nanometre size silicon pillars and cones, where the clusters are used as etch masks. The clusters used have been produced in two different ways. In the first case, Sect. 9.4.1, cluster films have been grown on the surface by magnetron sputter deposition, which then are used as masks in a RIE process, leading to the formation of silicon pillars or cones, depending on the etching conditions. In the second case, Sect. 9.4.2, clusters have been deposited after size selection onto the sample where they act as plasma etching masks to produce silicon pillars. These examples illustrate how different cluster growing methods can be employed for the production of nanostructures. Finally we will review two methods to create ordered arrays of silicon pillars, Sect. 9.4.3.

9.4.1 Fabrication of Silicon Pillars and Cones using Cluster Films Grown on the Surface

In this section we will consider a process which produces both *cones* and *pillars* of silicon, utilising cluster films grown on the silicon surface by magnetron sputter deposition. The samples are etched with reactive ion etching (RIE), employing a 1:1 mixture SF₆ and CF₄ (total flow rate 50 sccm). While SF₆ is known to produce isotropic etching, CF₄ leads to polymer formation. A mixture of these two gases thus allows anisotropic etching, because polymers are deposited on the side walls of the silicon structures, preventing undercut. The pressure is 6 mTorr and the temperature of the sample is kept at 10°C.

Figure 9.7 shows a schematic of the whole fabrication process. A silver film is deposited onto a silicon (111) wafer by magnetron sputtering. Silver is known to grow as three dimensional islands rather than layer by layer at higher coverages (see Sect. 9.3.1). This leads to the formation of a rough film (Fig. 9.7 a), consisting of clusters with typical diameters of 20 to 40 nm (as demonstrated by the AFM image of Fig. 9.4). The sample is then etched with

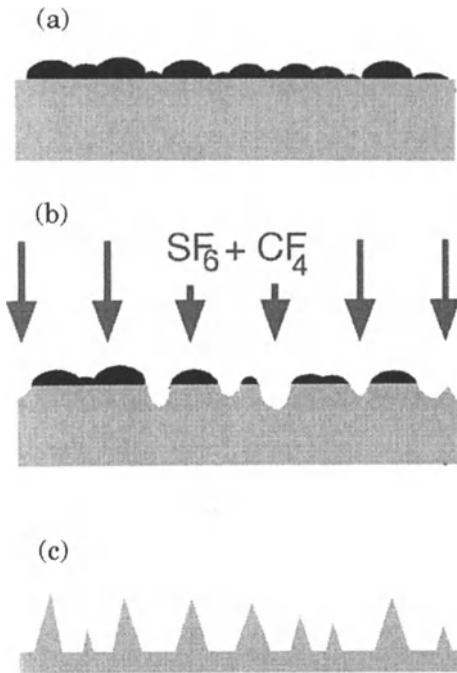


Fig. 9.7. Schematic of the fabrication process for silicon cones. (a) A rough silver film is formed by sputter deposition. (b) RIE etching sputters the silver film, exposing the underlying silicon to the reactive gas. (c) After the etching process silicon cones remain on the surface [43]

the RIE process described above. The ions start to sputter the silver film, leaving separated islands on the surface and exposing other areas of the silicon surface to the reactive ions. This shows why it is important to have a film of 3D clusters rather than a smooth metal film, allowing the clusters to resist the etching longer than the thinner parts. Chemical etching of the silicon in areas where the silver has been sputtered off leads to the formation of crater-like structures in the surface, Fig. 9.7 b. As the etching process progresses, the silver islands reduce in size by sputtering, exposing more of the substrate to the etching gas, which leads to the formation of silicon cones, Fig. 9.7 c. If the silver islands are completely sputtered off, the tips of the cones are etched away, leaving a featureless sample surface without structures, so it is important to stop the etching at the right time.

Variation of the applied RF power has quite a dramatic effect on the resulting silicon structures. Figure 9.8 shows scanning electron micrographs of samples etched at 200 W, 150 W and 100 W (Fig. 9.8 a–c, respectively). At 200 W cones are formed with a wide apex angle, α , but the cones produced at 150 W have much steeper side walls. At 100 W pillars with straight walls are formed, still having silver clusters on top. An analysis of the angle enclosed by the side walls is shown in Fig. 9.8 d. The distribution of cone angles of the structures formed at 120 W, 150 W and 200 W are displayed. This graph shows clearly how the cone angle distribution shifts to larger values for higher etching powers. At 120 W typical angles are between 4° and 28° , while at

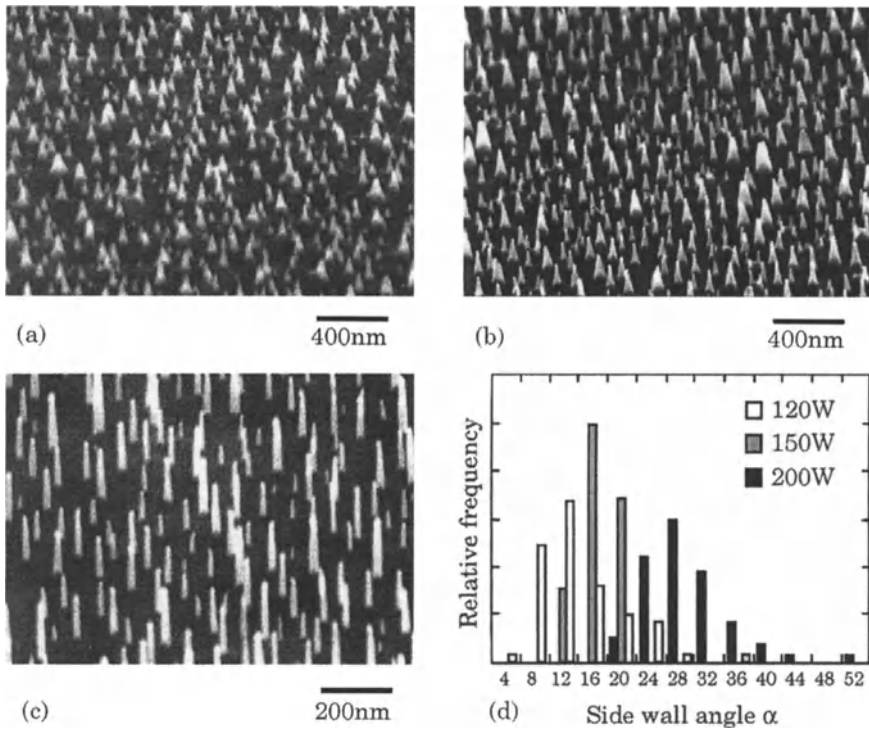


Fig. 9.8. Scanning electron micrograph of samples after 2 min etching at (a) 200 W, (b) 150 W and (c) 100 W RF power, and (d) distribution of apex angle of cones for various etching powers [43]

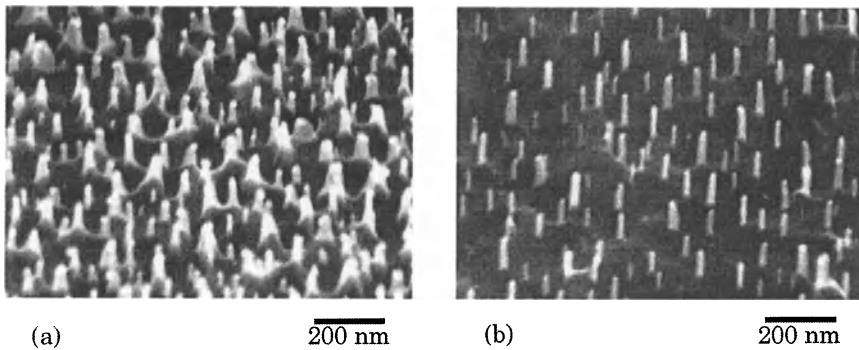


Fig. 9.9. Silicon pillars formed after an etch duration of (a) 2 min and (b) 2 minutes 45 seconds at 100 W [43]

200 W the angles lie between 20° and 44° . This effect can be explained by the relative speeds of the sputtering of the silver film and of the chemical etching of the silicon. At 200 W the islands are sputtered off very fast, which leads to a continuously shrinking etching mask, i.e., an ever smaller part of

the surface is protected, leading to a conical shape. At a power of 100 W the silver film is sputtered very slowly, so that the etching mask more or less retains the same size; thus the silicon is etched straight down, leading to formation of pillars not cones.

The development of the etching process was explored through experiments conducted with a low etching power of 100 W as a function of etching time. Figure 9.9 shows scanning electron micrographs of samples etched for (a) 2 min and for (b) 2 minutes 45 seconds. After 2 minutes etching time, the pillars have typical diameters of 20–35 nm, which can be related to the size of the silver clusters formed after magnetron sputter deposition (see Fig. 9.4). The typical height for this pillars is 60–120 nm. Increasing the etching time to 2 minutes 45 seconds leads to much thinner pillars with typical diameter of 10–25 nm (the smallest pillars are 5 nm in diameter), and a broad height distribution of 100–220 nm. At the same time, the pillar density of the pillars is much lower, i.e., some of the pillars have been completely etched away. This leads to the conclusion that a slow sideways etching takes place; pillars are eventually etched away from the side.

One major problem with the process described in this section is the non-uniformity of the resulting silicon nanostructures. Therefore it is desirable to use a more uniform cluster film, i.e. size-selected clusters. A process utilising size-selected clusters for the production of silicon pillars will be described in the following section.

9.4.2 Production of Silicon Pillars Using Cluster Beam Deposition

The clusters used in the next process we want to describe have been produced by the gas aggregation method. These clusters, which are size-selected prior deposition, act during the etching process as nucleation sites for the condensation of reaction products, which then act as efficient etching masks. It is possible to produce sub-10 nm pillars with this process [63]. A schematic of the formation process is shown in Fig. 9.10. After the deposition of clusters onto a silicon wafer, the sample is etched in an Electron Cyclotron Resonance (ECR) etching process with SF_6 at -130°C . During the etching process etching products such as Si_xF_y or S_xF_y condense around the clusters, protecting the clusters and the underlying silicon while the unprotected silicon is being etched. After an etching time of around 1 min pillars of approximate diameter 10 nm are formed. The temperature of the sample is very crucial for this process; it has to be very close -130°C . Changing the sample temperature to -120°C or -140°C prevents pillar formation, which supports the thesis of nucleation of the etching products; at a higher temperature no condensation occurs, while at a lower temperature the condensation happens all over the sample, protecting the whole surface from etching. The etching was performed at a pressure of 1.4×10^{-4} torr and a flow rate of 12.5 sccm.

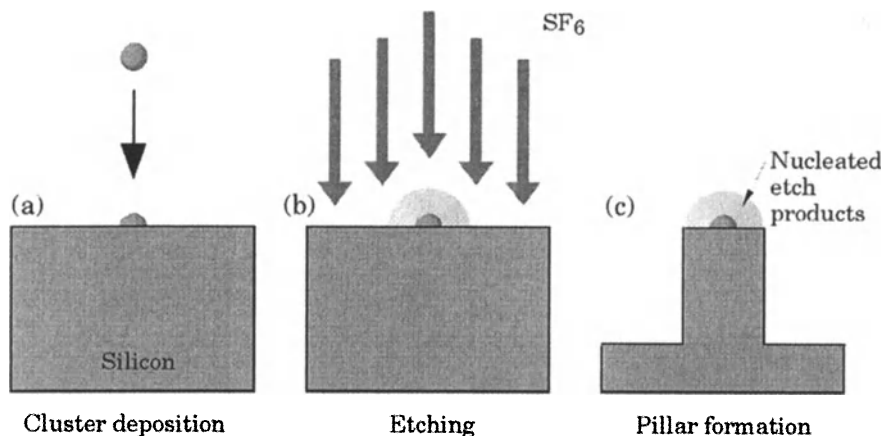


Fig. 9.10. Schematic of silicon pillar fabrication. After the deposition of size-selected clusters (a), the sample is etched in an ECR etching process. The clusters act as nucleation sites for etch products, forming a protective etching mask on top of the clusters while unprotected areas are isotropically etched (b). This leads to the formation of silicon pillars (c) [64]

The microwave power was kept at 250 W while an RF power of 10 W was applied to the sample.

In order to explore the influence of cluster sizes and material on the formation process different experiments were performed. Figure 9.11 shows scanning electron micrographs of pillars formed after deposition of size-selected silver clusters in the size range 200 to 600 ($\pm 10\%$) atoms per cluster. The clusters were produced with the gas aggregation cluster source described in Sect. 9.3.2. In Fig. 9.11 a, etching of the sample with 200 atom clusters does not lead to any pillar formation. For samples with 300 atom clusters, Fig. 9.11 b, some pillars are formed (note that the pillar diameter, ~ 17 nm, is significantly larger than the cluster diameter, ~ 2 –3 nm; see below). As the cluster size increases to 400 atoms, Fig. 9.11 c, the density of the pillars increases too. For cluster sizes of 600 atoms, Fig. 9.11 d, and bigger, the pillar density is approximately equal to the density of deposited clusters. A graphical representation of this behaviour is also displayed in Fig. 9.12 a, which shows a plot of the pillar density versus the cluster size. It also shows the initial cluster density, which was 3×10^{10} clusters cm^{-2} for these samples. The increasing effect of pillar formation can be explained by the process of mask condensation. On this view, in order to produce a stable mask by nucleation of the etch products, the clusters need to have a minimum size. A possible explanation is that clusters with a size below 300 atoms are etched away before stable etching masks have time to form. Figure 9.12 b displays the distribution of pillar diameters against cluster size, and shows that the cluster size has little influence on the pillar diameter. This effect can also be

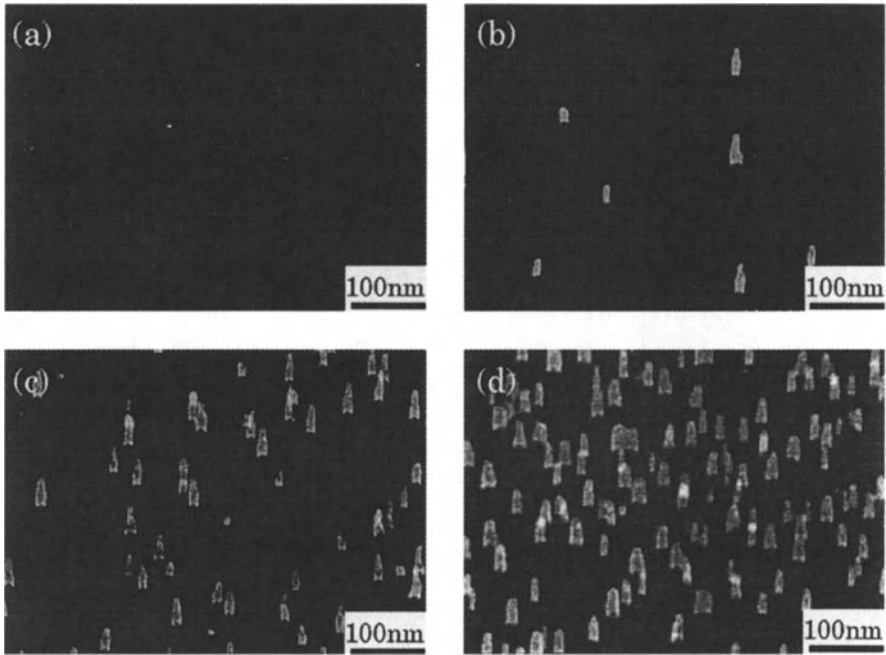


Fig. 9.11. Silicon samples etched after deposition of size-selected clusters of (a) 200 atoms, (b) 300 atoms, (c) 400 atoms and (d) 600 atoms [65]

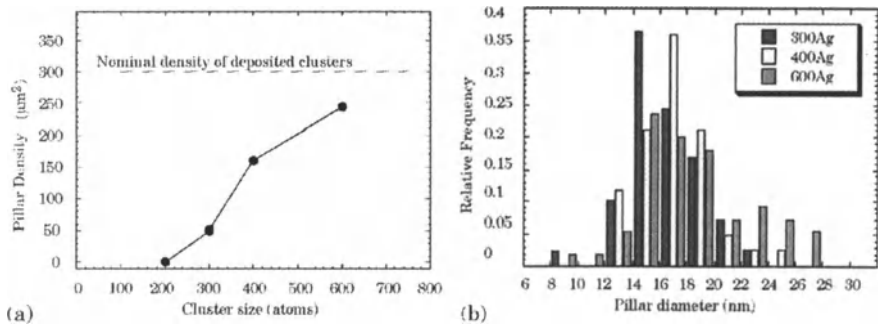


Fig. 9.12. (a) Pillar density after etching versus cluster size. The density of originally deposited clusters is marked with a *dashed line*. (b) The diameter of the pillars is independent of the cluster size

assigned to the mask formation process. Since the pillars have a diameter of around 17 nm, the masks must be much bigger than the original clusters, which have a diameter of 2 to 3 nm. This suggests that the mask size does not depend on the cluster size, hence, the resulting pillars have the same diameter for all cluster sizes.

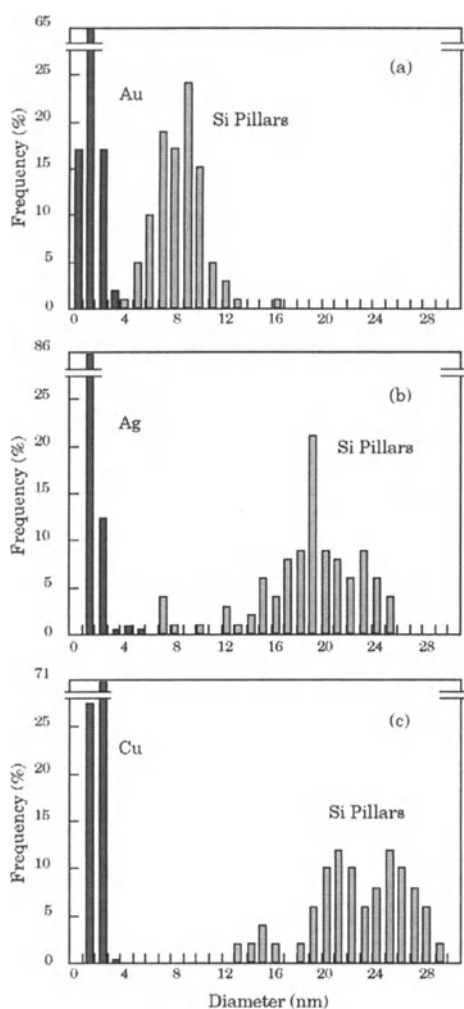


Fig. 9.13. Size distribution of deposited clusters *black bars* and the diameters of the fabricated pillars *grey bars* for (a) Au, (b) Ag and (c) Cu clusters [66]

In addition to the cluster size, the influence of the cluster material was also investigated. Clusters of gold, silver and copper atoms, this time produced by the vapour condensation method but without mass selection, were used as nucleation sites for the etching masks. Figure 9.13 shows the size distributions of clusters deposited, obtained from TEM studies, and the related diameter of the pillars formed from those clusters, from SEM studies. The diameters of the different clusters were similar, lying between 2 and 4 nm, but the diameters of the pillars formed differ significantly (again, the pillars are significantly bigger than the original clusters). For gold clusters an average pillar diameter of 9 nm was achieved, while for silver the value was 19 nm. Pillars formed with copper clusters as the nucleation sites for mask formation have an average diameter of 24 nm. A possible explanation for the size effect would centre

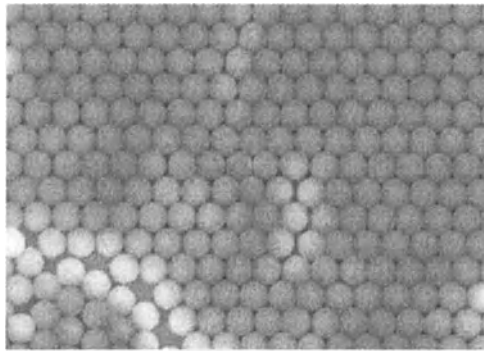
on the different chemical reactivity of the clusters towards S and F. The condensation of the reaction products seems to be more efficient in the case of copper and silver clusters than gold, leading to larger etching masks and hence to pillars of increased diameter. This result shows that it is possible to control the pillar size by choosing the cluster material.

A different method to produce pillars from size-selected clusters has been reported by Lewis et al. [67], who used gold colloidal particles as etch masks. The clusters were deposited onto the sample by submerging the pretreated sample into the solution containing the clusters. The cluster density could be varied by variation of the time the sample spent in the solution. The sample then was etched with a RIE process, using SiCl_4 as etching gas (flow rate: 20 sccm, pressure: 20 mtorr, RF power: 0.42 W/cm^2). The etching time and the colloid diameter influences the resulting pillars height and diameter. Colloids of 15 nm diameter were used to produce pillars of up to 80 nm height (diameter $<10 \text{ nm}$). Increasing the etching time leads to nonuniformity in pillar shapes, because eventually the cluster material will be sputtered away. The shape of the silicon pillars was also varied into a more conical form by dry oxidation and a subsequent oxide strip. The silicon tips formed show diameters of $\leq 5 \text{ nm}$.

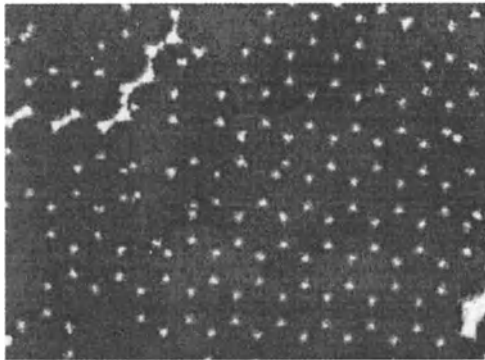
9.4.3 Ordered Arrays of Silicon Pillars

Finally, we want to review two methods to create ordered patterns of clusters which then are used to create ordered arrays of pillars. In Sect. 9.3.3, different processes were described which allow to organise clusters into arrays. First we want to demonstrate the application of self-assembled rafts of polymer balls as template for the deposition of etch masks. Figure 9.14 illustrates the different stages in the process. Fig. 9.14 a shows a scanning electron micrograph of a silicon sample covered with self-assembled polymer balls of size 500 nm. The solution containing the balls was dropped onto the sample and then dried slowly. The balls arrange themselves in close packed hexagonal patterns. Then silver is sputtered onto the sample, reaching the silicon surface only in the gaps between the balls. After dissolving the balls in chloroform in an ultrasonic bath, hexagonal arrays of silver clusters are left on the surface, as shown in Fig. 9.14 b. The sample is subsequently etched with an RIE process, as described in Sect. 9.4.1 at 100 W for 2 minutes 45 seconds. The result is displayed in Fig. 9.14 c. Regular hexagonal arrays of pillars are formed on the sample with a mean diameters of 35 nm and a height of 500 nm.

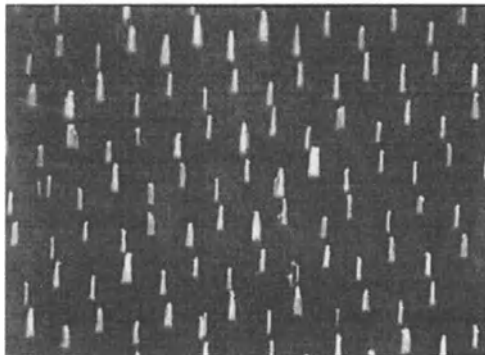
Tada et al. [68] demonstrate a different method to fabricate regular arrays of pillars. They pattern a sample with e-beam lithography, creating an array of 30 nm holes in the e-beam resist. Then metal atoms are deposited, forming clusters of a few nm in these small holes. After lifting off the resist, ordered arrays of nanoclusters remain on the sample, which then can be etched with the ECR etching technique described in Sect. 9.4.2. The process has been



(a)

1.5 μm 

(b)

1 μm 

(c)

500nm

Fig. 9.14. Fabrication of ordered arrays of pillars. (a) Polymer balls of 500 nm diameter are deposited onto the silicon sample and dried slowly. (b) Sputter deposition of silver and subsequent removal of the balls leads to a hexagonal patterning of silver on the surface. (c) Ordered arrays of pillars are formed after RIE etching [69]

tested with clusters of Au, Ag and Fe, which leads to ordered arrays of silicon nanopillars with dimensions depending on the cluster material as described earlier. Typical dimensions for pillars formed for example from Au clusters are 70 nm in height and 10 nm in diameter.

9.5 Summary

In this chapter we have discussed the application of clusters in nanotechnology, with emphasis on a specific illustration – the application of clusters as "tools" in the well-controlled fabrication of silicon nanostructures. To set these new developments in context, the advantages and disadvantages of conventional fabrication techniques have also been discussed. We have considered a range of techniques to produce cluster films for fabrication purposes, which meet the requirement to create a cluster film with a strongly 3-dimensional morphology. Specific examples of nanofabrication with cluster films have centred on the recent production of nanoscale silicon pillars and cones by dry plasma etching. Cluster films, grown on the surface by magnetron sputtering, can be utilised as etch masks, taking advantage of the rough morphology of the film. Size-selected clusters, deposited from the gas phase, can be used as nucleation sites for the condensation of etch masks, and allow the production of silicon pillars of 10 to 20 nm diameter. Similarly, colloidal gold particles, deposited from solution, can again be employed to fabricate silicon nanopillars by plasma etching. The creation of a hexagonal template on the sample surface by deposition of self-assembling polymer nanospheres, followed by magnetron sputter deposition of silver, creates hexagonal patterns of silver clusters on the surface, which can be used to fabricate ordered arrays of silicon pillars. The combination of e-beam lithography and growth of clusters allows the formation of arbitrary patterns of silicon nanostructures. These examples considered clearly demonstrate the advantage of clusters, and in particular of size-selected clusters, in nanofabrication.

The field of nanofabrication is, of course, only one of a variety of possible application areas in which clusters are the subject of growing interest. Indeed, the unique, size-dependent properties of clusters provide a host of new technological opportunities in diverse fields, ranging from optics, electronics and magnetics to catalysis and gas sensing. A considerable body for further research will need to be developed to set these technological development on a sound scientific footing.

References

1. H. Haberland, M. Moseler, Y. Qiang, O. Rattunde, Y. Thurner, and Th. Reiners. In Proc. of Int. Conf. on Beam Processing of Adv. Mat. (1995)
2. A. Perez, P. Melinon, V. Dupuis, P. Jensen, B. Prevel, J. Tuaille, L. Bardotti, C. Martet, M. Treilleux, M. Broyer, M. Pellarin, J.L. Vaille, B. Palpant, and J. Lerme. *J. Phys. D* **30**, 709 (1997)
3. U. Heiz, F. Vanolli, A. Sanchez, and W.D. Schneider. *J. Am. Chem. Soc.* **120**, 9668 (1998)
4. C.R. Henry. *Surf. Sci. Reports* **31**, 231 (1998)
5. Y. Dirix, C. Bastiaansen, W. Caseri, and P. Smith. *Adv. Mater.* **11**, 223 (1999)
6. W. Prost, F.E Kruis, F. Otten, K. Nielsch, B. Rellinghaus, U. Auer, A. Peled, E.F. Wassermann, H. Fissan, and F.J. Tegude. *Microelectr. Eng.* **42**, 535 (1998)

7. R.A. Smith and H. Ahmend. *J. Appl. Phys.* **81**, 2699 (1997)
8. D. Tsoukalas, P. Normand, C. Aidinis, E. Kapetanakis, and P. Argitis. *Microelectr. Eng.* **41**, 523 (1998)
9. C. Schönberger, H. van Houten, and H.C. Donkersloot. *Europhys. Lett.* **20**, 249 (1992)
10. R.P. Andres, T. Bein, M. Dorogi, S. Feng, J.I. Henderson, C.P. Kubiak, W. Mahoney, R.G. Osfichin, and R. Reifenberger. *Science* **272**, 1323 (1996)
11. S. Chen, R.S. Ingramm, M.J. Hostetler, J.J. Pietron, R.W. Murray, T.G. Schaaff, J.T. Khoury, M.M. Alvarez, and R.L. Whetten. *Science* **280**, 2098 (1998)
12. T. Sato and H. Ahmed. *Appl. Phys. Lett.* **70**, 2759 (1997)
13. J. Matsuo, N. Toyoda, and I. Yamada. *J. Vac. Sci. Technol. B* **14**, 3951 (1996)
14. J. Gspann. *Nucl. Instr. and Meth. in Phys. Res. B* **112**, 86 (1996)
15. L.T. Canham. chemical dissolution of wafers. *Appl. Phys. Lett.* **57**, 1046 (1990)
16. L.T. Canham, W.Y. Leong, M.I.J. Beale, T.I. Cox, and L. Taylor. *Appl. Phys. Lett.* **61**, 2563 (1992)
17. P.M.M.C. Bresser, J.W.J. Knapen, E.A. Meulenkamp, and J.J. Kelly. *Appl. Phys. Lett.* **61**, 108 (1992)
18. V. Lehmann and U. Gosele. *Appl. Phys. Lett.* **58**, 856 (1991)
19. A. Nakajima, Y. Sugita Y. Nara, T. Itakura, and N. Nakayama. *Jpn. J. Appl. Phys.* **32**, 415 (1993)
20. V.G. Baru, A.P. Chernushich, V.A. Luzanov, G.V. Stepanov, L.Y. Zakharov, K.P. O'Donnell, I.V. Bradley, and N.N. Melnik. *Appl. Phys. Lett.* **69**, 4148 (1996)
21. M.S. Brandt, H.D. Fuchs, M. Stutzmann, J. Weber, and M. Cardona. *Solid State Commun.* **81**, 307 (1992)
22. J.C. Tsang, M.A. Tischler, and R.T. Collins. *Appl. Phys. Lett.* **60**, 2279 (1992)
23. J.M. Lavine, S.P. Sawan, Y.T. Shieh, and A.J. Bellezza. *Si. Appl. Phys. Lett.* **62**, 1099 (1993)
24. B. Hamilton. *Semicond. Sci. Technol.* **10**, 1187 (1995)
25. J.P. Proot, C. Delerue, and G. Allan. *Appl. Phys. Lett.* **61**, 1948 (1992)
26. C. Delerue, G. Allan, and M. Lannoo. *Phys. Rev. B* **48**, 11024 (1993)
27. L.W. Wang and A. Zunger. *J. Phys. Chem.* **98**, 2158 (1994)
28. B. Delley, for Katrin, E.F. Steigmeier. *Phys. Lett.* **67**, 2370 (1995)
29. M. Hirao, T. Uda, and Y. Murayama. *Mater. Res. Soc. Symp. Proc.* **283**, 425 (1993)
30. C. Delerue, M. Lannoo, and G. Allan. *Properties of Porous silicon*, Chap. 7. INSPEC, The Institute of Electrical Engineers (1997)
31. H. Yorikawa, H. Uchida, and Muramatsu. *J. Appl. Phys.* **79**, 3619 (1996)
32. A.G. Nassiopoulos, S. Grigoropoulos, and D. Papadimitrou. *Appl. Phys. Lett.* **69**, 2267 (1996)
33. P. Rai-Choudhury. *Handbook of Microlithography, Micromachining, and Microfabrication, Vol. 1: Microlithography*. SPIE Optical Engineering Press (1997)
34. W.M Moreau. *Semiconductor Lithography: Principles, practices, and materials*. Plenum Press (1988)
35. G.W. Jones, S.K. Jones, M.D. Walters, and B.W. Dudley. *IEEE Trans. Electr. Dev.* **36**, 2686 (1989)
36. G. Hashiguchi and H. Mimura. *Jpn. J. Appl. Phys.* **33**, 1649 (1994)
37. H. Jansen, H. Gradeniers, M. de Boer, M. Elwenspoek, and J. Fluitman. *J. Micromech. Microeng.* **6**, 14 (1996)

38. Russ. A. Morgan. *Plasma Technology 1, Plasma etching in semiconductor fabrication*. Elsevier (1985)
39. K. Suzuki and N. Itabashi. *Appl. Chem.* **68**, 1011 (1996)
40. K. Tsujimoto, S. Okudaira, and S. Tachi. *Jpn. J. Appl. Phys.* **30**, 3319 (1991)
41. P. Rai-Choudhury. *Handbook of Microlithography, Micromachining, and Microfabrication, Vol. 2: Micromachining and Microfabrication*. SPIE Optical Engineering Press (1997)
42. G.M. Francis, I.M. Goldby, L. Kuipers, B.v. Issendorff, and R.E. Palmer. *J. Chem. Soc., Dalton Trans.*, p. 665 (1996)
43. K. Seeger and R.E. Palmer. *Appl. Phys. Lett.* **74**, 1627 (1999)
44. J.H. Je, T.S. Kang, and D.Y. Noh. *J. Appl. Phys.* **81**, 6716 (1997)
45. H.V. Nguyen, I. An, and R.W. Collins. *Phys. Rev. B* **47**, 3947 (1993)
46. Y. Taga, and R. Takahasi. *Surf. Sci.* **386**, 231 (1997)
47. W.A. de Heer. *Rev. Mod. Phys.* **65**, 611 (1993)
48. I.M. Goldby, B. v. Issendorff, L. Kuipers, and R.E. Palmer. *Rev. Sci. Instrum.* **68**, 3327 (1997)
49. S.J. Carroll, P. Weibel, B. v. Issendorff, L. Kuipers, and R.E. Palmer. *J. Phys.: Condens. Matter* **8**, 617 (1996)
50. S.J. Carroll, S. Pratontep, M. Streun, R.E. Palmer, S. Hobday, and R. Smith. unpublished
51. R.L. Whetten, J.T. Khoury, M.M. Alvarez, S. Murthy, I. Vazmar, Z.L. Wang, P.W. Stephens, C.L. Cleveland, W.D. Luedtke, and U. Landman. *Adv. Mater.* **8**, 428 (1996)
52. Z.L. Wang. *Adv. Mater.* **10**, 13 (1998)
53. P.C. Ohara, J.R. Heath, and W.M. Gelbart. *Angew. Chem. Int. Ed. Engl.* **36**, 1078 (1997)
54. T. Vossmeier, E. DeIonno, and J.R. Heath. *Angew. Chem. Int. Ed. Engl.* **36**, 1080 (1997)
55. P.J. Durston, R.E. Palmer, and J.P. Wilcoxon. *Appl. Phys. Lett.* **72**, 176 (1998)
56. B. Bretzger, Th. Schulze, U. Drodofsky, J. Stuhler, S. Nowak, T. Pfau, and J. Mlynek. *J. Vac. Sci. Technol. B* **15**, 2905 (1997)
57. H.W. Deckman and J.H. Dunsmuir. *Appl. Phys. Lett.* **41**, 377 (1982)
58. J. Boneberg, F. Burmeister, C. Schäfle, P. Leiderer, D. Reim, A. Fery, and S. Herminghaus. *Langmuir* **13**, 7080 (1997)
59. H.W. Deckman, J.H. Dunsmuir, and B. Abeles. *J. Vac. Sci. Technol. A* **3**, 950 (1985)
60. F. Burmeister, C. Schäfle, B. Keilhofer, C. Bechinger, J. Boneberg, and P. Leiderer. *Adv. Mater.* **10**, 495 (1998)
61. J.C. Hulteen and R.P. van Duyne. *J. Vac. Sci. Technol. A* **103**, 1553 (1995)
62. F. Burmeister, C. Schäfle, T. Matthes, M. Böhmisch, J. Boneberg, and P. Leiderer. *Langmuir* **13**, 2983 (1997)
63. T. Tada, T. Kanayama, K. Koga, P. Weibel, S.J. Carroll, K. Seeger, and R.E. Palmer. *J. Phys. D* **31**, 21 (1998)
64. K. Seeger, S.J. Carroll, R.E. Palmer, T. Tada, and T. Kanayama. In *Inst. Phys. Conf. Ser. No 153* (1997)
65. T. Tada, T. Kanayama, P. Weibel, S.J. Carroll, K. Seeger, and R.E. Palmer. *Microelectr. Eng.* **35**, 293 (1997)
66. T. Tada, T. Kanayama, K. Koga, K. Seeger, S.J. Carroll, P. Weibel, and R.E. Palmer. *Microelectr. Eng.* **42**, 539 (1998)

67. P.A. Lewis, H. Ahmed, and T. Sato. *J. Vac. Sci. Technol. B* **16**, 2938 (1998)
68. T. Tada and T. Kanayama. *J. Vac. Sc. Technol. B* **16**, 3934 (1998)
69. K. Seeger and R.E. Palmer. To be published

Index

- absorption frequency, 261
- acetylene, 251, 258
- activation volume, 232
- adatom diffusion, 70
- adiabatic approximation, 58
- adiabatic expansion, 13
- adsorbate, 37, 88
- adsorbate-surface interaction, 62
- Ag, 21, 26, 58, 73, 79, 92, 107, 116, 119, 122, 126, 129, 135, 155, 165, 168, 185, 199, 249, 254, 284, 289, 295
- Ag(110), 53, 55
- Ag(111), 78, 118
- aggregates, 256
- aggregation, 75
- Al, 74, 129, 133, 139, 180, 181, 185, 189–193, 196, 199, 201, 244
- Al₂O₃, 257
- Al(111), 74
- alkali metals, 41
- Andreev reflection, 188, 189
- angle-resolved photoemission, 41
- anion photoelectron spectroscopy, 16
- anisotropic substrates, 86
- anisotropy
 - energy, 212, 216, 226
 - field, 218, 219, 230
- antibonding, 264
- antiferromagnetism, 24
- apparent gap, 165, 166
- Ar, 110, 123
- arrays of pillars, 297
- Arrhenius plot, 72, 93
- ARUPS, 41
- atomic chain, 86, 88, 186, 200, 201
- atomic force microscope (AFM), 97
- atomic-size contact, 175, 179
- attachment, 79
- attractive point defects, 97
- Au, 1, 21, 79, 131, 138, 153, 179, 181–184, 191, 193, 195, 196, 198, 199, 201, 243, 247, 251, 266, 277, 295
- Au(001), 159
- Au(110), 53
- Au(111), 74, 90
- avoided level crossing, 227, 228
- backdonation, 264
- BaFeO, 220, 233
- ballistic
 - deposition, 112
 - point contact, 176
- band gap, 50, 55
- band gap engineering, 269
- beam depletion spectroscopy, 20
- benzene, 258
- Berry phase, 233
- Bi, 123
- bimetallic, 269
- blocking temperature, 30
- bonding, 37
- break junction, 192
- Brillouin function, 221
- buffer layer, 122
- buried cluster, 129
- C, 124, 132
- C₂H₂, 258
- C₆₀, 52, 53, 56, 111, 124, 138
- cage effect, 126
- Car–Parinello, 10
- catalysts, 239
- catalytic
 - activity, 258
 - behaviour, 264
 - oxidation, 239, 263

- processes, 265
- properties, 247, 249
- reactivity, 267
- CCl₄, 137
- chain of atoms, 186, 200, 201
- charge
 - exchange dynamics, 138
 - transfer, 41, 46, 123
 - transport, 159, 160
- chemical developing technique, 130
- chemical sensors, 239, 269
- chemisorption, 37, 244
- clearing-the-way effect, 129
- closed shell clusters, 6
- cluster
 - abundance spectrum, 175, 184
 - array, 92, 95, 287
 - beam, 26
 - binding energy, 72
 - growth, 283
 - impact, 132
 - impact chemistry, 113, 134
 - polarisability, 19
 - reactivity, 242
 - shape, 90
 - size distribution, 74, 94
 - source, 12, 114, 285
 - stability, 237
- cluster impact lithography, 278
- cluster–surface collisions, 116
- cluster–surface interaction, 58, 152, 155, 268
- clusters
 - passivated clusters, 286
 - as etchant, 278
- CO, 82, 241, 243, 251, 261
- Co, 28, 81, 220, 231
- CO₂, 136, 251, 261
- coalescence, 72, 120, 267
- coarsening, 86
- cohesive energy, 111, 114, 116
- collective
 - diffusion coefficient, 70
 - electron excitation, 21, 158
 - motion, 129
 - spin, 226, 233
- collision cascade, 132, 138
- colloidal gold, 1
- colloidal polymer particles, 288
- commensurate phase, 38
- compact clusters, 81
- compression, 110
- conductance
 - channel, 177, 187, 191
 - fluctuations, 175, 196, 199, 200, 205
 - histogram, 183, 197, 200, 201, 206
 - mode, 177, 187, 191
 - quantisation, 165, 175, 177, 181
 - quantum, 175, 177, 203
- conductivity, 158, 164
- confined nucleation, 94
- confinement, 154, 165
- confining potential, 164
- contact potential, 152
- Cooper pair, 188
- coordination, 77, 156, 263
- corner diffusion, 77
- correlated motion, 140
- Coulomb
 - barrier, 159
 - blockade, 214, 276
 - staircase, 159
- covalent, 37, 41
- Cr, 29, 288
- crater formation, 113
- critical ensemble, 258
- crossover temperature, 229, 230, 232
- crystalline facets, 259
- Cs, 43
- CsI, 138
- Cu, 76, 88, 108, 118, 129, 133, 185, 199, 295
- Cu (13 × 13), 95
- Cu(100), 108, 133
- Cu(111), 118
- cubo-octahedral, 264
- Curie temperature, 29
- Curie behaviour, 221
- current-voltage characteristic, 188, 191
- cyclisation, 258
- cyclotrimerisation, 251, 258
- de Broglie wavelength, 165
- decarbonylation, 255
- dendrites, 77
- density functional theory (DFT), 259, 264

- desorption, 259
- diamagnetism, 4
- dielectric function, 1
- diffusion, 76, 120, 160, 165
 - anisotropy, 86, 90
 - barriers, 74
 - in the presence of defects, 88
 - limited aggregation, 75
 - prefactor, 74
- dimer bond energy, 86
- dipole
 - coupling, 253
 - moment, 19
 - sum rule, 21
- dislocation network, 90
- dissociation, 264
- domain wall, 39
- domain wall width, 211, 212, 226
- double-layer model, 46
- drop deposition, 288
- Drude, 1

- edge diffusion, 79, 80
- EELS, 46, 59
- effective anisotropy, 216, 218
- elastic channels, 160
- electrocatalytic, 250
- electron
 - affinity, 17
 - capture, 137
 - confinement, 23, 166
 - emission, 136
 - holography, 213
 - scattering, 163
- electron beam lithography, 280
- electron cyclotron resonance (ECR)
 - etching, 281
- electron energy loss spectroscopy, 46, 59
- electronic
 - contrast, 40
 - level structure, 151
 - periodic table, 237
 - pressure, 8
 - response, 10
 - shells, 168
 - spin susceptibility, 6
 - structure, 3, 6, 9, 16, 154, 158, 166, 237, 263
- ellipsoidal clusters, 9
- embedded atom method (EAM), 263
- energetic cluster impact, 107, 132
- energetic deposition, 107, 122
- energy
 - gap, 3
 - level spacing, 4, 5
 - level spectrum, 227
- ensemble effect, 259
- epitaxial growth, 133
- ErAs, 231
- etch masks, 289, 295
- evaporation, 20
- exchange length, 211, 226
- extended X-ray absorption fine structure (EXAFS), 250

- Fano, 163, 164
- Fe, 28, 81, 95, 159, 213, 227
- Fe₂O₃, 213
- femtosecond spectroscopy, 120
- femtosecond timescale, 58
- Fermi
 - momentum, 11
 - velocity, 3
 - wavelength, 11
- Fermi level
 - crossing, 48
 - onset, 58
- ferromagnetic clusters, 32
- ferromagnetism, 24
- final state, 55, 58, 154
- Fokker–Planck equation, 221
- force fluctuations, 203
- Fourier transform infrared (FTIR), 252
- fractal dimension, 79, 80
- fragmentation, 113, 120, 122, 124, 125, 264
- free electron lasers, 157
- frontier orbitals, 264
- fullerene, 52
- functionalised support materials, 269

- GaAs(110), 159
- gas aggregation, 13, 115, 286
- Gd, 31
- geometric periodic table, 239
- geometrical shell structure, 14
- giant spin model, 227

- Gilbert equation, 221
 gold colloids, 286
 gold nanocrystals, 287
 graphite, 38, 58
 growth, 67

 H_2O , 137
 Hall probe magnetometry, 214
 hard landing, 122
 Hausdorff dimension, 76
 heating cycle, 265
 herringbone pattern, 91
 heterogeneous
 – catalysis, 265
 – nucleation, 97
 hexairidium, 250
 high energy deposition, 275
 HOMO, 52, 241, 264
 HOMO–LUMO, 57, 166
 homoepitaxy, 82
 HOPG, 59, 111, 138, 160, 161
 Hund's rules, 24
 hydrogenation, 255

 icosahedral, 264
 image-charge screening, 55
 impact induced erosion, 135
 implantation, 113, 118, 120, 122, 128
 incommensurate phase, 38
 inelastic channels, 160
 infrared spectroscopy, 267
 initial-state, 55, 58
 interlayer diffusion, 71
 inverse photoemission, 41, 42, 158, 160
 ion beam, 250
 ionic, 37, 41
 ionisation potential, 15, 241
 ionised cluster beam deposition, 132
 IPES, 41
 Ir, 86, 255
 $\text{Ir}_4(\text{CO})_{12}$, 255
 irreversible growth, 71
 islands, 122
 isotopic exchange, 253

 Jahn–Teller effect, 8, 206
 jellium, 7, 153, 160, 237
 jellium model, 10
 Josephson junction, 214

 K, 16, 18, 19, 43, 48, 166, 183, 185, 203
 kinetic
 – effects, 245
 – emission, 137
 – Monte-Carlo, 77, 80, 88
 – roughening, 71
 Kohn–Sham eigenvalues, 153
 Kr, 123

 Landau damping, 3
 Langevin function, 27, 31, 221
 laser light, 158
 laser vapourisation source, 13, 115, 250
 latent image, 249, 254
 lateral interactions, 74
 lateral sputtering effect, 132
 LDA, 10
 Levine's chain model, 46
 Li, 44, 50, 185, 203
 light emission, 160
 liquid clusters, 11
 lithium, 44, 50
 local density approach, 18, 263
 local temperature, 108
 Lorentz microscopy, 213
 low energy deposition, 276
 low-dimensional systems, 58
 low-temperature catalytic combustion, 247
 low-temperature oxidation, 247
 LUMO, 52, 241

 Mackay icosahedra, 15, 239
 macroscopic quantum tunnelling, 215, 226
 magic number, 6, 19, 176, 184, 204, 237
 magnetic
 – alloys, 33
 – deflection, 26
 – domain, 214, 232
 – force microscopy, 213
 – linear dichroism, 214
 – magic numbers, 32
 – molecular clusters, 226
 – moment, 27–29
 – particles, 24
 – quantum tunnelling, 228
 – susceptibilities, 5

- magnetisation, 27, 206
- magnetisation reversal, 218
- magnetism, 24, 211, 224
- magnetocrystalline anisotropy, 216, 219, 220
- magneto-resistance, 214
- majority spin band, 29
- mass
 - selection, 250
 - spectra, 6, 15, 237
 - spectrometer, 12
- matrix isolation spectroscopy, 119, 122
- MCB, 175, 178
- mean free path, 199
- mean-field nucleation theory, 72, 97
- mechanically controllable break junction, 175, 178
- melting, 11, 114
- mesoscopic
 - conductor, 196
 - physics, 225
- metal oxides, 247
- metallic, 37, 269
- metallic droplets, 6
- metallisation, 41, 46, 49
- Mg(OH)₂, 266
- MgO, 251
- MgO(100), 96, 246, 261
- micromechanical sensors, 269
- Mie, 1, 20, 21
- migration, 267
- minority spin band, 29
- Mn, 213, 227
- model catalysts, 243, 259
- molecular
 - beams, 5
 - clusters, 257
 - dynamics MD, 10, 45, 108, 112, 116, 122, 123, 133, 201, 206
 - effects, 138
- molecular beam epitaxy (MBE), 67, 68, 75
- momentum and spatial compression, 115
- monodispersed, 249
- monolayer-protected metal clusters (MPCs), 250
- morphology, 245
- MoS₂, 98
- Mullins-Sekerka instability, 76
- multichannel contact, 195
- multiple particle tunnelling, 188, 189
- Néel–Brown model, 221, 222, 224, 225, 232, 233
- Na, 16, 19, 21, 44, 50, 153, 167, 183, 199, 203, 237
- NaCl, 110
- nano-
 - materials, 239
 - particle, 211, 214, 215, 218, 220, 224–226, 228, 231–233
 - pits, 58
 - science, 239
 - technology, 239, 275
 - wires, 176
- Nb, 185, 186, 188, 191, 193, 199, 241
- Nb–AlO_x–Nb trilayer, 214
- Ni, 28, 91, 232, 249, 252
- Ni(100), 76
- NiAl(110), 243
- noble gas matrix, 3
- nucleation, 67, 72, 74
- O₂, 135, 251
- ohmic damping, 231
- open shell clusters, 8
- optical
 - absorption, 119, 125
 - response, 21
 - spectra, 125
 - spectroscopy, 99
- ordered overlayer, 38
- organic ligands, 250
- organometallics, 250
- Ostwald ripening, 84, 94
- oxidation, 135, 261
- oxide
 - powder, 250
 - surfaces, 95, 243
- PACIS, 13, 115, 160
- paramagnetism, 4
- parity effect, 228
- partial oxidation, 247
- passivated gold clusters, 277
- Pauli exclusion principle, 24
- Pb, 154, 185, 191–193

- Pd, 96, 97, 155, 243, 247, 251, 258
 Pd(100), 108, 116
 Pd(110), 88
 Pd(111), 258
 penetration depth, 130
 percolation, 72
 Periodic Table, 237
 periodicities, 237
 PES, 163, 167
 phase transition, 15, 30
 phase-space compressor, 250
 photo-
 - catalytic, 269
 - emission, 42
 - fragmentation, 156
 - hole, 59
 - lithography, 280
 - luminescence, 279
 photoelectron spectroscopy, 18, 153
 photographic image, 254
 photon
 - emission, 136
 - map, 168
 physisorption, 37
 pit, 130
 plasma etching, 281
 plasmon, 59, 99, 160, 170
 point contact, 175, 176
 porous silicon, 279
 post-nucleation, 85
 potential emission, 137
 predissociation, 253
 proximity induced superconductivity,
 192
 Pt, 139, 155, 161, 180, 181, 243, 251,
 261
 Pt(111), 73, 92, 95, 107, 122, 136, 263
 Pulsed Arc Cluster Ion Source (PACIS),
 160

 quadrupole mass filter, 14, 251
 quantisation, 165, 203
 quantum
 - channel, 175
 - confinement, 279
 - dot, 168
 - force, 182, 203
 - force fluctuations, 203
 - mode, 175
 - size effect, 249
 - tunnelling, 213, 218, 225-230, 232,
 233
 - wire, 175

 radiation damage, 113, 114, 128, 157
 Raman spectroscopy, 118, 255
 rare earth metals, 31
 rare gas monolayer, 38
 Rb, 50
 reaction kinetics, 249
 reactive ion etching (RIE), 281
 reactivity, 237, 263
 reconstruction, 37
 red shift, 23
 reflection, 113
 rehybridisation, 258
 relaxation energy, 57, 58
 restructuring, 269
 Rh, 32, 243, 244
 row-by-row growth, 86
 RPA, 10
 rubidium, 50

 saturation
 - coverage, 46
 - limits, 253
 - of channel transmission, 200, 201,
 205
 Sb, 123
 scanning tunnelling
 - microscopy (STM), 158, 178, 248
 - spectroscopy (STS), 158, 249
 scattering, 123
 secondary ion emission, 136
 seeded cluster beams, 13
 self organisation, 165
 self-assembled polymer balls, 296
 self-organized growth, 94
 shallow implantation, 107
 shape
 - anisotropy, 31, 216, 218, 220
 - transition, 79
 shattering, 124
 shell
 - correction, 10
 - model, 6, 10
 - structure, 167, 176, 203, 237, 264,
 268

- shock wave, 110
- shot noise, 175, 194, 200, 205
- Si, 41, 118, 125, 132, 135, 159, 278
- Si(100), 46, 48, 53, 56
- Si(111), 43, 156
- silicon
 - cones, 289, 290
 - pillars, 289, 292
- silver bromide, 254
- silver clusters, 58, 254
- single crystal surfaces, 245
- single domain particles, 25, 213
- single electron devices, 276
- SiO₂, 153
- SiO_x, 134
- site selective exchange, 92
- size effects, 3, 239, 242
- smoothing, 133
- sodium, 44, 50
- soft landing, 112, 115, 116, 118, 120, 251
- spillout, 16, 19
- spin
 - dynamics, 32
 - operator, 227, 228
 - relaxation, 26, 31
- spin-dependent tunnelling, 214
- SPM lithography, 280
- sputter deposition, 285
- sputtering, 107, 113–115, 131, 250
- SQUID, 214
- stable nucleus, 70
- step and kink density, 239
- step bunching, 53
- step edge barrier, 71
- Stern–Gerlach, 26
- sticking coefficient, 86
- STIPE, 160, 162, 170
- STM, 38, 53, 75, 120, 178
- stochastic fluctuations, 224
- Stoner model, 29
- Stoner–Wohlfarth model, 215, 217–221
- STS, 158, 159, 162–164, 166
- subgap structure, 187, 200, 205
- sudden approximation, 58
- super-shell, 11
- super-exchange, 32
- superconducting
 - contact, 175, 187, 200, 205
 - energy gap, 188
 - tunneljunction, 188
- superheated cluster, 111
- superparamagnetism, 32, 221
- superstructure, 161
- supported catalysts, 95
- surface
 - anisotropy, 216, 218–220
 - band, 49
 - band gap, 50
 - contamination, 5
 - dislocations, 90
 - intermediate, 258
 - reconstruction, 90
 - roughness, 133
 - state, 41, 47
- switching
 - field, 216, 218, 223, 224
 - rate, 222, 229, 231
- synchrotron, 157
- synthesis, 255
- technological application, 275
- telegraph noise, 223, 231
- temperature programmed reaction (TPR), 251
- tetrairidium, 255
- thermal desorption spectroscopy (TDS), 252
- thermal energy helium scattering, 108
- thermal spike, 132, 138
- thermionic emission, 137
- thermodynamic equilibrium shape, 81
- thermopower, 175, 199, 200
- thin film growth, 67
- thin films, 107
- Ti, 247
- tight binding calculation, 191
- time-of-flight mass spectrometer, 14
- time-of-flight (TOF) PES, 156, 157
- TiO₂(110), 159
- TiO₂, 247
- tip convolution, 98
- toluene, 255
- tracer diffusion coefficient, 70
- transient
 - exchange, 69
 - mobility, 69

- transition metal clusters, 28
- transition state theory, 70, 74
- transmission electron microscope (TEM), 201, 206
- transmission probability, 177, 188, 195
- tunnel splitting, 227
- tunnelling, 163
- tunnelling spectroscopy (STS), 54, 153
- turnover frequency, 245, 247

- ultra-high vacuum, 67
- uniform rotation mode, 218
- UPS, 58

- Va, 138
- valence orbital, 191
- van der Waals
 - clusters, 123
 - interaction, 37

- Vegard's law, 95
- vibrating reed magnetometry, 213
- vibrational coupling, 253

- W, 138
- W(110), 162
- W(110)/C-R(15×3), 162
- waiting time measurements, 222, 224
- wave vector, 42
- weakly incommensurate layers, 90
- weakly interacting supports, 96
- wedge effect, 123
- weird wires, 202
- wetting, 111
- Wulff
 - construction, 81
 - polyhedron, 96

- Xe, 38